

REPORT DOCUMENTATION PAGE

Form Approved
OMB No. 0704-0188

The public reporting burden for this collection of information is estimated to average 1 hour per response, including the time for reviewing instructions, searching existing data sources, gathering and maintaining the data needed, and completing and reviewing the collection of information. Send comments regarding this burden estimate or any other aspect of this collection of information, including suggestions for reducing the burden, to the Department of Defense, Executive Services and Communications Directorate (0704-0188). Respondents should be aware that notwithstanding any other provision of law, no person shall be subject to any penalty for failing to comply with a collection of information if it does not display a currently valid OMB control number.

PLEASE DO NOT RETURN YOUR FORM TO THE ABOVE ORGANIZATION.

1. REPORT DATE (DD-MM-YYYY) 31-08-2010	2. REPORT TYPE Final Technical Report (2 volumes)	3. DATES COVERED (From - To) Jun 2005 - Aug. 2010		
4. TITLE AND SUBTITLE "Basic Research Investigations into Multimode Laser and EM Launchers for Affordable, Rapid Access to Space" (Volumes 1 and 2)		5a. CONTRACT NUMBER FA9550-05-1-0392		
		5b. GRANT NUMBER FA9550-05-1-0392		
		5c. PROGRAM ELEMENT NUMBER		
		5d. PROJECT NUMBER		
		5e. TASK NUMBER		
		5f. WORK UNIT NUMBER		
7. PERFORMING ORGANIZATION NAME(S) AND ADDRESS(ES) Rensselaer Polytechnic Institute Mechanical, Aerospace, and Nuclear Engineering Department 110- Eighth Street, Troy, NY 12180-3590		8. PERFORMING ORGANIZATION REPORT NUMBER RPI-TR-A11602/ TR-A11848		
9. SPONSORING/MONITORING AGENCY NAME(S) AND ADDRESS(ES) Air Force Office of Scientific Research (AFOSR) Arlington, VA 22203		10. SPONSOR/MONITOR'S ACRONYM(S) AFOSR		
		11. SPONSOR/MONITOR'S REPORT NUMBER(S) FA9550-05-1-0392		
12. DISTRIBUTION/AVAILABILITY STATEMENT Unclassified. Distribution Unlimited				
13. SUPPLEMENTARY NOTES None				
14. ABSTRACT This basic research effort on pulsed airbreathing/rocket laser propulsion, investigates the physics of laser energy deposition into stationary and hypersonic working fluids, inclusive of electrical breakdown, ignition of laser-supported detonation waves (LSD), and blast wave propagation over thruster impulse-generating surfaces. The future application of AFOSR interest for this basic research endeavor is the laser launch of nano- and micro-satellites (i.e., 1-100 kg payloads) into Low Earth Orbit (LEO), at low cost and "on-demand." The present dual-pronged, combined experimental/numerical research campaigns centered on both static and hypersonic experiments with representative 2D and 3D laser-thruster geometries, using the Lumonics TEA-622 (~200J, ~100ns) and K922M (20-40J, ~100ns) CO2 lasers. Laser scramjet experiments were performed in the T3 tunnel at the Henry T. Nagamatsu Laboratory of Aerothermodynamics and Hypersonics (HTNLAH). Time-dependent surface pressure distributions were measured over thrust-generating surfaces following laser energy deposition; delivered impulse and momentum coupling coefficients (Cm) were obtained; Schlieren movies of the impulse generation process were recorded with a high-speed Cordin digital camera, to study the laser breakdown/ blast wave expansion process, and evolving flow field structures in both stationary and hypersonic flow. Time-resolved visualizations of inlet and absorption chamber flowfields, enabled qualitative analysis of dominant phenomena impacting laser-propulsion physics.				
15. SUBJECT TERMS Laser propulsion; beamed energy propulsion; advanced propulsion; laser/gas interaction; laser-induced breakdown; laser physics; airbreathing and rocket propulsion; lasers; lightcraft.				
16. SECURITY CLASSIFICATION OF: a. REPORT U b. ABSTRACT U c. THIS PAGE U		17. LIMITATION OF ABSTRACT UU	18. NUMBER OF PAGES 305	19a. NAME OF RESPONSIBLE PERSON Prof. Leik N. Myrabo
				19b. TELEPHONE NUMBER (Include area code) 802-989-2874

– FINAL REPORT –
– PART 1 –

Volume 1: Static and Hypersonic Experimental Analysis of Impulse
Generation in Air-Breathing Laser-Thermal Propulsion

MURI 05 Grant Title: “Basic Research Investigations into Multimode Laser and EM Launchers for Affordable, Rapid Access to Space”

Principal Investigator: Professor Leik N. Myrabo
Rensselaer Polytechnic Institute,
110 8th Street, Troy, NY 12180-3590

Major Contributors: Drs. Israel I. Salvador and David A. Kenoyer

AFOSR Award: FA9550-05-1-0392

Research Period: June 1, 2005 through August 31, 2010 (5 year grant)



Prepared for

Dr. Mitat Birkan

Air Force Office of Scientific Research (AFOSR)
Arlington, VA 22203

31 August 2010

CONTENTS

CONTENTS.....	ii
LIST OF TABLES	v
LIST OF FIGURES.....	vi
ACKNOWLEDGMENTS	Error! Bookmark not defined.
ABSTRACT.....	xiii
1. Introduction	1
1.1 Worldwide State-of-the-Art on Beamed Energy Propulsion	4
1.1.1 United States.....	6
1.1.2 Europe	10
1.1.3 Japan	12
1.1.4 Russia	15
1.1.5 Brazil.....	17
1.1.6 China	18
1.2 Motivation and Objectives.....	18
1.3 Thesis Outline	22
2. Laser Induced Breakdown and Impulse Generation Process.....	24
2.1 Early Stage – Cascade Ionization and Plasma Formation	24
2.1.1 Metal Surface Air-Breakdown	26
2.2 Post-Breakdown Phenomena and Absorption Waves	28
2.3 Analytical Model of Surface Pressure History and Impulse Generation	35
3. Experimental Apparatus and Procedure	40
3.1 Hypersonic Shock Tunnel.....	40
3.2 Lumonics TEA-620 Laser and Beam Propagation	44
3.2.1 Laser Beam Diagnostics and Calibration.....	50
3.3 2-D Cross Section Lightcraft Model	52
3.4 General Instrumentation	56

3.5	Schlieren Visualization Setup	57
3.6	Data Acquisition.....	59
4.	Static Experiments	Error! Bookmark not defined.
4.1	Surface Pressure Distribution	Error! Bookmark not defined.
4.2	Blast Wave Schlieren Visualization	Error! Bookmark not defined.
4.3	Impulse Generation Analysis from Surface Pressure Distribution	Error! Bookmark not defined.
5	Hypersonic Experiments.....	Error! Bookmark not defined.
5.1	Hypersonic Test Conditions.....	Error! Bookmark not defined.
5.2	Hypersonic Campaign Results for 2D Model...	Error! Bookmark not defined.
5.2.1	Runs 1 to 4 – Initial Runs.....	Error! Bookmark not defined.
5.2.2	Runs 5 to 11 – Troubleshooting Runs...	Error! Bookmark not defined.
5.2.3	Runs 12 to 15 – Shroud Removed	Error! Bookmark not defined.
5.2.4	Runs 16 to 19 – Mid-channel Breakdown	Error! Bookmark not defined.
5.2.5	Runs 20 to 24 – Surface Breakdown	Error! Bookmark not defined.
5.3	Discussion of the Results.....	Error! Bookmark not defined.
6	Conclusions and Future Work.....	Error! Bookmark not defined.
6.1	Conclusions.....	Error! Bookmark not defined.
6.1.1	Static Experiments	Error! Bookmark not defined.
6.1.2	Hypersonic Experiments	Error! Bookmark not defined.
6.2	Future Experimental Work	Error! Bookmark not defined.
6.2.1	Phase II Hypersonic Campaign with 2D Model	Error! Bookmark not defined.
6.2.2	2 nd Generation Two-Dimensional Model	Error! Bookmark not defined.
6.2.3	Axi-symmetric Hypersonic Lightcraft Model	Error! Bookmark not defined.
6.2.4	Airbreathing Laser-Electromagnetic Propulsion	Error! Bookmark not defined.

References.....	Error! Bookmark not defined.
Appendix A – Sensors and Calibration	Error! Bookmark not defined.
Appendix B – USA/Brazil BEP Collaboration.....	Error! Bookmark not defined.
Appendix C – Hypersonic Shock Tunnels.....	Error! Bookmark not defined.
C.1 Requirements for Hypersonic Testing.....	Error! Bookmark not defined.
C.2 General Characteristics of a Hypersonic Shock Tunnel	Error! Bookmark not defined.
C.3 Modeling of Shock Tunnel Flow	Error! Bookmark not defined.
C.3.1 Thermodynamic Equilibrium Shock Tube Problem	Error! Bookmark not defined.
C.3.2 Nozzle Flow Expansion	Error! Bookmark not defined.
Appendix D – Dedicated Laboratory Setup for CO ₂ TEA Laser Propulsion Experiments	Error! Bookmark not defined.
D.1 Research Vision and Laboratory Strategy	Error! Bookmark not defined.
D.2 Laboratory Equipment and Facilities	Error! Bookmark not defined.
D.3 Basic Research Program.....	Error! Bookmark not defined.
D.3.1 Current Research	Error! Bookmark not defined.
D.3.2 Future Research	Error! Bookmark not defined.
D.4 Summary.....	Error! Bookmark not defined.

LIST OF TABLES

Table 2.1: Laser-supported absorption wave propagation modes (10.6 μm radiation).....	31
Table 3.1: Basic operating conditions of Lumonics TEA 620 laser (stable resonator mode).	45
Table 3.2: Lumonics TEA-620 laser pulse characteristics with high gain gas mixture. .	46
Table 3.3: Pressure sensor inventory and radial distance from laser focal line at the shroud's undersurface.....	55
Table 4.1: Static (quiescent flow) test run conditions.	Error! Bookmark not defined.
Table 4.2: Sensor longitudinal inclination Θ , and impulse adjustment factor $\sin(\Theta)$	Error! Bookmark not defined.
Table 4.3: Limits of integration for laser-generated impulse calculations.	Error! Bookmark not defined.
Table 4.4: Longitudinal Impulse for sample runs #1, #7, #11 and #12.	Error! Bookmark not defined.
Table 5.1: T3 HST initial conditions and reservoir stagnation conditions achieved during experimental campaign.	Error! Bookmark not defined.
Table 5.2: Free stream conditions obtained during experiments, calculated with STCALC (code assumes chemical and thermodynamic equilibrium).	Error! Bookmark not defined.
Table 5.3: Model centerbody and shroud inclinations, focal line location, and laser pulse energy for all hypersonic runs.	Error! Bookmark not defined.
Table A.1: 2-D Lightcraft sensor models, calibration and ports.	Error! Bookmark not defined.
Table A.2: T3 HST 2-D Lightcraft sensor models, calibration and ports.	Error! Bookmark not defined.
Table B.1: Division of responsibilities between RPI and IEAv-CTA in the present campaign..	Error! Bookmark not defined.
Table D.1: Single K922M laser operating conditions.	Error! Bookmark not defined.

LIST OF FIGURES

Figure 1.1 Future application for BEP: worldwide transportation. Left: LightPort serviced by space-based power-beaming station. Right: Lightcraft vehicle on launch pad. Palm et al. (2009).....	4
Figure 1.2 Type 200 Laser Lightcraft in nighttime WSMR free-flight (right); Type 100 Lightcraft with expanding luminous air-plasma exhaust (left). (<i>Photos by James Shryne III—Courtesy of NASA</i>).....	7
Figure 1.3 Cutaway view of German “bell” engine, with ignition pin. Schall and Eckel (2003).....	11
Figure 1.4 Hypersonic (M=5.0) CFD simulations of a 16 cm diameter Lightcraft flying at 20 km altitude. (Komurasaki et al., 2003).....	14
Figure 1.5 Microwave-powered Lightcraft (Nakagawa et al., 2003).....	14
Figure 1.6 LITA concept, upstream beam operation (Komurasaki, 2002).....	15
Figure 1.7 LITA features in a pusher beam configuration (Sasoh, 2004).....	15
Figure 1.8 The ALSPE concept vehicle (Rezunkov et al., 2005)	16
Figure 1.9 Laser-induced DEAS hypersonic experiments in Brazil. (Salvador, 2008) ...	17
Figure 2.1: Breakdown threshold dependence on incident radiation for Al at 10.6 μ m, and characteristics times for breakdown initiation. Weyl et al. (1980).....	28
Figure 2.2: Absorption wave zones of a laser supported plasma from a metallic surface. (Root, 1989)	30
Figure 2.3: One-dimensional propagating plasma regions following laser absorption waves. (Root, 1989).....	32
Figure 2.4: Absorption regions of the one-dimensional waves. (Root, 1989).....	32
Figure 2.5: Cylindrical blast wave expansion models. Left: vertical oriented axis; Right: horizontal oriented axis (following laser-induced surface breakdown).....	37
Figure 2.6: Surface pressure vs. time evolution, showing characteristic times. (Pirri, 1973)	38
Figure 3.1: T3 Hypersonic Shock Tunnel at the HTN-Laboratory of Aerothermodynamics and Hypersonics.	41
Figure 3.2: Hollow HST sting with IR window and mount installed.	43
Figure 3.3: ‘Petal catcher’ (left), and stainless steel diaphragms (right).....	44

Figure 3.4: TEA 620 Laser configuration with unstable resonator cavity.	47
Figure 3.5: TEA 622 laser system with Faraday cage (left), and beam footprint (right).	48
Figure 3.6: Laser beam transmission path through the laboratory to the test section.	50
Figure 3.7: Beam diagnostics table for analyzing laser beam energy and pulse profile.	50
Figure 3.8: Beam-splitter energy calibration curve for NaCl sting-window.	51
Figure 3.9: Laser pulse profile and integrated pulse energy sampled at NaCl sting-window.....	52
Figure 3.10: Pressure sensor positions within 2D model geometry.....	53
Figure 3.11: 2-D laser propulsion model installed in T3 hypersonic shock tunnel.	54
Figure 3.12: Sensor disposition on shroud undersurface and line focus position used during the static experiments.....	56
Figure 3.13: Schlieren visualization and Cordin camera system setup for T3 test section.	58
Figure 3.14: T3 Hypersonic Shock Tunnel showing Schlieren light path and Cordin 550 camera.	59
Figure 4.1: Regions for impulse-generation analysis: 1) Inlet compression ramp surface (ignored for static runs); 2) Shroud undersurface; and, 3) Primary Optics (rear parabolic mirror surface).....	Error! Bookmark not defined.
Figure 4.2: Run #12—Pressure distribution over compression ramp. ($P_{\infty} = 1$ bar, $E=180\pm20$ J)	Error! Bookmark not defined.
Figure 4.3: Run #12—Pressure distribution over shroud undersurface. ($P_{\infty} = 1$ bar, $E=180\pm20$ J)	Error! Bookmark not defined.
Figure 4.4: Run #12—Pressure distribution over focusing mirror ($P_{\infty} = 1$ bar, $E=180\pm20$ J). Notice the influence of mechanical vibration on the pressure signal.	Error! Bookmark not defined.
Figure 4.5: Run #1—Pressure distribution over shroud undersurface. (P_6-P_9 ; $P_{\infty} = 60$ mbar; $E_P=172\pm17$ J).....	Error! Bookmark not defined.
Figure 4.6: Run #1—Pressure distribution over focusing mirror. (P_{10-13} ; $P_{\infty} = 60$ mbar; $E_P=172\pm17$ J).....	Error! Bookmark not defined.
Figure 4.7: Run#7—Pressure distribution over shroud undersurface. (P_6-P_9 ; $P_{\infty} = 150$ mbar; $E_P=222\pm23$ J).....	Error! Bookmark not defined.

Figure 4.8: Run#7—Pressure distribution over focusing mirror. (P_{10-13} ; $P_{\infty}= 150$ mbar; $E_P=222\pm23$ J).....**Error! Bookmark not defined.**

Figure 4.9: Run#11—Pressure distribution over shroud undersurface. (P_6-P_9 ; $P_{\infty}= 300$ mbar; $E_P=231\pm23$ J).....**Error! Bookmark not defined.**

Figure 4.10: Run #11—Pressure distribution over focusing mirror. (P_{10-P13} ; $P_{\infty}= 300$ mbar; $E_P=231\pm23$ J).....**Error! Bookmark not defined.**

Figure 4.11: Data for blast wave front arrival time vs. Sedov's scaling law.....**Error! Bookmark not defined.**

Figure 4.12: Regions for impulse computation, using pressures measured during static tests.**Error! Bookmark not defined.**

Figure 4.13: Run #1—Peak surface pressure vs. distance from laser line focus. ($P_{\infty}= 60$ mbar; $E_P=172\pm17$ J).....**Error! Bookmark not defined.**

Figure 4.14: Run#7—Peak surface pressure vs. distance from laser focal line. ($P_{\infty}= 150$ mbar; $E_P=222\pm23$ J).....**Error! Bookmark not defined.**

Figure 4.15: Run #11—Peak surface pressure vs. distance from laser focal line. ($P_{\infty}= 300$ mbar; $E_P=231\pm23$ J).....**Error! Bookmark not defined.**

Figure 4.16: Run#12—Peak surface pressure vs. distance from laser focal line. ($P_{\infty}= 1$ bar; $E_P=180\pm20$ J).....**Error! Bookmark not defined.**

Figure 4.17: Run #12- Blast wave evolution with measured surface pressures (top), and corresponding Schlieren image/frame timing (bottom). $P_{\infty}= 1$ bar; $E_P=180\pm20$ J.**Error! Bookmark not defined.**

Figure 4.18: Run #11 - Blast wave evolution with measured surface pressures (top), and corresponding Schlieren image/frame timing (bottom). $P_{\infty}= 300$ mbar; $E_P=231\pm23$ J.....**Error! Bookmark not defined.**

Figure 4.19: Run#7 - Blast wave evolution with measured surface pressures (top), and corresponding Schlieren image/frame timing (bottom). $P_{\infty}= 150$ mbar, $E_P=222\pm23$ J.....**Error! Bookmark not defined.**

Figure 4.20: LSD wave propagation followed by radial expansion; α and β angles are indicated. *Left:* Run #8, $P_{\infty}= 300$ mbar, $E=205\pm21$ J. *Right:* Run #11, $P_{\infty}= 300$ mbar, $E=231\pm23$ J.....**Error! Bookmark not defined.**

Figure 4.21: Laser-induced breakdown with 2D model pitched forward 10-degrees.**Error! Bookmark not defined.**

Figure 4.22: The three zones and respective integration limits considered for the longitudinal impulse calculation.**Error! Bookmark not defined.**

Figure 4.23: Run #1—Peak surface pressure vs. distance from laser line focus. *Top*: Region 1; *Bottom*: Region 3. ($P_{\infty}= 60$ mbar; $E_p=172\pm17$ J)**Error! Bookmark not defined.**

Figure 4.24: Run#7—Peak surface pressure vs. distance from laser focal line. *Top*: Region 1; *Bottom*: Region 3. ($P_{\infty}= 150$ mbar; $E_p=222\pm23$ J)**Error! Bookmark not defined.**

Figure 4.25: Run #11—Peak surface pressure vs. distance from laser focal line. *Top*: Region 1; *Bottom*: Region 3. ($P_{\infty}= 300$ mbar; $E_p=231\pm23$ J)**Error! Bookmark not defined.**

Figure 4.26: Run#12—Peak surface pressure vs. distance from laser focal line. *Top*: Region 1; *Bottom*: Region 3. ($P_{\infty}= 1$ bar; $E_p=180\pm20$ J)**Error! Bookmark not defined.**

Figure 4.27: Momentum coupling coefficient vs. ambient pressure. (Assumes $\Theta_{\text{shroud}}=-34$ deg.)**Error! Bookmark not defined.**

Figure 4.28: C_m variation vs. ambient pressure calculated for finite flat plate by Pirri (1973) and Richard (1989) vs. present experimental data from shroud undersurface (adjusted for shroud inclination).**Error! Bookmark not defined.**

Figure 5.1: Altitude vs. Mach number schedule for optimized airbreathing LP launch to low Earth orbit (Frasier, 1987).**Error! Bookmark not defined.**

Figure 5.2: Reynolds number variation with Mach number along optimized laser launch trajectory by Frazier (1987), together with T3 HST data from present test campaign.**Error! Bookmark not defined.**

Figure 5.3: Run 24—Typical HST and Pitot pressure signals obtained during experiments.**Error! Bookmark not defined.**

Figure 5.4: Run #1-Pressure transducer traces for Ch2-14 (distributed over 2D model); Laser ON, Flow ON; $M=8.61$; $E_p=196\pm20$ J. Channel number corresponds to

pressure sensor. Note simultaneous sensor response to laser-induced blast, indicating excessive mechanical noise.**Error! Bookmark not defined.**

Figure 5.5: Run #2- Pressure transducer traces for Ch2-14 (sensors distributed over 2D model); Laser OFF, flow ON; $M=8.56$; $E_p= 0$ J. The signal stability throughout the time window indicates fully established hypersonic flow over the model.**Error! Bookmark not defined.**

Figure 5.6: Run#0-Pressure transducer traces for Ch2-14 (sensors distributed over 2D model); Laser ON, flow OFF; $M=7.8$; $E_p=180\pm20$ J; $P_\infty = 7.5E-02$ mbar. Note similarity to Run#1 results.**Error! Bookmark not defined.**

Figure 5.7: *Left*: Run #1—Erratic Schlieren image sequence . Note oversaturation of 2nd frame when laser induced breakdown occurred, and missing frames due to EMI. *Right*: Run #2—Schlieren image with laser OFF, revealing flow structure at $M=8.56$**Error! Bookmark not defined.**

Figure 5.8: *Left*: Diaphragm engraving geometry. *Right*: Burst diaphragm.**Error! Bookmark not defined.**

Figure 5.9: Run 10-Schlieren image with only the laser-induced air-breakdown glow visible. ($M=8.77$, $T_\infty=68.7$ K, $P_\infty=0.15$ kPa).....**Error! Bookmark not defined.**

Figure 5.10: Run 10-Pressure gage traces for P6, P7,P9 distributed over shroud undersurface; laser ON, flow ON; Mach 8.77; $E_p=207$ J. Sensor P9 pressure jump is from passage of blast wave.....**Error! Bookmark not defined.**

Figure 5.11: Run #13-Laser induced blast wave interaction with oblique shock. ($M=5.95$, $T_\infty=263.7$ K, $P_\infty=5.62$ kPa, $E_p=196\pm20$ J).....**Error! Bookmark not defined.**

Figure 5.12: Run#15-Laser induced blast wave interaction with oblique bow shock; -4° model pitch. The smearing of the focus is noticeable on the air-breakdown geometry. ($M=5.95$, $T_\infty=262.3$ K, $P_\infty=5.16$ kPa, $E_p=176\pm18$ J)**Error! Bookmark not defined.**

Figure 5.13: Run#16 - Laser induced blast wave interaction with oblique shocks from shroud and inlet center-body at 7.5° inclination. ($M=5.96$; $T_\infty=258.3$ K; $P_\infty=5.32$ kPa; $E_p=187\pm19$ J)**Error! Bookmark not defined.**

Figure 5.14: Run#16 - Measured pressure distribution over shroud under-surface; traces offset. Schlieren frames from Figure 5.13 are marked by diamonds.Error!
Bookmark not defined.

Figure 5.15: Run#17 - Laser induced blast wave interaction with oblique shocks and shroud under-surface; 2D model at -7.5° ; Shroud at -4° inclination. ($M=5.94$, $T_\infty=256.8$ K, $P_\infty=6.25$ kPa, $E_p=186\pm19$ J)Error! **Bookmark not defined.**

Figure 5.16: Run#17 - Long exposure color photograph of laser-induced breakdown geometry at Mach 5.96; 2D model at -7.5° ; Shroud at -4° inclination.Error!
Bookmark not defined.

Figure 5.17 Run#17 - Measured pressure distribution across shroud under-surface. Traces offset. Schlieren frames from Figure 5.15 are marked for with diamonds.Error! **Bookmark not defined.**

Figure 5.18: Run#18 - Laser induced blast wave interaction with oblique shocks and shroud under-surface. Both center body and shroud at -7.5° inclination. ($M=5.94$; $T_\infty=284.4$ K; $P_\infty=4.88$ kPa; $E_p=121\pm12$ J)Error! **Bookmark not defined.**

Figure 5.19: Run#18 - Measured pressure distribution across shroud under-surface. Traces offset. Schlieren frames from Figure 5.18 are marked for with diamonds.Error! **Bookmark not defined.**

Figure 5.20: Run#19 - Measured pressure distribution across shroud under-surface; traces offset. Photon-drag detector signal provides timing for laser pulse delivery.Error! **Bookmark not defined.**

Figure 5.21: Run#20 - Extended duration pressure distribution over 2-D model, also showing transients before full flow establishment. Shroud sensors offset for clarification. ($M=8.6$; $T_\infty=128.8$ K; $P_\infty=0.566$ kPa; $E_p=189\pm20$ J) **Error! Bookmark not defined.**

Figure 5.22: Run#20 - Pressure distribution over shroud under-surface showing P6, P7, P9 signals, masked by mechanical noise. Photon drag detector signal gives laser pulse timing (*bottom trace*). Pressure traces offset. **Error! Bookmark not defined.**

Figure 5.23: Run#21 - Laser induced blast wave interaction with oblique inlet shocks and shroud under-surface. Model and shroud at -7.5° inclination. ($M=9.44$, $T_\infty=108$ K, $P_\infty=0.301$ kPa, $E_p=196\pm20$ J)Error! **Bookmark not defined.**

Figure 5.24: Run#21 - Long exposure photograph of bifurcated air-breakdown geometry across inlet gap, and secondary breakdown on shroud undersurface.**Error!**

Bookmark not defined.

Figure 5.25: Run#21 - Measured pressure distribution across shroud undersurface; traces offset. Schlieren frames from Figure 5.23 are marked with diamonds.**Error!**

Bookmark not defined.

Figure 5.26: Run#23 - Laser induced blast wave interaction with oblique shocks and shroud under-surface. Model at -7.5° and shroud at -24° inclination. ($M=9.43$, $T_\infty=113.7$ K, $P_\infty=0.293$ kPa, $E_p=106\pm11$ J).....**Error!** **Bookmark not defined.**

Figure 5.27: Run#23 - Measured pressure distribution at shroud under-surface; traces offset. Schlieren frames from Figure 5.26 are marked for clarification.**Error!**

Bookmark not defined.

Figure 5.29: Peak pressures (ΔP) measured across shroud under-surface, measured from its leading edge. (Runs 16 through 19).....**Error!** **Bookmark not defined.**

Figure 6.1: Complete 2D model with full external compression inlet for Phase 2 tests.**Error!** **Bookmark not defined.**

Figure 6.2: Features to be added in 2nd generation 2D hypersonic models.**Error!**

Bookmark not defined.

Figure 6.3: Axi-symmetric Lightcraft model ready for hypersonic tests in the T3 tunnel.**Error!** **Bookmark not defined.**

Figure 6.4: Pulsed power supply and 2.0 T magnet system.**Error!** **Bookmark not defined.**

Figure B.1: Logo for the collaborative effort set between RPI and HTN-LAH under sponsorship of the AFOSR.....**Error!** **Bookmark not defined.**

Figure C.1: Shock tunnel operation diagram.**Error!** **Bookmark not defined.**

Figure C.2: Reflected and transmitted shock after contact surface interaction, encountered in the reflected mode of operation ($U_2=0$).**Error!** **Bookmark not defined.**

Figure D.3: Twin Lumonics TEA-922Ms and Schlieren setup in the laboratory....**Error!**

Bookmark not defined.

Figure D.4: Panoramic view of the Laser Propulsion Laboratory.**Error! Bookmark not defined.**

Figure D.5: Schlieren montage of Lightcraft model #200 with beam centered, taken at 120,000 fps.....**Error! Bookmark not defined.**

Figure D.6: Schlieren montage of Lightcraft model #200 with beam offset of 20 mm, taken at 50,000 fps.....**Error! Bookmark not defined.**

Figure D.7: Integrated setup in the present 7.9 m x 5.2 m available laboratory space with altitude supersonic flow facility.**Error! Bookmark not defined.**

ABSTRACT

The present research campaign centered on static and hypersonic experiments performed with a two-dimensional, repetitively-pulsed (RP) laser Lightcraft model. The future application of interest for this basic research endeavor is the laser launch of nano- and micro-satellites (i.e., 1-100 kg payloads) into Low Earth Orbit (LEO), at low-cost and “on-demand.” This research began with an international collaboration on Beamed Energy Propulsion between the United States Air Force and Brazilian Air Force to conduct experiments at the Henry T. Nagamatsu Laboratory of Aerothermodynamics and Hypersonics (HTN-LAH). The laser propulsion (LP) experiments employed the T3 Hypersonic Shock Tunnel (HST), integrated with twin gigawatt pulsed Lumonics 620-TEA CO₂ lasers to produce the required test conditions.

Following an introduction of the pulsed laser thermal propulsion concept and a state-of-the-art review of the topic, the principal physical processes are outlined starting from the onset of the laser pulse and subsequent laser-induced air-breakdown, to the expansion and exhaust of the resulting blast wave.

After installation of the 254 mm wide, 2D Lightcraft model into the T3 tunnel, static LP tests were performed under quiescent (no-flow) conditions at ambient pressures of 0.06, 0.15, 0.3 and 1 bar, using the T3 test-section/dump-tank as a vacuum chamber. Time-dependent surface pressure distributions were measured over the engine thrust-generating surfaces following laser energy deposition; the delivered impulse and momentum coupling coefficients (C_m) were calculated from that pressure data. A Schlieren visualization system (using a high-speed Cordin digital camera) captured the laser breakdown and blast wave expansion process. The 2D model’s C_m performance of 600 to 3000 N/MW was 2.5-5x higher than theoretical projections available in the literature, but indeed in the realm of feasibility for static conditions. Also, these C_m values exceed that for smaller Lightcraft models (98 to 161 mm in diameter), probably due to the more efficient delivery of laser-induced blast wave energy across the 2D model’s larger impulse surface area.

Next, the hypersonic campaign was carried out, subjecting the 2D model to nominal Mach numbers ranging from 6 to 10. Again, time-dependent surface pressure distributions were recorded together with Schlieren movies of the flow field structure

resulting from laser energy deposition. These visualizations of inlet and absorption chamber flowfields, enabled the qualitative analysis of important phenomena impacting laser-propelled hypersonic airbreathing flight. The laser-induced breakdown took an elongated vertically-oriented geometry, occurring off-surface and across the inlet's mid-channel—quite different from the static case in which the energy was deposited very near the shroud under-surface. The shroud under-surface pressure data indicated laser-induced increases of 0.7- 0.9 bar with laser pulse energies of \sim 170 J, off-shroud induced breakdown condition, and Mach number of 7.

The results of this research corroborate the feasibility of laser powered, airbreathing flight with infinite specific impulse ($I_{sp}=\infty$): i.e., without the need for propellant injection at the laser focus. Additionally, it is shown that further reductions in inlet air working fluid velocity—with attendant increases in static pressure and density—is necessary to generate higher absorption chamber pressure and engine impulse.

Finally, building on lessons learned from the present work, the future research plan is laid out for: a) the present 2D model with full inlet forebody, exploring higher laser pulse energies and multi-pulse phenomena; b) a smaller, redesigned 2D model; c) a 254 mm diameter axisymmetric Lightcraft model; and, d) a laser-electromagnetic accelerator model, designed around a 2-Tesla pulsed electromagnet contracted under the present program.

1. Introduction

Chemical rocket engines have been *THE* space launch “workhorse” technology ever since the dawn of the *Space Age* on October 4, 1957, when the former Soviet Union successfully launched Sputnik I. Now, a decade into the 21st century, it still remains the only propulsion technology available for Earth-to-Orbit (ETO) transport, with alternatives largely confined to paper studies, small lab experiments, academic exercises, and science fiction dreams. But why chemical rockets, and what makes *space access* so difficult?

As intriguing as it is, chemical rocket propulsion technology faces inherent problems that cannot be solved or mitigated. Take for example: 1) propellant explosion hazards—proven catastrophic on far-too-many occasions; 2) small propellant energy densities—i.e., the thermal energy released per unit mass of fuel; and, 3) performance is limited by physics—already “pressed up against the wall.” In short, such rocket physics is driven by thermochemistry and available chemical propellants, since ALL the energy required for the boost to orbit must be carried onboard. Even with the most energetic propellants we have—*i.e., the H₂/O₂ reactive mix @ 20 MJ/kg (at stoichiometric ratio)*—chemical rocket launchers need propellant mass fractions of 0.90 (and higher) to reach low earth orbit. No technological breakthrough can change this picture dramatically, since modern 21st century chemical rockets already operate at efficiencies so high that *substantial* improvements are deemed physically unattainable.

Propulsion physics and propellant energy density not only drive performance of chemical rockets, but also the cost of operation—at best, \$10,000 per kilogram of cargo delivered to orbit. Launch costs haven’t significantly improved over the past half century and are not predicted to fall in the foreseeable future, regardless of incremental evolutionary change. To cut the cost of space access by 10x-100x, we need “game-changing” space launch technology. Presently on the horizon, the only candidate with this kind of potential is Beamed Energy Propulsion (BEP), and the physics is very well understood.

BEP is a “disruptive” technology that portends to complement, then later supersede chemical rockets, at least for micro/nano-satellite launch applications. In this concept, high intensity electromagnetic radiation is beamed from a remote radiation source (laser

or mm-wave) to a vehicle in flight, for direct conversion into thrust. Quite unlike chemical rockets, BEP takes its flight propulsive energy from this transmitted beam, rather than carrying it onboard as a massive fuel load. In airbreathing BEP engines, the working fluid is air, so thrust is produced by momentum exchange with the atmosphere; in the rocket BEP engines, thrust is produced by heating and expelling onboard propellant at a high velocity—no heavy oxidizer is needed, so low molecular weight propellants give exceptionally high specific impulse performance (e.g., 1000 to 2000 seconds or more).

By not having to lift the propulsive energy source in flight, BEP vehicles can leave the most heavy and expensive components on the ground as reusable power-plant infrastructure, for which the capital cost is amortized over copious launches. No highly reactive propellants are carried onboard, so the risk of catastrophic failure is minimal. The structural redundancy, safety equipment, and procedures that drive the mass and operational costs of conventional rockets upward, is neatly circumvented. Furthermore, BEP represents “green” transport technology that emits no pollutants during operation—100% environmentally friendly technology. Although *no* critical scientific or technological breakthroughs prevent the realization of BEP single-stage-to-orbit (SSTO) flights in the foreseeable future, the venture will require an arduous process of engineering adaptation. Plus, some of the critical technology apparently falls under ITAR or DoD restrictions.

Three potential liabilities of BEP (among others) must also be mentioned: 1) high initial cost and complexity of deploying requisite BEP infrastructure—multi-megawatt repetitively pulsed lasers (not available at this moment but within the realm of engineering feasibility); 2) transmitter adaptive optics for precise atmospheric turbulence compensation—“Star Wars” program spinoff, successfully applied in modern astronomical telescopes; and 3) eye safety—small glints (reflections) off Lightcraft engines could conceivably cause eye injuries at considerable downrange distances. To circumvent the last issue, laser launch facilities could be installed on remote, 3km high mountain peaks, employ source wavelengths that are “eye safe” (e.g., 1.62 um), and exploit boost trajectories that reduce reflected-beam intensity profiles to eye-safe

thresholds for all potentially affected populated areas (e.g., locate flight paths over sparsely populated deserts or the oceans).

The requisite BEP infrastructure is essentially a multi-megawatt class ground based laser (GBL) power station, which in the near term, would be designed for launching small satellites with payloads in the range of 1 to 10 kg (i.e., “nanosats”) into low earth orbit (LEO). As suggested above, adaptive optics, along with the appropriate choices of transmitter diameter and wave train characteristics (laser pulse energy, pulse duration, pulse repetition frequency, pulse shape, etc.) can minimize beam propagation losses through the atmosphere—an integral feature of the GBL power station. Although nanosatellite laser launchers would be the first natural step, once achieved, those technological foundations will soon enable more ambitious, 10x larger microsatellite payloads (10 to 100 kg). Ultimately, with a billion watts (~1GW) of beam power, payloads exceeding one tonne will become feasible, as proposed in the seminal work by **Kantrowitz (1972)**.

GBL launch stations offer high launch frequencies and short response times—an inherent strategic value that is hard to ignore (e.g., communications, surveillance, and intelligence needs). With GBL laser launchers, any part of the world is touchable in 50 minutes or less. Small payloads can be boosted on short notice and inserted into almost any desired orbit, or pitched into suborbital ballistic trajectories to any global destination. In fact, entire communications or navigation nano/microsatellites constellations could be launched “at will,” for low cost as suggested in **Kare, (1990)**, to replace recently negated military space assets.

BEP technology will eventually enable the visionary future applications outlined in **Myrabo and Ing (1985)** and **Myrabo and Lewis (2009)** that exploit both terrestrial and space-based power-beaming infrastructures. Imagine, for example, a global ultra-fast Lightcraft transportation system designed to replace the present congested hub and spoke commercial jet transport system, with ballistic launched Lightcraft flights linking any two cities on the planet. Imagine convenient flights to just about anywhere 50 minutes or less, operating from 100x to 1000x more “hub” airports than commercial airlines use today. The renderings in Figure 1.1 portray one such future Lightcraft port (left) and Lightcraft design (right) created by Palm.et.al.: the “LightPort” would function much

like a bus terminal today with no advanced reservations needed; the 5-m diameter Lightcraft vehicle, poised for liftoff, is sized to transport five people. These concepts were created in 2009 during a 10 week Masters-level design course at the Umea University Institute of Design, in Sweden, by one of 11 participating design teams.

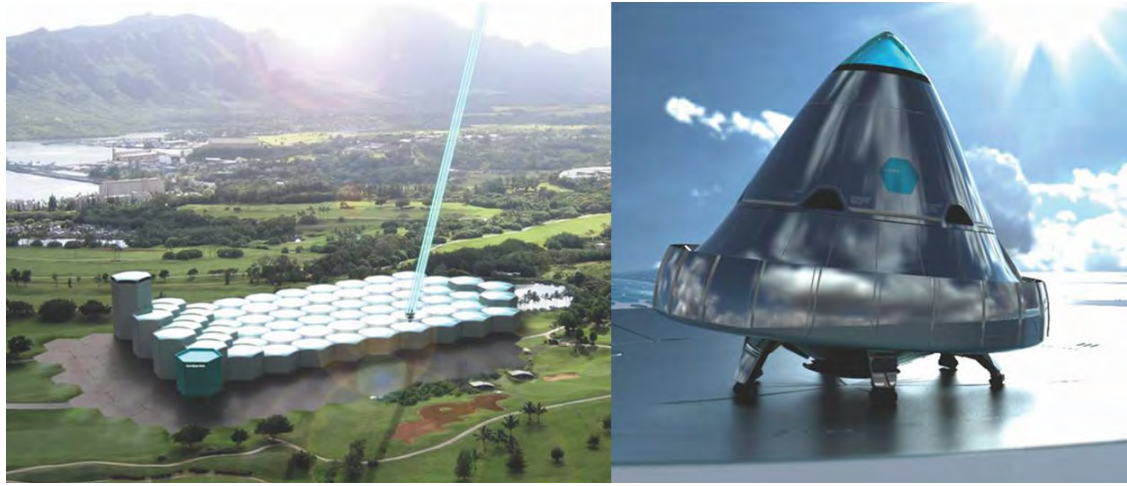


Figure 1.1 Future application for BEP: worldwide transportation. Left: LightPort serviced by space-based power-beaming station. Right: Lightcraft vehicle on launch pad. Palm et al. (2009)

1.1 Worldwide State-of-the-Art on Beamed Energy Propulsion

Research on Beamed Energy Propulsion began in the early 1960's, right after the first high energy laser was invented, when scientists started investigating laser induced breakdown phenomena and plasma ignition, upon which the LP concept studied herein is based. As mentioned above, the concept for BEP earth-to-orbit launch was first proposed in 1972 by Arthur Kantrowitz, who claimed that a gigawatt ground-based laser could lift a 1 ton cargo into space (**Kantrowitz, 1972**). His work was closely followed by the first experiments on laser propulsion performed by **Pirri and Weiss (1972)** who worked with Kantrowitz at the AVCO Everett Research Lab in Everett, MA. That same year **Minovich (1972)** conceived an ‘in-space’ laser rocket system utilizing a remote laser power station.

These seminal events launched the *first wave* of worldwide Laser Propulsion (LP) research, along with related physics investigations. The sheer magnitude of relevant research produced in the past four decades, prevents all but the most recent to be mentioned here—most notably, those of relevance to the specific Laser Propulsion (LP)

concept pursued in the present research. For further reviews on seminal BEP work, see **Kare, (Ed.) (1987, 1990), Pakhomov, (Ed.) (2002, 2004, 2007)** and **Komurasaki, (Ed.) (2003, 2005)**.

In 1997, a new worldwide wave of laser propulsion research was triggered by the Myrabo-Mead Lightcraft flights at the White Sands Missile Range (WSMR) in New Mexico, using the PLVTS (Pulsed Laser Vulnerability Test System) 10-kW CO₂ laser (**Myrabo et al., 1998**). Myrabo's LP experiments demonstrated the viability of this highly-integrated, beam-riding pulsejet engine/vehicle geometry which evolved directly from his 1987 Lightcraft Technology Demonstrator (LTD) concept, developed for the Strategic Defense Initiatives Office (SDIO). As with other LP researchers, Myrabo's over-riding goal has been to cut space access costs by at least two orders of magnitude below the ~\$10,000/kg milestone of today's chemical rockets, while greatly improving reliability.

Of all the LP concepts that researchers worldwide have created over the years, many believe the *repetitively-pulsed laser thermal propulsion* concept is the closest to near-term ETO launch system realization. International teams in the USA, Russia, Japan, Germany, and China have investigated a wide variety laser pulsejet engine cycles (e.g., airbreathing Laser Supported Detonation (LSD) mode, Solid Ablative Rocket (SAR) mode, combined-cycle airbreathing/rocket modes, among others for a variety of different vehicle concepts). So far most of the research on the topic has been focused on the evaluation of the Momentum Coupling Coefficient (C_m), which is a measure of how effectively id the incoming radiations transferred into kinetic impulse of the LP vehicle. This coupling coefficient is defined as the ratio between thrust and beam power ($C_m=T/P$) for the case of continuous sources, given in units of N/MW. It can also be defined as the ratio between impulse and pulse energy ($C_m=I/E_p$) for the case of pulsed sources, also given in units of N/MW.

Outside the USA's initial systems studies, several international LP research teams (e.g., in Germany, Japan, and ESA) have investigated the feasibility of commercial LP launchers for small payloads, while also exploring technical, economic, beam propagation, systems analysis and integration challenges. Even in countries just entering the field, BEP researchers universally recognize the revolutionary potential of laser

propulsion for low-cost space access. And judging from the rising list of Asian LP investigators in both Japan and now China, these teams are busy assembling resources to pursue LP launch technology; some interest clearly extends beyond purely academic research.

The following is a brief state-of-the art (SOA) review of global laser propulsion research relevant to near-term, nanosat/microsat laser launch systems.

1.1.1 United States

Pioneering LP research in the United States began in the 1970's and has evolved ever since. In the broadest sense, all laser electrothermal propulsion schemes can be classified as either Continuous Wave (CW) engines (**Nebolsine and Pirri, 2002**), or Repetitively Pulsed (RP) engines falling in three main categories: 1) Solid Ablative Rocket (SAR) (**Kare, 2002**); 2) Airbreathing (**Myrabo, 2002**); and 3) combined-cycle airbreathing/rocket (**Myrabo, 1987**).

In ablative laser rocket propulsion, an exposed solid propellant is rapidly vaporized by the incident laser beam, and thrust is generated as a result of the subsequent gas expansion process. Several alternative SAR concepts have been theoretically examined and experimentally demonstrated throughout the entire history of laser propulsion. Most recently, ablative laser propulsion studies were carried out at the University of Alabama by **Pokhamov et al. (2002)**. His investigations have screened a wide variety of materials (including lead, aluminum, Delrin®, Teflon®, water, ice, etc.) under different laser flux intensities, beam incidence angles, etc., searching for the optimum combination of momentum conversion efficiency and specific impulse. He has employed sophisticated diagnostics (including Schlieren imaging/visualization) to characterize the ablation process, mass consumption rates, blast wave velocities, and the like.

From the perspective of demonstrated beam-riding abilities, perhaps the most extensively explored laser propulsion concept to date is the Myrabo laser Lightcraft, in both its airbreathing and solid ablative rocket propulsion modes. Myrabo's initial BEP concept (**Myrabo, 1976**) proposed a single-stage-to-orbit (SSTO) shuttle concept based on a novel airbreathing magnetohydrodynamic (MHD) engine, powered by an orbital laser. As mentioned above, in the mid 1980's under contract to the Strategic Defense

Initiatives Office (SDIO), Myrabo's concept evolved to the Lightcraft Technology Demonstrator (LTD) concept—sized for launching 100 kg payloads to LEO)—which lead to the Ph.D. thesis of **Richard (1989)** that theoretically analyzed the performance of its airbreathing pulsed laser detonation engine vs. altitude and Mach number.

Ten years later, Myrabo further evolved this LTD concept directly into an even simpler family of Lightcraft vehicles used in proof-of-concept flights at the High Energy Laser Systems Test Facility (HELSTAF) on White Sands Missile Range (WSMR). This free-flight test campaign (**Myrabo et al., 1998**) was carried out with 97.7 to 161.2 mm in diameter vehicles with masses up to 50 g, scaled to fly on the 10 kW PLVTS pulsed CO₂ laser. The 6061T6 aluminum vehicles with purely airbreathing pulse-detonation engines (i.e., infinite specific impulse) could fly up to 30 m altitude before the annular shroud melted/failed (**Mead Jr., 2007**). To resolve this issue and increase thrust by ~2.5x, a solid ablative rocket (SAR) version was created by inserting a thin band of Delrin (used as propellant) at the annular laser focus just inside the shroud, at the expense of a finite specific impulse. **Figure 1.2** shows a long exposure night-time photograph of an airbreathing Type 200 Lightcraft flight (right), along with an enlarged view of a stationary Type 100 Lightcraft (left) undergoing thrust stand tests (note the luminous laser-induced plasma exhaust expanding below the engine/vehicle).

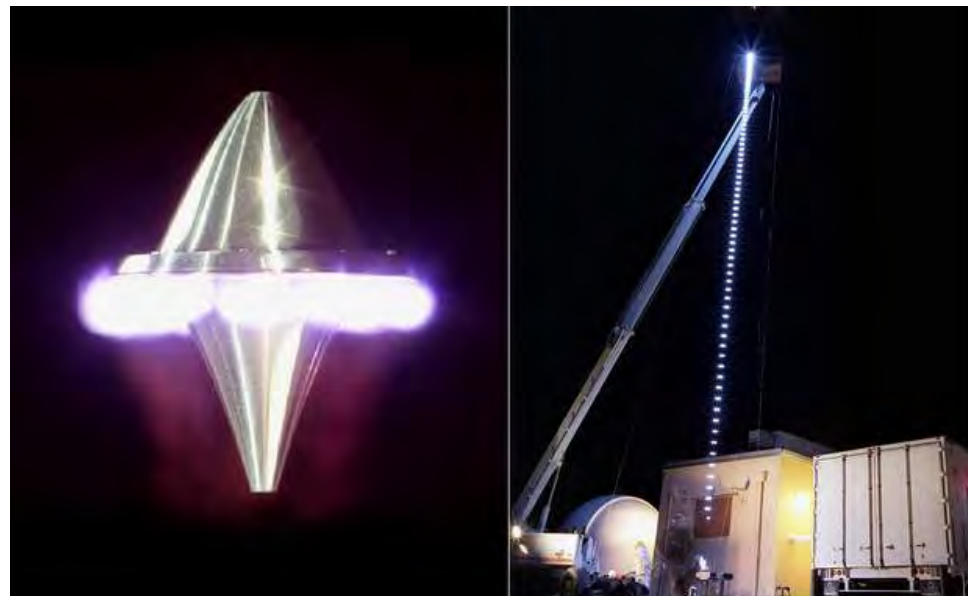


Figure 1.2 Type 200 Laser Lightcraft in nighttime WSMR free-flight (right); Type 100 Lightcraft with expanding luminous air-plasma exhaust (left). (*Photos by James Shryne III—Courtesy of NASA*)

Sophisticated numerical LP research on the Lightcraft concept was conducted by (**Wang et al., 2002**) at the NASA Marshall Space Flight Center. His CFD simulations embody the most complete and complex axisymmetric numerical model of airbreathing Lightcraft engine physics attempted to date. Wang's model includes nonequilibrium thermodynamics and air-plasma finite rate kinetics, ray tracing, laser absorption and refraction by plasma, nonequilibrium plasma radiation, and plasma resonance. His code results have been extensively calibrated upon the experimental data of **Myrabo et al. (1998)** from WSMR laboratory tests of the Type 200 airbreathing Lightcraft engine. It is important to note that Wang's model simulates only a stationary airbreathing Lightcraft engine with a closed annular inlet, but it could, in principle, be extended to encompass an entire engine/vehicle flying at supersonic or hypersonic speeds through the atmosphere, with an open external-compression inlet, but MSFC has no current plans to pursue this objective.

BEP research at the AFRL Propulsion Directorate (Edwards Air Force Base, CA) has examined the energy conversion in LP engines—performed by **Larson, et al. (2002)**, and the experimental/ numerical analysis of laser launch technology—conducted by **Mead Jr., et al. (2005)** and **Knecht, et al. (2005)**. Larson studied the propellant chemistry, expansion process, and overall conversion efficiency: i.e., specifically the transformation of laser energy to ejected mass internal energy and exhaust kinetic energy, for SAR and airbreathing Lightcraft engines, assuming equilibrium and frozen flow. **Mead Jr. et al. (2005)** developed two scaled-up versions of the Myrabo Lightcraft: one 25 cm in diameter and the other, 50 cm (designated XL-25LR and XL-50LR, respectively). The objective was to deploy an actual vehicle for suborbital “sounding rocket” flights in the near term, subsequently followed by orbital launch attempts in the future. Static laboratory bench tests were conducted with the XL-25LR model, along with launch trajectory studies and other subcontracted hardware development (under SIBRs)—e.g., electronic systems and micro thrusters for attitude control and orbit circularization. SAR Lightcraft engines and small conical rocket nozzles were used to test the performance of different types of Delrin® (both black and white varieties), revealing minimal coupling coefficient differences. Trajectory simulations were performed for the X-25LR by **Knecht et al. (2005)** using the *Optimal*

Trajectories by Implicit Simulation (OTIS) numerical code, assuming a 1 MW GBL operating at 10.6 μm with a beam power capture fraction of 82% into the combined-cycle pulsed LP engine. These simulated full-scale laser launches to LEO modeled the propulsion performance of both air-breathing and rocket phases of the flight trajectory.

Another critical research front is investigating the flight dynamics, stability, and control of repetitively-pulsed laser-propelled launch vehicles. One must clearly understand the beam-riding physics of existing and successful, spin-stabilized Lightcraft in order to acquire the wisdom to identify and create LP engine/vehicle configurations with exceptional merit and promise. In the near future, realistic/functional attitude control systems will be needed to maintain desired LP craft orientations and headings, in controlled flight along a launch trajectory to orbit.

Kenoyer, et al. (2007) have created a sophisticated, non-linear, 7 Degree of Freedom (7-DOF) flight dynamics model specifically for investigating the flight behavior of laser-boosted Lightcraft. The 7-DOF model, now precisely calibrated against 16 Lightcraft flights at WSMR, provides a realistic research tool for assessing beam-riding flight physics of innovative Lightcraft configurations that don't yet exist. The non-linear 6-DOF code incorporates all essential components (e.g., fully integrated engine, beam, aerodynamics, structures, and dynamics models), and permits such effects to be isolated so that the influence of any one may be studied separately and adjusted at will. Further RPI laboratory experiments with the Lumonics K922M laser system have measured the "beam riding" behavior of several engine LP configurations (e.g., Type #150, #200, and #250), using detailed diagnostics to record forces and moments, along with high speed Schlieren movies; these LP configurations were all previously flown at WSMR in test campaigns employing the 10-Kw PLVTS carbon dioxide laser.

Again, as mentioned earlier, several dozen research laboratories, institutes/centers, and universities—worldwide—have now investigated a staggering variety of concepts and applications for beamed energy propulsion: e.g., light sails, in-space laser-heated rockets, laser- and microwave energized airspikes—to name just a few. However, the present research emphasizes the SOA of basic research relevant only to the LP concept studied in this thesis.

1.1.2 Europe

European and Asian research in laser propulsion is relatively new and not so consolidated as in the United States and Russia. The German activity is centered in Stuttgart at the German Aerospace Center (DLR), and began right after Myrabo's successful WSMR indoor and outdoor flight experiments in 1997.

Bohn and Schall's (2002) initial research emphasized the interaction of high power CO₂ laser radiation with simple parabolic bell engines (see **Figure 1.3**), applying optical and other techniques to analyze the physics of breakdown and plasma generation. The static performance of their bell thruster, along with the Myrabo Lightcraft (#200-3/4) was tested with and without SAR propellants (e.g., Delrin®), at pressures ranging from sea level to a high vacuum. With DLR's high power CO₂ laser (11 µs pulse duration), their parabolic bell thruster clearly outperformed Myrabo's #200-3/4 Lightcraft engine in both airbreathing and SAR rocket modes. However, note that the bell geometry has not yet flown more than a second or two in free-flight, without the aid of wire guidance. In contrast, Myrabo's Lightcraft is a highly integrated vehicle/optics/engine platform for which stable "beam-riding" has already been achieved (a mandatory condition for successful free flights under laser power). The "German Lightcraft" has yet to demonstrate this essential feature beyond 5mm lateral offsets from the laser beam centerline.

Note also that the current Type 200 Lightcraft is simply the current baseline, proof-of-concept vehicle/engine that has flown outdoors on a laser waveform (i.e., pulse duration, PRF, and pulse energy—provided by the 10-kW PLVTS laser) that lies far outside the optimum requirements for this LP thruster. Further refinements in the plug-nozzle (i.e., off-axis parabolic) Lightcraft engine/vehicle, along with a more ideal laser source, will enable dramatic increases in engine performance throughout the subsonic, supersonic, and hypersonic regimes.

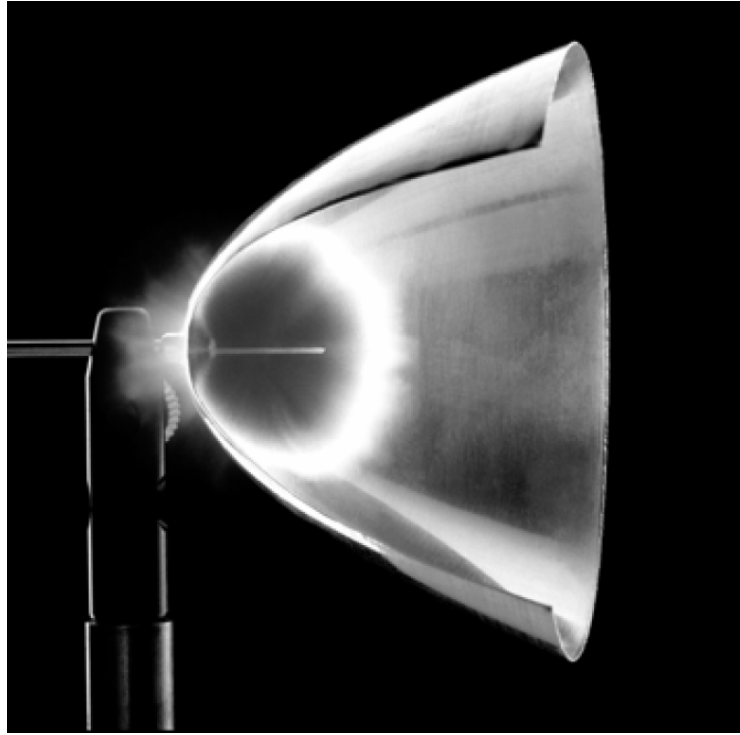


Figure 1.3 Cutaway view of German “bell” engine, with ignition pin. Schall and Eckel (2003)

More recently, **Schall and Eckel (2003)** have continued their experimental research on parabolic aluminum thrusters, with brief wire guided and free-flights, ballistic pendulum tests, etc. In the wire-guided tests, model mass varied from 17 to 55 grams (to simulate a payload), while maintaining engine geometry and scale unchanged. An indoor flight altitude of 8 m was achieved with DLR’s repetitively-pulsed CO₂ electron discharge laser (175 J at 45 Hz, pulse width of 11 μ s) and the bell thruster in airbreathing mode, dynamically refreshed from the nozzle exit between pulses. Ballistic pendulum experiments were performed under various static pressures to simulate the effects of altitude upon the momentum coupling coefficient (C_m).

In Portugal, **Resendes et al. (2004, 2007)** at the Instituto Superior Técnico in Portugal, under contract for the European Space Agency (ESA) performed an extensive review of laser propulsion SOA, and compared the applied LP research performed to date. The basic theory and concepts were also addressed. The work concludes with an analysis of the most promising concepts and provides suggestions for further experiments. Within this work, a basic first-order analysis of the trajectories and dynamics of the Myrabo Lightcraft was carried out (**Resendes et al., 2007**). This

analysis, which provides several insightful results, approximates the vehicle by a point-mass, with no beam-riding forces or moments; only the forces of gravity, drag, and thrust were simulated.

1.1.3 Japan

Outside the United States and Russia, Japan has produced the most extensive body of research on laser propulsion to date. Several renowned institutions have turned their attention to the concept in the last decade. Among them are: Tohoku University, the National Aerospace Laboratory, the University of Tokyo, Tokai University, and the Institute for Laser Technology (**Niino, 2002**).

Komurasaki et al. (2002) have performed numerical and experimental research on both laser and microwave propulsion concepts, addressing RP as well as CW thruster modes. Their numerical studies have investigated airbreathing, pulsed LP-ramjet schemes **Katsurayama, (2001)** with engine/vehicle geometries that closely resembled the Lightcraft Technology Demonstrator (LTD) concept proposed by **Myrabo et al. (1988)**. Various CFD analyses (see **Figure 1.4**) of this LP-ramjet concept have examined: 1) alternative Lightcraft forebody and shroud geometries, under various flight conditions (Mach number, ambient pressures/densities); 2) overall engine performance, and, 3) the influence of laser focal ring location upon laser energy conversion efficiency into thrust. One RP ramjet numerical model simulated the time-dependent behavior of a single thrust generating pulse. Another numerical model was built for CW laser rocket simulations to address the critical issues of wall heat losses, radiative losses, and laser absorption efficiency.

On the experimental front, **Mori et al. (2002)** and **Komurasaki et al. (2002)** linked a 10 J/pulse CO₂ laser system to a small-scale M=2.0 wind tunnel to investigate the laser-plasma expansion characteristics and blast wave production efficiency of a focused beam within the free stream. Also, a 2kW-class CW model thruster was built and tested, with the objective of measuring the efficiency of laser energy conversion into thrust.

Japanese researchers have also examined the feasibility of applying millimeter wave sources for beamed energy propulsion. **Nakagawa et al. (2003)** used a 1 MW gyrotron (operating in repetitive pulsed mode) to conduct proof-of-concept free flight and thrust

stand experiments with the airbreathing parabolic reflector model pictured in **Figure 1.5**. The momentum coupling coefficient (C_m) performance generally fell in the same range as laser thrusters.

Sasoh (2004) introduced the Laser-driven In-Tube Accelerator (LITA) which is perhaps one of the most prominent Japanese concepts. Collaborative numerical and experimental research on the LITA concept has been carried out by Japan and South Korea investigators. As shown in **Figure 1.6**, a repetitively pulsed laser beam is projected down onto a primary mirror integrated with the vehicle forebody, then is refocused by the cylindrical secondary mirror (i.e., the shroud inner surface) to just underneath the vehicle. The projectile is propelled up the guide tube by a sequence of laser supported detonations that drive blast waves against the aft centerbody surface.

The launch tube may easily be filled with any propellant gas (e.g., air, nitrogen or argon). Hence, Sasoh's experiments have been performed with a variety of gas mixtures at various pressures, with the laser beam admitted either from upstream ("tractor beam" version as in **Figure 1.6** or downstream ("pusher beam" version) as in **Figure 1.7**, depending on the model tested. The breakdown threshold may be reduced as desired, through the choice of propellant gas. The noticeably higher C_m performance and impulse levels of LITA can be attributed to the tube's confinement effect, according to **Ohnishi et al. (2005)** who also performed a brief numerical analysis. Note that LITA is conceptually identical to one of Myrabo's 1983 "tractor beam" lightcraft designs reported in **Myrabo et al. (1983)** and **Myrabo and Ing (1985)**.

Seoul National University and Pusan National University, both in South Korea, have collaborated with the numerical analysis on Sasoh's LITA concept (**Sasoh, 2004**). The investigation, which retained the exact same vehicle/engine/optics configuration, examined the in-tube flight aerodynamic characteristics and internal flow field features (e.g., including the inlet unstarting process) occurring within LITA. Aerodynamic visualization experiments and subsequent analyses were also performed on the LITA model geometry in a supersonic wind tunnel (**Kim and Cho et al., 2002** and **Kim and Pang et al., 2002**).

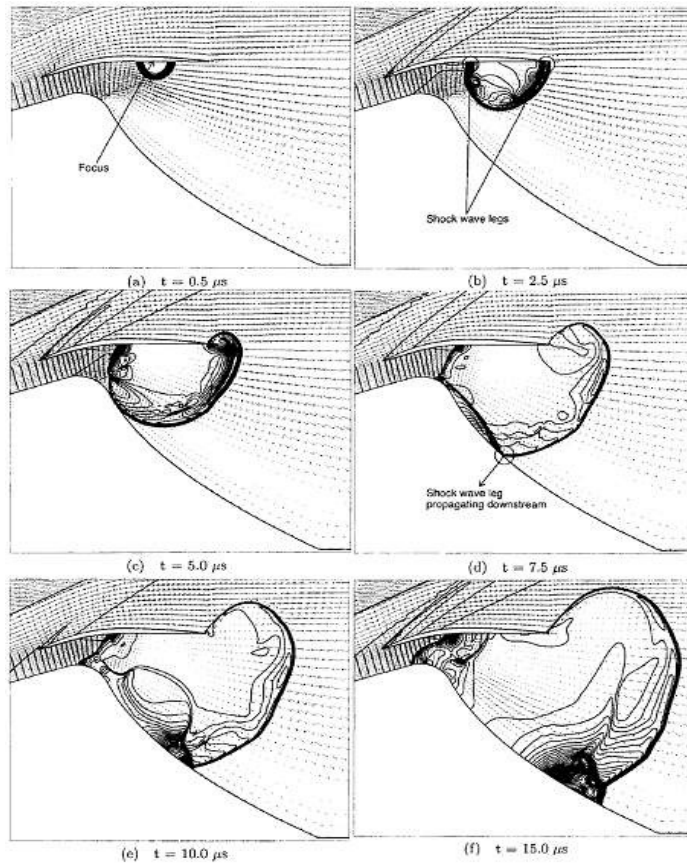


Figure 1.4 Hypersonic (M=5.0) CFD simulations of a 16 cm diameter Lightcraft flying at 20 km altitude. (Komurasaki et al., 2003)

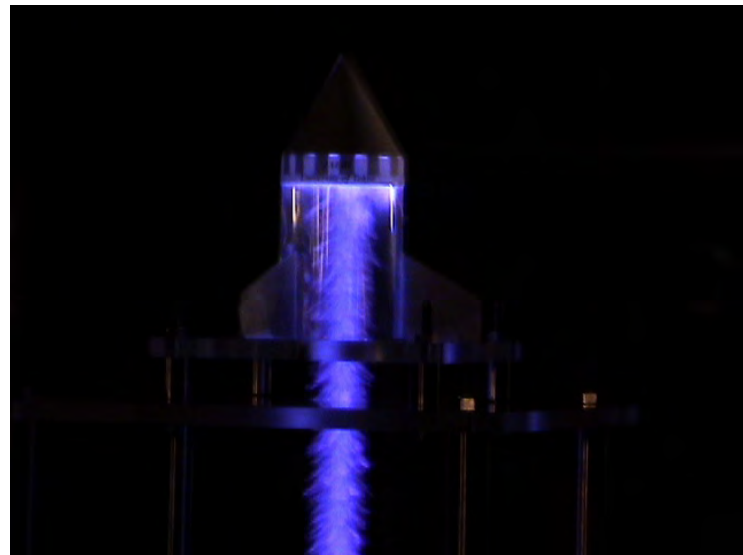


Figure 1.5 Microwave-powered Lightcraft (Nakagawa et al., 2003)

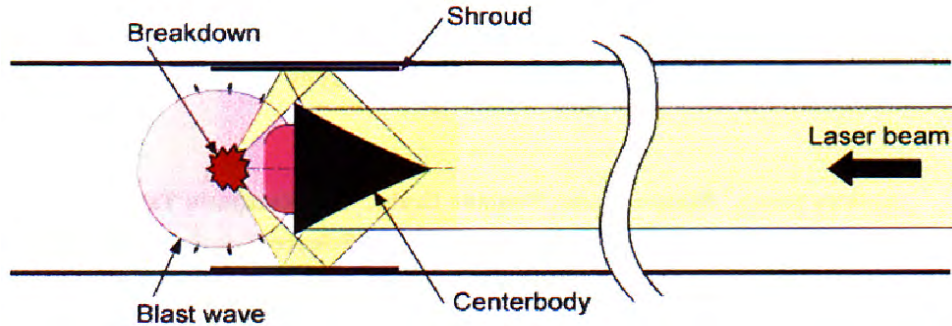


Figure 1.6 LITA concept, upstream beam operation (Komurasaki, 2002)

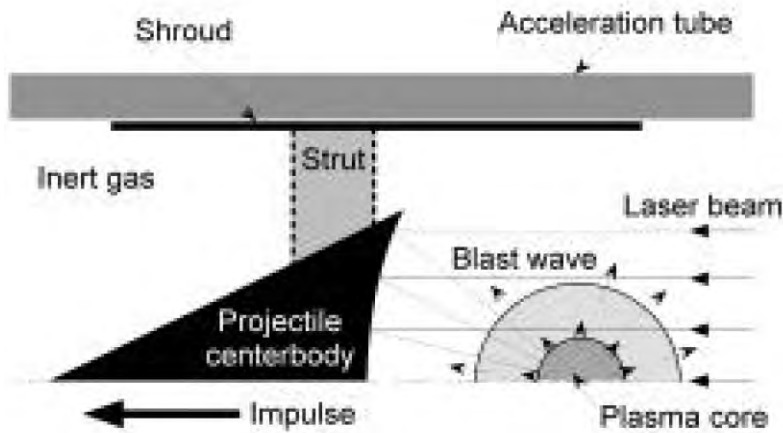


Figure 1.7 LITA features in a pusher beam configuration (Sasoh, 2004)

1.1.4 Russia

Russians laser propulsion pioneers, as with the United States, also began their work in the early 1970's. Fundamental theoretical studies on laser-induced breakdown, and heating of gases by laser radiation had already been accomplished in the mid-1960's: e.g., the classical works of Raizer (**Raizer, Yu. P. (1965)** and **Raizer, Yu. P. (1966)**). Recent interesting works on the physics of laser propulsion include those by Apollonov (**Apollonov and Tishchenko, 2004a**, **Apollonov and Tishchenko, 2004b**, **Apollonov et al., 2005**) and Tishchenko (**Tishchenko et al., 2002**, **Tishchenko, 2003**). Apollonov proposed the use of a *pulse periodic mode* induced in high power gas dynamic lasers for the transmission of ultra-high PRF waveforms (while maintaining high pulse energy) into innovative LP engine concepts. Tishchenko's experimental and numerical research on moving Optical Pulsed Discharges (OPD) has shed insight into the conditions

necessary for successfully tailoring subsequent shock waves into the so-called Quasi-Stationary Wave (QSW) heating mode. In the QSW mode, a strong, almost planar shock wave is created by the merging of several shocks resulting from a high PRF laser-induced blast train. Significant improvements are claimed for the momentum coupling coefficient of QSM-heated engines, in comparison with the *no QSW tailoring* case, and experiments are underway to substantiate this assertion.



Figure 1.8 The ALSPE concept vehicle (Rezunkov et al., 2005)

Rezunkov et al. (2005), another Russian research team, has conducted recent experiments with a novel AeroSpace Laser Propulsion Engine (ASLPE). This LP concept (see Figure 1.8) shares two features with Sasoh's LTIA "tractor beam" concept: 1) an axisymmetric forebody that serves as a primary receptive mirror, and, 2) an annular, ring-shaped secondary mirror. Note that ASLPE refocuses its annular beam *through narrow slits in its truncated conical nozzle* into a central laser absorption chamber; LITA has no such nozzle. The team claims: a) the unique engine geometry permits successful operation in both repetitively-pulsed (RP) and continuous wave (CW) propulsion modes, with roughly comparable efficiencies, b) optical windows are not required for the CW mode. Also demonstrated, was an inclined wire-guided flight of the ASLPE, propelled by a 6 kW repetitively-pulsed CO₂ laser (120J @ 50 Hz). Ballistic pendulum experiments with ASLPE gave momentum coupling coefficients (C_m) in the

range of 25 to 40 dynes/W with that 6 kW RP laser, and 10 to 13 dyne/W with their 30 kW CW CO₂ laser.

1.1.5 Brazil

Brazilian interest in laser propulsion began in the 1990's and has, until recently, been focused largely on Directed Energy Air Spike (DEAS) research (**Minucci et al., 2003; Minucci et al., 2005; Oliveira et al., 2005; Salvador et al., 2008**) of relevance to streamlining hypersonic blunt forebodies. The DEAS concept employs beamed laser energy to create a “virtual spike” that diverts hypersonic airflow away from a vehicle’s flight path, thereby reducing aerodynamic drag and heat transfer upon the blunt forebody. Experimental results have shown that hypersonic drag can be cut by as much as 40%. Investigations (see **Fig. 5**) are underway to quantitatively assess DEAS disruptions of established flow fields (**Oliveira et al., 2005**), and heat flux rates across blunt forebodies (**Salvador et al., 2008**).

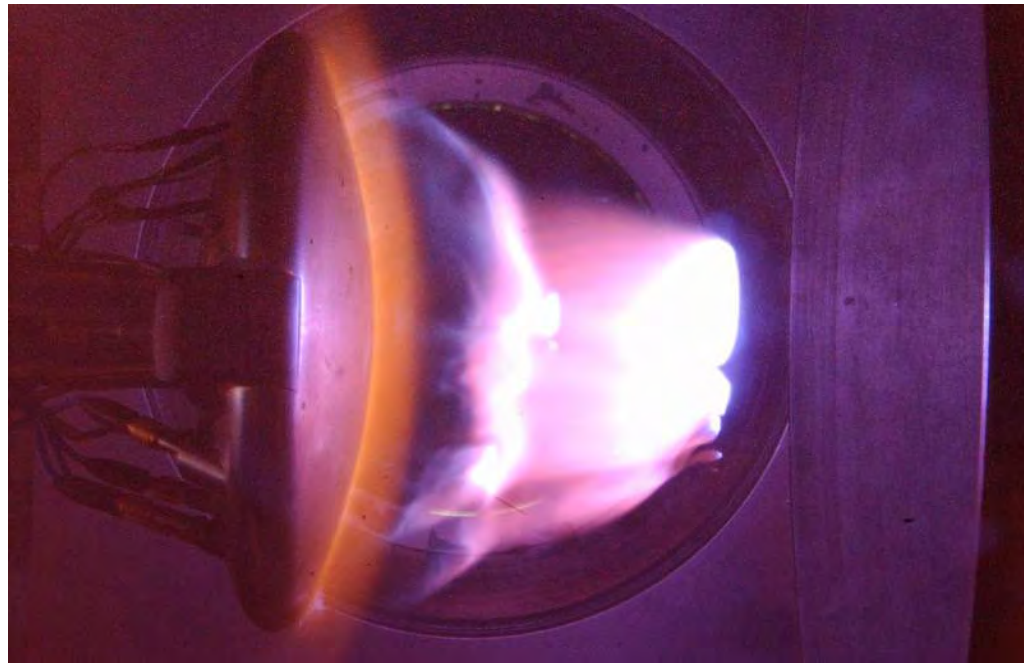


Figure 1.9 Laser-induced DEAS hypersonic experiments in Brazil. (Salvador, 2008)

Hypersonic shock tunnels at the *Henry T. Nagamatsu Laboratory for Aerothermodynamics and Hypersonics* (HTN-LAH) in Brazil are linked to powerful CO₂ TEA lasers in preparation for ground-breaking LP experiments and related hypersonics research. HTN-LAH is the only research facility in the world capable of

simulating flow conditions inside (and around) LP ramjet and scramjet engines, with the capability of providing deposition of laser energy into the flow. The fabrication of several large-scale, two and three-dimensional LP engine segments and vehicles is presently underway, for which basic research experiments, of which this work is the first one of them, are being performed.

1.1.6 China

China has revealed a sharply increasing interest in laser propulsion, judging by their growing list of conference and journal articles published around the world. At present, this LP research appears constrained to experimental and theoretical studies of relevant basic physics issues, possibly retracing historical foundations laid down by USA, Russia, and other researchers. Some observers believe this work will soon blossom (if it hasn't already) into a formidable world presence in laser propulsion research.

Cui et al. (2005) with the Northwestern Polytechnic Institute at Xi'an, has carried out basic LP experiments and numerical simulations to investigate the effects of nozzle structure upon laser thruster performance. **Dou et.al. (2005)**, from the Zhuangbei Institute of Technology, conducted experimental research with a 100 J pulsed CO₂ laser to assess the impact of various gas mixtures upon the momentum coupling coefficient (C_m) of simple laser thrusters. At the same institution, **Li et al. (2005)** examined the thrust generation mechanism within a RP thruster, comparing Sedov's self similar theory for strong explosions with numerical simulations of a single laser pulse focused at the centerline of a conventional nozzle.

At the University of Science and Technology of China, **Gong and Tang (2005)** performed a multi-pulsed simulation of an airbreathing bell nozzle thruster using FLUENT®. **Tang et al. (2005)** used a TEA CO₂ laser to conduct experiments on a parabolic thruster for a variety of pulse repetition rates and ambient pressures, within a vacuum chamber.

1.2 Motivation and Objectives

The work outlined in this thesis represents a solid initial “building block” for a future ambitious program that thoroughly investigates (both experimentally and

numerically) all LP propulsion modes and flight regimes encountered by a Lightcraft in its ETO flight, from liftoff to final orbit circularization. This thesis, to keep the research objectives both feasible and manageable, focuses on the Mach 7-10 laser scramjet regime which, represents a narrow portion of the entire Lightcraft flight trajectory, such as studied in (**Richards, 1989**) and (**Frasier, 1990**).

Extensive research into, and analyses of the subsonic/supersonic/hypersonic flight envelope facing a Lightcraft launch are clearly needed. Such investigations must include the consideration of novel engine/vehicle geometrical and design iterations that go well beyond the first embryonic Lightcraft concepts created (and available in the literature), as well as new trajectory profiles, laser beam parameters, beam propagation, infrastructure and cost analysis, and so on. All such needs will drive LP research objectives for years to come, of which the present thesis is just a first, but important step.

As briefly summarized in Section 1.1 above, prior research on airbreathing laser propulsion has been limited to: 1) stationary thrust stand tests; 2) short free-flights (some wire- and tube-guided) at low subsonic flight speeds; 3) laser energy deposition and static thrust generation studies (the most extensive studies), wherein the impulse and momentum coupling coefficients are measured with ballistic pendulums and/or load cells; and 4) numerical studies (very few of which are calibrated on real experimental data). These direct force/impulse measurements fail to reveal interdependent relationships between engine/optics/vehicle geometry, the blast wave expansion dynamics, and impulse generation process.

To adequately assess the impact of such Lightcraft geometrical features upon the impulse generation process—to a far greater extent than accomplished in past LP research—requires a completely different experimental technique, wherein: a) resultant impulse is measured by integrating time-variant pressure distributions created over engine surfaces; b) such pressure traces are correlated with high speed Schlieren movies that track positions of expanding, laser-generated blast waves; and, c) the time-variant thermal imprint of such laser-generated blast waves, as they expanded over the engine’s “hot section” and impulse surfaces, is recorded for subsequent analysis. The first item requires an array of appropriately placed piezoelectric pressure transducers over the Lightcraft model; the second item, a digital camera with a frame rate of 1000 fps or

better. To address the last item, in-depth knowledge of the distributed heat transfer load over the LP engine can be enabled with an array of heat transfer gages distributed/concentrated near the heavily loaded engine “hot section” surfaces.

Hence, now having in mind the limitations and advantages of pulsed laser propulsion, the SOA of previous LP research performed to date and the overall goals for future LP research, we can move forward to identify specific primary and secondary objectives for the present thesis research, as follows:

Primary Objectives:

- 1) Measurement of time-dependent surface pressure distributions over a 2-D Laser Lightcraft engine cross-section, including “hot section” (absorption chamber) and other internal surfaces;
- 2) Visualization of laser-induced blast wave expansions responsible for pressure increase —thus impulse generation—as well as its interaction with incoming hypersonic flow.

The first campaign would be conducted under quiescent air conditions at various ambient pressures up to 1 bar, to de-bug the complex experimental apparatus, and prepare for tests with flow. The second campaign would be performed at hypersonic flow conditions ranging from approximately Mach 6 to Mach 10. To secure the realization of these *primary objectives*, several complex apparatus and sophisticated tools must be made available and operational—thus leading to the *secondary objectives* given below.

Secondary Objectives:

- 1) *Develop and integrate the required experimental test facilities:* Link the HTN-LAH T3 Hypersonic Shock Tunnel with the Lumonics TEA-622 laser. This involved the transport (to Brazil), installation, and repair of the existing TEA-622 and the acquisition/design/manufacturing of the unavailable/needed equipment;
- 2) *Design, manufacture, and install 2D Lightcraft model:* This required the transport of the model to Brazil, insertion of pressure gages, installation of the model in the T3 tunnel, and de-bugging all instrumentation;

- 3) *Generate quality data for calibrating CFD tools:* The 2D model must give the kind of data needed to develop and calibrate sophisticated computational tools (CFD), for simulating design iterations and optimizing the LP engine concept;
- 4) *Determine airbreathing LP transition Mach numbers:* The Lightcraft concept under investigation, encompass a full-spectrum of LP propulsion modes that will transition from ramjet, to scramjet, and finally to rocket (i.e., using on-board propellant) modes along an earth-to-orbit launch trajectory. Hence, another secondary objective concerns the optimum transition points (i.e., Mach numbers) between operational modes, which is beyond this thesis. First is the LP subsonic-supersonic flow transition (analog to ramjet/scramjet transition), whereupon the inlet gap be widened to allow supersonic flow through the inlet throat. The second transition occurs when the LP scramjet inlet gap is closed at the upper limits of the sensible atmosphere—i.e., end of infinite specific impulse ($I_{sp}=\infty$) regime—and the engine switches to the LP rocket mode.
- 5) *“Pave the way” for future, continuing research:* Once the present thesis campaign is concluded, the present work will be handed off as a legacy to other investigators, so that airbreathing LP research progress can continue unabated. At that point, the HST/laser facilities at IEAv-DCTA would be integrated and operational, well equipped for subsequent campaigns with the same or different LP models, and much extended regime of Mach numbers. The overriding goal is to avoid the (far-too-common) interval of “dead” scientific advancement, after a research campaign terminates—wherein all the time and effort spent assembling formidable new facilities, models, and tools is lost. Fortunately, the host organization for the present experimental research (IEAv-DCTA) has a long-range vision for LP, involving scientists and faculty at institutes in both Brazil and the USA, researchers with the interest and commitment to jump in, provide continuity, and keep advancing the SOA.

Even though the present thesis work has intended to tackle these questions and supply tentative answers, it is known *a priori*, that the closure to such issues lies far ahead. Years of arduous research will be required before solid, quantitative conclusions can be obtained. Hence, an overarching goal of the research presented herein is to foster

fertile grounds for future long-term research on the complex multidisciplinary science and technology of hypersonic airbreathing laser propulsion.

1.3 Thesis Outline

The main body of this dissertation is divided in 6 chapters. The first is an extensive review of the world-wide “state-of-the-art” in laser thermal propulsion, which motivated the present work and clarified its objectives. Chapter 2 introduces the phenomenology taking place within a laser Lightcraft’s absorption chamber, from the moment of laser beam influx to final expulsion of the laser-induced blast wave. It also introduces the theoretical impulse generation models used in the past by prominent researchers. Chapter 3 details the research facilities assembled and used, including the Hypersonic Shock Tunnel (HST), TEA CO₂ lasers, two-dimensional Lightcraft model, and all instrumentation assembled for the setup.

The experiments performed under static conditions at various ambient pressures are described in Chapter 4, wherein surface pressure measurements were acquired and used to assess the momentum coupling coefficient (C_m)—the defining figure-of-merit for any airbreathing laser propulsion engine. Together with the pressure measurements, Schlieren visualization of the breakdown phenomena and subsequent blast wave expansion was obtained.

The hypersonic portion of the experimental campaign is described and discussed in Chapter 5, covering simulated hypersonic flight conditions ranging from Mach 6 to 10. Time-dependent pressure distributions over the 2-D model’s impulse surfaces were measured; the interaction of laser-induced blast waves with engine boundaries and the established flow field was photographed and analyzed. Finally, the predominant conclusions extracted from all this acquired data are summarized here.

Logically, the appendix material follows the main body of the work: Appendix A covers the instrumentation and calibration procedures. Appendix B explains the international collaboration specifically set up between United States and Brazil for beamed energy propulsion research, which enabled the present work. Appendix C describes the basic flow modeling in a Hypersonic Shock Tunnel, aimed at the reader unfamiliar with this formidable experimental tool. Finally, Appendix D details some of

the work performed at RPI, where a dedicated laser propulsion laboratory was created. The vision for this laboratory is explained along with its capabilities, a few of the experiments performed to date, and others planned for the future.

2. Laser Induced Breakdown and Impulse Generation Process

The science of Laser Thermal Propulsion is a complex multidisciplinary affair involving quantum electrodynamics, optics, fluid mechanics, gas dynamics, high temperature plasma dynamics, and the like. Deep theoretical developments on such subjects lie beyond the scope of this thesis, so the interested reader is encouraged to seek out the original references for more thorough treatments than presented here.

In the present research, laser impulse generation and overall efficiency aspects are the principal foci. This chapter addresses the basic phenomena taking place following the laser energy deposition into a Lightcraft engine's absorption chamber, and the subsequent phenomena leading to the generation of impulse. These processes are laid out herein, in sequence, starting with pulsed laser illumination of the rear optic/afterbody, and finalizing with the blast wave exiting the engine boundaries.

As noted by **Raizer (1977)**, the laser spark generation process can be divided into three successive stages: 1) air breakdown, where ionization develops in the cold gas and the initial plasma appears; 2) interaction between the remainder of the laser pulse energy and the initially formed plasma, which includes the motion of the plasma front maintained by the laser radiation (e.g. LSD wave), heating of the plasma to very high temperatures, and absorption and reflection of the laser light by the plasma (plasma mirror effects); 3) formation of the detonation phenomena, resembling a small-scale nuclear fireball. Subsequently, the blast wave relaxes in an unpowered manner, delivering impulse while expending its strength, until it exits the engine/vehicle boundaries into the surrounding environment.

Section 2.2 below provides a cursory description of the essential physical processes, followed by Sect. 2.3 which gives a brief analytical formulation for impulse generation, leading to the principal LP engine performance parameters: a) Momentum Coupling Coefficient (C_m), and, b) overall efficiency (η_o). The C_m formulation is based on extensive theoretical work by **Pirri (1973)**, **Reilly et al. (1979)**, and **Richard (1989)**.

2.1 Early Stage – Cascade Ionization and Plasma Formation

The first step in laser energy absorption by a gas is the optical breakdown, which is characterized by a reduction of the molecular gas into ionized gas (plasma). Breakdown

of a gas by strong optical radiation is caused by two mechanisms (**Weil, 1989**): 1) cascade ionization (Inverse Bremsstrahlung - IB), and, 2) Multiphoton Ionization (MPI).

The first mechanism involves the absorption of laser radiation by electrons through collision with neutral particles, in a region in space subjected to a strong electromagnetic (EM) field and where free electrons (also called seed electrons) are present. These electrons will begin an oscillatory motion triggered by the EM field and collide with gas particles (with kinetic energy transfer), either increasing the random motion of the particles or causing energy losses by scattering, appearing as heat generation. If the electron kinetic energy is high enough, it can collide with a neutral molecule ionizing it on the impact, as described by **Eq. 2.1**



As shown, the result of the interaction is two slower free electrons, which repeat the process leading to an increase in the number of electrons in an electronic avalanche or cascade ionization process (Inverse Bremsstrahlung–IB). If the acting field is strong enough, breakdown occurs in the gas under consideration, otherwise loss processes slow down the avalanche preventing the formation of the breakdown. The necessary conditions are the existence of an initial electron on the focal volume, and that the acquisition by the electrons of an energy greater than the ionization.

The second process has a purely quantum nature and is typical of the optical frequency range. This process, called Multiphoton Ionization (MPI), occurs when electrons absorb simultaneously a certain number of photons (n) with energy $E_{\text{photon}} = h\nu$, gaining enough energy ($n\nu$) to detach from atoms or molecules, which are then ionized. The condition for ionization is $n = (E_i/h\nu) + 1$, where E_i is the molecule ionization energy. This MPI process is described by **Eq. 2.2**



The probability of a multiphoton process is small, but increases with the light irradiance (photon flux). According to Weyil (1989), the importance of the MPI process is restricted to shorter wavelengths ($\lambda < 1 \mu\text{m}$) and at CO₂ laser frequency ($h\nu = 0.1 \text{ eV}$) is highly improbable, since ionization potentials of most gases are larger than 10 eV,

requiring simultaneous absorption of over 100 photons for the total energy (mhv) to exceed the ionization potential. Both IB and MPI require laser irradiances higher than 10^8 W/cm² in gases, with this value decreasing to 10^6 W/cm² in the case of solids. Note that this considers actual gaseous environments, containing aerosols and other particulates, which aids in the breakdown process by being heated up under the laser irradiation and generating electrons by thermionic emission. For clean air devoid of any impurity, the breakdown threshold can be as high as 10^{12} W/cm² for short pulses. Under normal conditions, there are over 10^4 particles/cm³ larger than 0.1 μ m in the atmospheric air (**Reilly et al., 1977**), which acts towards the reduction of the breakdown threshold in atmospheric conditions.

In the present work, the laser breakdown is located on the inner surface of the Lightcraft's aluminum shroud, that leads to reduced breakdown thresholds, since the threshold for solids and liquids are significantly lower than that for gases. In the case of metal breakdown, plasma formation is preceded by metal vaporization, which occurs on thermally insulated defects with characteristic length of the order of 10^{-6} m, which can attain temperatures higher than 5×10^3 K (for $I \sim 10^8$ W/cm² and $\tau \sim 5 \times 10^{-8}$ s). (**Walters et al., 1978**).

2.1.1 Metal Surface Air-Breakdown

As pointed out by **Walters et al. (1978)** and **Weil (1989)**, plasma ignition on a metallic target surface occurs at the rising portion of the beam pulse profile spike, with the plasma formation preceded by surface vaporization, following absorption of the radiation in a skin depth on the order of 10^{-10} angstroms. With a pulse width of tens of nanoseconds (as with the present experiments), the thermal diffusion length is much larger than the skin depth, so the surface temperature is given by

$$T = T_0 + \left(\frac{2I}{K} \right) \left(-t \right)^{\frac{1}{2}} \quad (2.3)$$

Assuming the interaction of a clean aluminum surface and a CO₂ laser pulse ($\lambda = 10.6$ μ m), absorptivity (α) ~ 0.05 , thermal conductivity (K) = 2.4 W/cm, and thermal diffusivity (χ) = 1 cm²/sec, and considering the laser irradiance (I) as 10^8 W/cm² and

pulse time of $(\tau_p) = 5 \times 10^{-8}$ s, **Eq. 2.3** yields $T - T_0 = 500$ K, which is lower than the melting temperature for the metal. This shows that the ignition occurs on thermally insulated defects of thickness $d = 0.1$ to 0.3 μm , which is much smaller than the thermal diffusion depth and has its temperature governed by the equation

$$T = T_0 + \frac{I \cdot t}{Cd} = T_0 + \frac{0.0102}{d} \quad (2.4)$$

where ρ and C are the density and specific heat of aluminum, respectively. Under the same circumstances ($d = 2$ μm) $T - T_0 = 5100$ K, a temperature rise high enough for vaporization within the laser pulse spike.

Modeling of the breakdown initiated on metal (Al) surface defects was first examined by **Weyl et al. (1980)**. This model assumes a three-part event sequence, following laser energy deposition: 1) evaporation of thermally insulated metal flakes, 2) laser induced breakdown in the metal vapor with a 1-D expansion, and, 3) breakdown with a 3-D expansion of the vapor in later times. It is stipulated that breakdown threshold depends on the ratio of vaporization temperature to the ionization energy, which in turn determines the initial electron concentration required for the inverse Bremsstrahlung -- and it is time dependent, varying with the incident irradiance, as shown in **Figure 2.1**. If the breakdown is sufficiently rapid ($I > 10^8$ W/cm² for Al at 10.6 μm) the expansion can be treated as one-dimensional. For lower intensities, three-dimensional effects become important due to previous over expansion of the vapor and later onset of the breakdown in the vapor behind the shock.

The presence and size of defects (flakes) depend on the mechanical properties and method of preparation for the surface; both play pivotal roles in the surface-initiated breakdown process. Surface preparation has proven important in recent experiments performed at RPI with aluminum Lightcraft engines that demonstrated higher impulse from increasing the surface roughness (by sanding) around the laser focus. A simple explanation for this effect can be postulated: With a reduction in initial breakdown energy, a larger portion of the total incident laser energy is deposited into the local air plasma, thus increasing the subsequent blast wave's strength. Faster breakdown times means less laser energy reaches the surface prior to the onset of absorption by the

attached gas layer. Enhanced early breakdown might also reduce wall heating at the focus; however, future research must verify this hypothesis.

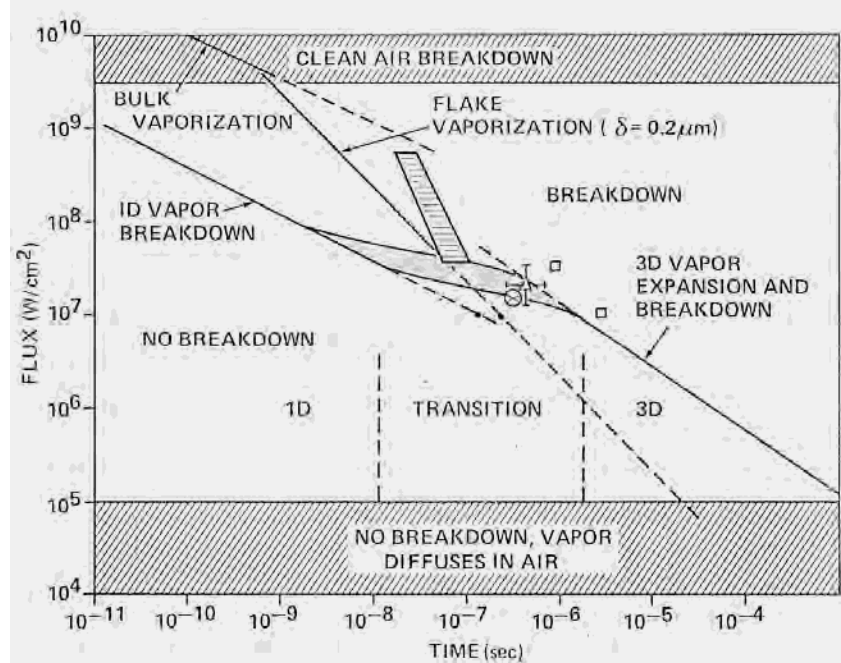


Figure 2.1: Breakdown threshold dependence on incident radiation for Al at 10.6 μm , and characteristics times for breakdown initiation. Weyl et al. (1980).

The laser energy spent on electrical breakdown of the aluminum surface can likely be neglected in the present experiments, even though the laser focus “burn” (about 1 mm wide and 12.5 cm long—a surface area of only 1.25 cm^2) upon the shroud is clearly distinguishable after several laser shots. At the irradiances necessary for flake vaporization, $I > 10^9 \text{ W/cm}^2$, only 10^{-9} s (see Fig. 2.1) is invested on breakdown or about 1/100th of the energy available in the $\sim 100 \text{ ns}$ pulse width (FWHM) obtained in the present experiments. Hence, the inner surface of the shroud serves not as an ablatant, but as a catalyst for enhancing surface air-breakdown—a kind of “spark plug” that ejects free electrons into the gas to trigger air breakdown and expedite the ignition of LSD waves. Close examination of the focal burns during the present campaign reveals that negligible mass had been ablated from the shroud along the focus.

2.2 Post-Breakdown Phenomena and Absorption Waves

Following the initial stages of plasma formation, several transient phases take place throughout the plasma evolution sustained by the laser, during the pulse. The nature of

the plasma and resulting effects over the ignition surface are a function of the ambient atmosphere, irradiance, pulse duration, and wavelength. Depending on these parameters, three types of plasma waves can be observed to propagate into the surrounding atmosphere: 1) Laser Supported Combustion (LSC) waves; 2) Laser supported Detonation (LSD) waves; and 3) Laser Supported Radiation (LSR) waves. These three different absorption waves can be distinguished on the basis of their propagation velocity, pressure and expansion process during the subsequent plasma evolution process.

Following the hot vapor formation and initial plasma generation over a surface, the plasma becomes strongly absorbing and interacts with the surrounding air in two ways (**Root, 1989**): 1) rapid expansion of the high pressure vapor, driving a shock wave into the atmosphere, and 2) energy transfer to the atmosphere by a combination of thermal conduction, radiative transfer (i.e., re-radiation), and shock wave heating. For the high laser irradiance levels encountered throughout the present research, shock heating of the adjacent atmosphere dominates as adjacent gases that were previously transparent to the beam (when cold), start to absorb the laser radiation.

With the creation of an absorbing gas layer, the plasma becomes a fully developed propagation wave, absorbing most of the laser energy in its advancing front while shielding the remaining plasma from direct laser interaction. Such absorption waves propagate towards the laser source until the beam is terminated, or the irradiance falls to levels insufficient to support the absorption wave (**Raizer, 1977**).

The general configuration of an absorption wave is sketched in **Figure 2.2** (applicable to all 3 types) which identifies the principal zones and their evolution in time. Radial expansion of the plasma is always present but can be considered negligible in comparison with the axial plasma propagation effects; however, when the rarefaction waves begin to coalesce into the central axis, they dominate the evolution of the plasma at the surface. The radial expansion effects upon the propagation zone front (if any) are dependent on the nature of the propagation mechanism (i.e., LSC, LSD, or LSR).

Table 2.1 summarizes the main differences between these three absorption wave propagation regimes. **Figures 2.3** and **2.4** give idealized, qualitative illustrations of the differences in a one-dimensional reference frame, highlighting the distinct gasdynamic

regions (from ambient to the wall) and dominant characteristics of each type, together with variations in gas velocity, pressure, temperature, and density. Although highly idealized representations, they still provide a clear first-order representation of the underlying physics.

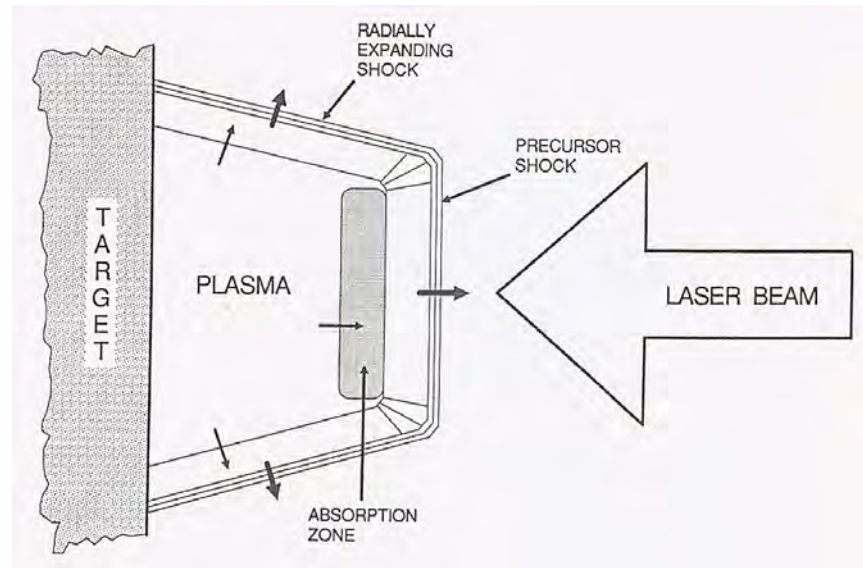


Figure 2.2: Absorption wave zones of a laser supported plasma from a metallic surface. (Root, 1989)

Table 2.1: Laser-supported absorption wave propagation modes (10.6 μm radiation).

Propagating Absorption Wave	General Features
LSC – Laser Supported Combustion	<ul style="list-style-type: none"> - Low laser Irradiance ($I < 10^7 \text{ W/cm}^2$); - Precursor shock separated from centimeters-thick absorption zone and plasma; - Analog to 1-D chemical deflagration wave; - LSC wave advances at supersonic speed in the laboratory frame, but subsonic relative to precursor shock; - Thermal conduction and radiation as propagation mechanisms; - Equilibrium heating process.
LSD – Laser Supported Detonation	<ul style="list-style-type: none"> - Occurring at intermediate irradiance levels ($10^7 < I < 10^9 \text{ W/cm}^2$); - Millimeters-thick absorption zone follows directly behind precursor shock, with shocked gas at sufficiently high temperature to absorb laser energy directly → analog to chemical detonation wave; - Supersonically advancing LSD wave; - Non-equilibrium heating process (two temperature gas; electrons @ 2-3+ ev) gives lower temperature ions and neutrals than with LSC waves.
LSR – Laser Supported Radiation	<ul style="list-style-type: none"> - Highest level of irradiance ($I > 10^9 \text{ W/cm}^2$); - Ambient gas heated to light absorption temperatures prior to shock arrival; - Low pressure increase, but high temperature increase (taking place at constant pressure); - Non-equilibrium heating process (two temp. gas)

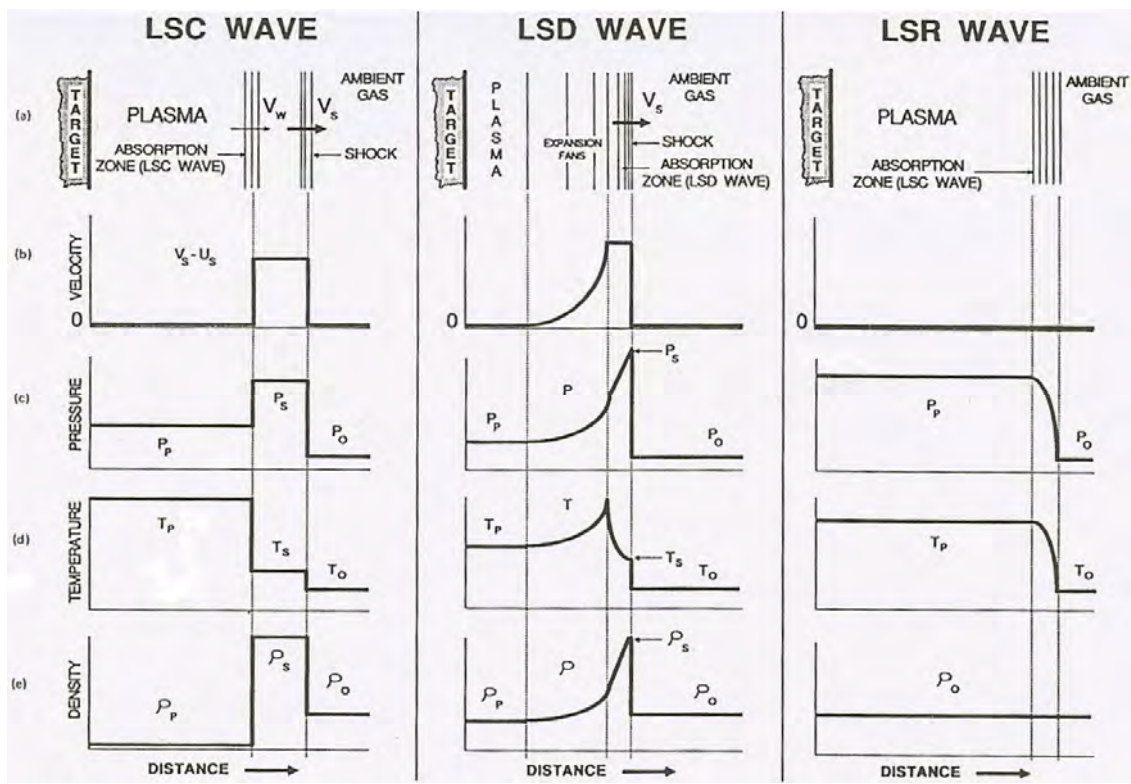


Figure 2.3: One-dimensional propagating plasma regions following laser absorption waves. (Root, 1989)

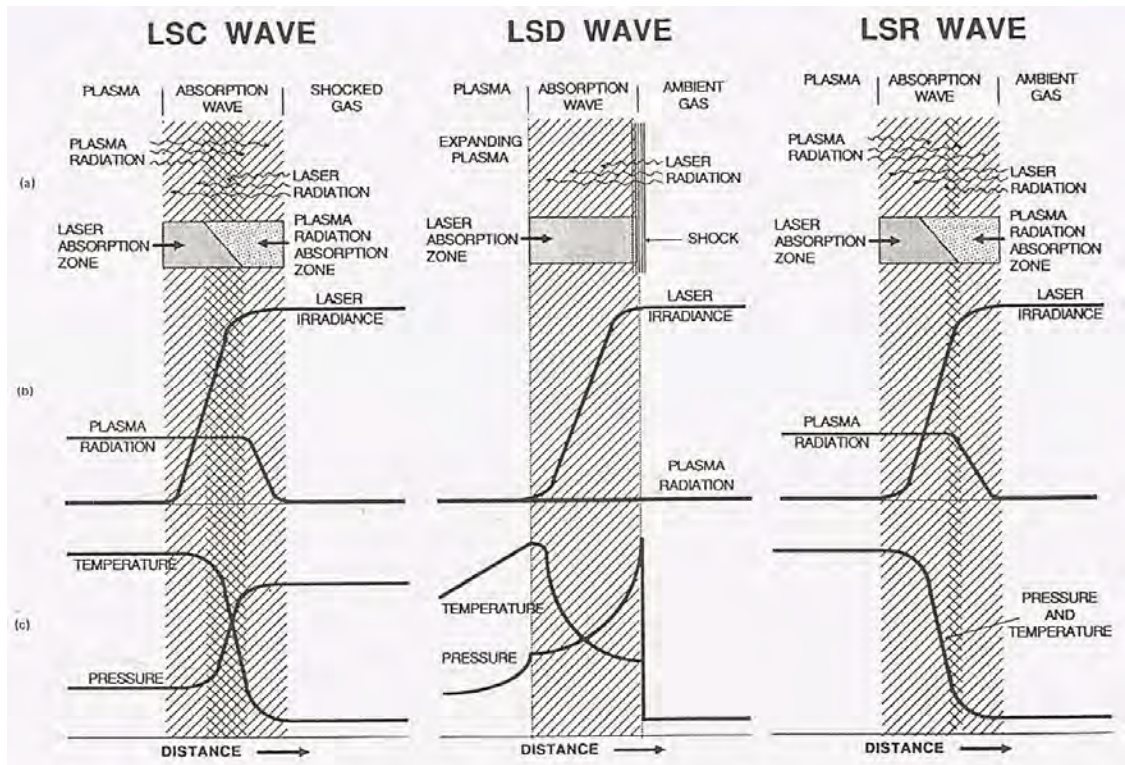


Figure 2.4: Absorption regions of the one-dimensional waves. (Root, 1989)

Previous studies on laser-supported absorption waves ignited off aluminum surfaces have observed the onset of LSC waves in irradiance levels as low as $3 \times 10^4 \text{ W/cm}^2$ for CO₂ lasers at 10.6 μm (**Reilly et al., 1979**). In the present experiments, an analysis of our Lumonics TEA622 laser pulse profile shows that intensities in the order of 10^8 W/cm^2 are achieved at the line focus, throughout most of the pulse. Henceforth, it can safely be assumed that LSD waves are the only powered type of absorption waves taking place here.

Raizer (1965) was first to model LSD wave propagation by comparing it to a chemical detonation wave, wherein the laser heats up the gas immediately behind the advancing shock wave, until the local gas velocity becomes sonic at the Chapman-Jouget (C-J) point. LSD wave propagation speed is determined by laser energy deposited between the shockwave and the C-J point; behind the C-J point the behavior is uncoupled, with no effect on the propagating plasma.

Initial gas/plasma properties before the rapid absorption are given by the shock wave jump conditions. LSD plasma conditions can be assessed by assuming conservation of momentum, mass and energy at the C-J point, and the complete absorption of laser power. Here, the shock velocity V_s is identical to the LSD wave speed, as given by (**Raizer, 1965, 1966, 1977; Zeldovich and Raizer, 1966; Root, 1989**)

$$V_s = \left[\frac{2(\gamma^2 - 1)I_0}{\gamma + 1} \right]^{1/3} \quad (2.5)$$

The LSD wave properties are characterized by their values at the C-J point, with the density (ρ_s), pressure (p_s) and enthalpy (h_s) given as

$$\rho_s = \frac{\gamma + 1}{\gamma - 1} \rho_0 \quad (2.6)$$

$$p_s = \frac{\rho_0 V_s^2}{\gamma + 1} = \frac{\left[2(\gamma^2 - 1)I_0 \sqrt{\rho_0} \right]^{2/3}}{\gamma + 1} \quad (2.7)$$

$$h_s = \frac{2}{(-1)(+1)^2} V_s^2 \quad (2.8)$$

For an LSD wave propagating away from a wall, the effects of that surface must be included. Behind the C-J point, expansion fans will appear which permit the gas velocity to drop to zero at the wall (**Pirri, 1973, 1978; Reilly et al., 1979**). These properties at the wall are determined by isentropic expansion through the rarefaction waves, with the values at the wall given by

$$p_w = p_s \left(\frac{+1}{2} \right)^{\frac{2}{-1}} \quad (2.9)$$

$$w = s \left(\frac{+1}{2} \right)^{\frac{2}{-1}} \quad (2.10)$$

$$h_w = h_s \left(\frac{+1}{2} \right)^2 \quad (2.11)$$

Although the above equations neglect real gas effects (excitation, dissociation and recombination) and heat transfer losses, they nonetheless provide insight to the essential physics. In the present research, these equations enable first-order initial estimates for the surface pressures near the focal line on the Lightcraft shroud, which drove the selection of pressure transducers purchased for the present 2D laser scramjet experiments.

Root (1989) also notes that his theoretical models do not account for laser beam angle of incidence relative to the surface. His one-dimensional analysis assumes that both the LSD wave and leading shock propagate away normal to the target surface, whereas at later times when the initial transient from plasma initiation has died out, the LSD wave propagates up the beam axis towards the laser source.

Likewise, in the present 2D laser scramjet experiments, breakdown occurs at the shroud undersurface, subsequently igniting a LSD wave that cuts a wedge-shaped swath across the supersonic inlet in roughly 1.5 μs (i.e., the laser pulse duration); the laser

beam centerline is oblique to the shroud undersurface. This LSD-wave powered portion of the laser propulsion cycle, resembles a pulsed “planar heater” (wedge-shaped, actually) that slices across the supersonic inlet air working fluid, producing a strong blast wave that subsequently expands and decays during the unpowered portion engine cycle. This unpowered blast wave expansion is responsible for the great majority of the impulse generation in this pulsed detonation engine. The extremely high pressure LSD wave momentarily acts on only a very small region/volume of absorption chamber air, over a time span orders of magnitude shorter than that of the unpowered blast wave expansion.

2.3 Analytical Model of Surface Pressure History and Impulse Generation

Presented below is a first-order theoretical analysis of the laser-induced pressure distribution across a flat impulse surface, analogous to the thruster surface considered in the present pulsed LP scramjet experiments. This theory will later be applied to the analysis of pressure transducer data acquired in the initial experiments carried out under static (i.e., no flow) conditions. A more extensive and general development of the theory for laser-generated impulse, imparted to a surface under static atmospheric conditions, can be found in the works of **Pirri (1973)**, **Reilly et al. (1979)**, **Reilly et al. (1984)** and **Richard (1989)**.

The basic objective of the theory presented here is the quantitative prediction of the momentum coupling coefficient (C_M) in a laser irradiance regime where a Laser Supported Detonation (LSD) wave launches a subsequent unpowered blast wave that dominates the momentum transfer process. This process begins with the onset of local air breakdown at a moment $t < \tau_p$, where τ_p is the laser pulse duration, followed by the LSD wave propagation and extinction at τ_p . The impulse generated during this process is small due to the short, $\sim 1\mu\text{s}$ pulse duration, as will be shown later. Following next, is the unpowered blast wave expansion, driven by the piston-like behavior of the LSD wave, wherein the impulse magnitude can be calculated from the gas dynamic motion of the relaxing blast wave using self-similar relations. As initially developed by **Pirri (1973)**, the blast wave motion is modeled by matching an analysis of the one-dimensional shock

dynamics to the relaxing blast wave model, including two-dimensional expansion effects, as described in **Reilly et al. (1979)**. The surface pressure and impulse are then calculated as a function of time as the blast wave propagates over and away from the flat impulse surface.

The dominant time scale in the problem is the total time (τ_0) over which impulse is delivered to the surface. Under the action of the laser pulse, the initial motion of the LSD wave can be modeled as one-dimensional propagation, turning into a two-dimensional propagation once the leading edge of the rarefaction fan initially at the laser spot edge, propagates to the centerline. This characteristic time is given by

$$\tau_{2D} = \frac{R_s}{V_s} \quad (2.12)$$

where R_s is the spot radius and V_s is the LSD wave speed. Slightly different definitions are given for the value of τ_{2D} in the literature.

Thus, the impulse delivered to the thruster surface consists of the combined contributions from a) when the laser pulse is on, and b) after the laser pulse has terminated. While the laser pulse is on ($t \leq \tau_p$), the impulse contribution per unit area can be given by

$$\frac{I}{A} = \int p dt = p_w t \quad (2.13)$$

For short pulses ($\tau_p < \tau_{2D}$), the relaxation is assumed to take place in a one dimensional form until $\tau_p = \tau_{2D}$, with the propagation becoming two-dimensional before the gas pressure decays to ambient. **Pirri (1973)** and **Reilly et al. (1979)** adopt a two-dimensional model for the initial blast wave propagation assuming a circular spot area over the surface leading to a cylindrical high pressure plasma generated by the one-dimensional LSD propagation towards the laser source. The unpowered cylindrical expansion laws developed by **Sedov (1951)** are then used to model the blast wave expansion and relaxation: i.e., the surface pressure versus time history.

Richard (1989) uses the same cylindrical blast wave expansion laws, but models the plasma formation along a line focus lying on the impulse surface (see **Figure 2.5** below), assuming this LSD-generated plasma takes on a horizontal semi-cylindrical

geometry over the impulse (target) surface. An unpowered blast wave is then assumed to be launched from the leading edge of the LSD wave upon laser pulse termination. This geometrical configuration more closely resembles to the impulse generation geometry in the present Lightcraft engine experiments. The two cylindrical configurations are compared in **Figure 2.5** below.

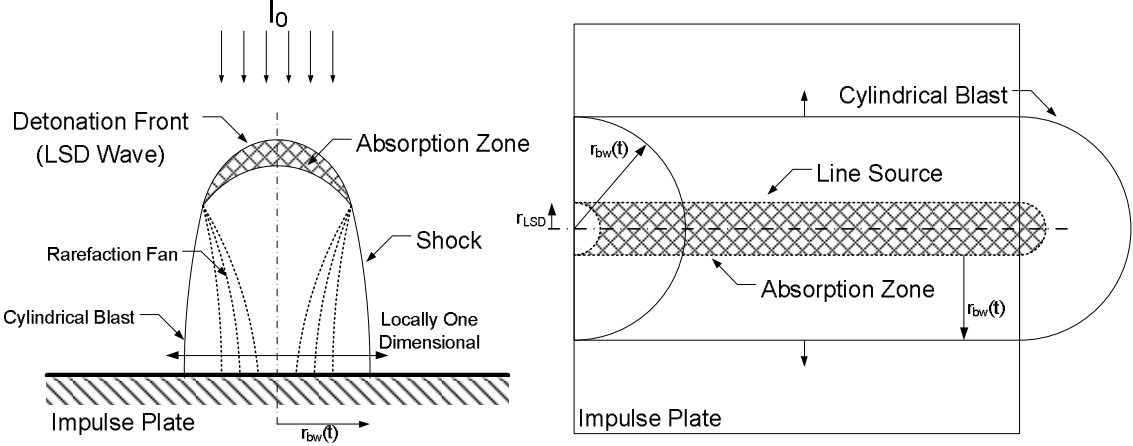


Figure 2.5: Cylindrical blast wave expansion models. Left: vertical oriented axis; Right: horizontal oriented axis (following laser-induced surface breakdown).

Then $t = \tau_{2D}$, the surface pressure for the case of $\tau_p \leq \tau_{2D}$ can be defined as

$$P_w(\tau_p \leq \tau_{2D}) = p_w \left(\frac{\tau_p}{\tau_{2D}} \right)^{\frac{2}{3}} \quad (2.14)$$

And when $t > \tau_{2D}$, Sedov's (1973) cylindrical blast-wave theory predicts

$$p_w(t) = P_w(\tau_p \leq \tau_{2D}) \left(\frac{\tau_{2D}}{t} \right)^{\frac{1}{3}} \quad (2.15)$$

Hence, the total impulse per unit area over the impulse surface, assuming $\tau_0 \geq \tau_{2D}$ and $\tau_p \leq \tau_{2D}$, can now be calculated as

$$\begin{aligned} \frac{I}{A} &= p_w \tau_p + p_w \tau_p^{\frac{2}{3}} \int_{\tau_p}^{\tau_{2D}} t^{-\frac{2}{3}} dt + P_w(\tau_p \leq \tau_{2D}) \int_{\tau_{2D}}^0 t^{-1} dt \\ &= p_w \tau_p \left\{ 1 + 3 \left[\left(\frac{p_w}{P_w(\tau_p \leq \tau_{2D})} \right)^{\frac{1}{2}} - 1 \right] + \left(\frac{p_w}{P_w(\tau_p \leq \tau_{2D})} \right)^{\frac{1}{2}} \ln \left(\frac{P_w(\tau_p \leq \tau_{2D})}{P_\infty} \right) \right\} \end{aligned} \quad (2.16)$$

A schematic of the model for surface pressure versus time is presented by Pirri (1973) and is reproduced below in **Figure 2.6**. When $\tau_p < \tau_{2D}$, the surface pressure is p_w until $t = \tau_p$, with the pressure decay following Sedov (1959) planar blast wave model until $t = \tau_{2D}$. For $t > \tau_{2D}$, the surface pressure decays with time following Sedov's cylindrical blast wave model. For long pulses where $\tau_p \geq \tau_{2D}$, the surface pressure is p_w until $t = \tau_{2D}$, following the cylindrical decay model afterwards.

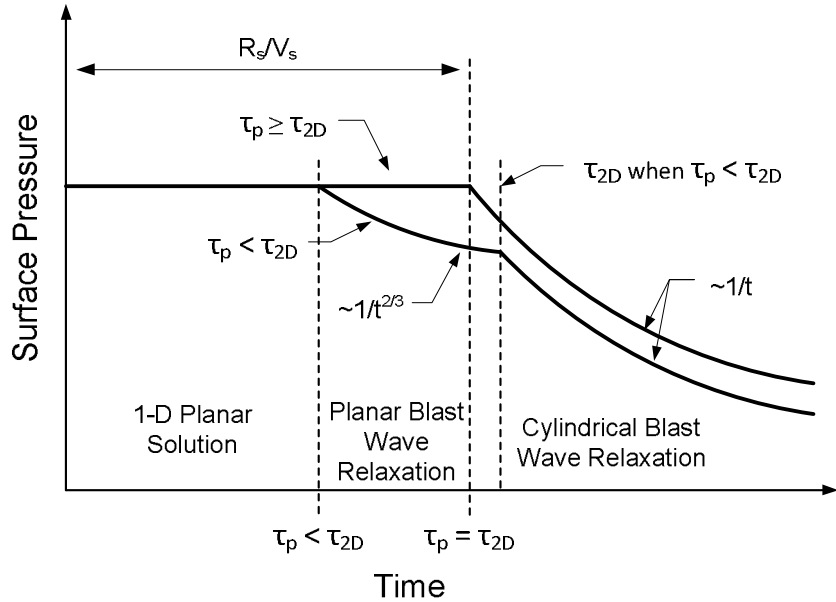


Figure 2.6: Surface pressure vs. time evolution, showing characteristic times. (Pirri, 1973)

A calculation was also performed for the impulse and coupling coefficient for the case of a finite diameter target surface. With a finite target, the blast wave pressure is not relaxed to atmospheric before “spilling” around the target’s periphery. Here a new characteristic time is introduced: τ_D , which is the time taken by the cylindrical blast to reach the edges of the target—given by

$$D = 2D \left(\frac{r_T}{r_s} \right)^2 \quad (2.17)$$

With r_T and r_s being the radius of the target and the radius of the laser spot, respectively. When $t > \tau_D$, the initial force is no longer preserved, due to the decaying pressure across the finite (constant) target area. Hence, the total impulse for a finite target size when $\tau_p \leq \tau_{2D}$ and $\tau_0 > \tau_D$, is then given by

$$\begin{aligned}
I_{total} &= A_s \int_0^{2D} p_s(t) dt + \int_{2D}^D \int_0^{r_{bw}} p_s(t)(2-r)dr dt + A_T \int_D^0 p_s(t) dt \\
&= A_s p_w \left\{ 1 + 3 \left[\left(\frac{p_w}{P_w(p \leq 2D)} \right)^{1/2} - 1 \right] \right\} + P_w(p \leq 2D) A_s \left[- \frac{A_T}{A_s} \int_{2D}^0 \ln \left(\frac{0}{D} \right) dt \right] \quad (2.18)
\end{aligned}$$

with r_{bw} as the radius of the cylindrical blast wave, and A_s and A_T being the laser spot area and target area, respectively. The momentum coupling coefficient can then be calculated from $C_m = I_{total}/E_p$, in which the laser pulse energy is $E_p = A_s I_0 \tau_p$.

Slightly different results are obtained by **Richard (1989)**, where cylindrical blast wave relations were used to calculate the impulse on a horizontal line focus case, as described earlier. The equation describing the total impulse in this particular situation being

$$I_{total} = A_s p_s \int_{2D}^0 \left\{ 1 + 2 \left[\left(\frac{p_s}{P_\infty} \right)^{1/2} - 1 \right] - 2 \left(\frac{p_s}{P_\infty} \right)^{1/2} - \left(\frac{P_\infty}{p_s} \right) \right\} dt \quad (2.19)$$

These analytical formulations will be applied next in analyzing experimental pressure transducer data obtained from the present test campaign.

3. Experimental Apparatus and Procedure

The LP experimental setup involved a Hypersonic Shock Tunnel (HST), one CO₂ laser, a 2-D cross-sectional LightCraft model, and requisite instrumentation/data acquisition system. Accurate triggering of all events was mandatory since the entire HST test window was typically ~ 3.0 ms depending on the desired HST flow condition, whereas the laser energy deposition time (~ 1 μ s) and subsequent blast wave expansion (~ 200 μ s) were substantially shorter. A more detailed description of the experimental setup is given below.

3.1 Hypersonic Shock Tunnel

This experimental research was carried out at the Henry T. Nagamatsu Laboratory for Aerothermodynamics and Hypersonic (HTN - LAH) in Sao Jose dos Campos, Brazil, using the T3 HST facility to drive hypersonic flow over a 2-D LightCraft model for pulsed laser scramjet tests. The physics of shock tunnels is comprehensively covered in several references such as **Liepmann & Roshko (1964)**, **Lukasiewicz (1973)**, **Anderson (1990)**, and **Nascimento (1997)**, and won't be addressed further here except for a general technical description of the T3 facility. A more thorough introduction to Hypersonic Shock Tunnels is given in **Appendix C**, which includes the theory and modeling of impulsive HST flows. **Figure 3.1** shows the T3 hypersonic tunnel in the HTN-LAH laboratory.

The T3 tunnel enables test section flow conditions varying from low to high enthalpies, simulating Mach numbers from approximately 6 up to 15, by replacing the nozzle throat and exit sections and varying the driver section pressure and gas composition (i.e., dry air for low enthalpy runs, and helium for higher enthalpies). For this particular HST, test times vary from 2 to 10 ms, with longer test times for lower Mach numbers. The tunnel can generate flows with enthalpies up to 10 MJ/kg, with reservoir pressures up to 25 MPa, which leads to stagnation pressures up to 200 atm and stagnation temperatures up to 7500 K in the test section.



Figure 3.1: T3 Hypersonic Shock Tunnel at the HTN-Laboratory of Aerothermodynamics and Hypersonics.

This tunnel is composed of a 4.08 m long driver section that can operate at pressures up to 35 MPa (5000 psi, 345 bar), even though in the present experiment most test runs were performed with 3000 psi of filling pressure. A double diaphragm section (DDS) is placed between the driver and driven sections. The DDS houses four solenoid valves and the stainless steel diaphragms that control the exact moment of the experiment initiation; a third diaphragm can be used to operate the tunnel in the Gaseous Piston mode if required (Nascimento, 1997). This DDS section is usually filled at half of the driver's pressure and once this section is rapidly vented by activating the solenoid valves, the higher differential pressure forces the rupture of both diaphragms and hence, the onset of HST operation. Argon was selected for DDS working fluid since it is an inert gas with high molecular weight, which helps to prevent gas diffusion between the (Helium/Air) contact surface formed after the diaphragms burst.

A contraction region is placed just downstream of the DDS which reduces the diameter of the driver section to match that of the driven, reduced from 190.5 mm to 127

mm; this produces a stronger shock wave than the same driver-to-driven pressure ratio could produce in a comparable, constant-area shock tube.

The driven section is 10.5 m long with 127 mm internal diameter, and its downstream nozzle-end is strengthened to serve as a “reservoir” for the high pressure reflected region, when operated in the reflected mode. Instrumentation ports are distributed along the entire length of the tunnel to accommodate all diagnostics required for a given experiment. In the present work, this section was fitted with three pressure transducers, two of which were separated 400 mm apart and used to measure the incoming shock wave speed. The third pressure transducer, installed at the end section close to the diverging nozzle entrance, was used to measure the reservoir pressure as well as to trigger the remaining test equipment, including the Cordin high speed digital camera, the Lumonics 622 CO₂ laser, and the data acquisition system. Installed at the downstream end of the driven section is an aluminum diaphragm that separates this section from the evacuated dump tank. Upon the arrival of the incident shock wave, this diaphragm breaks from the sudden pressure increase, and releases the shock-compressed test gas into the nozzle section.

The convergent-divergent nozzle section comprises a replaceable “throat” insert and 15° half-angle, multi-section conical nozzle. For most experiments performed in the present research, the last nozzle section was removed to decrease the standard 610 mm exit diameter (which gives an ideal Mach number of 10.0), down to 491.0 mm for an ideal Mach number of 9.12. The nozzle resides inside an evacuated, two-segment dump tank; the hypersonic flow exits into a horizontal 1.8 m diameter by 1.26 m long segment (containing the test section), joined to a vertical segment measuring 1.89 m diameter by 4.35 m tall. The test section is fitted with a horizontal hollow sting mount (designed to support test models) that also provides a 20 cm (clear-aperture) beam tube for laser beam injection. An anodized aluminum infra-red (IR) window mount had to be designed, constructed, and installed onto the external end of this hollow sting (see **Figure 3.2**), and fitted with a 2 inch thick NaCl window.



Figure 3.2: Hollow HST sting with IR window and mount installed.

The test section/dump tank is equipped with four orthogonally-placed ports with 50 cm aperture for optical diagnosis (e.g., Schlieren visualization) and instrumentation feed-throughs. The top and bottom ports are strong enough to support heavy models, as in the current research, and also provide electrical feed-throughs for instrumentation such as pressure and heat transfer gages. In the present experiments the test section side ports were fitted with 30 cm quartz windows for maximum quality Schlieren photographs.

The T3 tunnel was a recent acquisition of the HTN-LAH so a few operational issues were still being addressed, and had to be tackled during the present campaign. One such issue was the lack of HST nozzle inserts that could permit operation at Mach numbers other than 10; this was resolved by the design and machining of five new stainless steel throat inserts for nominal Mach numbers of 6, 7, 8, 12, and 15.

Two new batches of stainless steel plates of the proper thickness were acquired for DDS diaphragm manufacture, with slightly different material compositions and thus different rupture dynamics. DDS diaphragms must be cross-cut machined (i.e., crucifix pattern) into the downstream-facing surface to enable them to burst open in the desired manner, with the creation of four petals (see **Figure 3.3**, central image). An incorrect cut depth (i.e., too deep) might lead to petal detachment and acceleration downstream through the driven tube, with fragments passing through the small HST nozzle throat and

impacting the model at ballistic speeds, often causing severe damage. Several test runs were performed with the two families of diaphragms until the right cut depth was found, as will be explained later. Furthermore, to reduce the risk of detached diaphragm petals damage, a “petal catcher” was designed and manufactured, as shown in **Figure 3.3** (left); at the far right is a pre-scored diaphragm, along with a burst diaphragm (center).



Figure 3.3: ‘Petal catcher’ (left), and stainless steel diaphragms (right).

The turnaround time for the experiments performed at the T3 facility is approximately 6 hours, including: a) replacement of used diaphragms at DDS and nozzle sections, b) purge of the residual gases, c) refill of driver and driven sections with new ‘gas loads’, and d) vacuum purge of the test section dump tank. Future improvements to this facility will greatly reduce this turnaround time, allowing multiple experiments in a single day.

3.2 Lumonics TEA-620 Laser and Beam Propagation

Pulsed infrared laser energy was supplied by one of the two Lumonics TEA-620 CO₂ lasers available, which share the same resonator cavity. An attractive feature of these TEA-620 lasers is their ability to deliver a very short ($\sim 1 \mu\text{s}$), high energy pulse, up to 500 J each, while operating in the stable resonator mode with peak powers of 2.2 GW, according to the manufacturer. In the unstable resonator mode used throughout this work, the TEA-620 has a small output beam divergence measured in the sub-miliradian

range, with pulses up to 300 J. Concerns about the limited lifespan of the high voltage capacitors (8 per laser), and the potential damaging effects of supply-side over-voltage oscillations—all led to conservative decision to operate the 620s at 65 to 70 % of their rated maximum capacitor charge of 100 kV; higher supply voltages produced frequent electric arcs, and lower voltages, inconsistent glow discharges. This decision reduced the 620's available output laser energy to approximately 150 to 230 J/pulse, but greatly increased reliability.

Note that both 620 lasers are now “on line” and they can be fired sequentially for multi-pulse LP experiments to examine the interaction of two laser-induced blast wave within a laser scramjet engine, under simulated ultra-high PRF conditions (e.g., 10 to 20 kHz). However, throughout the present campaign technical issues with one capacitor bank put it out of commission. Future experiments will be able to take advantage of the two lasers operating together. **Table 1** shows the basic operating conditions for each TEA-620 operating as a standalone unit, assuming 90kV for the charging voltage.

Table 3.1: Basic operating conditions of Lumonics TEA 620 laser (stable resonator mode).

Electrode Gap	200	mm	Capacitor	0.15	μF ea.
Electrode length	600	mm	# Caps	2	/ stage
Charging Voltage	90	kV	# Stages	4	/ Marx
Electrical Energy	4860	J	Total C	0.075	μF
Rep rate	0.03	Hz	Power input	145.8	W
Discharge volume	24	liters	FWHM	~100	ns
Energy density (input)	202.5	J/l			
Electric Field	18	kV/cm			
Output Energy(Photons)	500	Joules			
Electrical Efficiency	0.1029				

Lumonics TEA 620 lasers can operate with several different gas mixtures that produce different laser output pulse profiles and energies. The lasers currently operate in a “flow-through,” open-cycle mode wherein the gas mixture is controlled by varying the flow rate of each gas constituent; in the future, the system will likely be converted to closed-cycle operation, aided by an existing catalytic converter. Throughout the present test campaign a high gain (HG) mixture was used, which produced a short ~1 μs pulse with a higher fraction of the pulse energy contained in the initial ~90 ns spike than in the

long tail. The laser pulse characteristics achieved with this HG mixture are displayed in **Table 3.2**.

The physics and operating principles for TEA CO₂ lasers can be found in several useful references (**Patel, 1968; Siegman, 1986; Svelto, 1998 and Verdeyen, 1994**), and need not be addressed further here.

Table 3.2: Lumonics TEA-620 laser pulse characteristics with high gain gas mixture.

<i>Parameter (units)</i>	<i>Value</i>
Energy per pulse, J	150-230
Wavelength, μm	10.6
Peak pulse duration (FWHM), ns	90-100
Maximum peak power, MW	~1800
Total pulse duration, μs	~1.0
HG gas mixture flow, ft^3/hr	16.0 He; 6.5 CO ₂ ; 3.2 N ₂
Power supply voltage, kV	65-70

These TEA lasers were shipped from the United States to the HTN-LAH laboratory in Brazil in dire condition, basically having been ‘mothballed’ since mid- 1980s being last used as amplifiers in the “Paladin” seed laser that fed the Induction-LINAC Free Electron Laser (FEL) experiment at Lawrence Livermore National Laboratory (LLNL). Hence, for the present campaign, the laser optics had to be designed for the 622-TEA unstable resonator configuration, wherein the same resonator cavity shared by both 620 modules. An *unstable* resonator was selected over the *stable* resonator configuration for one principal reason: i.e., the elevated mezzanine planned for the 622 installation placed them at a distance of ~25 meters from the HST test section, which demanded the lower divergence beam from an unstable resonator, even though the output pulse energies were lower (e.g., 320J vs. 500J from each 620 module).

The unstable resonator optics for the 622 configuration (see **Figure 3.4**) are comprised of a large concave parabolic mirror (the primary reflector) and a smaller convex parabolic mirror or output-coupler, separated by 3.75 m length; the cavity encompasses both 620 modules that are precisely positioned, in line, upon two steel rails. The aluminum primary reflector is 254 mm (10”) in diameter and 50.8 mm thick,

diamond turned to a concave geometry with 15 m surface radius. The output coupler is a 120 mm diameter aluminum mirror with truncated sides and 100 mm in width, diamond turned to a 7.5 m convex surface radius. Thus, these mirrors form a resonating cavity with a magnification of 2, giving a collimated output beam, as shown in **Figure 3.5**.

Sturdy welded steel support stands were fabricated for the resonator optics, and anchored firmly into the mezzanine's reinforced concrete floor (see **Figure 3.5**). These detached optic stands neatly isolated the resonator optics from shock-wave-induced vibrations from 620 laser firings that could misalign the output optics, if they had been attached directly to the laser modules and/or their support rails. This was of extreme importance since precise alignment of the unstable resonator optics is a labor intensive, time consuming process. Finally, note in **Figure 3.5** (left) that the 622 system is completely enclosed by a Faraday cage which attempted to provide an EM leak-proof envelope; displayed at the right is a typical laser beam footprint "burned" onto ThermoFax paper.

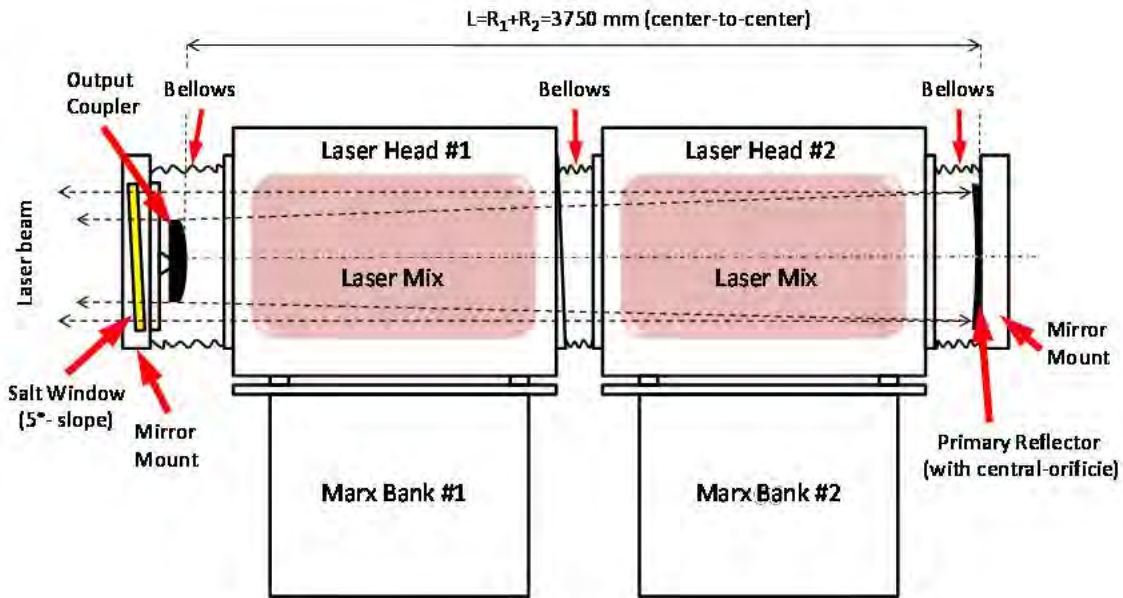


Figure 3.4: TEA 620 Laser configuration with unstable resonator cavity.

In addition to the laser resonator optics, other critical parts had to be designed, constructed, and/or acquired in order to reactivate the laser. One of these was the NaCl laser output window (transparent to 10.6 um infrared radiation, and installed into the output coupler framework) to seal off the internal laser gas mixture from infiltration and

contamination by the surrounding atmosphere. To complete the cavity isolation from the lab environment, three rubber bellows were installed: one between the two laser modules, another at the rear primary mirror, and another to seal off the output window.

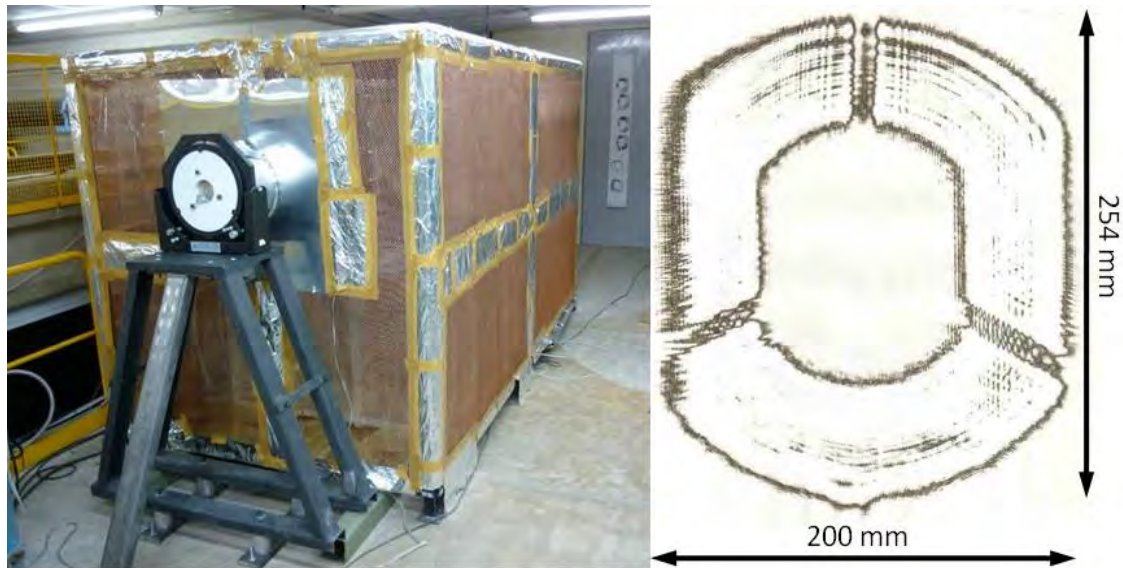


Figure 3.5: TEA 622 laser system with Faraday cage (left), and beam footprint (right).

Due to limited space available in the HTN-LAH laboratory, an adjacent elevated mezzanine was acquired for installation of the 622-TEA laser system, as mentioned earlier. Since this mezzanine was ~25 meters from the HST sting-entry window, a special “light-tight” laser beam delivery tube (made from 350 mm diameter PVC pipe) had to be erected to safely transmit laser power into the HST test section. Also, the three 45-deg. turning points in this beam tube, required 30cm diameter turning flats—additional metal mirrors that had to be designed and manufactured, and then bolted to adjustable mirror mounts.

As shown in Figure 3.6 the laser beam delivery path, starting at the 622 laser, encounters a sequence of optical elements (i.e., the “optical train”) which are arranged in the following order: First, the beam leaves the 622-TEA output coupler with a diameter of 254 mm (10 in) and arrives at the 0.75x magnification (reducing) telescope. This telescope was designed around a pre-existing 300 mm (12 in.) diameter concave copper mirror with surface radius of 10 m, and hence required the fabrication of one additional convex metal mirror. After reflecting off the concave mirror, the incident beam strikes a 228.6 mm (9 in) diameter convex aluminum mirror placed 1.25 m away, requiring a

mirror curvature of 7.5 m to regain beam collimation. This reduced aperture beam fit nicely through the three 300 mm diameter turning mirrors (placed at 45 degrees to the incident beam at the corners of the beam delivery tube in **Figure 3.6**), as well as clearing the 200 mm aperture window installed with a 7 deg. incidence at the HST hollow sting (see **Figure 3.2**).

After the reducing telescope is properly aligned to “burn” a centered ThermoFax pattern at the first turning flat, all three 300 mm flats (two aluminum and one copper) must then be precisely adjusted (in sequence, again by burning thermally sensitive paper) to deliver a centered “burn” at the HST sting-mount window. This 250 mm diameter, 50 mm thick NaCl window serves a dual purpose: 1) a physical boundary to isolate the high vacuum dump tank volume (necessary for the HST operation) from the lab environment; and, 2) a beam splitter that diverts a small portion of laser pulse energy into a calorimeter (*joule meter*)—a sensitive diagnostic unit used to precisely measure and record the delivered laser pulse energy—as well as a photon drag detector to measure the pulse profile, at every shot. This arrangement is depicted in **Figure 3.6**.

The NaCl windows reflect approximately 8% of the incident 10.6 μm beam energy, which is diverted onto a concave copper mirror of 250 mm diameter and 2 m surface radius, which concentrates the focused beam through a second NaCl window and onto a Gentec UP60N-40S-H9 thermopile calorimeter. This second oblique NaCl window (labeled #2 in Figure 3.7) diverts ~0.64% of the laser energy into a Hamamatsu B749 photon drag detector, for the measurement of the pulse profile.

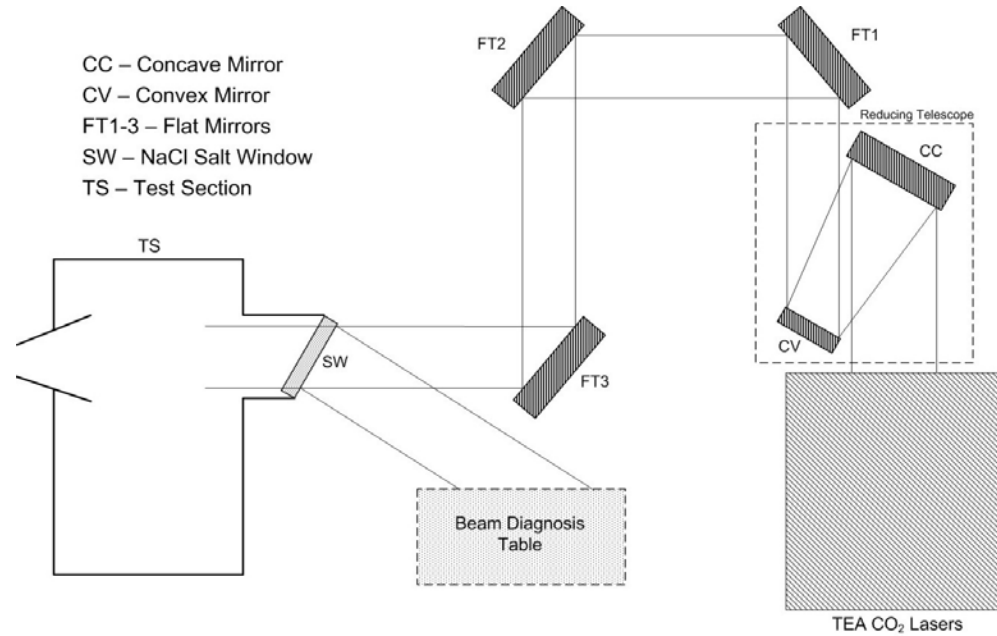


Figure 3.6: Laser beam transmission path through the laboratory to the test section.

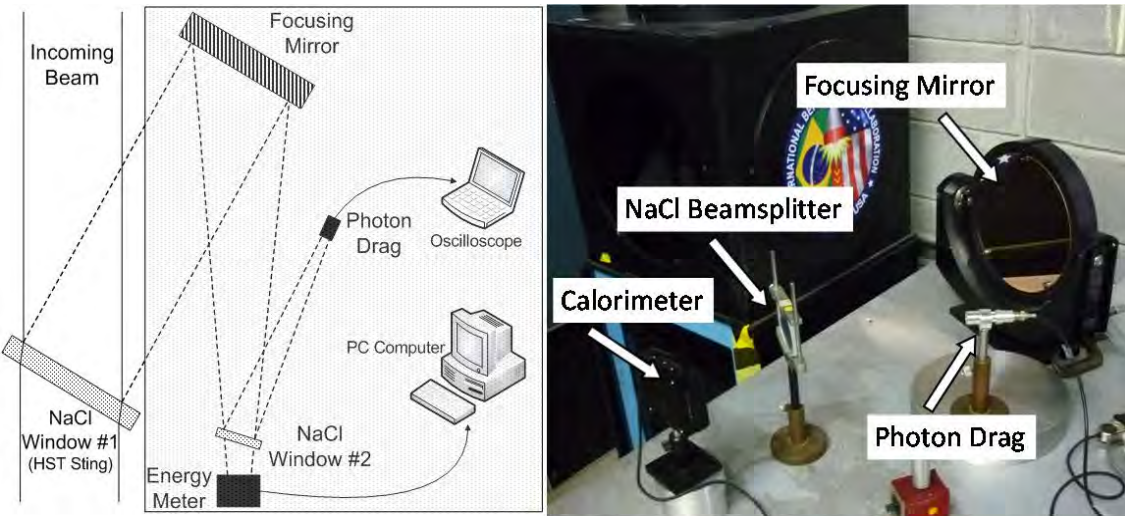


Figure 3.7: Beam diagnostics table for analyzing laser beam energy and pulse profile.

3.2.1 Laser Beam Diagnostics and Calibration

As indicated above, a beam diagnostics table was set up for measuring laser pulse energy for every test run. The following describes the calibration procedure. First, the large NaCl window/beam-splitter (see **Figure 3.2**) had to be calibrated, which required two calorimeters: 1) one placed inside the HST test section, just downstream of the 2D Lightcraft model (Scientech Astral Series S, 200 mm aperture) to capture the actual energy incident onto the test model, and, 2) a second calorimeter placed outside, near the

sting, to collect the reflected portion of the beam (Gentech UP60N-40S-H9) entering the sting window. The NaCl windows supplier specified a reflectivity of 7.5%, but the actual reflectivity was measured at 7.9%. The beam-splitter calibration plot is given in **Figure 3.8**, together with the linear fit results and corresponding instrument measurement error.

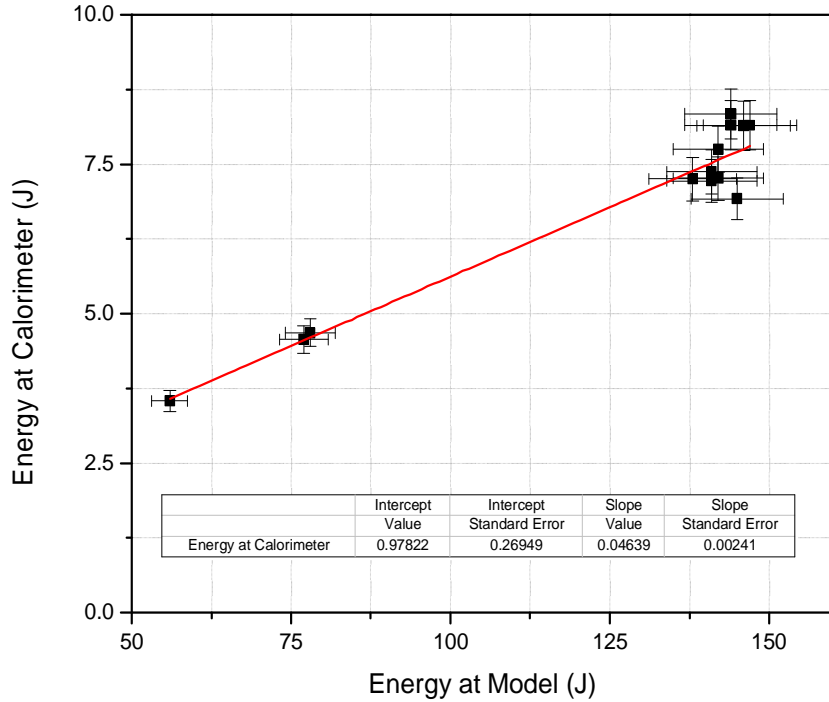


Figure 3.8: Beam-splitter energy calibration curve for NaCl sting-window.

The laser pulse profile (or time-history of irradiance) was obtained with the use of a secondary beam-splitter and a photon drag detector as mentioned above (see **Figure 3.7**). This pulse profile was obtained/ recorded at every laser shot, and is dictated by the laser kinetics for the gas composition filling the active cavity volume. It is also dependent on the final Marx bank voltage, available energy, and discharge dynamics; the Hyptronics power supply was set to either 65 kV or 70 kV for the charge.

The energy profiles sampled throughout this experimental campaign revealed little variation, because the laser gas mixture composition was kept unchanged. The pulse profile in **Figure 3.9** below indicates that approximately 70% of the pulse energy resides in the spike, with the remaining 30% in the 1.5 μ s pulse tail.

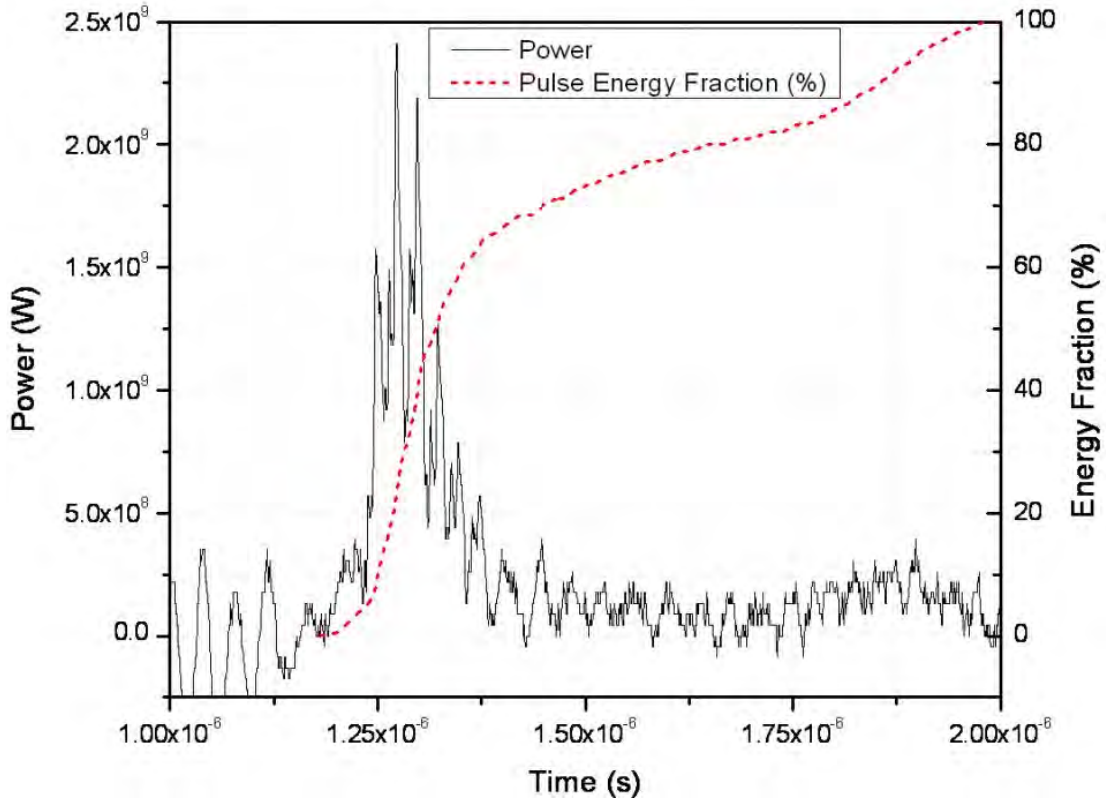


Figure 3.9: Laser pulse profile and integrated pulse energy sampled at NaCl sting-window.

3.3 2-D Cross Section Lightcraft Model

This 2-D airbreathing engine model is approximately a half-scale representation of a 1/24th annular section of the 1.4 m diameter LightCraft Technology Demonstrator (LTD) analyzed by **Myrabo (1989)** and **Richard (1989)** for the now-defunct SDIO Laser Propulsion Program, and is scaled to fit inside the HST 0.6 m T3 test section. A derivative of previous LP research performed at RPI, the 250 mm wide, 2-D aluminum model is comprised of three basic parts: i) forebody compression ramp; ii) inlet/shroud; and, iii) primary parabolic mirror/expansion surface. The external compression inlet forebody directs the captured airflow, across the shroud's flat plate (lower) impulse surface that bounds the laser absorption chamber. When the incoming laser beam is brought to a line focus (as shown in **Figure 3.10**) upon this shroud undersurface, the aluminum "igniter" material greatly lowers the incident laser intensity and fluence required to trigger the optical air breakdown, as explained in **Chapter 2**.

The geometry for this model's external compression air inlet is similar to that studied by **Richard (1989)** and reminiscent of the work performed by **Sienel (1992)**, but the length was truncated to represent only part of an actual scale nosecone in order to fit within the T3 HST nozzle. **Figure 3.10** depicts the 2-D model contour together with the position of the pressure sensors. The compression ramp section is instrumented with 3 pressure transducers (P_2 , P_3 , and P_4) distributed lengthwise along the centerline.

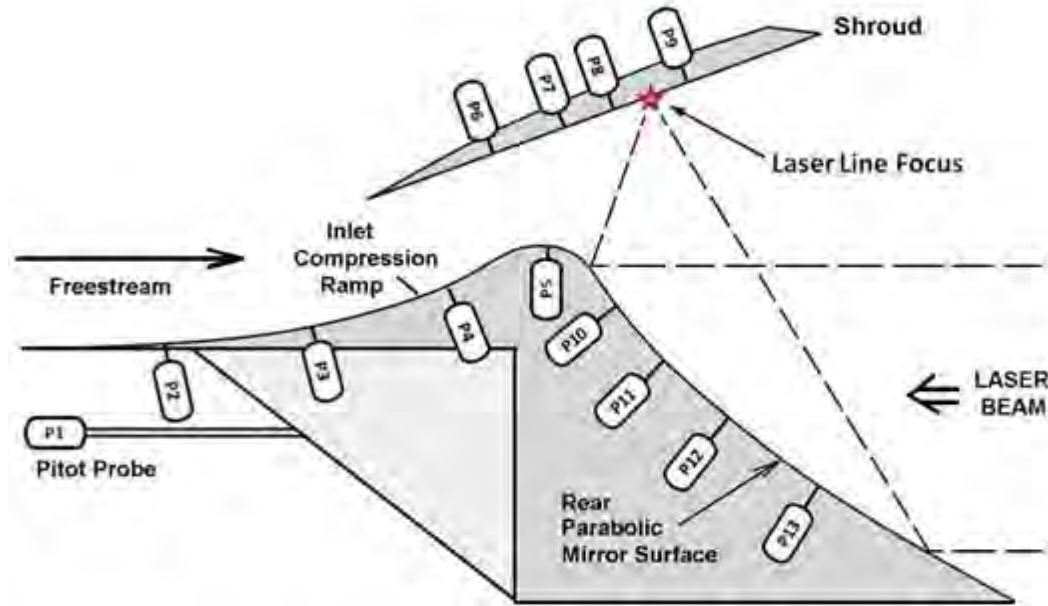


Figure 3.10: Pressure sensor positions within 2D model geometry.

Following the compression ramp, comes a smooth transition or “throat” section (fitted with P_5 in **Figure 3.10**) just upstream of the primary focusing optics. This rear parabolic reflector has three main functions: 1) focus the incoming laser beam to cause the electrical air breakdown on the shroud undersurface; 2) act as an inner lower boundary of the absorption chamber, containing the subsequent cylindrical blast wave generated by laser induced breakdown; and, 3) participate as an expansion (2D plug nozzle) surface for the blast-wave-processed engine working airflow. In this 2-D model the primary reflector is composed of a sturdy aluminum “hardback” machined with the desired parabolic contour, to which a polished OFHC copper faceplate was attached to create the 2-D mirror; this optic was designed for unrealized LP experiments proposed by **Fernandez (1990)** and by **Sienel (1992)**. The primary rear reflector was fitted with four pressure sensors (P_{10} thru P_{13} in **Figure 3.10**).

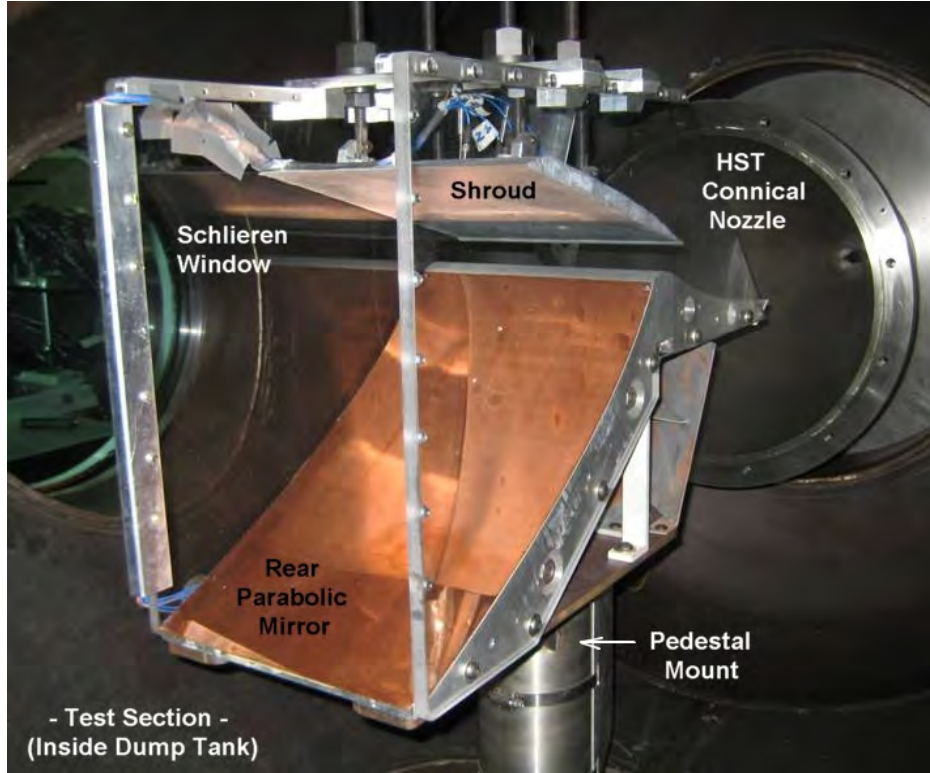


Figure 3.11: 2-D laser propulsion model installed in T3 hypersonic shock tunnel.

The 2-D shroud provides both air inlet capture and absorption chamber functions, and its shape is similar to that adopted by Katsurayama (2001-2004) in his $M=5.0$ numerical analysis, as well as the LTD's shroud contour used in the previous conceptual studies. The 2-D shroud is comprised of a simple planar inner wall, with a streamlined cylindrical exterior surface that is of lesser importance in the current experiments; the shroud was also fitted with four pressure transducers (P_6 thru P_9 in **Figure 3.10**). **Figure 3.11** shows the model installed in the HST test section.

Because of the varied test conditions that can be simulated in the HST, the 2-D laser scramjet model was designed in a modular manner so that most parts can be exchanged with the current configuration—considered the first in a series of Lightcraft engines to be tested in the near future. The shroud can be placed at different positions with respect to the model's center-body (i.e., compression ramp + primary reflector), since the mechanical support system for the articulating shroud was designed for three degrees of freedom: 1) fore and aft translation; 2) up and down translation; and, 3) free rotation for changing angle-of-attack. For the static (i.e., quiescent flow) experiments performed in this work, the laser line focus was kept at the same axial position upon the shroud

undersurface as shown in **Figure 3.12**; to change angle-of-attack for the static and initial hypersonic experiments, the shroud is simply rotated about this line focus. **Table 3.11** shows the radial distance of the sensors to the laser line focus for the initial axial shroud position. During the hypersonic experiments, the axial focal line position was varied across the shroud to accommodate desired test conditions.

Table 3.3: Pressure sensor inventory and radial distance from laser focal line at the shroud’s undersurface.

<i>Sensor</i>	<i>Radial distance from focus[mm]</i>	<i>Sensor</i>	<i>Radial distance from focus[mm]</i>
1	Pitot	8	25
2	294	9	25
3	234	10	130
4	175	11	160
5	116	12	200
6	125	13	260
7	55	-	-

The influence of the radially expanding flow field exiting the HST conical nozzle was neglected in the present experiments; the hypersonic flow is “channelized” to some extent by the 2-D model’s polycarbonate side panels. The principal function of the side panels was to support the shroud while providing an unobstructed view of the laser-induced gasdynamic phenomena taking place within the absorption chamber. These side panels introduce oblique shock waves into the engine interior flow field, phenomena which was deliberately not visualized (i.e., purposefully avoided) in the Schlieren setup. Future detailed investigations of such shock-induced perturbations, as well as more detailed analyses of the external compression inlet characteristics, must await further instrumentation and testing. Nevertheless, to accomplish the principal research objectives of the present campaign (i.e., first-order analysis of impulse generation physics, and overall process efficiency), these interference/ perturbation effects can be neglected.

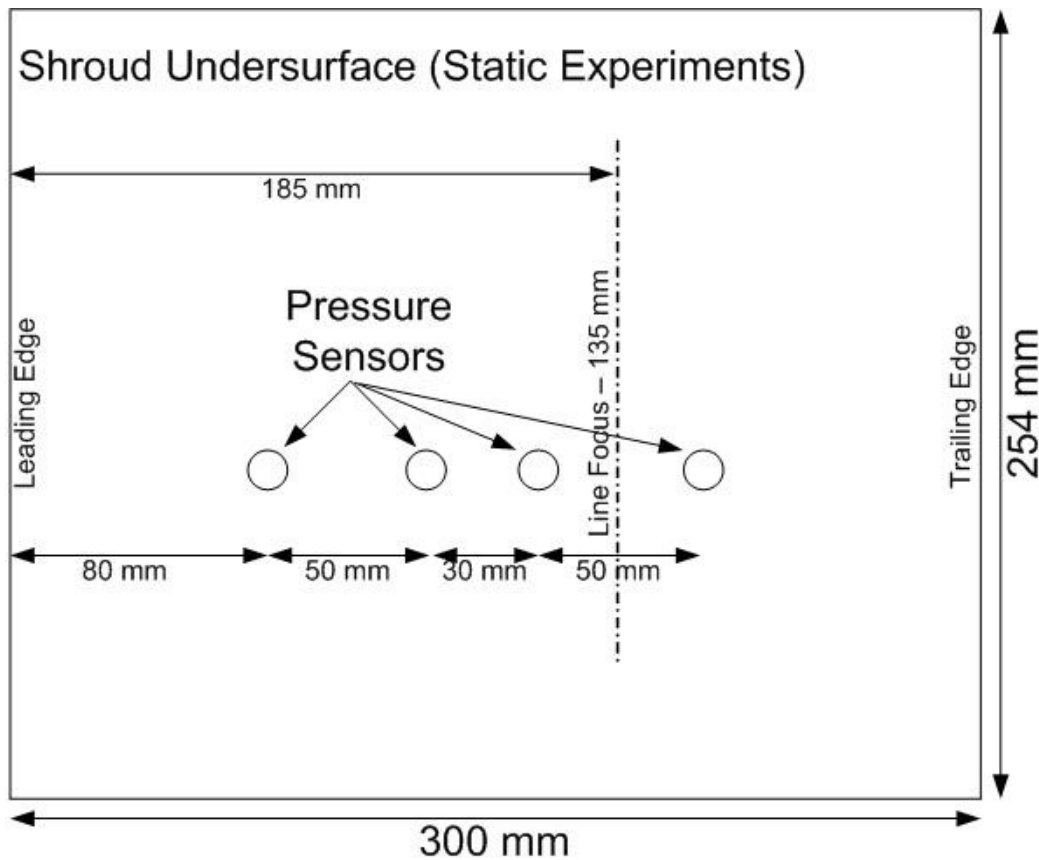


Figure 3.12: Sensor disposition on shroud undersurface and line focus position used during the static experiments.

3.4 General Instrumentation

A full diagnostic array is required to monitor all essential components of the experimental setup which includes the T3 tunnel, 622 laser system, and experimental model. The T3 shock tunnel is instrumented with three piezoelectric pressure transducers: two Kistler Model 701A gages for measuring the incoming shock wave speed in the driven section, and one Kistler 701K for the sensing reservoir pressure—needed to calculate T3 test section flow conditions upon the model. The initial pressure (i.e., prior to HST “firing”) inside the evacuated dump tank and test section is measured by a BOC Edwards APG-L-NW16 Active Pirani vacuum gauge, read by a Model 1575 pressure display. All remaining critical HST pressures (e.g., driver, DDS, etc.) are measured by analog Heise mechanical/analog gauges installed into the T3 control panel. Finally, a Schlieren visualization setup with high speed digital Cordin camera captures the hypersonic flow structure through the T3 test section, for subsequent analysis.

The TEA-620 laser system is fitted with a Teledyne Model 3190 trace oxygen analyzer for measuring O₂ contamination levels in the laser gas mix, to assure that a “glow discharge” is established across the resonator electrodes instead of damaging arcs; note that O₂ concentrations of 500 ppm and higher can encourage electrical arcs during laser firings. These arcs prevent the uniform, ‘glow’ discharge required for an effective lasing of the active media (CO₂) greatly reducing the energy output and also inducing strain in the system, what reduces its lifespan. As mentioned before, the incoming laser pulse energy from the TEA-620’s is measured by two thermopile calorimeters: Gentec UP60N-40S-H9, and Scientec Astral 360801S. Both TEA-620 lasers are controlled by a single customized control panel, with separate controls for the 100 kV Hyptronics power supply that charges the Marx banks.

The 2-D model was instrumented with thirteen piezoelectric PCB pressure transducers: twelve for measuring the pressure distribution vs. time along the model centerline, and one installed in a separate pitot probe for sensing the stagnation impact pressure of incoming hypersonic flow, as mentioned in the previous section.

The 2-D laser scramjet model was also fitted with four Nanmac Type K surface junction thermocouples (Model E6-Q7982-2): two located upon the shroud inner surface and two in the primary reflector, to record the time-variant surface temperatures from which local heat transfer rates were to be obtained using the Cook-Felderman technique (**Cook and Felderman, 1966**). As later revealed in tests, these sensors proved to lack the desired sensitivity for single-pulse LP experiments. More sensitive sensors, as used by **Salvador (2005, 2007)** will have to be used in future multi-pulse experiments, in an attempt to directly measuring the global heat transfer onto interior engine surfaces.

3.5 Schlieren Visualization Setup

An ultra-high speed Cordin digital movie camera was implemented with a Schlieren optical visualization setup for analyzing the time-dependent flow-field structure inside the 2D laser scramjet engine; the objective was to capture the evolving LSD wave driven, expanding blast wave dynamics, and subsequent unpowered blast/flow interactions within the engine working fluid. This visualization system uniquely provides the ability to observe density variations in the flow during pulsed operation of the

Lightcraft engine. More details on the design and setup of Schlieren systems and associated theory is given by **Settles (2006)**, and will not be further addressed here.

The mirror-based Schlieren setup adopted a standard ‘Z’ configuration with two flat folding mirrors with the test section in between. A schematic of this system is depicted in **Figure 3.13**. The effective viewing aperture 250 mm in diameter, dictated by the size of the quartz windows installed in the two test section ports bounding the test section. This Schlieren system is composed of a pulsed xenon flash lamp, an optical slit and focusing lens, two parabolic and three flat mirrors, the knife edge which provides the necessary light cut-off, and the Cordin 550 rotating mirror, ultra-high speed camera. The photo in **Figure 3.14** shows the Schlieren light beam path and placement of the Cordin camera, with respect to the T3 test section.

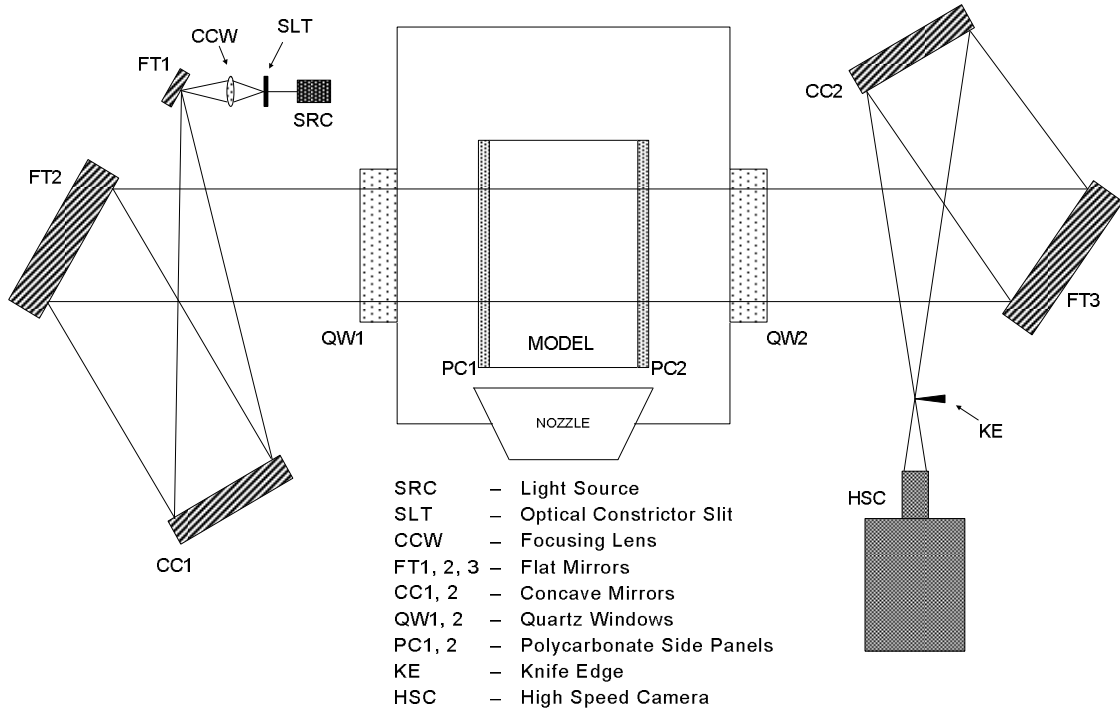


Figure 3.13: Schlieren visualization and Cordin camera system setup for T3 test section.

The Cordin 550 camera can acquire 32 frames with a maximum resolution of 1000 x 1000 pixels at up to 2 million frames per second (fps) in full color. Such frame rates are achieved by a multi-faceted mirror spinning at high speeds, surrounded by 32 CCD elements which acquire images as the mirror rotates. Mirror rotation is driven by a turbine wheel supplied with high pressure N₂ for frame rates up to 500,000 fps, and pressurized He for the highest speeds. Even though extremely high speeds can be

achieved, the present work demanded more modest 50,000 to 100,000 fps because of technical reasons related to the high Electro-Magnetic Interference (EMI) generated when the 620-TEA lasers were fired. This EMI impaired the Cordin's ability to acquire uninterrupted image sequences, as well as the loss of triggering precision which must be on the order of microseconds to capture the desired "window" that images the laser breakdown and subsequent flow field evolution. Hence, the requirement for lower frame rates and the implementation of a specific, known camera pre-trigger to insure capture of the desired "test window." Since triggering precision is closely tied to frame rate, attempts to run the camera at the highest frame rates in that excessive EMI environment, has caused several HST runs to miss the intended "window" altogether—sometimes by a large margin.

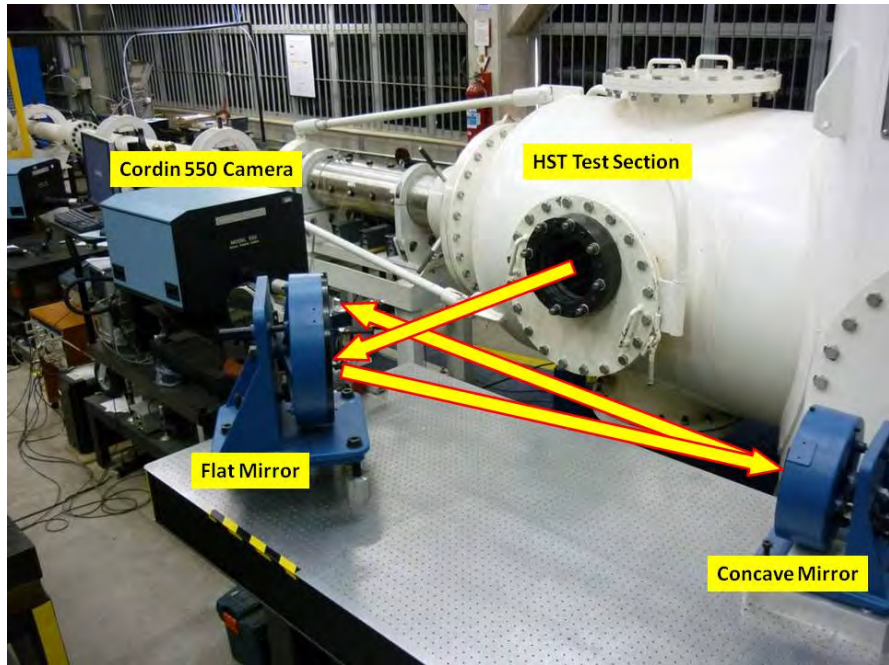


Figure 3.14: T3 Hypersonic Shock Tunnel showing Schlieren light path and Cordin 550 camera.

3.6 Data Acquisition

For the present laser scramjet experiments performed in the T3 tunnel, the data acquisition system required more than 18-20 channels, depending on the test objectives. For the 2-D Lightcraft model alone, 13 channels were needed for the piezo-electric pressure transducers, whereas the HST instrumentation required another set of 4 channels; additional channels were needed for TEA-620 laser diagnostics.

Two 16-channel Yokogawa DL750 Scopewriters comprised most of the data acquisition system: one for the LP model pressure distributions, and the other for HST instrumentation. These DL750s can record up to 10 MS/s for all 16 channels for the duration of the test window (e.g., 10 ms for the HST scope, and 5 ms for the 2-D model scope); that provides the required 10 sample points per microsecond of test time—judged sufficient to resolve all physical phenomena under investigation. Raw pressure data from the model's piezo-electrics was pre-amplified by a 16-Channel PCB 481A02 signal conditioner. The Yokogawa DL750 easily interfaced with the favored data analysis software (Microcal Origin), without the need for preprocessing.

Data acquisition for the TEA-620's diagnostic instrumentation was performed by a Tektronix TDS2014 (100 MHz, 1GS/s); the laser pulse profile was sensed by a Hamamatsu B749 Photon Drag detector. The Gentec's UP-60N calorimeter readout was acquired by a Pentium PC computer.

All remaining data gathered during the LP experiments (laser gas constituent feed rates, HST driver/driven pressures, etc) was hand recorded from direct readouts on standard analog gauges and other stand-alone instruments.

- FINAL REPORT -

- PART 2 -

Volume 1: Static and Hypersonic Experimental Analysis of Impulse
Generation in Air-Breathing Laser-Thermal Propulsion

MURI 05 Grant Title: “Basic Research Investigations into Multimode Laser and EM Launchers for Affordable, Rapid Access to Space”

Principal Investigator: Professor Leik N. Myrabo
Rensselaer Polytechnic Institute,
110 8th Street, Troy, NY 12180-3590

Major Contributors: Drs. Israel I. Salvador and David A. Kenoyer

AFOSR Award: FA9550-05-1-0392

Research Period: June 1, 2005 through August 31, 2010 (5 year grant)



Prepared for

Dr. Mitat Birkan

Air Force Office of Scientific Research (AFOSR)
Arlington, VA 22203

31 August 2010

CONTENTS

CONTENTS.....	ii
LIST OF TABLES	iv
LIST OF FIGURES.....	v
1. Static Experiments.....	61
1.1 Surface Pressure Distribution	62
1.2 Blast Wave Schlieren Visualization.....	74
4.3 Impulse Generation Analysis from Surface Pressure Distribution	81
5 Hypersonic Experiments.....	91
5.1 Hypersonic Test Conditions.....	93
5.2 Hypersonic Campaign Results for 2D Model.....	100
5.2.1 Runs 1 to 4 – Initial Runs.....	100
5.2.2 Runs 5 to 11 – Troubleshooting Runs.....	104
5.2.3 Runs 12 to 15 – Shroud Removed	107
5.2.4 Runs 16 to 19 – Mid-channel Breakdown.....	111
5.2.5 Runs 20 to 24 – Surface Breakdown	120
5.3 Discussion of the Results.....	128
6 Conclusions and Future Work.....	136
6.1 Conclusions.....	136
6.1.1 Static Experiments	136
6.1.2 Hypersonic Experiments	138
6.2 Future Experimental Work	141
6.2.1 Phase II Hypersonic Campaign with 2D Model.....	141
6.2.2 2 nd Generation Two-Dimensional Model.....	143
6.2.3 Axi-symmetric Hypersonic Lightcraft Model.....	145
6.2.4 Airbreathing Laser-Electromagnetic Propulsion	147
References.....	149

Appendix A – Sensors and Calibration	158
Appendix B – USA/Brazil BEP Collaboration.....	160
Appendix C – Hypersonic Shock Tunnels.....	163
C.1 Requirements for Hypersonic Testing.....	163
C.2 General Characteristics of a Hypersonic Shock Tunnel.....	164
C.3 Modeling of Shock Tunnel Flow	166
C.3.1 Thermodynamic Equilibrium Shock Tube Problem.....	168
C.3.2 Nozzle Flow Expansion	170
Appendix D – Dedicated Laboratory Setup for CO ₂ TEA Laser Propulsion Experiments	173
D.1 Research Vision and Laboratory Strategy	173
D.2 Laboratory Equipment and Facilities	175
D.3 Basic Research Program.....	178
D.3.1 Current Research	179
D.3.2 Future Research	181
D.4 Summary.....	185

LIST OF TABLES

Table 4.1: Static (quiescent flow) test run conditions.	62
Table 4.2: Sensor longitudinal inclination Θ , and impulse adjustment factor $\sin(\Theta)$	83
Table 4.3: Limits of integration for laser-generated impulse calculations.	84
Table 4.4: Longitudinal Impulse for sample runs #1, #7, #11 and #12.....	87
Table 5.1: T3 HST initial conditions and reservoir stagnation conditions achieved during experimental campaign.	97
Table 5.2: Free stream conditions obtained during experiments, calculated with STCALC (code assumes chemical and thermodynamic equilibrium).	98
Table 5.3: Model centerbody and shroud inclinations, focal line location, and laser pulse energy for all hypersonic runs.	99
Table A.1: 2-D Lightcraft sensor models, calibration and ports.....	158
Table A.2: T3 HST 2-D Lightcraft sensor models, calibration and ports.	159
Table B.1: Division of responsibilities between RPI and IEAv-CTA in the present campaign.	161
Table D.1: Single K922M laser operating conditions.	175

LIST OF FIGURES

Figure 4.1: Regions for impulse-generation analysis: 1) Inlet compression ramp surface (ignored for static runs); 2) Shroud undersurface; and, 3) Primary Optics (rear parabolic mirror surface).....	64
Figure 4.2: Run #12—Pressure distribution over compression ramp. ($P_{\infty} = 1$ bar, $E=180\pm20$ J)	65
Figure 4.3: Run #12—Pressure distribution over shroud undersurface. ($P_{\infty} = 1$ bar, $E=180\pm20$ J)	65
Figure 4.4: Run #12—Pressure distribution over focusing mirror ($P_{\infty} = 1$ bar, $E=180\pm20$ J). Notice the influence of mechanical vibration on the pressure signal.	66
Figure 4.5: Run #1—Pressure distribution over shroud undersurface. (P_6-P_9 ; $P_{\infty} = 60$ mbar; $E_P=172\pm17$ J).....	67
Figure 4.6: Run #1—Pressure distribution over focusing mirror. (P_{10-13} ; $P_{\infty} = 60$ mbar; $E_P=172\pm17$ J).....	67
Figure 4.7: Run#7—Pressure distribution over shroud undersurface. (P_6-P_9 ; $P_{\infty} = 150$ mbar; $E_P=222\pm23$ J).....	68
Figure 4.8: Run#7—Pressure distribution over focusing mirror. (P_{10-13} ; $P_{\infty} = 150$ mbar; $E_P=222\pm23$ J).....	68
Figure 4.9: Run#11—Pressure distribution over shroud undersurface. (P_6-P_9 ; $P_{\infty} = 300$ mbar; $E_P=231\pm23$ J).....	69
Figure 4.10: Run #11—Pressure distribution over focusing mirror. (P_{10-P_13} ; $P_{\infty} = 300$ mbar; $E_P=231\pm23$ J).....	69
Figure 4.11: Data for blast wave front arrival time vs. Sedov's scaling law.....	71
Figure 4.12: Regions for impulse computation, using pressures measured during static tests.	72
Figure 4.13: Run #1—Peak surface pressure vs. distance from laser line focus. ($P_{\infty} = 60$ mbar; $E_P=172\pm17$ J).....	73
Figure 4.14: Run#7—Peak surface pressure vs. distance from laser focal line. ($P_{\infty} = 150$ mbar; $E_P=222\pm23$ J).....	73
Figure 4.15: Run #11—Peak surface pressure vs. distance from laser focal line. ($P_{\infty} = 300$ mbar; $E_P=231\pm23$ J).....	74

Figure 4.16: Run#12—Peak surface pressure vs. distance from laser focal line. ($P_{\infty} = 1$ bar; $E_P = 180 \pm 20$ J).....	74
Figure 4.17: Run #12- Blast wave evolution with measured surface pressures (top), and corresponding Schlieren image/frame timing (bottom). $P_{\infty} = 1$ bar; $E_P = 180 \pm 20$ J... 77	
Figure 4.18: Run #11 - Blast wave evolution with measured surface pressures (top), and corresponding Schlieren image/frame timing (bottom). $P_{\infty} = 300$ mbar; $E_P = 231 \pm 23$ J.....	78
Figure 4.19: Run#7 - Blast wave evolution with measured surface pressures (top), and corresponding Schlieren image/frame timing (bottom). $P_{\infty} = 150$ mbar, $E_P = 222 \pm 23$ J.....	79
Figure 4.20: LSD wave propagation followed by radial expansion; α and β angles are indicated. <i>Left:</i> Run #8, $P_{\infty} = 300$ mbar, $E = 205 \pm 21$ J. <i>Right:</i> Run #11, $P_{\infty} = 300$ mbar, $E = 231 \pm 23$ J.....	81
Figure 4.21: Laser-induced breakdown with 2D model pitched forward 10-degrees.....	81
Figure 4.22: The three zones and respective integration limits considered for the longitudinal impulse calculation.....	84
Figure 4.23: Run #1—Peak surface pressure vs. distance from laser line focus. <i>Top:</i> Region 1; <i>Bottom:</i> Region 3. ($P_{\infty} = 60$ mbar; $E_P = 172 \pm 17$ J)	85
Figure 4.24: Run#7—Peak surface pressure vs. distance from laser focal line. <i>Top:</i> Region 1; <i>Bottom:</i> Region 3. ($P_{\infty} = 150$ mbar; $E_P = 222 \pm 23$ J)	85
Figure 4.25: Run #11—Peak surface pressure vs. distance from laser focal line. <i>Top:</i> Region 1; <i>Bottom:</i> Region 3. ($P_{\infty} = 300$ mbar; $E_P = 231 \pm 23$ J)	86
Figure 4.26: Run#12—Peak surface pressure vs. distance from laser focal line. <i>Top:</i> Region 1; <i>Bottom:</i> Region 3. ($P_{\infty} = 1$ bar; $E_P = 180 \pm 20$ J)	86
Figure 4.27: Momentum coupling coefficient vs. ambient pressure. (Assumes $\Theta_{\text{shroud}} = -34$ deg.)	88
Figure 4.28: C_m variation vs. ambient pressure calculated for finite flat plate by Pirri (1973) and Richard (1989) vs. present experimental data from shroud undersurface (adjusted for shroud inclination).	90
Figure 5.1: Altitude vs. Mach number schedule for optimized airbreathing LP launch to low Earth orbit (Frasier, 1987).....	92

Figure 5.2: Reynolds number variation with Mach number along optimized laser launch trajectory by Frazier (1987), together with T3 HST data from present test campaign.	92
.....
Figure 5.3: Run 24—Typical HST and Pitot pressure signals obtained during experiments.	95
Figure 5.4: Run #1-Pressure transducer traces for Ch2-14 (distributed over 2D model); Laser ON, Flow ON; $M=8.61$; $E_p=196\pm20$ J. Channel number corresponds to pressure sensor. Note simultaneous sensor response to laser-induced blast, indicating excessive mechanical noise.	102
Figure 5.5: Run #2- Pressure transducer traces for Ch2-14 (sensors distributed over 2D model); Laser OFF, flow ON; $M=8.56$; $E_p= 0$ J. The signal stability throughout the time window indicates fully established hypersonic flow over the model.	102
Figure 5.6: Run#0-Pressure transducer traces for Ch2-14 (sensors distributed over 2D model); Laser ON, flow OFF; $M=7.8$; $E_p=180\pm20$ J; $P_\infty = 7.5E-02$ mbar. Note similarity to Run#1 results.	103
Figure 5.7: <i>Left</i> : Run #1—Erratic Schlieren image sequence . Note oversaturation of 2 nd frame when laser induced breakdown occurred, and missing frames due to EMI. <i>Right</i> : Run #2—Schlieren image with laser OFF, revealing flow structure at $M=8.56$	104
Figure 5.8: <i>Left</i> : Diaphragm engraving geometry. <i>Right</i> : Burst diaphragm.	105
Figure 5.9: Run 10-Schlieren image with only the laser-induced air-breakdown glow visible. ($M=8.77$, $T_\infty=68.7$ K, $P_\infty=0.15$ kPa).....	107
Figure 5.10: Run 10-Pressure gage traces for P6, P7,P9 distributed over shroud undersurface; laser ON, flow ON; Mach 8.77; $E_p=207$ J. Sensor P9 pressure jump is from passage of blast wave.....	107
Figure 5.11: Run #13-Laser induced blast wave interaction with oblique shock. ($M=5.95$, $T_\infty=263.7$ K, $P_\infty=5.62$ kPa, $E_p=196\pm20$ J).....	109
Figure 5.12: Run#15-Laser induced blast wave interaction with oblique bow shock; -4° model pitch. The smearing of the focus is noticeable on the air-breakdown geometry. ($M=5.95$, $T_\infty=262.3$ K, $P_\infty=5.16$ kPa, $E_p=176\pm18$ J).....	111

Figure 5.13: Run#16 - Laser induced blast wave interaction with oblique shocks from shroud and inlet center-body at 7.5° inclination. (M=5.96; T _∞ =258.3 K; P _∞ =5.32 kPa; E _p =187±19 J)	113
Figure 5.14: Run#16 - Measured pressure distribution over shroud under-surface; traces offset. Schlieren frames from Figure 5.13 are marked by diamonds.	114
Figure 5.15: Run#17 - Laser induced blast wave interaction with oblique shocks and shroud under-surface; 2D model at -7.5°; Shroud at -4° inclination. (M=5.94, T _∞ =256.8 K, P _∞ =6.25 kPa, E _p =186±19 J).....	116
Figure 5.16: Run#17 - Long exposure color photograph of laser-induced breakdown geometry at Mach 5.96; 2D model at -7.5°; Shroud at -4° inclination.....	117
Figure 5.17 Run#17 - Measured pressure distribution across shroud under-surface. Traces offset. Schlieren frames from Figure 5.15 are marked for with diamonds. 117	
Figure 5.18: Run#18 - Laser induced blast wave interaction with oblique shocks and shroud under-surface. Both center body and shroud at -7.5° inclination. (M=5.94; T _∞ =284.4 K; P _∞ =4.88 kPa; E _p =121±12 J)	118
Figure 5.19: Run#18 - Measured pressure distribution across shroud under-surface. Traces offset. Schlieren frames from Figure 5.18 are marked for with diamonds. 119	
Figure 5.20: Run#19 - Measured pressure distribution across shroud under-surface; traces offset. Photon-drag detector signal provides timing for laser pulse delivery.	120
Figure 5.21: Run#20 - Extended duration pressure distribution over 2-D model, also showing transients before full flow establishment. Shroud sensors offset for clarification. (M=8.6; T _∞ =128.8K; P _∞ =0.566 kPa; E _p =189±20 J)	121
Figure 5.22: Run#20 - Pressure distribution over shroud under-surface showing P6, P7, P9 signals, masked by mechanical noise. Photon drag detector signal gives laser pulse timing (<i>bottom trace</i>). Pressure traces offset.	122
Figure 5.23: Run#21 - Laser induced blast wave interaction with oblique inlet shocks and shroud under-surface. Model and shroud at -7.5° inclination. (M=9.44, T _∞ = 108 K, P _∞ = 0.301 kPa, E _p =196±20 J).....	123
Figure 5.24: Run#21 - Long exposure photograph of bifurcated air-breakdown geometry across inlet gap, and secondary breakdown on shroud undersurface.	124

Figure 5.25: Run#21 - Measured pressure distribution across shroud undersurface; traces offset. Schlieren frames from Figure 5.23 are marked with diamonds.	125
Figure 5.26: Run#23 - Laser induced blast wave interaction with oblique shocks and shroud under-surface. Model at -7.5° and shroud at -24° inclination. ($M=9.43$, $T_\infty=113.7$ K, $P_\infty=0.293$ kPa, $E_p=106\pm11$ J).....	127
Figure 5.27: Run#23 - Measured pressure distribution at shroud under-surface; traces offset. Schlieren frames from Figure 5.26 are marked for clarification.	128
Figure 5.28: Peak pressures (ΔP) measured across shroud under-surface, measured from its leading edge. (Runs 16 through 19).....	133
Figure 6.1: Complete 2D model with full external compression inlet for Phase 2 tests.	142
Figure 6.2: Features to be added in 2 nd generation 2D hypersonic models.	144
Figure 6.3: Axi-symmetric Lightcraft model ready for hypersonic tests in the T3 tunnel.	146
Figure 6.4: Pulsed power supply and 2.0 T magnet system.	148
Figure B.1: Logo for the collaborative effort set between RPI and HTN-LAH under sponsorship of the AFOSR.....	160
Figure C.1: Shock tunnel operation diagram.	165
Figure C.2: Reflected and transmitted shock after contact surface interaction, encountered in the reflected mode of operation ($U_2=0$).....	169
Figure D.1: Twin Lumonics TEA-922Ms and Schlieren setup in the laboratory.....	177
Figure D.2: Panoramic view of the Laser Propulsion Laboratory.	178
Figure D.3: Schlieren montage of Lightcraft model #200 with beam centered, taken at 120,000 fps.	180
Figure D.4: Schlieren montage of Lightcraft model #200 with beam offset of 20 mm, taken at 50,000 fps.	181
Figure D.5: Integrated setup in the present 7.9 m x 5.2 m available laboratory space with altitude supersonic flow facility.	183

1. Static Experiments

This chapter covers the static tests (i.e., quiescent flow) of a 2D Lightcraft engine performed in the T3 dump tank at 1Bar ambient and three lower pressures, with the model installed in the tunnel’s test section; the subsequent campaign (see **Chapter 5**) moved on to LP scramjet tests with laser energy deposition into hypersonic flow. Although the TEA-622 can deliver up to 1000 joules (i.e., 500 J per 620 module in the stable resonator mode), the static tests were carried out with ~200 J from a single 620 deposited along a 13.5 cm line focus on the shroud undersurface—which equates to ~15 J/cm, or about 20% of the 80 J/cm needed for optimum LP engine performance (to be explored in future tests). Several problems delayed reactivation of the Lumonics TEA-620 lasers, which were joined into the 622 geometry to share the same unstable resonator cavity (as was explained earlier), but these issues were ultimately resolved.

The two principal objectives of the static experiments were to: 1) record high speed Schlieren camera movies of the laser-induced blast waves; and 2) determine the laser-induced impulse and momentum coupling coefficient from direct measurements of time-resolved pressure distributions produced over the 2D model’s absorption chamber surfaces—comprised of the shroud undersurface, and the rear parabolic optic (a copper 2D focusing mirror that also serves as a plug nozzle). This experimental data is then compared to impulse predictions from first-order theoretical models. A third objective of the quiescent-flow experiments is to acquire data essential for validating future full-engine numerical (CFD) simulations, which could be used in the future to simulate pulsed laser energy deposition and subsequent unpowered hydrodynamic processes taking place in the absorption chamber of any Lightcraft engine/vehicle geometry. Such tools will play a major role in the design optimization of future laser Lightcraft, revealing geometrical and operational features necessary for successful operation.

Numerous tests were performed under quiescent conditions at four different ambient pressures (0.60, 0.15, 0.30, and 1 bar), from which seventeen—listed in **Table 4.1**—were specifically selected for analysis. Note that the laser pulse energy and shroud incidence (measured relative to the Lightcraft model’s horizontal axis) vary through the campaign.

Table 1.1: Static (quiescent flow) test run conditions.

<i>Test Run #</i>	<i>Ambient Pressure, bar</i>	<i>Shroud Angle, deg.</i>	<i>Laser Energy, J</i>
1	60E-3	34	172±17
2	60E-3	34	218±22
3	60E-3	34	158±16
4	150E-3	34	205±21
5	150E-3	34	211±21
6	150E-3	34	222±23
7	150E-3	34	222±23
8	300E-3	34	205±21
9	300E-3	34	198±20
10	300E-3	34	235±24
11	300E-3	34	231±23
12 ^a	1	25	180±20
13 ^a	1	25	180±20
14	1	25	156±16
15 ^{a,b}	1	25	180±20
16 ^{a,b}	1	25	180±20
17 ^{a,b}	1	25	180±20

^aConducted prior to final beam-splitter calibration setup; estimated laser pulse energy $E_p= 180 \text{ J}$.

^bSchlieren images only; pressure discarded due to excessive mechanical induced vibration.

1.1 Surface Pressure Distribution

PCB piezoelectric pressure transducers were used to measure the time-variant pressure distributions over the 2D model's absorption chamber surfaces; the gages were installed perpendicular to local interior surfaces, to register the static pressure history at each sensor port location. Ideally these sensors should be installed flush with such surfaces to avoid any delay in the response (which might approach $\sim 1 \mu\text{s}$), but a flush installation was not possible for two reasons: 1) direct laser beam exposure of the sensor head would probably damage (ablation, ionized plasmas, non-linear strain, and/or overpressures) the delicate sensing element; and, 2) laser-induced thermal transients in

the sensor head would likely cause significant deviations from calibrated (i.e., cool head) pressure readouts (**Walter, 2004**). These factors forced the decision to install the sensor heads 3mm from the surface, and provide an on-axis 1.5 mm diameter, 3 mm deep hole to remotely read the surface pressure. This configuration protects the sensing element at the expense of a small time lag in sensor response. This delayed response is clearly visible in the acquired pressure traces, but not so long as to prohibit accurate readings of both shock arrival time and peak pressures.

Another compromise that reduced sensor response was the application of thermal shielding to the PCB sensing heads. The 3 mm tapered PCB installation provided insufficient thermal isolation from the hot, high pressure laser-induced plasmas, so the affected, incoherent data acquired over the first few static tests had to be discarded. To resolve this issue, a single layer of black electrical tape was applied to each sensor head surface, which subsequently eliminated the transient temperature-induced effects upon the pressure readouts/signal output.

For laser-generated impulse analysis purposes, the 2D Lightcraft engine surfaces can be divided into three pressure-acquisition regions (see **Figure 4.1**): 1) inlet compression ramp, 2) shroud undersurface and 3) primary optics (focusing mirror). In the impulse analysis of static test results, compression ramp pressures were neglected since the inlet would ideally be closed for during liftoff; any blast wave energy escaping forward through inlet throat would be considered as loss. Hence, under quiescent-flow conditions, the dominant impulse contributions would come from integrated, time-variant pressure increases over the shroud undersurface and aft mirror surfaces.

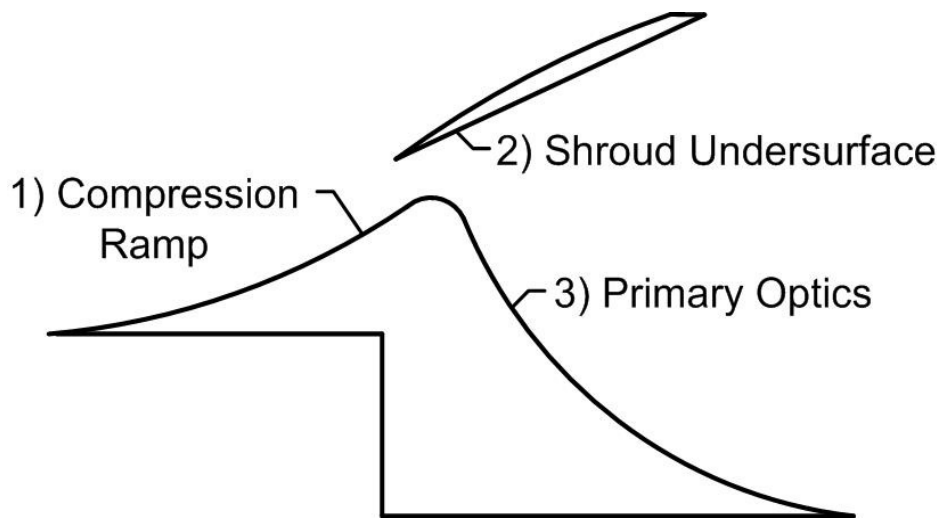


Figure 1.1: Regions for impulse-generation analysis: 1) Inlet compression ramp surface (ignored for static runs); 2) Shroud undersurface; and, 3) Primary Optics (rear parabolic mirror surface).

Time-variant pressure distributions over the 2D model surfaces for the Quiescent Runs in **Table 4.1** are given in **Figures 4.2** to **4.4** below. These sample traces clearly reveal the influence of mechanical vibrations that reduced measurement precision (inducing errors with magnitude equivalent to its amplitude), which was considerable in some sensors: e.g., sensors P12 and P13 show vibration-induced amplitudes reaching 20% of the actual pressure signal. These errors will, of course, propagate forward into any analysis performed using this data; hence, further refinement and vibration suppression must be considered in future data acquisition strategies.

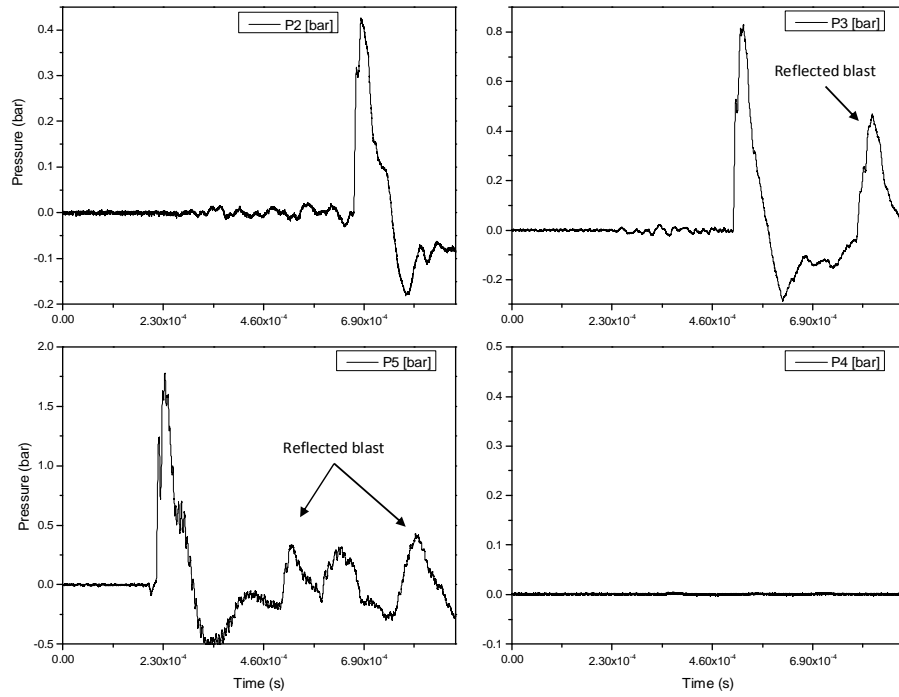


Figure 1.2: Run #12—Pressure distribution over compression ramp. ($P_{\infty} = 1$ bar, $E = 180 \pm 20$ J)

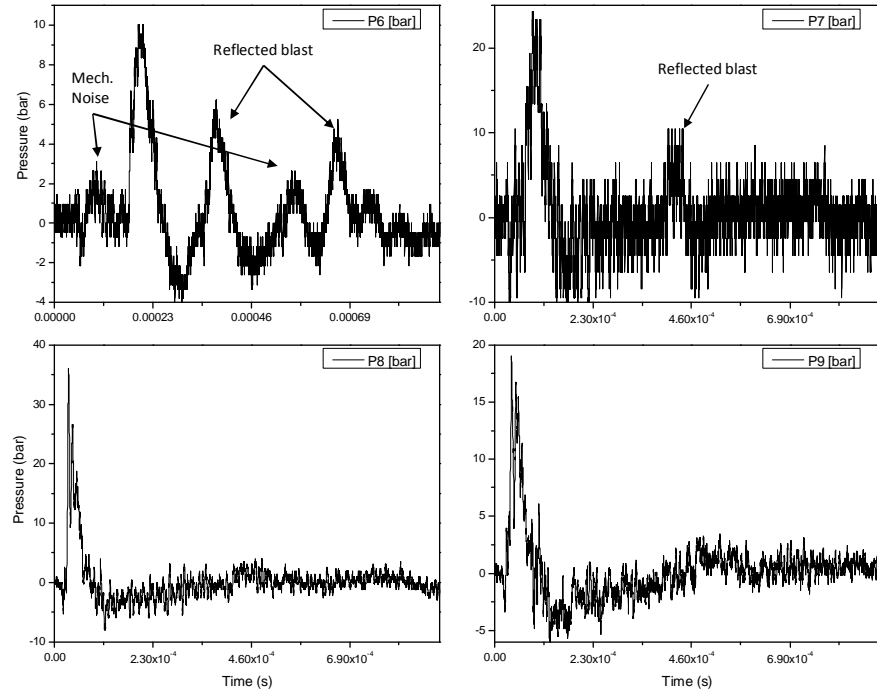


Figure 1.3: Run #12—Pressure distribution over shroud undersurface. ($P_{\infty} = 1$ bar, $E = 180 \pm 20$ J)

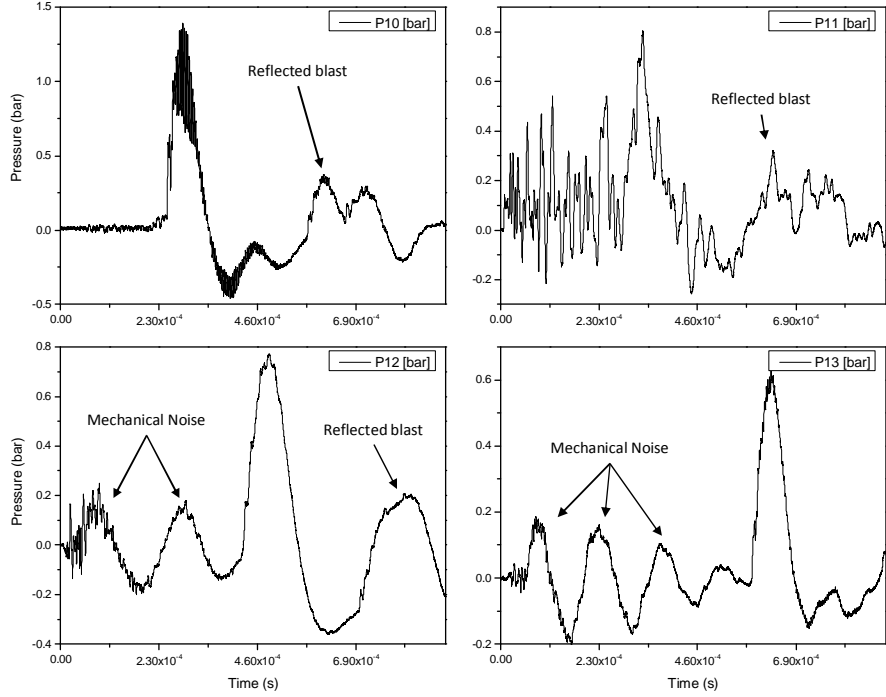


Figure 1.4: Run #12—Pressure distribution over focusing mirror ($P_{\infty} = 1$ bar, $E=180\pm20$ J).

Notice the influence of mechanical vibration on the pressure signal.

Several steps were taken to reduce the initial (severe) vibration noise to the far-lower levels captured in the above plots. The first action taken was to remount the model onto 10 mm polyurethane rubber chimes, in an attempt to vibration-isolate it from the metal support base that was bolted directly to the HST dump tank. The next step was to increase the 2D model's mass by installing several “dead weights” onto the shroud support structure. Finally, a stabilizing strut-fork was added to the two polycarbonate plates (aft end) to restrict their movement and stiffen the whole assembly. These three modifications resolved the PCB gage vibration noise problem and enabled the successful acquisition of the pressure traces presented here, which was impossible with the initial setup.

Sample pressure trace results for Runs #1, #7, and #11 are given in **Figures 4.5** to **4.10** for the shroud undersurface and primary optics surface. During these runs P11 was malfunctioning, so its signal was unavailable. All traces have the same time scale, ranging from 0 (i.e., master trigger for firing the laser) up to 1 ms max.

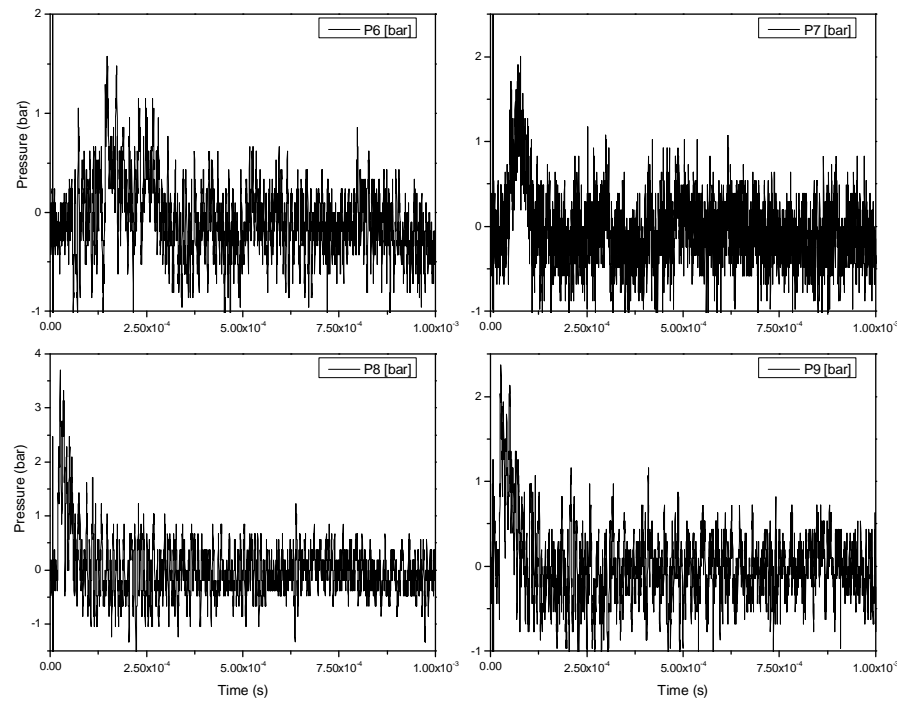


Figure 1.5: Run #1—Pressure distribution over shroud undersurface. (P6-P9; $P_{\infty} = 60$ mbar; $E_p = 172 \pm 17$ J)

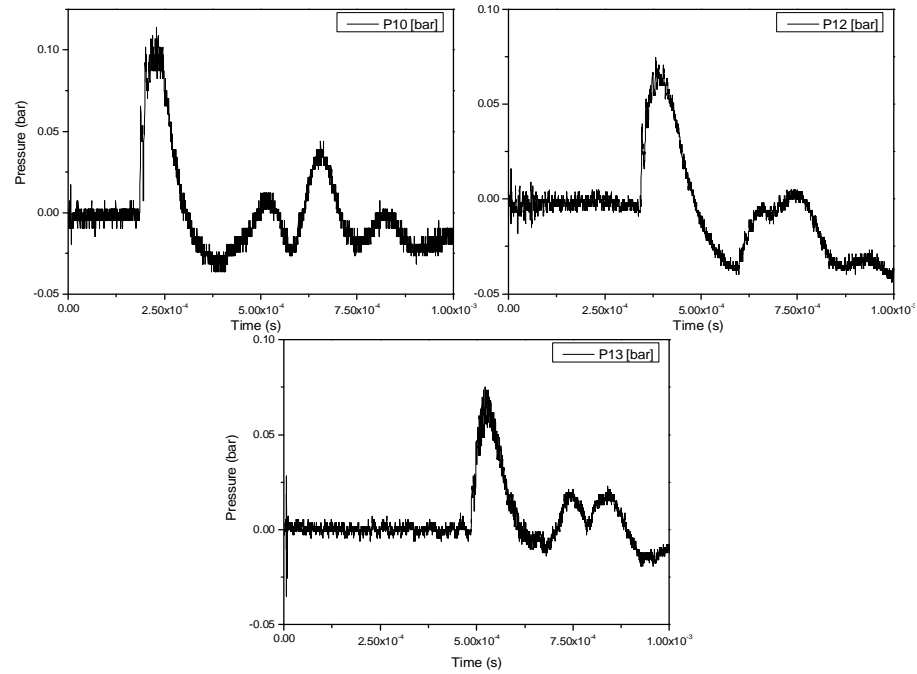


Figure 1.6: Run #1—Pressure distribution over focusing mirror. (P10-13; $P_{\infty} = 60$ mbar; $E_p = 172 \pm 17$ J)

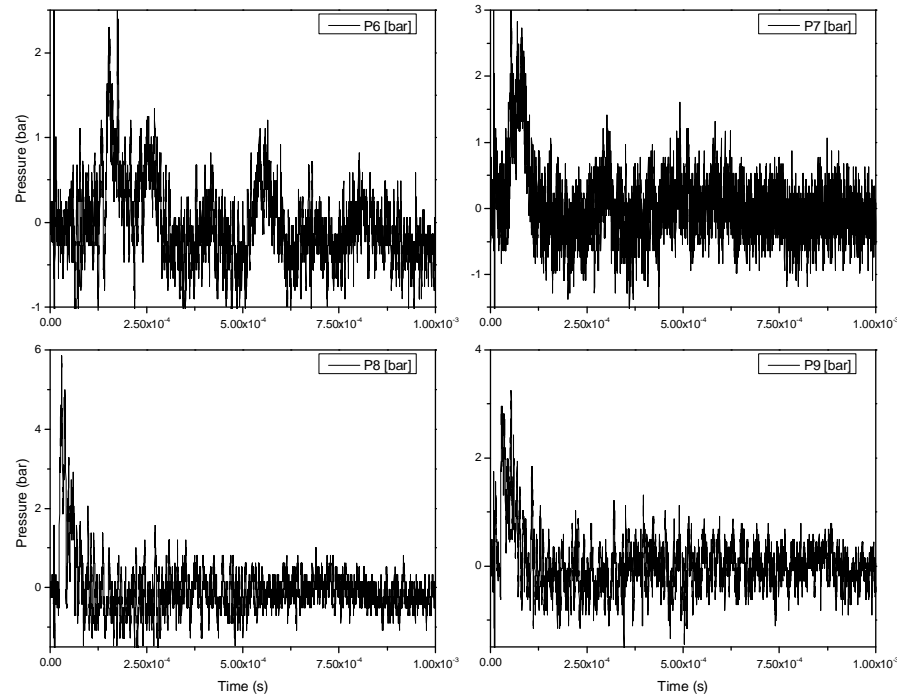


Figure 1.7: Run#7—Pressure distribution over shroud undersurface. (P_6 - P_9 ; $P_\infty = 150$ mbar; $E_p = 222 \pm 23$ J)

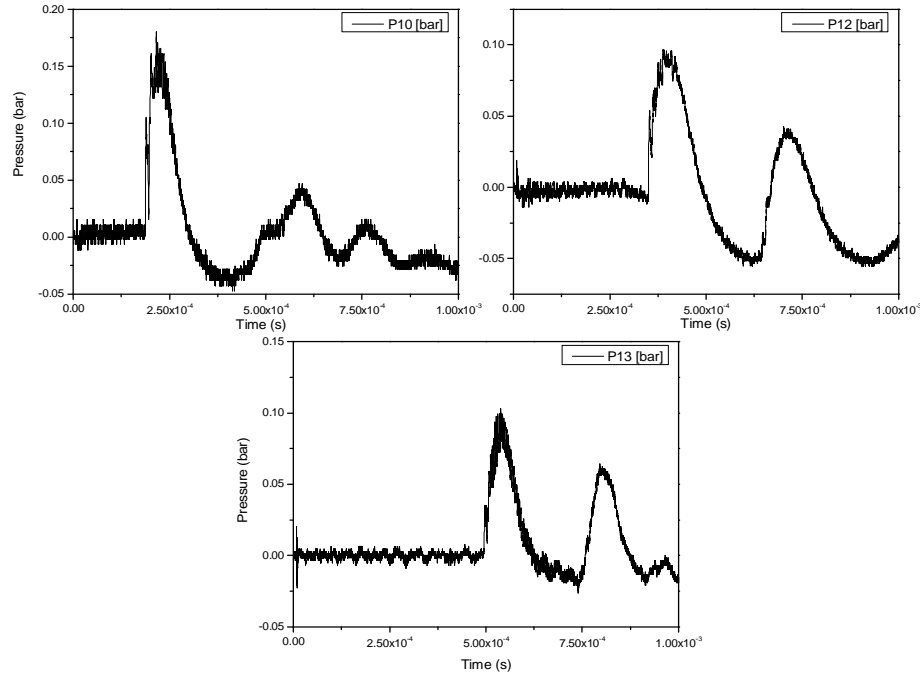


Figure 1.8: Run#7—Pressure distribution over focusing mirror. (P_{10-13} ; $P_\infty = 150$ mbar; $E_p = 222 \pm 23$ J)

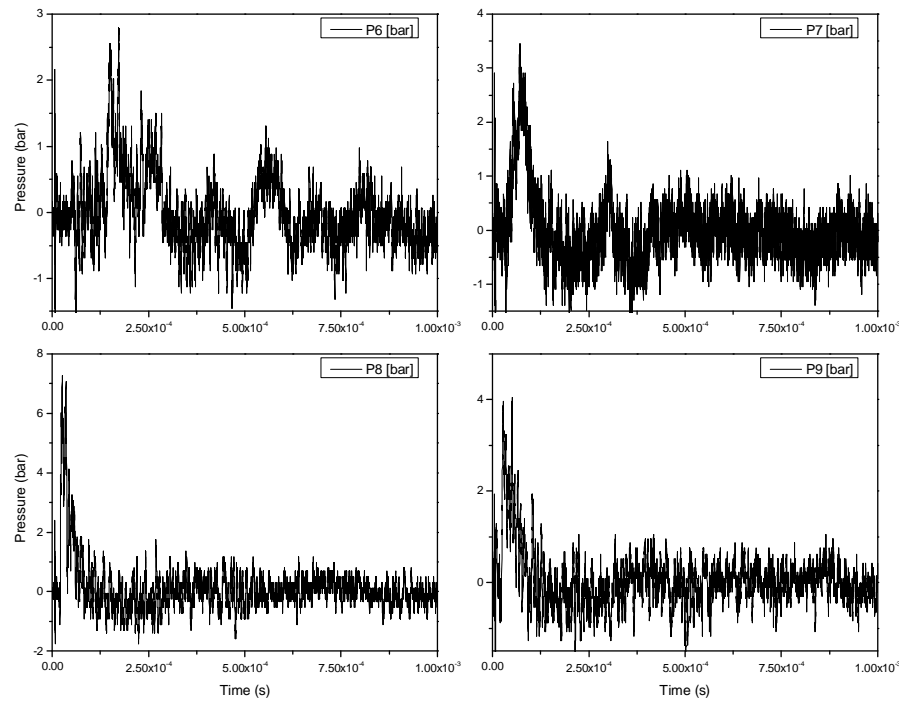


Figure 1.9: Run#11—Pressure distribution over shroud undersurface. (P_6 - P_9 ; $P_\infty = 300$ mbar; $E_p = 231 \pm 23$ J)

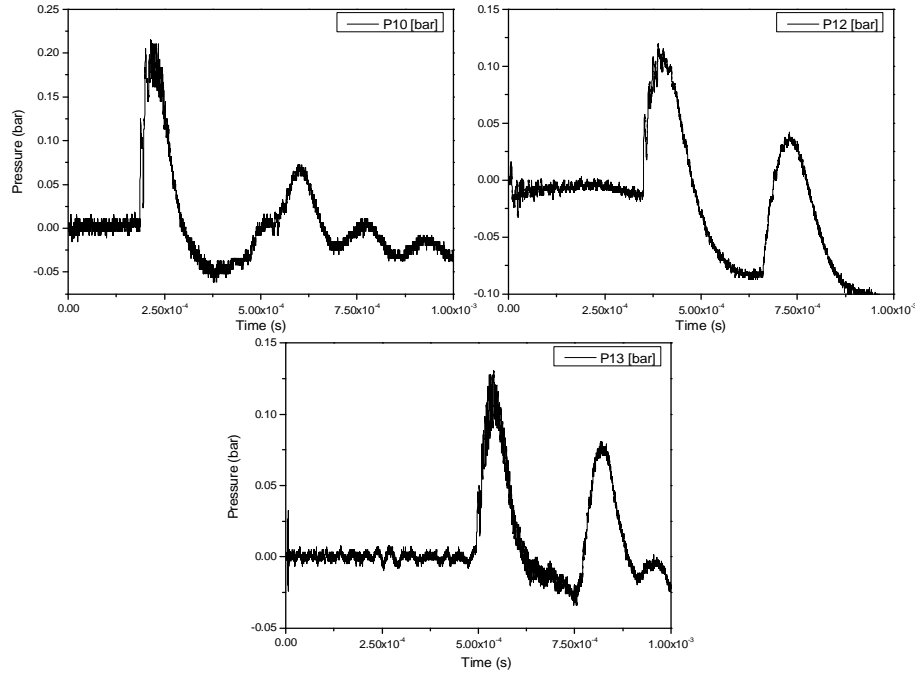


Figure 1.10: Run #11—Pressure distribution over focusing mirror. (P_{10} - P_{13} ; $P_\infty = 300$ mbar; $E_p = 231 \pm 23$ J)

Note in reduced P_∞ runs that lower mechanical noise was present in the pressure traces, especially for sensors P12 and P13. Also, random noise was a considerable portion of the signal amplitude from sensors P6 through P9 (shroud) due to the lower measured pressures, that contributed to the high total error in the measurement. This could have been avoided if pressure transducers of higher sensitivity had been used, better matched with the expected pressure levels. These sensors were better tailored to laser-induced pressure increases from the 1 bar background case.

For any given sensor location, the blast wave arrival time is heralded by the initial sensor response (beginning of sensor signal slope). In **Figure 4.11**, this time of arrival is plotted against the distance traveled by the blast and is nearly constant regardless of varying ambient pressure. The only noticeable difference was for sensors P6 and P10—located 12.6 cm and 13 cm (respectively) from the laser focal line—possibly due to the weak pressure jump on sensor P6, and indeterminate slope of sensor P10 response to the incoming blast wave.

In the P6 traces, three blast wave reflections can be distinguished as corresponding to the successive reflections between the initial blast and the inlet throat transition region residing between the compression ramp and the primary rear reflector. The second blast reflection can also be seen in the trace from P7; these reflections become more evident (stronger) as the ambient pressure raises, and the signal overcomes the background noise. Blast wave reflections are more clearly seen in the pressure traces of sensor P10 to P13 due to their higher sensitivity, despite the lower pressures that were measured.

This blast wave expansion rate data was compared with that predicted by self-similar blast wave theory developed by **Sedov (1951)** for the cylindrical, unpowered expansion of the form $r/r_{\text{ref}} = (t/t_{\text{ref}})^{1/2}$, and plotted vs. time of arrival in **Figure 4.10**. This self-similar theory predicts the expansion of planar, cylindrical and spherical blast waves, in the powered (while energy is being added) and un-powered (after the energy addition has ceased) cases. Divergence of the experimental data with respect to self-similar theory, indicates that these relations don't accurately model the blast wave expansion at later times, but do track the initial moments after local energy deposition.

The discrepancy in the shock wave position increases with time, as noticed from **Figure 4.10**; Sedov's self-similar theory is valid only for $P_{\text{blast}}/P_\infty > 6$: i.e., for strong

shocks. Self-similar blast wave relations have been extensively used in theoretical analysis of laser propulsion phenomena (Reilly, 1979; Richards, 1989), but cannot provide accurate predictions at longer time-scales.

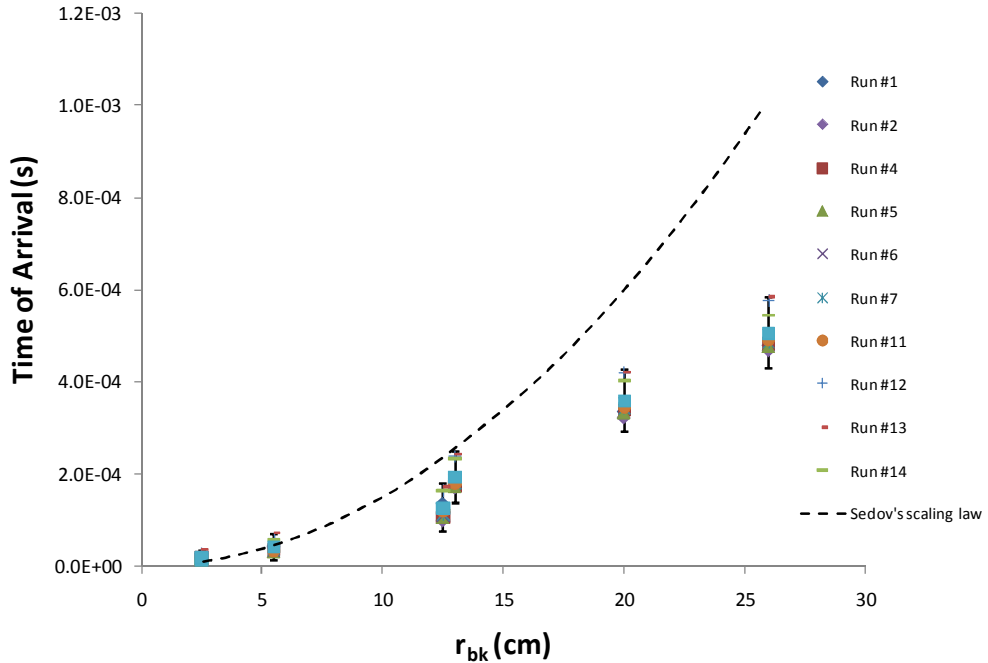


Figure 1.11: Data for blast wave front arrival time vs. Sedov's scaling law.

Examination of the measured surface pressure distributions revealed features that suggest a strong dependence on beam/optics/engine geometry. The first discrepancy is the apparent disparity between the pressures measured by sensors P8 and P9 (see **Figures 4.13 to 4.16**). Note that sensor P8 gave higher pressure readings than P9, despite their equal distance from the laser line focus and blast wave origin. In part, this phenomenon might be explained by a non-perpendicular orientation (i.e., relative to the flat shroud undersurface) of the wedge-shaped, high pressure plasma created by the LSD wave, as it propagates towards the source. If, for example, this asymmetry favors P8, the tilted LSD kernel could momentarily drive pressures higher at P8, than reach P9, well before transition to an unpowered blast wave. More insight to this feature is given in Section 4.2 with the Schlieren visualization analysis. Further assessment of this asymmetry dependence must be performed in the future, since a definite conclusion is hard to reach with the data at hand—as the magnitude of error in the measurements reveals.

The second discrepancy in **Figures 4.13 to 4.16** is the even greater disparity between the pressures measured by P6 on the shroud undersurface, and P10 on the primary mirror (very much lower), even though there is no significant difference in their radial distance from the laser focal line or blast wave arrival times (see **Figure 4.11**). One clue might be the incidence angle with which the blast wave hits and then reflects off the oblique surface at P10. Future experiments should be performed to either refute or confirm these results. If proven correct, the optimization of such geometrical dependences might lead to advanced thruster geometries with maximized pressure distributions, and hence impulse.

Finally, it should be noted that the error bars on data displayed in **Figures 4.2 to 4.10** reflect the sum of distinguishable mechanical noise and random noise of the measurements. For a better exposition of these discrepancies obtained from the pressure measurements, the data plotted in **Figures 4.13 to 4.16** was divided in three regions of interest. Regions 1 and 2 correspond to the shroud under-surface, with 1 encompassing the area bounded by the line focus and the shroud's leading edge, and 2 bounded between the line focus and the shroud's trailing edge. Region 3 corresponds to the primary optics surface. These three regions are identified in **Figure 4.12**.

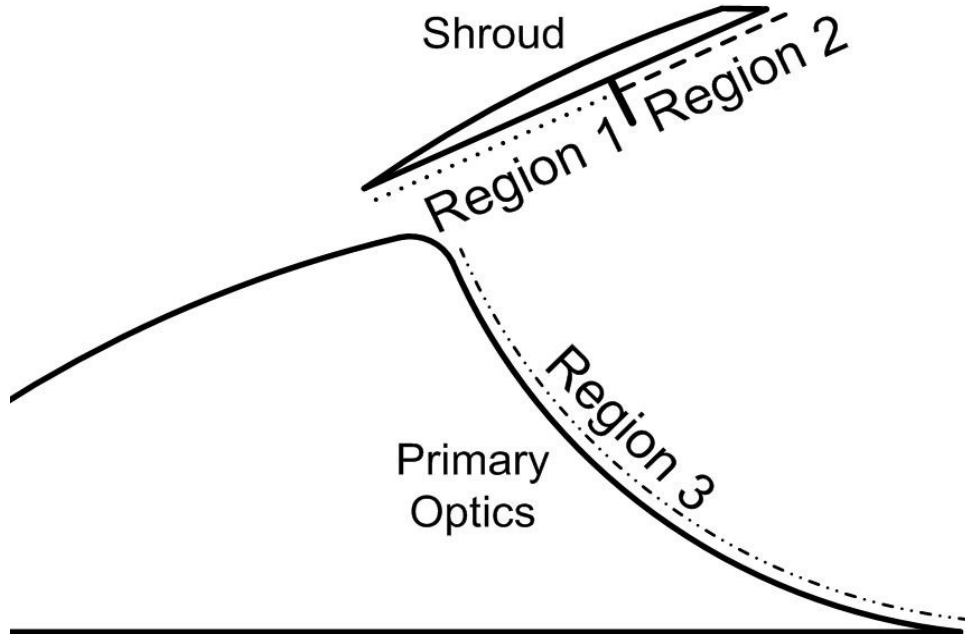


Figure 1.12: Regions for impulse computation, using pressures measured during static tests.

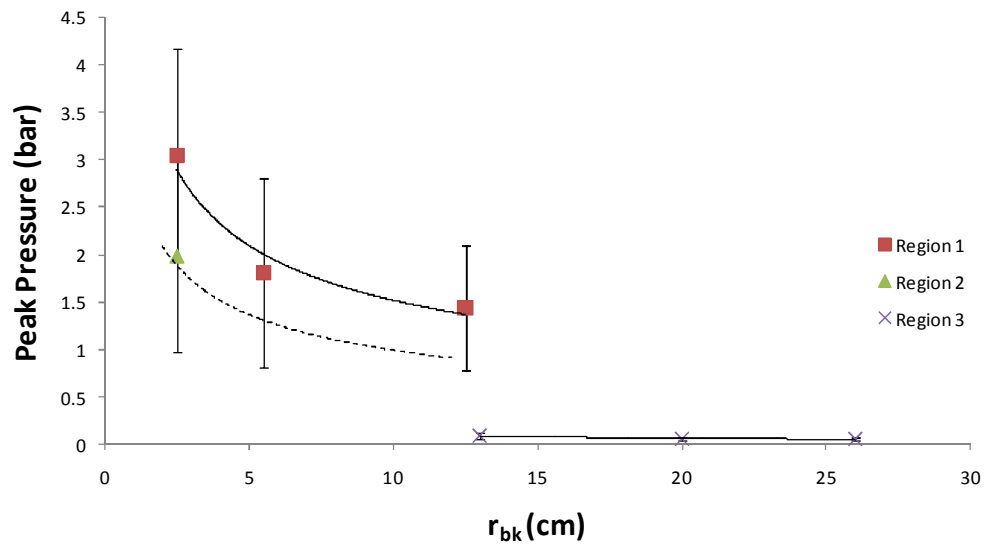


Figure 1.13: Run #1—Peak surface pressure vs. distance from laser line focus. ($P_{\infty} = 60$ mbar; $E_p = 172 \pm 17$ J)

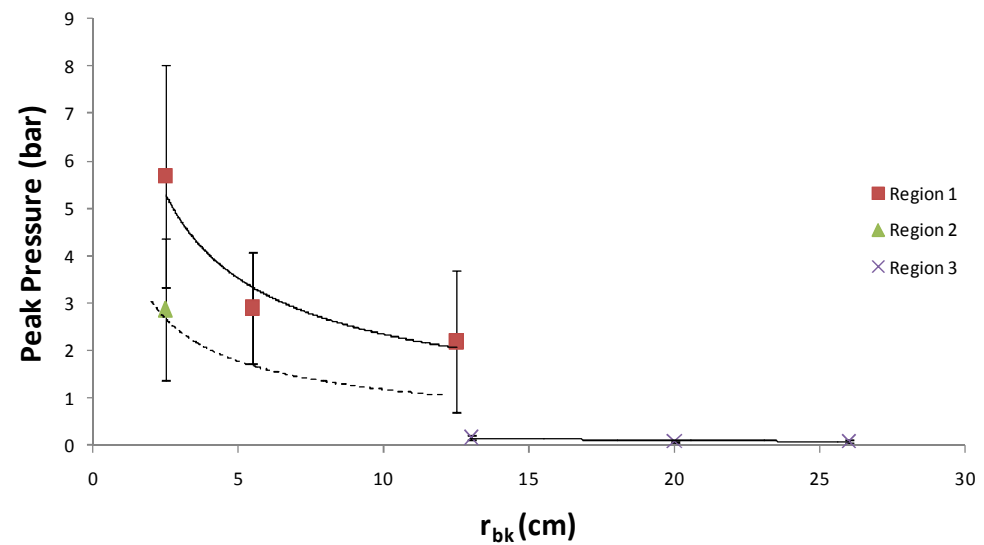


Figure 1.14: Run #7—Peak surface pressure vs. distance from laser focal line. ($P_{\infty} = 150$ mbar; $E_p = 222 \pm 23$ J)

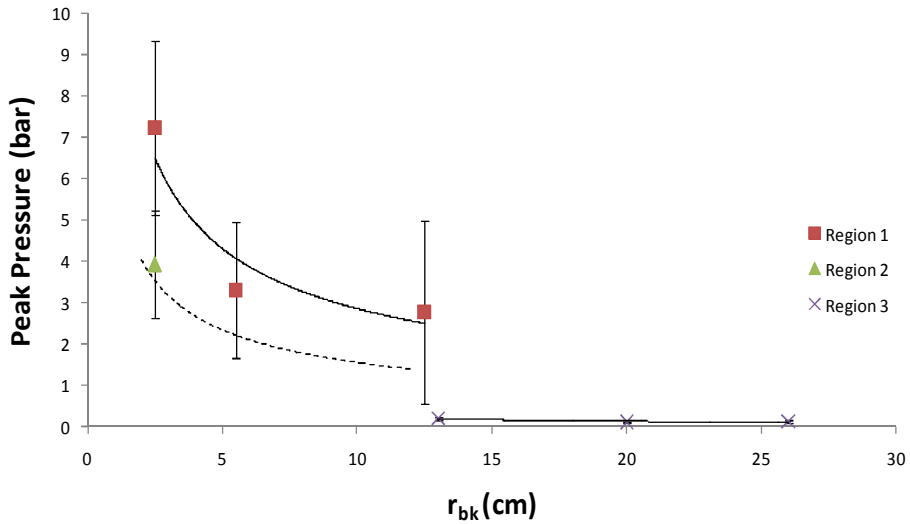


Figure 1.15: Run #11—Peak surface pressure vs. distance from laser focal line. ($P_{\infty} = 300$ mbar; $E_p = 231 \pm 23$ J)

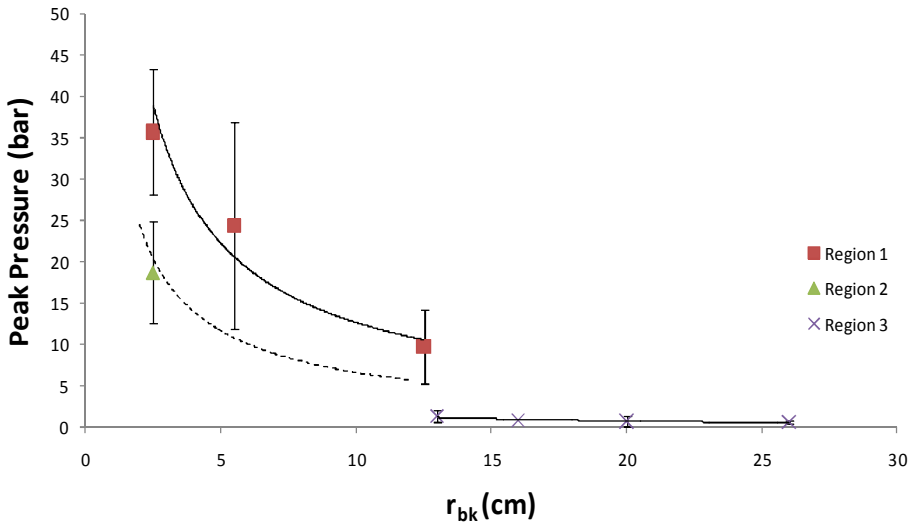


Figure 1.16: Run #12—Peak surface pressure vs. distance from laser focal line. ($P_{\infty} = 1$ bar; $E_p = 180 \pm 20$ J)

1.2 Blast Wave Schlieren Visualization

2. For each static run, Schlieren visualization of the time-dependent, laser-induced blast wave propagation was attempted. Not all attempts were successful due to the excessive Electro Magnetic Interference (EMI) generated by the laser's Marx bank capacitor which is rated for peak discharges up to 34 gigawatts (see Table 3.1; 4860 J released, of which $\sim 70\%$ is in the 100ns FWHM spike). However for the present test campaign, the Marx bank was charged to only 70 kV instead of its maximum rated 90

kV, which reduced the stored energy to 2940J and yielded peak discharges of ~20 GW; these conservative operating conditions for the 620-TEA yielded reliable laser output pulses of 150-200 J, as mentioned earlier. Throughout the static tests, several time-consuming attempts to mitigate such EMI effects were met with minimal success, as covered previously in **Chapter 3**, but greater success was finally realized in the hypersonic campaign—see **Chapter 5**.

The laser's EMI disrupted all instrumentation to some degree, but was especially pronounced with the Cordin High Speed Camera. More often than not, several of the 32 frames acquired by the camera during each run were lost (i.e., completely blank), or scrambled the sequences—activating each of the eight CCD banks (each bank acquires four successive images) in a random order. Despite the image acquisition difficulties, good quality Schlieren images were finally obtained for static LP tests at three dump tank pressures (1.0, 0.3, and 0.15 Bar), but no distinguishable blast waves appeared at 0.06 Bar. These Schlieren sequences are presented in **Figures 4.15 to 4.17** together with surface pressure traces; note the diamond-shaped symbols which mark the exact times that photos were recorded. In **Figure 4.15**, note the upper left Schlieren photo was taken at -28.5 μ s; the negative marker is due to the -100 μ s delay between the laser and camera triggering (i.e., “pre-trigger”). Note also that in **Figure 4.17**, a dashed line is drawn slightly ahead of the blast wave to enhance visibility of that weak shock produced at 0.15 bar; however, detachment of the blast wave from the plasma contact surface was not distinguishable in these Schlieren images. Such features were only visible at the higher static pressures of 0.3 and 1.0 bar.

For static tests at ambient pressures below 0.15 bar, the evolving blast wave structure is barely visible with the present system, so significant improvements in Schlieren sensitivity are mandated. With only minor modifications of the existing experimental setup, this objective becomes feasible: 1) use a higher quality light source—a pulsed visible laser unit in place of the existing Xenon flash unit (**Settles, 2006**); and, 2) replace the 12.7 mm polycarbonate plates that channelize the 30cm flow (installed on both sides of the 2D model), but severely degrade the Schlieren image quality. The strong polycarbonate material is of low optical uniformity, and such non-uniformities appear as dark spots in the field of view, obscuring the blast wave structure.

This kind of optical interference was not present in previous experiments performed at the T3 HST using only the quartz windows installed at the test section side ports (**Rolim, 2009**).

At the 150 mbar run the detachment of the blast wave shock from the contact surface cannot be distinguishable, with this phenomena only being visible at the higher pressure Schlieren images (0.3 and 1.0 bar).

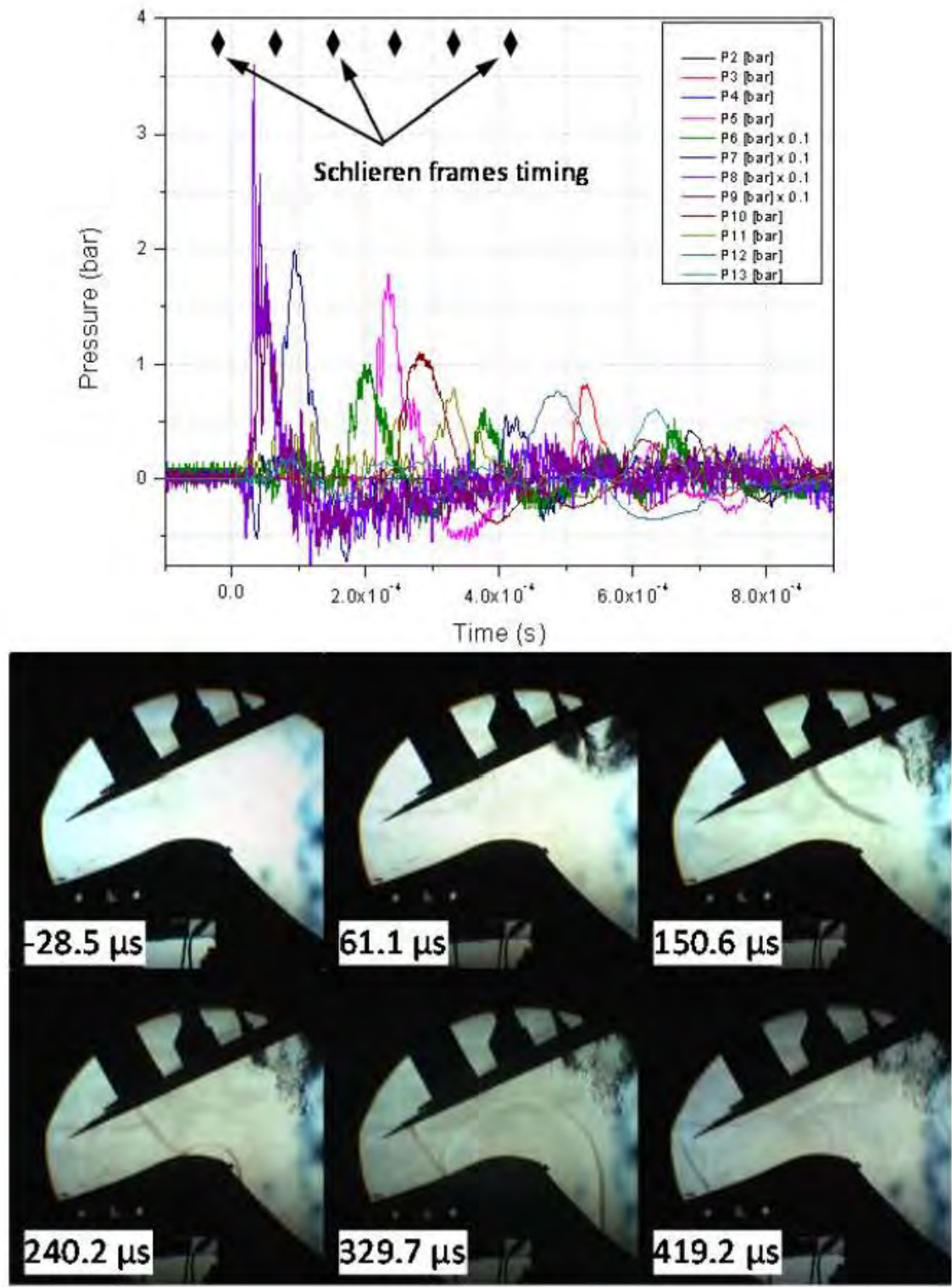


Figure 1.17: Run #12- Blast wave evolution with measured surface pressures (top), and corresponding Schlieren image/frame timing (bottom). $P_\infty = 1$ bar; $E_P = 180 \pm 20$ J.

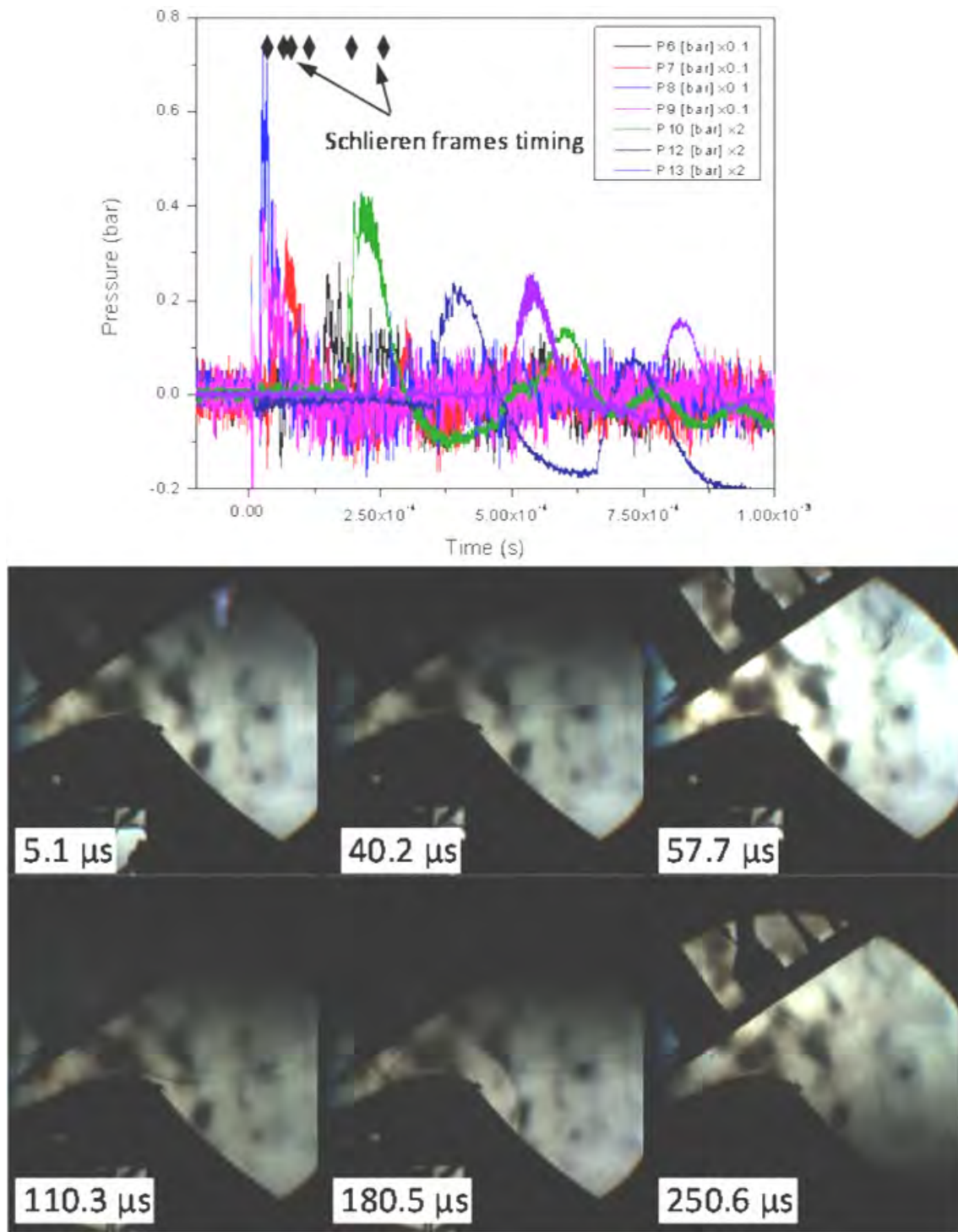


Figure 1.18: Run #11 - Blast wave evolution with measured surface pressures (top), and corresponding Schlieren image/frame timing (bottom). $P_{\infty} = 300$ mbar; $E_p = 231 \pm 23$ J.

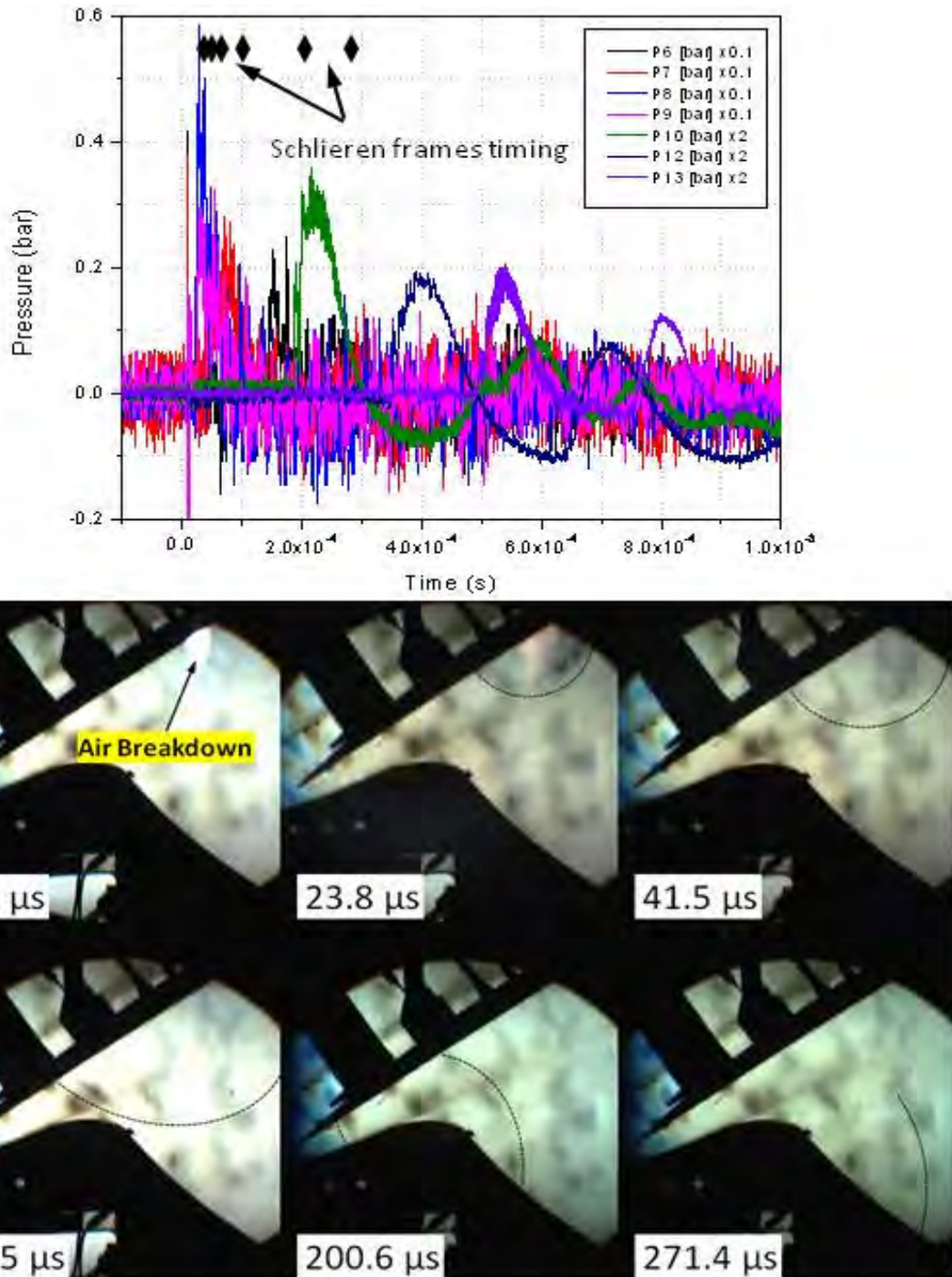


Figure 1.19: Run#7 - Blast wave evolution with measured surface pressures (top), and corresponding Schlieren image/frame timing (bottom). $P_\infty = 150$ mbar, $E_p = 222 \pm 23$ J.

Further examination of Schlieren images that managed to capture the exact instant of laser energy deposition, seems to corroborate the previous explanation given for the asymmetry in pressures measured by sensors P8 and P9. **Figure 4.20** shows a geometrical analysis overlaid upon two Schlieren images of the laser-induced

breakdown upon the inclined shroud. Here α corresponds to the angle between the incoming (focused) laser beam centerline and a perpendicular reference line to the flat shroud undersurface. The included angle β defines the boundaries of the wedge-shaped incoming laser beam that is focused upon the shroud undersurface, causing breakdown and ignition of a LSD wave that propagates away from the shroud and towards the laser source. The physical model describing the propagation of this LSD wave was previously explained in **Figure 2.5**.

The influence of α and β over the resulting asymmetrical shape of the high pressure, high temperature plasma kernel as it expands against the inclined shroud, is clearly in evidence. **Figure 4.21** displays the initial moments of the laser-induced breakdown and blast generation with the model center-body tilted in 7.5° . Here the boundaries of the incoming beam defined by β are more pronounced than in **Figure 4.20**, due to the model's tilt and resulting breakdown, which takes place in the air, away from the surface. Note that the exposure time of each frame in **Figures 4.20 and 4.21** is approximately $4 \mu\text{s}$, long enough to capture the entire process.

Further insight to this phenomenon must await results forthcoming from the planned LP experiments with a 3.5cm wide shroud section instrumented with 4 PCB pressure transducers, to be targeted with 40 J pulses from a Lumonics K922M CO₂ laser; the effects of varying shroud incidence angle upon the pressure traces will be of particular interest. Note that with 13.3 J/cm deposited along the 3.5 cm line focus, the test conditions provide a close match with the 620-TEA experiments (i.e., 12.5 cm line focus with 180-200 J => 14.4 to 16 J/cm). High speed Schlieren movies will also be recorded to study the interaction between the expanding blast and the shroud surfaces, as a function of shroud inclination. This data will also be useful in validating of future CFD models developed for the design and optimization of laser Lightcraft engine/vehicle geometries.

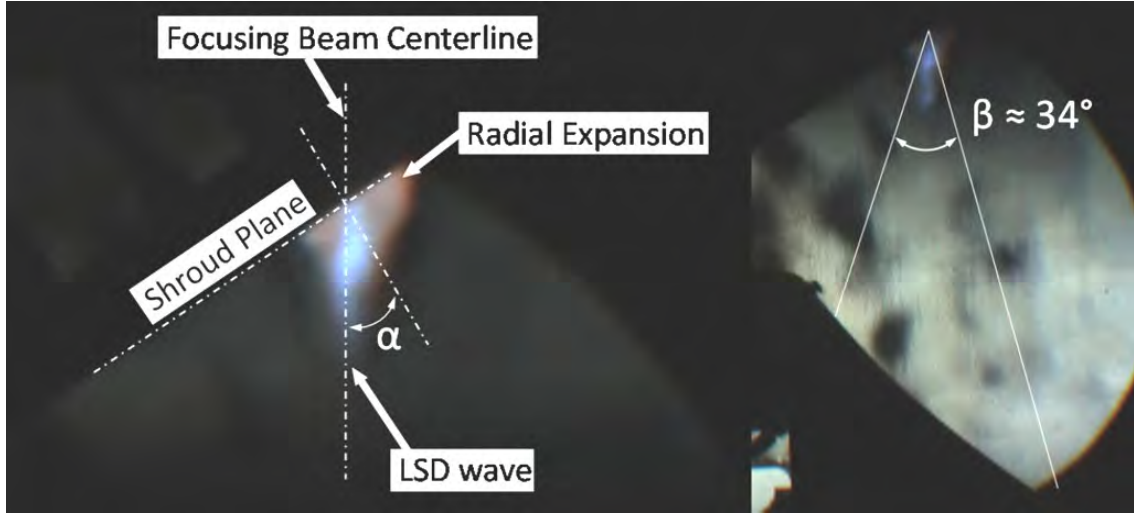


Figure 1.20: LSD wave propagation followed by radial expansion; α and β angles are indicated.

Left: Run #8, $P_\infty = 300$ mbar, $E = 205 \pm 21$ J. Right: Run #11, $P_\infty = 300$ mbar, $E = 231 \pm 23$ J.

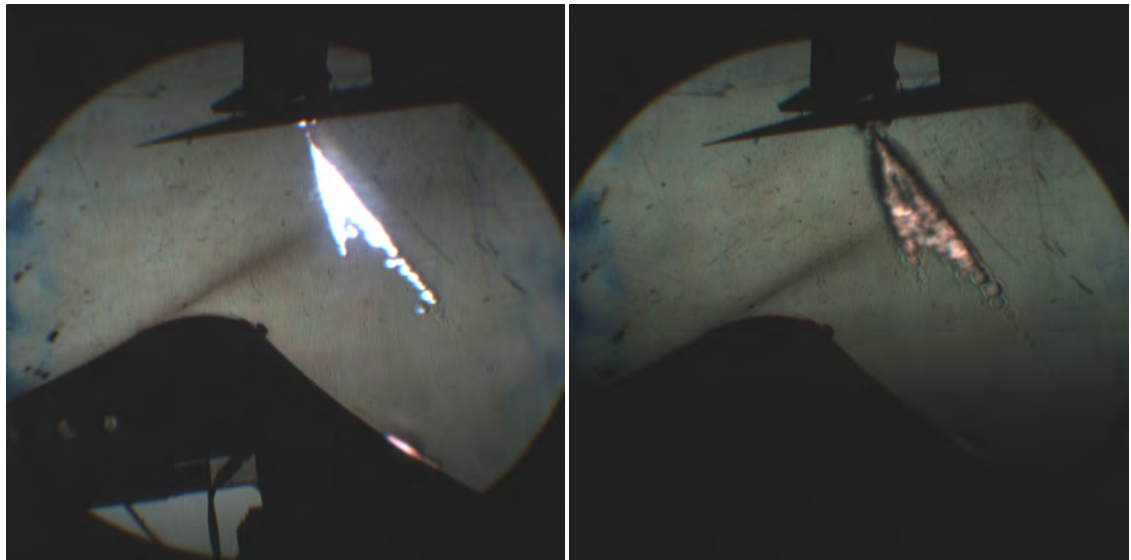


Figure 1.21: Laser-induced breakdown with 2D model pitched forward 10-degrees.

4.3 Impulse Generation Analysis from Surface Pressure Distribution

First-order estimates of the total impulse departed to a 2D Lightcraft engine from a single laser pulse can be calculated from pressure sensor data, taken across engine internal surfaces, under static test conditions. The resultant laser-induced breakdown, LSD wave propagation, and subsequent blast wave expansion comprises one complete pulsed-detonation cycle of duration $\tau_{cycle} = 1/PRF$, where PRF is the pulse repetition frequency of laser source. These static experiments revealed that the blast front transit time (starting from the laser line focus) to reach sensor P13 (near the engine's outer

extremities) is on the order of 700 μs and largely independent of ambient pressure. Hence, the maximum engine *PRF* under these static conditions (e.g., typical of the liftoff and initial subsonic portion of the launch trajectory) would be ~ 1430 Hz if the engine working fluid could be instantly refreshed, which of course is not feasible. Some minimal refresh time interval will be necessary before the engine can again be pulsed.

The momentum coupling coefficient (C_m) and overall efficiency (η_o) of any airbreathing Lightcraft engine (which are vary with flight Mach number and altitude), may be considered the two principal performance criteria targeted for optimization. The momentum coupling coefficient (C_m) is simply the impulse (I) divided by the laser pulse energy (E_p), as given by

$$C_m = \frac{IMPULSE}{PULSE.ENERGY} = \frac{I}{E_p}, \quad \left[\frac{N \cdot s}{J} \right] \quad (4.1)$$

and since time-average thrust given by I/τ_{cycle} and the beam power is $E_p \times PRF$

$$C_m = \frac{THRUST}{BEAM .POWER}, \quad \left[\frac{N}{MW} \right] \quad (4.2)$$

The single-pulse impulse can be directly assessed from surface pressure measurements,

$$I = \iint F dA dt = \int \Delta P \cdot A dt \quad (4.3)$$

and assuming constant area for the 2-D Lightcraft model, the local impulse per unit area is,

$$\frac{I}{A} = \int P_{measured} dt \quad (4.4)$$

For each pressure trace $P(t)$, numerical integration of the area under the curve was readily accomplished with Microcal Origin[®] data analysis software. Once I/A was obtained at each pressure gage site, its magnitude was adjusted to account for the local inclination of the thruster surface with respect to the 2D model's longitudinal axis, since only the axial component of the impulse is of present interest. The radial component will play a pivotal role in autonomous beam-riding characteristics of the Lightcraft engine

(Kenoyer, 2010); however, this shall not be addressed here. Note that all pressure sensors (P6 to P13) were installed perpendicular to the local tangential engine surface, and their inclinations relative to the model’s longitudinal axis are given in **Table 4.2**. Note that the shroud inclination was 25 degrees for the 1 bar static run, but 34 degrees for all lower pressure runs (60, 150, and 300 mbar).

Hence, the adjusted total impulse per unit area contribution is given by $I_{\text{total}}/A = (I/A)\sin(\Theta)$. A simple power law was then fitted to this data to obtain an expression for the I/A over the inner surface of each region bounding the absorption chamber, as displayed in **Figures 4.23 to 4.26**; only Regions 1 and 3 are plotted, since Region 2 is modeled just like Region 1, but off-set by the ratio $(I/A)_9/(I/A)_8$.

Table 1.2: Sensor longitudinal inclination Θ , and impulse adjustment factor $\sin(\Theta)$.

Pressure Sensor	Sensor Location	Sensor Inclination Θ (deg.)	Adjustment $\sin(\Theta)$
P6	Shroud	25/34	0.42/0.56
P7	Shroud	25/34	0.42/0.56
P8	Shroud	25/34	0.42/0.56
P9	Shroud	25/34	0.42/0.56
P10	Primary Optic	51.3	0.78
P11	Primary Optic	45.2	0.71
P12	Primary Optic	39.6	0.63
P13	Primary Optic	32.5	0.53

Next, the I/A distributions were integrated over three distinct absorption-chamber regions (1 and 2 for the shroud; 3 for the rear optics—as shown in **Figure 4.22**) using the integration limits in **Table 4.3**. The influence of LSD-wave/kernel inclination (alpha) with respect to the shroud undersurface (i.e., causing disparate pressure readings of P8 and P9) was also evident in the I/A values. Blast wave energy that propagates out the air inlet gap was neglected (i.e., “lost” contribution to thrust production).

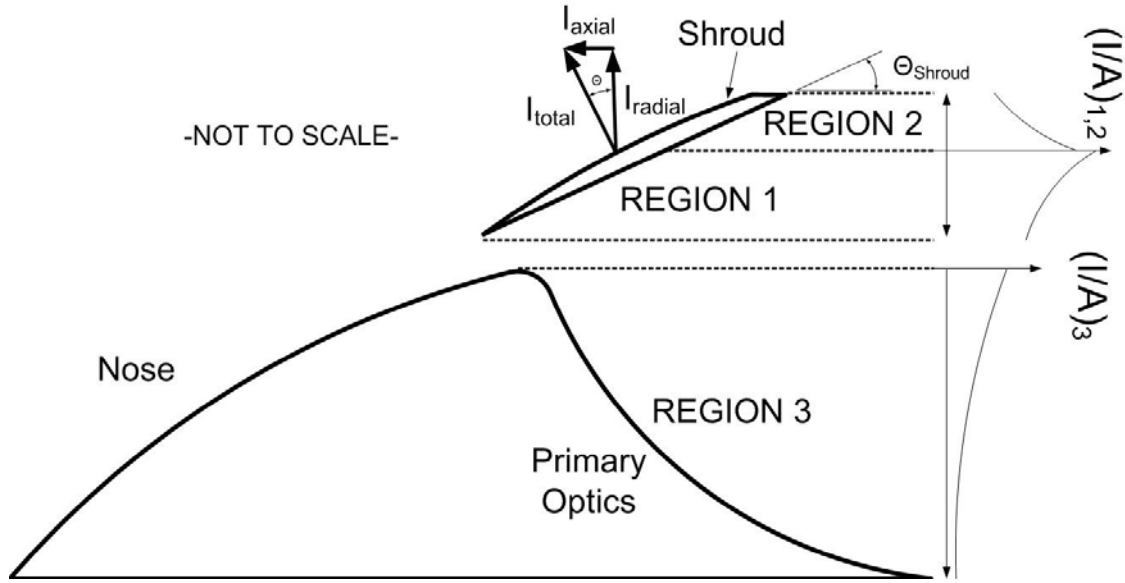


Figure 1.22: The three zones and respective integration limits considered for the longitudinal impulse calculation.

Table 1.3: Limits of integration for laser-generated impulse calculations.

Limits of integration		
Region	Min (m)	Max (m)
1	0	0.185
2	0	0.115
3	0.099	0.353

The small overlap on the integration limits for the case of 34 degrees was neglected. For both cases, the part of the blast wave traveling through the aperture of the inlet was considered as losses, since it is not useful for thrust generation. For the case of static flight the inlet would have to be closed and this blast wave energy loss would be computed in the secondary reflection inside the engine, which as mentioned before was neglected here and as will be seen, its influence would have a magnitude smaller than the measurement errors.

The error relative to the computed I/A was assumed to be the same relative error for the pressure measurements, which already computed for both the random and mechanical noise and are shown in the (I/A) vs. (Axial Distance) plots for Runs #1, #7, #11 and #12, in **Figures 4.23** through **4.26**. Note that the only regions being plotted are Regions 1 and 3, with Region 2 considered as an off-set of the fitted curve of region 1 by the ratio $(I/A)_9/(I/A)_8$.

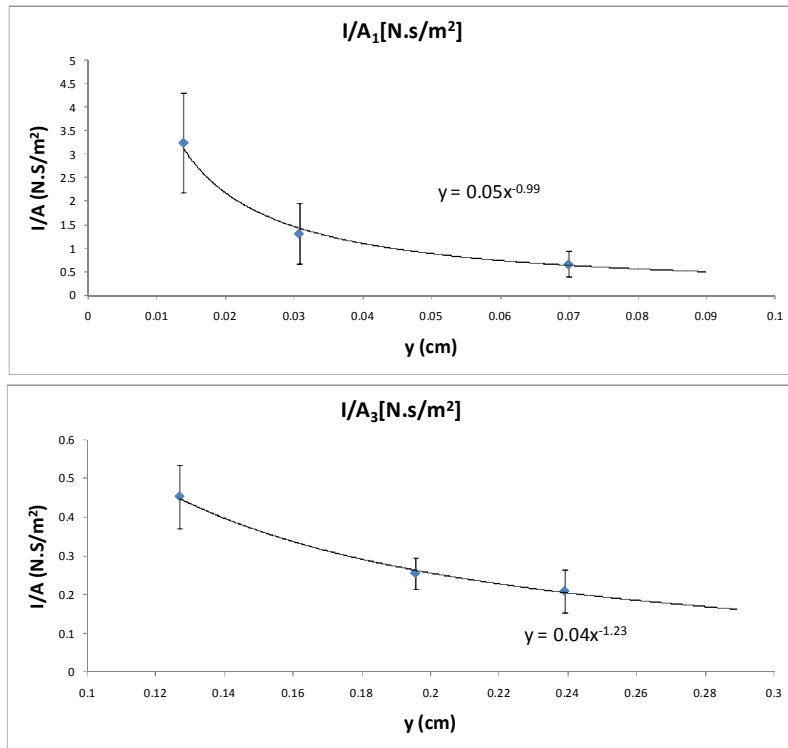


Figure 1.23: Run #1—Peak surface pressure vs. distance from laser line focus. *Top: Region 1; Bottom: Region 3.* ($P_\infty = 60$ mbar; $E_p = 172 \pm 17$ J)

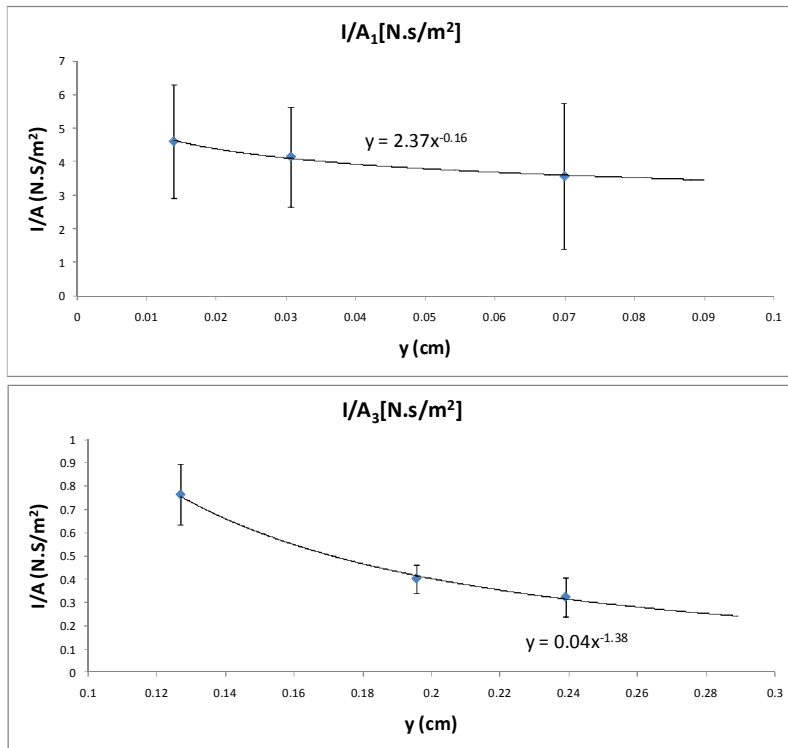


Figure 1.24: Run#7—Peak surface pressure vs. distance from laser focal line. *Top: Region 1; Bottom: Region 3.* ($P_\infty = 150$ mbar; $E_p = 222 \pm 23$ J)

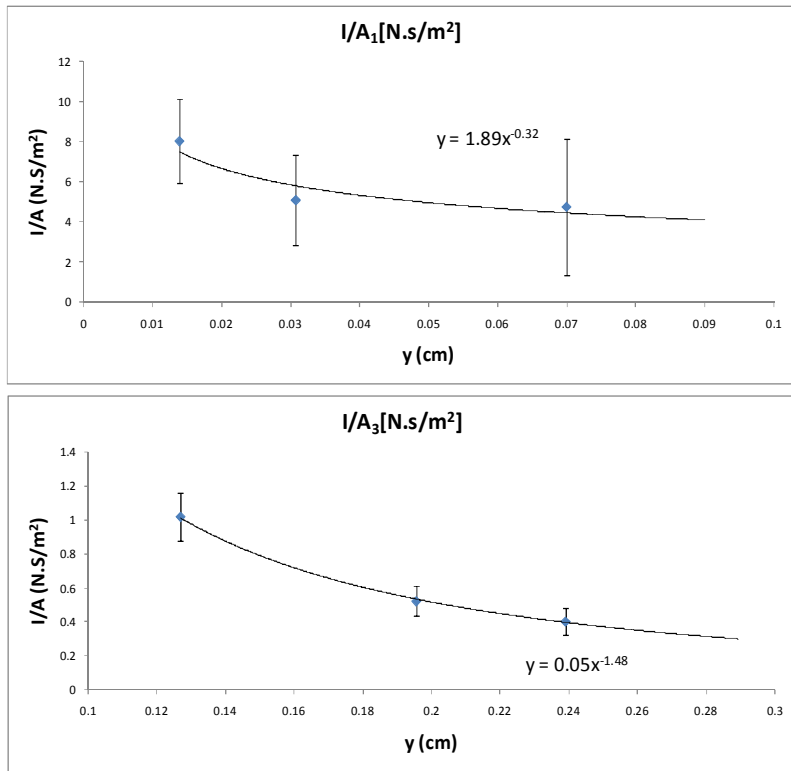


Figure 1.25: Run #11—Peak surface pressure vs. distance from laser focal line. **Top:** Region 1; **Bottom:** Region 3. ($P_\infty = 300$ mbar; $E_p = 231 \pm 23$ J)

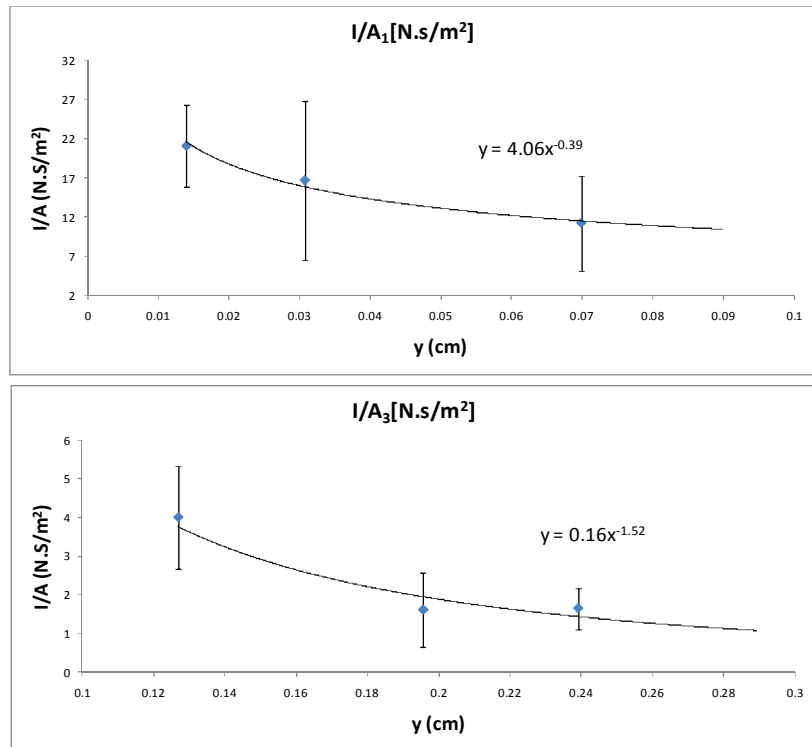


Figure 1.26: Run #12—Peak surface pressure vs. distance from laser focal line. **Top:** Region 1; **Bottom:** Region 3. ($P_\infty = 1$ bar; $E_p = 180 \pm 20$ J)

The next step was to integrate the (I/A) curves over the limits given in **Table 4.3**, to obtain the total impulse (per unit depth) over the surface in the longitudinal direction, I/L (N.s/m). Considering only the 135 mm depth of the laser line focus, the total impulse and momentum coupling coefficient C_m were then calculated and are given in **Table 4.4**.

Table 1.4: Longitudinal Impulse for sample runs #1, #7, #11 and #12.

Region, I/L	Run#1	$\sigma_{\#1}$	Run#7	$\sigma_{\#7}$	Run#11	$\sigma_{\#11}$	Run#12	$\sigma_{\#12}$
Region 1	0.25	0.12	0.42	0.21	0.59	0.31	1.40	0.55
Region 2	0.18	0.09	0.27	0.14	0.29	0.10	0.41	0.14
Region 3	0.08	0.02	0.10	0.02	0.14	0.03	0.50	0.27
Total I/L [N-s/m]	0.51	0.23	0.79	0.37	1.03	0.44	2.31	0.96
I (x0.135) [N-s]	0.07	0.03	0.11	0.05	0.14	0.06	0.31	0.13
C_m [N/MW]	396.2	181.7	478.7	232.1	600.5	265.4	1734.8	742.2

Following this same procedure, C_m was calculated for each of the 14 runs considered and plotted in **Figure 4.27**, together with the averaged value for each condition (i.e., averaged over all runs at a given ambient pressure), which includes the averaged standard deviation from each run. Calculation of the C_m standard deviation was not attempted due to run-to-run variations in E_P . Also displayed in the image, is the -34 degree equivalent C_m result for the atmospheric pressure runs. As mentioned before, the atmospheric runs were made with the shroud positioned at -25 degrees inclination, so to compare with the reduced ambient pressure runs, those results were adjusted for -34 degrees inclination.

From these results it can be seen that the calculated C_m —based on surface pressure distributions—are approximately 2.5 to 5 times higher than the C_m obtained in previous research on the Myrabo Lightcraft models (**Kenoyer et al., 2010; Myrabo, 2002; Wang, 2002**). This would come as a surprise if not for the differences in model size, laser energy, and pulse-widths employed in these experiments.

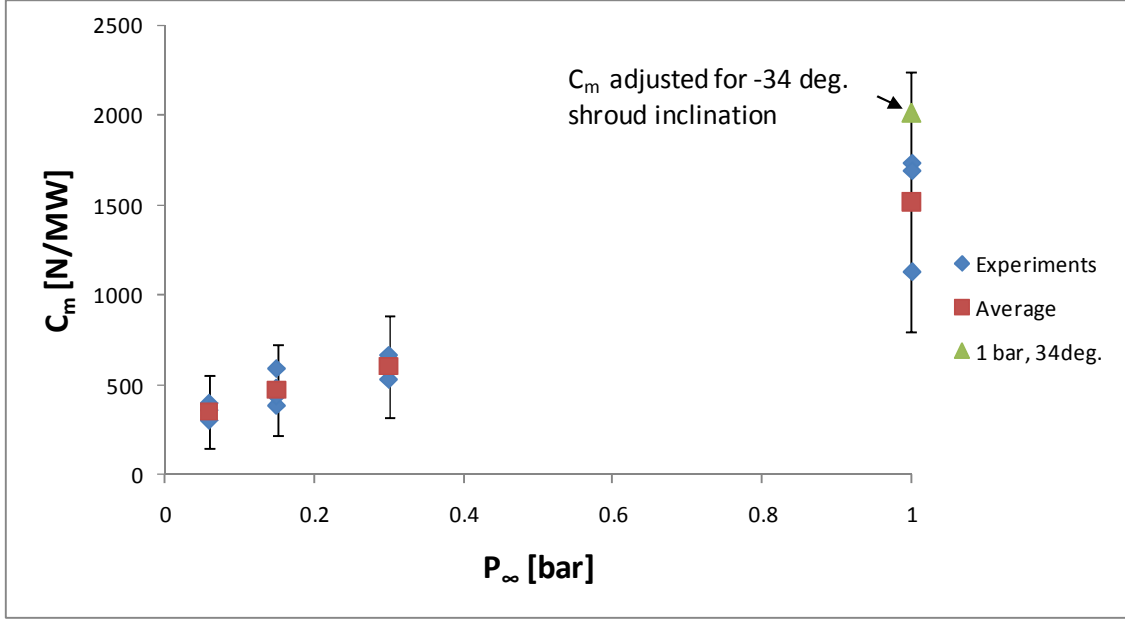


Figure 1.27: Momentum coupling coefficient vs. ambient pressure. (Assumes $\Theta_{\text{shroud}} = -34$ deg.)

First, note that the small 10-cm to 16-cm diameter lightcraft used in previous experiments by **Myrabo (1998)**, **Messitt (1999)**, and **Mead (2007)**—with associated numerical simulations performed by **Wang (2002)**—employed the PLVTS CO₂ laser with a nominal pulse energy of ~420 J and pulse-width of 18 μ s (i.e., 180x longer than the Lumonics 622-TEA laser). A principal conclusion from this former research is that, the 420 J far exceeds optimal pulse energy levels for the small Lightcraft tested; hence, much of that laser energy was lost/ spilled out of the engine’s absorption chamber in the form of excessive blast wave energy. In other words, most of the blast wave expansion happened outside the engine boundaries.

Note that **Pirri (1973)**, **Reilly (1979)**, and **Wang (2002)** assessed the effect of laser pulse-width upon momentum transfer to targets by surface-induced LSD waves, and found that the maximum impulse is delivered when the laser pulse width (τ_p) equals the LSD radial expansion (τ_{2D}) time, which was of the order of 1 μ s; however, the PLVTS pulse-width is 18x longer than this. In contrast, the 622 laser used in the present campaign delivers pulses on the order of 1.5 μ s, but the FWHM of the leading spike is roughly 90 ns and contains approximately 70 % of the total pulse energy. These pulse characteristics are much closer to the optimal values indicated by the research of **Pirri (1973)**, **Reilly (1979)**, and **Wang (2002)**, thus lending credibility to the higher axial C_m

performance observed in the present static test campaign with the 25.4 cm 2D Lightcraft engine.

Furthermore, the largest Lightcraft vehicle studied in the previous experimental research was only 16-cm in diameter (Myrabo, 1998), with an 8 cm primary optic focal radius. However, the present 2D Lightcraft model has an equivalent radius at the focus of 35.3 cm, which enables a much longer blast wave residence time inside the absorption chamber. Hence, it is entirely conceivable that the 2.5-5x enhanced C_m was actually achieved, in large part due to increased thruster dimensions that enable blast waves to fully expand within the thruster, and thereby transfer most of its energy to the impulse surfaces before dissipating. Measured pressures at the furthermost sensors in the present 2D engine seem to corroborate this hypothesis, wherein peak pressures at the extremities were only fractionally higher than background ambient levels.

This dimensional dependence on blast wave expansion and total impulse should be further studied in future experiments, with laser pulse energies up to 1000 joules (if possible) with the present 25.4 cm 2D engine. Also, more precise impulse measurements must be attempted, say perhaps by using larger arrays of more sensitive PCB gages; also, “noise” levels must be reduced significantly to enable measurements of secondary blast wave reflections.

The results reported herein are quite comparable to the analytical predictions made by **Richard (1989)** for the Lightcraft Technology Demonstrator (LTD) because of the close similarity of its pulsed detonation engine and model geometry; Richard’s calculations assumed a cylindrical unpowered blast wave expansion launched from a laser line focus lying flush on flat impulse surface of finite dimensions. In contrast, the theoretical model by **Pirri (1973)** employed a circular laser focal point at the center of a flat impulse surface of finite dimensions, with a vertically propagating LSD wave (perpendicular to the impulse surface) and subsequent cylindrical blast wave geometry, for which a close agreement was not achieved. **Figure 4.28** displays the variation of axial C_m vs. ambient (background) pressure calculated from **Equations 2.18 (Pirri, 1973)** and **2.19 (Richard, 1989)**, where $A_s = 3.6 \text{ cm}^2$, $A_T = 0.04 \text{ m}^2$, $\tau_p = 1.5 \mu\text{s}$, $\tau_{2D} = 350 \mu\text{s}$, $E_p = 200 \text{ J}$, and $I_0 = 2.0\text{E+08 W/cm}^2$. Since the axial C_m values obtained from the present experimental pressure distributions were adjusted for shroud inclination (i.e.,

from 25° to 34°), the same kind of correction was applied in **Figure 4.28** for the theoretical results of Richard and Pirri.

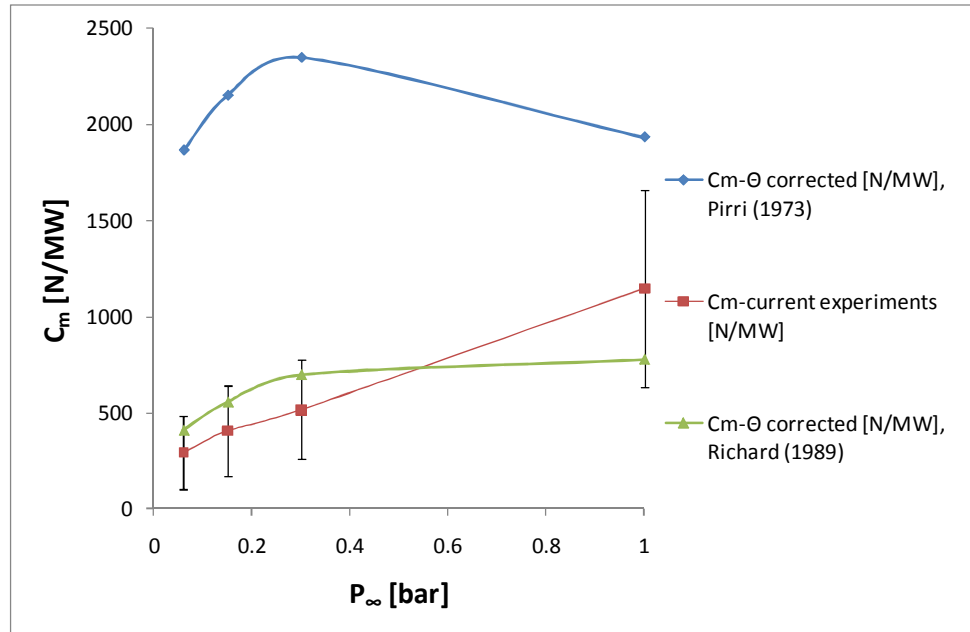


Figure 1.28: C_m variation vs. ambient pressure calculated for finite flat plate by Pirri (1973) and Richard (1989) vs. present experimental data from shroud undersurface (adjusted for shroud inclination).

5 Hypersonic Experiments

Following the static run campaign, T3 hypersonic experiments were performed on the 2-D model with the intent of assessing the feasibility of laser powered flight for purely airbreathing Lightcraft engines in the Mach 6-10 regime. This section presents a qualitative analysis of the laser-scramjet impulse generation process and dominant features, identified from high-speed Schlieren visualizations of the flow structure, along with measured pressure histories over inner surfaces of the 2-D engine's laser absorption chamber. Quantitative results and discussions are limited to cases/runs in which the desired experimental conditions were achieved.

The objective of these ground tests was to explore the hypersonic performance of a laser Lightcraft engine along an airbreathing flight trajectory to low Earth orbit. The hypersonic shock tunnel (HST) is known to be the flow facility of choice, in duplicating such environmental conditions. The two principal parameters that assure similitude are the Reynolds number and Mach number. Matching of these two nondimensional parameters is necessary to achieve similitude in velocity and pressure; however, if similitude in temperature, heat transfer, reaction rates, and continuity are also to be achieved (which exceeds the scope of the present work), additional parameters including the Prandtl, Damköler, and Knudsen numbers (among others) must be considered.

As mentioned earlier, the Lightcraft Technology Demonstrator (LTD) concept vehicle was used for the reference point in designing the present 2-D laser scramjet model. An optimized Earth-to-orbit launch trajectory (**Figure 5.1**) for laser launch was developed by **Frazier (1987)** using SORT flight dynamics software. This altitude vs. Mach number trajectory was subsequently applied by **Langener (2006)** in his Fluent® numerical simulations of flow fields over (and through) various Lightcraft engine/vehicle geometries, at speeds ranging from low subsonic up to Mach 5. The Reynolds numbers encountered along this optimized laser-launch trajectory are plotted vs. Mach number in **Figure 5.2**, along with T3 experimental conditions for the present test campaign. However approximate these flow conditions are, improved matching of similarity parameters must await future experiments, and model designs specifically tailored for such requirements. The existing 2-D laser scramjet model was tested under “off-design” (inlet and absorption chamber) conditions throughout the hypersonic

campaign, with more exact scaling of physical parameters (representative of actual flights) being a secondary, iterative objective for a subsequent campaign. Further information on hypersonic test requirements and similarity can be found in **Lu and Marren (2002)**, **VKI/AEDC Special Course (1993)**, and **Lucasiewicz (1973)**.

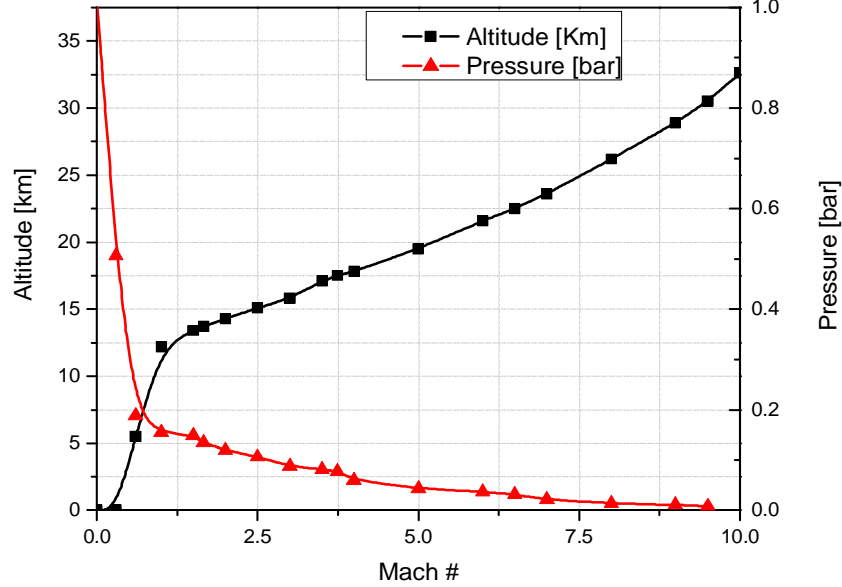


Figure 5.1: Altitude vs. Mach number schedule for optimized airbreathing LP launch to low Earth orbit (Frasier, 1987).

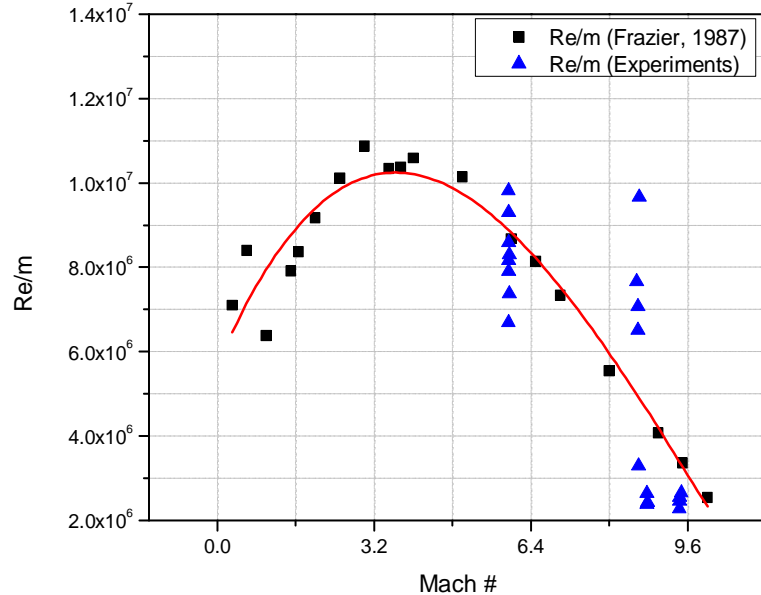


Figure 5.2: Reynolds number variation with Mach number along optimized laser launch trajectory by Frazier (1987), together with T3 HST data from present test campaign.

5.1 Hypersonic Test Conditions

The direct measurement of the test section conditions in any ground test facility is possible only with the aid of proper sensors. Calculation of free-stream properties such as stagnation pressure and temperature is made from specific measurements from sensors positioned at critical locations throughout the tunnel. For the T3 HST facility, such instrumentation was described in Chapter 3, and the theoretical model for computing test section flow conditions is given in **Appendix C**.

The STCALC code, developed at the HTN-LAH laboratory (Rosa et al., 2009), was used to calculate free-stream properties incident upon the 2-D laser scramjet model, directly from gas conditions behind the incident/reflected shock wave at the downstream end of the driven section, which acts as the HST expansion nozzle's reservoir. This code accounts for real gas effects in the T3 tunnel, through the use of tabulated air properties assuming chemical and thermodynamic equilibrium. The code requires as input: a) the gas constant and specific heat ratio, b) the initial driven-section pressure and temperature, and c) the incident shock wave transit time through the driven tube. This transit time is measured by two pressure sensors located at known positions at the end of the driven section. The STCALC program requires the input of the measured reservoir pressure, instead of that calculated by reflected shock relations, which enables the calculation of both “*flow through*” operation, as well as for the operation in the “*reflected mode*” in the HST (**Minucci, 1991; Nascimento 1997**), wherein different reservoir conditions are achieved depending on the mode of operation. The stagnation pressure, temperature, and density, together with the incident and reflected shock wave Mach numbers are given in **Table 5.1** for every test run performed.

Once the reservoir conditions are obtained, the next step is the calculation of free stream flow conditions at the exit station of the conical nozzle, which is also the entrance to the test section. Two calculation modes can be used: one that assumes the nozzle area ratio, and the other takes pressure data from a Pitot probe positioned in the test section. For the results presented herein, the nozzle area ratio mode was used. Hence, the test section free-stream conditions displayed in **Table 5.2** are calculated using STCALC (using the specified diagnostics inputs), for the entire campaign of 24 test runs, using three different nozzle area ratios.

The T3 HST expansion nozzle is composed of three conical sections, for which the final section has an exit diameter of 610 mm. When the present hypersonic campaign began, the initial nozzle had an area ratio of 535.9 with a throat diameter of 26.3 mm—thus giving an isentropic expansion to $M=10$. Since the 2-D model had initially been intended to operate at Mach numbers up to 5-6, the final nozzle section was removed to reduce the nozzle exit diameter to 491 mm for an isentropic expansion of $M=9.12$. This also facilitated the installation of the 2-D model, by avoiding interference with the nozzle. Shortly thereafter, a new family of nozzle throat inserts and a new nozzle transition section were designed for the T3 HST, which now enable test section Mach numbers of 6, 7, 8, 10, 12, and 15—assuming isentropic expansion. Of these, only the $M=10$ insert was available at the start of the present hypersonics campaign.

Runs 1 to 11 were performed with an isentropic nozzle expansion to $M=9.12$, whereas in Runs 12 to 20 the nozzle throat was replaced for $M=6.34$. In Run 20, the throat section was returned to $M=9.12$, but the remaining runs were carried out at $M=10$ by reinstalling the last section of the conical expansion nozzle. Schlieren images revealed that the test section flow conditions at the model site could not be assumed one-dimensional, because conical flow effects were clearly perceptible. In addition, the shortened nozzle prevented full expansion of the flow field, leading to under-expanded conditions at the (shortened) nozzle exit. Hence the actual flow Mach number over the model was lower than that calculated with the measured nozzle area ratio.

Successful operation of the combined system—T3 HST, 620-TEA laser, high speed camera, 2-D model and HST diagnostics—required precise timing of all involved systems, exacerbated by the inherent complexity of the entire setup, and multiple short duration phenomena. The entire test-time-widow supplied by the HST flow is on order of ~ 3 ms, whereas the TEA 620 spike (FWHM) lasts approximately 100 ns followed by a ~ 1 μ s tail; the laser induced air-breakdown, subsequent blast wave expansion, and downstream convection lasts no longer than 150 μ s. All these events must be triggered in the desired sequence with high precision and low jitter. Timing complexity is further increased by the need for acquiring diagnostics from HST instrumentation, TEA 620 laser, and the 2-D model’s pressure transducers, beam diagnosis (energy meter and photon drag), and high-speed Cordin camera system. To assure proper timing for the

experiments reported here, the delays were evolved from instrumentation signals acquired in prior runs, and the principal reference time used was the incident shock arrival time at the nozzle entrance. To assure that the flow over the model was fully established, the main trigger signal followed 1.320 ms later, which then triggered the data acquisition system, Schlieren light source, and secondary trigger. This secondary trigger activated the laser with a 50 μ s delay and the camera with a 250 μ s delay. The camera pre-trigger was set at -220 μ s, so it actually started acquiring images before the laser fired.

Figure 5.3 displays HST instrumentation signals from four pressure transducers during a sample hypersonic run, whereby the pressure increase confirms passage of an incident shock wave. Shown are the measured reservoir and test-section Pitot pressure signals. This figure provides insight to the time scales involved in sequencing the whole system, wherein the raise in the reservoir pressure is used as the reference for all trigger delays, as mentioned before.

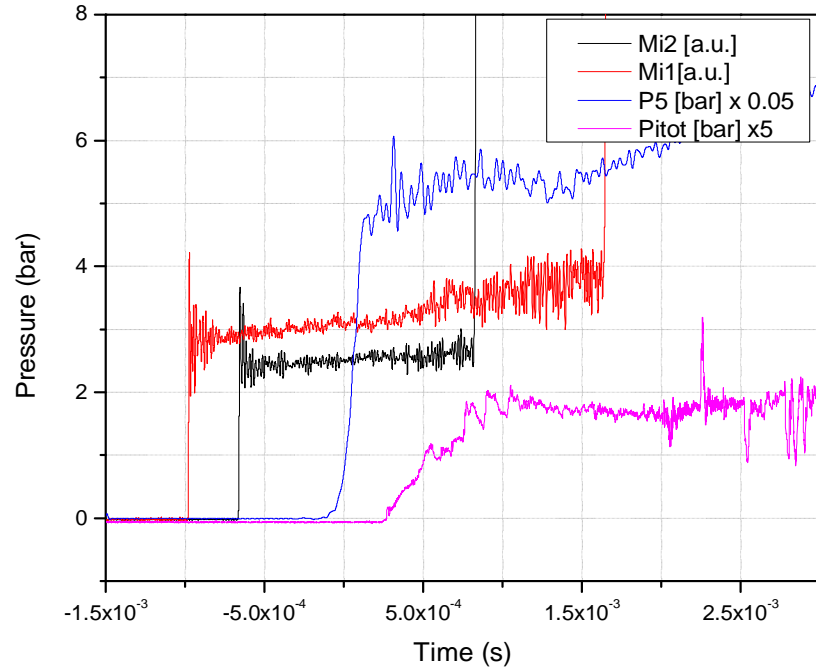


Figure 5.3: Run 24—Typical HST and Pitot pressure signals obtained during experiments.

Test-to-test variations throughout the hypersonic campaign were not restricted just to variations in HST test-section flow conditions. The entire 2-D Lightcraft model itself was tilted downward up to 10-degrees in some tests, and the shroud placement was

frequently altered. The shroud support structure, as explained earlier, permits three degrees of freedom in movement; hence the shroud can be easily repositioned between runs to examine flow structures over the new geometries. For each run, **Table 5.3** lists the different shroud positions with respect to the model's center body and laser focal line, along with the measured pulse energy; the model's center body inclination in respect to the test section centerline is also given.

Later in the hypersonic campaign, the entire model was tilted downward at 0, 4, and 7.5 degrees from horizontal, providing stronger inlet bow shock waves, larger inlet capture areas, and more highly compressed inlet flows. This was explored to help ameliorate the 'off-design' inlet operation (i.e., without the triangular flat plate forebody extension). Note that the LTD engine/vehicle geometry was designed for lower design Mach numbers of 5 (**Richards 1989; Fernandez, 1990**), and higher laser pulse energies (e.g., linear energy density at the focal line up to 87.5 J/cm around the 1.2m diameter focal ring).

Table 5.1: T3 HST initial conditions and reservoir stagnation conditions achieved during experimental campaign.

Run #	Initial Conditions				Incident Mach #	Reflected Mach #	Stagnation Conditions		
	Gas	P_4 (psi)	P_1 (atm)	T_1 (°C)			P_0 (bar)	T_0 (K)	ρ_0 (Kg/m ³)
1	He	3000	2.5	19	2.80	2.04	197.0	133	51.0
2	He	3000	2.5	18	3.40	2.22	213.4	160	45.8
3	He	3000	2.5	21	3.57	2.24	184.0	161	39.3
4	He	3000	2.5	20	3.44	2.21	193.6	157	42.4
5	He	3000	2	22	-	-	N/A	-	-
6	He	3000	1	23	-	-	N/A	-	-
7	Air	3000	1	23	-	-	N/A	-	-
8	Air	3000	1	24	2.52	1.95	33.0	102	11.0
9	Air	3000	1	21	-	-	N/A	-	-
10	Air	3000	1	22	2.69	2.01	31.6	106	10.2
11	Air	3000	1	22	2.52	1.95	27.9	981	9.8
12	He	3000	1	20	3.91	2.31	88.8	186	16.5
13	He	3000	1	18	3.83	2.29	106.4	188	19.5
14	He	2800	1	20	3.82	2.29	100.4	186	18.5
15	He	3000	1	24	3.82	2.29	98.0	188	17.9
16	He	3250	1	22	3.77	2.28	101.2	185	18.8

17	He	3000	1	21	3.60	2.25	118.4	$\frac{184}{5}$	22.2
18	He	3200	1	23	4.17	2.35	92.0	$\frac{201}{2}$	15.8
19	He	3000	1	23	3.59	2.24	110.0	$\frac{182}{2}$	20.9
20	He	3000	1	22	3.57	2.24	111.6	$\frac{181}{5}$	21.3
21	He	3000	1	21	3.60	2.25	110.0	$\frac{181}{5}$	20.9
22	He	3000	1	20	3.41	2.21	102.8	$\frac{170}{5}$	20.8
23	He	3000	1	20	3.82	2.29	106.4	$\frac{189}{5}$	19.4
24	He	3000	1	22	3.63	2.25	108.0	$\frac{182}{4}$	20.5

**Table 5.2: Free stream conditions obtained during experiments, calculated with STCALC
(code assumes chemical and thermodynamic equilibrium).**

Run #	Free Stream Conditions (equilibrium)						
	P _{Pitot} (kPa)	p _∞ (kPa)	ρ _∞ (Kg/m ³)	T _∞ (K)	M _∞	h _∞ (kJ/kg)	Re _∞ (m ⁻¹)
1	95.5	0.975	3.70E-02	91.1	8.61	91.82	9.67E+06
2	104.5	1.082	3.30E-02	113.4	8.56	114.33	7.66E+06
3	90.2	0.931	2.80E-02	113.6	8.58	114.54	6.51E+06
4	94.7	0.978	3.00E-02	110.5	8.58	111.43	7.07E+06
5	N/A	-	-	-	-	-	-
6	N/A	-	-	-	-	-	-
7	N/A	-	-	-	-	-	-

8	15.9	0.157	8.20E-03	66	8.77	66.57	2.64E+06
9	N/A	-	-	-	-	-	-
10	15.2	0.15	7.60E-03	68.7	8.77	69.23	2.39E+06
11	13.4	0.132	7.30E-03	62.6	8.78	63.11	2.43E+06
12	217.5	4.66	6.29E-02	257.7	5.96	259.89	7.37E+06
13	262.9	5.621	7.40E-02	263.7	5.95	265.9	8.59E+06
14	248.0	5.289	7.00E-02	260	5.95	262.12	8.17E+06
15	235.7	5.164	6.80E-02	262.3	5.95	264.44	7.91E+06
16	249.8	5.329	7.10E-02	258.3	5.96	260.4	8.30E+06
17	292.0	6.254	8.40E-02	256.8	5.94	258.96	9.82E+06
18	228.5	4.884	5.90E-02	284.4	5.94	286.76	6.69E+06
19	271.1	5.79	7.90E-02	252.4	5.95	254.51	9.30E+06
20	55.0	0.566	1.50E-02	128.8	8.6	129.85	3.29E+06
21	35.3	0.301	9.70E-03	108	9.44	108.9	2.54E+06
22	32.9	0.279	9.70E-03	100	9.47	100.88	2.66E+06
23	34.2	0.293	8.90E-03	113.7	9.43	114.68	2.27E+06
24	34.6	0.296	9.40E-03	108.6	9.44	109.53	2.46E+06

Table 5.3: Model centerbody and shroud inclinations, focal line location, and laser pulse energy for all hypersonic runs.

Run#	2D Model Inclination (deg.)	Shroud L.E. distance from laser focal line, (cm)		Shroud Angle (deg.)	Laser Pulse Energy, E_P (J)
		X	Y		
1	0	14.2	6.6	25	196±20
2	0	14.2	6.6	25	Off
3	0	14.2	6.6	25	Off
4	0	14.2	6.6	25	58±6
5	0	14.2	6.6	25	Off
6	0	15.5	10.7	34	155±16
7	0	15.5	10.7	34	138±14

8	0	15.5	10.7	34	Off
9	0	15.5	10.7	34	Off
10	0	15.5	10.7	34	207±21
11	0	15.5	10.7	34	Off
12	0	15.5	10.7	34	Off
13	0	No shroud	No shroud	-	196±20
14	0	No shroud	No shroud	-	198±21
15	4	No shroud	No shroud	-	176±18
16	7.5	8.7	0.1	4	187±19
17	7.5	8.7	0.1	4	186±19
18	7.5	8.6	2.5	7.5	121±12
19	7.5	8.6	2.5	7.5	177±18
20	7.5	8.6	2.5	7.5	189±20
21	7.5	8.6	2.5	7.5	196±20
22	7.5	9.3	6.1	24	183±19
23	7.5	9.3	6.1	24	106±11
24	7.5	9.3	6.1	24	150±16

5.2 Hypersonic Campaign Results for 2D Model

This section provides an analysis and discussion of the 24 runs with the 2-D laser scramjet model that comprise the hypersonic test campaign. These results are grouped by similar test section conditions (free-stream properties and Mach number), and model configuration—specifically: a) center body inclination with respect to HST nozzle axis, and b) shroud leading edge (L.E.) distance from the laser focal line, and shroud pitch with respect to the nozzle axis (see **Table 5.3**).

5.2.1 Runs 1 to 4 – Initial Runs

Runs 1 through 4 were carried out at $M \sim 8.6$ with the 2D model installed in the HST test section; the shroud was set at -25° inclination. The driven section was pressurized to 2.5 times atmospheric with synthetic air. Runs 1 and 4 were performed with laser energy

pulses of 196 J and 58 J, respectively; but in Runs 2 and 3, the laser system was not active. **Figures 5.4** and **5.6**. show pressure traces for all the sensors from Runs 1 and 2. Figure 5.7 shows the “Run 0” results (*laser ON, flow OFF*), for which the tunnel was evacuated to $P_{\infty} = 7.5\text{E-}02$ mbar.

Thus, during these first runs three different situations were analyzed: 1) Laser ON with hypersonic flow; 2) Laser OFF with the same hypersonic flow conditions; and, 3) Laser ON while the model was rested in the evacuated dump tank right before the onset of the test flow.

From the pressure data obtained over the model during these runs, it could be seen a simultaneous response of the signals at every sensor when the laser was fired. This does not correspond to the pressure increase from the laser-induced blast, which has to take place with a delay between sensors, as the blast wave expands, and shown in the previous chapter at static conditions.

This behavior was found to be caused by a ‘hammering effect’ produced by the laser induced breakdown and subsequent blast over the surface of the shroud with reduced local pressure, analog to a hammer impact at the laser focal point. This response is not seen at higher ambient pressures due to a larger amount of the laser energy being transferred to the air at the inner surface of the shroud. This mechanism of energy transfer to the shroud surface behaves as a ‘soft hammer’, dampening the mechanical impact cause during the process. This differs from the case of a near vacuum environment where little of the breakdown energy is absorbed by the surrounding air.

The complete mitigation of this ‘hammer’ effect is a difficult task however; reduction of its influence on the pressure data can be achieved with a different design for the shroud fixation and use of a sturdier model less prone to the effects of vibration. In addition, the signal generated due to the vibration can be accessed using the techniques suggested by **Walter (2004)**. This is performed by the use of strain isolated pressure transducers as well as ‘check’ transducers. This enables for the documentation of the vibration response alone, guiding modifications to the model until their output becomes negligible. Furthermore, pressure port inserts can be manufactured with low density material providing a higher level of mechanical insulation for the sensor.

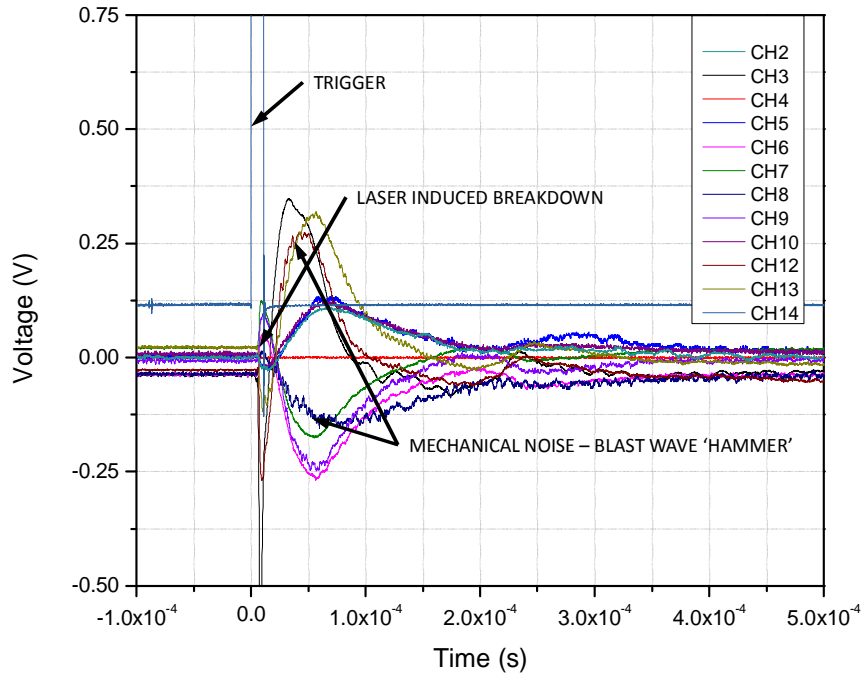


Figure 5.4: Run #1-Pressure transducer traces for Ch2-14 (distributed over 2D model); Laser ON, Flow ON; $M=8.61$; $E_p=196\pm20$ J. Channel number corresponds to pressure sensor. Note simultaneous sensor response to laser-induced blast, indicating excessive mechanical noise.

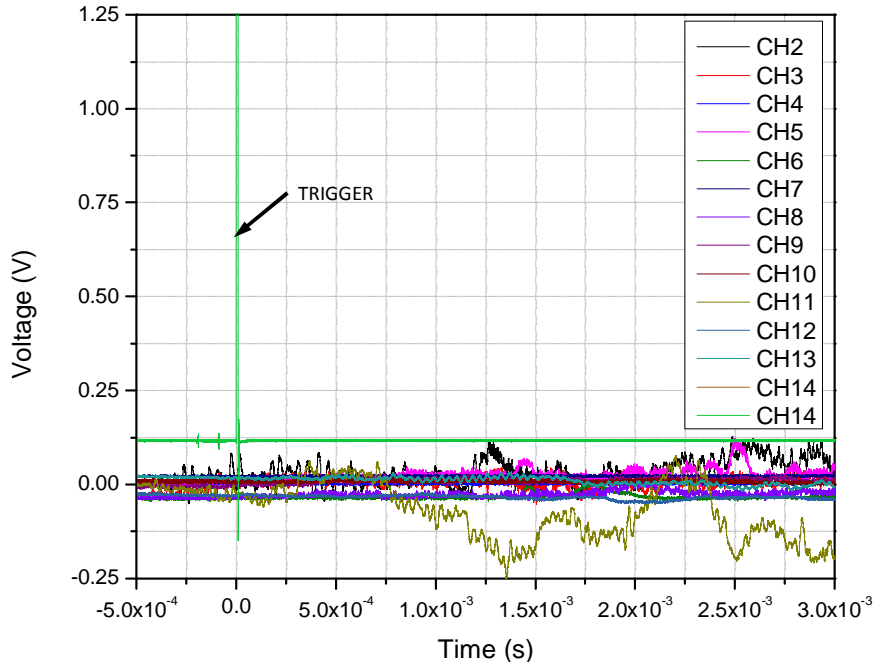


Figure 5.5: Run #2- Pressure transducer traces for Ch2-14 (sensors distributed over 2D model); Laser OFF, flow ON; $M=8.56$; $E_p=0$ J. The signal stability throughout the time window indicates fully established hypersonic flow over the model.

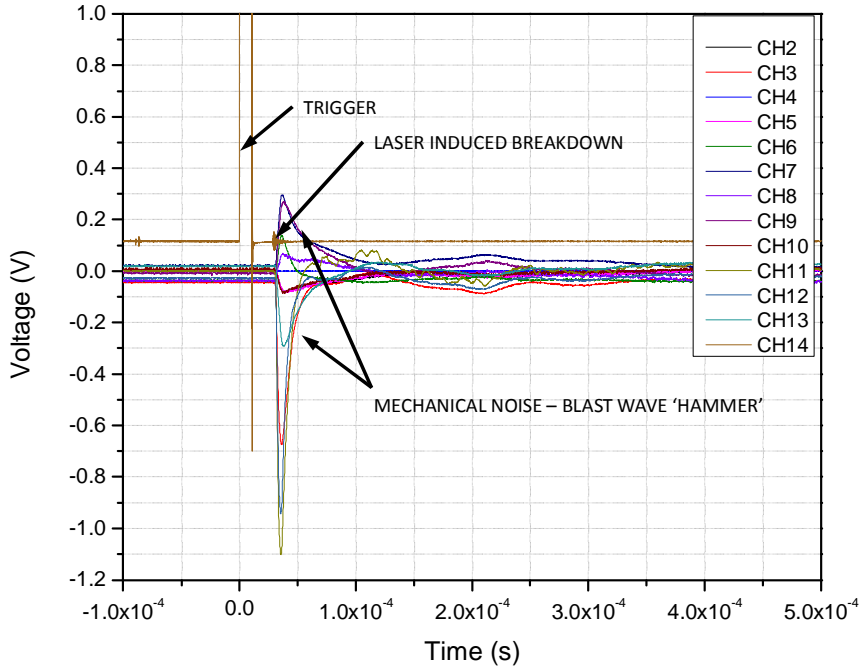


Figure 5.6: Run#0-Pressure transducer traces for Ch2-14 (sensors distributed over 2D model); Laser ON, flow OFF; $M=7.8$; $E_p=180\pm20$ J; $P_\infty = 7.5E-02$ mbar. Note similarity to Run#1 results.

During this phase the high speed camera used for the Schlieren imaging of the phenomena operated erratically due to the EMI noise generated by the TEA 620 lasers. Most of the 32 frames available for the camera acquisition were lost, with some of the visible frames left in a scrambled order. Only the runs performed without laser energy deposition were flawlessly acquired. The Schlieren sequence acquired during Run #1 is shown on the left of **Figure 5.7**, with the image on the right showing one of the frames obtained in Run #2.

EMI problems with the high speed Cordin camera were eventually resolved (with a specific pre-trigger) during the next phase of troubleshooting experiments, along with other issues affecting the experimental setup.



Figure 5.7: Left: Run #1—Erratic Schlieren image sequence . Note oversaturation of 2nd frame when laser induced breakdown occurred, and missing frames due to EMI. **Right:** Run #2—Schlieren image with laser OFF, revealing flow structure at M=8.56.

5.2.2 Runs 5 to 11 – Troubleshooting Runs

During the initial four HST runs, several problems affected the quality of data acquisition from model instrumentation and Schlieren imaging system. In addition, operational issues with the T3 HST and TEA-620 laser system had to be resolved, which required several troubleshooting runs.

For Runs 1 through 4, a previous batch of stainless steel diaphragms was available and used between the driver and driven sections. These diaphragms had been thoroughly characterized during the previous campaign (**Rolim, 2009**). However, a new batch of diaphragms (different material) had to be manufactured for the remaining experiments, and new diaphragm manufacturing specifications had to be found.

To achieve the desired rupture dynamics for the diaphragms, careful engraving of one surface must be made, with the rupture pressure determined by the cut depth, cut geometry, and diaphragm material. The diaphragm engraving and test procedure followed the guidelines set by **Rolim (2009)**, with the basic geometry depicted in **Figure 5.8.**, together with a ruptured diaphragm. For these tests only the DDS section of the tunnel was pressurized until the rupture was achieved. Once the desired rupture pressure between 2000 and 2500 psi was achieved, full tests of the T3 HST could be performed.

This procedure had to be executed before Run 6 and Run 7 until a suitable engraving depth and geometry was achieved. Due to poor rupture dynamics from the diaphragms the incident shock wave was not formed properly in Runs 5 through 7, and the data obtained had to be discarded. In these runs the laser was active, but the flow field was not properly established. The diaphragm problem was finally solved for Run 8, whereupon the engraving geometry was frozen.

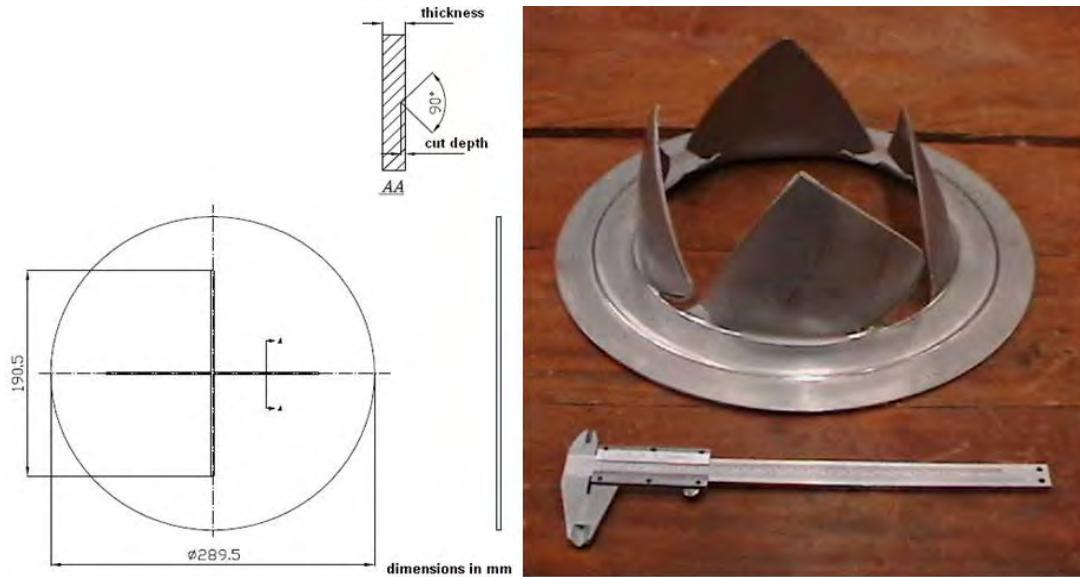


Figure 5.8: Left: Diaphragm engraving geometry. Right: Burst diaphragm.

Run 9 had to be discarded due to issues with the delay generator. In this run the HST worked properly, but none of the instrumentation or the laser was activated.

Throughout these runs (except Runs 5 and 6) air was used as the driver gas (instead of Helium) to reduce costs. In most of these experiments the laser was active (Runs 6, 7, 9, and 10) but the issues described above did not allow for any consistent data acquisition until Run 10.

The static analysis from the previous chapter was performed during this phase of troubleshooting hypersonic experiments. With the noticeable reduction in pressure from the data, the need of a higher sensitivity sensor for the hypersonic runs became evident. For this reason all the shroud sensors (PCB 113A22) were changed to increase the sensitivity from 1.45mV/kPa to 14.5 mV/kPa (PCB 112A22), as shown in **Appendix A**.

During Run 10, the laser was active and the pressure distribution over the model was acquired. This run was performed at $M=8.7$, with the model shroud inclined at -34

degrees, in an attempt to capture the shock wave generated off the compression ramp; the shroud axial position and the ‘focus-on-shroud’ restriction were maintained. The results obtained are in accordance to those from the previous experiments, with the mechanical noise making impossible the accurate measurement of the pressure increase caused by the laser induced blast wave expansion. This situation was emphasized by the extremely small capture and inlet area, aided by the reduce flow pressure and density at the focus.

At these conditions no blast wave expansion visualization was possible by the Schlieren technique, with only the air-breakdown glow being distinguishable, as shown in **Figure 5.9**. The acquired signal from P6, P7 and P9 are displayed in **Figure 5.10**, where the initial simultaneous peak can be clearly seen. The P8 presented problems and its signal was lost. Figure 5.10 clearly show the result of the blast wave ‘hammer’ effect and the subsequent increase in noise caused by the arrival of the expanding blast. Due to its proximity to the focus, sensor P9 shows a distinguishable peak from the pressure increase caused by the incoming blast, which was not present in P6 and P7, due to their distance from the focus, with the blast reaching them with greatly reduced strength.

Following the solution of the issues with the HST, the efforts were concentrated on the TEA 620 lasers, which were experiencing power supply premature discharge. These problems were solved with a major overhaul and enabled the successful operation during the final 13 experiments.

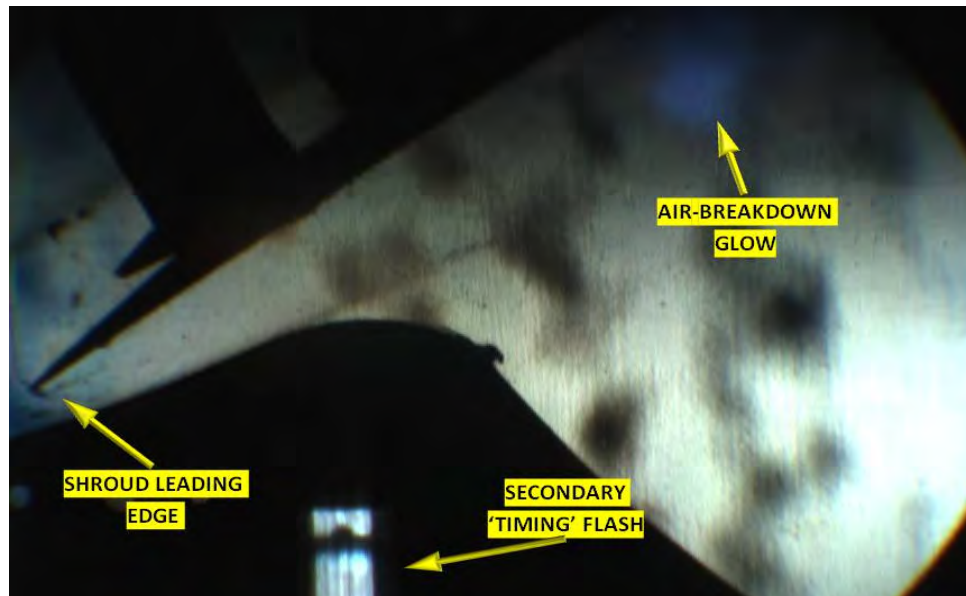


**Figure 5.9: Run 10-Schlieren image with only the laser-induced air-breakdown glow visible.
($M=8.77$, $T_{\infty}=68.7$ K, $P_{\infty}=0.15$ kPa).**

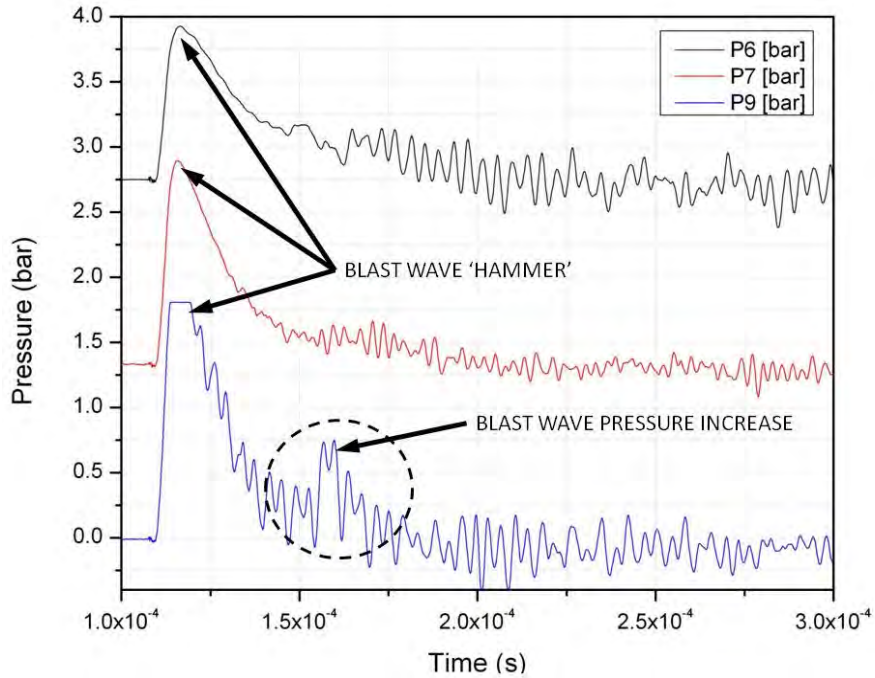


Figure 5.10: Run 10-Pressure gage traces for P6, P7, P9 distributed over shroud undersurface; laser ON, flow ON; Mach 8.77; Ep=207J. Sensor P9 pressure jump is from passage of blast wave.

5.2.3 Runs 12 to 15 – Shroud Removed

Now that the initial issues with HST tunnel operation, instrumentation, TEA 620s were resolved, the fully integrated hypersonic experiments could resume.

Prior attempts to capture high-speed Schlieren movies of laser-induced blast waves within the laser scramjet engine were unsuccessful for two main reasons: 1) The low static pressure at the laser focal line, caused by the rapid expansion (and acceleration) of flow captured through the inlet gap, lead to weak laser-induced air breakdowns and blast waves; and, 2) the 620-TEA's EMI pulse disrupted the Cordin camera, causing erratic behavior—i.e., frame scrambling, blank frames, and loss of trigger precision. Solutions to these two issues were discovered in this test series, finally enabling the acquisition of desired data.

The EMI solution emerged from a creative application of the camera's pre-trigger and banks that record photographic frame sequences. The Cordin 550 is fitted with eight CCD camera banks that capture four frames each. Previous to receiving the trigger

signal, these banks are continuously acquiring and storing images into the camera's cache. With the proper pre-trigger, these banks are sequentially activated to deliver previously-acquired images that are stored in the cache memory. This pre-trigger procedure creatively circumvented the former EMI-induced camera disruptions.

To investigate the influence of local static pressure variations upon laser-induced breakdown focal line of the rear parabolic optic, the model's shroud was temporarily removed. This significant modification of the model geometry (readily performed), eliminated the rapid expansion produced by a sharply inclined shroud and parabolic optic, that acted as a diverging nozzle, accelerating the captured airflow through the inlet gap. At the same time, this modification produced a high pressure and density region behind the bow shock, favorable to laser-induced air-breakdown and strong blast waves.

Figure 5.11 displays 4 of the 32 frames acquired in Run 13 which, for the first time ever, captured images of a laser-induced blast wave evolving in Mach 5.5 flow. Note the disturbed upper end of the oblique bow shock (formed off the inlet forebody), as this blast wave structure is convected downstream in hypersonic flow. The elapsed time for the whole cycle, from the moment of laser energy deposition/ air-breakdown, through the reestablishment of the original inlet flow structure was about 70 ± 4 μ s. The first camera frame, which was to image the air-breakdown, was not successfully acquired.

The removal of the shroud did not allow for the acquisition of the time-dependent pressure distribution, which was performed in the later runs.

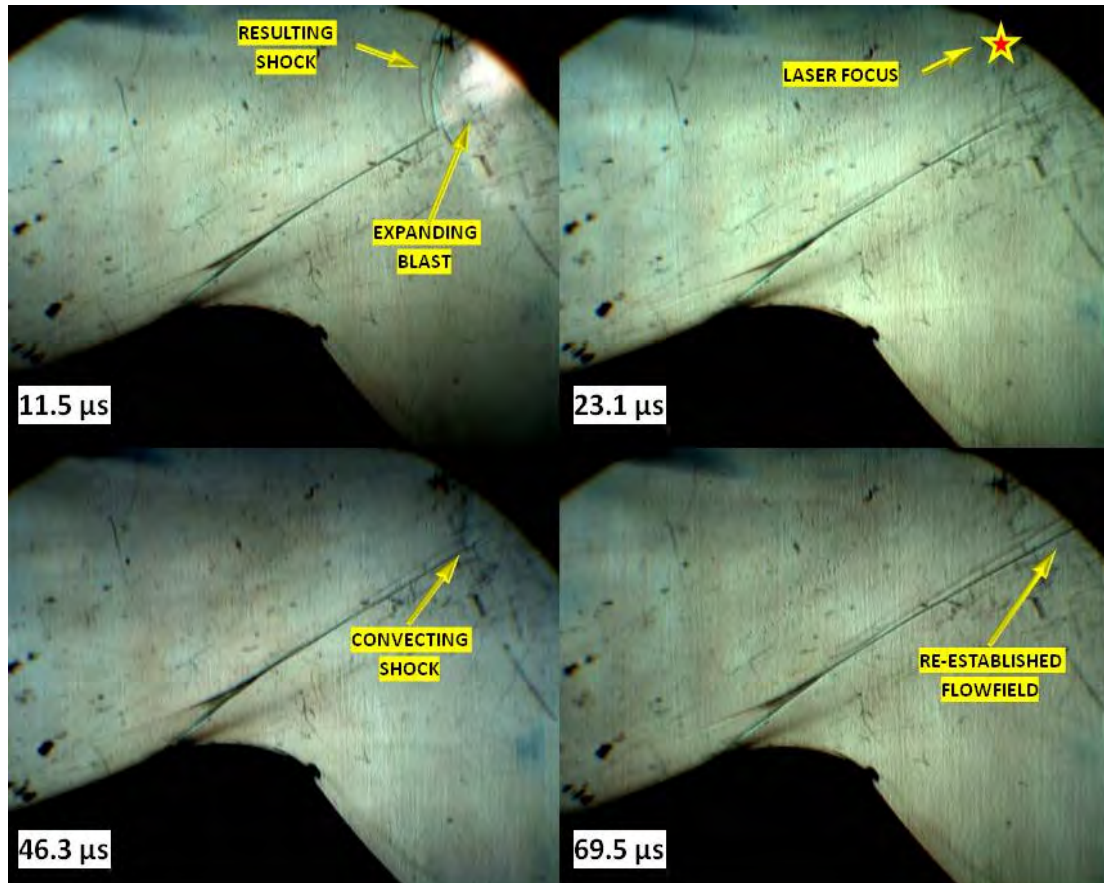


Figure 5.11: Run #13-Laser induced blast wave interaction with oblique shock. (M-5.95, $T_{\infty}=263.7$ K, $P_{\infty}=5.62$ kPa, $E_p=196\pm20$ J)

In Run 14 the identical setup conditions were maintained, except for the Schlieren camera whose frame rate was increased—hoping for images of the blast wave structure evolution; however, no images were acquired.

The objective of this test series was to investigate the laser “focus-on-shock” condition. Note that for each of the Run 13 images in Figure 5.11, this focus of the primary optics is marked by a pair of closely spaced X’s (see upper right), residing just above the bow shock wave. So for Run 15, an attempt was made to lift the bow shock position above this focus, by pitching the entire model forward ~4 degrees counterclockwise.

Note that experimental studies have measured the C_M performance of Type 200 Lightcraft engines as a function of pitch angle (relative to the laser axis). As the engine pitch increases, coma aberrations around the optic’s focal ring cause local laser intensities to decrease, and hence C_M declines because the laser-induced blast wave

pressures also decline. For example at 4-deg pitch, C_M falls to 80% (of max for the aligned case), 70% at 7.5-deg, and declining linearly with pitch angle—to 66% at 10-deg. pitch

As seen in **Figure 5.12**, the 4-deg pitch did elevate the bow shock to a position much closer to the focus while increasing inlet airflow compression, but at the expense of coma aberrations in the focused laser beam (caused by the 4-deg tilt of the primary parabolic optic)—made evident by the broadening of the laser focal waist at the breakdown location. This wider focal waist reduces the local laser flux, and influences the laser-induced breakdown geometry, giving it an elongated appearance (accentuated towards the laser source) as in **Figure 5.12**.

The direct comparison of Schlieren images from **Figure 5.11** (Run 13) and **Figure 5.12** (Run 15) reveals an increase in bow shock slope and compression for the -4 deg. case. This slows airflow velocity over the forebody ramp and extends the residence time for the laser-induced blast in **Figure 5.12** images, which extend approximately $80\pm4\ \mu\text{s}$ before leaving the field-of-view, despite the lower laser pulse energy ($176\pm18\ \text{J}$).

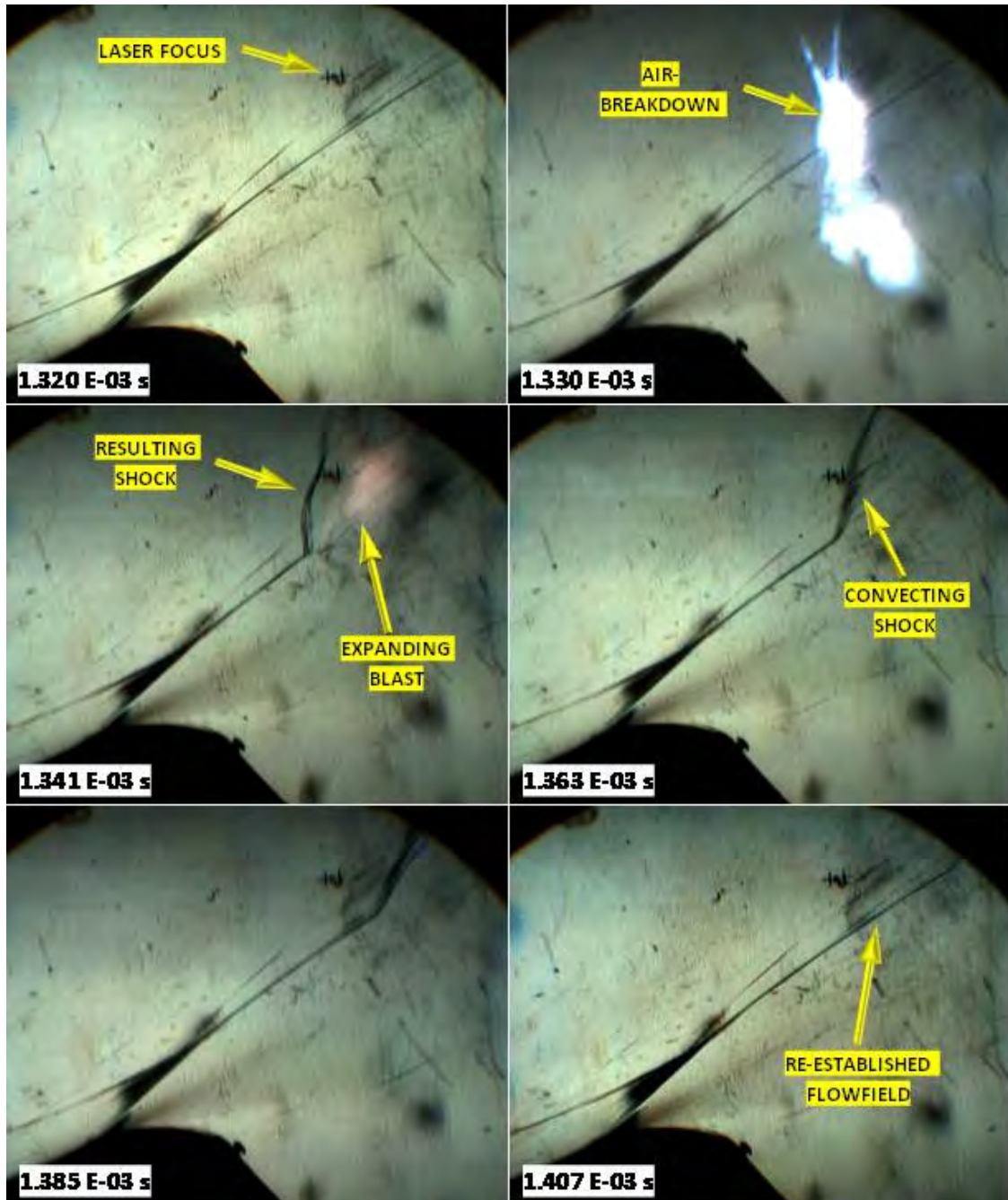


Figure 5.12: Run#15-Laser induced blast wave interaction with oblique bow shock; -4° model pitch.

The smearing of the focus is noticeable on the air-breakdown geometry. (M=5.95, $T_{\infty}=262.3$ K,

$$P_{\infty}=5.16 \text{ kPa}, E_p=176 \pm 18 \text{ J}$$

5.2.4 Runs 16 to 19 – Mid-channel Breakdown

For Runs 16 to 19, the shroud was re-installed on the model. For Run 16, the shroud was set at -4° incidence (from horizontal), with the undersurface positioned slightly

above the primary optics' focal line. The entire model was pitched further forward from -4° to -7.5° (counterclockwise). Otherwise, Run 16 was performed at the same flow conditions as the previous.

A six-frame Schlieren image montage from Run 16 is displayed in **Figure 5.13**, wherein the shock wave off the lower leading edge of the shroud is clearly visible. The bow shock wave formed over the inlet compression ramp/forebody meets with the shroud's shock wave at a point near where the laser-induced breakdown occurs. As it is convected downstream, the resultant expanding blast wave appears to interact with the shroud undersurface (see image at $22.6\ \mu\text{s}$); however, the reflected shock off the shroud under-surface appears unaffected. Also, note the secondary shock that has formed off the inlet compression ramp/forebody; it may be triggered off a small surface discontinuity on the inlet compression ramp just before the cylindrical transition section to the rear optics. **Figure 5.14** gives the pressure traces measured by the PCB sensors across the shroud undersurface. The blast wave arrival times are clearly registered by P9 and P7, but negligible perturbation is seen by P6.

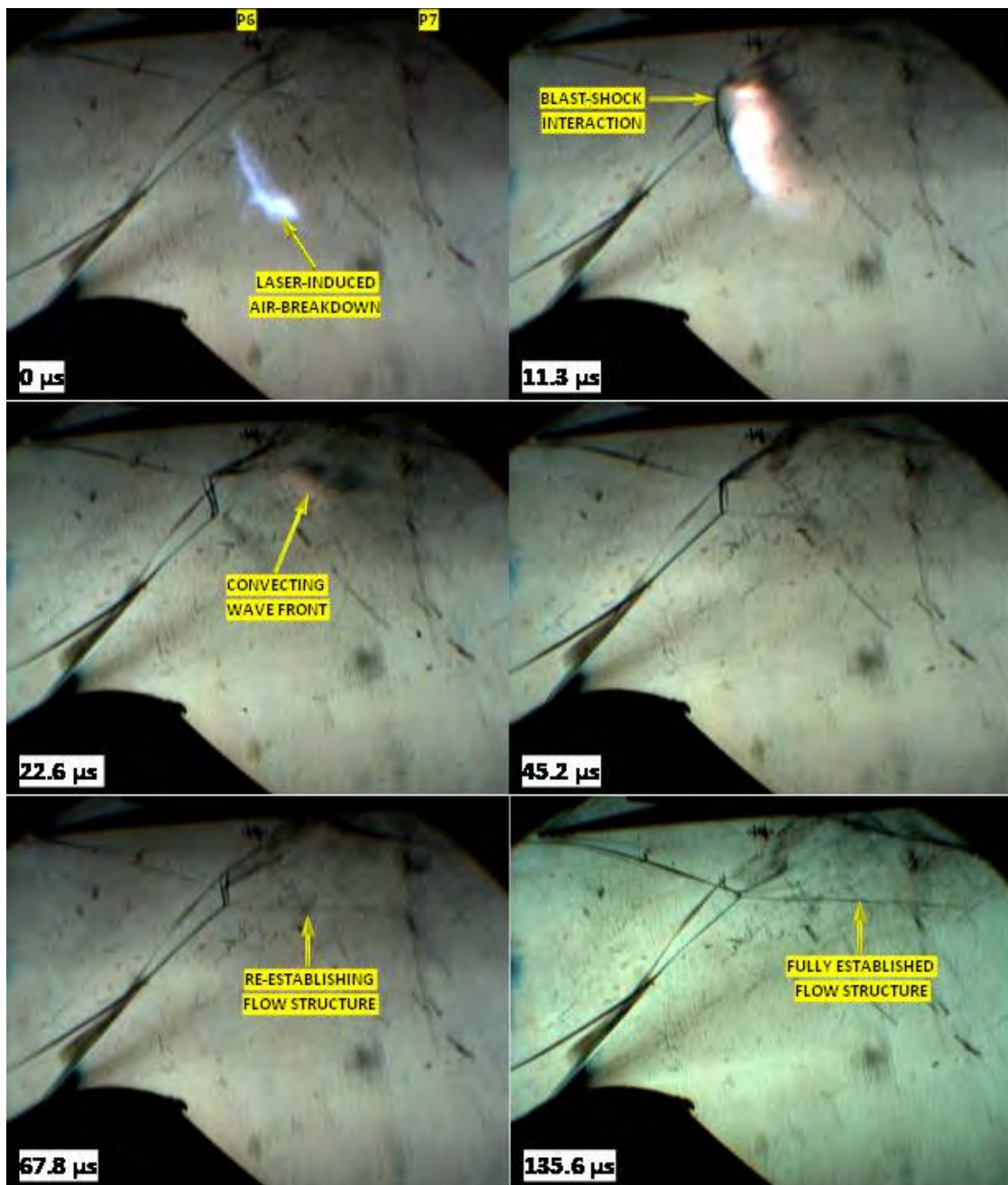


Figure 5.13: Run#16 - Laser induced blast wave interaction with oblique shocks from shroud and inlet center-body at 7.5° inclination. ($M=5.96$; $T_{\infty}=258.3$ K; $P_{\infty}=5.32$ kPa; $E_p=187\pm19$ J)

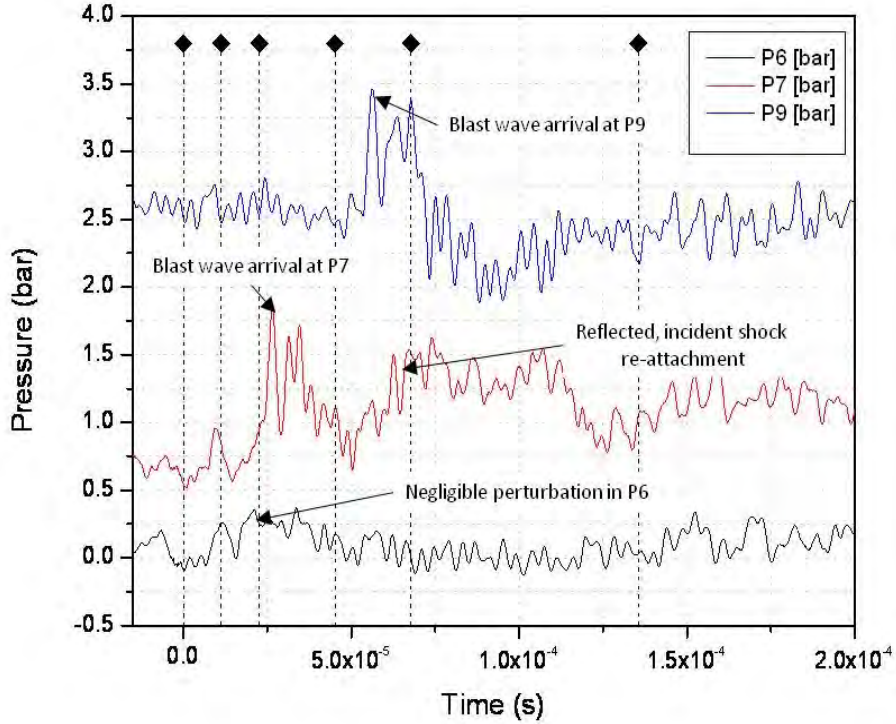


Figure 5.14: Run#16 - Measured pressure distribution over shroud under-surface; traces offset.

Schlieren frames from **Figure 5.13** are marked by diamonds.

Run 17 was performed with the same HST setup configuration used in Run 16, but the Schlieren images in **Figure 5.15** were considerably different, perhaps in large part because of dissimilar free-stream conditions (see **Table 5.2**) in the test section. The 19% increase in P_∞ and 22% increase in ρ_∞ between Runs 16 and 17, was likely caused by atypical rupture dynamics of DDS diaphragms. Considering the driver pressure of 3000 psi for Run 17, and 3250 psi for Run 16, the latter was expected to give higher free-stream P_∞ and ρ_∞ properties. A similar discrepancy was observed in Run 18 in which the driver was charged to 3200 psi, but the test registered lower free-stream properties than either Run 16 or 17 (see **Tables 5.1** and **5.2**).

Despite the differences in test section free-stream properties, and diverse laser-induced blast-wave dynamics captured in the Schlieren movies, Runs 16 and 17 displayed very similar pressure distributions across the shroud undersurface. A comparison of these distributions in **Figure 5.14** (Run 16) and **Figure 5.17** (Run 17) reveals that the blast wave in Run 16 propagated further upstream on the shroud before dissipating—note the small perturbation in the P6 signal; a similar response was not

registered in Run 17, however. Other features observed in the Run 17 Schlieren images (**Figure 5.15**), and long exposure photograph in **Figure 5.16** are: 1) a more pronounced interaction of the laser-induced blast wave with the pre-established flow structure and shroud; 2) earlier re-stabilization of the disturbed flow field, probably accentuated by the higher free-stream P_∞ and ρ_∞ .

For Run 18, the shroud was pitched to -7.5° (further counter-clockwise), to align its undersurface parallel with the model center-body which was kept at -7.5° from horizontal; the free stream P_∞ and ρ_∞ were considerably reduced relative to the previous runs (see **Table 5.2**); and, the laser pulse energy of 121 ± 12 J was also lower. Several important features are captured in the Schlieren images of **Figure 5.18**. Note the bifurcated shape of the laser-induced breakdown in the first image (also appearing in **Figure 5.15**), and the subsequent sequence—possibly portraying the dynamics of an inlet “unstart”—which could be due to two factors: 1) the reduced static pressure under the shroud, thus less resistance to blast wave propagation upstream; and, 2) the lower shroud pitch angle (-7.5°) with respect to free-stream flow, causing a weaker shock off the shroud leading edge. These results are corroborated by the PCB traces in **Figure 5.19**, which track the blast wave arrival at P6, P7, and P9, and subsequent re-establishment of the flow after the disturbance is swept downstream.

As seen in **Figures 5.13, 5.15, and 5.18**, an oblique shock wave is attached at the shroud leading edge, despite the 7.5° negative inclination with respect to the test section axis. This result supports the hypothesis that the smaller (491 mm) HST nozzle exit delivers a conical expanding flow field into the test section with a non-negligible radial component striking the inclined 2-D model and shroud, which is a clear departure from the desired condition of quasi-parallel flow over the model in the test section. In the following Runs 21-23, this effect was reduced, albeit not entirely mitigated, with the reinstallation of the last section (610 mm) of the HST expansion nozzle. Future tests may have to employ reduced size Lightcraft engine models, to keep its boundaries within the central core section of the expanded flow field where the parallel flow assumption is valid.

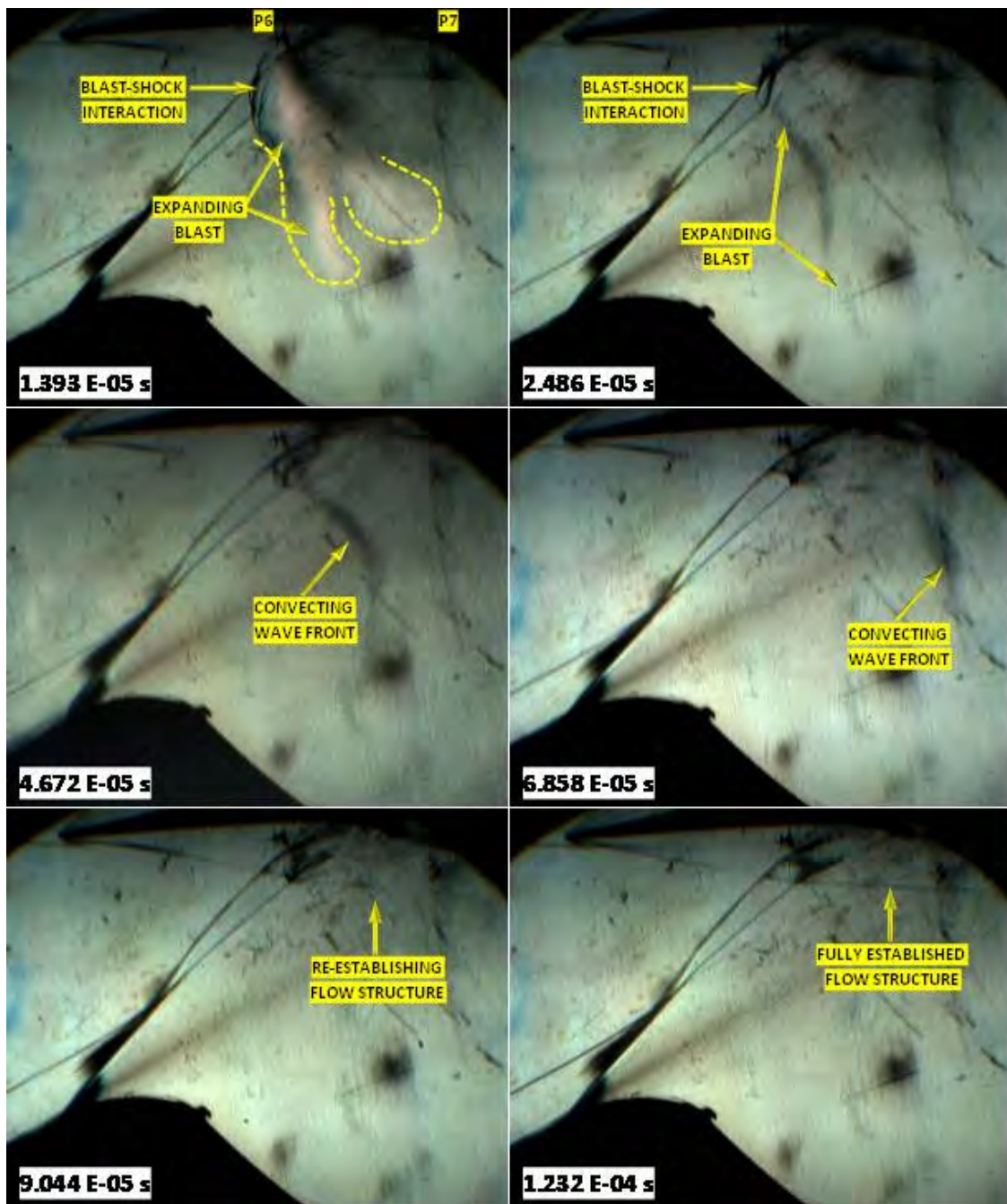


Figure 5.15: Run#17 - Laser induced blast wave interaction with oblique shocks and shroud under-surface; 2D model at -7.5° ; Shroud at -4° inclination. (M-5.94, $T_\infty=256.8$ K, $P_\infty=6.25$ kPa, $E_p=186\pm19$ J)



Figure 5.16: Run#17 - Long exposure color photograph of laser-induced breakdown geometry at Mach 5.96; 2D model at -7.5°; Shroud at -4° inclination.

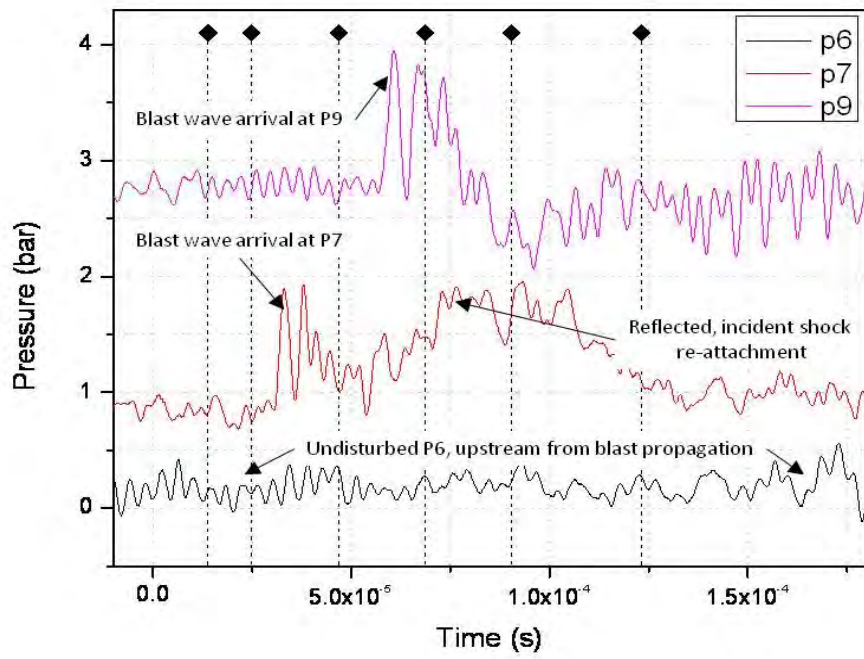


Figure 5.17 Run#17 - Measured pressure distribution across shroud under-surface. Traces offset. Schlieren frames from Figure 5.15 are marked for with diamonds.

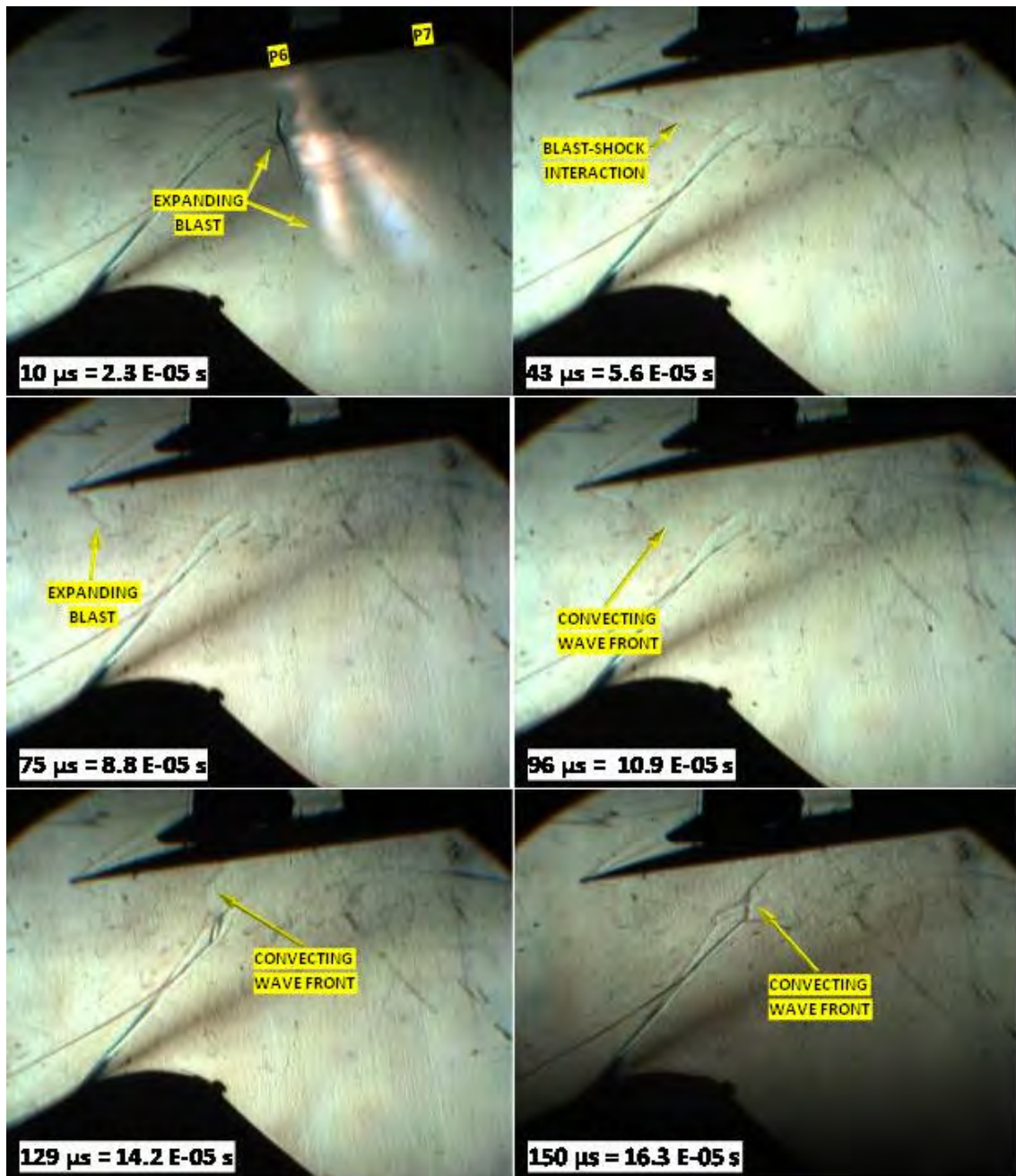


Figure 5.18: Run#18 - Laser induced blast wave interaction with oblique shocks and shroud under-surface. Both center body and shroud at -7.5° inclination. ($M=5.94$; $T_\infty=284.4$ K; $P_\infty=4.88$ kPa; $E_p=121\pm12$ J)

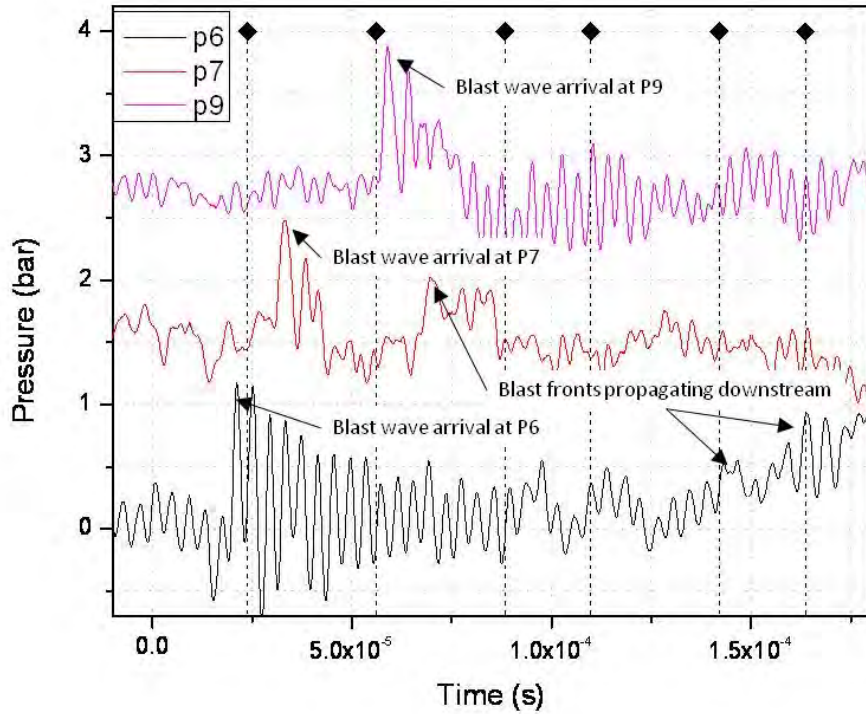


Figure 5.19: Run#18 - Measured pressure distribution across shroud under-surface. Traces offset. Schlieren frames from Figure 5.18 are marked for with diamonds.

Run 19 was performed at test conditions identical to Run 18, with only a slight difference in the free stream conditions and laser pulse energy (177 ± 18 J). Due to EMI, the Schlieren image sequence following laser-induced air-breakdown was lost. The pressure distribution across the under-surface of the shroud is displayed in **Figure 5.20**, along with the photon drag detector (near sting salt window - see **Chapter 3**) trace that provides laser pulse timing.

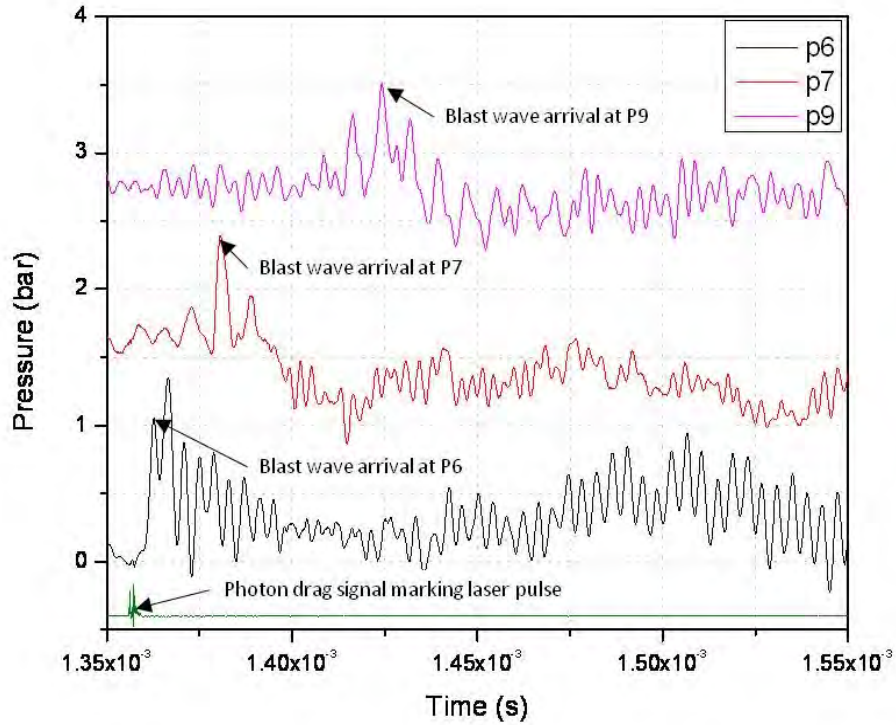


Figure 5.20: Run#19 - Measured pressure distribution across shroud under-surface; traces offset. Photon-drag detector signal provides timing for laser pulse delivery.

5.2.5 Runs 20 to 24 – Surface Breakdown

New HST test conditions were set for the remaining Runs 20 to 24. The free-stream Mach number was increased substantially from the prior series (Mach 5.95), with the same stagnation temperature of about 1850 K.

For Run 20, the same 2-D model center body and shroud configuration was retained, both inclined -7.5 degrees (counterclockwise) from horizontal. The T3 test section Mach number was increased from 5.95 to 8.6 simply by changing the nozzle throat insert, with the enthalpy kept unchanged. The lower free stream P_∞ and ρ_∞ produced a noticeable weakening of the shock waves in the Schlieren images, which became less visible. Unfortunately, the Schlieren camera triggered too late, capturing only the re-stabilized steady flow—well after the expanding laser-induced blast wave had faded. Such Schlieren data loss is still common, despite the progress made in EMI mitigation. On the other hand good pressure traces were acquired, as displayed in **Figures 5.21** and **5.22**. Note the expanded timescale shown in **Figure 5.21** which extends over the entire experiment duration of ~1.8 ms, from HST incident shock arrival

at the nozzle entrance, through diaphragm rupture and flow establishment in the test section (confirmed by pressure transients), and finally the laser firing and blast-induced mechanical noise. **Figure 5.22** zooms into a 200 μ s long time-window (same as previous runs) that highlights only the shroud sensor pressure signals (P6,P7,P9) following the laser energy deposition. The photon drag detector trace in **Figure 5.22** (bottom) gives the laser pulse timing. Note that sensor response to the laser-induced blast and subsequent mechanical noise is similar to that in Runs 1-4: i.e., all signals simultaneously jumped when the laser was fired, and the subsequent pressure increases (caused by the propagating blast wave) are seen as offset peaks in **Figure 5.22**—quite in contrast to previous results from Runs 16-19, even though the 2-D model geometrical settings were kept unchanged.

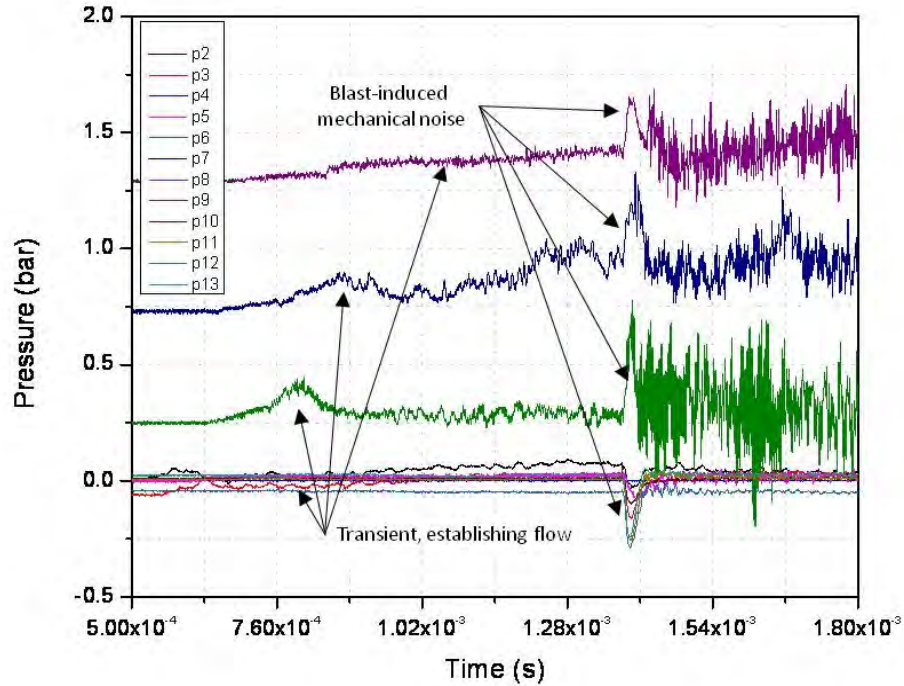


Figure 5.21: Run#20 - Extended duration pressure distribution over 2-D model, also showing transients before full flow establishment. Shroud sensors offset for clarification. (M=8.6; $T_{\infty}=128.8\text{K}$; $P_{\infty}=0.566\text{ kPa}$; $E_p=189\pm20\text{ J}$)

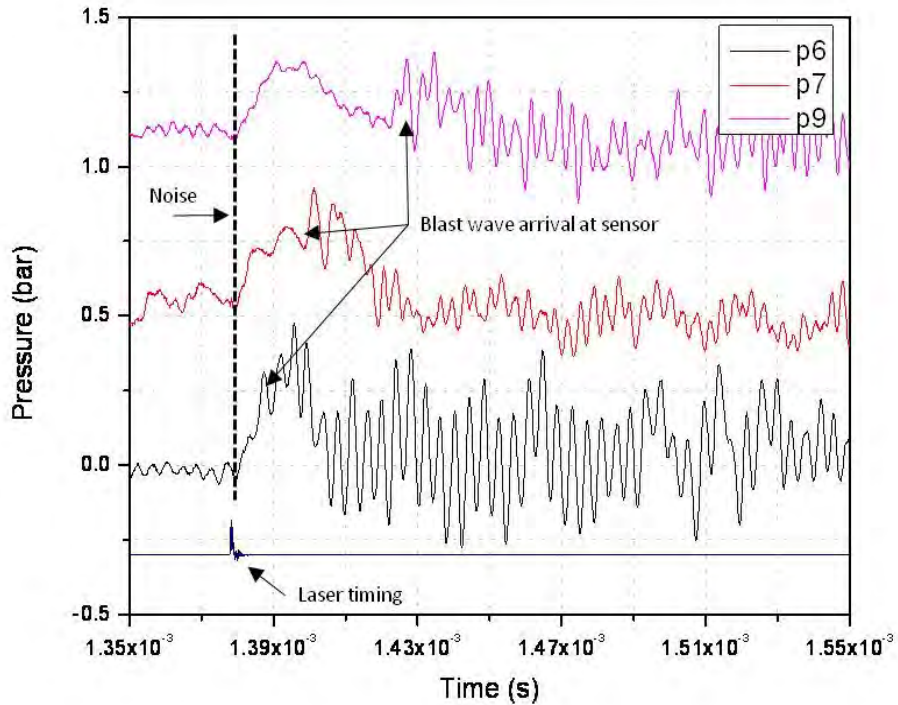


Figure 5.22: Run#20 - Pressure distribution over shroud under-surface showing P6, P7, P9 signals, masked by mechanical noise. Photon drag detector signal gives laser pulse timing (bottom trace). Pressure traces offset.

For Runs 21 to 24, the last section of the conical divergent nozzle leading to the test section was re-installed, bringing the exit diameter from 491 mm back up to 610 mm, for a nominal Mach number of 10.0 (Table 5.2 gives the calculated equilibrium condition of $M \sim 9.45$). In Run 21 the model/shroud geometry was unchanged from Run 20; the only difference in the test setup being the free stream condition and laser pulse energy of 196 ± 20 J. Notable Schlieren and pressure distribution data were obtained, as shown in **Figures 5.23 and 5.25**. The long exposure photograph in **Figure 5.24** was also taken during the run, where the unique bifurcated luminous plasma is likely caused by the hollow laser beam emitted from the 620-TEA unstable resonator.

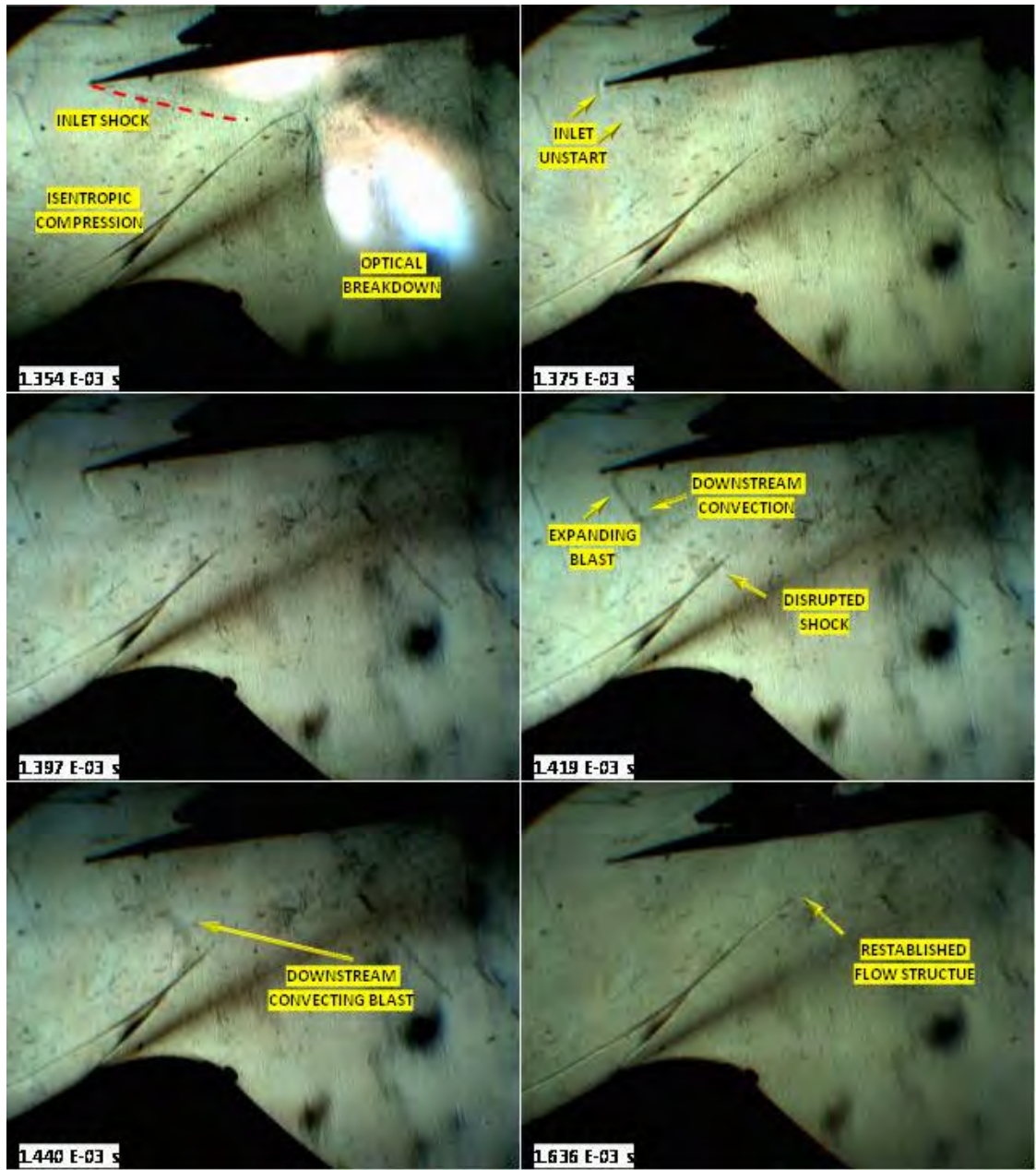


Figure 5.23: Run#21 - Laser induced blast wave interaction with oblique inlet shocks and shroud under-surface. Model and shroud at -7.5° inclination. ($M=9.44$, $T_\infty = 108$ K, $P_\infty = 0.301$ kPa, $E_p=196\pm20$ J)

Figure 5.23 reveals the interaction dynamics for the laser-induced breakdown and blast wave with the established Mach 9.44 flow structure and shroud undersurface. The upper left Schlieren image reveals that air-breakdown is triggered in two regions (or lobes) simultaneously: a) a lower bifurcated breakdown centered across the inlet gap; and b) a second surface-induced breakdown initiated at the focal line on the shroud

undersurface. The cylindrical blast wave launched from the laser focal line is seen to propagate upstream (against the shroud undersurface) into the region directly behind the weak oblique shock attached to the shroud's leading edge; this causes the inlet to unstart at 22 ± 4 μ s, just as this oblique shock detaches from the leading edge. Next, as the expanding blast wave is convected downstream, its interaction with the lower oblique bow shock wave formed off the compression ramp/ forebody is clearly visualized. The whole process, from laser-induced breakdown to the restoration of the original flow field takes just 292 ± 4 μ s.

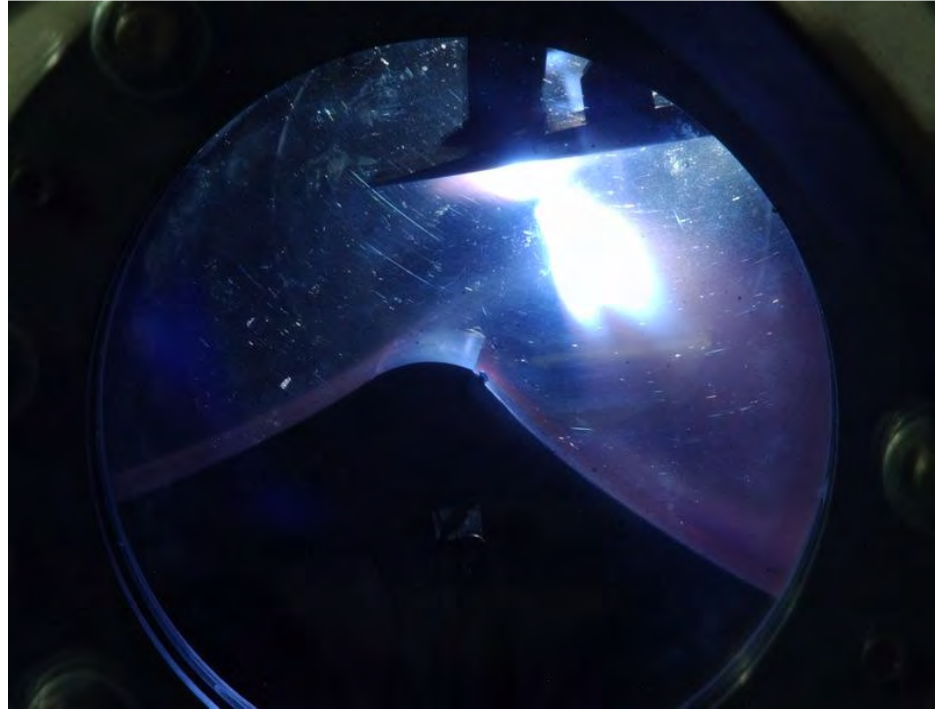


Figure 5.24: Run#21 - Long exposure photograph of bifurcated air-breakdown geometry across inlet gap, and secondary breakdown on shroud undersurface.

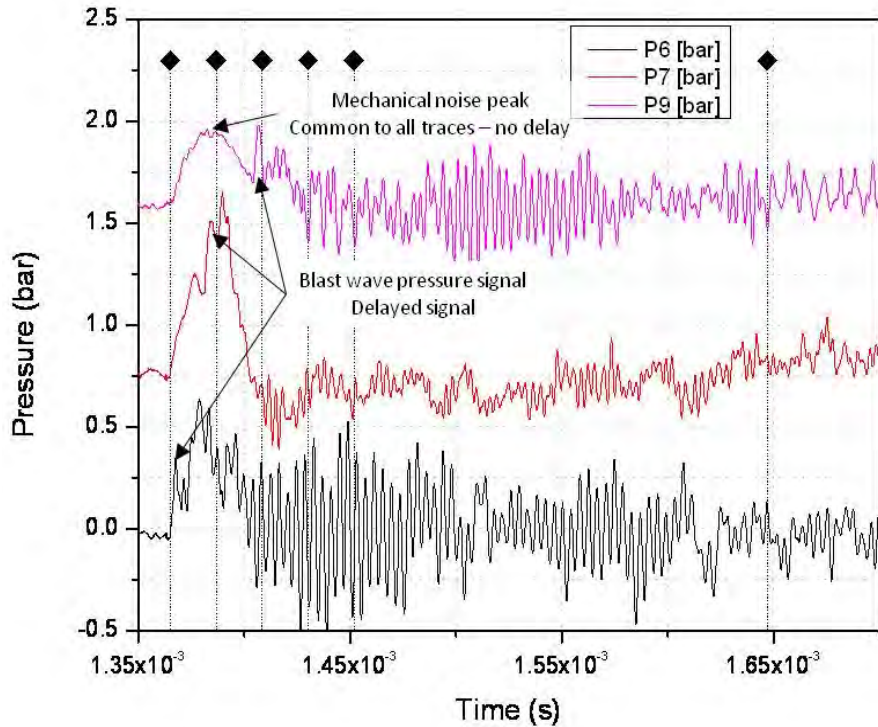


Figure 5.25: Run#21 - Measured pressure distribution across shroud undersurface; traces offset. Schlieren frames from Figure 5.23 are marked with diamonds.

After correlating dominant phenomena from the Schlieren image sequence in **Figure 5.23** (Run 21), against the sensor traces in **Figure 5.25**, there can be little doubt that the common source of high-frequency mechanical vibration (noise) is due to the timing of laser-induced breakdown at the shroud undersurface—delivering the “hammer” effect, previously discussed. In contrast, the previous runs were performed at higher static pressures, wherein much of the laser energy was deposited across the inlet flow-field at some distance removed from the shroud undersurface—delivering a smoother interaction with reduced noise levels. Due to the excessive noise interference, accurate pressure readings across the shroud undersurface with P6/P7/P9 could not be quantified; only the arrival times for the propagating laser-induced blast wave can be inferred by the small “blips” on the high frequency noise signature.

Prior experience with the present 2-D model proves that shroud pressures can be accurately read only in runs for which no “hammer” effects are present. However, with sophisticated signal processing software, it may be possible to decouple the pressure signals from the noise signatures, but this challenge must await future test campaigns.

For the near term, a more promising and immediate solution was already mentioned: i.e., simply install all shroud PCB sensors into vibration-isolating plastic inserts manufactured from a range of materials with different properties, and then through actual HST testing, down-select the ideal choice of insert material on the basis of signal quality.

Runs 22 to 24 were carried out with HST setup conditions identical to Run 21 except that the shroud was pitched even further forward to -24° with respect to horizontal, and its lower surface was placed 1.5 cm below the laser focus. All previous runs had the laser focal line placed coincident with the shroud under-surface to facilitate laser-induced breakdown—i.e., ‘focus-on-shroud’ configuration.

Figure 5.26 (Run 23) revealed a much weaker laser-induced blast wave on the shroud undersurface than for Run 21. Also, absence of the bifurcated, mid-channel breakdown (seen in Run 21) may be attributed to: a) the low laser pulse energy of 106 ± 11 J, which was lower than usual; and, b) the -24° shroud inclination, which generated an expansion wave off the shroud’s leading edge—that interacted with the shock off the inlet compression ramp and further reduced the local static pressure across the inlet channel/gap.

As in Run 21, the Schlieren image sequence in **Figure 5.26** captures a similar inlet unstart at 22 ± 4 μ s following the air-breakdown for Run 23, driven by the laser-induced blast wave expanding across the shroud undersurface. The duration of the entire event was measured at 114 ± 4 μ s—roughly half that seen in Run 21—again, probably due to the lower local static pressure and weaker laser pulse.

Just prior to Run 22, the faulty sensor P8 was finally replaced with a new PCB unit to enable pressure measurements at *four* positions across the shroud undersurface, as had originally been planned. **Figure 5.27** shows these four traces for Run 23 along with the timing of Schlieren frames (shown in **Figure 5.26**), marked with diamond-shaped symbols. Significantly lower pressure increases were registered by passage of the laser-generated blast wave, and the signal magnitudes in **Figure 5.27** were very near the random noise level, once more due to the reduced local static pressure and laser energy. Also, the “hammer” effect was absent, in large measure due to the low laser pulse energy, and more importantly, because the shroud lower surface was positioned below

the laser focal line. [Note: Results from Runs 22 and 24 were so similar to that of 21 and 23 in this same series, that they are not included here].

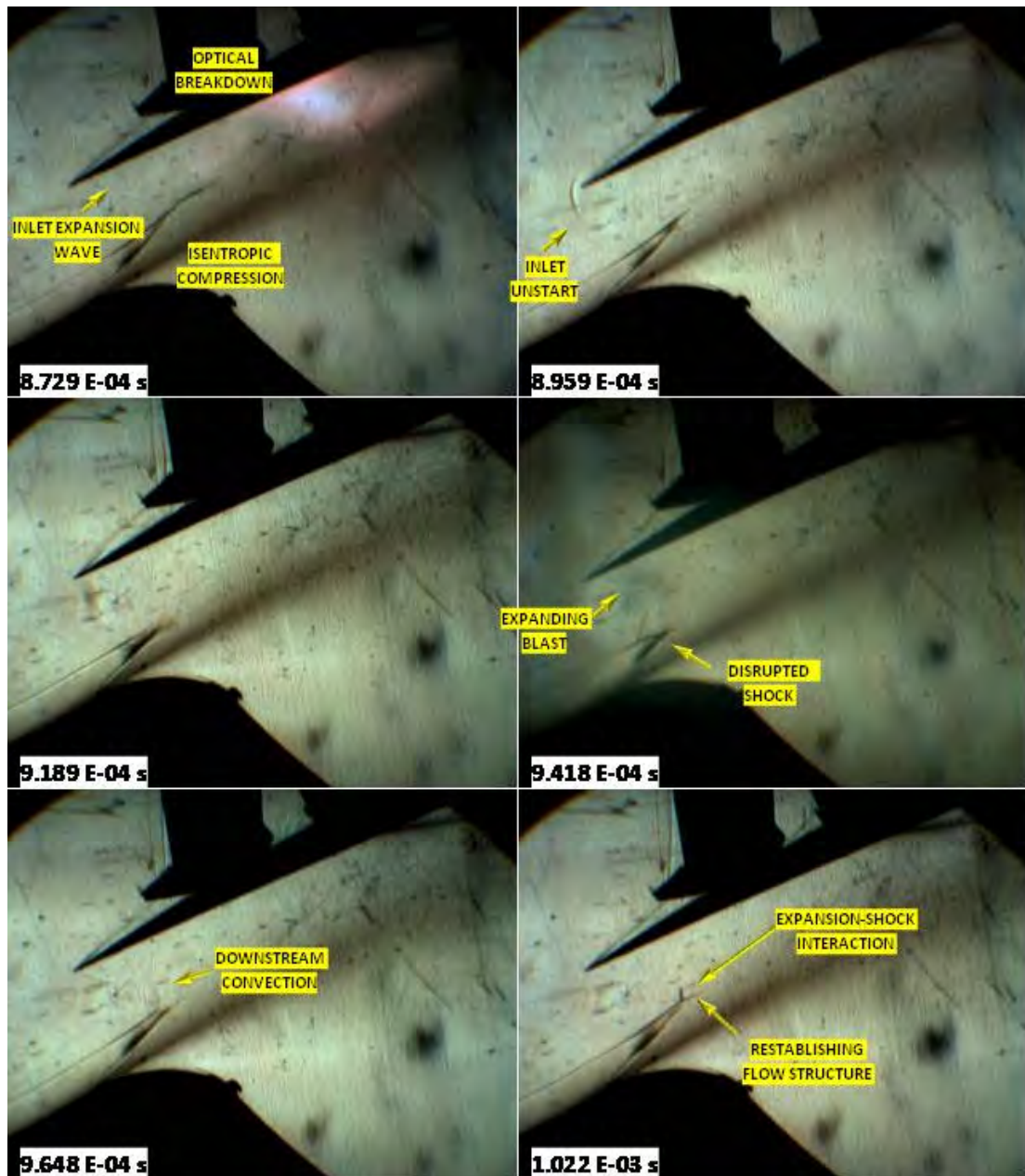


Figure 5.26: Run#23 - Laser induced blast wave interaction with oblique shocks and shroud under-surface. Model at -7.5° and shroud at -24° inclination. ($M=9.43$, $T_\infty=113.7$ K, $P_\infty=0.293$ kPa, $E_p=106\pm11$ J)

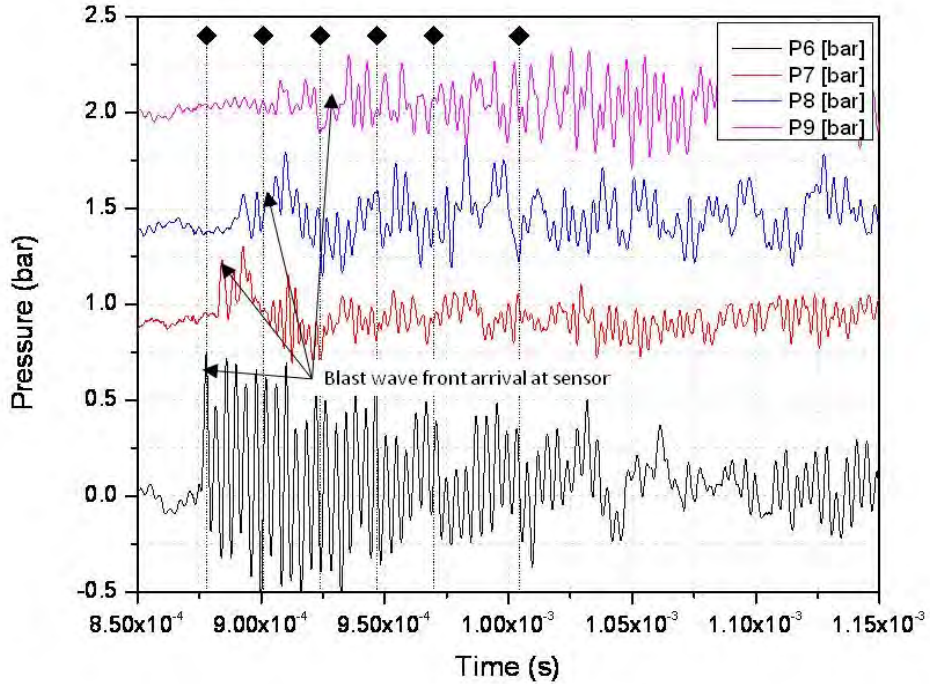


Figure 5.27: Run#23 - Measured pressure distribution at shroud under-surface; traces offset. Schlieren frames from Figure 5.26 are marked for clarification.

5.3 Discussion of the Results

The Phase I hypersonic experiments, described herein, accomplished two major objectives: a) measurement of static pressure distributions across the shroud under-surface of the existing 2-D lightcraft engine model; and, b) Schlieren visualization of time-dependent compressible flow structures affected by pulsed laser energy deposition at free-stream Mach numbers ranging from 6 to 10.

At this point in the Phase I hypersonic effort, only the “off-design” inlet condition (i.e., swallowed inlet bow shock; no “shock-on-lip”) was demonstrated, and geometrical similarity has not yet been achieved with the 2-D engine/vehicle model—awaiting attachment of a triangular flat-plate forebody that will complete the external-compression inlet geometry. To expedite progress in Phase I, the flat-plate forebody was omitted in order to simplify the “shakeout” process for this unusually complex experimental apparatus (i.e., laser/HST/Schlieren/data-acquisition/etc.) and thereby concentrate the focus upon resolving “show-stopper” problems with HST operation, laser activation, EMI, Cordin camera issues, debugging data acquisition, and all

attendant timing issues. With such challenges now successfully resolved, the groundwork has finally been laid for the upcoming “*direct-connect*” engine tests—Phase 2 of the hypersonics effort—wherein the full external-compression inlet will extend far into the HST conical nozzle. With this planned addition, geometric similarity will be achieved, along with the shock-on-lip condition, using higher laser pulse energies (e.g., 400 J and beyond).

Given the above caveats on the Phase I setup (with non-ideal, off-design operating conditions with the truncated inlet), several conclusions can be derived from the results to date. From the Schlieren flow visualization movies, it can be seen that the 2-D model is prone to “inlet unstart” even at reduced laser pulse energies of 100-200 J, depending on the shroud inclination and free-stream conditions. Also, a comparison of the time-dependent Schlieren photographs from Runs 13 and 15 with those from Runs 16-18, reveals that the ability of laser-induced blast wave disturbances to propagate upstream, is accentuated by the presence and inclination of the shroud, and hence by the local static pressure across the shroud undersurface. With the lower free-stream pressure in Run 18, the blast wave disturbance clearly disrupts the established structure of the shroud shock, which becomes even more pronounced at the higher Mach numbers in Runs 20 to 24, wherein the inlet flow is “unstarted” by the upstream-propagating portion of the laser-induced blast wave. This is distinguishable by the detached bow shock that appears at the leading edge of the shroud.

The Phase I test results (despite the off-design inlet geometry) suggest that at hypersonic Mach numbers, efficient laser impulse generation—without unstarting the inlet—will be difficult if not impossible, without assuring the shock-on-lip condition for optimum inlet pressure recovery, especially considering that 5x the present linear energy densities will be required for sustained hypersonic flight. An inlet unstart dramatically increases drag while cutting thrust and cycle efficiency to zero—i.e., a complete loss of the laser-induced blast wave energy fraction available for conversion into impulse.

The design process for an airbreathing laser PDE engine is difficult to summarize succinctly. First, the inlet must sport a reasonably efficient pressure recovery schedule (vs. Mach number), and deliver working fluid with the desired properties (P_a , ρ_a , V_a) and mass flow rate into the laser focus line and “absorption chamber.” Second, the laser

pulse energy (vs. Mach number and altitude) will be limited by thermal choking and inlet unstart (from the upstream-propagating blast wave), and the maximum PRF is set by the “refresh” interval. Several methods for avoiding or mitigating such unstarts from thermal choking have been incorporated in today’s chemical-fueled jet propulsion systems, and some of those could conceivably be applied to future lightcraft—e.g., inlet bleeds and relief valves (Seddon and Goldsmith, 1985). Inlet unstart prevention/mitigation is just as critical (possibly more so) with laser PDE engines, as with their chemical-fueled scramjet counterparts, due to: a) high pressure pulses inherent with unsteady, “constant volume” PDE Lightcraft engines; and, b) short distance from the laser focus to the inlet entrance and shroud leading edge. In contrast, conventional chemical-fueled scramjets operate in the “constant pressure” mode, with thermal power released into the working fluid continuously and with considerably-longer combustion chambers than a Lightcraft’s short absorption chamber. Furthermore, the aspect ratios (i.e., vehicle length-to-width ratio) of conventional scramjet-powered aircraft are generally much higher than those for spin-stabilized Lightcraft; the laser-boosted craft flown at White Sands Missile Range, all had aspect ratios close to one—a restriction driven by flight-dynamics, stability, and control requirements (Kenoyer et al., 2010).

The inlet unstart phenomena may also limit operational envelopes of *combined-cycle laser PDE engines*—at the very highest altitudes (i.e., top of the atmosphere) and speeds; here, the injection of on-board propellant (or seedant) into the absorption chamber can be used to increase the static pressure/density of the mixed working fluid flowing into the laser focus, to enhance laser-induced blast wave strength up to the limits of inlet unstart. Future laser Lightcraft engine designs must forge a compromise between inlet pressure recovery schedule and attainable thrust over the desired operational envelope; this will ultimately dictate the transition Mach number and altitude between laser Airbreathing and Rocket modes along an airbreathing launch trajectory to LEO. But, the Phase I hypersonic experiments have not yet investigated such combined-cycle engines, nor the transition point, and hence cannot quantify the limits. Judging from the results attained thus far, would not be surprising, however, to learn that the transition must occur earlier in the trajectory than proposed by Frasier (1987)—perhaps before reaching Mach 10.

Schlieren images from the Phase I results reveal that a good fraction of the inlet air working fluid is engaged with, and heated by the laser pulse but only a small portion of the resultant blast wave impacts the shroud undersurface (i.e., impulse generation thru pressure increase), although the laser pulse energy was still only ~20% of ideal. The remaining blast wave energy appears convected downstream and lost. Hence, future Lightcraft engine geometries must increase transitory confinement of such initial blast waves, and facilitate thrust generation over the absorption chamber/nozzle surfaces.

Schlieren images prove that the shape of any air-breakdown geometry is driven strongly by the rear-optic focusing geometry, whether the focal line is placed coincident, below, or above the shroud undersurface, or directly into hypersonic flow (i.e., shroud absent). Runs 17, 18, and 21 clearly reveal a dual lobe shaped air-breakdown, which can certainly be ascribed to the focused, hollow-center laser beam emitted from the 620-TEA unstable resonator.

Finally, the occurrence and geometry of laser-induced breakdown across the mid-section of the inlet channel was completely unforeseen, especially since the irradiance level there is much smaller than at the surface focal line ($\sim 2 \times 10^8$ W/cm²); the air-breakdown is taking place without catalytic or “spark plug” effect of the aluminum shroud undersurface (see Chapter 2). The location of the air-breakdown site is important because it plays a key role in optimizing future LP engine cycles and Lightcraft designs. The existence of high particulate concentrations in the HST free-stream flow (including humidity, oil residues from driver-tube compressors, and microscopic diaphragm particles) is tentatively deemed the cause for this low irradiance air-breakdown. Whether this breakdown occurs almost simultaneously, or through surface-induced breakdown followed by a propagating LSD wave, or both is presently unknown, and must await further research. An ideal instrument for this investigation would be a Gated Optical Imaging (GOI) camera with nano-second resolution to reveal the exact details of breakdown and/or LSD wave propagation phenomena. In future HST experiments, a more controlled, free-stream HST gas composition should be used to examine the effects of particulates and humidity levels on the laser-induced air-breakdown.

In the Phase I hypersonic experiments, measurement of engine surface pressure distributions was restricted to the shroud under-surface. The pressure measurements

along the compression ramp were used solely for ascertaining the time to reach fully established free-stream conditions in the test section; pressure traces of gages installed on this ramp were not disturbed by laser-induced blast waves in any run. The same can be said for the primary optic surface, since the laser-induced blast did not possess sufficient strength to expand radially and make contact before being convected downstream.

Two main noise sources impacted all the PCB pressure sensor signals that were displayed previously: a) Mechanical noise from the “hammer” effect, which hindered quantitative analysis (present in most runs depending on test setup); and, b) High frequency “ringing” noise following the passage of the laser-induced blast wave (present in every run). Despite the “ringing” noise, a fair assessment of the peak pressures caused by blast wave interaction with the shroud undersurface was indeed accomplished in some runs, as reported earlier.

The peak pressures (ΔP) measured by P6, P7 and P9 are given in **Figure 5.29** for Runs 16 through 19, at $M=5.95$. The shroud was tilted at -4 degrees for Runs 16 and 17, and -7.5 degrees for Runs 18 and 19; the model centerbody was held unchanged at -7.5 degrees. Note the trend in Figure 5: the larger shroud tilt angle of -7.5° induces the laser-induced blast wave to propagate further upstream towards the shroud leading edge than with the -4° tilt. Experimental measurement error was not estimated due to the varying HST test conditions for each run.

From **Figure 5.29**, it can be seen that considerable pressure increases (ΔP) were achieved over the shroud’s under-surface; however, the delivered impulse is negligible for this 2-D model at the present $\sim 200J$ level, which is $\sim 20\%$ of that required for efficient impulse delivery with the shock-on-lip inlet condition (**Richard, 1989**).

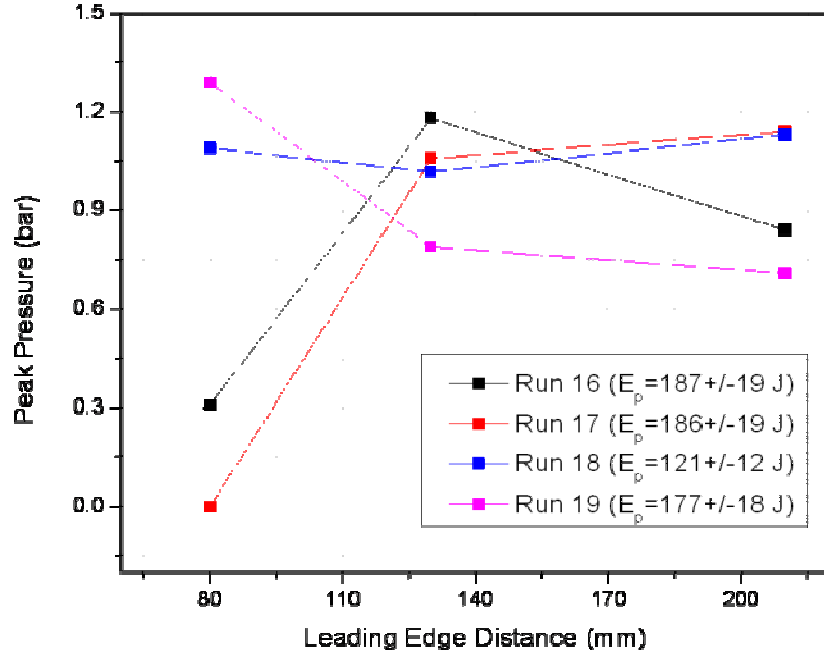


Figure 5.28: Peak pressures (ΔP) measured across shroud under-surface, measured from its leading edge. (Runs 16 through 19)

The ideal shroud inclination is presently unknown because increasingly higher pressures will be applied over the shroud upper surface, in direct proportion to the incidence of the oncoming hypersonic free-stream flow. For the lower shroud (i.e., thrust generating) surface, the resulting axial impulse component (i.e., in the flight direction) is proportional to $\sin(\Theta_{\text{shroud}})$, where Θ_{shroud} is the shroud inclination to horizontal. With the shock-on-lip condition satisfied and laser pulse energies increased towards the 1 kJ level, the more powerful laser-induced blast waves will expand to engage the primary optic surface—as originally intended; all surfaces bounding the absorption chamber must actively participate if efficient impulse generation is the objective. Prior experimental and numerical LP studies have proven that total impulse can benefit greatly from exploiting primary optics that are inclined sharply to the flight axis. In the present 2-D Lightcraft model geometry, blast waves reflected off this large surface can deliver much impulse before accelerating downstream and exiting the Lightcraft’s absorption chamber.

In light of the results presented herein, the quantitative analysis of the hypersonic impulse generation process was not performed in this Phase I campaign. The high noise levels in the data prevents the kind of impulse analysis performed on the static run

results in Chapter 4, wherein time-resolved pressure increases (ΔP) over the shroud and optic surfaces were integrated to obtain the total impulse and C_m . For the Phase II hypersonic campaign, substantial improvements in PCB pressure data quality will be sought for the shock-on-lip condition and 2x-5x higher laser pulse energies

The “air-refresh” time (i.e., Δt to convect fresh air across the laser focus line, or $1/PRF$) for the off-design, 2-D engine operation can be estimated by analysis of the shroud undersurface pressure distributions and associated Schlieren images. The refresh time can also be considered the propulsion cycle duration (τ_{cycle}) which dictates the maximum laser pulse repetition frequency (PRF). From the Schlieren images in Run 23, it can be seen that the blast wave perturbation was convected downstream of the focal point in approximately 149 μs . A more precise estimate is difficult to ascertain from the Run 23 PCB pressure trace disturbances, but can be judged to fall between 100 and 200 μs . This indicates an engine PRF of approximately 10,000 Hz for the given “off-design” inlet conditions. Similar blast wave residence times are observed in Runs 16 through 19. Run 21 revealed the longest residence time of 292 μs , based on the Schlieren image sequence that confirms re-establishment of the original flow field, and the PCB pressure disturbances that lasted on the order of 300 μs . Clearly, τ_{cycle} is highly dependent on the local inlet flow field (for which “shock-on-lip” is optimum), and therefore engine/vehicle geometry.

The principal conclusion extracted from these Phase I results is that powered flight at hypersonic speeds is likely feasible, but fundamental improvements in the inlet flow field, laser pulse energies, and engine/vehicle geometry are required. These changes must optimize inlet performance (e.g., “shock-on-lip”) for refined absorption chamber geometries that maximize static pressure and density convected across the laser line focus, with big enough laser pulse energies to fully engage the shroud undersurface and rear parabolic optic in the impulse generation process. Refined afterbody geometries must efficiently direct the exhaust (blast wave expansion) in the axial direction, but not at the sacrifice of autonomous beam-riding abilities: i.e., the Lightcraft engine must still generate sufficient radial-directed impulse to re-center itself if disturbed (momentary lateral offset from beam centerline) during flight.

Further analysis of the total impulse produced by surface pressure distributions measured over absorption chamber surfaces was not possible, and will require improved pressure signals, the shock-on-lip inlet condition, and 2x to 5x larger laser pulse energies—along with a substantial increase in the number of pressure transducers installed over critical model surfaces, and great reduction in noise levels in their signals. In conclusion, the quantitative performance analysis must await the hypersonic Phase II test campaign, which will identify the operational performance envelope (i.e., high and low limits) of PDE propulsive modes of interest; the *Full* treatment will demand experimental research into the supersonic flight regime as well.

6 Conclusions and Future Work

6.1 Conclusions

The present Phase I research campaign was facilitated through an international collaboration (at top governmental-to-government level) between the United States Air Force and the Brazilian Air Force, and carried out at the Henry T. Nagamatsu Laboratory of Aerothermodynamics and Hypersonics (HTN-LAH) in São José dos Campos, Brazil. This IEAv-CTA experimental facility is the first in the world to be set up expressly for hypersonic laser propulsion (LP) research. The HTN-LAH facility comprises the T3 Hypersonic Shock Tunnel (HST), the Lumonics 622-TEA laser system, and dedicated instrumentation. The present two-dimensional LP model—based on the Lightcraft Technology Demonstrator (LTD) concept—was designed, manufactured, and installed into the T3 HST for the present campaign.

Phase I experiments were carried out under static (i.e., quiescent flow) and then hypersonic flow conditions with two principal research objectives in mind: 1) measurement of time-dependent surface pressure distributions subsequent to pulsed laser energy deposition and the resulting laser-induced blast wave expansion through the 2-D model's absorption chamber; and, 2) Schlieren visualization of the evolving flow field and blast wave structures, and their interaction with impulse generating surfaces. The results collected thus far have yielded invaluable insight for the Phase 2 hypersonic campaign, as well as useful R&D data for future airbreathing LP engine concepts.

6.1.1 Static Experiments

The Phase I test campaign began with static experiments performed with the 2-D Lightcraft model installed in the T3 test section. These initial runs were plagued with the typical troubleshooting, de-bugging, and systems integration challenges that normally plague complex experimental setups, but once brought online, the apparatus yielded valuable data on the momentum coupling coefficient (C_m) performance of the 2-D model. The HST test section and dump tank can be evacuated to extremely low pressures, which enabled the static experiments to be conducted in laboratory-quality air at various pressures of 60 mbar, 150 mbar, 300 mbar, and 1 bar. The 150-230 J pulses from the 620-TEA laser were concentrated by the 2-D model's rear parabolic optic onto

a 135 mm line focus, centered on the 254 wide shroud undersurface which was inclined at 25 and 34 degrees (from horizontal) for these static tests.

Until now, no references in the LP literature had covered or reviewed the direct use of time-variant surface pressure distributions in assessing the momentum coupling coefficient (C_m) performance of a LP engine. However, prior studies had often applied a single pressure transducer to monitor time-variant pressures inside various LP engines, typically as a diagnostic tool (Mead, 2007). To first order, C_m can succinctly specify the airbreathing LP engine performance over its operational envelope (i.e., vs. Mach number and altitude), so the present test campaign had as its major objective to collect such experimental data.

From the Phase I static test results, the following conclusions can be reached:

- The 2-D laser propulsion model was designed for 500-1000 J output pulses from the Lumonics 622-TEA laser in the stable resonator mode (Marx bank charged to 90 kV); deposited along the 135cm focal line, this gives a linear-energy-density of 37-74 J/cm;
- With an available laser pulse energy of 200 J (for a single 620-TEA laser charged to 70 kV), the 2-D engine's focal line received 15 J/cm or just 20-40% of design;
- Laser focal line intensities reached $\sim 2 \times 10^8$ W/cm² (on average) for the 1 μ s laser pulse duration, which gives peak LSD wave pressures up to 40 bar in a 1 atmosphere lab environment;
- Over 60 % of the laser-generated impulse appears on the “upstream” portion (i.e., between the focal line and shroud leading edge) of the inclined shroud undersurface, whereas the parabolic mirror sees minimal impulse; however, at the full 1 kJ level, a much larger fraction of the impulse will be generated off this rear-facing optic;
- The focused laser beam's incidence angle (α) and included angle (β) exert considerable influence on the resultant laser-induced pressure distribution over the shroud under-surface; this warrants further investigation and must be quantified vs. α and β ;

- Momentum coupling coefficients (C_m) from the 2-D model were 2.5x to 5x higher than previously achieved with much smaller LP engines. This result can be attributed to a greater fraction of blast wave energy being transferred to larger impulse surfaces within the present 2-D engine. This important relationship between E_P , linear-energy-density along the focal line, and characteristic dimensions of impulse generating surfaces clearly warrants further investigation. Present C_m experimental results comply with prior theoretical predictions by **Richard (1989)**, within measurement error.
- Since only axial-directed components of surface pressure distributions generate impulse in the flight direction, optimization of engine geometry for more efficient conversion of laser-generated impulse is clearly mandated.
- The present Phase I static test database (i.e., time-variant pressure distributions and Schlieren movies) will be useful in calibrating future CFD codes, and such codes will prove indispensable to developing refined Lightcraft designs in the future.

6.1.2 Hypersonic Experiments

As with the static experiments, the Lumonics 622TEA laser again delivered ~200 J pulses into the T3 tunnel -- but this time for **hypersonic** airbreathing laser propulsion tests with the same 2D model. Other than analytical/numerical studies of similar laser ramjet/scramjet geometries, no prior hypersonic investigations of this nature have been reported in the literature. The two principal experimental goals were to: a) measure the time-variant pressure distributions over the model's internal thrust-generating surfaces (i.e., absorption chamber); and, b) capture high speed Schlieren flow field visualizations of the thrust production process -- to reveal the influence of engine geometrical features during blast wave expansion. These Mach 6-9 experiments constitute the first attempt to measure C_m performance from an array of pressure transducers distributed over the model. Such data is important for future LP research in guiding modifications and improvements to the basic engine/vehicle geometry studied here.

The following conclusions were achieved from the Phase I hypersonic campaign:

- The 2D Lightcraft model (~30 cm focal “radius”) is roughly modeled after a half-scale Lightcraft Technology Demonstrator (LTD); the LTD had a focal ring radius of 60 cm and linear focal energy density (E_{FD}) requirement of 87.5 J/cm at Mach 5 and 30 km altitude; to first order, E_{FD} scales with the focal ring radius so the 2D model needs 43.8 J/cm for optimum performance.
- The 2D hypersonic model has a 135 mm focal line, so ~590 J is needed for optimum impulse generation; at 200 J (single 620-TEA laser charged to 70 kV; *unstable* resonator mode), the linear focal energy density is 14.8 J/cm or 34% of ideal; doubling E_P to 400 J (622-TEA charged to 70 kV; *unstable* resonator mode) brings it up to 68%—very close to optimum;
- Only “off-design” inlet conditions have been tested to date; geometrical similarity was not achieved with the present 2-D engine/vehicle model (awaiting installation of flat-plate forebody in Phase II campaign);
- The present 2-D model is prone to “inlet unstart” even at reduced pulse energies; inlet unstart is accentuated with increasing shroud inclination, and sub-ideal internal working fluid properties (static p & ρ);
- Efficient laser impulse generation without inlet unstart requires the “shock-on-lip” condition -- to be studied in the Phase II campaign;
- Improved Lightcraft inlet designs will permit higher E_P , greater peak engine pressures, and elevated impulse levels;
- Increased blast wave confinement times and reduced working fluid flow speeds (with higher static pressure and density) will enhance impulse delivery in the absorption chamber and plug nozzle;
- The laser-induced air-breakdown geometry (inside the engine) is driven by the parabolic rear-optic focusing geometry upon shroud (α & β), but can also be dominated by particulate-induced breakdown triggered off “contaminants” in the T3 hypersonic flow;
- PCB pressure sensor noise levels are very high, and because of the “hammer” effect and excessive ringing, no C_m analysis was possible;

- An analysis of the time-variant pressure distributions and Schlieren movies reveals that engine's air refresh time (or propulsion cycle duration, τ_{cycle}), equates to a maximum **PRF** of approximately 10 kHz;
- Powered flight at hypersonic speeds is likely feasible, but requires the “shock on lip” inlet condition, an optimum shroud angle, and other refinements in engine/vehicle geometry; CFD analysis will be needed for optimization;

Developing an airbreathing (i.e., I_{SP} =infinite) Lightcraft engine/vehicle is a complex multidisciplinary task for which the difficulty grows with increasing flight Mach number and altitude objectives. As with any innovative/future airbreathing engine, only extensive R&D can reveal the feasible flight operational envelope, but several features unique to laser propulsion must be kept in mind:

With BEP launchers, the overall engine efficiency can be relaxed in favor of **high acceleration** performance, which is in sharp contrast with existing airbreathing chemical propulsion (e.g., hydrogen/hydrocarbon-fueled) designed for **efficient “cruise”** performance. With the latter, a reduction in chemical-fueled scramjet efficiency negatively impacts specific fuel consumption, which dictates larger propellant loads and tankage penalties, higher structural mass fractions, and ultimately, increased fixed and recurrent costs. However with ground-based power-beaming infrastructure, such engine/vehicle liabilities can be transferred to the GBL, where infrastructure capital costs can be amortized over copious launches (e.g., life cycle of 10-20 yrs), with recurring costs limited to maintenance and electric power rates.

From the present hypersonic results, it is obvious that the laser-induced breakdown and time-variant compressible flow-field over a Lightcraft engine/vehicle and through the absorption chamber is an exceedingly complex process. Hence, expedient progress in evolving future Lightcraft engine/vehicle can only be made with a combined numerical/experimental approach. Specialized CFD codes with full-blown chemistry can provide fundamental insight to the plasma physics, but they must be fully calibrated against experimental data—which will take time. Meanwhile, rudimentary insight can be gained with commercial CFD packages that accurately model just the propagating blast waves, using input initial conditions from actual experiments. This approach can enable more

detailed analyses of time-variant surface pressure distributions in the absorption chamber, as well as interactions between two sequential blasts within the engine.

In summary, the research work presented herein has paved the way for future investigations into hypersonic airbreathing laser propulsion physics. The present results set an important historical precedent, since prior hypersonic LP research has largely been speculative—limited only to theoretical and numerical studies—and lacking the necessary experimental data to “anchor” such simulations against nature.

6.2 Future Experimental Work

This section introduces the “follow-on” hypersonic airbreathing laser propulsion research planned for the near future, which for the most part can be considered direct spin-offs of work covered in the previous chapters. This next campaign constitutes a family of LP experimental investigations in the hypersonic regime, that a laser Lightcraft would typically encounter along a launch trajectory into orbit.

6.2.1 Phase II Hypersonic Campaign with 2D Model

As mentioned above, the Phase I hypersonic effort demonstrated an initial “off-design” inlet condition (i.e., swallowed inlet bow shock; no “shock-on-lip”) with the 2D engine/vehicle model, and geometrical similarity had not yet been achieved. Nonetheless, important information can be drawn from the Phase I results for the first “laser scramjet” PDE experiments ever conducted, wherein the laser detonation line (optic focus) is refreshed at supersonic speeds. [Note that the Phase 1 experiments achieved a linear focal-line energy density of just 13.3 J/cm with a 180 J pulse, and this 135 mm focal line represents the half-width of the 254 mm wide 2D model.]

In the Phase II hypersonic campaign, a triangular flat-plate forebody will be added to complete the external-compression inlet geometry—see **Fig. 6.1** below. With this addition, geometric similarity will be achieved, along with the shock-on-lip condition to enable much higher laser pulse energies (e.g., 400 J and beyond).

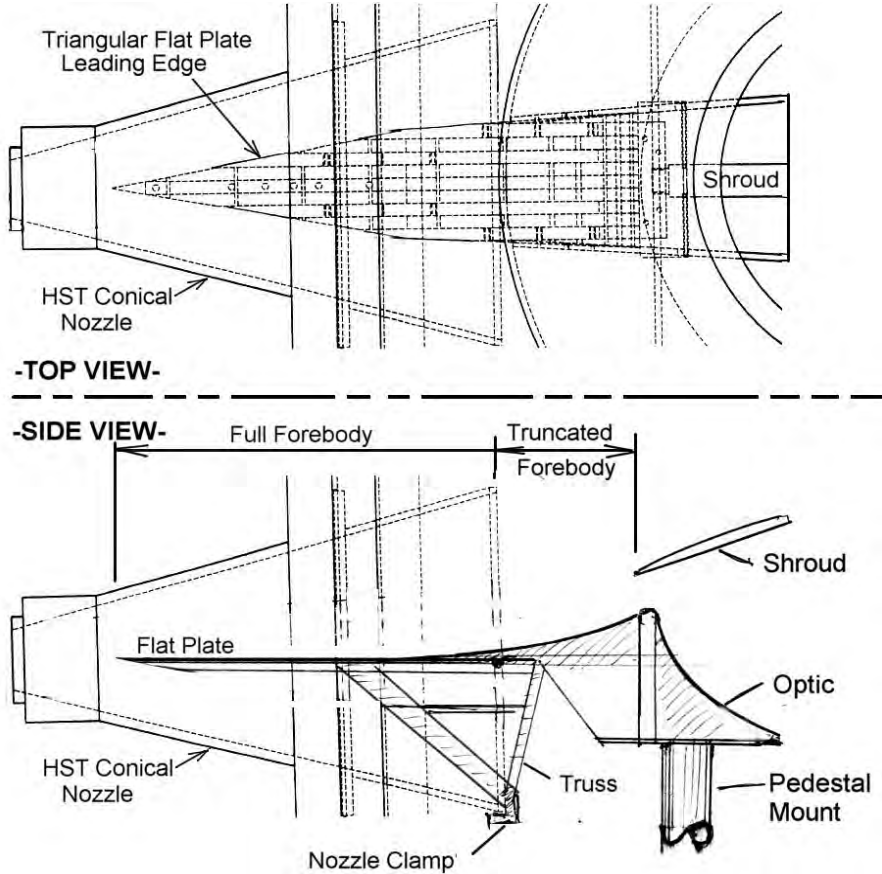


Figure 6.1: Complete 2D model with full external compression inlet for Phase 2 tests.

Again, note that the current 2D engine/vehicle model geometry was derived from (Richard, 1989; Fernandez, 1990; Sienel, 1992) for the Lightcraft Technology Demonstrator concept, in which the inlet gap is assumed to operate in the choked condition (i.e., Mach 1 or transonic refresh of laser focus)—a so-called “*laser ramjet*” or pulsed detonation engine (PDE) mode; the LTD had a design Mach number of 5 and maximum altitude of 30 km. In contrast, the present T3 experiments are being conducted at Mach numbers of 5.95 to 9.47, extending far beyond that of Richard’s analytical studies of the LTD “constant volume” PDE cycle. At these higher Mach numbers, the inlet air is driven across the 2D laser focus at supersonic speeds—a so-called “*laser scramjet*” PDE mode.

As originally designed, the leading edge flat plate extension (note triangular planform in top view) was to be inserted far into the HST nozzle along the centerline axis (see Fig. 6.1). This inlet forebody extension will allow the boundary layer to form much farther upstream at a lower Mach number within the nozzle. Hence by the time the

flow enters the lightcraft inlet gap, the flow Mach number would be lower than in Phase 1 runs, and the compressed inlet flow will expand to fill the entire inlet gap (~10cm thick, for the “shock on lip” condition). With the inclusion of the flat plate forebody in Phase 2 tests, more realistic boundary layer thicknesses, representative of full-scale LTD vehicles will be simulated. [Note that the inlet design automatically bleeds off the boundary layer over primary receptive optics, which would normally see separated flow in operation anyway.]

6.2.2 2nd Generation Two-Dimensional Model

Lessons learned in the Phase I campaign have spawned the design of an improved 2D hypersonic model—see **Figure 6.2**. This new 2nd generation 2D model design attempts to mitigate several problems encountered with the current 2D model, and its dimensions have been scaled down to match the reduced beam size entering the test section. Whereas the 622-TEA emits a 180 x 170 mm laser beam into the 0.75 reducing telescope, it measures 135 x 115 mm at the sting window. The 2nd-gen model has the following attractive features:

- Reduced manufacturing time, cost, and setup complexity;
- More compact and rigid construction to reduce mechanical vibration levels that resulted in high PCB pressure transducer noise with the current 2D model.
- Improved Schlieren visualization setup, wherein the entire 2D model fits within the viewing aperture;
- Satisfaction of the one-dimensional HST flow assumption over the model extremities—i.e., the core flow emerging from the conical nozzle exit is quasi-parallel; no model interaction with the conical nozzle’s boundary layer;
- Enhanced match of available laser energy (~200 J per 620-TEA module) and *linear focal energy densities* (E_{FD}) with Lightcraft model dimensions; as mentioned earlier, E_{FD} scales with the focal ring radius so the 2D model (to first order);

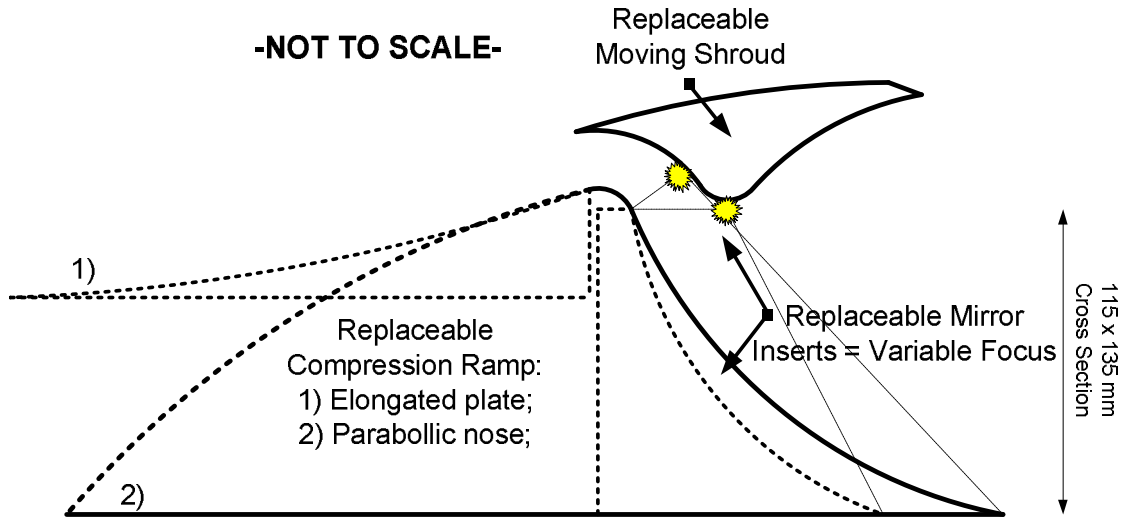


Figure 6.2: Features to be added in 2nd generation 2D hypersonic models.

Adjustable stagnation pressure rakes will be installed in the 2nd-gen 2D model to survey the inlet gap and absorption chamber “off-wall” gas properties. This inlet data is essential for analysis of: a) the inlet’s pressure recovery and captured air mass flow rate, and, b) air flow properties (V , ρ , P) refreshing the laser focal line. The data will also prove useful for numerical analysis (CFD codes) and guiding refinement of Lightcraft engine/vehicle geometries.

Judging from the Phase 1 hypersonic results, the present 2D model has a number of liabilities that have hampered or prevented collection of desired/critical data. Take, for example, the two parallel polycarbonate plates that: a) structurally support the shroud; b) enable Schlieren visualization of the internal engine flow fields; and, c) channelize the compressible flow field through the engine and into the absorption chamber. The thick polycarbonate plates greatly reduced the contrast achieved with the current Schlieren setup, and its varying optical quality (i.e., non-uniform optical properties) across the plate material often obscured interesting features of the time-variant compressible flow structure. Also, after a number of shots, the debris and soot that was convected down the tunnel had eroded and blackened the inward facing polycarbonate surfaces in critical (observing) areas near the inlet gap. Hence, other easily-replaceable, transmissive materials with superior optical quality should be explored in the future. One option is to use high quality optical glass inserted into a special metal frame or into machined-inserts in the polycarbonate plates. Future models should also consider more rigid

methods of supporting the shroud—e.g., by bolting the shroud securely to the side plates once the optimum shroud position has been determined—since excessive mechanical vibration-induced noise (possibly from a loosely supported shroud) had made many pressure transducer traces unreadable.

Along with these 2nd-gen model modifications, further improvements in the T3 tunnel and TEA-622 laser are anticipated for the next test campaigns. For example, to date both TEA-620 lasers have only been fired individually (~200 J), but very soon the combined TEA-622 will be able to deliver 400+ J into the test section. Note also that the laser’s multi-pulse capability (i.e., two pulses sequentially fired with a specific delay interval) has not yet been explored in the present work due to technical issues. But when such issues are finally resolved, the enhanced laser flexibility will greatly expand the scientific output of future hypersonic LP experiments.

6.2.3 Axi-symmetric Hypersonic Lightcraft Model

During the present campaign, an axisymmetric Lightcraft model was designed and manufactured using a geometry studied by **Langener (2006)** in CFD simulations up to Mach 5.0 along an airbreathing launch trajectory proposed by **Frazier (1987)**. As shown in **Figure 6.3**, the 3D model is composed of an aluminum “power-law” nose, transparent cylindrical shroud, and an off-axis rear parabolic mirror truncated at the tip to admit the SS support sting for T3 tunnel installation. The model is mounted on linear bearings so that the aerodynamic drag force and time-variant laser-generated impulse can be measured with a piezoelectric load cell (see **Figure 6.3**). A PCB pressure transducer may be installed at the tip of the nosecone to monitor stagnation pressure.

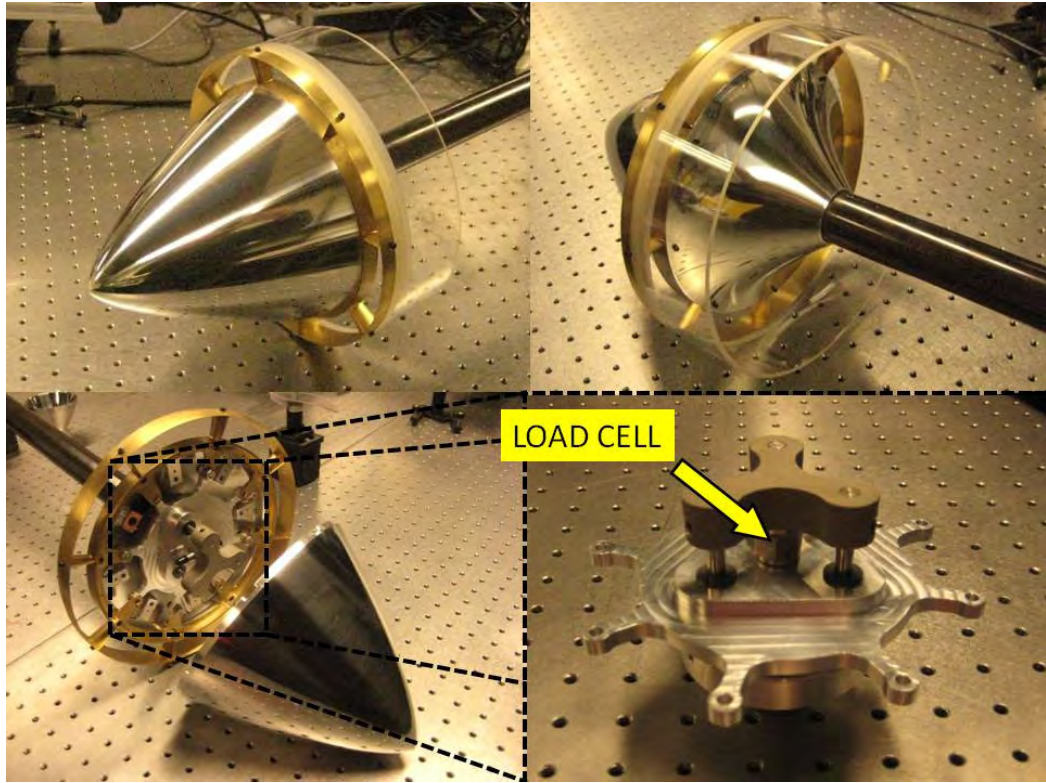


Figure 6.3: Axi-symmetric Lightcraft model ready for hypersonic tests in the T3 tunnel.

The model's cylindrical shroud (254 mm diameter) was manufactured from 3-mm thick optical quality Lexan to enable direct Schlieren visualization of the laser-induced air-breakdown and blast wave expansion process taking place within the absorption chamber. This model will allow direct comparison of the external compression inlet performance and “unpowered” ram drag data obtained by **Langener (2009)** with FluentTM; the planned hypersonic experiments will extend this investigation into the “powered regime” with the deposition of pulsed laser energy, and also explore flight angles of attack other than zero. This 254 mm diameter model is considerably smaller than the current 2-D model, having a center body optic diameter of 203 mm (8”), so that the laser beam nearly fills the rear optics.

The center section structure of the 3-D model was manufactured from brass, offering superior structural support for the existing nosecone and primary optics, which can be interchanged with others to make different Lightcraft geometries in future tests. The center section also supports the shroud leading edge structure which can also be replaced.

Once the direct load-cell measurement system for laser-induced impulse is “debugged” and operational, it will become an invaluable asset for calibrating CFD codes, and for assessing the overall efficiency (η_0) and C_M of Lightcraft engine/vehicles.

6.2.4 Airbreathing Laser-Electromagnetic Propulsion

An even more exotic propulsion experiment planned for the T3 tunnel is the *laser-initiated, MHD slipstream accelerator*, which promises to extend the hypersonic airbreathing regime up to orbital velocities and beyond (Myrabo, 1976); the engine is also designed to annihilate the vehicle bow shock so that no sonic boom is generated. In this engine concept, the incoming laser beam is focused by the rear parabolic optic into the compressed slipstream air, triggering air-breakdown at a position just above the shroud; as mentioned earlier, preliminary experiments with the 2D model (shroud removed) have already demonstrated this breakdown process. The objective of this laser pulse is to create/prepare an ionized air-plasma “paddle” for subsequent acceleration using MHD forces in a repetitively-pulsed thruster mode (Myrabo, 1976), as briefly described below.

After striking the primary parabolic optic, the laser beam passes through an aerodynamic window or physical infra-red (IR) window (installed flush with the shroud upper surface) and triggers air breakdown in the compressed hypersonic working fluid between the bow shock wave and the shroud upper surface. The laser-induced breakdown forms an electrically conductive plasma “paddle” between a pair of parallel high voltage electrodes positioned at both sides of MHD accelerator channel, thereby closing the electric circuit; a capacitor bank then discharges a strong electric current through the conductive plasma “paddle” in the presence of an “on-board” 2 Tesla magnetic field. The plasma “paddle” is then accelerated downstream by the action of Lorentz forces ($\vec{F} = \vec{J} \times \vec{B}$), entraining air ahead of it like a “snow plow” (Myrabo, 1976).

The objective of this research is not only the direct measurement of the MHD impulse, but also the Schlieren visualization of the laser-induced breakdown and plasma acceleration phenomena, including annihilation of the bow shock wave. The most complex and expensive component in this model/apparatus is the 2.0 T magnet shown in

Figure 6.4, which was custom designed and built for this experiment. Successful system tests of the magnet/power-supply at a charge voltage of 5.6 kV and peak current of 59.9 kA demonstrated a peak magnetic induction of 2.01 Tesla at a distance of 75 mm above the magnet's exterior surface. The 2-Tesla goal was attained 1.92 ms after initiation of the discharge, with a time constant of 8.3 ms (for magnetic induction field decay). The next step is to manufacture the new model from high strength plastics and ceramic materials, and install the magnet, capacitor bank, and MHD accelerator electrodes.

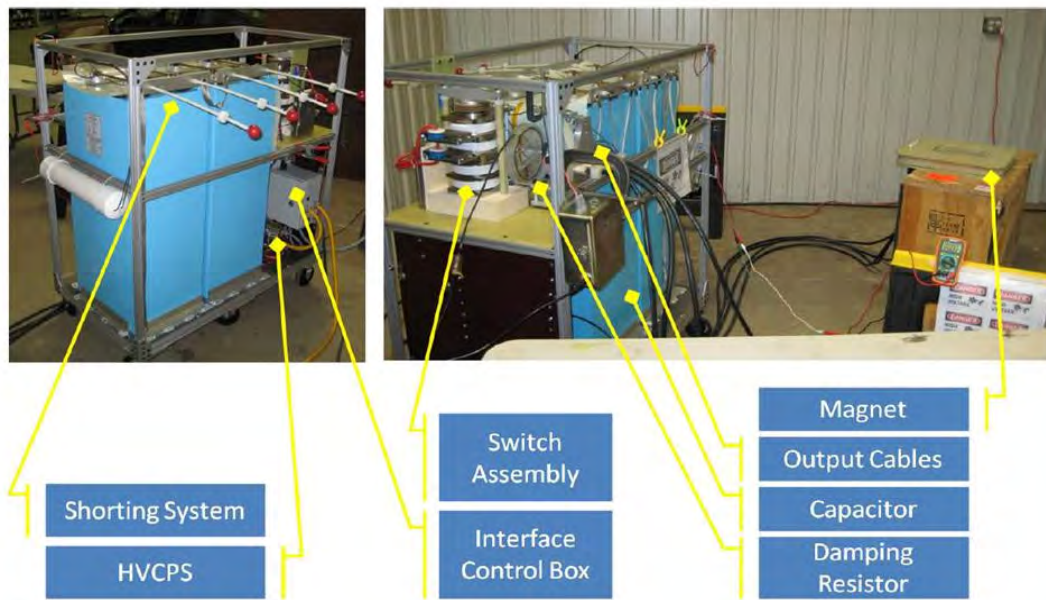


Figure 6.4: Pulsed power supply and 2.0 T magnet system.

To avoid undesirable particulate-induced air breakdowns, and guarantee the desired line-focus breakdown geometry for the MHD experiment, potential contaminants (i.e., pump oil, metallic and HC particulates, etc.) must be removed from the T3 internal passageways. This can be achieved by thoroughly cleaning the driver and driven sections of the HST after every run, and by using only dry synthetic air or pure N₂ as the working gas in the driven section.

This experiment will attempt to demonstrate the physics and feasibility of the laser-electromagnetic accelerator concept.

References

Anderson, J. D., (1990). *Modern Compressible Flow: With Historical Perspective*, McGraw-Hill Inc., 2nd ed.

Apollonov, V.V., Tishchenko, V.N., (2004). “Mechanism of Shock Wave Merging in a Laser Jet Engine”, *Quantum Electronics (Kvantovaya Elektronika)*, 34(12), 1143-1146, 2004.

Apollonov, V.V., Tischenko, V. N., (2004). “Stable Generation and Merging of Shock Waves for ‘Lightcraft’ Applications: Part 1”, 3rd International Symposium on Beamed Energy Propulsion (ISBEP), AIP Conference Proceedings 766, October 2004.

Apollonov, V.V., Kijko, V.V., Kislov, V.I., Tischenko, V.N., (2005). “Pulse-Periodic Lasers for Lightcraft Application”, XV International Symposium on Gas Flow, Chemical Lasers, and High Power Lasers, Proc. SPIE Vol. 5777, 2005.

Bohn, W. L., Schall, W. O., (2002). “Laser Propulsion Activities in Germany,” 1th International Symposium on Beamed Energy Propulsion (ISBEP), AIP Conference Proceedings 664, pp. 79 - 94, November 2002.

Cook, W. J., Felderman, E. J., (1966). “Reduction of Data from Thin-Film Heat-Transfer Gages: A Concise Numerical Technique”, *AIAA Journal*, vol. 4, no. 3, pp. 561-562, March.

Cunyan Cui, Yanji Hong, Ming Wen, Jun Wang, and Guoqiang He, (2005). “Effects of Nozzle Structure on Laser Thruster Performance,” 4th International Symposium on Beamed Energy Propulsion (ISBEP), AIP Conference Proceedings 830, pp. 33-37, November 2005.

Fernandez, J., (1990). “Design and Analysis of a Laser Impulse Experiment for a Multi-Cycle Laser Pulsejet Engine,” MSc. Thesis, Rensselaer Polytechnic Institute, Troy, NY.

Frazier, S. R., (1987). “Trajectory Analysis of a Laser-Energized Transatmospheric Vehicle,” MSc. Thesis, Rensselaer Polytechnic Institute, Troy, NY.

Gong, P., Tang, Z., (2005). “Numerical Simulation for Laser Propulsion of Air Breathing Mode Considering Moving Boundaries and Multi-Pulses,” 4th International Symposium on Beamed Energy Propulsion (ISBEP), AIP Conference Proceedings 830, pp. 87-94, November 2005.

Kantrovitz, A. (1972). *Propulsion to Orbit by Ground-Based Lasers*. Astronautics & Aeronautics, Vol. 10, pp. 74-76.

Kare, J. T. (Ed.) (1987) *SDIO/DARPA Workshop on Laser Propulsion, 1986*. Conference Proceedings, Livermore, CA.

Kare, J. T. (Ed.) (1990). *1987 SDIO Workshop on Laser Propulsion*. Conference Proceedings, Los Alamos, NM.

Kare, J.T., (2002). “Laser Launch – Second Wave,” 1th International Symposium on Beamed Energy Propulsion (ISBEP), AIP Conference Proceedings 664, pp. 22-33, November 2002.

Katsurayama, H., Komurasaki, K., Arakawa, Y., (2001). “Numerical Analyses on Pressure Wave Propagation in Repetitive Pulse Laser Propulsion”, AIAA-2001-3665, 37th Joint Propulsion and Conference, July 2001.

Katsurayama, H., Komurasaki, K., Arakawa, Y., “Computation Performance Estimation of Laser Ramjet Vehicle”, AIAA-2002-3778, 38th Joint Propulsion and Conference, July 2002.

Katsurayama, H., Hirooka, Y., Komurasaki, K., Arakawa, Y., “Feasibility Study of a Laser Ramjet Single Stage to Orbit Vehicle”, 41st Aerospace Sciences Meeting and Exhibit, AIAA-2003-0497, January 2003

Katsurayama, H., Ushio, M., Komurasaki, K., Arakawa, Y., “Analytical Study on Flight Performance of an Air-Breathing RP Laser Launcher”, AIAA-2004-3585, 40th Joint Propulsion and Conference, July 2004.

Kenoyer, D. A., Anderson, K. S., Myrabo, L. N., Nagler, B. N., (2007). “Validation and Calibration of 6-DOF Laser Propelled Lightcraft Flight Dynamics Model vs. Experimental Data,” JANNAF Propulsion Meeting, 2007.

Kenoyer, D. A., Salvador, I. I., Myrabo, L. N., Notaro S. S., Bragulla, P. W., (2010). “Experimental Investigation of Axial and Beam-Riding Propulsive Physics with TEA CO₂ Laser,” 2010 International High-Power Laser Ablation Conference, Santa Fe NM, April.

Kim, S., Cho, H., Choi, J.-Y., Jeung, I.-S., (2002). “Flow Characteristics of Two-Dimensional Supersonic Laser Propulsion Vehicle,” AIAA-2002-2204, 33rd Plasmadynamics and Lasers Conference, May, 2002.

Kim, S., Pang, J. -S., Jeung, I.-S., Choi, J.-Y., (2002). “Numerical Simulation of Flow Characteristics of Supersonic Airbreathing Laser Propulsion Vehicle,” 1th International Symposium on Beamed Energy Propulsion (ISBEP), AIP Conference Proceedings 664, pp. 160-169, November 2002.

Knecht, S. D., Mead, F. B., Micci, M. M., Larson, C. W., (2005). “Trajectory Simulations, Qualitative Analyses and Parametric Studies of A Laser-Launched Micro-Satellite Using OTIS,” 4th International Symposium on Beamed Energy

Propulsion (ISBEP), AIP Conference Proceedings 830, pp. 522-533, November 2005.

Komurasaki, K., Arakawa, Y., Hosoda, S., Katsurayama, H., Mori, K., (2002). “Fundamental Researches on Laser Powered Propulsion,” AIAA-2002-2200, 33rd Plasmadynamics and Lasers Conference, May, 2002.

Komurasaki, K. (Ed.) (2003). *Second International Symposium on Beamed Energy Propulsion*. AIP Conference Proceedings, 702, Sendai, Japan.

Komurasaki, K., Yabe, T., Uchida, S., Sasoh, A. (Eds.) (2005). *Fourth International Symposium on Beamed Energy Propulsion*. AIP Conference Proceedings, 830, Nara, Japan.

Langener, T. (2006). “Numerical Investigations on the Inlet Aerodynamics and Ram-Drag of Laser Lightcraft Vehicles,” Diplomarbeit IRS-06-S30, Institute für Raumfahrtsysteme Universität Stuttgart, July.

Larson, C.W., Mead Jr., F.B., Kallioma, W.M., (2002). “Energy Conversion in Laser Propulsion III,” ,” 1th International Symposium on Beamed Energy Propulsion (ISBEP), AIP Conference Proceedings 664, pp. 170-181, November 2002.

Libeau, M. A., Myrabo, L. N., Filippelli, M., and McInerney, J., (2002). “Combined Theoretical and Experimental Flight Dynamics Investigation of a Laser-Propelled Vehicle,” AIAA 2002-3781.

Liepmann, H.W., Roshko, A., (1964). *Elements of Gasdynamics*, Dover Publications Inc., 2001, 443p.

Lukasiewicz, J., (1973). *Experimental Methods of Hypersonics*. Marcel Dekker, Inc. NY.

Lu, F. K., Marren, D. E., (2002). *Advanced Hypersonic Test Facilities*, AIAA Progress in Astronautics and Aeronautics, v. 198, Reston, VA.

Mead Jr., F. B., Larson, C. W., Knecht S. D., (2005). “An Overview of the Experimental 50-cm Laser Ramjet (X-50LR) Program,” 4th International Symposium on Beamed Energy Propulsion (ISBEP), AIP Conference Proceedings 830, pp. 534-552, November 2005.

Mead Jr., F. B., (2007). “Part 1 – The Lightcraft Technology Demonstration Program,” AFRL-RZ-ED-TR-2007-0078, Final Report.

Minovitch, M. A. (1972). *Reactorless Nuclear Propulsion – The Laser Rocket*, 8th AIAA/SAE Joint Propulsion Specialist Conference, New Orleans.

Minucci, M. A. S., (1991) "An Experimental Investigation of a 2-D Scramjet Inlet at Flow Mach Numbers of 8 to 25 and Stagnation Temperatures of 800 to 4,100 K", Ph.D. Thesis, Rensselaer Polytechnic Institute, Troy, NY, May.

Minucci, M. A. S., Toro, P. G. P., Chanes Jr., J. B., Ramos, A. G., Pereira, A. L., Nagamatsu, H. T., Myrabo, L. N., (2003). "Investigation of a Laser-Supported Directed-Energy 'Air Spike' in Hypersonic Flow – Preliminary Results," *Journal of Spacecraft and Rockets*, Vol. 40, No. 1, pp. 133-135, 2003.

Minucci, M. A. S., Toro, P. G. P., Oliveira, A. C., Ramos, A. G., Chanes Jr., J. B., Pereira, A. L., Nagamatsu, H. T., Myrabo, L. N., (2005). "Laser-Supported Directed-Energy "Air Spike" in Hypersonic Flow," *Journal of Spacecraft and Rockets*, Vol. 42, No. 1, pp. 51-57, 2005.

Mori, K., Komurasaki, K., Arakawa, Y., (2002). "Laser Plasma Production and Expansion in a Supersonic Flow," AIAA 2002-0634, 40th Aerospace Sciences Meeting and Exhibit, Reno, NV, January.

Myrabo, L.N., (1976). "MHD Propulsion by Absorption of Laser Radiation," AIAA Paper No. 76-706, AIAA/SAE 12th Propulsion Conference, Palo Alto - CA, July.

Myrabo, L.N., et al., (1983). "Advanced Beamed-Energy and Field Propulsion Concepts," BDM/W-83-225-TR, prepared for the Jet Propulsion Laboratory under NASA Contract NAS7-100, Task Order No. RE-156, The BDM Corporation, McLean, VA, 1983, p. V11.

Myrabo, L.N., and Ing, D., (1985). *The Future of Flight*, Baen Books, distributed by Simon & Schuster, New York, NY, 1985, p. 102.

Myrabo, L.N., (Ed.), (1989). "Lightcraft Technology Demonstrator," Final Technical Report, SDIO Laser Propulsion Program, prepared under contract to Lawrence Livermore National Laboratory, No. 2073803.

Myrabo, L.N., Messit, D. G., Mead Jr., F. B., (1998). "Ground and Flight Tests of a Laser Propelled Vehicle," AIAA paper 1998-1001, 36th Aerospace Sciences Meeting and Exhibit, Reno, NV.

Myrabo, L.N., (2002). "Brief History of the Lightcraft Technology Demonstrator (LTD) Project," 1th International Symposium on Beamed Energy Propulsion (ISBEP), AIP Conference Proceedings 664, pp. 49-59, November 2002.

Myrabo, L. N., (Ed.), (2006). "Basic Research Investigation into Multimode Laser and EMI Launchers," MURI Progress Report, AFOSR Award: 9550-05-0392.

Myrabo, L. N., Lewis, D. S., (2009). *Lightcraft Flight Handbook LTI-20: Hypersonic Flight Transport for an Era Beyond Oil*. Collector's Guide Publishing, Inc.

Nascimento, M. A. C., (1997). "Gaseous Piston Effects in Shock Tube/Tunnel When Operating in the Equilibrium Interface Condition," São José dos Campos, Doctorate Thesis – Instituto Tecnológico de Aeronáutica, Brazil.

Nakagawa, T., Mihara, Y., Matsui, M., Komourasaki, K., Takahashi, K., Sakamoto, K., Imai, T., (2003). "A Microwave Beaming Thruster Powered by 1 MW Microwave," AIAA 2003-4430, 39th AIAA/ASME/SAE/ASEE Joint Propulsion Conference and Exhibit, July, 2003.

Nagamatsu, H. T., Sheer, R. E., (1965). "Vibrational Relaxation and Recombination of Nitrogen and Air in Hypersonic Nozzle Flows," AIAA Journal, Vol. 3, No. 8, 1965, p.p. 1386-1391, .

Nebolsine, P.E., Pirri, A.N., (2002). "Laser Propulsion: The Early Years", 1th International Symposium on Beamed Energy Propulsion (ISBEP), AIP Conference Proceedings 664, pp. 11-21, November 2002.

Niino, M., (2002). "Activities of Laser Propulsion in Japan," 1th International Symposium on Beamed Energy Propulsion (ISBEP), AIP Conference Proceedings 664, pp. 71-78, November 2002.

Ohnishi, N., Ogino Y., Sawada K., Ohtani T., Mori K., Sasoh A., (2005). "Numerical Simulation of Laser-Driven In-Tube Accelerator Operation," 4th International Symposium on Beamed Energy Propulsion (ISBEP), AIP Conference Proceedings 830, pp. 191-198, November 2005.

Oliveira, A. C., Minucci, M. A. S., Toro, P. G. P., Channes Jr, J. B., Salvador, I. I., (2005). "Schilieren Visualization Technique Applied to the Study of Laser-Plasma Induced Breakdown in Low Density Hypersonic Flow," 4th International Symposium on Beamed Energy Propulsion (ISBEP), AIP Conference Proceedings 830, pp. 504-509, November 2005.

Pakhomov, A. V., Thompson, M. S., Gregory, D. A., (2002). "Ablative Laser Propulsion: A Study of Specific Impulse, Thrust and Efficiency," 1th International Symposium on Beamed Energy Propulsion (ISBEP), AIP Conference Proceedings 664, pp. 49-59, November 2002.

Pakhomov, A. (Ed.) (2002). *First International Symposium on Beamed Energy Propulsion*. AIP Conference Proceedings, 664, Huntsville, Alabama.

Pakhomov, A., Myrabo, L. N., (Eds.) (2004). *Third International Symposium on Beamed Energy Propulsion*. AIP Conference Proceedings, 766, Troy, New York.

Pakhomov, A. (Ed.) (2007). *Fifth International Symposium on Beamed Energy Propulsion*. AIP Conference Proceedings, 997, Kailua-Kona, Hawaii.

Palm, N., Kaplan, M., Lim, T-Y, (2009). *Aurora Spacelines – Laser Powered Business Trips*. Umea Institute of Design, Sweden.

Patel, C. K. N. (1968). "High-Power Carbon Dioxide Lasers", *Scientific American*, Vol. 219, Iss. 2, pp 22-33, August.

Pirri, A.N., (1973). "Theory for Momentum Transfer to a Surface With a High Power Laser," *Physics of Fluids*, vol. 16, Is. 9, pp.1435-1440, September.

Pirri, A.N, Root, R.G., Wu, P.K.S., (1978). "Plasma Energy Transfer to Metal Surfaces Irradiated by Pulsed Lasers," *AIAA Journal*, vol.16, No. 12, pp. 1296-1304, December.

Pope, A. and Goin, K., (1965). *High-Speed Wind Tunnel Testing*, Wiley, New York.

Qian Li, Yanji Hong, Jinhu She, Zhengrui Cao, and Junhua Wang, (2005). "Thrust Generating Mechanism of Nozzle Powered by Single Laser Pulse," 4th International Symposium on Beamed Energy Propulsion (ISBEP), AIP Conference Proceedings 830, pp. 121-129, November 2005.

Radziemaski, L. J., Cramers, D. A., (Ediors) (1989). *Laser-Induced Plasmas and Applications*, Marcel Dekker, Inc., New York.

Raizer, Yu. P., (1965). "Heating of a Gas by a Powerful Light Pulse," Soviet Physics JETP, Vol. 21, No. 5, pp. 1009-1017, November.

Raizer, Yu. P., (1966). "Breakdown and Heating of Gases Under The Influence of a Laser Beam," Soviet Physics Uspekhi, Vol. 8, No. 5, pp. 650-673, March-April.

Raizer, Yu. P., (1977). *Laser-Induced Discharge Phenomena*, Consultants Bureau, New York.

Reilly, J. P., Sing, P., and Weil, G., (1977). "Multiple pulse propagation Through Atmospheric Dust at 10.6 microns." AIAA Paper 77-697, 10th Fluid and Plasma Dynamics Conf., New Mexico, June 27-28.

Reilly, J.P., Ballantyne, A., Woodroffe, J.A., (1979). "Modeling of Momentum Transfer to a surface by Laser-Supported Absorption Waves", *AIAA Journal*, vol.17, no. 10, pp. 1098-1105, October.

Resendes, D. P., Mota, S., Sorasio, G., Mendonça S. T., Sanders, B., Encarnação, J., (2004). "Laser Propulsion for ESA Missions," Contract No. 17048/03/NL/PA, November.

Resendes, D. P., Mota, S., Mendonça S. T., Sanders, B., Encarnação, J., del Amo, J. G., (2007). "Laser Propulsion for Ground Launch", *Journal of Propulsion and Power*, Vol. 23, No.1, pp. 73-80, January-February.

Richard, J.C., (1989). "Analysis of Pulsed Laser-Generated Impulse in an Advanced Airbreathing Thruster," PhD Thesis, Rensselaer Polytechnic Institute, Troy, NY.

Rolim, T. C. (2009). "Experimental Analysis of a Hypersonic Waverider," MSc. Thesis, Aeronautics Institute of Technology – ITA, São José dos Campos, Brazil.

Root, R. G., (1989). "Modeling of Post-Breakdown Phenomena," in Radziemski, L. J., Cramers, D. A. (Eds.), *Laser-Induced Plasmas and Applications*, pp. 67-103, Marcel Dekker, NY.

Rosa, M. A. P. ; Rocamora Jr., F. D., Menezes, A. C., (2009). "STCALC - A Hypersonic Shock Tunnel Calculator". 20th International Congress of Mechanical Engineering, COBEM 2009, Gramado, RS, Brazil.

Salvador, I. I., Minucci, M. A. S., Toro, P. G. P., Oliveira, A. C., Channes Jr, J. B., Myrabo, L. N., and Nagamatsu, H. T., (2005). "Experimental Analysis of Heat Flux to a Blunt Body in Hypersonic Flow with Upstream Laser Energy Deposition — Preliminary Results," 4th International Symposium on Beamed Energy Propulsion (ISBEP), AIP Conference Proceedings 830, pp. 163-171, November.

Salvador, I. I., Minucci, M. A. S., Toro, P. G. P., Oliveira, A. C., Channes, J. B. Jr, (2005). "Development of Surface Junction Thermocouples for High Enthalpy Measurements," 4th International Symposium on Beamed Energy Propulsion (ISBEP), AIP Conference Proceedings 830, pp. 481-491, November.

Salvador, I. I., Minucci, M. A. S., Toro, P. G. P., Oliveira, A. C., Channes, J. B. Jr, (2007). "Surface Heat Flux and Pressure Distribution on a Hypersonic Blunt Body with DEAS," 5th International Symposium on Beamed Energy Propulsion (ISBEP), AIP Conference Proceedings 997, pp. 367-378, November.

Sasoh, A., Yu, X., Ohtani, T., Ogawa, T., Kawahara, T., Kim, S., Jeung, I. -S., (2004). "Laser Impluse Generation in Flight," AIAA 2004-650, 42nd AIAA Aerospace Science Meeting and Exhibit, January.

Schall, W. O., Eckel, H. A., (2003). "Pulsed Laser Propulsion Experiments," IAC-03-S.6.04, 54th International Astronautical Congress, October.

Seddon, J., Goldsmith, E.L., (1985). *Intake Aerodynamics*, AIAA Education Series, New York.

Sedov, L.I., *Similarity and Dymensional Methods in Mechanics*, 10th edition, CRC Press, 1993.

Settles, G.S., (2006). *Schlieren and Shadowgraph Techniques*. Springer Verlag, Berlin.

Siegman, A. E. (1986), *Lasers*, University Science Books, Mill Valley, CA.

Sienel, T. H., (1992). "Design of a 2-D Full-Scale Variable Geometry Engine Inlet Model for a Multy-Cycle Laser Powered Transatmospheric Vehicle," MSc. Thesis, Rensselaer Polytechnic Institute, Troy, NY.

Srinivasan, S.; Tannehill, J. C.; Weilmuenster, K. J., (1987). "Simplified curve fits for the thermodynamic properties of equilibrium air," Nasa Technical Report NASA-RP-1181.

Svelto, O. (1998). *Principles of Lasers*. Plenum Press, NY.

Tang, Z., Cai J., Gong, P., Hu, X., Tan, R., Zheng, Z., Wu, J., Lu, Y., (2005). "Experimental Study of the Momentum Coupling Coefficient with the Pulse Frequency and Ambient Pressure for Air-Breathing Laser Propulsion," 4th International Symposium on Beamed Energy Propulsion (ISBEP), AIP Conference Proceedings 830, pp. 104-113, November.

Tischenko, V.N., (2003). "Generation of a Low-Frequency Wave by an Optical Discharge Moving in a Gas at a Subsonic Speed," Quantum Electronics (Kvantovaya Elektronika), 33(9), 823-830.

Tischenko, V.N., Grachev, G. N., Zapryagaev, V.I., Smirnov, A.L., Sobolev, A.V., (2002). "Spectrum of Shock Waves Produced by an Optical Discharge at a High -Pulse Repetition Rate", Quantum Electronics (Kvantovaya Elektronika), 32(4), 329-334.

Toro, P. G. P., (1998). "Experimental Pressure and Heat Transfer Investigation over a 'Directed Energy Air-Spike' Inlet at Flow Mach Numbers of 10 to 20, Stagnation Temperature of 1000K, and Arc Power up to 127kW", PhD Thesis, Rensselaer Polytechnic Inst., Troy, NY, August.

VKI/AEDC Special Course, (1993). *Methodology of Hypersonic Testing*, Von Karman Institute for Fluid Dynamics, Lecture Series 1993-03.

Verdeyen, J. T., (1995). *Laser Electronics*. Prentice Hall, Englewood Cliffs, NJ.

Yu. A. Rezunkov, A. L. Safronov, A. A. Ageichik, M. S. Egorov, V. V. Stepanov, V. S. Rachuk, V. Yu. Guterman, A. V. Ivanov, S. G. Rebrov, and A. N. Golikov, (2005). "Performance Characteristics of Laser Propulsion Engine Operating both in CW and in Repetitively-Pulsed Modes," 4th International Symposium on Beamed Energy Propulsion (ISBEP), AIP Conference Proceedings 830, November.

Walter, P. L. (2004). "Air blast and the Science of Dynamic Pressure Measurements," Sound and Vibration, pp. 10-16, December.

Walters, C.J., Barnes, R.H., Beverly, R.E., (1978). "Initiation of Laser Supported Detonation Waves," Journal of Applied Physics, Vol. 49, pp. 2937-2949.

Wang, T. -S., Chen, Y. -S, Liu, J., Myrabo, L. N., Mead Jr., F. B., (2002). "Advanced Performance Modeling of Experimental Laser Lightcraft," Journal of Propulsion and Power, Vol. 18, No. 6, November-December.

Weyl, G. M., Pirri, A., Root, R., (1980). "Laser Ignition of Plasma Off Aluminum Surfaces," AIAA-1980-1319, 13th Fluid & Plasma Dynamics Conference, Snowmass, CO.

Weyl, G. M., (1989). "Physics of Laser-Induced Breakdown: An Update," in Radziemski, L. J., Cramers, D. A. (Eds.), *Laser-Induced Plasmas and Applications*, pp. 1-67, Marcel Dekker, NY.

Zeldovich, Ya. B., Raizer, Yu. P., (1966). *Physics of Shock Waves and High Temperature Hydrodynamic Phenomena*, 2002 Edition, Dover Publications Inc., New York.

Zhiguo Dou, Honglin Yao, Jun Wang, Ming Wen, Peng Wang, Jan Yang, and Chong Li, (2005). "Experimental Investigation for 100-Joule-class TEA CO₂ Laser and Gas Interaction," 4th International Symposium on Beamed Energy Propulsion (ISBEP), AIP Conference Proceedings 830, pp. 81-86, November.

Appendix A – Sensors and Calibration

The 2-D Lightcraft model used was equipped with 13 pressure transducer ports. Not all the sensors were kept the same throughout the experiments, with the sensors located at the model's shroud being exchanged depending on the environment pressure. The environment pressure dictates the blast wave pressure induced by the laser air-breakdown.

This appendix presents the sensors used throughout the experiments and their respective calibration and position on the model, according to **figure 3.10** and presented in **Table A.1**. The sensors used in the T3 HST for the measurement of the incident shock wave transit time and the reservoir pressure are described in **Table A.2**.

Table A.1: 2-D Lightcraft sensor models, calibration and ports.

<i>Sensor model</i>	<i>S/N</i>	<i>Sensitivity [V/bar]</i>	<i>Port</i>
112A22	25585	1.466	Pitot
112A22	8340	1.344	p2
112A22	8341	1.404	p3
112A22	9181	1.609	p4
112A22	9183	1.489	p5
113A26	18669	0.143	p6
112A22	25593*	1.395	p6
113A22	17882 ^a	0.0149	p7
113A26	18671*, ^a	0.146	p7
112A22	25601*	1.429	p7
113A26	18670 ^a	0.142	p8
112A22	26671*	1.467	p8
113A21	18665	0.335	p9
113A26	18672*, ^a	0.145	p9
112A22	26673*	1.436	p9
112A22	26670	1.453	p10
112A22	13070	1.35	p11
112A22	10373	1.491	p12
112A22	10372	1.323	p13

* replacement sensors; ^a used in the static experiments;

Table A.2: T3 HST 2-D Lightcraft sensor models, calibration and ports.

<i>Sensor model</i>	<i>S/N</i>	<i>Sensitivity [pC/bar]</i>	<i>Port</i>
Kistler 701A	598603	-81	P2 (Shock transit)
Kistler 701A	255465	-78.5	P3 (Shock transit)
Kistler 7005	588222	-47	P5 (Reservoir)

Appendix B – USA/Brazil BEP Collaboration



Figure B.1: Logo for the collaborative effort set between RPI and HTN-LAH under sponsorship of the AFOSR.

When the present AFOSR-sponsored, 5-year Multi-University Research Initiative (MURI) grant on laser propulsion (LP) began on June 1, 2005, Rensselaer Polytechnic Institute (RPI) was undergoing strategic changes that included the decommissioning of the former Gas Dynamics Laboratory (GDL) in the Ricketts Building, after it had hosted 5+ decades of cutting-edge research in aerodynamics, hypersonics, and advanced propulsion. After 7 months in limbo, a new ~ 550 ft² laboratory was authorized (by RPI) in the Johnsson Engineering Center under the direction of Prof. Leik Myrabo—the Laser Propulsion Laboratory (LPL)—which retained some useful equipment from the GDL but, unfortunately, lost the capacity for performing high speed flow research.

It then became necessary to seek an alternative to the operational RPI Hypersonic Shock Tunnel (HST) in Ricketts, so that the promised MURI research objectives could be pursued in an off-campus location. An exceedingly viable alternative emerged in the form of an international collaboration with the Henry T. Nagamatsu Laboratory of Aerothermodynamics and Hypersonics (HTN-LAH) located at the Instituto de Estudos Avançados (IEAv-CTA) in São José dos Campos, Brazil. This partnership was forged by the shared research goals envisioned by both parties (RPI and IEAv-CTA), and the unique facilities and equipment made available for this AFOSR research: i.e., a) the operational T3 hypersonic shock tunnel at the HTN-LAH; and, b) RPI's two Lumonics TEA 620 lasers that were transported to Brazil with the approval of AFOSR.

Another important consideration was the high cost of running hypersonic ground tests (facilities, workforce personnel, and consumables) which could strain the limited funding available under the AFOSR grant. Costs were effectively shared between both laboratories throughout the research campaign presented here. Helium, purchased in Brazil, was the most expensive consumable, running at about \$1350 per HST test; one bottle of pure helium at \$600 USD for the Lumonics 622-TEA (3hrs/test, including preparatory purge time), and three bottles of "fly balloon" helium for the HST driver at \$250 USD each. Hence, a typical 30 run campaign costs over \$40,000 USD for just the helium.

Table A.1 show how the responsibilities were divided for successful realization of the HST experiments, with RPI focusing on the CO₂ lasers, Lightcraft models (the present 2D model, and 3D-axisymmetric model for future experiments) and associated instrumentation. HTN-LAH was responsible for T3 tunnel operation and related instrumentation, data acquisition systems, installation of CO₂ lasers and all consumables. The workforce was supplied by both parties.

Table B.1: Division of responsibilities between RPI and IEAv-CTA in the present campaign..

RPI (USA)	LAH - IEAv (Brazil)
2x Lumonics TEA CO ₂ Lasers Optics and related equipment/instrumentation 2-D Hypersonic Lightcraft Model TEA CO ₂ lasers installation Logistics	T3 Hypersonic Shock Tunnel and instrumentation Data acquisition systems T3 technical support personnel T3 Consumables (Gases+Diaphragms) TEA CO ₂ lasers installation

This collaborative effort also enabled RPI's donation of experimental flow facilities from the decommissioned GDL to the newly created HTN-LAH at IEAv-CTA. Among the equipment donated was the 0.6 m (test section diameter) HST, designed and built by Prof. Henry T. Nagamatsu (now deceased) being in use at RPI for over 30 years; a half-scale HST of the same design was also donated. The other HST donated was a powerful combustion-driven HST (capable of Mach 8 to 50), which was also designed by Prof. Nagamatsu when affiliated with General Electric R&D in Schenectady, NY; this tunnel was never installed in the GDL lab (for lack of a suitable space), and was preserved in storage since GE R&D gave it to RPI nearly 27 years ago. In addition, a 12 m long brass, low pressure (Toro, 1998) shock tube (conventional cylindrical cross-section), and another 8 m long shock tube with a square cross-section were donated as well. Much ancillary equipment including electronic instrumentation, vacuum pumps, compressors, and the like, were shipped with these tubes and tunnels by sea freight loaded into two shipping containers. The outdated electronic instrumentation was discarded, and new modern replacements are being acquired by the HTN-LAH. One exciting development: a brand new building is presently under construction at IEAv to house all these shock tunnels and tubes—Prof. Nagamatsu's legacy—which now continues to live on, in Brazil.

Finally, it bears mentioning that Professor Nagamatsu's entire technical library on hypersonics research, collected since the dawn of the Space Age, was transferred to the archives of the IEAv's library as a part of this donation. This personal gift was kindly facilitated by Prof. Nagamatsu's wife and surviving family, who also sponsored its shipment to the HTN-LAH.

Appendix C – Hypersonic Shock Tunnels

The main tools used in the present experiments were the T3 Hypersonic Shock Tunnel (HST) and the Lumonics 622-TEA CO₂ laser. The theory and operation of a HST are reviewed in depth *here* (i.e., not in the main body of the dissertation), so as not to distract readers already familiar with such physics. Those unfamiliar with HST dynamics grasp are invited to read further.

After a brief introduction to the requirements for hypersonic testing, the general characteristics of a HST are introduced along with modeling of the flow field, starting from rupture of the main diaphragm to the establishment of flow in the test section.

C.1 Requirements for Hypersonic Testing

As noted by Lukasiewicz (1973) the main difficulty in obtaining reliable hypersonic data from ground testing, is the large number of similarity parameters that should be satisfied, in addition to the specific desired atmospheric and velocity conditions that would be encountered in hypersonic flight.

Assuming ideal compressible viscous flow, the similarity parameters are basically the Mach, Reynolds and Prandtl numbers, ratio of specific heats, and a temperature-viscosity law. As long as these parameters are satisfied, we can assume the flow properties are duplicated for the simulation in question. However, ideal compressible viscous flow is limited to lower Mach numbers flows, with the requirements for hypersonic similitude being more stringent due to real (high temperature) gas effects encountered at higher enthalpies. These thermochemical effects include vibrational excitation, dissociation, ionization, and radiation. Thus, to satisfy the similitude under hypersonic conditions (real gas), one would be required to duplicate the flight velocity, vehicle size and atmospheric environment, which can rarely be accomplished. However, specific phenomena such as aerodynamics forces and pressures, are insensitive to real gas effects under certain hypersonic conditions (usually below 5.0 km/s), so Mach and Reynolds numbers usually suffice for similitude.

Another important factor that must be considered in hypersonic ground simulations is the amount of energy involved in simulating flows at these conditions. The huge amounts of energy make impractical the use of continuous and even long duration test

facilities to operate, due to thermal and structural limitations. The most common solution for this problem is to use extremely short duration (i.e., impulsive) test facilities, with test times ranging from 10^{-2} to 10^{-6} s of operation, coupled with small flow field cross-sections. This is the context in which Hypersonic Shock Tunnels have seen widespread acceptance in hypersonic experimental science.

C.2 General Characteristics of a Hypersonic Shock Tunnel

The Hypersonic Shock Tunnel (HST) is the easiest and cheapest method for simulating high enthalpy conditions characteristic of hypersonic flight. Basically, a HST is comprised of a standard shock tube fitted with an expansion nozzle at the end of the driven section.

A conventional shock tube is comprised of a high pressure section (driver) separated by a diaphragm from a low pressure section (driven). With the rupture of the diaphragm a strong shock wave is formed and propagates downstream into the low pressure section, compressing and heating the air in this section at the same time it accelerates the gas as it travels through the tube. From this moment on, the flow field can be considered as unsteady and one-dimensional with all properties a function of space (x) and time (t). Meanwhile an expansion wave is propagated upstream into the driver section and a contact surface is formed in the interface of the gases of the two sections, which succeeds the shock wave at lower speed. After reaching the opposite end wall of the driven section (nozzle entrance) the incident shock wave is reflected. This reflection increases the enthalpy of the driven gas even further by transforming the gas kinetic energy into increased temperature and pressure and, depending on the initial conditions and shock strength, leading to the onset of high temperature effects in the gas (i.e., rotational and vibrational mode excitations as well as dissociation and ionization). Depending on the temperature achieved at this reservoir, after the incident shock wave reflection, the flow can then be classified according to its enthalpy, with low enthalpy being the case of $T_R < 1000$ K, medium enthalpy if $1000 \text{ K} < T_R < 2000$ K, and high enthalpy for $T_R > 2000$ K.

In the HST, a second diaphragm is positioned at the end of the driven section and is dynamically ruptured by the pressure rise caused by the incoming shock wave; the

nozzle's reservoir condition is generated by this incident shock wave reflection which processes the air, thereby generating the desired high enthalpy reservoir conditions. A basic diagram of the operation of a shock tunnel is shown in **Figure C.1..**

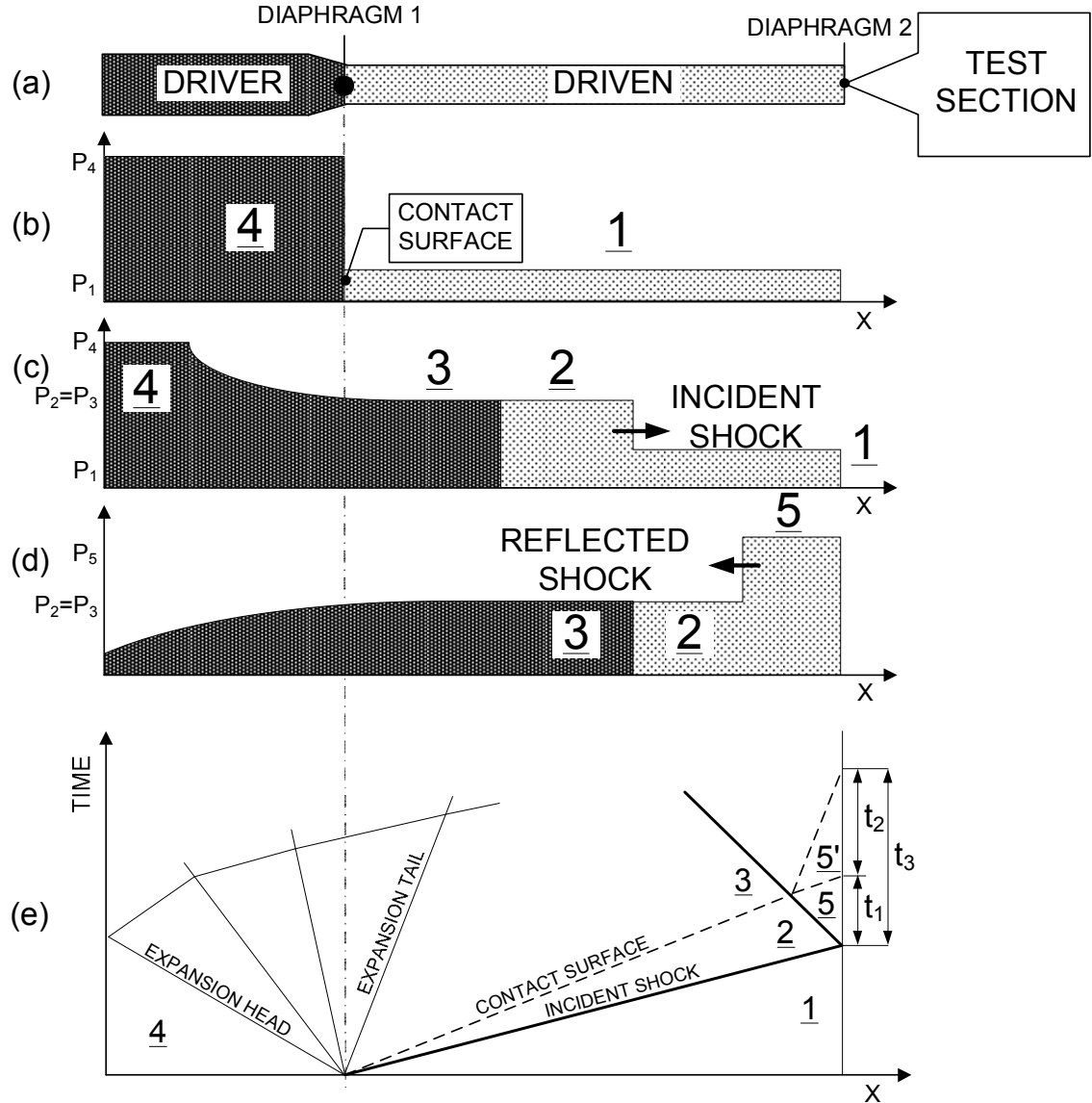


Figure C.1: Shock tunnel operation diagram.

Figure C.1 displays the basic configuration of a reflected shock HST (a), showing the driver/driven/test sections and diaphragms position, together with its initial pressure distribution (b). Also displayed are the pressure states achieved following the driver/driven diaphragm burst (c), and the resulting high pressure created at the nozzle entrance (d). At the bottom, (e) is a diagram of the time evolution of the incident shock, contact surface and expansion wave. In this figure the driver section is indicated by the

subscript (4), while the driven section is indicated by the subscript (1). The region indicated by (3) is the one processed by the expansion wave, and the region processed by the incident shock wave is indicated by (2). The reflected shock conditions are indicated by the subscript (5) and (5'). Region (5) corresponds to the case of flow through operation of the shock tunnel, with a test time t_1 , while region (5') corresponds to the tailored case where the shock impedance of the driver and driven gases are matched, resulting in a t_2 increase in test time (t_3 total).

C.3 Modeling of Shock Tunnel Flow

Most of the HST flow can be modeled by separating the shock tube flow from the nozzle flow, which is present only in the HST. The basic parameter of the shock tube is the diaphragm pressure ratio P_4/P_1 . Both the driver and the driven sections can operate with different gases and at different temperatures. This condition determines the shock and expansion strengths, P_2/P_1 and P_3/P_4 respectively, which can be obtained by using the conservation equations (continuity, momentum, and energy).

Considering a stationary shock wave, these equations are given as

$$\begin{aligned} {}_1u_1 &= {}_2u_2 \\ p_1 + {}_1u_1^2 &= p_2 + {}_2u_2^2 \\ h_1 + \frac{u_1^2}{2} &= h_2 + \frac{u_2^2}{2} \end{aligned} \quad (c.1)$$

with u_1 and u_2 being the velocities ahead and behind the shock wave (relative to the wave). If a moving shock reference is adopted, we then have $u_1 = u_s$ and $u_2 = (u_s - u_p)$, where u_s is the shock speed and u_p is the contact surface velocity.

Rearranging these equations and assuming thermically and calorically perfect gases in a constant section shock tube with negligible viscous effects, one can obtain the equations below

$$u_p = u_2 = a_1 \left(\frac{p_2}{p_1} - 1 \right) \left(\frac{2}{\left(\frac{1}{\gamma} + 1 \right) \frac{p_2}{p_1} + \left(\frac{1}{\gamma} - 1 \right)} \right)^{\frac{1}{2}} \quad (c.2)$$

$$u_3 = \frac{2a_4}{\gamma - 1} \left[1 - \left(\frac{p_3}{p_4} \right)^{\frac{(\gamma-1)/2}{\gamma-1}} \right] \quad (c.3)$$

which can be rearranged into the basic shock tube relation (Anderson, 1990), knowing the pressure and velocity relations $p_2 = p_3$ and $u_2 = u_3 = u_p$

$$\frac{p_4}{p_1} = \frac{p_2}{p_1} \left(1 - \frac{(\gamma-1)(a_1/a_4)(p_2/p_1 - 1)}{(2 - [2 - (\gamma+1)(p_2/p_1 - 1)])^{1/2}} \right)^{-2 \frac{1}{\gamma-1}} \quad (c.4)$$

In these equations p_1 , p_2 , p_3 , and p_4 are the pressures in the different sections, a_1 and a_4 are the sound speeds, γ is the specific heat ratio, and u_3 and u_p are the expansion wave and contact surface speed, respectively.

This equation is of great importance since it relates the shock strength (p_2/p_1) not only with the pressure ratio but also with the sound speed ratio (a_1/a_4), showing that the smaller the sound speed ratio, the stronger the shock wave will be. With $a = \sqrt{(\gamma/MM)T}$, the incident shock wave strength can be maximized by the use of a low molecular mass gas at high temperature in the driver and a high molecular mass gas at low temperature in the driven. Further analysis on the operation and use of shock tunnels can be found in the literature. (**Anderson, 1990; Nascimento, 1997; Toro, 1998 and Rolim 2009.**)

The above analysis is restricted to thermally perfect gases and considers ideal diaphragm rupture and no viscous effects inside the tunnel. For a better analysis of the real conditions, a direct method of measurement must be used where the shock wave and contact surface propagation speed are measured. Minucci (1991) developed a numerical routine to calculate the shock tunnel test conditions; he divided the problem into two parts wherein the phenomena is modeled assuming the gas is in thermodynamic equilibrium. The first part is the shock tube problem which results in the reservoir conditions and test time, and the second is the nozzle flow expansion which gives the test section free stream conditions. A similar code, used in Chapter 5, was developed (Rosa et al., 2009) which also solves the shock tunnel problem assuming chemical and thermodynamic equilibrium. This is performed by the input of the gas constant and

specific heat ratio, the initial driven pressure and temperature, as well as the incident shock wave transit time.

C.3.1 Thermodynamic Equilibrium Shock Tube Problem

The elevated temperature after the incident and reflected shocks means that the perfect gas mathematical assumption is no longer valid. Therefore, real gas effects must be accounted for estimation of the processed gas conditions. At high temperatures, the physical and chemical properties change due to the excitation of molecular vibrational modes, dissociation, and ionization. Also, several new chemical products are formed in high temperatures such as NO, NO⁺, CO, among others.

For this case the conservation equations are used (Figure C.1)

$$\begin{aligned} \rho u_w &= \rho(u_s - u_2) \\ p_1 + \rho_1 u_s^2 &= p_2 + \rho_2 (u_s - u_2)^2 \\ e_1 + \frac{p_1}{\rho_1} + \frac{u_s^2}{2} &= e_2 + \frac{p_2}{\rho_2} + \frac{(u_s - u_2)^2}{2} \end{aligned} \quad (c.5)$$

which are solved by using the equilibrium thermodynamic properties given by the equations of state

$$p_2 = p_2(e_2, \rho_2) \quad (c.6)$$

$$T_2 = T_2(e_2, \rho_2) \quad (c.7)$$

This non-linear system of equations can then be solved numerically by using the solution obtained in the ideal gas case as an initial guess. The values for the equations of state can be found in the work of Srinivasan et al. (1987), where their values were plotted for temperatures up to 25,000 K and densities varying from 10⁻⁷ to 10³ atmospheres.

Once the incident shock wave reflects at the end of the driven section, as in the reflected mode of operation, state 2 is then reprocessed by the reflected shock into state 2', which constitutes the reservoir stagnant condition.

A new set of conservation equations can then be used to calculate state 2'

$$\rho_2(u_2 + u_r) = \rho_2 u_r$$

$$p_2 + \rho_2(u_2 + u_r)^2 = p_{2'} + \rho_{2'} u_r^2 \quad (c.8)$$

$$e_2 + \frac{p_2}{\rho_2} + \frac{(u_2 + u_r)^2}{2} = e_{2'} + \frac{p_{2'}}{\rho_{2'}} + \frac{u_r^2}{2}$$

where u_r is the reflected shock velocity. This non-linear system of equations can be solved in a similar manner as the equations for the incident shock wave assuming perfect gas, by interpolating with the equilibrium state relations (Eqs. c.6 and c.7).

Finally, higher enthalpies and longer test times can be achieved by operating the HST in what is called the Equilibrium Interface condition. In this condition, the reflected shock wave is reflected once again when it encounters the moving contact surface. After a few of these interface reflections between the end wall and the contact surface, only Mach waves are produced with no further changes to the gas properties, establishing a quasi-stationary contact surface before the nozzle entrance. This mode of operation can be achieved given the appropriate conditions of gas composition and temperatures are achieved. A schematic showing the reflected and transmitted shock wave through the contact surface is shown in **Figure C.2**.

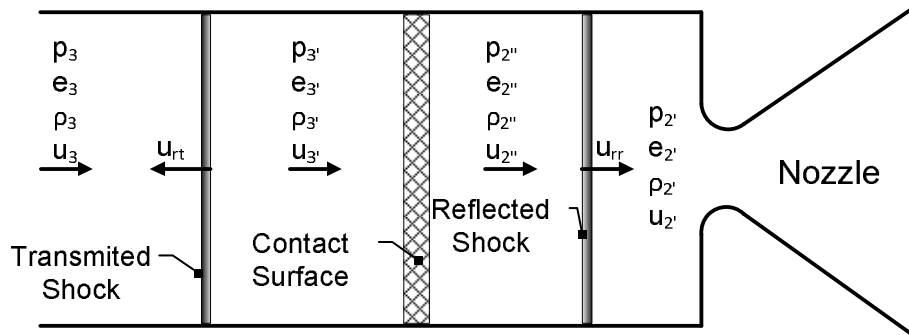


Figure C.2: Reflected and transmitted shock after contact surface interaction, encountered in the reflected mode of operation ($U_2=0$).

The interaction between the reflected shock and the contact surface can create three distinctive situations. The first one is the Equilibrium Interface situation explained above. The other situations are either an expansion wave or a Mach wave being reflected back. If the pressure behind the contact surface immediately after the shock passage is lower than the one existing in front of the contact surface, the expansion wave will be

formed; in the opposite case the a shock wave will be reflected. However, if these pressures are equal, the reflection will be a Mach wave.

We can now write the equations for the flow through the reflected and transmitted shock wave as:

Interface-reflected wave

$$\begin{aligned}\rho_{2'} u_{rr} &= \rho_{2''} (u_{rr} - u_{2''}) \\ p_{2'} + \rho_{2'} u_{rr}^2 &= p_{2''} + \rho_{2''} (u_{rr} - u_{2''})^2 \\ e_{2'} + \frac{p_{2'}}{\rho_{2'}} + \frac{u_r^2}{2} &= e_{2''} + \frac{p_{2''}}{\rho_{2''}} + \frac{(u_{rr} - u_{2''})^2}{2}\end{aligned}\quad (\text{c.9})$$

Interface-transmitted wave

$$\begin{aligned}\rho_3 (u_{rt} + u_3) &= \rho_{3'} (u_{rt} + u_{3'}) \\ p_3 + \rho_3 (u_{rt} + u_3)^2 &= p_{3'} + \rho_{3'} (u_{rt} + u_{3'})^2 \\ e_3 + \frac{p_3}{\rho_3} + \frac{(u_{rt} + u_3)^2}{2} &= e_{3'} + \frac{p_{3'}}{\rho_{3'}} + \frac{(u_{rt} + u_{3'})^2}{2}\end{aligned}\quad (\text{c.10})$$

where u_{rr} is the interface-reflected wave speed and u_{rt} is the interface-transmitted wave speed, as shown in **Figure C.2**.

C.3.2 Nozzle Flow Expansion

The flow in a HST is composed of the *Shock Tube Problem*, stated in the previous section, with the addition of a converging-diverging nozzle at the driven tube's end wall, to generate the required free stream flow conditions by expanding the reservoir gases into the test section. Thus, the reservoir condition comes from the solution of the shock tube problem, which is then used to calculate the expansion through the nozzle and the free stream conditions achieved in the test section.

Due to the reservoir's high temperature conditions, the perfect gas assumption cannot be applied to the flow; characteristics of the flow are dominated by its thermochemical properties. A multitude of chemical reactions dictate the concentration of an equally high quantity of chemical species. If the characteristic time for these

reactions to reach an equilibrium state is on the order of the test time, the phenomenon is considered as non-equilibrium flow. On the other hand, if the characteristic time is much longer than the test time, the flow is considered ‘frozen,’ with the chemical composition of the flow considered unchanged throughout the test.

Ideally, equilibrium flow would be reached in the case of infinite reaction rate constants; however, for hypersonic flow through nozzles, a state of equilibrium can be assumed for reservoir temperatures up to 4500 K and pressures considerably higher than 500 psi, as noted by **Nagamatsu and Sheer (1965)**.

For the calculation of free stream conditions in the test section, the first step is obtaining the sonic conditions at the nozzle throat. This is accomplished by assuming the expansion to be isentropic, one-dimensional, neglecting viscous effects and considering thermodynamic equilibrium throughout the expansion process, despite the high reservoir temperatures achieved. Following these assumptions, the conservation equations can be reduced to

$$e_0 + \frac{p_0}{\rho_0} = e^* + \frac{p^*}{\rho^*} + \frac{u^*^2}{2} \quad (c.11)$$

$$s_0 = s^*$$

Once the conditions at the throat are reached, isentropic flow expansion can be used to calculate the test section conditions from

$$\rho^* u^* A^* = \rho_\infty u_\infty A_\infty$$

$$e^* + \frac{p^*}{\rho^*} + \frac{u^*^2}{2} = e_\infty + \frac{p_\infty}{\rho_\infty} + \frac{u_\infty^2}{2} \quad (c.12)$$

$$s^* = s_\infty$$

These results can then be used, together with the conservation equations, in the calculation of the expected Pitot pressure in the test section. As mentioned before two numerical routines are available for calculation of the free stream conditions from data obtained during the experiments, as further described in Minucci (1991) and Rosa et al. (2009), which assessed the difference in the results from these routines. These results

vary within 2 % of the calculated shock tube reflected (reservoir) pressure, temperature, and density, but up to 5 % for HST test section stagnation conditions (i.e., at higher enthalpies of $T_0 > 2500$ K). The code used for the calculating the test section conditions in the present work was developed by Rosa et al. (2009).

Appendix D – Dedicated Laboratory Setup for CO₂ TEA Laser Propulsion Experiments

In January 2006, Rensselaer Polytechnic Institute was not equipped with any facilities for conducting BEP experiments; only an empty 650 ft² basement laboratory was provided. The experimental equipment and setup necessary for pursuing the research was nonexistent at this moment in time.

Two solutions were envisioned for the successful realization of this BEP research: 1) seek an external partnership/ collaboration with a research institution (academic or industrial) interested in the current research; or, 2) set-up a dedicated BEP laboratory in-house at RPI, capable of fostering all research envisioned for the near future. The later solution was ultimately selected, and pursued. How this laboratory was brought into operational status is thoroughly described below, along with research plans for the future.

D.1 Research Vision and Laboratory Strategy

The research and development of an actual and complete nano/micro-satellite launch system is a multidisciplinary endeavor involving a staggering range of disciplines: e.g., laser power systems architecture, atmospheric beam transmission physics (turbulence, thermal blooming, jitter, and diffraction effects), adaptive optics, pointing and tracking systems, and the like. Furthermore, Lightcraft vehicle R&D must consider the airbreathing/rocket impulse generation processes, propellant handling, flight dynamics, stability & control issues, and trajectory optimization, as well as vehicle size, mass, and inertial properties—to highlight just some of the essential elements. No single academic research facility could tackle all these research requirements simultaneously, nor would one want to. However, the affordable assembly of a small dedicated laboratory, targeting a few critical propulsion research issues, is eminently feasible. Such a lab can make extremely valuable research advances in selected fields.

The facilities described in the following sections were envisioned to tackle the more immediate research issues facing the present Lightcraft engine/vehicle concept, such as impulse generation physics, internal and external aerodynamics, attitude control, propellant delivery, etc. With these objectives in mind, an analysis was performed of the

needed lab equipment, which was then acquired, refurbished, and/or upgraded-- while exploiting (to the extent possible) any miscellaneous equipment already available from the decommissioned Gas Dynamics Laboratory at RPI. Once the “arsenal” of equipment furnishing the Laser Propulsion (LP) laboratory was known, a set of achievable objectives was laid out:

- Explain the Lightcraft engine’s ‘beam-riding’ physics, so that suitable attitude control and guidance systems can be developed in the future;
- Improve the understanding of LP impulse generation physics so that momentum coupling coefficients, specific impulse, and overall efficiencies can be optimized, and the losses that come into play during the impulse generation phenomena can be precisely quantified;
- Confirm the feasibility and operating envelope for completely airbreathing ($I_{sp} = \infty$) Lightcraft propulsion along Earth-to-Orbit boost trajectories;
- Assess the performance of novel LP propellants including both solid ablative and liquids (including feasible injection/atomization methods) being fed to the focus of the Lightcraft’s absorption chamber ;
- Examine surface heat transfer rates inside LP engine absorption chambers, and assess survivability of “hot section” and primary optics materials;
- Study the influence of different laser beam parameters upon the impulse generation process: e.g., pulse shape (achieved by varying laser active media mixture), pulse width, pulse energy, and pulse repetition frequency (PRF). These parameters drive the final selection of an optimum laser system tailored for a given launch application;
- Analyze the influence of Lightcraft engine geometry in generating thrust, by visualizing the expanding blast wave, and measuring the surface pressure distributions and thrust (force), to ascertain the interaction between the engine surfaces and the thrust-generating phenomena;
- Investigate the influence of magnetostatic fields on laser-induced breakdown, propagating LSD waves, and thrust generation processes.

These objectives are being pursued at the RPI Laser Propulsion Laboratory through a well planned set of basic research experiments; additional experiments will pursued in

the near future once the new low-cost flow facilities, presently under construction, come on line.

D.2 Laboratory Equipment and Facilities

The RPI Laser Propulsion Laboratory is equipped with a twin Lumonics K-922M laser system. These lasers, which were completely rebuilt recently at LightMachinery Inc., were originally part of the “Paladin” master oscillator used for induction Linac FEL (Free Electron Laser) experiments at the Lawrence Livermore National Laboratory (LLNL) during the 1980s. Each identical K-922M is composed of two Lumonics K-920 modules upgraded with Marx Bank capacitors (hence, the “M” designation) to supply higher pulse energies, and linked to operate as a single oscillator. An internal view of one of the twin lasers is picture in **Figure D.1**.

These lasers can be sequentially pulsed with any delay interval to simulate any desired PRF; they can also be operated in burst mode (see **Table D.1**). The single pulse energy is measured with a Gentec QE50-LP Pyroelectric calorimeter located after a ZnSe beamsplitter. Burst mode power is measured directly with a Gentec UP60G Thermopile calorimeter which has a max rating of 500 W.

Table D.1: Single K922M laser operating conditions.

<i>Power Supply Load (kV)</i>	<i>Energy/Pulse (J)</i>	<i>Repetition Rate (Hz)</i>	<i>Burst Duration 100 shots (s)</i>
25	10	12	8.3
30	13	10	10
35	16	8	12.5
40	20	6	16.6

The pulse profile for these lasers can be modified with the use of different active media mixtures, with two mixtures selected for the current experiments: 1) a high gain mixture (CO₂-28%, N₂-16%, CO-4%, H₂-0.5%, H_e balance) and the LaserMark V laser mixture (CO₂-8%, N₂-16%, CO-4%, H₂-0.5%, H_e balance). With stable resonator optics installed, the K-922Ms produce a solid rectangular beam in the near-field, as shown in **Figure D.2**. A sample of the beam profiles, operating with the high gain mixture, acquired with a Hamamatsu B749 photon drag and using the two different mixtures is

also shown together with Lightcraft engine illuminated by air breakdown following laser pulse.

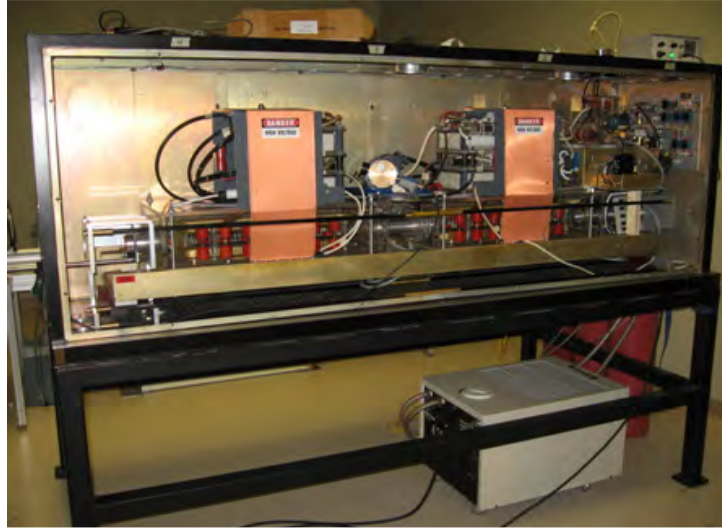


Figure D.1: Interior view of Lumonics K-922M TEA CO2 laser module.

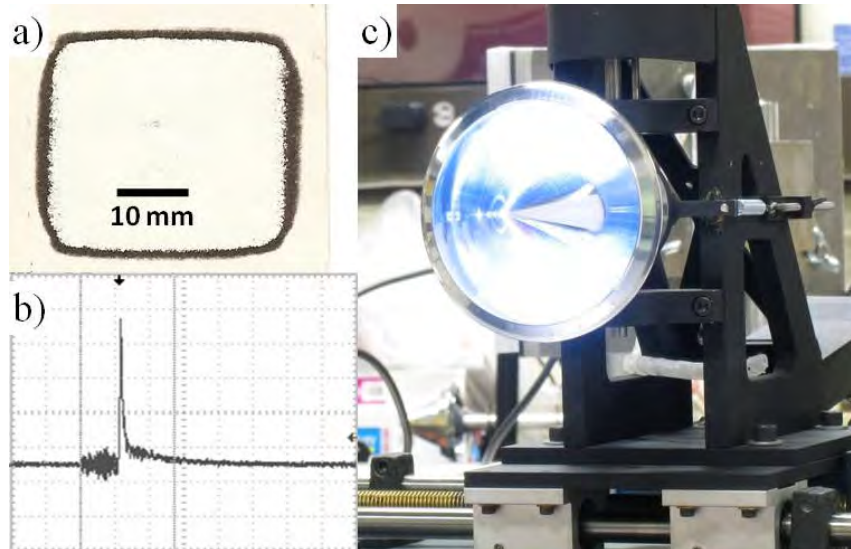


Figure D.2: Lumonics TEA-622M beam characteristics; a) Burn pattern in the near field; b) Beam profile for the High Gain mixture; c) Plasma formation in Lightcraft engine.

Another powerful tool employed in the present research is the Cordin 530 High Speed camera, used for flow visualization, e.g. Schlieren movies of the post laser-induced breakdown structure. This rotating drum CCD camera is can capture a sequence of 16 images at frame rates up to 200,000 frames per second. The Schlieren system mirrors have a total aperture of 200 mm (8 in). Two light sources are available: a flash

unit that is triggered simultaneously with the camera, and a continuous Xenon arc lamp. One of the Schlieren setups used is depicted in **Figure D.3**.

Several different static thrust stands are employed for impulse and attitude measurements in the laboratory. One is the Angular Impulse Measuring Device (AIMD), designed to measure both the lateral (linear) and the pitching (angular) impulse which act upon the Lightcraft's center of gravity, and are induced by the off-set of the laser beam axis from the vehicle longitudinal axis. Two ballistic pendulums are also available at the lab: 1) one heavy unit used in previous experiments with larger Lightcraft models tested with the PLVTS CO₂ laser at WSMR; and 2) a new lightweight pendulum for the RPI small engine experiments. The reduced energy available from the K922M lasers (i.e., relative to the 420 J/pulse of PLVTS) required a lighter pendulum to accurately measure the engine's time-integrated impulse. The angular displacements of the AIMD's rotor and both ballistic pendulums are acquired with a Schavetz Rotary Variable Differential Transformer.

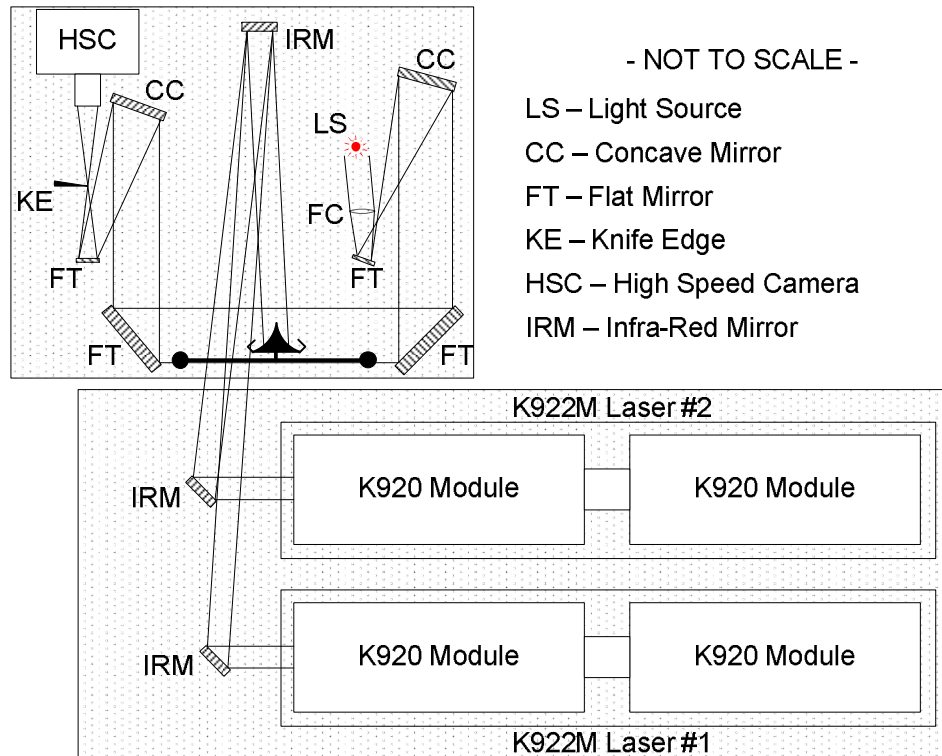


Figure D.1: Twin Lumonics TEA-922Ms and Schlieren setup in the laboratory.

Other essential LP laboratory equipment includes piezoelectric pressure transducers and force sensors, surface junction thermocouples, signal amplification systems,

pulse/delay generators, optical tables, data acquisition, high precision balances, various optics for Schlieren and the K922M IR lasers, environmental control, among others. A panoramic view of the LP laboratory is given in **Figure D.4**.

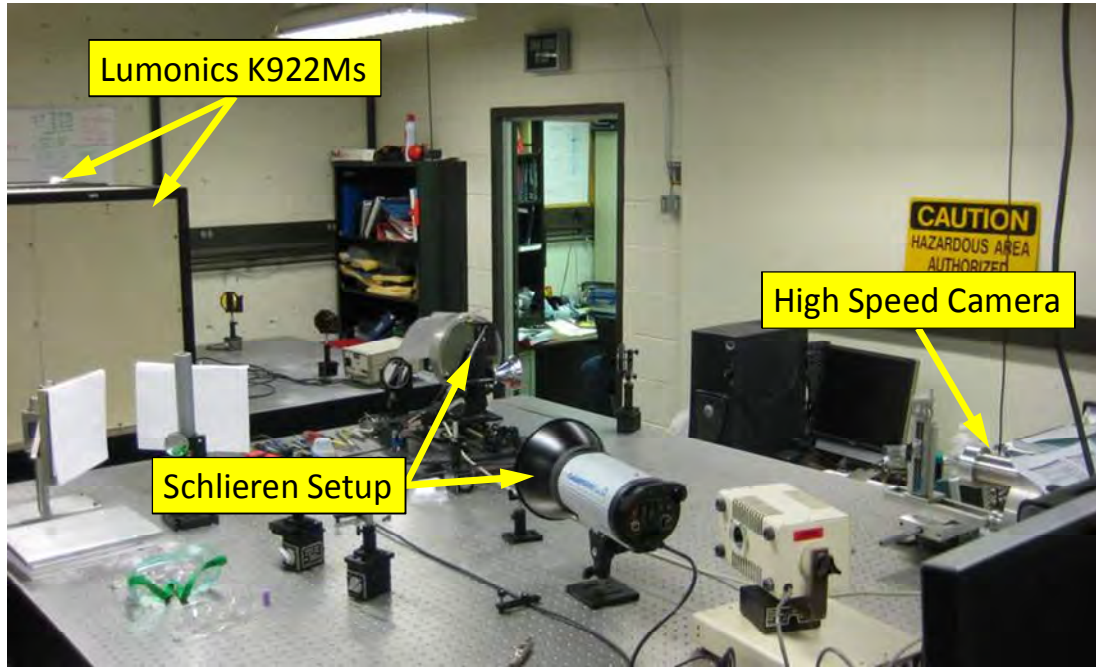


Figure D.2: Panoramic view of the Laser Propulsion Laboratory.

D.3 Basic Research Program

At the present moment, the LP laboratory is supporting basic research into the beam-riding and static thrust performance of new and previously tested Lightcraft engine geometries, using ballistic pendulums and the AIMD apparatus. The post laser-induced breakdown phenomena is being studied with a Schlieren high speed digital visualization system; also, pressure and heat flux measurements are being acquired for different engine geometries, including solid ablative and liquid propellant injection schemes. Upcoming experiments will embrace investigations into the influence of magnetostatic fields upon laser induced breakdown and impulse generation.

In preparation for a future laboratory expansion, two blow-down test facilities have been designed for the LP laboratory; one will be down-selected for manufacture and assembly in the near future, pending fund availability. These blow-down facilities will accommodate a wide variety of two-dimensional Lightcraft engine geometries, and will significantly expand the LP laboratory's ability to investigate airbreathing laser

propulsion physics, from the transonic into the supersonic regime—which is necessary for the study of laser launchers based on combined-cycle LP engines.

D.3.1 Current Research

The current test campaign at Rensselaer Polytechnic Institute includes an in-depth investigation of beam-riding and laser propulsion physics for sub-microsecond laser pulses. These investigations involve the AIMD apparatus (**Libeau et al., 2002; Kenoyer et al., 2010**) and a lightweight ballistic pendulum using the twin Lumonics K922M TEA CO₂ laser system whose output characteristics provide a much improved match with the small Lightcraft engines previously flown at WSMR. Already measured are the axial impulses, side impulses and pitching angular impulses vs. lateral offset generated by three different sizes of #200 Lightcraft engines ranging from 97.7 to 122mm in diameter. The momentum coupling coefficients (C_M) obtained for these models were far superior to the previous performance demonstrated with the “non-ideal” PLVTS laser at WSMR.

Next, the laser ablative rocket mode performance with Teflon and Delrin propellants in 1 atm air, are being examined with the smallest #200-2/3 engine (97.7mm diameter). Subsequently, the beam-riding performance of #150-2/3 and #250-2/3 airbreathing Lightcraft (97.7mm diam.) will be investigated and contrasted with that of a 100mm Bohn bell engine. Once the #150 and #250 beam-riding data is available, these non-ideal Lightcraft geometries can be simulated in the numerical flight dynamics code, to see how well these results compare with actual Lightcraft flight trajectory data. The results of this numerical study can then guide the evolution of optimized Lightcraft engine geometries for maximum performance in the future. Note that the 7-Degree Of Freedom (DOF) flight dynamics code, which has been calibrated against 16 actual trajectories of small scale Lightcraft previously flown at WSMR on the PLVTS laser, is comprised of individual models for aerodynamics, engine, laser beam propagation, variable vehicle inertia, reaction controls system, and dynamics—fully integrated to represent all major phenomena in a single framework.

A Schlieren visualization system is presently being set up and linked to a high speed Cordin digital camera to study the laser induced blast waves ejected from the various models. The flow visualization system reveals blast structure variations with laser beam

offset (i.e., measured relative to the engine longitudinal axis)—thereby giving insight into beam-riding and thrust vectoring phenomena, as shown in **figures 5 and 6**, where the Lightcraft Model #200-2/3 was photographed at 120,000 and 50,000 frames per second, with the beam centered and offset in 20 mm, respectively.

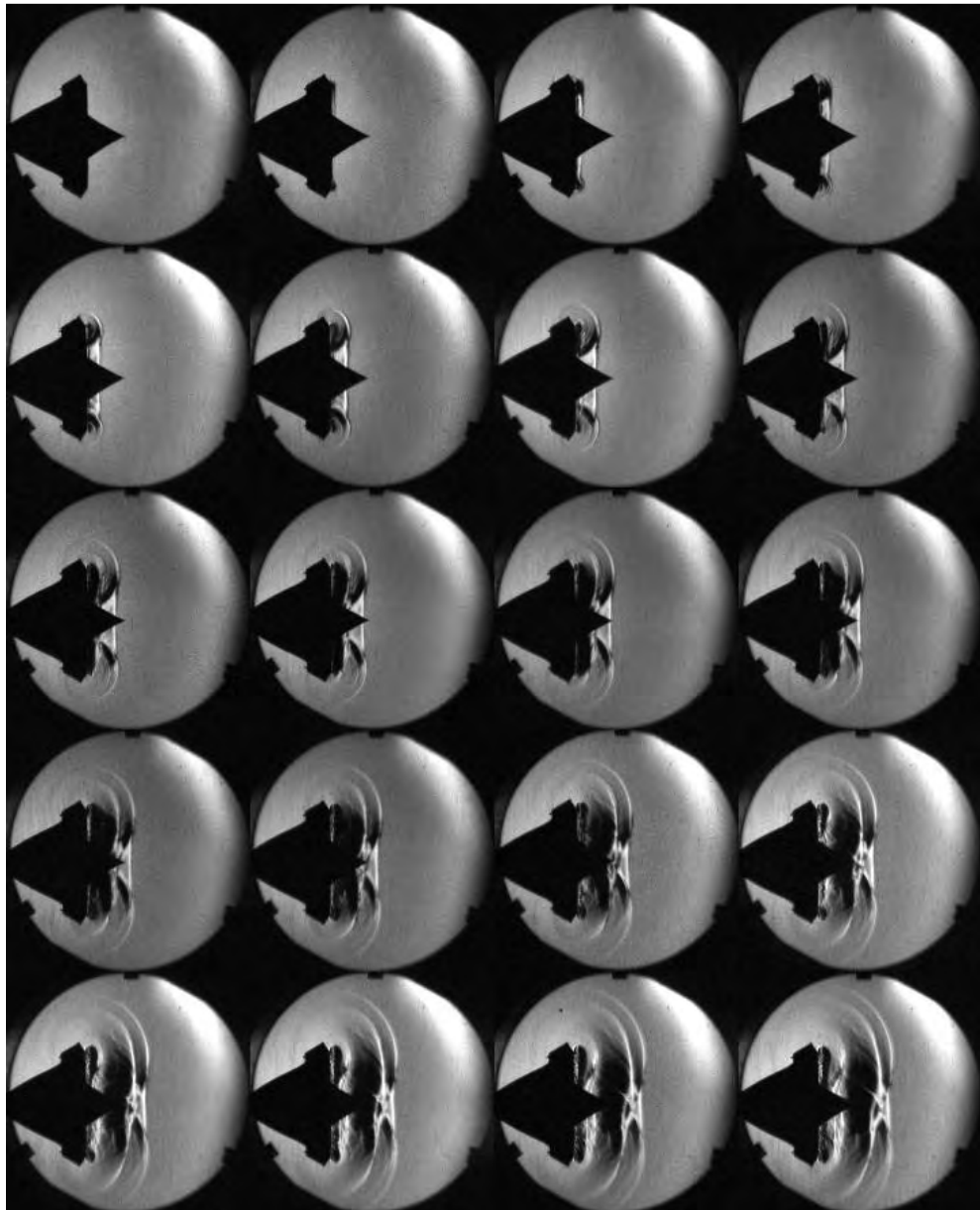


Figure D.3: Schlieren montage of Lightcraft model #200 with beam centered, taken at 120,000 fps.

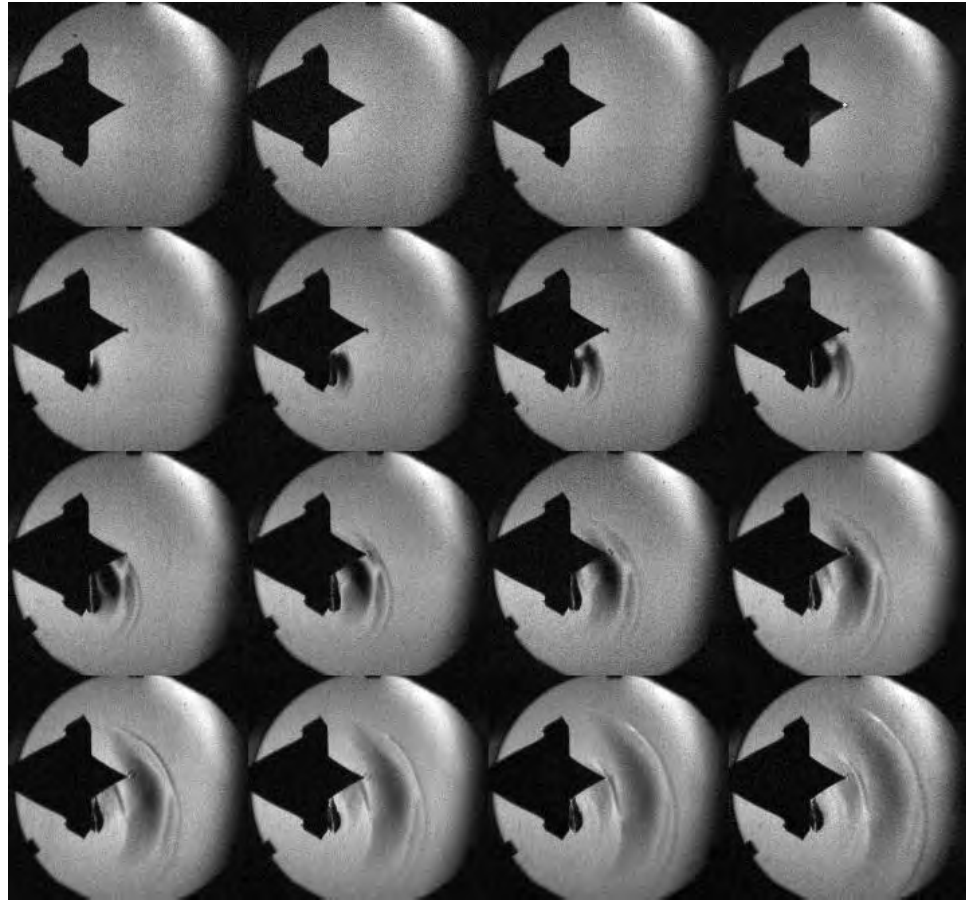


Figure D.4: Schlieren montage of Lightcraft model #200 with beam offset of 20 mm, taken at 50,000 fps.

D.3.2 Future Research

The next step in the ongoing basic research program is the experimental investigation of airbreathing LP engine physics under subsonic, transonic, and low supersonic conditions. The requirement for this facilities expansion comes from the flight regimes anticipated for the vehicle along its boost trajectory into orbit (Frazier, 1987). As a multi-cycle LP engine/vehicle climbs up through the atmosphere, it may transition through as many as five different laser-thermal propulsion modes: e.g., airbreathing Pulsed Detonation Engine (PDE), ramjet, scramjet, ducted rocket, and upon leaving the atmosphere, purely rocket (i.e., onboard propellant only). It is necessary to analyze each propulsion mode separately within its respective optimum flight envelope.

D.3.2.1 Flight Simulation and Flow Facilities

Small-scale supersonic, blow-down type flow facilities (**Pope and Goin, 1965**) can be designed and manufactured at modest cost, and tailored to support a wide variety of LP experiments, thus yielding an excellent cost/return ratio. Two of these facilities have been thoroughly designed, with all the required equipment dimensioned and component suppliers selected. The construction and assembly of the down-selected facility is now dictated largely by manufacturing time and available research funds.

The first of these flow facilities is a supersonic blow down wind tunnel, capable of simulating transonic through Mach 3.0 conditions, expected from launch up to the high altitude flight regime. This tunnel consists of a high pressure, dry air reservoir composed of stacked DOT-E 9421 – 4500 psi storage tanks, fed by a high pressure compressor/dryer (Star Air 6000 compressor unit), followed by a Fisher 1" HPS Body ball-type valve connected to a 4160K 2-Mode electrically actuated pressure controller for the control of the air feed pressure as the reservoir is emptied.

Following the pressure control valve is a settling chamber to guarantee flow uniformity in the test section. Due to the flow facility's modular design concept several different test sections can be inserted, as dictated by the goal of the experimental research: e.g., a “direct-connect” 2D inlet test section modeling any given vehicle geometry; or a “straight through,” constant area test section measuring 50mm×50mm. To simulate the desired flight altitude, the test section exit station is evacuated to a vacuum tank, with its discharge pressure controlled by throttling another fast-action valve that assures the desired static pressure within the test section. The whole system can be easily integrated and run on a LabView equipped computer. A simplified representation of the entire flow and laser system is given in **Figure D.7**, showing the distribution of the main components within the laboratory.

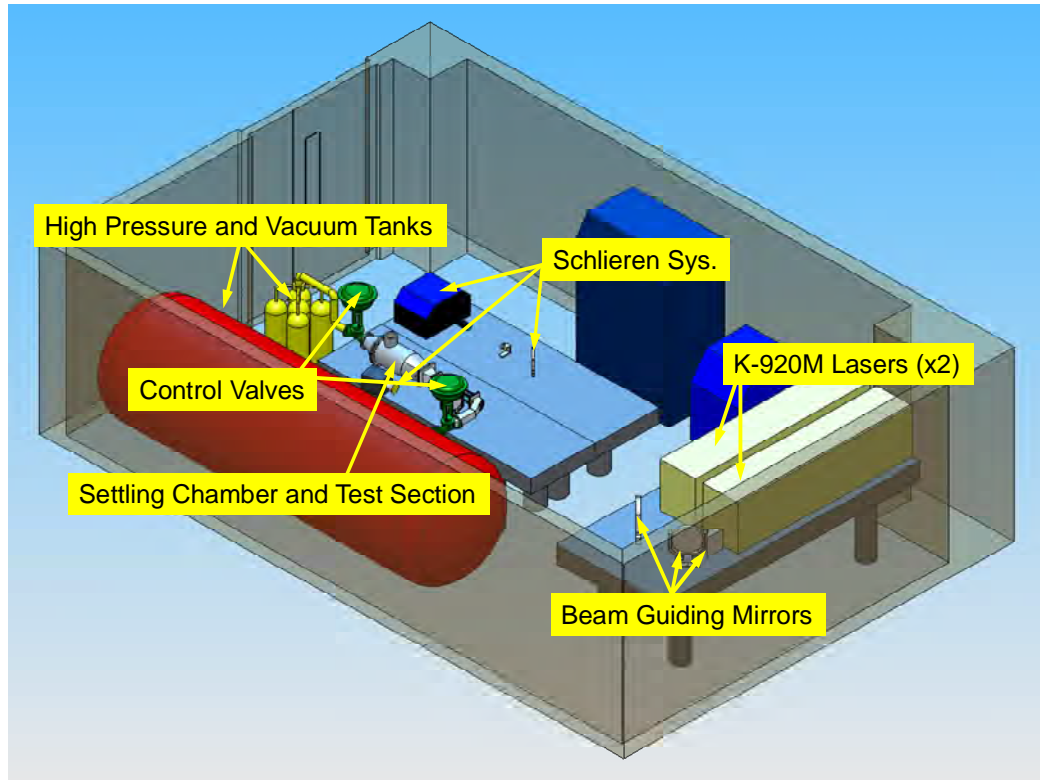


Figure D.5: Integrated setup in the present 7.9 m x 5.2 m available laboratory space with altitude supersonic flow facility.

The second candidate flow facility is a Ludwieg tube-driven system, capable of simulating both transonic and low supersonic flight conditions, depending on the test section and model inserts. This facility has a simpler design and reduced costs (as compared with the previous option), but is not capable of simulating high altitude flight conditions: i.e., the test section always discharges directly into a 1Bar laboratory environment. This facility is basically composed of a high pressure reservoir equipped with a pressure actuated sting for diaphragm rupture, a truncated convergent nozzle, and a modular test section. The test conditions are dictated by the reservoir pressure and the geometry of the model installed inside the test section, which acts to throttles the flow. This facility have reduced precision and increased limitations, but at considerable lower costs and reduced complexity.

The main goal in designing these flow facilities was to create research tools capable of simulating all essential phenomena involved in supersonic airbreathing laser propulsion, from the inlet flow field, to laser energy absorption and impulse generation. The facilities' small size, simple operational procedures, and low acquisition cost present

an optimum match with the available Lumonics K-922M laser system. Several of the research objectives stated previously in this thesis will require such tools. Furthermore, these flow systems are also an important asset to the validation of CFD codes that can rapidly evolve the design of future Lightcraft. Without such experimental data it will be impossible to assess the accuracy of any numerical predictions, nor the validity of their assumptions.

D.3.2.2 Static Experiments

The principal goal is to study the temporal force history delivered by laser-induced blast waves as they expand rapidly over thruster/vehicle surfaces. Direct thrust measurements of this force/time history for several 2-D and 3-D lightcraft engine geometries will be taken with piezoelectric force sensors, using the high speed Schlieren visualization system (with the Cordin digital camera) for insight into the hydrodynamic phenomena. The integrated impulse obtained from force sensors traces will then be compared and contrasted with ballistic pendulum data, using Schlieren movie frames to track expanding shock positions, for validation.

Another test campaign will investigate the physics of liquid propellant injection schemes for pulsed laser rocket propulsion. Essentially, a fine mist or cloud of water vapor (or other liquid propellant of interest) will be injected into the laser focal point of an absorption chamber, to examine the hydrodynamics and efficiency of the laser heating process. A family of parabolic mirrors, sized for the unexpanded K922M laser beam, has already been manufactured, and their injection systems are now being installed. Subsequent static and dynamic LP experiments will involve liquid propellant injection into various 2-D Lightcraft geometries.

Later experiments will investigate influence of intense magnetostatic fields applied to the laser focal heating point, to improve airbreathing and rocket LP engine performance, specifically with regard to: 1) impulse enhancement, 2) magnetic thrust vectoring, 3) magnetic nozzles, and 4) laser-to-impulse conversion efficiency. Note that 0.5 to 1.0 Tesla magnetostatic fields are readily available from existing rare-earth permanent magnets. Although the laser-induced electrical air breakdown and plasma formation processes, which take place on nano-second timescales, can only be captured

by ultra-fast framing cameras, our 200,000 FPS Cordin/ Schlieren visualization system can certainly capture the post-breakdown hydrodynamic phenomena and impulse delivery process—easily tracking the laser-induced blast wave structure.

D.4 Summary

Assembling a laboratory is a difficult, time consuming task which requires careful planning. Even though fundamental and gratifying, it is often a task that researchers naturally try to avoid (or minimize), since most of the splendor of the research itself lies in performing the experiments and publishing the data—i.e., tasks that demand a fraction of the time and work invested in creating the laboratory in the first place. Take for example, the time spent on obtaining the funds, searching for suitable equipment while trading-off between price restrictions and technical specifications, gathering competitive price quotes from several different OEM sources, persuading management of essential equipment needs, negotiating subcontracts with suppliers, issuing purchase orders, hiring and training a dedicated workforce (i.e., students in this case), delays in equipment delivery, etc. These issues, among countless others, can turn the task of paving the way to innovative research into a long and arduous work.

That was the road traveled for the past few years by the Laser Propulsion Laboratory team at RPI. Finally the experiments can now be set up and performed using the available facilities using the strategy laid out previously. Several fundamental and basic experiments are underway and many more are being set up, with the laboratory's continuity and future success dependent upon funding and institutional interests.

– FINAL REPORT –
– PART 3 –

Volume 2: *Combined Experimental and Numerical Investigations into Laser Propulsion Engineering Physics*

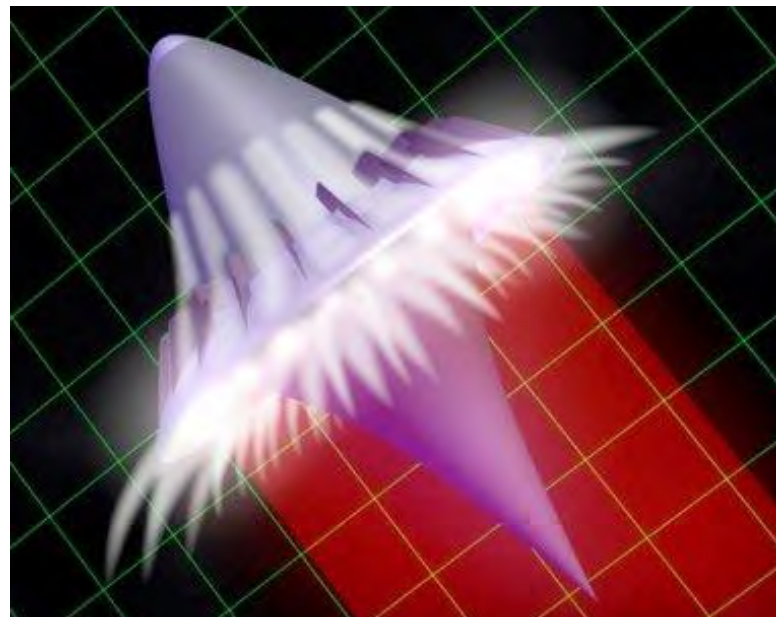
MURI 05 Grant Title: “Basic Research Investigations into Multimode Laser and EM Launchers for Affordable, Rapid Access to Space”

Principal Investigator: Professor Leik N. Myrabo
Rensselaer Polytechnic Institute,
110 8th Street, Troy, NY 12180-3590

Major Contributors: Drs. David A. Kenoyer and Israel I. Salvador

AFOSR Award: FA9550-05-1-0392

Research Period: June 1, 2005 through August 31, 2010 (5 year grant)



Prepared for
Dr. Mitat Birkan
Air Force Office of Scientific Research (AFOSR)
Arlington, VA 22203

31 August 2010

CONTENTS

CONTENTS.....	i
LIST OF TABLES	iv
LIST OF FIGURES.....	v
ABSTRACT.....	ix
NOMENCLATURE.....	x
1. INTRODUCTION AND HISTORICAL REVIEW.....	1
1.1 Background.....	2
1.1.1 Off-axis Parabola Lightcraft.....	3
1.1.2 Bell Lightcraft	6
1.2 Type #200 Aerodynamics	7
1.3 7-DOF Code Development	10
1.4 Objectives and Impact	11
2. EXPERIMENTAL APPARATUS AND LABORATORY SETUP.....	13
2.1 K-922M Laser System.....	13
2.2 Lightcraft Geometries.....	16
2.3 Angular Impulse Measuring Device.....	18
2.4 Lightweight Ballistic Pendulum.....	23
2.5 Experimental Setup	25
2.6 Experimental Error Analysis.....	27
2.7 Schlieren Photography.....	27
3. NUMERICAL FLIGHT DYNAMICS SIMULATION DEVELOPMENT.....	29
4. RESULTS	38
4.1 Airbreathing Propulsion Experiments	38
4.1.1 Axial Impulse Investigation	39
4.1.2 Lateral and Angular Impulse Investigation.....	44
4.1.3 Engine Refresh Investigation	56

4.2	Ablative Propellant (Rocket Mode) Experiments	57
4.3	Numerical Investigation: 7-DOF Code	62
4.3.1	Code Calibration on 16 WSMR Flights	62
4.3.2	Code Calibration Results	64
4.3.3	Simulations of 240cm Lightcraft Flights	69
4.3.4	Simulations Using Experimental Results	83
5.	DISCUSSION AND CONCLUSIONS	85
5.1	AIMD and LWBP Experimental Results	85
5.2	7-DOF Flight Dynamics Code Results	87
6.	FUTUTRE WORK	89
6.1.1	Flight Simulation and Flow Facilities	89
6.1.2	Static Experiments	91
6.1.3	Vacuum Chamber Experiments	92
6.1.4	Engine Geometry Optimization Studies	92
6.1.5	Windtunnel Experiments	93
7.	REFERENCES	89
8.	APPENDICES	98
8.1	Appendix A: AIMD Spring Calibration	98
8.2	Appendix B: Sample RVDT Outputs	99
8.3	Appendix C: Simulations	101
8.3.1	Flight 1	103
8.3.2	Flight 3	104
8.3.3	Flight 4	106
8.3.4	Flight 6	108
8.3.5	Flight 7	109
8.3.6	Flight 8	111
8.3.7	Flights 10 and 11	113

8.3.8 Flight 12	113
8.3.9 Flight 13	114
8.3.10 Flight 14	114
8.3.11 Flight 15	115
8.3.12 Flight 16	115
8.4 Appendix D: Impact Hammer Calibrations	116
8.5 Appendix E: Sanded vs. Unsanded Optics	118
9. Acronyms	119

LIST OF TABLES

Table 1.1. PTFE/AP mixture compositions [11].....	5
Table 2.1. Reconfigurable, four-module K-920M laser system.	13
Table 2.2. Laser gas compositions for K-922M laser system.....	16
Table 2.3. Lightcraft properties.....	17
Table 2.4. Experimental error associated with experimental data acquisition devices.	27
Table 4.1. K-922M Laser gas mixture compositions.	40
Table 4.2. WSMR Lightcraft flight trajectory database [12].....	64
Table 4.3. Initial launch conditions for airbreathing lightcraft flights.	65
Table 4.4. Assumed propellant characteristics for 7-DOF simulations.....	70
Table 4.5. MOI and mass of lightcraft components modeled in 7-DOF code.....	73
Table 4.6. Initial launch conditions and results for suborbital flights	81
Table 8.1. AIMD Spring Calibration.....	98
Table 8.2. Calibration data for models on LWBP.....	117

LIST OF FIGURES

Figure 1.1. Inverse parabolic laser lightcraft, Type #200.....	2
Figure 1.2. Original Type 100 lightcraft with laser induced air plasma.....	3
Figure 1.3. Specific impulse and C_M data for various PTFE/AP mixtures [11].	5
Figure 1.4. German 10 cm bell-type lightcraft in DLR ballistic pendulum[6].	6
Figure 1.5. Momentum coupling coefficients for the #200 SAR and German bell	7
Figure 1.6. Lightcraft model 200-5/6 for 2'x2' subsonic wind tunnel experiments.	8
Figure 1.7. Lightcraft sting mount and force diagrams.	9
Figure 1.8. Flow visualization using helium filled bubbles.....	10
Figure 1.9. Research objectives tree.....	12
Figure 2.1. Interior view of Lumonics K-922M TEA CO ₂ laser module.	14
Figure 2.2. Reconfigurable laser system setup for LP laboratory use.	14
Figure 2.3. Laser beam burn patterns of a) Laser 1, and b) Laser 2.....	15
Figure 2.4. Laser pulse traces from LaserMark V mix and High Gain mix.	15
Figure 2.5. Lightcraft engine family cross-sections.	16
Figure 2.6. Lightcraft engine family	17
Figure 2.7. 97.73 mm teacup mount and family of engine geometries	17
Figure 2.8. German “Bohn” bell 10 cm diameter engine with teacup mount.....	18
Figure 2.9. AIMD apparatus with lightcraft engine, teacup mount, and spacers.....	19
Figure 2.10. AIMD rotor geometry	19
Figure 2.11. AIMD rotor diagram.	22
Figure 2.12. Calibration setup used in WSMR lab experiments with PLVTS.	24
Figure 2.13. Lightweight ballistic pendulum (LWBP).....	24
Figure 2.14. Optical setup for ballistic pendulum with calibrated beam-splitter.....	25
Figure 2.15. Optical setup for AIMD test stand with calibrated beam-splitter.....	26
Figure 2.16. Schlieren setup in RPI Laser Propulsion Laboratory.	28
Figure 3.1. Lightcraft model 200-5/6 spin deceleration exponential decay function.	33
Figure 3.2. Lightcraft Aerodynamic Force Diagram.	34
Figure 3.3. Cutaway of 2.4m #200 lightcraft.....	35
Figure 3.4. Laser beam orientation with respect to launch pad and lightcraft.	35
Figure 3.5. Laser launch scheme	36

Figure 3.6. Critical BEP engine beam-riding and performance criteria	37
Figure 4.1. Axial C_M vs. E_p for #200-11/10 engine	39
Figure 4.2. Axial C_M vs. E_p for two different laser gas mixes (#200-2/3).....	40
Figure 4.3. Induced focus angle, α , for #200-2/3, #200-3/4, and #200-5/6 engines.	41
Figure 4.4. Axial C_M vs. E_p for High Gain laser mix (#200 family).....	42
Figure 4.5. Axial C_M vs linear energy density for #200 sizes and HG mix.....	42
Figure 4.6. Axial C_M vs. E_p for the family of lightcraft geometries.....	43
Figure 4.7. Axial C_M vs. E_p comparing the bell and #200 geometries	44
Figure 4.8. Rear view of #200-3/4 engine and circular laser beam	44
Figure 4.9. Lateral C_M vs. offset; $E_p = 20$ J (#200-3/4).....	45
Figure 4.10. Lateral C_M vs. offset; $E_p = 20$ J (#200 lightcraft family).	46
Figure 4.11. Lateral C_M vs. lateral offset for various AB lightcraft geometries.	48
Figure 4.12. Lateral C_M vs. lateral offset for the 10 cm German bell geometry.....	49
Figure 4.13. Pitching angular impulse vs. lateral beam offset (#200 engine family).	50
Figure 4.14. Pitching angular impulse vs. lateral offset	51
Figure 4.15. Schlieren photography of #150-2/3 with laser offset	52
Figure 4.16. Schlieren photography of #200-2/3 with laser offset	53
Figure 4.17. Schlieren photography of #250-2/3 with laser offset	54
Figure 4.18. Schlieren photography of German bell with laser offset	55
Figure 4.19. Average axial C_M vs. repetition pulse interval	56
Figure 4.20. Axial C_M vs. pulse energy for airbreathing and “rocket mode”	58
Figure 4.21. Lateral C_M vs. offset for #200-2/3 airbreathing and “rocket mode”.....	59
Figure 4.22. Angular pitching moments vs. lateral offset for AB and RM	60
Figure 4.23. Specific impulse vs. pulse energy for axial impulse experiments.	61
Figure 4.24. Ablative laser propulsion efficiency vs. pulse energy	61
Figure 4.25: Methodology for validation and calibration of upgraded 6-DOF Code.	62
Figure 4.26. Flight simulation vs. climb trajectory data for Flight #2.	65
Figure 4.27. Flight simulation vs. trajectory data in the Y-Z plane for Flight #2.....	66
Figure 4.28. Flight simulation vs. climb trajectory data for Flight #5	67
Figure 4.29. Flight simulation vs. trajectory data for Flight #5	67
Figure 4.30. Flight simulation vs. climb trajectory data for Flight #9	68

Figure 4.31. Flight simulation vs. trajectory data Y-Z comparison for Flight #9	68
Figure 4.32. Cutaway of 2.4m #200 lightcraft.....	69
Figure 4.33. Altitude vs. time trajectories for Teflon® and Delrin®.	71
Figure 4.34. Mach number vs. time trajectories for Teflon® and Delrin® trajectories ...	71
Figure 4.35. Propellant remaining vs. time trajectories for Teflon® and Delrin®.	71
Figure 4.36. Propellant mass consumption vs. time for vertical ascent	72
Figure 4.37. Crosswind tolerance of #200-2.4m craft in vertical flight.....	74
Figure 4.38. Beam riding behavior of #200-2.4m craft in vertical flight.....	74
Figure 4.39. a) RCS and main PTFE propellant usage for a vertical flight.....	75
Figure 4.40. Altitude vs. range for selected constant zenith boost angles.....	76
Figure 4.41. Velocity vs. time for selected constant zenith boost angles.....	76
Figure 4.42. Laser beam boost reference angle schedules with respect to launch pad. ...	77
Figure 4.43. Mach number vs. altitude for pop-up to 12 km.....	78
Figure 4.44. a) Velocity vs. time, b) Altitude vs. time for several pop-up schedules.....	79
Figure 4.45. PTFE propellant mass vs. time for several Mach 0.6 pop-up schedules	79
Figure 4.46.RCS propellant mass vs. time for several Mach 0.6 pop-up schedules	80
Figure 4.47. Flight 5 altitude and range vs time	81
Figure 4.48. Flight 5 absolute and azimuthal velocity vs. time	81
Figure 4.49. Launch vehicle velocity and altitude vs. time	82
Figure 4.50. Laser thruster and RCS propellant usage vs. time.....	83
Figure 4.51. Visualization of launch trajectory to scale over Earth.....	83
Figure 4.52. . WSMR Flights 10 and 11 vs. updated model simulations	84
Figure 6.1: Integrated setup in the laboratory with altitude supersonic flow facility.	90
Figure 6.2: Proposed vacuum chamber for LP experiments.....	92
Figure 6.3: Lightcraft model with AXi brushless outrunner motor	93
Figure 8.1. Sample output from AIMD	99
Figure 8.2. Sample output from AIMD	99
Figure 8.3. Sample output from LWBP (#250-2/3, ~39 J pulse, HG Mix).	100
Figure 8.4. Sample LWBP output	100
Figure 8.5. WSMR Flights 10 and 11 vs. updated model simulations	101
Figure 8.6. Simulation vs. climb trajectory data for Flight #2.....	102

Figure 8.7. Simulation vs. trajectory data in the Y-Z plane for Flight #2	102
Figure 8.8. Simulation vs. trajectory data of Flight #1.....	103
Figure 8.9. Simulation vs. trajectory data in the Y-Z plane for Flight 1.....	103
Figure 8.10. 3-D Simulation vs. trajectory for Flight 1.....	104
Figure 8.11. Simulation vs. trajectory data of Flight #3.....	104
Figure 8.12. Simulation vs. trajectory data in the Y-Z plane for Flight #3	105
Figure 8.13. 3-D Simulation vs. trajectory for Flight 3.....	105
Figure 8.14. Simulation vs. trajectory data of Flight #4.....	106
Figure 8.15. Simulation vs. trajectory data in the Y-Z plane for Flight #4	107
Figure 8.16. 3-D Simulation vs. trajectory for Flight 4.....	107
Figure 8.17. Simulation vs. trajectory data of Flight #6.....	108
Figure 8.18. Simulation vs. trajectory data in the Y-Z plane for Flight #6	108
Figure 8.19. 3-D Simulation vs. trajectory for Flight 6.....	109
Figure 8.20. Simulation vs. trajectory data of Flight #7.....	109
Figure 8.21. Simulation vs. trajectory data in the Y-Z plane of Flight #7	110
Figure 8.22. 3-D Simulation vs. trajectory data of Flight #7	110
Figure 8.23. Simulation vs. trajectory data of Flight #8.....	111
Figure 8.24. Simulation vs. trajectory data for the Y-Z plane of Flight #8	112
Figure 8.25. 3-D Simulation vs. trajectory for Flight 8.....	112
Figure 8.26. Simulation vs. trajectory data of Flights #10 and #11	113
Figure 8.27. Simulation of Flight #12 vs. trajectory data.....	113
Figure 8.28. Simulation of Flight #13 vs. trajectory data.....	114
Figure 8.29. Simulation of Flight #14 vs. trajectory data.....	114
Figure 8.30. Simulation of Flight #15 vs. trajectory data.....	115
Figure 8.31. Simulation of Flight #16 vs. trajectory data.....	115
Figure 8.32. LWBP Impulse vs. initial angular velocity calibration for #200-2/3	116
Figure 8.33. LWBP Impulse vs. initial angular velocity calibration for #150-2/3.	116
Figure 8.34. LWBP Impulse vs. initial angular velocity calibration for #250-2/3.	117
Figure 8.35. LWBP Impulse vs. initial angular velocity calibration for German Bell. .	117
Figure 8.36. Axial C_M for sanded vs. non-sanded foci of #200-2/3.....	118

ABSTRACT

The RPI pulsed Laser Propulsion (LP) research effort focuses on the future application of launching nano- and micro-satellites (1-10 kg payloads) into Low Earth Orbit (LEO), using a remote Ground Based Laser (GBL) power station to supply the required energy for flight. This research program includes both experimental and numerical studies investigating the propulsive performance of several engine geometries (constituting a lightcraft family). Using the Lumonics twin K-922m TEA pulsed laser system, axial and lateral thrust, C_m , I_{sp} , and η measurements were made for these engine geometries, examining the effects of several critical factors including: engine orientation (e.g. lateral and angular offset), laser pulse energy, pulse repetition frequency, pulse duration, propellant type, and engine size-scaling effects. Investigation into the origins of lateral “beam riding” forces was of particular interest. Lateral impulse measurements and high speed Schlieren photography were utilized to provide an understanding of laser beam-riding/propulsive physics.

The acquired lightcraft database was used to further develop an existing 7-Degree Of Freedom (DOF) flight dynamics model extensively calibrated against 16 actual trajectories of small scale model lightcraft flown at White Sands Missile Range, NM on a 10 kW pulsed CO₂ laser called PLVTS. The full system 7-DOF model is comprised of updated individual aerodynamics, engine, laser beam propagation, variable vehicle inertia, reaction controls system, and dynamics models, integrated to represent all major phenomena in a consistent framework. This flight dynamics model and associated 7-DOF code provide a physics-based predictive tool for basic research investigations into laser launched lightcraft for suborbital and orbital missions. Simulations were performed to demonstrate the flight capabilities of each engine geometry using the updated lightcraft propulsion database, the results of which further demonstrate that autonomous beam riding capability is an essential component for a stable launch to orbit and the future of LP.

NOMENCLATURE

\vec{a}	Acceleration of the lightcraft centre of mass with respect to the inertial reference frame
	Dextral basis vectors fixed in reference frame (body) B
C_L	Coefficient of aerodynamic lift
C_D	Coefficient of aerodynamic drag
C_M	Aerodynamic moment coefficient
C_M	Momentum coupling coefficient
E_p	Pulse energy
	Sum of all applied non-impulsive forces acting on the lightcraft
g	Gravitational acceleration constant
I_{xx}	Moment of inertia about the x-axis
I_{yy}	Moment of inertia about the y-axis
I_{zz}	Moment of inertia about the z-axis
I_{sp}	Specific impulse
I_R	Moment of inertia of the rotor at position R
	ij element of the central inertial matrix of despun platform/carrier B
	Rotor central moment of inertia about the spin axis
F_S	Side force
F_T	Time-variant thrust
	Impulse imparted to the lightcraft by the laser
k	Spring constant
m_a	Mass ablated
	component of the moment exerted on the rotor R by the carrier B
M^B	Sum of all external moments applied to the carrier B from outside the system
M_{TOT}	Total moment
M_P	Time-variant pitching moment
M_c	Time-variant torque
$1, 2, 3$	Basis vectors, standard de-spun Earth reference frame

r_T	Time-variant thrust moment arm
r_C	AIMD moment arm
T	Period
V_e	Exhaust velocity
α	Included focus angle
η_{ALP}	Ablative Laser Propulsion Efficiency
δ	Dirac delta function
τ	Reference time
	Rotor rotation rate relative to B
θ	Angular position
	Angular velocity
	Angular acceleration
	Initial angular velocity of the rotor with respect to the Newtonian (inertial) reference frame
	System angular acceleration

1. INTRODUCTION AND HISTORICAL REVIEW

The long term goal of this LP research is to lead to: 1) affordable, rapid access to space for time-critical commercial and military payloads of 1-100 kg; 2) reduced operation costs for launching nano- and micro-satellites in the near term (e.g., 5-10 years); 3) increased simplicity and safety since a remote ground-based laser power station beams all the energy consumed by the propulsion system; and 4) greatly reduced on-board propellant mass penalties relative to conventional chemical rockets – since beamed energy propulsion (BEP) specific impulses are far higher (e.g., 2x to 4x).

This effort involved an extensive series of experiments, including various laser characteristics (e.g., pulse duration, energy, and repetition rate) and engine-related geometrical features (e.g. focal point of receptive optics) and their influence upon the internal flowfield structure, as well as the resultant impulse (i.e. both lateral and axial), momentum coupling coefficient (C_m), specific impulse (I_{sp}), and ablative laser propulsion efficiency (η_{ALP}). Wind tunnel data was taken to validate the current computational fluid dynamic (CFD) analysis of lightcraft aerodynamic coefficients (e.g., lift, drag, and pitching moment), and preparations have been made for future experiments to investigate the aerodynamics of a spinning body during flight (e.g., investigate Magnus force coefficients) and to complete the previously unfinished lightcraft aerodynamic database. Additionally, for the rocket propulsion mode, the use of a solid ablative propellant to increase engine impulse was investigated.

The data acquired from these experiments has been modeled in a 7-DOF flight dynamics simulator [1], developed to improve the understanding of lightcraft engine/vehicle capabilities and enable prediction of future flight performance to orbit. This code has been validated using a 16 flight experimental database obtained at the White Sands Missile Range (WSMR) [2] and extended to simulate suborbital boost trajectories for several launch scenarios, incrementally working up to a final, circularized low Earth orbit (LEO) trajectories.

Both the experimental and numerical phases of this effort had overlapping objectives and features. The numerical phase results identified optimum flight conditions (i.e., speed, “pop-up” altitude, aim point offset, airbreathing/rocket transition velocity, etc.) for the trajectory to LEO and geostationary Earth orbit (GEO) as well as confirming the capabilities of the engine geometries investigated in the present experiments. The LP experimental effort identified the optimum beam-riding engine geometry, and clarified what causes the stable beam riding phenomenon that is essential to the future of laser launch systems. The behavior of stable beam-riding lightcraft in flight is analogous to a stable aircraft, or missile, for example.

1.1 Background

Since Kantrowitz [3] first proposed the concept of laser propulsion in 1972, there have been many efforts world-wide to turn this idea into reality. Currently there is great international interest in Beamed Energy Propulsion (BEP), not only with lasers, but mm-wave sources as well. The vehicles investigated in the present effort are two pre-existing variations of laser lightcraft; i.e., ultra-lightweight vehicles that employ BEP engines linked to ground-based laser power stations. The first lightcraft variation utilizes an off-axis parabolic optic, pictured in Fig. 1.1, which evolved directly from an RPI study [4] for the now defunct Strategic Defense Initiatives Office (SDIO). The second design is an on-axis parabolic “bell” engine, experimentally investigated extensively in the USA[5], Russia, China, and Germany [6]. While there have been many other BEP vehicle designs proposed, these have exhibited the most promising experimental performance to date.



Figure 1.1. Inverse parabolic laser lightcraft, Type #200.

1.1.1 Off-axis Parabola Lightcraft

The off-axis parabola lightcraft is assembled from three parts: nose, annular shroud, and rear optic. The rear optic, which also serves as a plug nozzle, is an off-axis parabolic reflector that concentrates incident pulsed laser energy into an annular ring focus just inside the shroud. Here, air or on-board solid ablative propellant is explosively heated, and impulsive thrust is generated as the high temperature, high pressure exhaust gases expand out the plug nozzle (Fig. 1.2). This Pulsed Detonation Engine (PDE) cycle has been extensively demonstrated in laboratory and outdoor flight experiments at WSMR in New Mexico [2]. One lightcraft model in particular, the Type 200, has exhibited an unusual ability to “ride” the laser beam, consistently re-centering itself after being perturbed. Because of these characteristics, the #200-5/6 model lightcraft holds the current world altitude record of 71 meters set on October 2, 2000.



Figure 1.2. Original Type 100 lightcraft with laser induced air plasma.

In an attempt to improve the understanding of WSMR flight data, thrust performance, and beam-riding characteristics of the Type 200 lightcraft, several computer-based flight dynamics models have been developed that included accurate dynamics, aerodynamics, engine, and laser beam models. The first attempt at modeling the flight dynamics with a 6-DOF code was performed by Libeau [7]; this was followed by Ballard et. al [8], and

several subsequent iterations [1,9] before arriving at the most current model [10]. The ultimate goal is a research tool that can facilitate invention of new lightcraft engine/vehicle geometries, assist creation of active flight control systems, and enhance understanding of experimental flight trajectories.

To date, all off-axis parabola lightcraft flown at WSMR and investigated in the RPI Laser Propulsion Laboratory have been constructed from 6061-T6-511 aluminum as thin-shell (e.g., 0.245 mm wall thickness) bodies of revolution, completely symmetric about the vertically-oriented spin axis. In the outdoor demonstration flights, the vehicle was boosted by a 10 kW CO₂ electric discharge laser known as the Pulsed Laser Vulnerability Test System (PLVTS), located on the High Energy Laser System Test Facility (HELSTF) at WSMR. The laser produces a 10 x 10 cm hollow square beam profile whose dimensions can be varied with telescope-like optics to match the size of the lightcraft shroud.

The propulsive reaction received by the lightcraft system from repetitive laser-induced detonations embodies three linear impulses and three angular impulses. However, of these, only the thrust impulse, side (restoring) impulse, and pitching moment impulse dominate the craft's flight behavior. The thrust impulse propels the vehicle skyward, whereas the side impulse attempts to re-center the lightcraft in the laser beam; the pitching impulse, which results from a lateral offset, tends to tip the vehicle. To minimize effects from this pitching impulse, and to prevent tumbling, the lightcraft is spun to approximately 10,000 RPM prior to launch.

To improve engine thrust beyond that attainable with the airbreathing mode, a solid ablative propellant ring of Delrin® is inserted into the annular shroud at the focus of the primary optic. Not only does this propellant increase engine thrust by a factor of 2.5, but the ablating Delrin® helps to cool the shroud. Without such cooling, the aluminum shroud predictably fails at the 100th laser pulse—e.g., after 4 seconds of PLVTS operation at 25 Hz with 420 Joule pulses. Hence, all altitudes beyond 30 m have used Delrin® (AP). Other investigations into solid ablative propellants [11] have since found

PTFE (commonly called Teflon®) to be a superior laser ablative rocket propellant, with a specific impulse (I_{sp}) of ~ 800 seconds and an ablative laser propulsion efficiency of 60% (compared to ~ 200 seconds and 50%, respectively, for Delrin®). The C_M and I_{sp} performances of various mixtures of these two propellants, the components of which are provided in Table 1.1, can be seen in Fig. 1.3. The intention of this study was to capitalize upon the desirable C_M of 100% AP for liftoff and the high I_{sp} of 100% PTFE propellant by transitioning throughout a flight. The Type 200 lightcraft currently under development serves as a research craft for evolving future laser-propelled launch vehicles with superior performance.

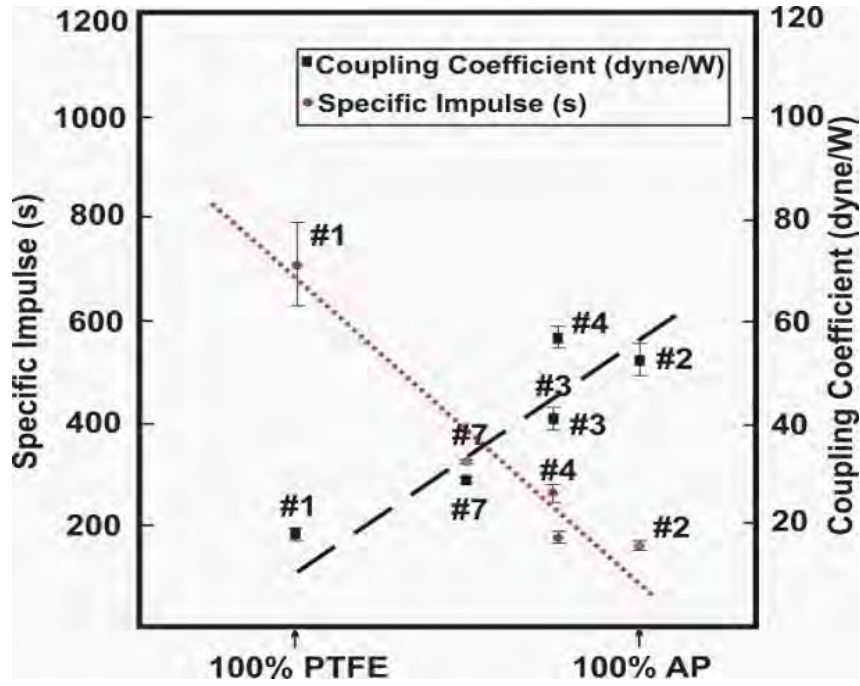


Figure 1.3. Specific impulse and C_M data for various PTFE/AP mixtures [11].

Table 1.1. PTFE/AP mixture compositions [11].

Propellant #	1	2	3	4	5	6	7
% PTFE	100	0	18	19	0	15	49
%AP	0	100	80	80	0	80	49
% Other	0	0	2	1	100	5	2

1.1.2 Bell Lightcraft

The on-axis parabolic “bell” engine variant of lightcraft is typically one solid piece, as seen in Fig. 1.4 [6]. The interior surface is polished and serves to focus the incident laser beam onto a central focus at some distance from the apex of the paraboloid. A central metal pin is often used, which extends along the axis of symmetry to the focal point and beyond, with the purpose of ensuring reliable breakdown even at low laser pulse energies. This pulsed detonation engine generates thrust in the same manner as the off-axis parabolic lightcraft engine, as high temperature, high pressure exhaust gases expand out the nozzle. A 10 cm German bell engine has been extensively demonstrated in laboratory experiments using a pulsed, electron beam sustained, CO₂ electric discharge laser capable of up to 450 J at 100 Hz (average power of 45 kW), at the DLR-Institute of Technical Physics in Stuttgart, Germany [6,12]. Prior German investigations into the beam-riding capabilities of this bell engine have used free-flight video analysis to find local lateral CM values, but leaving much of the “flight envelope” unexplored [12] Bohn’s experiments measuring the axial performance of the German bell and type #200 lightcraft indicate that the #200 provides superior C_M values with Delrin® propellant in a vacuum and at lower pressures, but inferior performance at ambient pressures of 0.4 atm and above, as seen in Fig. 1.5.

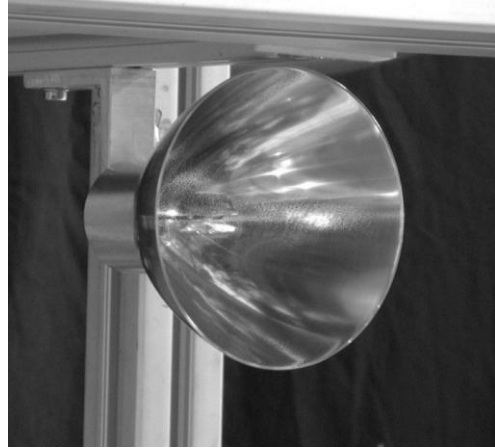


Figure 1.4. German 10 cm bell-type lightcraft in DLR ballistic pendulum[6].

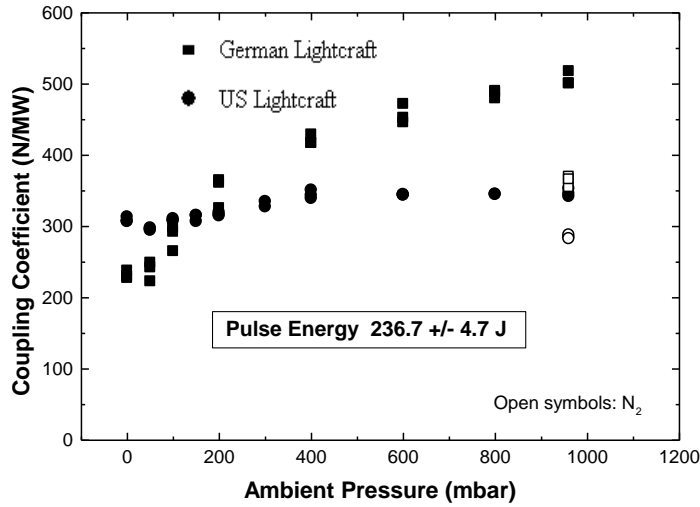


Figure 1.5. Momentum coupling coefficients for the #200-3/4 SAR and German 10 cm bell lightcraft engines as a function of ambient pressure in air and nitrogen with Delrin® propellant [6].

1.2 Type #200 Aerodynamics

In order to advance lightcraft technology, one must also investigate the vehicle aerodynamics throughout all phases of a trajectory to orbit: i.e., subsonic, supersonic, and hypersonic. As the #200 flight performance was superior, it has been the focus of several aerodynamic studies. Fluent® computational fluid dynamics (CFD) simulations [13] were performed for a 23 cm diameter lightcraft in the subsonic portion of a trajectory to orbit. These conditions were also relevant for the series of demonstration flights at WSMR by Myrabo et. al. [2]. Supersonic portions of launch trajectories (both ascent to orbit and re-entry) were also experimentally investigated in the RPI Mach 3, vacuum-driven wind tunnel [14]. These experiments investigated compressible flow-fields over lightcraft models, measured vehicle drag at Mach 3.0 with a closed inlet, and quantified aerodynamic lift generated in lateral flight (i.e., re-entry mode) vs. vehicle angle-of-attack (AoA). Later, another series of Fluent® CFD simulations [15] performed to study the inlet aerodynamic and vehicle drag properties for several 60 cm airbreathing laser-propelled lightcraft configurations. Features investigated included external-compression inlets flying at subsonic, transonic, and supersonic speeds to Mach 5, and

the resulting pressure, temperature, and velocity fields around the vehicles and the resulting drag coefficients. From this CFD study, an optimal engine/vehicle geometry for minimum drag was chosen for future experimental research at Mach 7-10 in Brazil.

A new and very accurate 200-5/6 sting-mounted lightcraft (Fig. 1.6) was constructed of 6061-T6 aluminum for experiments in RPI's 2'x2' subsonic wind tunnel.



Figure 1.6. Lightcraft model 200-5/6 for 2'x2' subsonic wind tunnel experiments.

The objective of the 61 cm by 61 cm subsonic wind tunnel test [16] was to gather the most accurate 200-5/6 lightcraft aerodynamics database generated to date. This subsonic wind tunnel has a smaller test section than that used previously [17], i.e. RPI's 4'x6' tunnel, but is equipped with a much more sensitive balance for measuring aerodynamic forces. A cross-sectional diagram of the sting and model investigated is provided in Fig. 1.7, showing the force diagram for both the *sting reference frame* and the *lightcraft reference frame*.

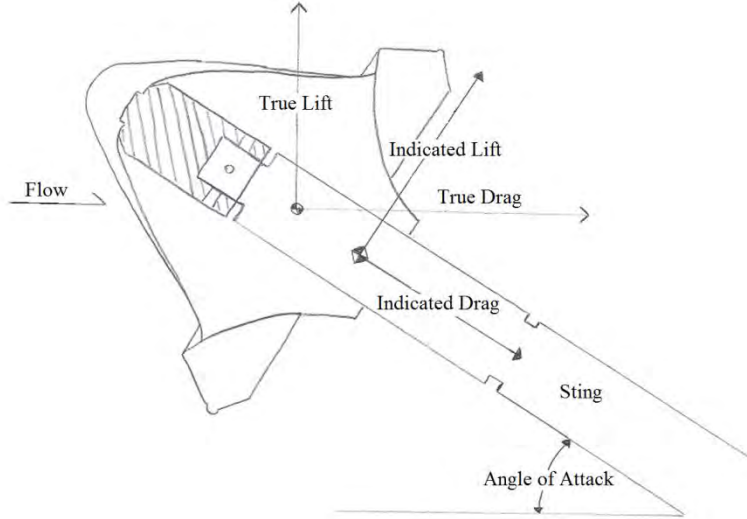


Figure 1.7. Lightcraft sting mount and force diagrams.

Although initially the model's aerodynamic center (AC) was assumed coincident with the vehicle center of mass (CM), one major objective of the wind tunnel experiments was to actually locate the real aerodynamic center. The results indicated the AC is near the aft end of the parabolic reflector. Although this location might seem an abstract concept, Hoerner [18] has assembled credible data on certain blunt bodies for which their AC is apparently aft of the body. Lift and drag data was obtained for angles of attack between 0 and 30° and matched well with previous experimental and numerical CFD results.

Visualization of the flow-field over the model at high AoA was performed using helium filled soap bubbles, which makes the separated flow region aft of the shroud, especially visible—see Fig. 1.8 below.

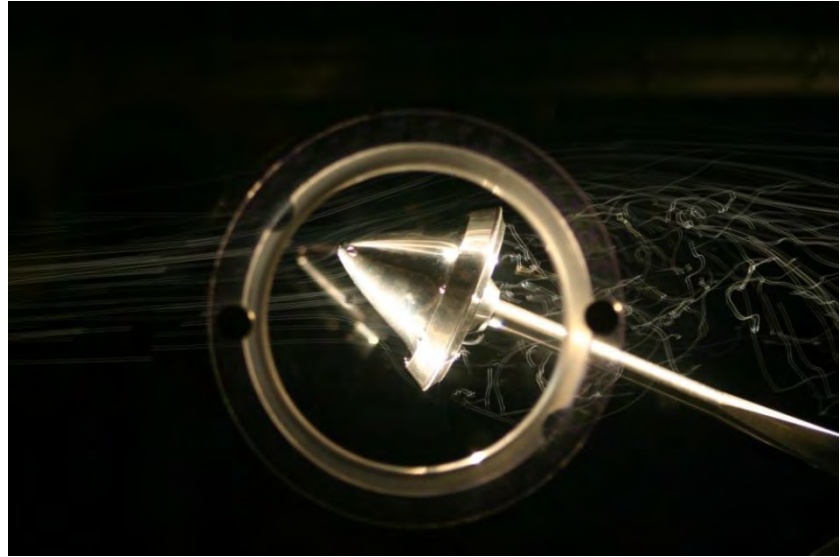


Figure 1.8. Flow visualization using helium filled bubbles.

1.3 7-DOF Code Development

The principal objective of the 7-DOF code development was to develop, validate, and calibrate a flight dynamics system model against existing experimental lightcraft flight trajectory data (from WSMR) to improve understanding of vehicle performance capabilities and enable prediction of future flight performance. The beam-riding and axial thrust characteristics of the Type 200 lightcraft engine have been modeled and verified using the processes described below. The flight dynamics system model was originally a six degree of freedom (6-DOF) model, but has been given a seventh degree of freedom for craft with a despun body. This 7-DOF tool can assess the prospects for new lightcraft geometries by predicting their flight behavior, and new models are being created specifically for this purpose. The goal is to create an accurate predictive tool which can enable users to design, predict, and assess the response of new lightcraft models to typical situations they may encounter in flight. Additionally, an active flight control system and accurate aerodynamics models have been incorporated into the model. This control system will be vital in future development of the lightcraft, because such controls are essential for any successful launch vehicle. The process by which this 7-DOF tool has been verified, validated, and calibrated is also described in detail in the following sections.

1.4 Objectives and Impact

The main objectives of this joint experimental and numerical investigation into beamed energy propulsion physics and 7-DOF flight dynamics research are: 1) determine why the #200 lightcraft geometry flies so well, and others don't; 2) obtain an understanding of the beam-riding phenomenon in varying engine geometries; and 3) determine the capabilities of the #200 geometry for trajectories transporting a payload to Low Earth Orbit (LEO). This involved:

- Experimentally investigating laser propulsion physics (e.g., C_M , I_{sp} , η_{ALP} , and laser pulse repetition frequency);
- Examining beam-riding behavior and performance of a specific lightcraft “family” (e.g., Type 150, 200, and 250 geometries) as well as the German “Bohn” bell design;
- Employing a 7-DOF flight dynamics simulator (after improving the associated aerodynamic and propulsion databases) to simulate trajectories and define the “flight envelopes” for lightcraft geometries investigated (#150, 200, 250).

This research will impact “Science” by providing a fundamental understanding of laser launch propulsion physics, including beam-riding behavior of airbreathing and rocket engines, and by creating an experimental database of propulsive characteristics vs. engine geometry, while searching for optimum engine/vehicle performance (e.g., both axial and lateral/restorative force behavior). The impact upon “Technology” will be to provide a clear understanding of laser propulsion physics for the specific application of nano-satellite launchers, and to ascertain the fundamental limits facing laser thermal propulsion technology (e.g., flight regime, airbreathing/rocket mode transition, etc.). An objectives tree for the present research program is provided in Fig. 1.9.

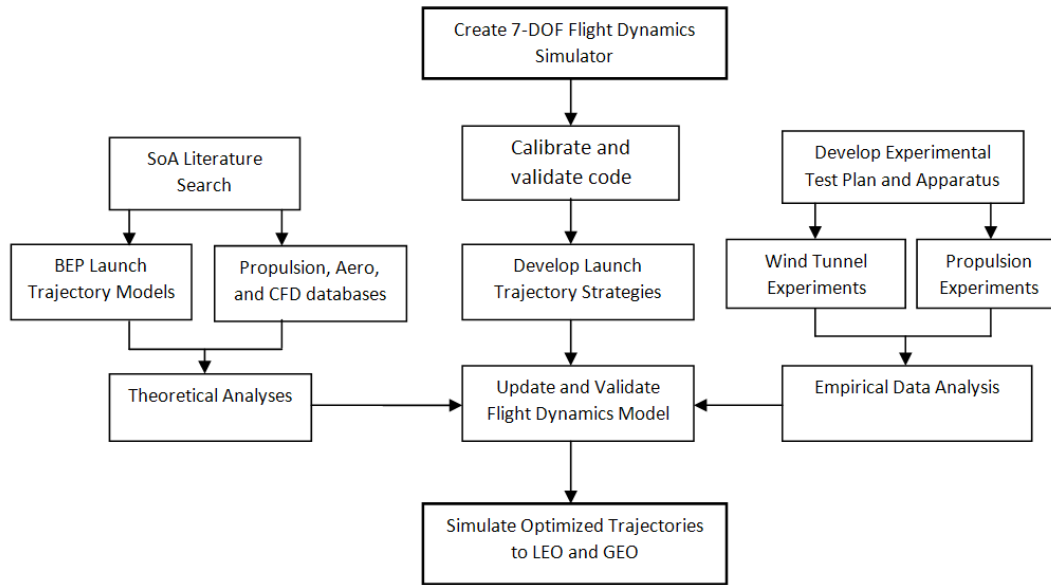


Figure 1.9. Research objectives tree.

2. EXPERIMENTAL APPARATUS AND LABORATORY SETUP

The experimental phase of this effort was conducted at the RPI Laser Propulsion Laboratory. The LP experiments were performed using the Lumonics K-922M Laser System, Angular Impulse Measuring Device (AIMD), two ballistic pendulums, and a high speed digital Cordin camera, amongst other laboratory equipment.

2.1 K-922M Laser System

The laser system for the LP experiments at RPI consists of two Lumonics K-922M CO2 TEA lasers, each comprised of two K-920M modules (see Fig. 2.1), upgraded with Marx Bank capacitors (“M”) to supply higher pulse energies. In the mid-1980s, they were originally part of the Paladin master oscillator that was configured for induction Linac FEL laser experiments at LLNL. Although the two K-920s could be reconfigured to fire independently as K-921Ms (10 J pulses), they are presently linked in series to fire as a K-922M, as seen in Figs. 2.1 and 2.2, delivering output pulse energies up to ~20 J at repetition rates up to 10 Hz, in bursts of up to 100 pulses. Table 2.1 presents the output characteristics of the reconfigurable, four-module K-920M system, assembled in the various configurations utilized in the RPI LP lab. With stable resonator optics installed, the K-922Ms produce a solid rectangular beam measuring 30x35mm in the near-field for the AIMD experiments at a range of 1 meter. For the ballistic pendulum experiments, the two beams were expanded slightly larger (see Fig. 2.3), measuring 41x35mm at a range of 4 meters from Laser 2, and 44x41mm at a range of 5 meters from Laser 1.

Table 2.1. Reconfigurable, four-module K-920M laser system.

Configuration	Pulse Energy [J]	PRF [Hz]
one K-922M	17	20
two K-922M	17	40
one K-924M	34	10



Figure 2.1. Interior view of Lumonics K-922M TEA CO2 laser module.

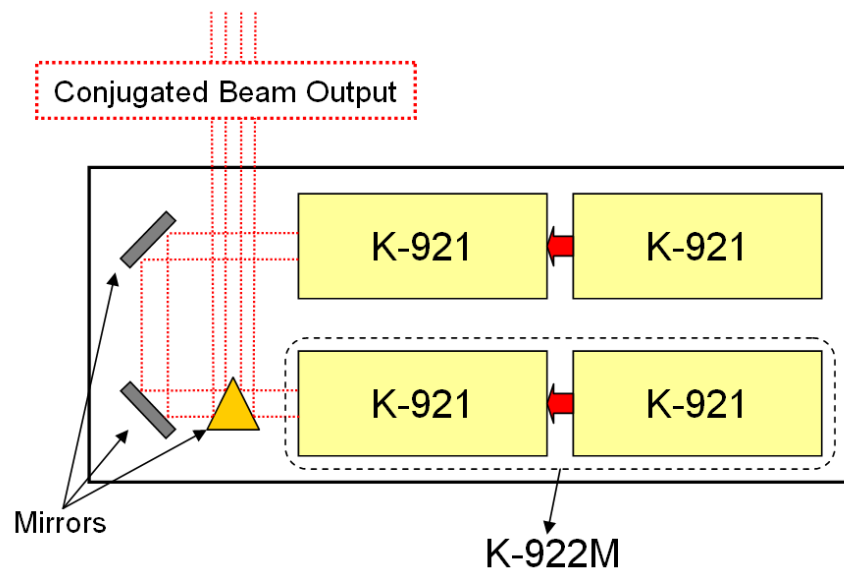


Figure 2.2. Reconfigurable laser system setup for LP laboratory use.

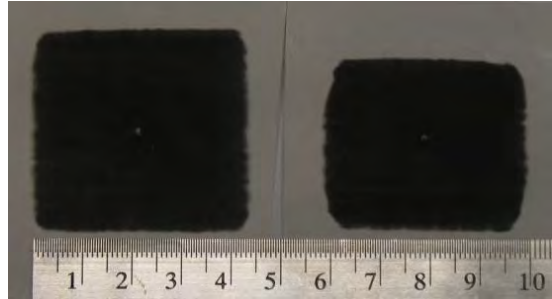


Figure 2.3. Laser beam burn patterns of a) Laser 1 (range of 5 m), and b) Laser 2 (range of 4 m).

Two different gas mixtures, LaserMark V (LM5) and High Gain (see Table 2.2,) were used exclusively throughout the current test campaign. The laser pulse shape from the LM5 mix has a much longer tail ($\sim 3.5 \mu\text{s}$) than the High Gain mix, as seen in Fig 2.4. In the LM5 mix, this tail contains $\sim 80\%$ of the pulse energy, with only 70% being delivered within $1.5 \mu\text{s}$. Conversely, the vast majority of the pulse energy (90%) is in the spike and first $1.5 \mu\text{s}$ of the HG mix. By defining the pulse duration as the FWHM of the spike, and the tail length as the time to deliver 90% of the pulse energy, it can be shown from Fig. 2.4 that the pulse duration of the HG mix and LM5 mixes are both less than 100 ns, while the tail length is ~ 1.5 and $2.5 \mu\text{s}$, respectively.

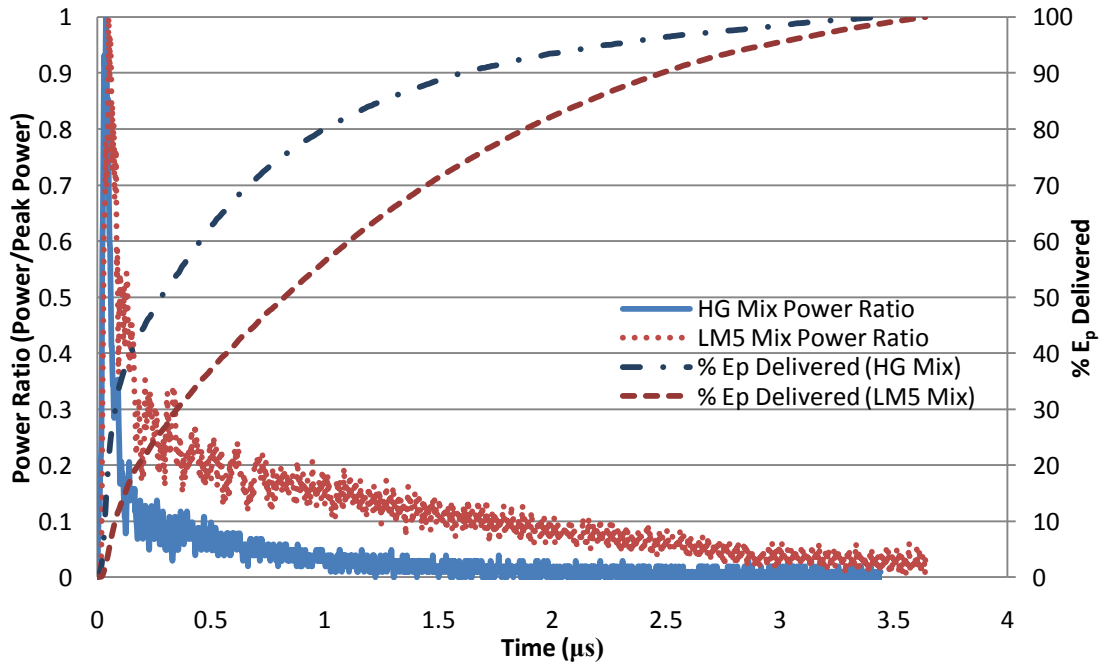


Figure 2.4. Laser pulse traces from LaserMark V mix and High Gain mix.

Table 2.2. Laser gas compositions for K-922M laser system.

Gas Mixture	CO ₂	N ₂	CO	H ₂	He
LaserMark V	8%	16%	4%	0.5%	71.5%
High Gain	28%	16%	4%	0.5%	51.5%

2.2 Lightcraft Geometries

During experiments at WSMR [2] Myrabo et. al. investigated the outdoor free flight performance of a series of several geometries (e.g., Types 100, 150, 200, 250, and 300) and sizes (e.g., 2/3, ¾, 5/6, 10/10, and 11/10, see Table 2.3 for dimensions) of a lightcraft family. Each engine type has a different focal and shroud configuration due to differences in the rear optic shape which affects the internal engine volume contained within the shroud. The designation (#) associated with each engine type represents the percent scale of the volume within the shroud compared to that within the type #100 (e.g., the #200 engine has twice the volume of the type #100). Figure 2.5 demonstrates the cross-section of each of these engine geometries, highlighting the differences. The full range of lightcraft sizes flown previously at WSMR is shown in Fig. 2.6. Note that all are #200, except the two at the far right, which are #150.

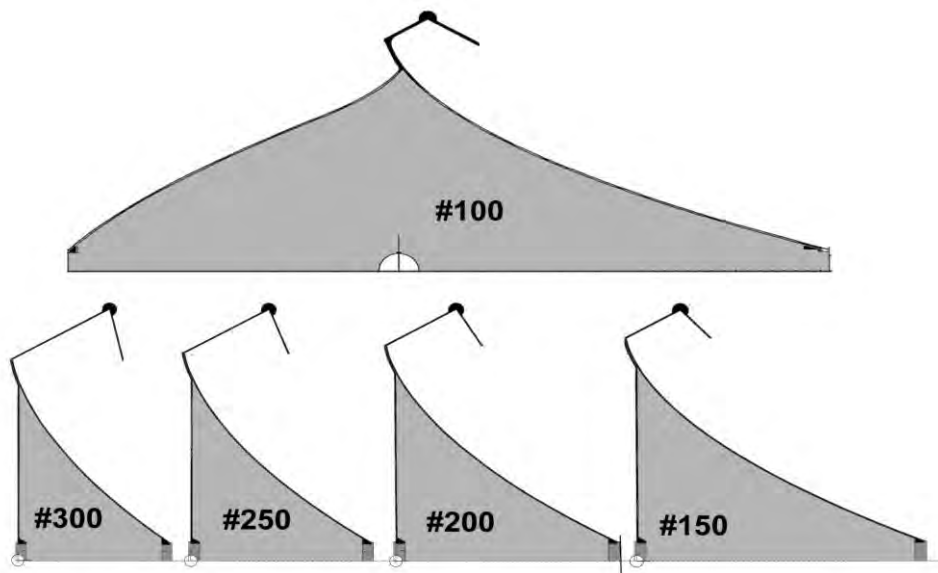


Figure 2.5. Lightcraft engine family cross-sections.



Figure 2.6. Lightcraft engine family (from left to right, #200-11/10, #200-10/10, #200-5/6, #200-3/4 #150-3/4, #150-2/3) .

Table 2.3. Lightcraft properties.

Engine	Mass (kg)	Diameter (mm)	$I_{xx} (\text{kg} \cdot \text{m}^2)$	$I_{yy} (\text{kg} \cdot \text{m}^2)$
200-2/3	0.02162	97.73	$2.25 \cdot 10^{-5}$	$1.8 \cdot 10^{-5}$
200-3/4	0.0269	109.9	$3.642 \cdot 10^{-5}$	$2.939 \cdot 10^{-5}$
200-5/6	0.0311	122.2	$6.027 \cdot 10^{-5}$	$4.653 \cdot 10^{-5}$
200-10/10	0.04863	146.6	$13.43 \cdot 10^{-5}$	$10.097 \cdot 10^{-5}$
200-11/10	0.0545	161.2	$18.049 \cdot 10^{-5}$	$13.63 \cdot 10^{-5}$

For each K-922M LP experiment, mounting of the lightcraft to the thrust stand is facilitated by a “teacup mount” that replaces the nose of each model. The 2/3 scale teacup nose is pictured (center-rear) in Fig. 2.7, as well as the shroud and optic of the #250, #200, and #150 (from left to right). Figure 2.8 pictures the 10 cm diameter German “Bohn” bell with an integral teacup-mount used for LP experiments at RPI.



Figure 2.7. 97.73 mm teacup mount and family of engine geometries



Figure 2.8. German “Bohn” bell 10 cm diameter engine with teacup mount.

2.3 Angular Impulse Measuring Device

The Angular Impulse Measuring Device (AIMD) [19] in Fig. 2.9, was designed to measure both the dominant side (lateral) linear impulse and the dominant pitching angular impulse about the flight vehicle’s center of mass, which is located approximately at the “quarter chord” (measured on the shroud’s conical frontal surface in Fig. 2.10). The AIMD apparatus allows experimenters to easily “dial in” any desired lateral and angular offsets (of the laser beam) for any mounted engine. During tests, the angular impulse generated by a lightcraft engine imparts an angular velocity to a vertical shaft through its special “teacup” mount (see Fig. 2.7). The shaft turns a Schaevitz Rotary Variable Differential Transformer (RVDT), which produces a voltage proportional to the angular displacement of the rotor over a range of 60 degrees. Because precise rotor/beam alignment is important for each test, the AIMD core sports a vertical pin to re-orient the rotor after each laser pulse is delivered.

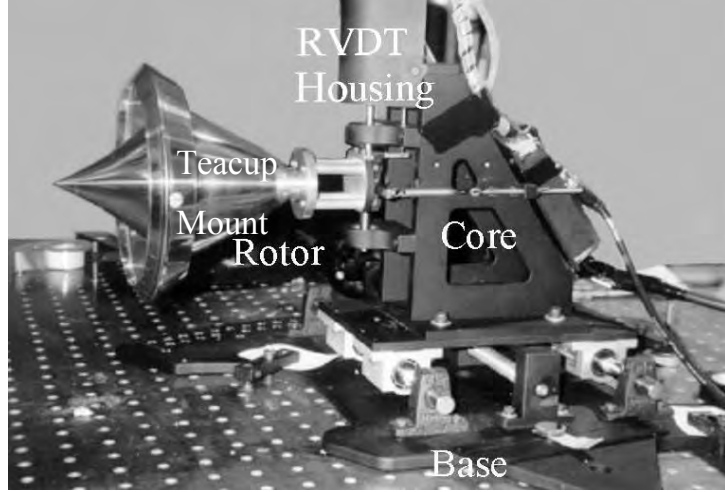


Figure 2.9. AIMD apparatus with lightcraft engine, teacup mount, and spacers.

The AIMD device employs two extension springs stretched with the proper tension between the rotor and core framework, to produce an oscillatory rotor response to laser delivered impulses applied to the engine; the spring constants are selected to limit rotor motion from becoming so large that it contacts the end stops. Precise selection of spring properties is crucial to AIMD successful operation (data gathering), since excessive stiffness will result in minimal angular displacement, while inadequate stiffness could possibly damage the rotor.

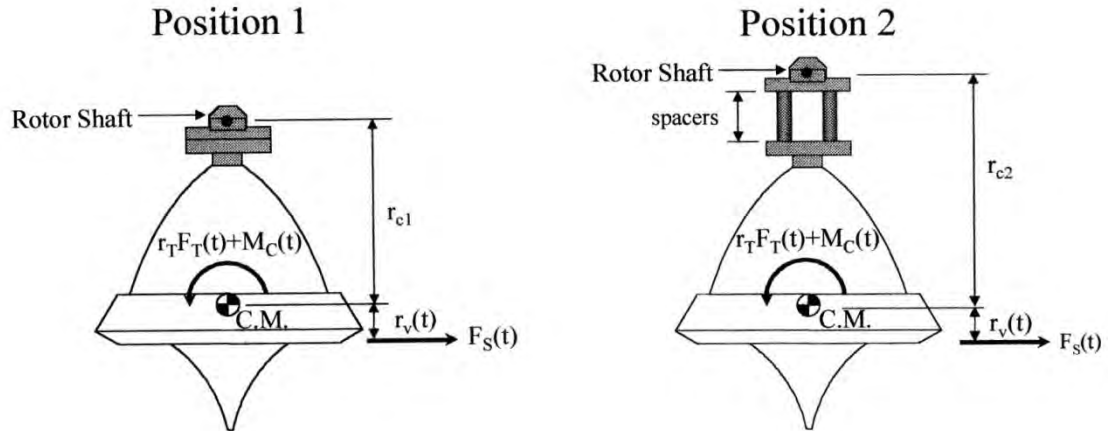


Figure 2.10. AIMD rotor geometry showing variable definitions, pivot shaft, and spacer placement.

The AIMD test stand actually measures the resultant impulse applied to the *rotor* (not forces and moments), because the briefly applied forces and moments—generated by a laser-induced detonation—persist for only milliseconds [20]. The measured angular

impulse includes components from both the side force and the pitching moment. The *rotor* is comprised of the shaft, lightcraft engine, and “teacup” mount, and is considered to be a rigid body (see Fig. 2.10). The total angular impulse applied to the *rotor* about the rotor axis r , , is given by:

(1)

where I_r is the moment of inertia of the rotor about the rotor axis and ω_0 is the initial angular velocity of the *rotor* about the rotor axis. An alternate form of the total angular impulse, given in Eqn. 2, is attributed to two components: 1) the side linear impulse acting on a moment arm, and 2) M_p , the time-variant pitching moment given in Eqn. 3. Equations 2 and 3 are simplified versions of the general form of Euler’s equation of motion, made possible by the system’s singular axis of rotation.

(2)

(3)

where T is the time-variant thrust, \mathbf{r}_c is the vector from the rotor shaft to the rotor center of mass, \mathbf{r}_t is the time-variant thrust moment arm, and \mathbf{M}_t is the time-variant torque comprised of various couples existing on the engine (see Fig. 2.10).

A second equation is obtained to solve for the two unknowns by moving the lightcraft a known distance radially outward from the axis of revolution using 34.9 mm aluminum spacers, as pictured in Fig. 2.10. Note that the impulse delivered by the laser-induced pressures expanding over the engine’s walls is identical regardless of the spacer length (i.e., the engine’s radial position) because the lightcraft’s lateral alignment with the incident laser beam at the time of the impulse delivery, has not changed; therefore, functions \mathbf{r}_c and \mathbf{r}_t are assumed to remain constant. However, the geometric alteration of the rotor does indeed change the rotor’s moment of inertia, and this change

must be considered when determining the angular impulse based on the initial rotor velocity, as given by:

(4)

(5)

where R_1 and R_2 represent engine positions 1 and 2, respectively. Extending the radially outward position of the engine also increases the moment arm r_C and, more importantly, it generates the second equation needed to find the two unknowns. The system of two equations is given as:

(6)

(7)

where subscripts 1 and 2 again denote positions 1 and 2 respectively. Figure 2.10 shows the changing moment arm. Simplifying the equations due to a singular degree of freedom, then solving for the unknown impulses yields:

_____ (8)

_____ (9)

The above equations allow both *side linear impulse* and *pitching angular impulse* (with respect to the vehicle's center of mass in free-flight) to be determined from the measured rotor angular velocities [19].

As first demonstrated by Libeau [21], a complete lightcraft engine (i.e., forebody/nose, shroud, and rear optic) is attached to the AIMD using a teacup type mount. Note that prior PLVS experiments at WSMR with a ballistic pendulum tested only ~~half~~ the engine—i.e., only the shroud and rear optic were mounted on the pendulum [22, 23, 24]; the nose was missing. This incomplete approach was discarded because larger laser

pulse energies (e.g., typical of PLVTS), will generate blast wave pressures strong enough to wrap back around the shroud and onto the vehicle's nose, thereby reducing the total impulse.

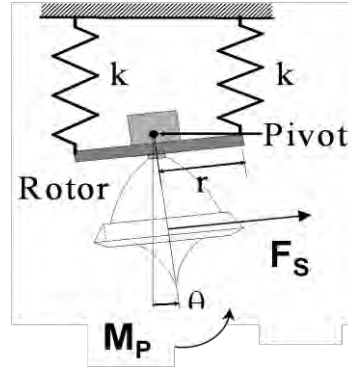


Figure 2.11. AIMD rotor diagram.

The spring constants K (confirmed by laboratory tests, see Appendix A) were used to obtain the rotor's moment of inertia and thereby convert the measured angular velocities into angular impulses. The rotor's moment of inertia is experimentally determined from the test data by modeling the rotor motion as a simple 2nd order system illustrated in Fig. 2.11 and described by

$$\ddot{\theta} + C\dot{\theta} + \frac{2r^2K}{I_R}\theta = 0 \quad (10)$$

where θ is the angular displacement of the rotor, C is the viscous damping term, r is moment arm of the springs, K is the average spring constant of the springs, and I_R is the moment of inertia of the rotor. The viscous damping term results in a damping coefficient of about 0.06 and does little to alter the natural frequency of the system. Finally, the spring constants of the two springs are assumed to be nearly equal and θ is assumed to be a small angle. With these three assumptions, the natural frequency of the rotor is

$$\omega_N = \sqrt{\frac{2r^2K}{I_R}} \quad (11)$$

where ω_N is given in radians/sec. By determining the period of rotor oscillation T , the above equation can be solved for rotor MOI in terms of period as

$$I_R = \frac{Kr^2T^2}{(2\pi)^2} \quad (12)$$

Note Eqn. 12 has been corrected from that presented by Libeau [19,21].

2.4 Lightweight Ballistic Pendulum

To measure the axial impulse provided by the engine, a ballistic pendulum was used. An engine is mounted on a pendulum, hanging a known distance from a rotating shaft which is connected to a RVDT device identical to the one used with the AIMD. The RVDT produces a voltage proportional to the angular displacement of the rotating shaft, which can be used to find the initial rotational velocity of the pendulum. Using a calibration taken with the impact hammer, a direct relation is found between this initial velocity and the impulse provided to the engine. The first tests employed a heavy ballistic pendulum originally used at WSMR [5, 21, 22, 23, 25], seen in Fig. 2.12. The large moments of inertia of this pendulum prevented angular displacements significantly beyond the RVDT noise level, so this necessitated the design and construction of the new, lightweight ballistic pendulum (LWBP), shown in Fig. 2.13. This sensitive ballistic pendulum was decreased the moments of inertia about the rotating shaft by approximately two orders of magnitude, allowing an accurate measurement of the axial impulse produced by small lightcraft engines. This pendulum is calibrated using a PCB 086C01 impact hammer, as shown in Fig. 2.12. Example outputs of the AIMD and LWBP, as measured by the Tektronix TDS 2014B four channel digital oscilloscope used for all impulse experiments, are provided in Appendix B.



Figure 2.12. Calibration setup with impact hammer and the original, heavy pendulum, used in WSMR lab experiments with PLVTS.



Figure 2.13. Lightweight ballistic pendulum (LWBP) with #200-3/4 engine and balancing mass.

2.5 Experimental Setup

For the first test campaign, the lightweight ballistic pendulum was anchored to an optical bench approximately 4 meters down range of Laser 2, and 5 meters from Laser 1 (see Fig. 2.14). In the subsequent campaign, the AIMD was fixed to the same optical bench as the K922 laser system, and oriented so that its translating core moved perpendicular to the laser beam axis (see Fig. 2.15); the beam was propagated about 1 m beyond the K922M cabinet (i.e., output aperture) before contacting the lightcraft engine, to eliminate interactions with the laser resonator cavity. Both the ballistic pendulum and the AIMD were aligned such that the laser beam axis was exactly centered onto the tip of the engine's parabolic optic, with zero lateral offset.

Just prior to beginning each test campaign, the beam -splitter was calibrated; the 75 mm diameter, 3 mm thick ZnSe window (set at ~ 45 degrees) had no anti-reflective coatings. This beam-splitter setup was retained in the optical train during all experiments, so that the laser energy delivered in every pulse could be precisely measured and recorded for every test run.

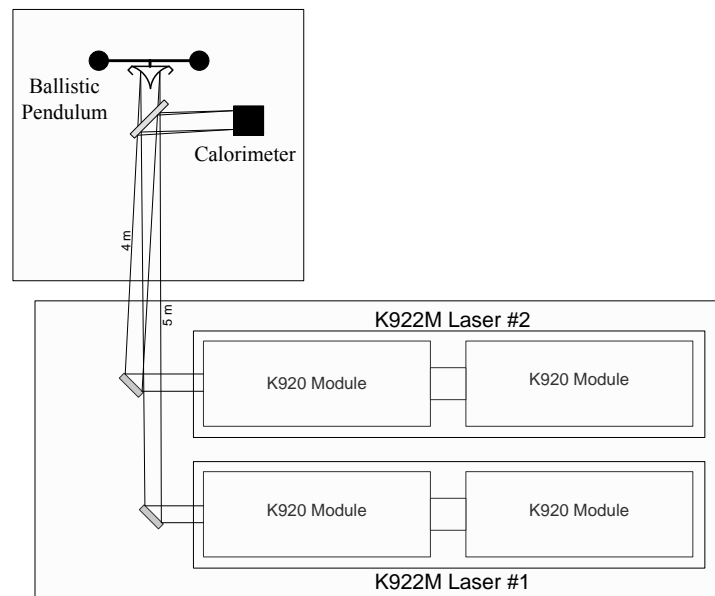


Figure 2.14. Optical setup for ballistic pendulum with calibrated beam-splitter.

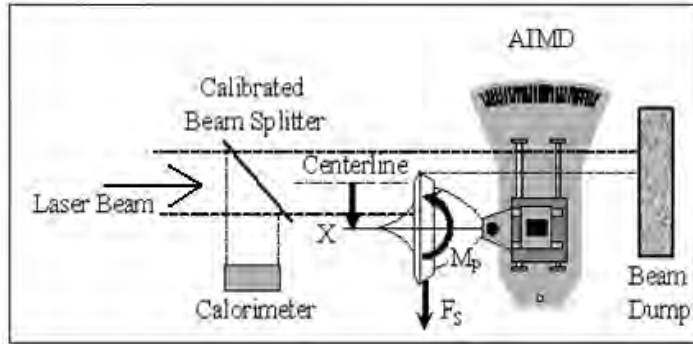


Figure 2.15. Optical setup for AIMD test stand with calibrated beam-splitter.

The ballistic pendulum test campaigns involved measuring the axial impulse generated by a series of engines with varying geometries, sizes, propellants, and laser gas mixes. The performance of each engine was investigated while delivering pulse energies ranging from approximately 12 to 40 J.

The AIMD test campaign comprised several experimental setups of a series of engines (again, utilizing varying geometries, sizes, propellants, and laser gas mixtures), with two different standoff distances (zero and 34.93 mm.) For each case, the lightcraft was traversed laterally through the fixed laser beam, beginning with an initial offset of at least -10 mm and ending with the engine completely outside the beam. Each lightcraft was initially attached flush to the rotor for the first test; then, 34.93 mm spacers were inserted for the second. At every lateral offset position (in 5 mm increments), several angular impulse measurements were recorded from sequential laser pulses; these data points were then averaged together. The twin springs used for the #150, #200, and #250 engines were Century Springs Model 5509, with a spring constant of ~ 150 N/m. Century Springs model 5305 (spring constants of ~ 25 N/m) was used for the 10 cm diameter German bell tests to greatly enhance AIMD rotor sensitivity, providing a higher degree of accuracy for experimental measurements of diminutive beam-riding response.

2.6 Experimental Error Analysis

Error bars are used throughout the experimental results to indicate the uncertainty in quantities measured to within one standard deviation (68% certainty). The uncertainty involved in each of the devices in the experimental apparatus and setups described above, are listed in Table 2.4. For apparatus and setups involving more than one piece of equipment in Table 2.4, the uncertainty of each propagates to cause the system uncertainty to be a quadratic sum of the parts, or:

(13)

where $error_{total}$ is the total error involved in the experiment, and $error_n$ is the error associated with device n used to obtain the experimental results. When the associated error is a percentage, the total error is calculated as the mean value of the series of experimental results times the associated percent error. For all experiments, three data points were obtained and averaged to provide the results shown below, unless otherwise stated.

Table 2.4. Experimental error associated with experimental data acquisition devices.

Equipment Model	Associated Error
Gentec-EO Model QE55 laser energy meter	$\pm 3\%$
Schaevitz® Model R30D RVDT	$\pm 0.25\%$
Tektronics® TDS 2014b oscilloscope	$\pm 3\%$
PCB Piezotronics® Model086E80 impact hammer	$\pm 1\%$
Ohaus® Model TP200S electronic balance	± 0.001 grams

2.7 Schlieren Photography

A conventional Schlieren system was implemented to capture a series of high speed digital photographs of the laser induced breakdown and resulting blast waves expelled from each engine. As shown in Fig. 2.16 below, this system captures images at point (e), between two 25.4-cm diameter parabolic mirrors with 1.52-m foci (marked $-d''$ and $-f''$)

and a Flashpoint II Model 1220A Moonlight with a xenon flashtube (a) to illuminate through a 1 mm slit (b) simulating a point source, before being expanded using a lens with a 220-cm focus (c). The images are filtered using a razor blade (g) and captured by a high speed Cordin Model 530 digital framing camera (h).

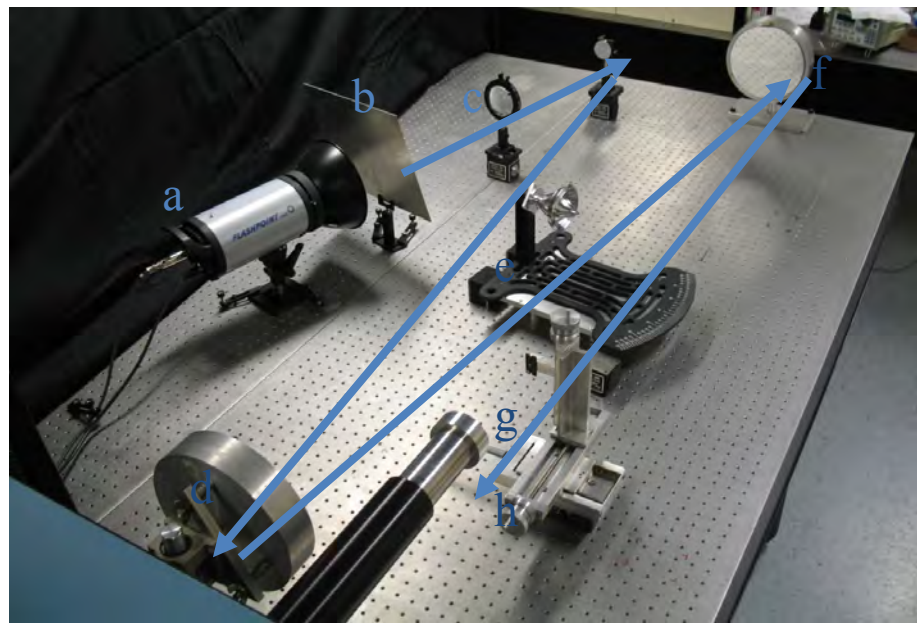


Figure 2.16. Schlieren setup in RPI Laser Propulsion Laboratory.

3. NUMERICAL FLIGHT DYNAMICS SIMULATION DEVELOPMENT

A detailed flight dynamics model has been developed for the purpose of providing a physics-based predictive tool, which may be used to evaluate the performance of proposed future lightcraft vehicle concepts, engine systems, beam shapes, and active control strategies, thereby aiding in the development of the next generation of laser propelled lightcraft. The full system model is composed of individual aerodynamic, engine, laser beam, variable vehicle inertial, and 7-DOF dynamics models which have been integrated to represent all major phenomena in a consistent framework. Other featured capabilities of the current model include full atmospheric models, multiple engine models (airbreathing, rocket, & combined-cycle), an active reaction control system (RCS), laser beam pointing models with a variable azimuth and zenith, and beam propagation models for a variable focus telescope. The resulting system level model and associated code was then validated and calibrated using experimental flight information from a 16 flight trajectory data base [1].

As shown by Ballard, Anderson, and Myrabo [8], the present model represents the spinning lightcraft as a six degree-of-freedom gyrostat [26] being acted upon by laser impulses and aerodynamic loads. An optional seventh degree-of-freedom has been added, allowing for a “despun” payload compartment/carrier, but not used for the results in this paper. The craft is represented as this “despun” payload compartment/ carrier; a symmetric spinning rotor R ; and the system center, all located relative to a well established design reference point P , and dextral basis vectors $\mathbf{e}_1, \mathbf{e}_2, \mathbf{e}_3$, fixed in reference frame (body) B . For all cases considered here the rotation axis of the rotor is defined to be parallel to direction \mathbf{e}_1 , which is nominally the preferred flight direction. The carrier is then acted upon by laser impulses and aerodynamic loads. *[This model has been produced with the intent of treating planned future lightcraft which will include such a despun equipment/ crew platform, and will contain some as yet to be determined active reaction control.]* The equations of motion for this system are:

$$\begin{aligned}
\begin{bmatrix} M_1^B \\ M_2^B \\ M_3^B \\ M_1^{R/B} \end{bmatrix} = & \begin{bmatrix} I_{11}^B & I_{12}^B & I_{13}^B & J^R \\ I_{12}^B & (I_{22}^B + I^R) & I_{23}^B & 0 \\ I_{13}^B & I_{23}^B & (I_{33}^B + I^R) & 0 \\ J^R & 0 & 0 & J^R \end{bmatrix} \begin{bmatrix} \dot{\omega}_1 \\ \dot{\omega}_2 \\ \dot{\omega}_3 \\ \ddot{\psi}_3 \end{bmatrix} \\
& + \begin{bmatrix} (I_{13}^B \omega_2 - I_{12}^B \omega_3) \omega_1 + (I_{23}^B \omega_2 - I_{22}^B \omega_3) \omega_2 \\ (I_{11}^B \omega_2 - I_{13}^B \omega_1) \omega_1 + (I_{12}^B \omega_3 - I_{23}^B \omega_1) \omega_2 \\ (I_{12}^B \omega_2 - I_{11}^B \omega_2) \omega_1 + (I_{22}^B \omega_1 - I_{12}^B \omega_2) \omega_2 \\ 0 \end{bmatrix} \\
& + \begin{bmatrix} (I_{33}^B \omega_2 - I_{23}^B \omega_3) \omega_3 \\ (I_{33}^B \omega_2 - I_{23}^B \omega_3) + J^R \omega_3 \dot{\psi} + (J^R - I^R) \omega_1 \omega_3 \\ (I_{23}^B \omega_1 - I_{13}^B \omega_2) \omega_3 + J^R \omega_2 \dot{\psi} + (I^R - J^R) \omega_1 \omega_2 \\ 0 \end{bmatrix} \quad (14)
\end{aligned}$$

where I_{ij}^B represents the ij element of the central inertial matrix of despun platform/carrier B, with angular velocity relative to the Newtonian frame N of

$\dot{\omega}_1, \dot{\omega}_2, \dot{\omega}_3$ is the sum of all external moments applied to the carrier B from outside the system, while J^R is the ω_1 component of the moment exerted on the rotor R by the carrier B. The moments I^R are due to laser impulsive loads, aerodynamic loads, and potentially some form of reaction control system. The quantity I^R is the central moment of inertia associated with the directions ω_2 and ω_3 , while J^R is the rotor central moment of inertia about the spin axis ω_1 . Lastly, the angular velocity of the rotor R relative to the carrier B is $\dot{\psi}_3$. For all lightcraft so far flown, the entire system acts as the rotor. The “despun” platform B is thus a massless reference frame and the system degenerates to a six degree-of-freedom spinning, axially symmetric body, where the rotor rotation rate relative to B is a prescribed $\dot{\psi}_3$. For this idealized system, the rotational equations of motion for the lightcraft then take the form

$$+ \quad (15)$$

For the results presented here, the lightcraft body spins at a constant rate with respect to a “despun” reference frame about the craft axis of symmetry. This despun reference frame nominally has a nonzero angular velocity ω_d , but is termed “despun” because $\omega_d = \omega_i$ ($i = 1, 2, 3$). The angular velocity of the lightcraft rotor with respect to the Newtonian (inertial) reference frame is then given by

(16)

And the system angular acceleration is

(17)

This form of the model exploits system symmetries and permits significantly larger temporal integration steps to be taken while maintaining both integrator stability and accuracy. The model was created using Autolev Ver. 4.1 [27], a dynamic modeling software that uses Kane's method [28] to develop the equations of motion. The actual mathematical model on which the associated simulation code was built is significantly more general than this, permitting the masses and associated mass properties of the carrier and/or rotor to vary with time, permitting the accurate consideration of propellant usage.

To accurately capture the behavior of future lightcraft flights to extreme altitudes, the Newtonian reference frame, with associated basis vectors $\mathbf{e}_1, \mathbf{e}_2, \mathbf{e}_3$ was taken to be the standard de-spun Earth reference frame [29] placed at the Earth's center and aligned such that \mathbf{e}_1 points outward toward the vernal equinox, \mathbf{e}_3 points outward along the Earth's rotation axis toward the north geometric pole, and $\mathbf{e}_2 = \mathbf{e}_3 \times \mathbf{e}_1$. The model uses an inverse square law gravitational field, and correctly accounts for centripetal and Coriolis acceleration variation with launch site location. Additionally, model state variables are defined with respect to the launch site reference frame (i.e., fixed at the launch point) as opposed to the despun system inertial frame, so that simulated quantities (position, velocity, and acceleration) may be directly related to the associated quantities

measured experimentally at the launch site. The vehicle mass, centre of mass, and mass moments of inertia were defined as time-variant to account for the consumption of rocket propellant. The model can additionally simulate the behavior of lightcraft under the influence of a crosswind that is variable in both magnitude and direction.

If t_k is the time at which the impulsive thrust occurs, then by using Newton's 2nd law with modification to account for impulses, the lightcraft translational equation of motion is written as:

(18)

where \mathbf{F}_{ext} is the sum of all applied non-impulsive forces acting on the lightcraft. These forces include gravitational forces, aerodynamic forces, and forces resulting from the firing of the Reaction Control System (RCS). \mathbf{F}_{imp} is the impulse imparted to the lightcraft by the laser and is a complex function of system geometry (Optic size and shape, orientation, location in the beam, and laser beam profile). $\delta(\tau - t_k)$ is the Dirac delta function, m the mass of the lightcraft at time τ , and \mathbf{a} is the acceleration of the centre of mass of the lightcraft with respect to the inertial reference frame.

In the demonstration flights at WSMR [2], the lightcraft is typically spun up to 13,000 RPM just prior to launch. During flight, skin friction forces apply a roll-damping torque on the vehicle that steadily reduces the vehicle spin rate. Since the vehicle is spin-stabilized, the spin rate is of critical importance in modeling lightcraft flight dynamics along laser-boost trajectories. To properly model the lightcraft's spin deceleration, an analytical function had to be developed that accurately captures the experimental behavior. Hence, a laboratory experiment was carried out at RPI to measure the spin deceleration rate of a model 200-5/6 lightcraft as a function of time, starting from >11,000 RPM. The spin deceleration of the craft was approximated by an exponential decay function, with the decay rate obtained from laboratory experiments. The spin deceleration is realized by the application of an appropriate aerodynamic moment T

about the spin axis. The exponential decay function in Eqn. (19) provides an excellent curve fit to this experimental data over the first 30 seconds:

$$\dot{\omega}_1 = -\gamma\omega_i e^{-\gamma t} = -0.0658\omega_i e^{-0.0658t} \quad (19)$$

where ω_i is the initial spin rate in rad/sec, and -0.0658 is the decay rate that comes from the exponential decay curve fit to the data presented in Fig 3.1.

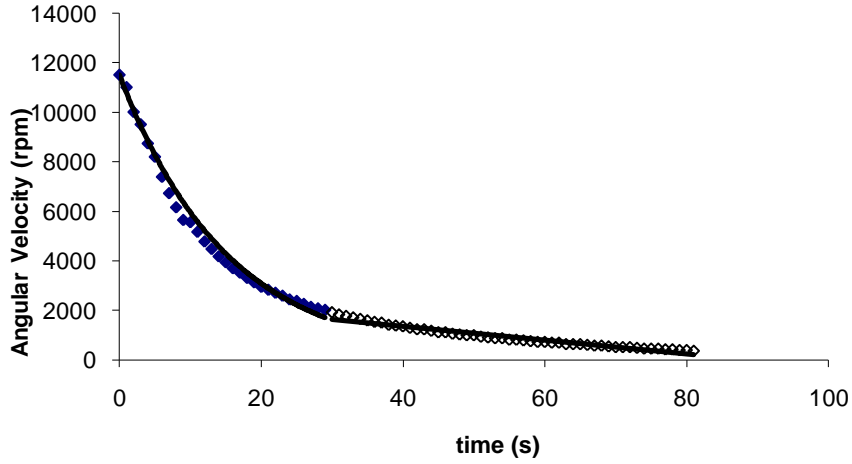


Figure 3.1. Lightcraft model 200-5/6 spin deceleration exponential decay function.

The spin deceleration is realized by the application of an appropriate aerodynamic moment T about the spin axis. This, in addition to the aerodynamic drag D , lift L , and tipping moment M , are modeled as:

$$D = 1/2 \rho V^2 S C_D \quad (20)$$

$$L = 1/2 \rho V^2 S C_L \quad (21)$$

$$M = 1/2 \rho V^2 S C_M c \quad (22)$$

$$T = J \dot{\omega}_1 \quad (23)$$

Within these equations, ρ is the local air density, V is of the speed of the craft relative to the air flow, S is the planform area, and c is reference chord, while C_D , C_L and C_M are the aerodynamic coefficients of drag, lift, and pitching moment, respectively. These

aerodynamic forces are then applied to the lightcraft in the convention indicated in Fig. 3.2.

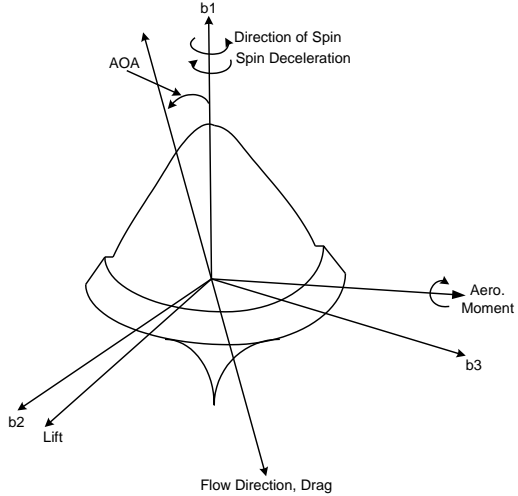


Figure 3.2. Lightcraft Aerodynamic Force Diagram.

The ultimate goal of the series of simulations, the results of which are presented below, was to develop flight control system strategies for a stable launch into LEO, to identify optimized trajectories that make maximum use of a lightcraft engine's autonomous beam-riding feature, and to define the capabilities or "flight envelope" of the investigated engine geometries, specifically the #200. The present two-body 7-DOF code enables users to quantify flight maneuvering forces/torques needed from the attitude control system (ACS) to assure boost stability in the presence of disturbing forces such as wind gusts, changing laser beam geometry, etc. Figure 3.3 reveals the lightcraft cross-section, indicating placement of the reaction control jet system relative to the vehicle center-of-mass. The maximum allowed RCS gas-jet thrust in the present study was 100 N with an assumed specific impulse of 200 seconds.

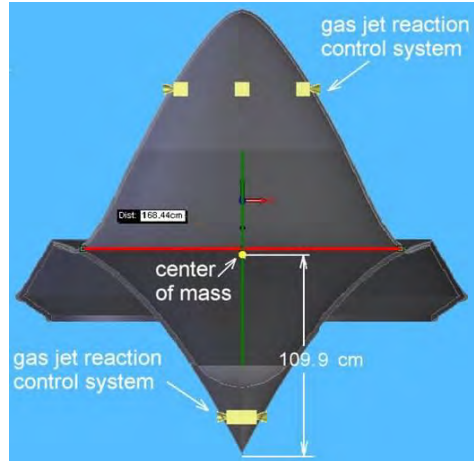


Figure 3.3. Cutaway indicating center of mass and placement of reaction control system, in 2.4m #200 lightcraft.

To achieve low earth orbit (LEO), a lightcraft must increase its azimuthal velocity to ~ 8 km/s. Since vertically oriented launches will not accomplish this objective (except possibly for direct flights to geostationary orbit), the beam must be scheduled to slew with time. Figure 3.4 shows the principal variables that define laser beam orientation with respect to the launch pad; zenith is measured from vertical, and azimuth from North, as indicated.

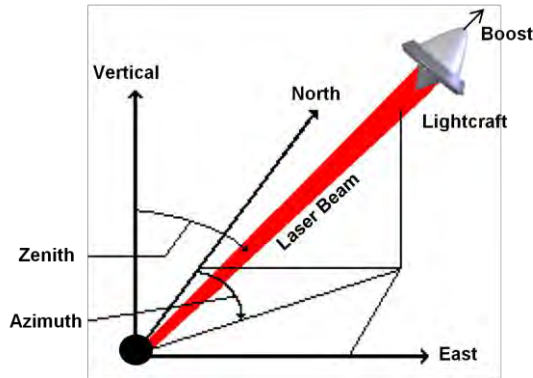


Figure 3.4. Laser beam orientation with respect to launch pad and lightcraft.

Figures 3.5 and 3.6 show the Aim Point laser launch scheme. Note the lightcraft orientation with respect to the laser beam –aim-point,” vehicle center of mass (C.M.) location, axial and lateral restorative (i.e., “beam-riding”) thrust vectors, vehicle angle-of-attack, and axial thrust vectoring angle. Figure 3.6 clearly indicates the anticipated

portions of the vehicle performance curves (i.e., axial and lateral impulse vs. angular and lateral offset) to be taken advantage of for trajectory simulations to LEO. Note that the beam riding forces are maximized while the axial forces are still very nearly at their maximum, as the entire beam is still captured by the engine and the tipping angle upon the beam is small. For the initial suborbital simulation results reported herein, the beam is not actively targeting a specific spot (i.e., “aim-point”) on the lightcraft; instead, the beam is either held at a constant orientation, or follows a scheduled slewing rate. Hence, the lightcraft “rides” the beam with only natural “beam-riding” restorative forces. For the final series of simulations to LEO, however, a designated aim-point was specified and utilized.

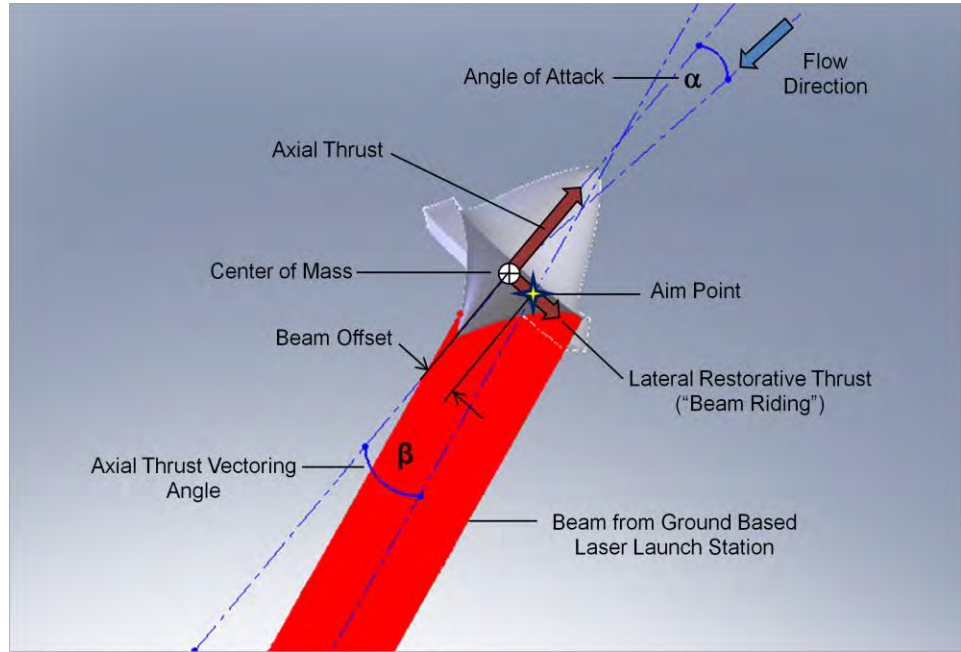


Figure 3.5. Laser launch scheme showing lightcraft boost orientation in relation to the aim point (beam offset), axial and lateral engine thrust, thrust-vectoring angle, vehicle angle-of-attack and center of mass.

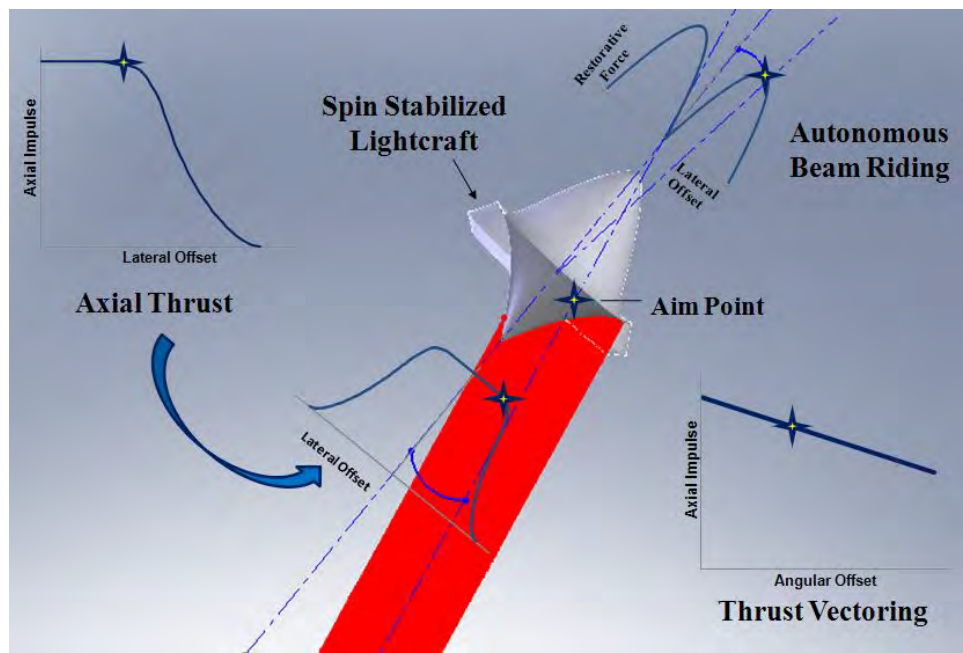


Figure 3.6. Critical BEP engine beam-riding and performance criteria required for stable laser-boosted launch.

4. RESULTS

The combined experimental and numerical test campaign investigating laser propulsion physics at Rensselaer Polytechnic Institute used a 7-DOF flight dynamics code and the twin Lumonics K922M TEA CO₂ laser system, whose output characteristics (20 joules each; ~200 ns FWHM spike with ~1 μs tail) provide a much improved match with the small lightcraft engines flown at WSMR. The laser propulsion performance of a series of lightcraft engines ranging from 97.7 mm to 161.2 mm in diameter (i.e., covering the -2/3, through -11/10 scale engines) was measured experimentally using the different apparatus discussed in previous chapters. Experiments were performed in the subsonic wind tunnel at RPI investigating the subsonic aerodynamics of vehicles during a launch trajectory to orbit. Trajectory simulations were also performed using historical laser propulsion databases and the flight envelope of the lightcraft family, specifically favoring the #200 geometry. The flight dynamics code was then updated with the results of new laser propulsion experiments carried out at RPI, and further trajectory simulations were performed. The ultimate goal of this effort was an in-depth investigation of laser propulsion physics for sub-microsecond laser pulses, to understand the beam-riding phenomena, and to discover why the Type # 200 lightcraft flies so well, and other geometries don't.

4.1 Airbreathing Propulsion Experiments

The physics of laser impulse generation in a lightcraft engine is a complex function of several variables including laser pulse energy and pulse width, lateral and angular offset of the beam, fluence upon the rear optic, and also the included focus angle, α , which is defined only for the centered, on-axis beam alignment case. Momentum coupling coefficients (C_M) were calculated from recorded impulse traces (Tektronix scope Model #2014B) using methods described above and the following relation:

$$C_M = \frac{\int F_s \mathbf{v} dt}{E_p} \quad (24)$$

It is important to note that the type #150 characteristically departed from the PLVTS beam in free flight at WSMR [2] soon after launch, while the #200 and #250 engines were able to demonstrate good beam-riding capabilities; the #200 proved superior. Due

to this historical precedence and WSMR flight video footage, these three lightcraft were selected for further investigation at RPI. Using the twin Lumonics K-922M laser system, the axial and beam-riding behavior of these engine geometries were investigated, as well as the German “Bohn” bell.

4.1.1 Axial Impulse Investigation

Early experiments (1996-1999) performed at WSMR with the PLVTS laser [30] found that C_M values were highly dependent on laser pulse duration, and peak power. The shortest pulse that PLVTS could deliver was 5 μs , and as presented in Fig. 4.1 for the #200-11/10 engine: the improvement in axial C_M over the 18 μs data is notable, especially at low pulse energies.

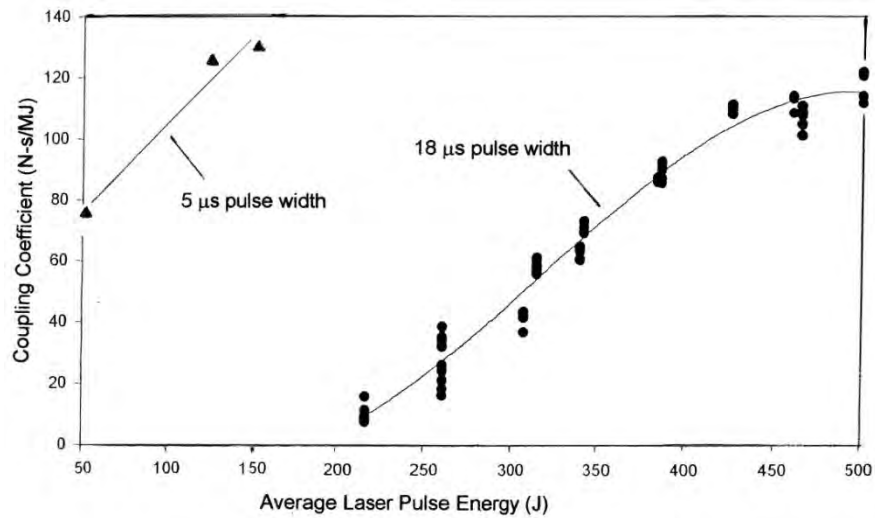


Figure 4.1. Axial C_M vs. E_p for #200-11/10 engine (PLVTS laser, 23-24 May 1999).

With the K-922M laser system, the C_M values obtained from the #200-2/3 engine using both High Gain and LaserMark 5 (LM5) laser gas mixtures (see Table 4.1) were investigated; the results are plotted in Fig. 4.2 against laser pulse energy. With the High Gain (HG) mix, C_M reaches a plateau at much lower energies than with the LM5 mix, due to elevated peak power in the spike (and decreased energy in the tail), as evidenced in Fig. 4.2. Since it generated superior performance throughout the lower pulse energies, the High Gain laser mixture was used in all subsequent ballistic pendulum experiments.

Table 4.1. K-922M Laser gas mixture compositions.

Laser Gas	CO ₂ (%)	N ₂ (%)	CO (%)	H (%)	He (%)
LM5	8	16	4	0.5	71.5
HG	28	16	4	0.5	51.5

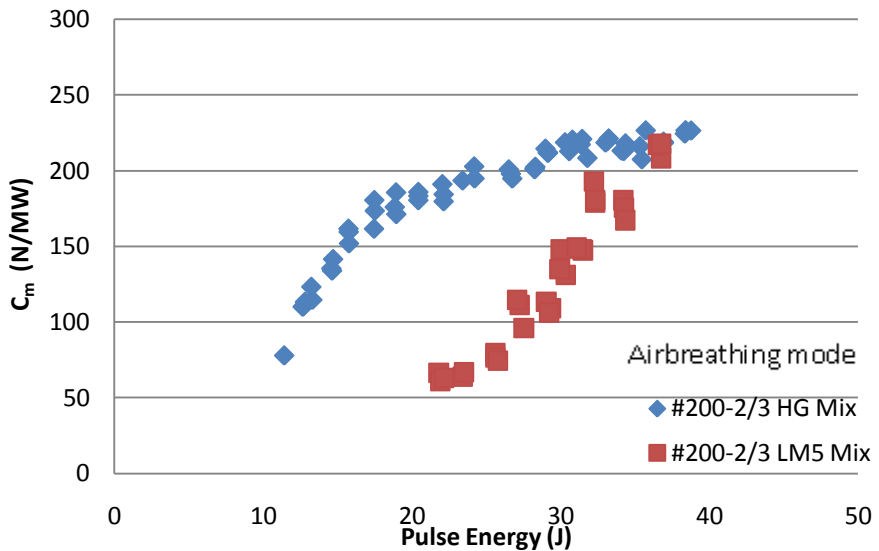


Figure 4.2. Axial C_M vs. E_p for two different laser gas mixes (#200-2/3).

Further experiments examined the effects of varying the ratio of incident beam size to the lightcraft optic diameter ratio. Figure 4.3 shows the relative scale of the three engine sizes investigated (#200-2/3, ¾, 5/6 scale; or 97.73 mm, 109.9 mm, and 122.2 mm, respectively) vs. a circular laser beam (36.6 mm diameter) with the same cross-sectional area as the K922M's 30 x 35 mm beam (used in the AIMD experiments). As indicated, the included focus angles, α , as the beam reflects off the rear parabolic optic for the #200-2/3, #200-3/4, and #200-5/6 engines are 26.4°, 23.5°, and 19.7°, respectively for this beam size. Larger engines employing the unexpanded beam have inherently smaller α angles. *[For the actual rectangular 30x35 mm beam, α would, in practice, vary as a function of position around the shroud; in order to simplify this analysis, the beam has been approximated as a circle with a cross-sectional area identical to the square beam.]* This variance in α , as expected, influenced the beam-riding performance data gathered test series.

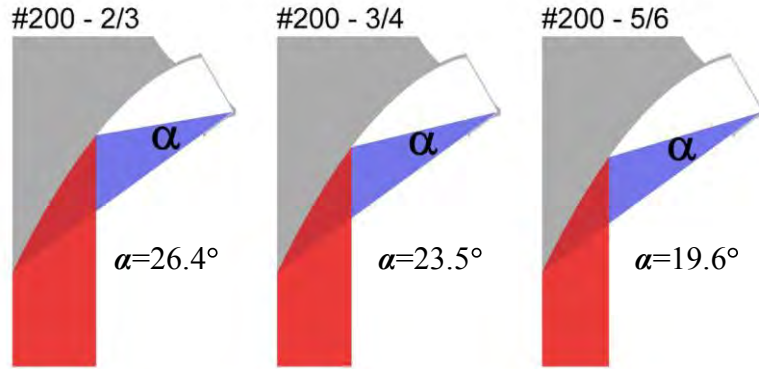


Figure 4.3. Induced focus angle, α , for #200-2/3, #200-3/4, and #200-5/6 engines.

Axial coupling coefficients are maximized with the HG and LM5 gas mixes (see Fig. 4.4), when the incident beam size to the optic diameter ratio is close to one (i.e., when α is maximized)—as with the #200-2/3. In the ballistic pendulum setup, α values for the 2/3, 3/4, and 5/6 engine sizes were 39.1° , 32.8° , and 28.2° , respectively; in the AIMD setup, they're 26.4° , 23.5° , and 19.7° , respectively. Note that with the #200-2/3 engine, axial C_M exceeds 200 N/MW for $E_P > 24$ J, whereas the larger 3/4 and 5/6 engines peak at only ~ 140 N/MW. One useful figure of merit that can provide useful insight is the engine's linear energy density (measured in Joules/cm) deposited into the annular focal ring (i.e., E_P /focal ring circumference). Note in Fig. 4.5 the axial C_M values are still reduced when plotted as a function of pulse energy, normalized by annular focal length to account for variations in engine scaling. For this reason, subsequent experiments standardized on the 2/3 scale engines (i.e., 97.73 mm diameter), in order to exploit the high α values.

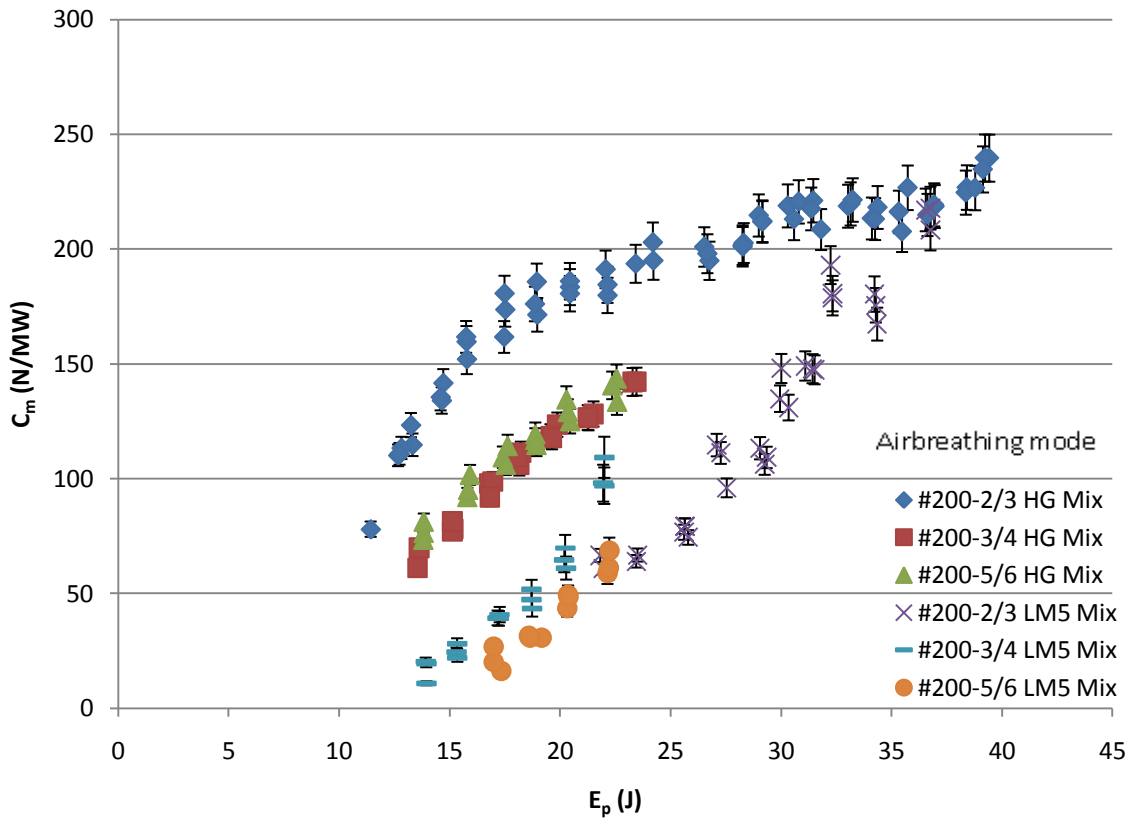


Figure 4.4. Axial C_M vs. E_p for High Gain laser mix (#200 family).

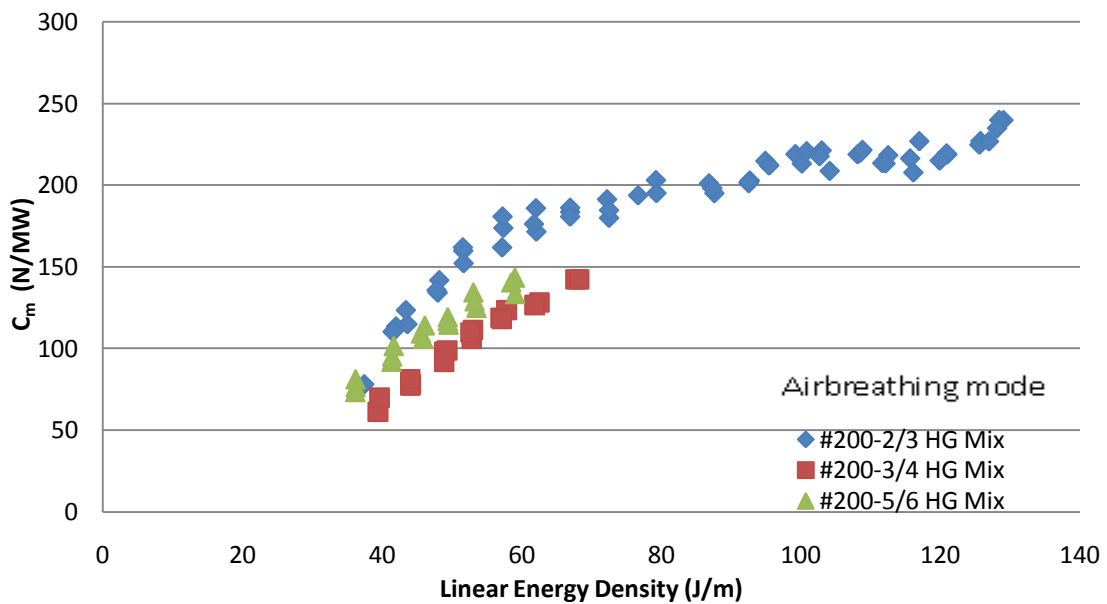


Figure 4.5. Axial C_M vs linear energy density for #200 sizes and HG mix.

As shown in Fig. 4.6, axial C_M performance of the three member lightcraft engine family is very similar, with the #150 only slightly outperforming the #200 and #250. This difference can perhaps be attributed to the #150 engine's longer optic over which the expanding blast wave can generate an improved axial impulse. All engine geometries achieve peak axial C_M values in the range of 220-250 N/MW. Further increases in laser energy deposition would produce stronger blast waves that wrap around the engine shroud and nose, reducing the axial C_M .

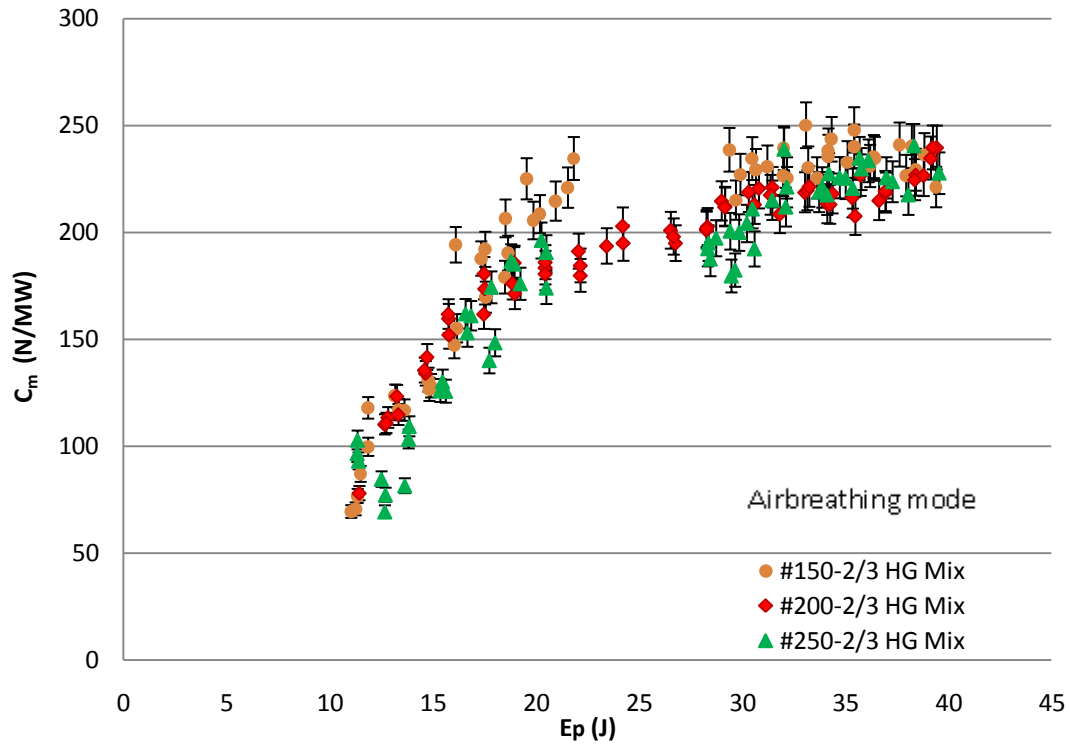


Figure 4.6. Axial C_M vs. E_p for the family of lightcraft geometries.

Prior German experiments on the “Bohn” bell [6] and the Type #200-3/4 lightcraft have indicated that the bell provides greater C_M values at 1 atm, as seen in Fig. 1.5; these tests employed a DLR electric discharge CO₂ laser with a pulse duration of 11 μ s. However, with the K-922M at pulse energies beyond 20 Joules, as seen in Fig. 4.7, the axial C_M values of the German bell are very similar to the Type #200; below 16-18 J, when the #200 engine is still “turning on,” the bell performance is slightly better.

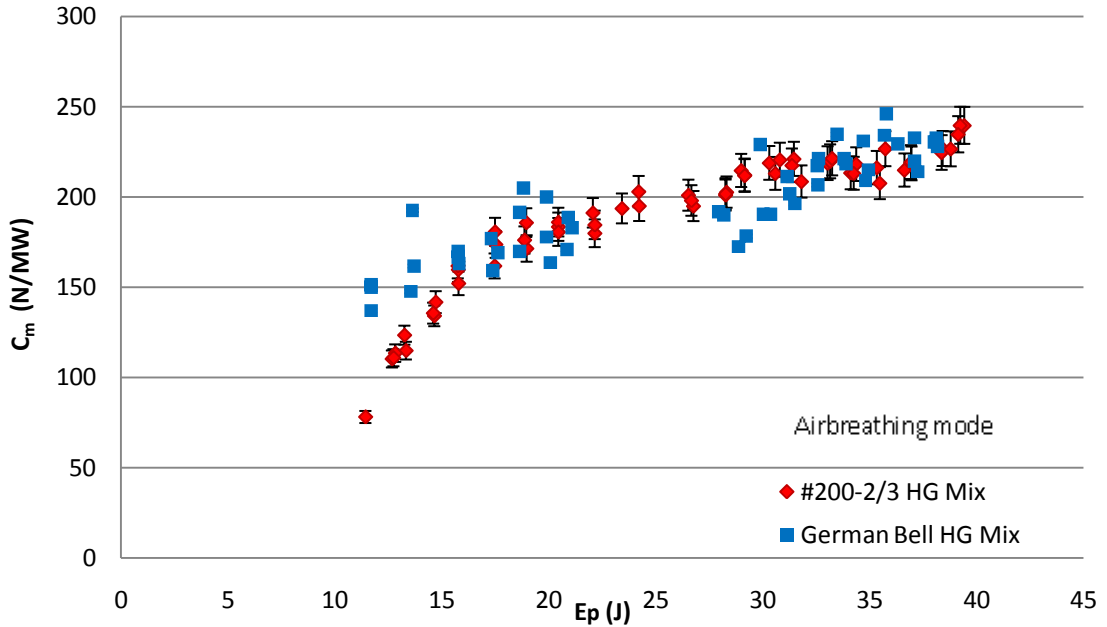


Figure 4.7. Axial C_M vs. E_p comparing the bell and #200 geometries using the K-922M laser system.

4.1.2 Lateral and Angular Impulse Investigation

The impulsive thrust generated by a lightcraft engine will be vectored when a lateral offset exists between the engine and laser beam centerlines; the lateral component of this impulse is referred to as the beam-riding impulse. This lateral impulse is generally zero when the vehicle or engine is “centered” on the laser beam, and grows with increasing lateral offset as long as all the laser beam energy is captured into the engine. Figure 4.8 gives a rear view of the #200-3/4 engine (109.9 mm diameter) showing relative scale of the 36.6 mm circular laser beam, for the on-axis “centered” and offset positions.

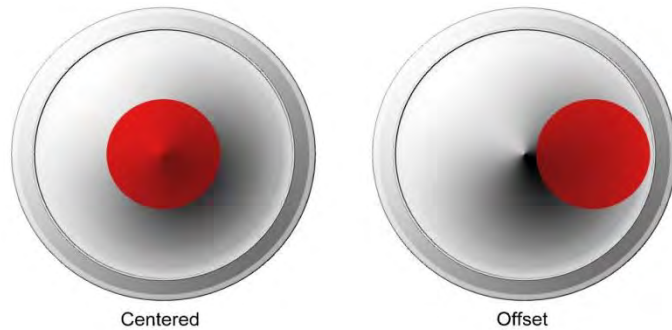


Figure 4.8. Rear view of #200-3/4 engine showing relative scale of circular laser beam with same cross-sectional area as K-922M's 30 x 35 mm rectangular beam (AIMD experiments).

Using the AIMD apparatus described earlier, a series of experiments were performed to determine the lateral and angular impulses imparted upon each of the engine geometries as a function of lateral offset. Figure 4.9 shows the lateral C_M vs. offset performance of the #200-3/4 engine with both LM5 and High Gain mixes, for a constant pulse energy of 20 J. Peak C_M values for both mixes are 75 N/MW, but the behavior at small offsets (i.e. less than ± 15 mm, or $\sim 13.6\%$ engine diameter) exhibits much less scatter with the High Gain mix. On larger engines, the laser flux and fluence around the annular focus is barely sufficient to ignite LSD waves, so resulting impulses are random (perhaps driven by small pulse-to-pulse energy variations, and laser-induced breakdown losses at the optic tip). Nevertheless, once lateral beam offset exceeds a certain threshold distance, focal flux/fluence becomes sufficiently elevated to generate consistent impulses.

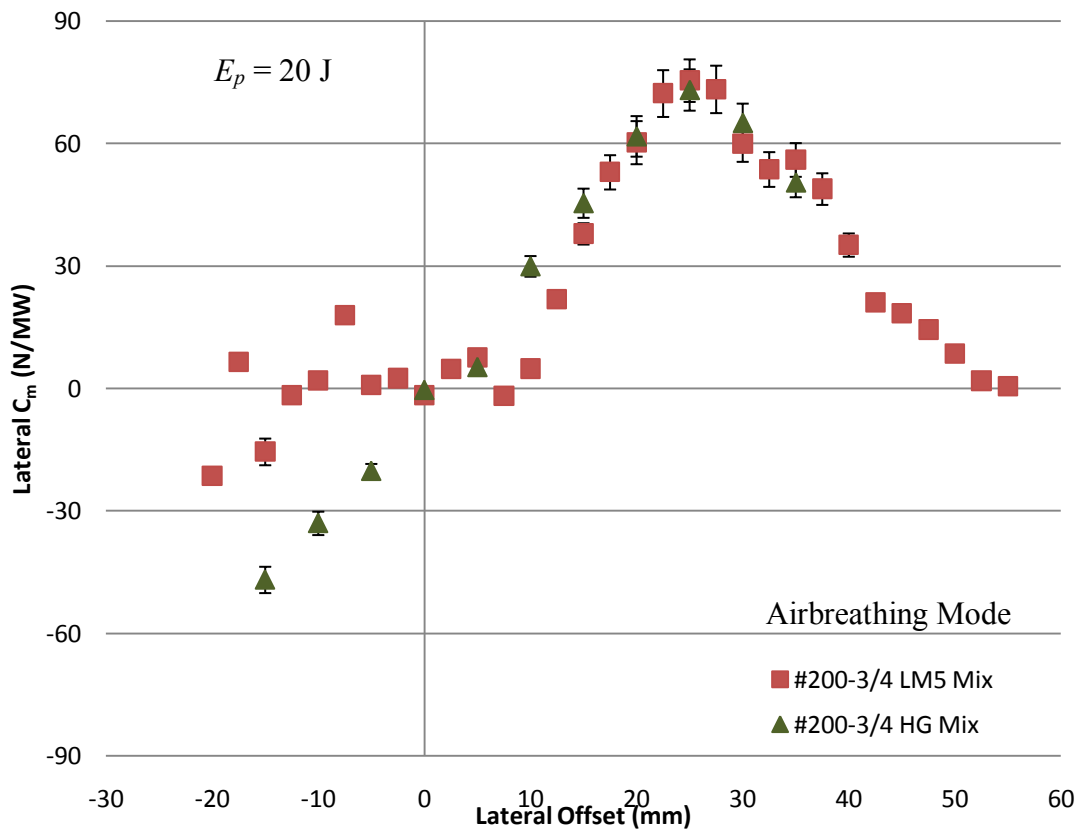


Figure 4.9. Lateral C_M vs. offset; $E_p = 20$ J (#200-3/4).

Lateral momentum coupling coefficients are plotted against lateral offset of the laser beam in Fig. 4.10 (20 J, LM5 mix). Note that maximum values ranged from 53 N/MW for the #200-5/6 engine to 75 N/MW for the #200-3/4 engine. This is a significant increase (5x) from prior values of 15-16 N/MW [9] with the PLVTS laser at WSMR.

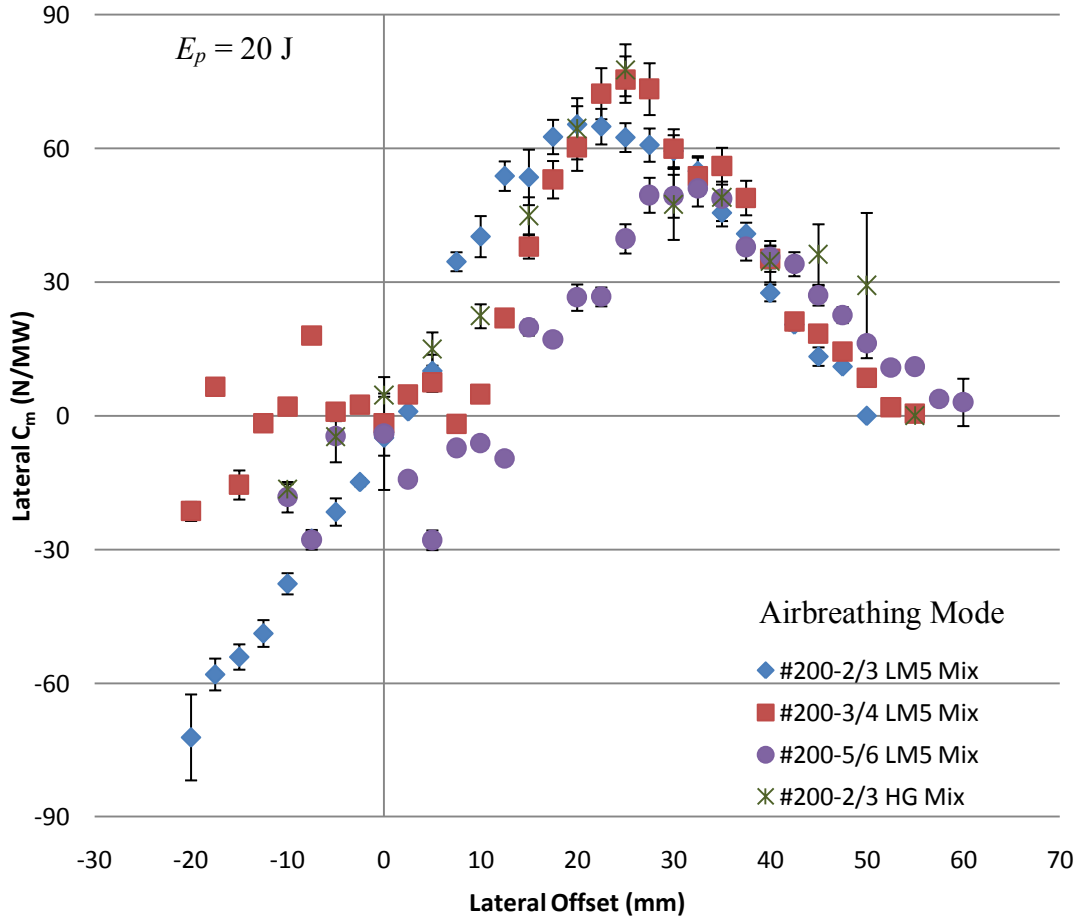


Figure 4.10. Lateral C_M vs. offset; $E_p = 20$ J (#200 lightcraft family).

For all AIMD tests, the laser beam size was maintained constant at the unexpanded 30 mm x 35 mm dimensions, but for larger engines, α decreases, as mentioned earlier. Note in Fig. 4.10 that the lateral C_M and impulse become vanishingly small at zero lateral offset, and increase with offset to a maximum, whereupon the engine begins to “spill” laser energy. This beam “spilling” condition, in turn, reduces the integrated impulse delivered by laser-generated blast waves expanding over the engine. Likely causes for the elevated lateral C_M (i.e., relative to PLVTS) include a much shorter laser pulse

duration (100 ns vs. 18 μ s of PLVTS), and reduced laser pulse energy—i.e., providing a significantly improved match for small lightcraft engine sizes examined here. Note in Fig. 4.10 that max lateral C_M values of the #200-3/4 are slightly higher than the #200-2/3 engine when using the LM5 mix, a surprising circumstance when compared to the axial results. However, the peak values obtained with the HG mix are very similar for these two engines, with the #200-2/3 model slightly outperforming the #200-3/4, as expected.

The #150-2/3 and #250-2/3 scale (97.7 mm diameter) geometries were investigated using the HG mix, as it improved reliability of the beam-riding behavior at small offsets. Note the 2/3 scale also provides optimal α values. The beam-riding capabilities of the engine geometries are evident in Fig. 4.11. The #200 geometry, as expected, provides the largest lateral impulse, peaking at \sim 75 N/MW, while the #250 reaches a peak at 35 N/MW. These values are both still significant increases over the PLVTS WSMR data found by both Libeau and Myrabo on 11/10 scale engines (162.2 mm diameter) [9]. As with the axial impulses, this is attributable to: 1) the too large pulse energies from PLVTS creating blast waves powerful enough to wrap around the shroud, and back up on the nose – negating available impulse, and 2) the short pulse duration and resulting high peak powers of the K-922M laser system. Note that the lateral C_M value for the #150 geometry goes negative, thereby pushing the vehicle off the laser beam rather than causing a beam-riding behavior. This result explains the trend noted by Myrabo at WSMR [2] for the #150 to predictably depart from the laser beam every time during free flights, shortly after launch.

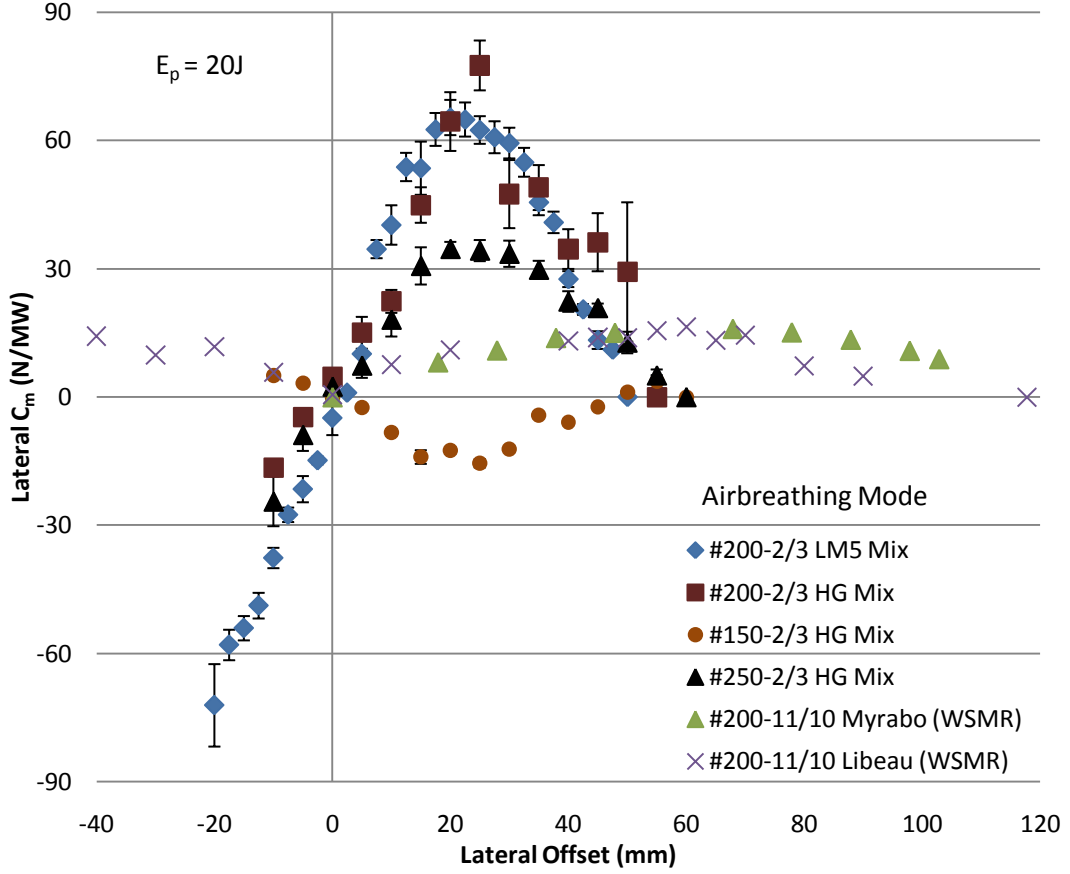


Figure 4.11. Lateral C_M vs. lateral offset for various AB lightcraft geometries.

German investigations of the beam-riding capabilities of the “Bohn” bell geometry [12, 31] have quantified only small portions of their engine’s beam-riding performance curve using video analysis of free flights. Lateral C_M values of 9 to 21 N/MW have been witnessed for orbital radii of 2.5 to 10 mm, respectively. However, the database is sparse and beam-riding performance curves vs. lateral offset had yet to be directly measured experimentally. Using the AIMD with the K-922M laser, lateral C_M values of the “Bohn” bell geometry were found for offsets from 0 to 45 mm (0-45% engine diameter), as shown in Fig. 4.12. Note how the values are at least 10x smaller than the off-axis parabolic #200 lightcraft engine’s. Also of note are the large error bars associated with C_M data greater than 2 N/MW. This experimental measurement error is due to large fluctuations shot-to-shot in the recorded angular velocity of the rotor, which is partially due to the diminutive lateral impulse and AIMD rotor response (with the bell engine

mounted) – all within the noise of the RVDT, despite the reduced spring constants applied in this bell engine experiment. The beam-riding abilities of the bell engine appear erratic and irregular at best. Regardless of the large error bars, the only region in which a non-zero beam riding impulse appears is for offsets up to 15 mm (15% engine diameter). At offsets of 20-35 mm, the craft will be pushed off the beam by lateral impulses, albeit small ones. This is consistent with the free flight results of Scharring et.al. [31]: the 100cm diameter bell engine will ride the beam in free flight, but only with very small offsets (i.e., $\sim 20\%$ engine diameter or less); otherwise it will depart from the beam.

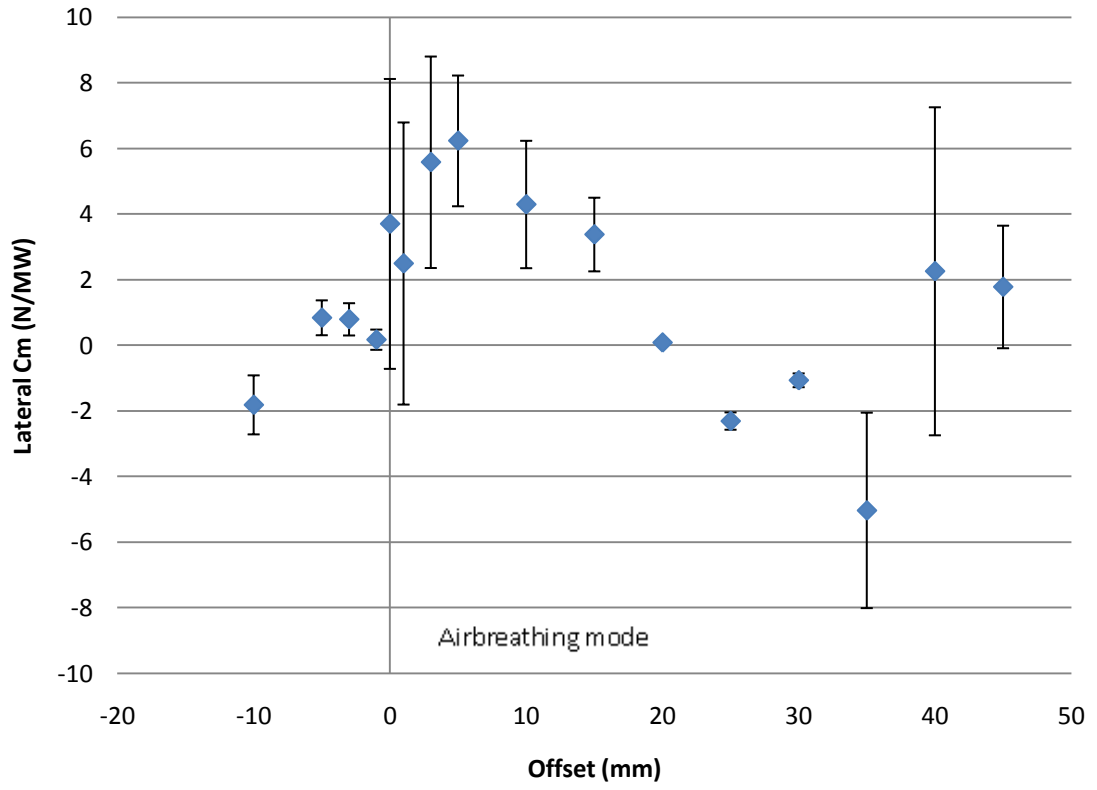


Figure 4.12. Lateral C_M vs. lateral offset for the 10 cm German “Bohn” bell geometry.

As is evident in Fig. 4.13 (mostly LM5 mix), pitching angular impulse data for the #200-2/3 is well behaved and basically reflects trends evident from the lateral C_M data in Fig. 4.10. However, LM5 data for the larger engines (3/4 and 5/6; i.e., with small α included angles) appears somewhat erratic for reasons that will hopefully become clear after

further testing with more expanded laser beams (i.e., designed to flood the entire rear optic). Apparently, when α is too small (i.e., small beam-to-engine diameter ratios), the pitching moment data may be influenced by asymmetric laser-induced breakdown effects around the annular line focus; this may be caused by lowered laser flux and fluence, when barely sufficient to ignite LSD waves. However, note that the $\frac{3}{4}$ engine data with the HG mix is well behaved, with minimal scatter at small offsets. As shown in Fig. 2.11, a negative moment means the vehicle nose will be tipped toward the center of the beam (for positive lateral offsets).

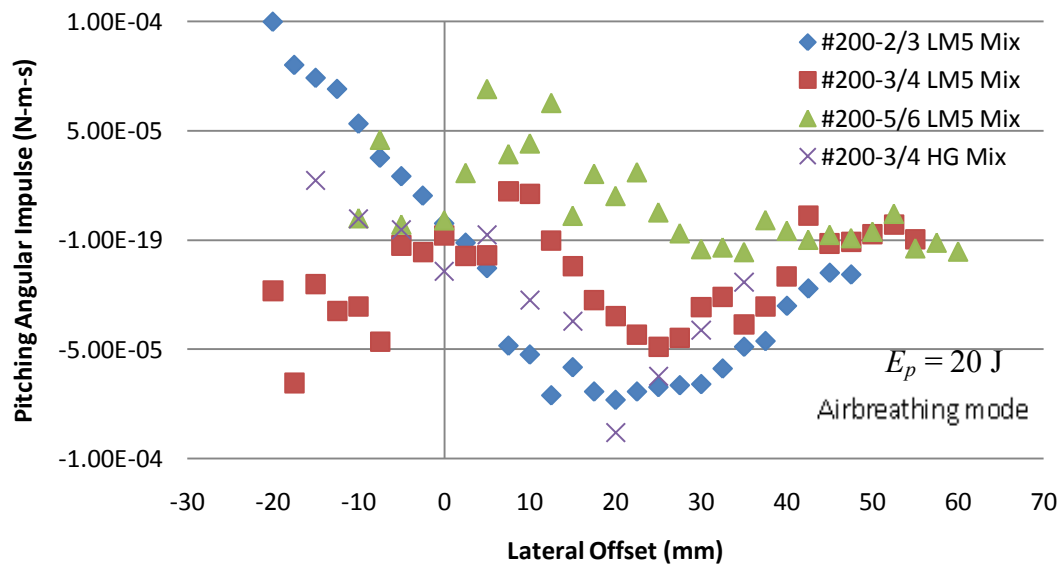


Figure 4.13. Pitching angular impulse vs. lateral beam offset (#200 engine family).

The angular impulses seen in Fig. 4.14 for the lightcraft family revealed that the #200 lightcraft nose will tip towards the laser beam, while the #250 and #150 generate tipping moments that tip their noses away from the beam axis. However, note the angular impulse values for the #250 are an order of magnitude smaller than the #150 and #200, so such moments probably have little effect on flight performance. Angular impulse data for the German “Bohn” bell data series was omitted from the figure because no discernable trend was evident, and the values were 10x smaller than for the #150 and #200. In summary, the flight-proven beam-riding capabilities of the #200 are apparently due to both the superior lateral restorative impulses provided, and also the

tendency for the engine or vehicle to tip itself, vectoring the axial impulse toward beam axis.

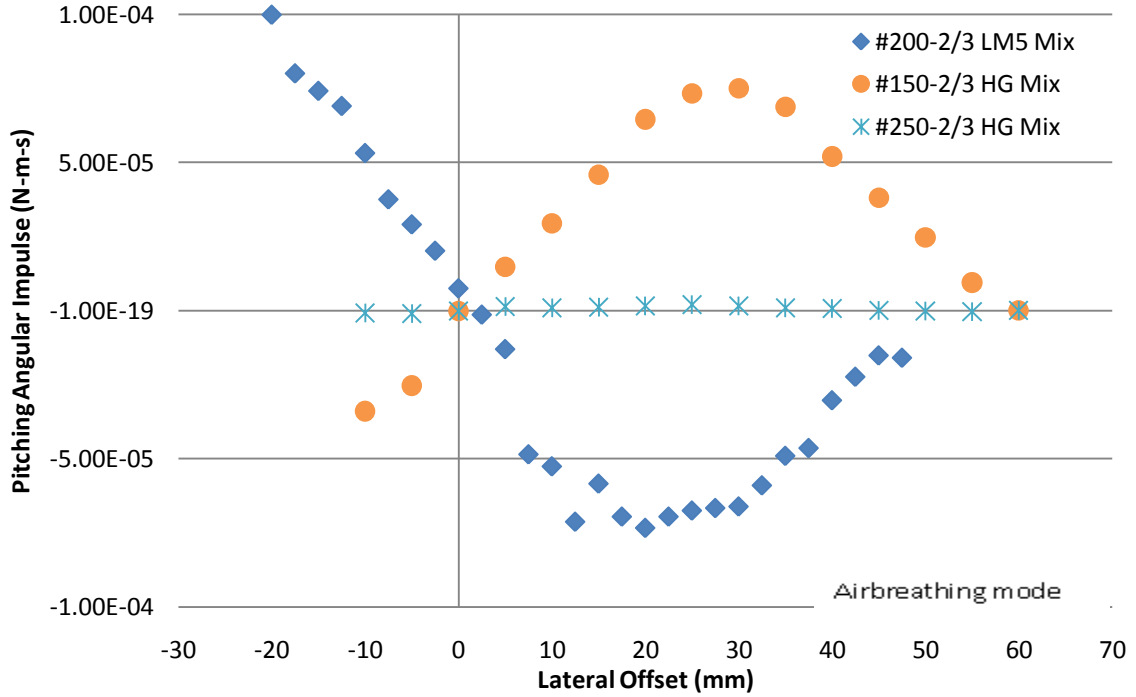


Figure 4.14. Pitching angular impulse vs. lateral offset for family of lightcraft geometries.

In order to visualize the vectored thrust measured in AIMD experiments, high speed Schlieren movies were recorded for each of the Lightcraft engine geometries at prescribed offsets of 10, 20, and 30 mm, representing $\sim 0\%$ engine diameter (D_e), 10% D_e , 20% D_e , and 30% D_e , respectively. This schedule of offset points considered the minimum and maximum lateral C_M values, as well as selected points along the beam-riding curve. The blast emerging from each engine can be clearly seen in Figs. 4.15 – 4.18; downward vectoring of the exhaust plume with increasing offsets is especially pronounced with the #200 and #250 engines. Note that the blast wave is much stronger off the illuminated (lower) side of the optic, providing enhanced lateral impulse to the shroud on that side. For the #150 geometry, it is possible that the lateral impulse generated from the blast wave reflected off the longer optic might be greater than the lateral impulse provided directly from the shroud, thereby resulting in a negative beam-riding effect. Finally note that the German bell vectors the blast wave minimally, indicating little or no beam riding ability, as confirmed experimentally.

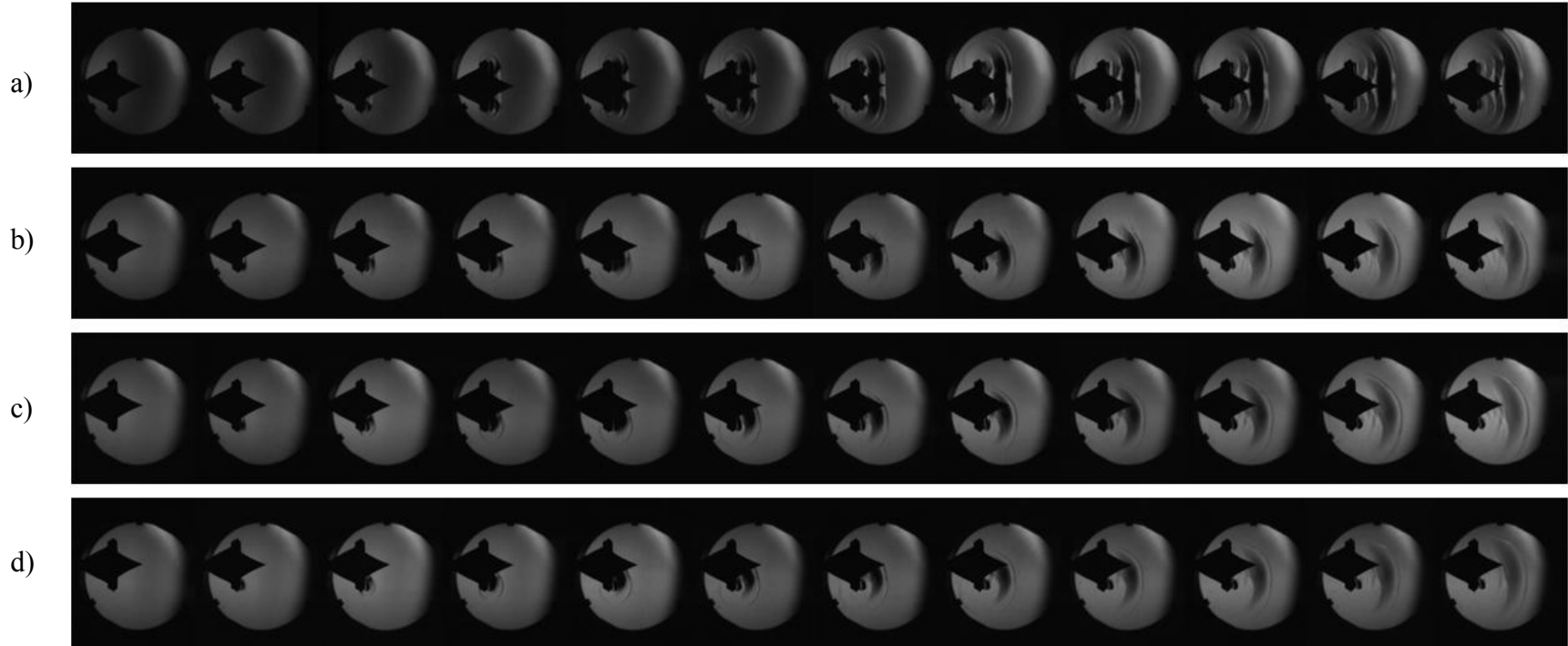


Figure 4.15. Schlieren photography of #150-2/3 with laser offset downward from engine centerline by: a) 0% engine diameter (D_e), b) 10% D_e , c) 20% D_e , d) 30% D_e . (~13 J pulse, ~20.5 μ s step).

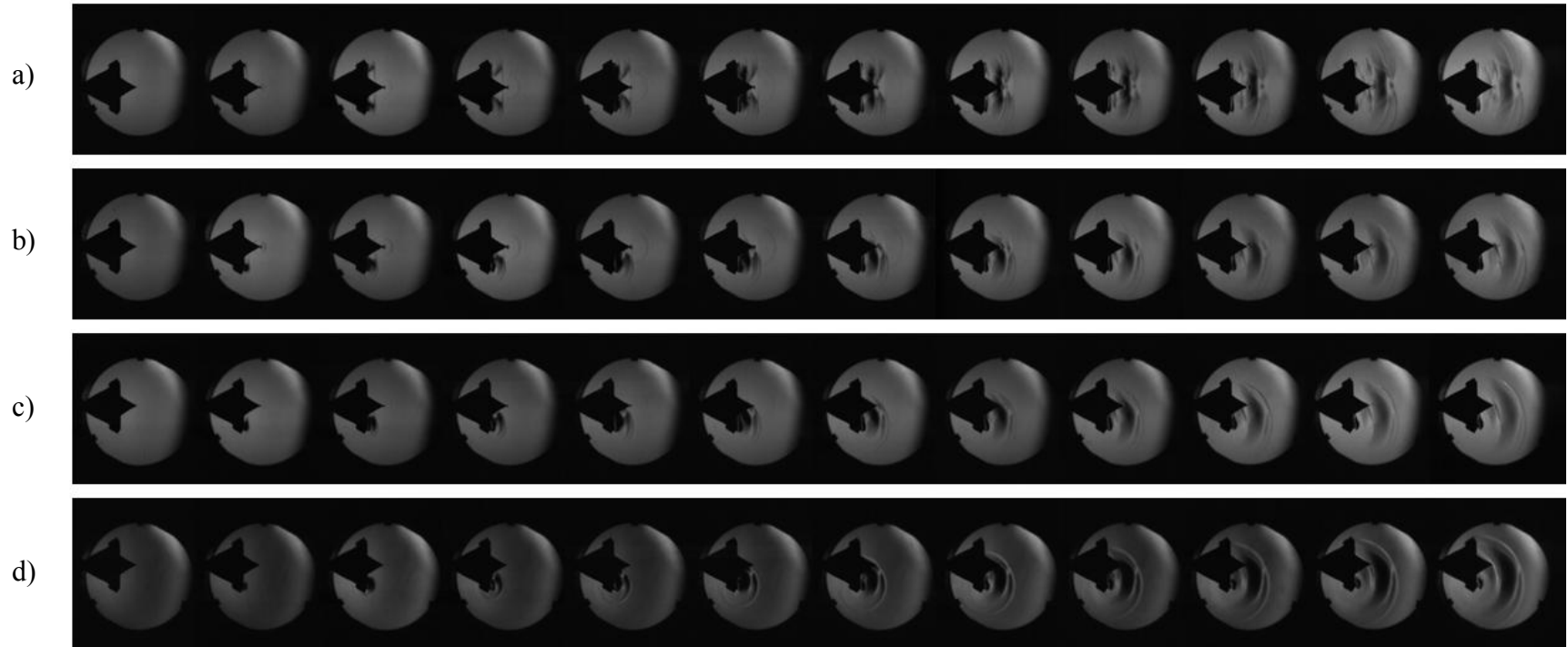


Figure 4.16. Schlieren photography of #200-2/3 with laser offset downward from engine centerline by: a) 0% D_e , b) 10% D_e , c) 20% D_e , d) 30% D_e . (~13 J pulse, ~20.5 μ s step).

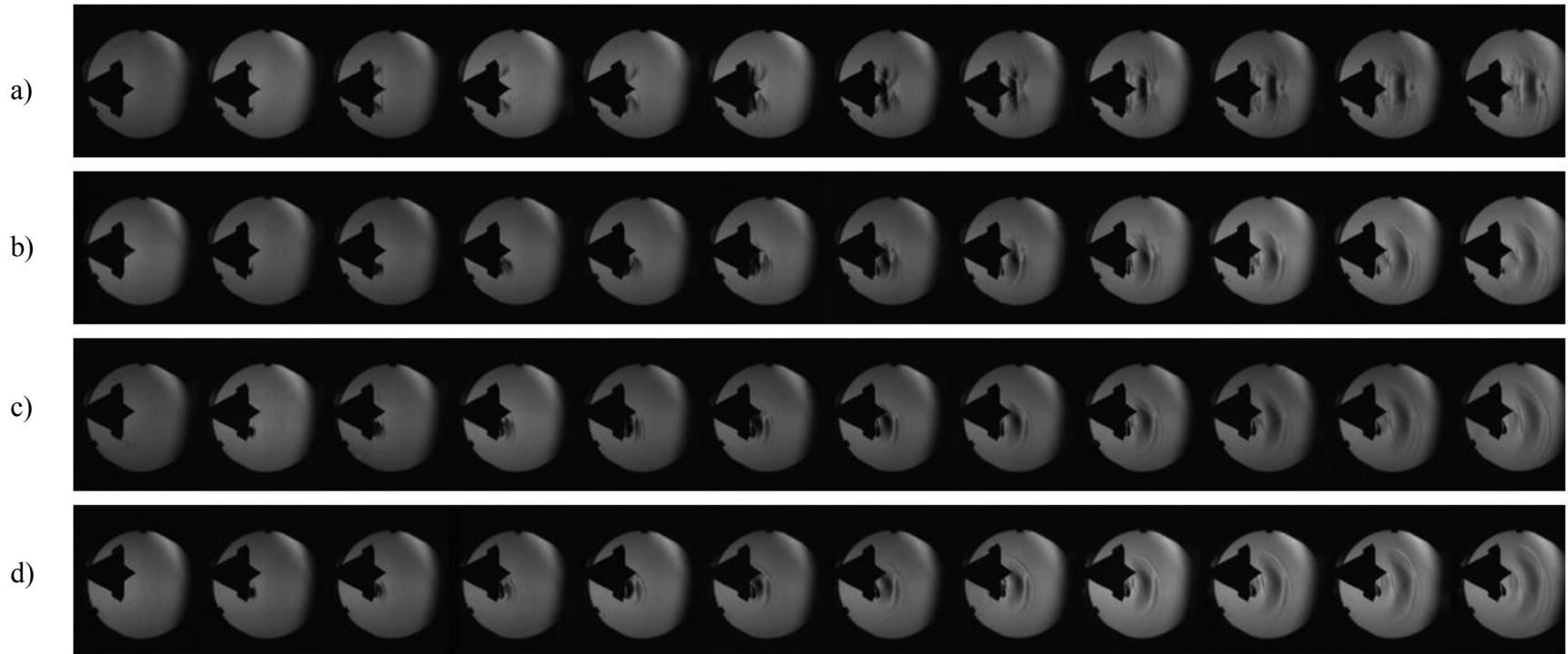


Figure 4.17. Schlieren photography of #250-2/3 with laser offset downward from engine centerline by: a) 0% D_e , b) 10% D_e , c) 20% D_e , d) 30% D_e . (~13 J pulse, $\sim 20.5 \mu\text{s}$ step).

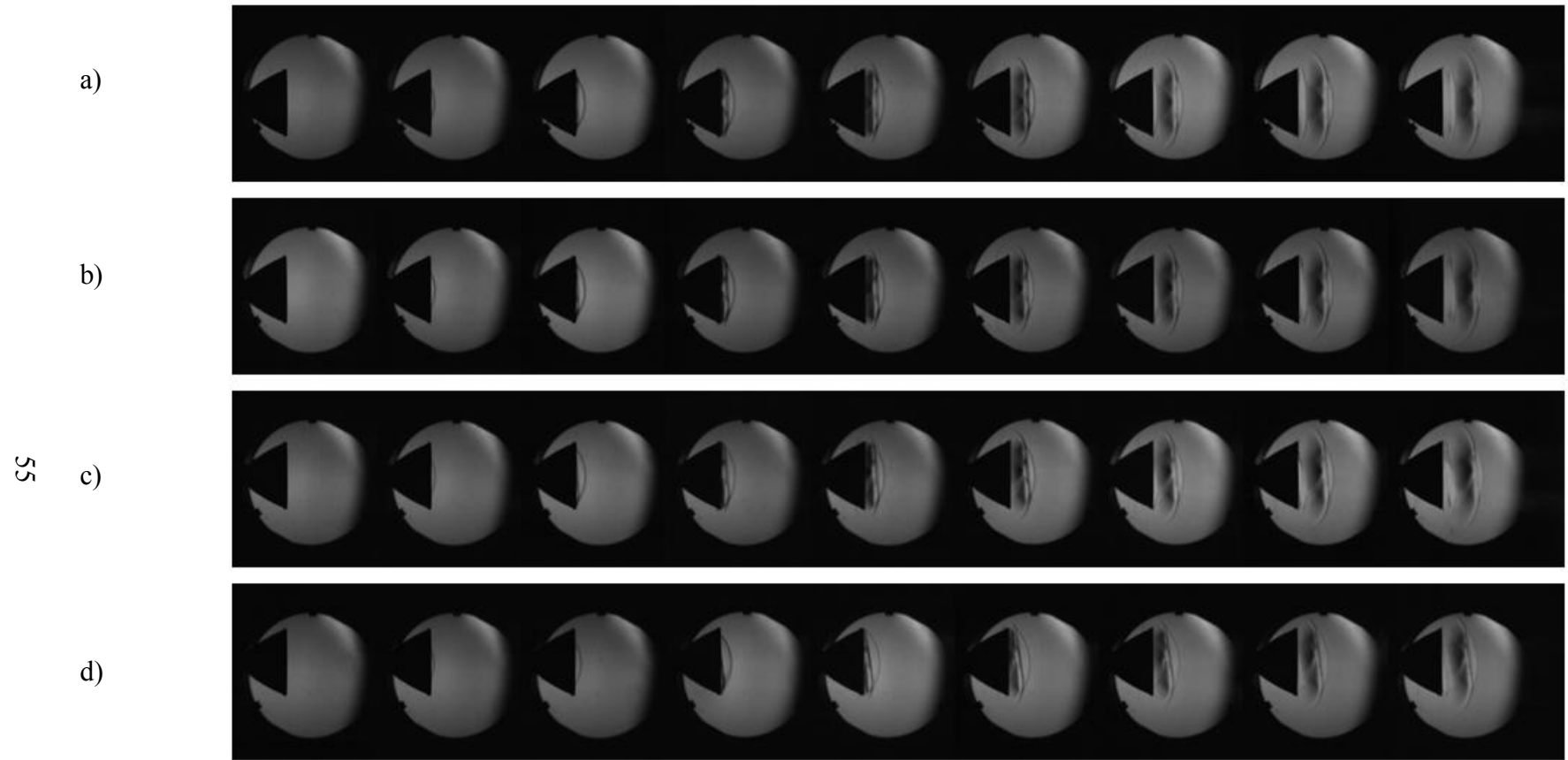


Figure 4.18. Schlieren photography of German bell with laser offset downward from engine centerline by: a) 0% D_e , b) 10% D_e , c) 20% D_e , d) 30% D_e (~13 J pulse, ~20.5 μ s step).

4.1.3 Engine Refresh Investigation

Optimal laser pulse repetition frequencies (PRF) will be required by lightcraft engines accelerating along airbreathing launch trajectories to orbit through subsonic, supersonic, and hypersonic regimes. The subsonic regime effects of PRF upon the axial C_M from a two-pulse series were investigated by firing both K-922M lasers with a variable delay between pulses, with the LWBP, to determine the optimal refresh delay interval for the static air-breathing #200 engine. As seen in Fig. 4.19, when two 16 J pulses are fired with zero delay, the result is equivalent to a single pulse at twice the energy (32 J). As the delay is increased to 50-200 μ s, the average axial C_M (for the two pulse series) drops to roughly half of that expected for a single 16 J pulse. This is largely due to a firing into hot, low density (partially refreshed) air still occupying the engine. With longer delays, shroud air is increasingly refreshed, so the second pulse provides larger impulses with larger time-average axial C_M values. [Beyond 3 ms, the LWBP has swung far enough between pulses to cause misaligned delivery of the second pulse, reducing the impulse expected from the second pulse.] The trend in Fig. 4.19 is clearly asymptotically approaching the line representing the expected C_M from a single pulse. Ideal PRFs for liftoff are likely between 250-350 Hz (3-4 ms delay interval), for the conditions investigated (static, closed inlet, ~1 atm background). With an open inlet, ram air would certainly reduce the necessary delay between pulses for ideal C_M values.

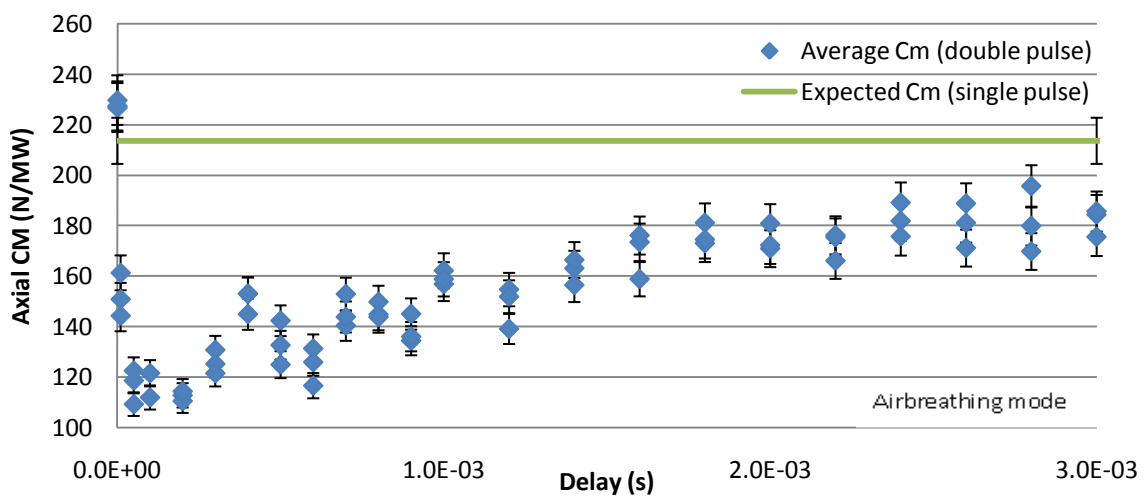


Figure 4.19. Average axial C_M vs. repetition pulse interval (#200-2/3 engine, K-922 M with HG mix).

4.2 Ablative Propellant (Rocket Mode) Experiments

The performance of ablative propellants in pulsed laser rocket engines can be experimentally measured in terms of their momentum coupling coefficients (C_M), specific impulse (I_{sp}), and ablative laser propulsion efficiency (η_{ALP}). Momentum coupling coefficients (C_M) can be calculated from recorded impulse traces (Tektronix scope Model #2014B) using methods and relations described previously. The impulse generated each pulse is given by:

$$\text{Impulse} = \text{_____} \quad (25)$$

The mass ablated per pulse (m_a) is represented by:

$$\text{_____} \quad (26)$$

where V_e is the exhaust velocity, also represented as:

$$\text{_____} \quad (27)$$

Rearranging Eqns. 26 and 27 to obtain I_{sp} :

$$\text{_____} \quad (28)$$

where g is the gravitational acceleration on the surface of the Earth at sea level ($\sim 9.81 \text{ m/s}^2$). The ablative laser propulsion efficiency of the propellant (η_{ALP}) is then:

$$\text{_____} \quad (29)$$

Due to its prior use in flight experiments at WSMR (and its existing performance database), Delrin® was selected for ablative rocket lightcraft experiments with the K-922M laser system. Historically, in US and German experiments, ablative “rocket mode”

engines with Delrin® as a solid ablative propellant have seen increased axial C_M values a factor of ~ 2.5 greater than the airbreathing equivalent [1,2], but this was with the CO₂ electric discharge lasers and 18 μ s pulse durations. Using the K-922M laser system (~ 100 ns FWHM pulse duration) and the #200-2/3 engine geometry with a Delrin® propellant ring, the maximum axial C_M values were found to be 467 N/MW, or an increase of 2x over airbreathing values, as seen in Fig. 4.20. Note the similarities in the airbreathing and “rocket mode” axial C_M trends.

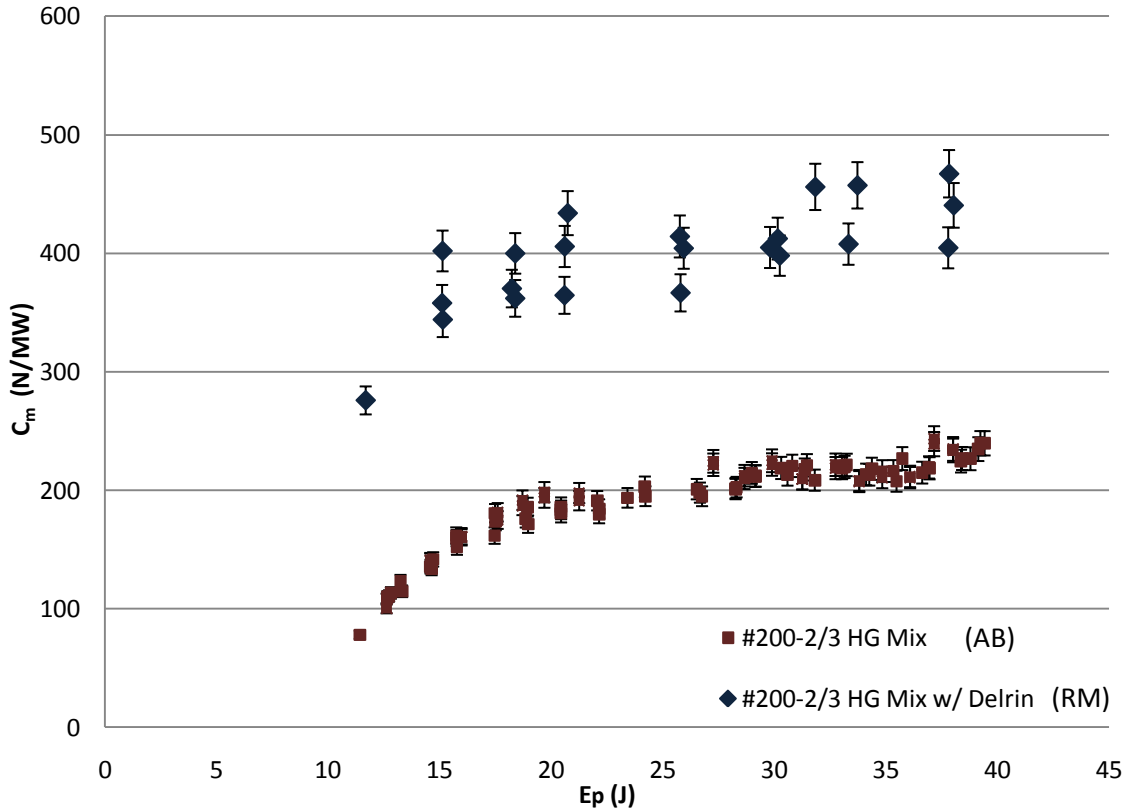


Figure 4.20. Axial C_M vs. pulse energy for airbreathing (AB) and “rocket mode” (RM) engines.

No previous experimental campaigns have investigated and quantified the beam-riding phenomena of “rocket mode” lightcraft engines. Prior numerical flight dynamics studies have assumed that “rocket mode” lateral impulses scale in the same manner as the axial impulse performance. Using the AIMD device, the lateral C_M values vs. offset were found to reach a maximum value of 125 N/MW, seen in Fig. 4.21. This value indeed is a

factor of 2 greater than the 65 N/MW associated with airbreathing engines using either HG or LM5 gas mixes, verifying the assumption made in previous numerical flight dynamics studies.

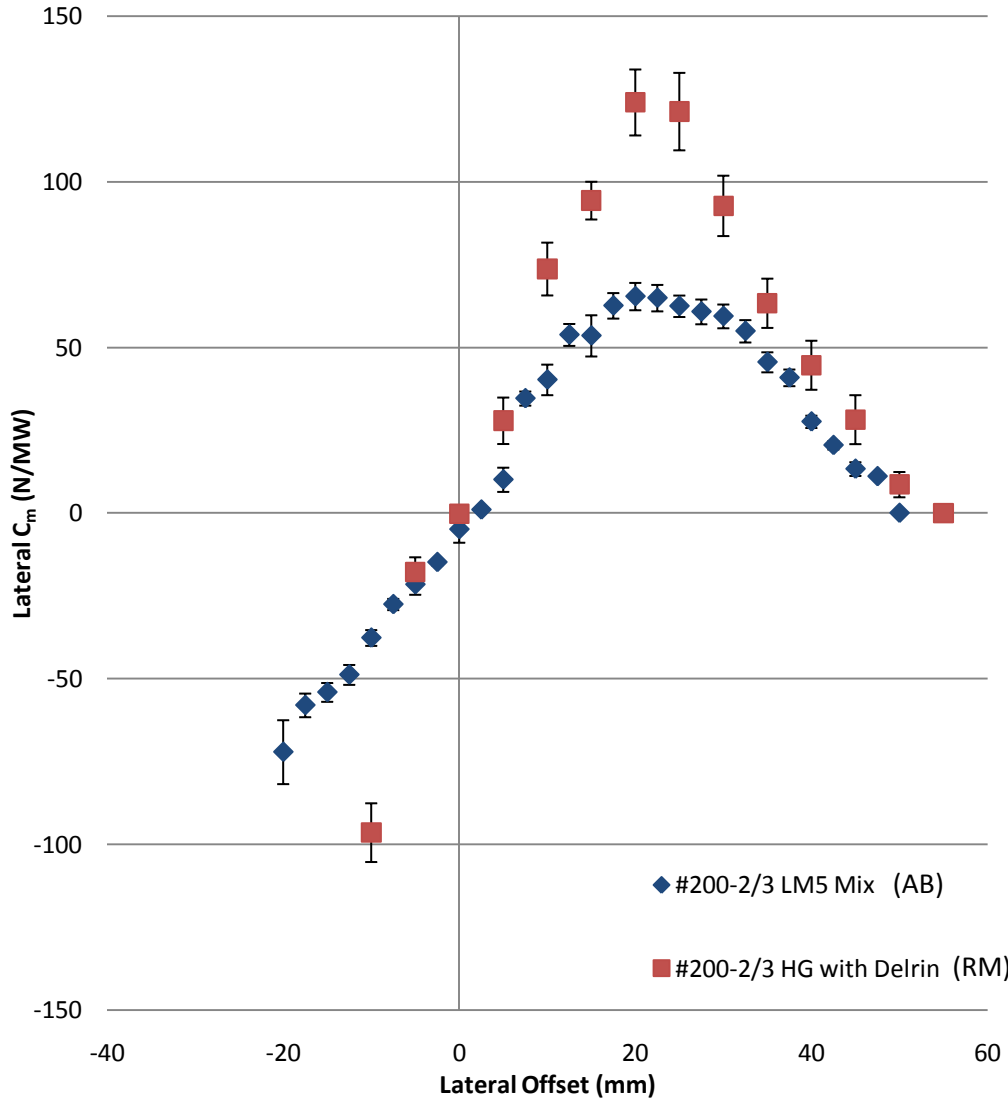


Figure 4.21. Lateral C_M vs. offset for #200-2/3 airbreathing (AB) and “rocket mode “ (RM) with Delrin®.

Quite surprisingly, ablative rocket mode lightcraft engines exhibit pitching impulse magnitudes similar to their airbreathing counterparts, but in the opposite direction (i.e., tipping the vehicle nose out of the beam rather than towards the beam centerline). Note

how similar the trend is to that of the #150 engine data given in Fig. 4.22. These magnitudes are small, and as such they don't prevent the vehicle from successfully riding the beam, as seen at WSMR. The erratic behavior seen at small offsets in Fig. 4.22 is likely due to chipping of the propellant, which occurred during that portion of both the extended and retracted portions of the AIMD experiment.

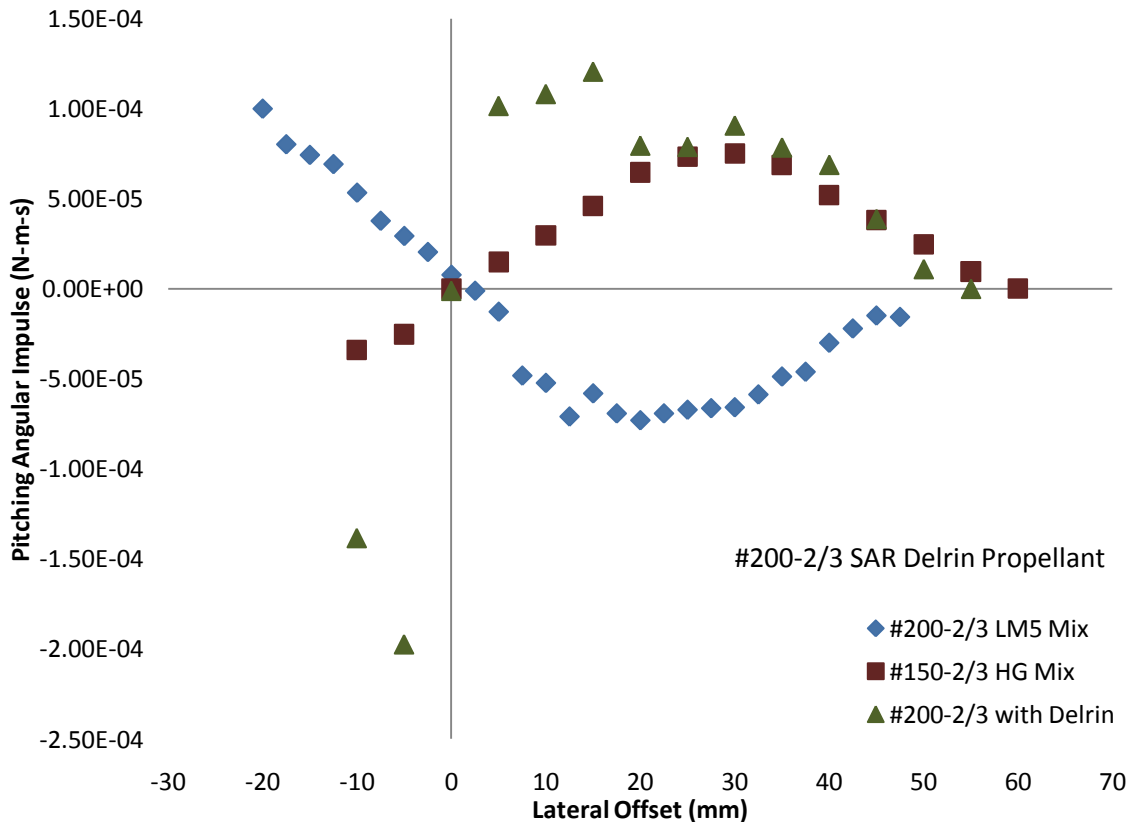


Figure 4.22. Angular pitching moments vs. lateral offset for airbreathing (AB) and “rocket mode” (RM) #200-2/3 engines.

The propellant ablated was measured every three pulses using a OHaus Model TP200S electronic balance, accurate to 0.001 grams. The total pulse energy deposited into the engine was also measured using a Gentec-EO Model QE55 laser energy meter. The average propellant ablated per joule laser pulse energy, and the total propellant mass ablated per pulse was then calculated. Using this value and the axial data above, the I_{sp} and ablative laser propulsion efficiency (η_{ALP}) were calculated. The I_{sp} was found to fall between 220 and 330 seconds, as seen in Fig. 4.23. These values slightly exceed the 190

seconds quoted by Pakhomov [11] in previous vacuum experiments; however, this can be attributed to augmentation from the 1 bar lab environment. The η_{ALP} (shown in Fig. 4.24) is generally 40-60%, which is very close to the 50% achieved in vacuum experiments.

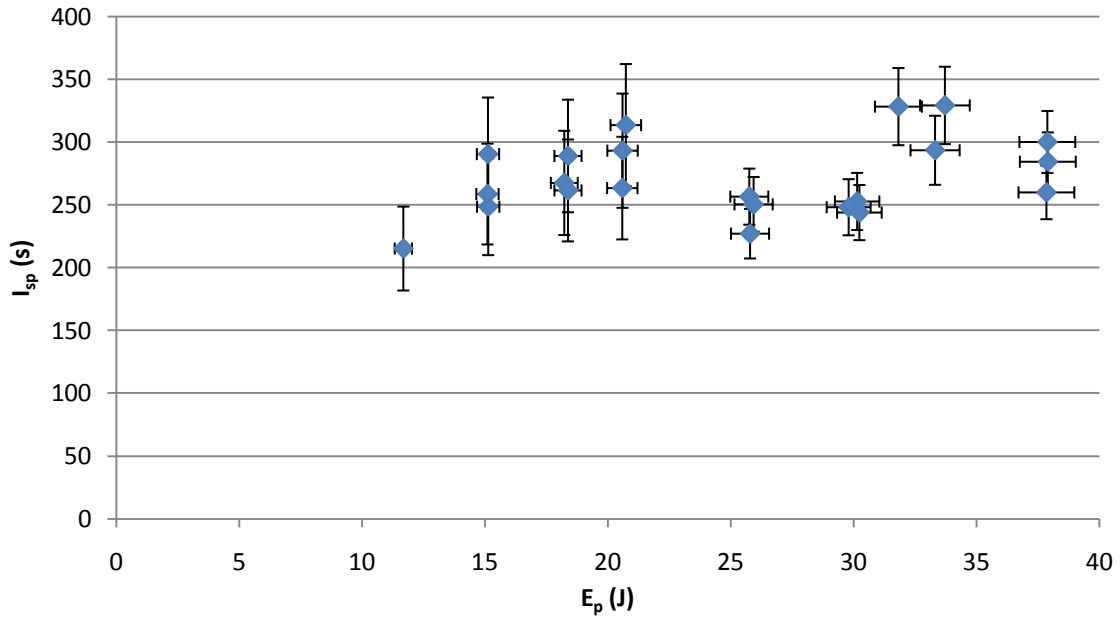


Figure 4.23. Specific impulse vs. pulse energy for axial impulse experiments.

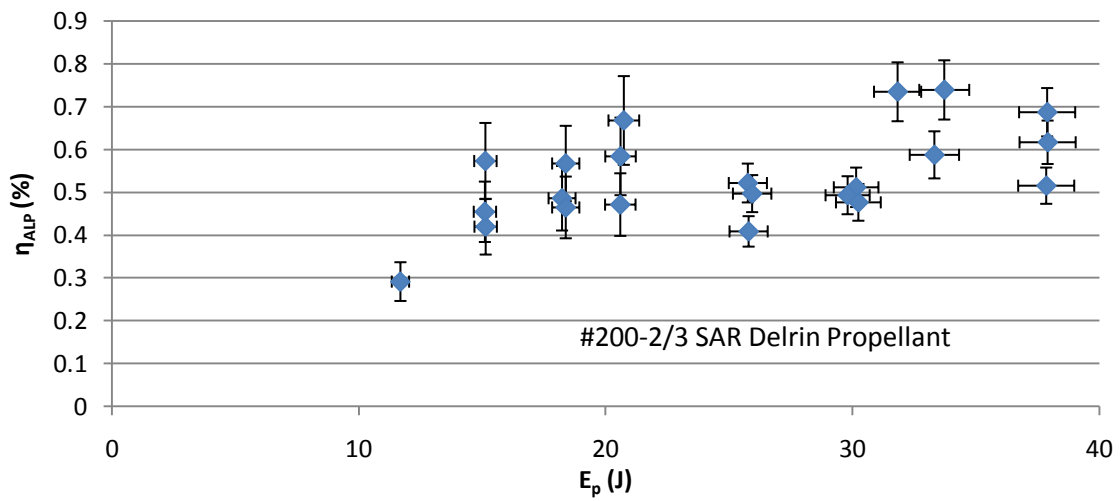


Figure 4.24. Ablative laser propulsion efficiency vs. pulse energy for a series of axial experiments.

4.3 Numerical Investigation: 7-DOF Code

4.3.1 Code Calibration on 16 WSMR Flights

The original 6-DOF code validation/calibration procedure (before the seventh degree of freedom was added) is given in Fig. 4.25. In validating the flight dynamics model, simulations were run, and re-run for all 16 lightcraft flights in the WSMR database. Using the methods described below, every component model (e.g., laser beam, engine, dynamics, etc.) was isolated such that its effects could be individually assessed and adjusted as necessary.

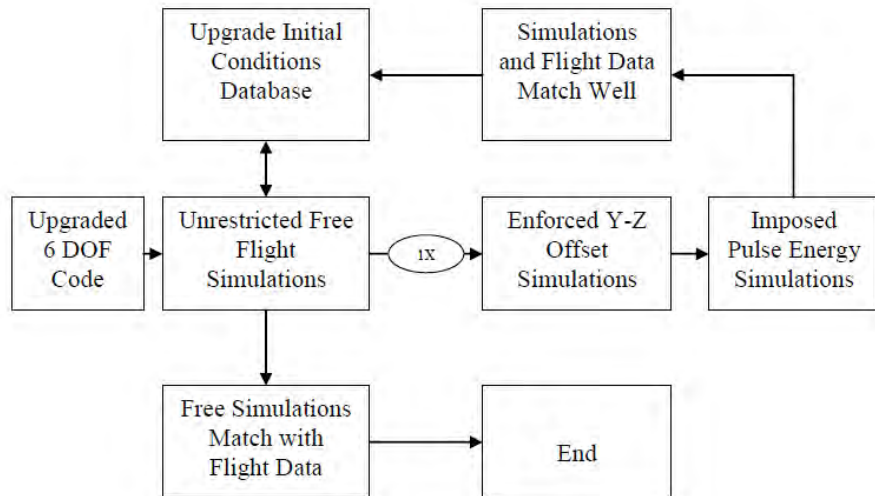


Figure 4.25: Methodology for validation and calibration of upgraded 6-DOF Code.

First to be attempted were 6-DOF simulations designated as “*Free-Flights*”: i.e., craft were permitted to “fly” self-determined trajectories without constraints of any kind imposed. Free-flight simulations successfully modeled the initial portion of the trajectories, but accuracy diminished for flight times extending beyond a few seconds duration. Hence, the 6-DOF component models were believed accurate to the first-order, but further refinement, verification, and calibration of the code was deemed necessary.

An “*Enforced y-z Offset*” study was executed to 1) confirm the validity of axial impulse equations for laser pulsejet engines, and 2) seek an improved “altitude vs. time”

- FINAL REPORT -
- PART 4 -

Volume 2: *Combined Experimental and Numerical Investigations into Laser Propulsion Engineering Physics*

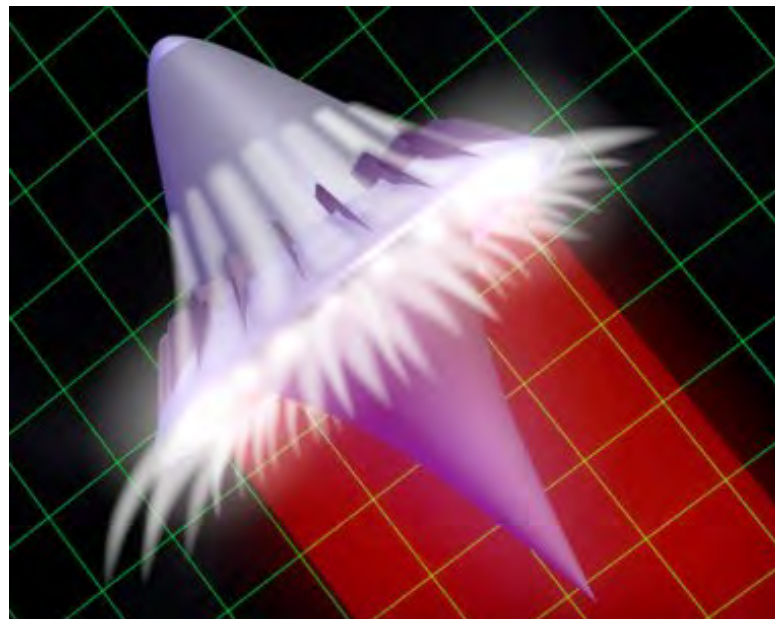
MURI 05 Grant Title: “Basic Research Investigations into Multimode Laser and EM Launchers for Affordable, Rapid Access to Space”

Principal Investigator: Professor Leik N. Myrabo
Rensselaer Polytechnic Institute,
110 8th Street, Troy, NY 12180-3590

Major Contributors: Drs. David A. Kenoyer and Israel I. Salvador

AFOSR Award: FA9550-05-1-0392

Research Period: June 1, 2005 through August 31, 2010 (5 year grant)



Prepared for
Dr. Mitat Birkan
Air Force Office of Scientific Research (AFOSR)
Arlington, VA 22203

31 August 2010

CONTENTS

CONTENTS	i
LIST OF TABLES.....	iii
LIST OF FIGURES	iv
4 RESULTS (CONTINUED)	62
4.4 Numerical Investigation: 7-DOF Code	62
4.4.1 Code Calibration on 16 WSMR Flights	62
4.4.2 Code Calibration Results	64
4.4.3 Simulations of 240cm Lightcraft Flights	69
4.4.4 Simulations Using Experimental Results.....	83
5 DISCUSSION AND CONCLUSIONS	85
5.1 AIMD and LWBP Experimental Results.....	85
5.2 7-DOF Flight Dynamics Code Results	87
6 FUTURE WORK.....	90
6.1.1 Flight Simulation and Flow Facilities.....	90
6.1.2 Static Experiments	92
6.1.3 Vacuum Chamber LP Experiments.....	93
6.1.4 LP Engine Geometry Optimization Studies.....	93
6.1.5 Windtunnel Experiments.....	94
7 REFERENCES	95
8 APPENDICES	99
8.1 Appendix A: AIMD Spring Calibration.....	99
8.2 Appendix B: Sample RVDT Outputs.....	100
8.3 Appendix C: Simulations	102
8.3.1 Flight 1	104
8.3.2 Flight 3	105
8.3.3 Flight 4	107

8.3.4	Flight 6	109
8.3.5	Flight 7	110
8.3.6	Flight 8	112
8.3.7	Flights 10 and 11	114
8.3.8	Flight 12	114
8.3.9	Flight 13	115
8.3.10	Flight 14	115
8.3.11	Flight 15	116
8.3.12	Flight 16	116
8.4	Appendix D: Impact Hammer Calibrations	117
8.5	Appendix E: Sanded vs. Unsanded Optics.....	119
9	Acronyms.....	120

LIST OF TABLES

Table 4.2. WSMR Lightcraft flight trajectory database [12].....	64
Table 4.3. Initial launch conditions for airbreathing lightcraft flights.	65
Table 4.4. Assumed propellant characteristics for 7-DOF simulations.....	70
Table 4.5. MOI and mass of lightcraft components modeled in 7-DOF code.....	73
Table 4.6. Initial launch conditions and results for selected suborbital flights	81
Table 8.1. AIMD Spring Calibration.....	99
Table 8.2. Calibration data for models on LWBP.	118

LIST OF FIGURES

Figure 4.25: Methodology for validation and calibration of upgraded 6-DOF Code.....	62
Figure 4.26. Flight simulation vs. climb trajectory data for Flight #2.....	65
Figure 4.27. Flight simulation vs. trajectory data in the Y-Z plane for Flight #2.	66
Figure 4.28. Flight simulation vs. climb trajectory data for Flight #5.....	67
Figure 4.29. Flight simulation vs. trajectory data for Flight #5.....	67
Figure 4.30. Flight simulation vs. climb trajectory data for Flight #9.....	68
Figure 4.31. Flight simulation vs. trajectory data Y-Z comparison for Flight #9	68
Figure 4.32. Cutaway indicating center of mass and placement of RCS	69
Figure 4.33. Altitude vs. time trajectories for Teflon® and Delrin®	71
Figure 4.34. Mach number vs. time trajectories for Teflon® and Delrin® trajectories ..	71
Figure 4.35. Propellant remaining vs. time trajectories for Teflon® and Delrin®	71
Figure 4.36. Propellant mass consumption vs. time for vertical ascent	72
Figure 4.37. Crosswind tolerance of #200-2.4m craft with 100 kg payload	74
Figure 4.38. Beam riding behavior of #200-2.4m craft with 100 kg payload	74
Figure 4.39. a) Propellant usage for a vertical flight in crosswind; b) Altitude vs. time.	75
Figure 4.40. Altitude vs. range for selected constant zenith boost angles.....	76
Figure 4.41. Velocity vs. time for selected constant zenith boost angles	76
Figure 4.42. Laser beam boost reference angle schedules with respect to launch pad....	77
Figure 4.43. Mach number vs. altitude for pop-up to 12 km.....	78
Figure 4.44. a) Absolute vehicle velocity vs. time; b) Altitude vs. time	79
Figure 4.45. Remaining PTFE propellant mass vs. time for several pop-up schedules ..	79
Figure 4.46. RCS propellant mass vs. time for several Mach 0.6 pop-up schedules ..	80
Figure 4.47. Flight 5 altitude and range vs time	81
Figure 4.48. Flight 5 absolute and azimuthal velocity vs. time.....	81
Figure 4.49. Launch vehicle velocity and altitude vs. time (100 MW beam power).	82
Figure 4.50. Laser thruster and RCS propellant usage vs. time	83
Figure 4.51. Visualization of launch trajectory to scale over Earth.	83
Figure 4.52. . WSMR Flights 10 and 11 vs. updated model simulations	84
Figure 6.1: Integrated setup in the present 7.9 m x 5.2 m available laboratory space....	91
Figure 6.2: Proposed vacuum chamber for LP experiments.....	93

Figure 6.3: Lightcraft model with AXi brushless outrunner motor.....	94
Figure 8.1. Sample output from AIMD	100
Figure 8.2. Sample output from AIMD	100
Figure 8.3. Sample output from LWBP (#250-2/3, ~39 J pulse, HG Mix).	101
Figure 8.4. Sample LWBP output.....	101
Figure 8.5. WSMR Flights 10 and 11 vs. updated model simulations	102
Figure 8.6. Simulation vs. climb trajectory data for Flight #2	103
Figure 8.7. Simulation vs. trajectory data in the Y-Z plane for Flight #2	103
Figure 8.8. Simulation vs. trajectory data of Flight #1	104
Figure 8.9. Simulation vs. trajectory data in the Y-Z plane for Flight 1.	104
Figure 8.10. 3-D Simulation vs. trajectory for Flight 1.....	105
Figure 8.11. Simulation vs. trajectory data of Flight #3	105
Figure 8.12. Simulation vs. trajectory data in the Y-Z plane for Flight #3	106
Figure 8.13. 3-D Simulation vs. trajectory for Flight 3.....	106
Figure 8.14. Simulation vs. trajectory data of Flight #4.....	107
Figure 8.15. Simulation vs. trajectory data in the Y-Z plane for Flight #4	108
Figure 8.16. 3-D Simulation vs. trajectory for Flight 4.....	108
Figure 8.17. Simulation vs. trajectory data of Flight #6.....	109
Figure 8.18. Simulation vs. trajectory data in the Y-Z plane for Flight #6	109
Figure 8.19. 3-D Simulation vs. trajectory for Flight 6.....	110
Figure 8.20. Simulation vs. trajectory data of Flight #7.....	110
Figure 8.21. Simulation vs. trajectory data in the Y-Z plane of Flight #7.....	111
Figure 8.22. 3-D Simulation vs. trajectory data of Flight #7.....	111
Figure 8.23. Simulation vs. trajectory data of Flight #8.....	112
Figure 8.24. Simulation vs. trajectory data for the Y-Z plane of Flight #8	113
Figure 8.25. 3-D Simulation vs. trajectory for Flight 8.....	113
Figure 8.26. Simulation vs. trajectory data of Flights #10 and #11.....	114
Figure 8.27. Simulation of Flight #12 vs. trajectory data.....	114
Figure 8.28. Simulation of Flight #13 vs. trajectory data.....	115
Figure 8.29. Simulation of Flight #14 vs. trajectory data.....	115
Figure 8.30. Simulation of Flight #15 vs. trajectory data.....	116

Figure 8.31. Simulation of Flight #16 vs. trajectory data.....	116
Figure 8.32. LWBP Impulse vs. initial angular velocity calibration for #200-2/3.....	117
Figure 8.33. LWBP Impulse vs. initial angular velocity calibration for #150-2/3.....	117
Figure 8.34. LWBP Impulse vs. initial angular velocity calibration for #250-2/3.....	118
Figure 8.35. LWBP Impulse vs. initial angular velocity calibration for German Bell..	118
Figure 8.36. Axial C_M for sanded vs. non-sanded foci of #200-2/3	119

4.4 Numerical Investigation: 7-DOF Code

4.4.1 Code Calibration on 16 WSMR Flights

The original 6-DOF code validation/calibration procedure (before the seventh degree of freedom was added) is given in Fig. 4.25. In validating the flight dynamics model, simulations were run, and re-run for all 16 lightcraft flights in the WSMR database. Using the methods described below, every component model (e.g., laser beam, engine, dynamics, etc.) was isolated such that its effects could be individually assessed and adjusted as necessary.

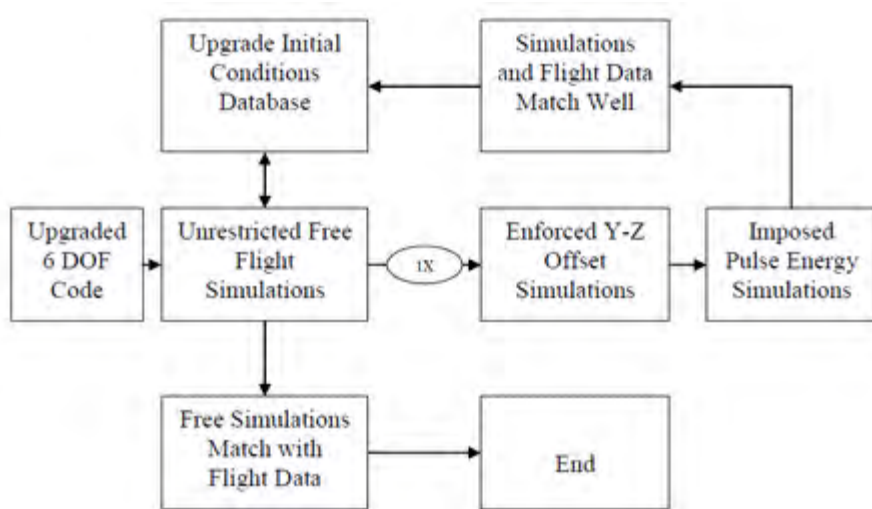


Figure 4.1: Methodology for validation and calibration of upgraded 6-DOF Code.

First to be attempted were 6-DOF simulations designated as “*Free-Flights*”: i.e., craft were permitted to “fly” self-determined trajectories without constraints of any kind imposed. Free-flight simulations successfully modeled the initial portion of the trajectories, but accuracy diminished for flight times extending beyond a few seconds duration. Hence, the 6-DOF component models were believed accurate to the first-order, but further refinement, verification, and calibration of the code was deemed necessary.

An “*Enforced y-z Offset*” study was executed to 1) confirm the validity of axial impulse equations for laser pulsejet engines, and 2) seek an improved “altitude vs. time” trajectory match with the WSMR database -- especially for the longer flights. A new subroutine enabled the input of known “y-z offset vs. time” data into the 6-DOF code, extracted from actual WSMR flight trajectories. This experimentally derived y-z data was then enforced over the entire 6-DOF flight simulation to ensure an exact y-z match with its WSMR counterpart. (Note that the actual trajectories are, of course, heavily influenced by crosswind and other launch anomalies.) By enforcing this “actual” transverse motion, the 6-DOF code enforced an axial impulse schedule that approached verifiable experimental values. Furthermore, these simulations simultaneously enforced a laser pulse energy schedule (i.e., captured into the engine) that should closely agree with that of a given WSMR trajectory, since captured E_p is a dictated function of offset and altitude (i.e., range). The results of the “enforced y-z offset” study proved that the 6-DOF code can accurately reproduce WSMR experimental trajectories, thereby verifying the axial impulse equations created for these pulsejet engines.

Next, the “*Imposed Pulse Energy*” study was carried out to verify the lateral or “beam-riding” impulse equations in the 6-DOF code. In contrast with the previous study, the captured laser pulse energy (E_p) vs. time was first calculated from a given WSMR flight trajectory, and then input into the 6-DOF code as an imposed pulse energy schedule. Next, each 6-DOF simulation was run as an unconstrained “free-flight” so that the y-z beam-riding behavior could be compared with the real data. The exceptional agreement in beam-riding (y-z) behavior between the simulations and WSMR data gives us a high degree of confidence in the code’s lateral impulse models.

A final study on “*Initial Launch Conditions*” examined the effects of environmental (e.g., cross-wind) and other launcher anomalies upon the resultant flight trajectory. Parametric variations in numerous effects were carried out with the 6-DOF code, in an effort to assess the impact of each effect. For example, lightcraft were observed to frequently “stick” to the launcher’s guide rod during the liftoff process, usually receiving a lateral impulsive “kick” upon final separation. Also, occasionally the laser beam

became unintentionally misaligned with the guide rod, which gave the craft an initial offset right at liftoff. Upon modeling such effects in a number of launch scenarios, the 6-DOF simulations were able to match specific WSMR flight trajectories to a high degree of accuracy.

4.4.2 Code Calibration Results

The excellent match in evidence for unrestricted “free flights” proves that the 7-DOF code is an ideal tool for simulating the flight behavior of existing, as well as future lightcraft. Each flight in the WSMR trajectory database, presented in Table 4.2, was run with numerous input conditions.

Table 4.1. WSMR Lightcraft flight trajectory database [12].

Flight Ref. #	Lightcraft Type and Size	Max. Altitude (feet)	Laser Telescope Separation	Launch Mass (grams)
1	200-5/6	58.9	8'-10.5"	32.5
2	200-11/10	39.2	9'-2"	54.5
3	200-5/6	55.0	10'-7"	32.5
4	200-11/10	25.2	none	54.5
5	200-5/6	55.8	8'-10.5"	32.5
6+	200-11/10	35.8	none	54.5
7	200-5/6	60.2	10'-7"	32.5
8	200-10/10	28.6	10'-7"	48.4
9++	200-10/10	22.8	none	48.4
10	200-2/3	47.2	10'-7"	21.5
11	200-2/3	78.3	10'-7"	21.5
12*	200-5/6 SAR	159.	9'-8.75"	49.02
13*	200-5/6 SAR	184.	none	49.02
14*	200-5/6 SAR	233.	9'-8.75"	50.62
15*	200-3/4 SAR	128.	9'-8.75"	26.3
16*	200-3/4 SAR	128.	9'-8.75"	29.02

* Rocket mode, with Delrin®; altitude vs. time data only.

+ Cross-wind = 3 m/s; ++ Cross-wind = 4.8 m/s.

4.4.2.1 Selected Calibration Flights

The excellent match in evidence for unrestricted “free flights” proves that the 6 DOF code is an ideal tool for simulating the flight behavior of existing as well as future lightcraft. Each flight in Table 4.2 was run with numerous input conditions. Parametric

variations in initial offset, wind speed, wind direction, and initial lateral velocity were all considered in the “*initial launch conditions*” study. The best results were obtained with the initial launch parameters displayed in Table 4.3.

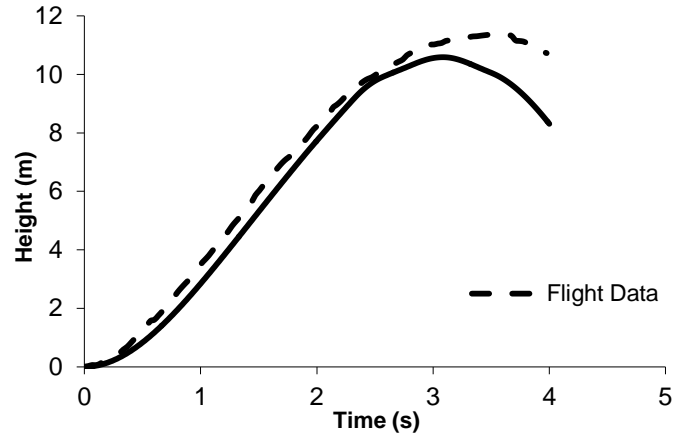


Figure 4.2. Flight simulation vs. climb trajectory data for Flight #2. (25 Hz at 400 J, 10 kW power; 200-11/10 airbreathing mode; 2.974m Telescope Spacing)

Table 4.2. Initial launch conditions for airbreathing lightcraft flights.

Flight Number (WSMR database)	Wind Speed (m/s)	Initial Velocity (m/s)	Z	Initial Y Offset (m)	Wind Direction (Radians)
1	0.5	0		0	$\pi/2$
2	0.5	0.2		0.005	$\pi/2$
3	0.5	0.1		0.01	π
4	1	0.2		0	$\pi/2$
5	0.5	0.1		0.005	$\pi/2$
6	0.5	0.2		0.01	$\pi/2$
7	1	0.3		0	π
8	0.5	0.2		0	$\pi/2$
9	4.8	-0.1		-0.005	$\pi/4$

For example, Fig. 4.26 shows a climb performance (i.e., x vs. time) comparison for an airbreathing flight of the #200-11/10 lightcraft in Flight #2 of the WSMR database. The 6-DOF code simulation was run with the initial input conditions in Table 4.3, for an unrestricted flight. The code simulation provides an accurate representation of the experimental trajectory until roughly ~ 3 seconds into the flight, whereupon the craft departs the beam at a time slightly earlier than in the experimental data. Figure 4.27 compares the lightcraft's y-z beam-riding behavior for the same flight; again, an excellent match.

Figure 4.28 shows a comparison of the climb performance for the #200-5/6 airbreathing craft in Flight #5. The 6-DOF simulation agrees extremely well throughout the entire flight trajectory, which verifies the accuracy of the #200-5/6 model. The y-z trajectory comparison for this same flight is given in Fig. 4.29.

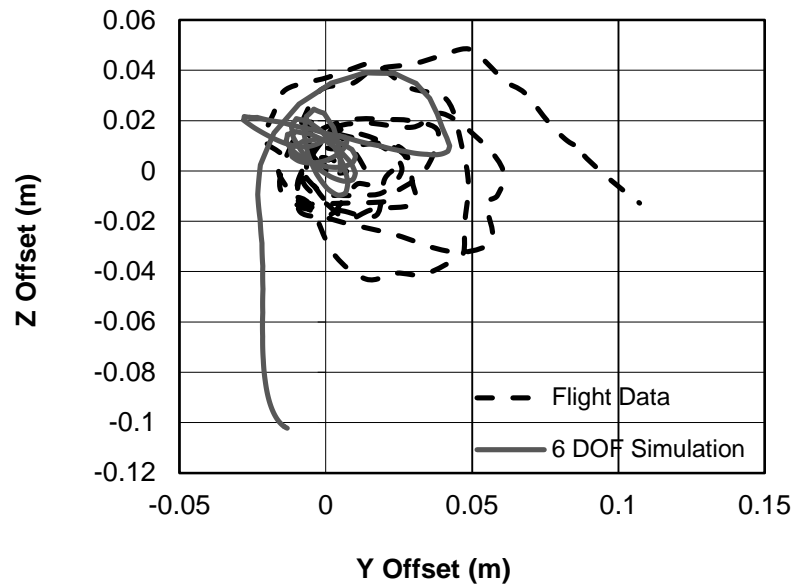


Figure 4.3. Flight simulation vs. trajectory data in the Y-Z plane for Flight #2. (25 Hz at 400 J, 10 kW power; 200-11/10 airbreathing mode; 2.974m Telescope Spacing)

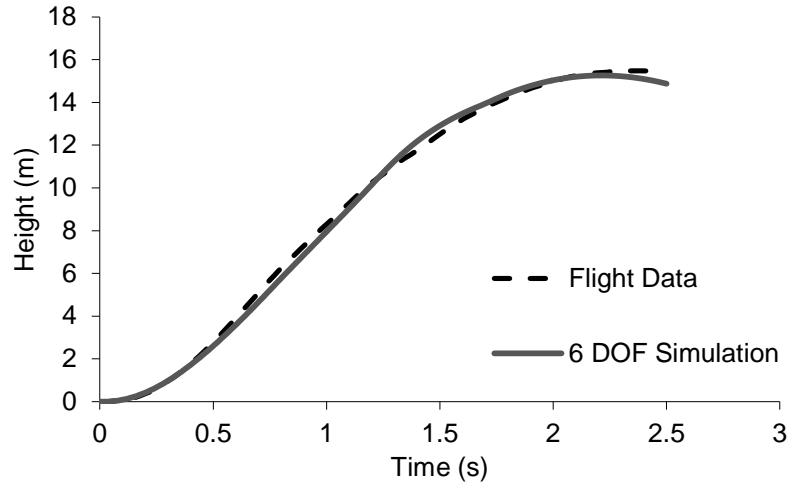


Figure 4.4. Flight simulation vs. climb trajectory data for Flight #5 (25 Hz; 200-5/6 airbreathing mode; 2.7m Telescope Spacing).

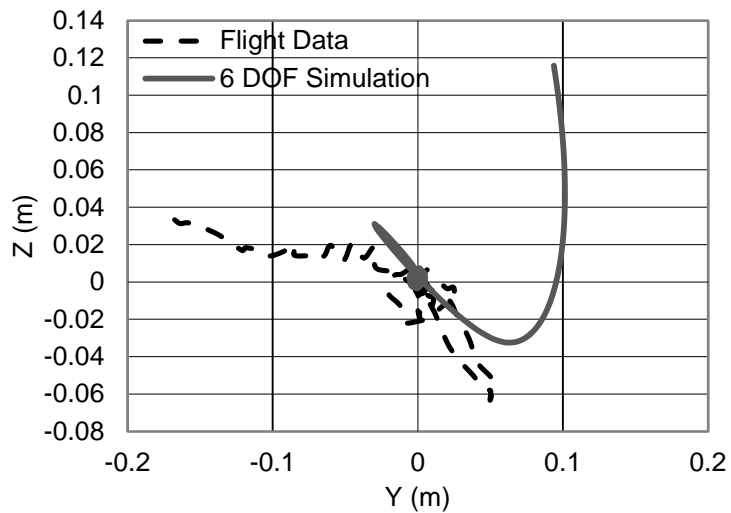


Figure 4.5. Flight simulation vs. trajectory data for Flight #5 (25 Hz; 200-5/6 airbreathing mode; 2.7m Telescope Spacing).

Figures 4.30 and 4.31 provide trajectory comparisons for Flight #9 with a #200-10/10 airbreathing craft in a crosswind. The 6-DOF climbing performance compares well with that of the experimental data until the 4 second mark, at which point the engine begins to overheat; thereafter, the craft begins to slip off the beam, and thrust declines. Note that the y-z simulation results also compare quite well with the experimental data. Both

figures demonstrate that the craft will “beam ride” to about the same point, and in roughly the same fashion.

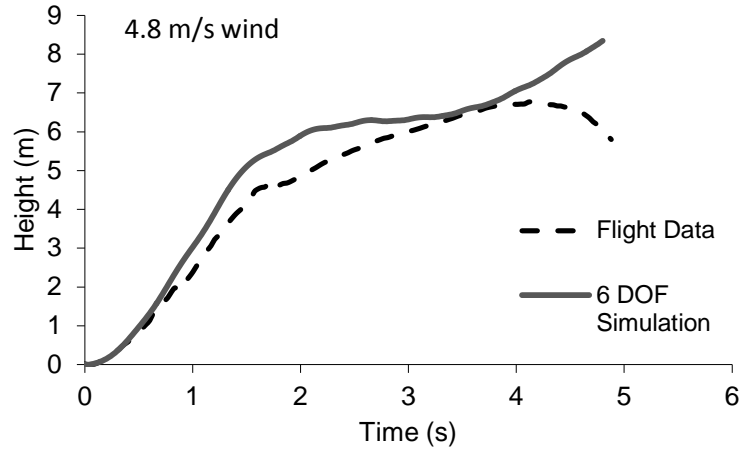


Figure 4.6. Flight simulation vs. climb trajectory data for Flight #9 (25 Hz; 200-10/10 airbreathing mode; No Telescope).

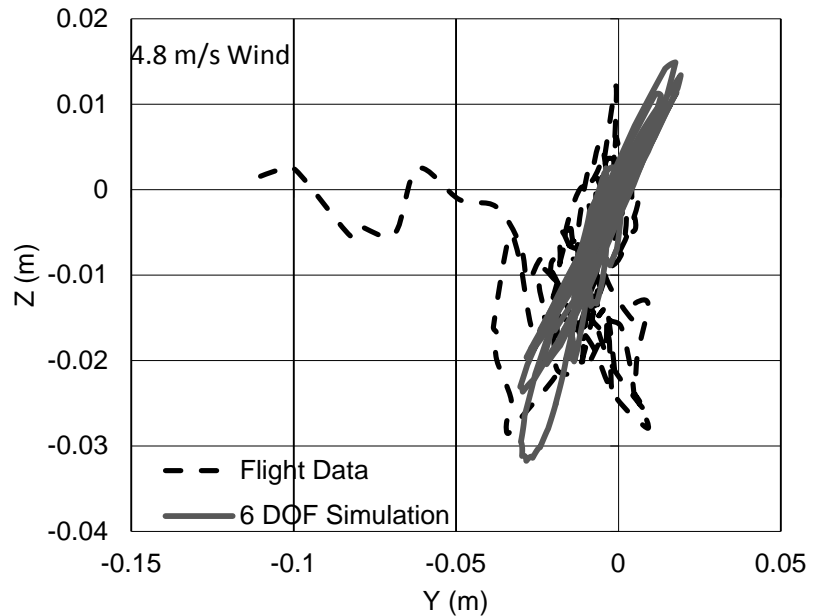


Figure 4.7. Flight simulation vs. trajectory data Y-Z comparison for Flight #9 (25 Hz; 200-10/10 airbreathing mode; No Telescope).

4.4.3 Simulations of 240cm Lightcraft Flights

Using the 7-DOF code, the flight dynamics, stability, and control of 240 cm diameter lightcraft (i.e., scaled for 100 kg class payloads), as shown in Fig. 4.32, under laser boost to extreme altitudes, and eventually into Low Earth Orbit (LEO) were investigated.

The suborbital boost trajectory results presented below are for a 100 kg payload (upper limit of microsatellite class) for four different launch scenarios: 1) liftoff and vertical climb-out on a vertically oriented laser beam; 2) liftoff and climb-out along a constant beam pointing angle (i.e., fixed azimuth and zenith) defined relative to the launch pad; 3) liftoff and climb-out with time-varying, beam pointing schedule (azimuth and zenith); and, 4) liftoff and climb-out using the Aim Point laser launch scheme described below. All exploit the engine’s autonomous beam-riding feature. A 100 MW ground-based laser (GBL) is assumed to propel the 240 cm craft’s rapid ascent through the atmosphere; the laser rocket engine mode is “optimized” for 100 kJ pulses at 1 kHz pulse repetition frequency, with ablative Teflon®-type (i.e., polytetrafluorethylene or PTFE) performance [11]. Note the laser pulsejet engine model in the 7-DOF code can be run in either the solid ablative rocket mode or combined-cycle (i.e., airbreathing/rocket) mode, the latter transitioning to rocket mode at some optimum point along the transatmospheric trajectory.

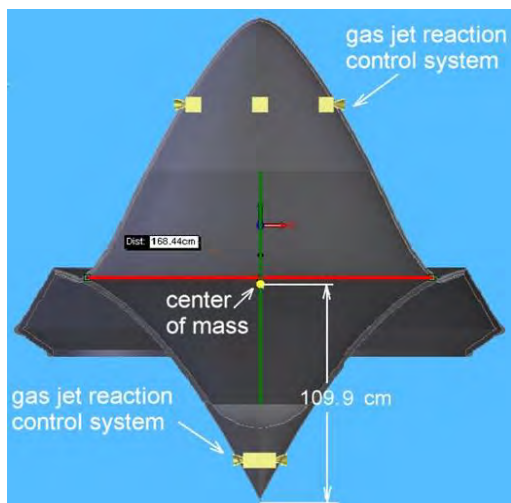


Figure 4.8. Cutaway indicating center of mass and placement of reaction control system, in 2.4m #200 lightcraft.

Delrin® has been used extensively in experiments with off-axis parabolic lightcraft engines, while Teflon® has been investigated by Pakhomov [11]. The assumed properties of both of these propellants are provided in Table 4.4. Delrin® has a higher coupling coefficient than Teflon® and consequently provides $\sim 2.7x$ more thrust per megawatt of captured beam power, although at a substantially reduced I_{sp} . Accordingly, launch trajectories simulated with the 7-DOF flight dynamics code utilizing Delrin® accelerated much more quickly than those with Teflon®-like propellant, as displayed in Fig. 4.34. This is the principal advantage to using Delrin®, however, as it is less efficient and has a 3.2x lower specific impulse, the propellant is consumed quickly.

The vertical launch trajectories (zenith = 0°) using 500kg of Teflon®-like propellant in a 2.4m lightcraft (see Fig. 4.32) achieved significantly higher altitudes, burnout velocities, and run durations, (100 km, Mach 8, and 225 seconds before burnout, respectively) as shown in Figs. 4.33 to 4.35. In Fig. 4.33, Teflon® gives an apogee of 460 km vs. 2 km for Delrin®. Figure 4.34 compares the Mach number schedule for both of these trajectories and Fig. 4.35 compares propellant consumption. These three figures clearly demonstrate the advantages of Teflon®-like ablative propellants for future launch trajectories. Delrin® provides a high initial acceleration, but exhausts the propellant load at a low altitude. As a result, Teflon®-like propellant characteristics were assumed in all subsequent simulations.

Table 4.3. Assumed propellant characteristics for 7-DOF simulations.

Propellant Type	C_m (N/MW)	I_{sp} (s)	η_{ALP} (%)	Ablation Rate (kg/J)
Delrin	510	200	50	$1.097 * 10^{-7}$
Teflon	190	644	60	$2.2004 * 10^{-8}$
Ideal Liquid (PTFE-like)	190	900	88	$1.575 * 10^{-8}$

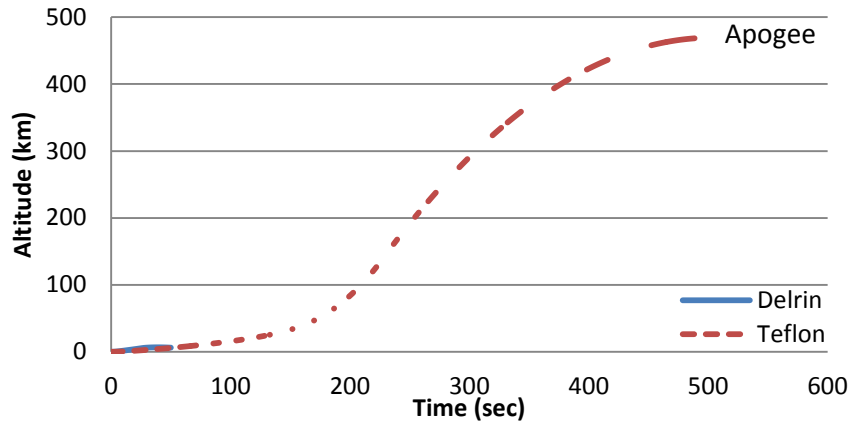


Figure 4.9. Altitude vs. time trajectories for Teflon® and Delrin®. Beam power = 100 MW with Zenith = 0 degrees; initial propellant mass = 500 kg.

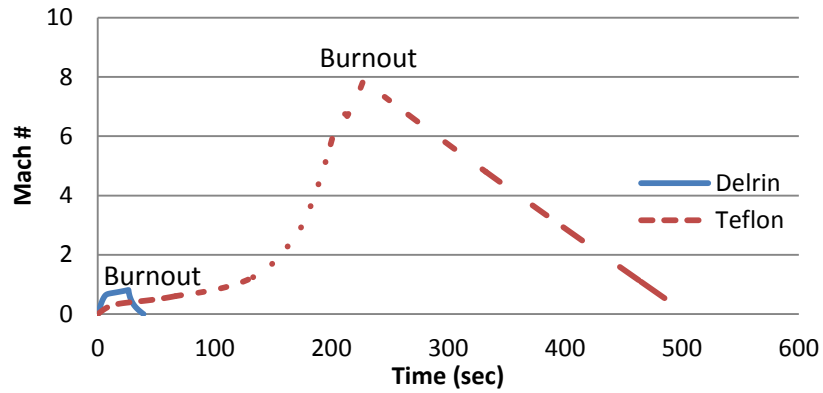


Figure 4.10. Mach number vs. time trajectories for Teflon® and Delrin® trajectories. Beam power = 100 MW with Zenith = 0 degrees; initial propellant mass = 500 kg.

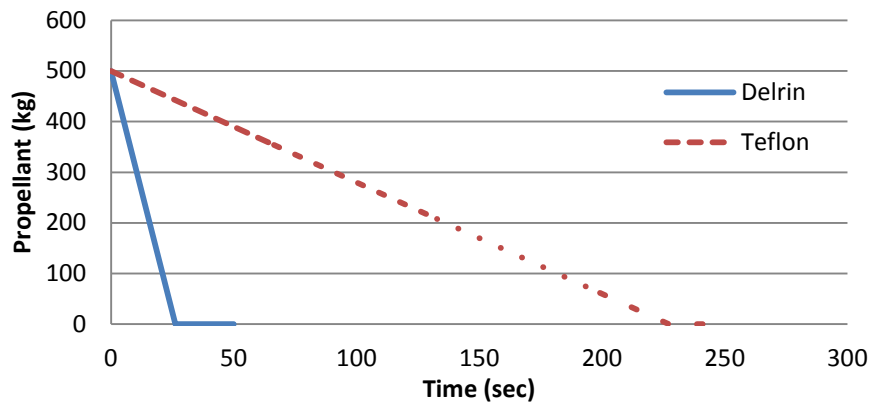


Figure 4.11. Propellant remaining vs. time trajectories for Teflon® and Delrin®. Beam power = 100 MW with Zenith = 0 degrees; initial propellant mass = 500 kg.

An investigation was performed into the propellant consumption of a 2.4 m lightcraft (specifications in Table 4.5) by both the main engine and the reaction control system (RCS) during vertical trajectories utilizing Teflon®-like, (PTFE) propellant; two trajectories were simulated. In the first simulation, the RCS was used to maintain the lightcraft's angular and lateral position within the beam (i.e., the autonomous beam-riding feature was turned off), but only the angular offset (i.e., pitch and roll tipping angles upon the beam) in the second. These simulations revealed that passive/autonomous beam-riding is an essential ingredient to successful laser launch, because without it, the RCS is severely overtaxed and rapidly exhausts all propellant within ~ 150 seconds. Utilizing the autonomous beam-riding feature allowed stable vertical laser launches to extreme altitudes in laser rocket mode (e.g., ablative PTFE propellant) with RCS propellant still remaining, as seen in Fig. 4.36.

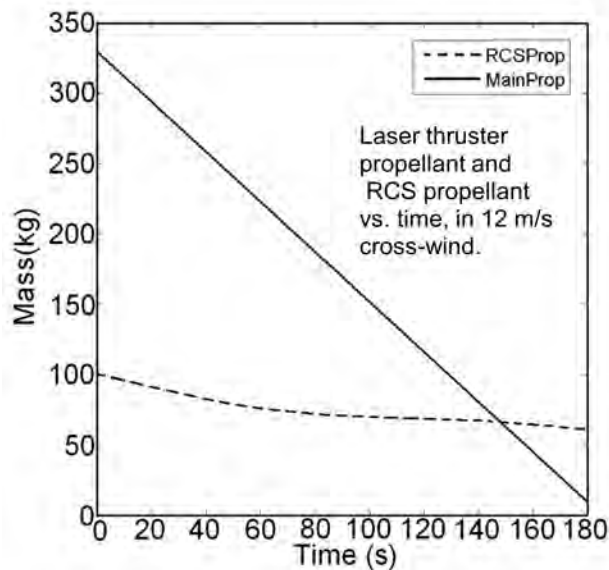


Figure 4.12. Propellant mass consumption vs. time for vertical ascent, autonomous beam-riding feature activated.

Again, Table 4.5 summarizes the liftoff mass and moments of inertia assumed for the 240 cm lightcraft. The vehicle forebody and/or micro-satellite payload are de-spun, and the annular engine parts (i.e., shroud, rim, and ablative propellant) rapidly rotate to impart gyroscopic stability. These studies assumed a constant shroud RPMs in the range

of 1920 to 6680, generally held constant as the PTFE propellant is consumed in flight; the ablative propellant is assumed to have a vacuum specific impulse of 644 seconds, momentum coupling coefficient of 190 N/MW, and ablative laser propulsion efficiency of 60% [11], as shown in Table 4.5. Note that 511 kg is the maximum Teflon® propellant load that will fit within the #200 type shroud’s volumetric constraints, outside the 1.0 meter radius. Assuming only 50% of the RCS propellant is consumed during the launch, which gives a mass ratio (MR) of 2.02, the rocket equation indicates an ideal delta-V (i.e., neglecting aerodynamic drag losses) of 4443 m/s, which is clearly suborbital.

Table 4.4. MOI and mass of lightcraft components modeled in 7-DOF code (240 cm vehicle).

Component	I_{XX} (kg-m ²)	I_{YY} (kg-m ²)	I_{ZZ} (kg-m ²)	Mass (kg)
Despun nose and payload	151.2	92.26	146.7	400.
Rotating shroud and afterbody	64.58	125.0	125.0	100.
Ablative PTFE propellant at lift-off	520.68	260.34	260.34	511.
RCS propellant at lift-off	-	-	-	100.
Total at lift-off	736.46	477.6	532.04	1111.

Note: PTFE propellant is modeled as a thin ring within the annular shroud/engine at $r=100$ cm; $I_{XX} = mr^2$; $I_{YY}=I_{ZZ}=(1/2)mr^2$

The next series of simulations were run to expand the “flight envelope” of the #200 laser launch vehicle. The first set examined vertical flights on a fixed laser beam orientation, specifically to determine the vehicle’s crosswind tolerance—i.e., altitudes at which a lightcraft is either able to maintain vertical flight, or is blown completely off the beam. The simulations were conducted for a laser ablative rocket mode with a lift-off propellant load of 511 kg (PTFE). Fig. 4.37 presents the cross-wind tolerance results for wind velocities ranging from 0 to 150 m/s. For crosswinds below 75 m/s, the 240 cm craft maintains small orbiting radii about the laser beam axis, and continues to climb until all propellant is exhausted. For flights in winds of 70 m/s to 150 m/s, the lightcraft orbits the laser beam at larger radii; beam power is “spilled” and lost when this radius gets too large, causing the craft to lose thrust and reach lesser altitudes. In crosswinds of 150 m/s and greater, lightcraft are blown off the beam shortly after launch. Figure 4.38 shows a “look-down” view of this beam-riding behavior for crosswinds of 20, 90, and 150 m/s. In these simulations, note that the RCS system only maintains the lightcraft axis parallel to laser beam, allowing the autonomous beam-riding feature to dominate.

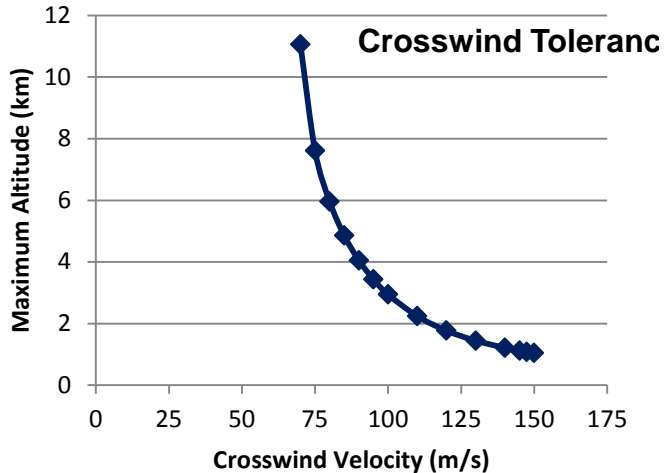


Figure 4.13. Crosswind tolerance of #200-2.4m craft with 100 kg payload in vertical flight.

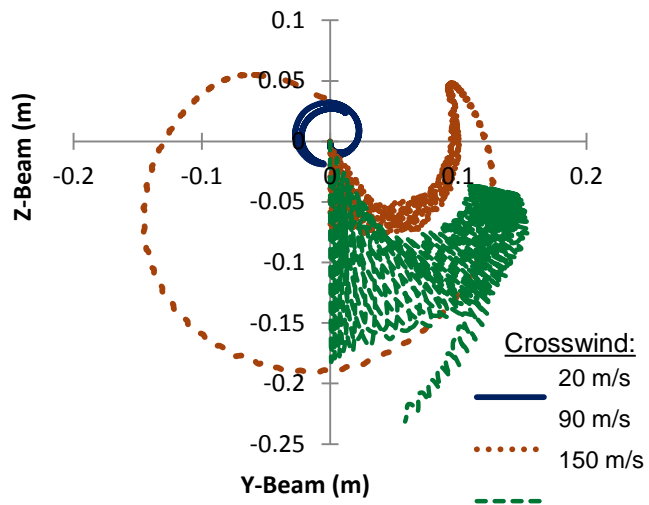


Figure 4.14. Beam riding behavior of #200-2.4m craft with 100 kg payload in vertical flight (look down view).

Figure 4.39a shows the RCS and main PTFE propellant consumption for vertical flight in a 20 m/s crosswind. Note that the ablative propellant is exhausted at ~ 235 seconds (i.e., “burn-out”), with roughly 50% of the RCS propellant remaining. When the engine’s autonomous beam-riding feature is “turned off” in the 7-DOF code, the RCS system propellant is quickly exhausted as its gas-jets struggle to center the lightcraft in the beam, exacerbated by high crosswinds. But when the RCS system allows the autonomous beam-riding feature to dominate, and only maintains the craft’s rotational

axis parallel to the laser beam, RCS propellant usage is dramatically decreased and achievable altitudes (see Fig. 4.39b) are increased. Hence, this proves that passive beam-riding engines will be an essential ingredient for a stable launch to orbit—requiring minimal RCS propellant loads—as evidenced by such crosswind trajectory studies.

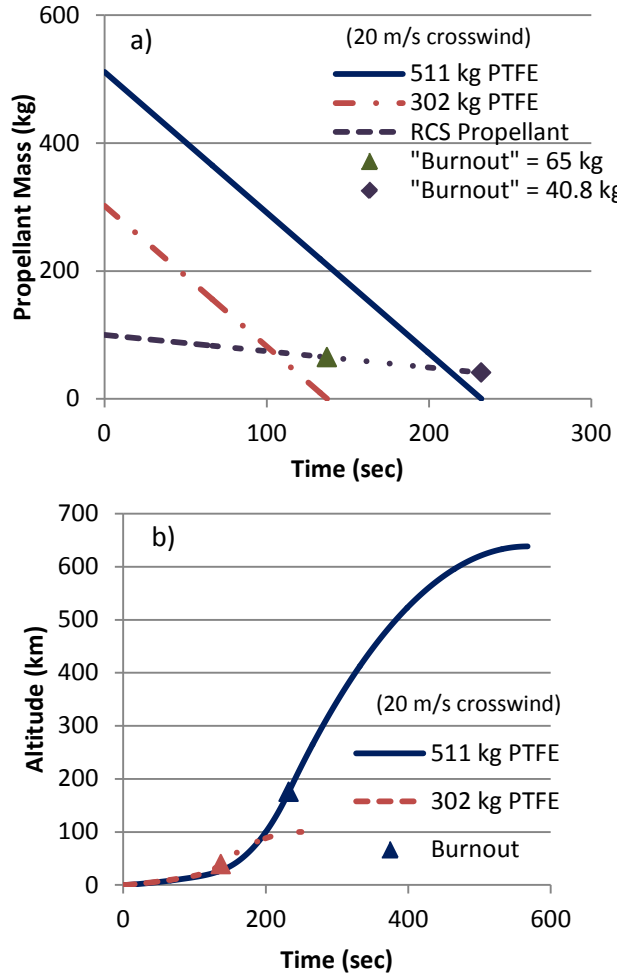


Figure 4.15. a) RCS and main PTFE propellant usage for a vertical flight in a 20 m/s crosswind; b) Altitude vs. time; beam power of 100 MW; Type #200-240 cm lightcraft; 302 kg vs. 511 kg initial PTFE propellant load).

Presented next are results from 7-DOF code attempts to “fly” suborbital trajectories that reach altitudes and/or velocities of interest. Figures 4.40 and 4.41 give trajectories for constant zenith boost angles, which indicate that smaller initial zenith angles (i.e., launch close to vertical) are desirable; but clearly, large zenith angles (i.e., $\sim 90^\circ$) at “burnout” are mandatory for orbital insertion. Note that the highest terminal velocities are obtained

at extreme altitudes, where atmospheric drag penalties are minimized. Larger zenith launch angles, which result in lower apogee and/or terminal velocities, penalize the craft with spending too much time accelerating through the dense atmosphere, thus wasting propellant (lost to drag) and beam power (to high atmospheric attenuation, which is not yet modeled here).

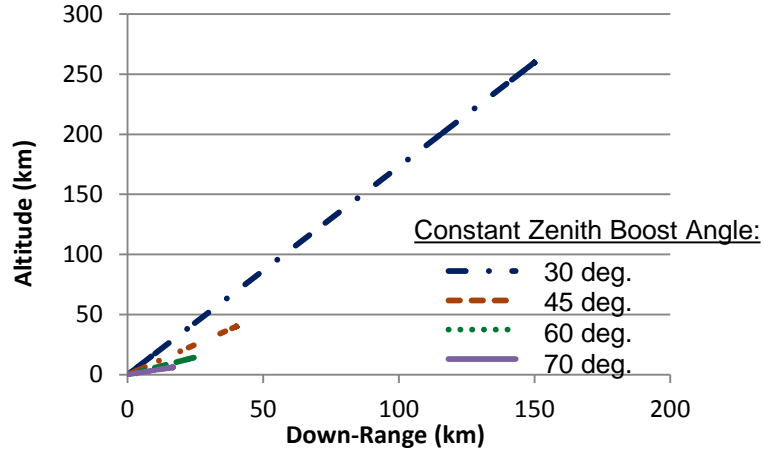


Figure 4.16. Altitude vs. range for selected constant zenith boost angles 100 MW beampower;

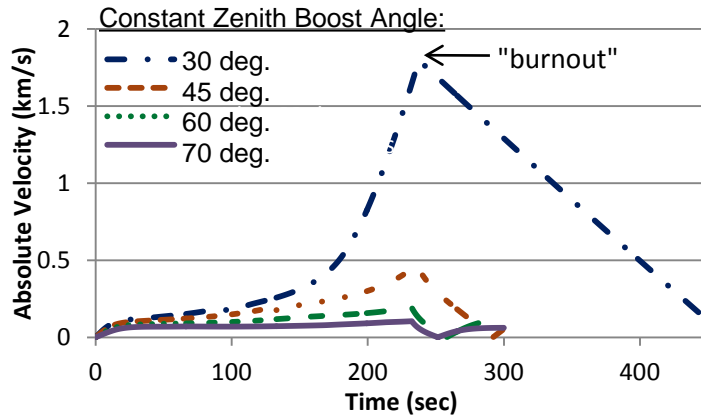


Figure 4.17. Velocity vs. time for selected constant zenith boost angles (100 MW power at 1 kHz);

Hence, a more optimum laser boost reference angle schedule—i.e., beam zenith angle vs. time, $Z(t)$ —would ideally begin with a small zenith angle at the moment of launch, but then slew to larger angles as the craft climbs up through, and exits the atmosphere. Clearly, the beam slewing rate can either be held constant, or vary as some function of

time. Take for example, a launch scenario requiring the highest beam slew rate near the launch pad, then decreasing logarithmically with increasing lightcraft range, as given by:

$$Z(t) = Z_0 + N * \ln(t + 1) \quad (30)$$

where “ N ” is a constant, “ t ” is time, and Z_0 is the initial zenith at liftoff.

Reaching circular orbit will of course require that the final velocity vector be directed circumferentially upon reaching the desired altitude, whereas during the laser boost phase, the craft’s rear optic must point directly at the ground-based laser and launch pad. For the original Lightcraft Technology Demonstrator (LTD) vehicle concept (mission of 100 kg payload to LEO), Myrabo et.al. [12] suggest an “optimized” laser boost reference angle schedule that slewed the beam from an initial zenith of 60 deg. to a final of 71 deg at “burnout.” This schedule, displayed in Fig. 4.42 for reference (along with others for $N=4$ to 6), minimized the delta-V for orbit circularization required of an on-board chemical-kick rocket.

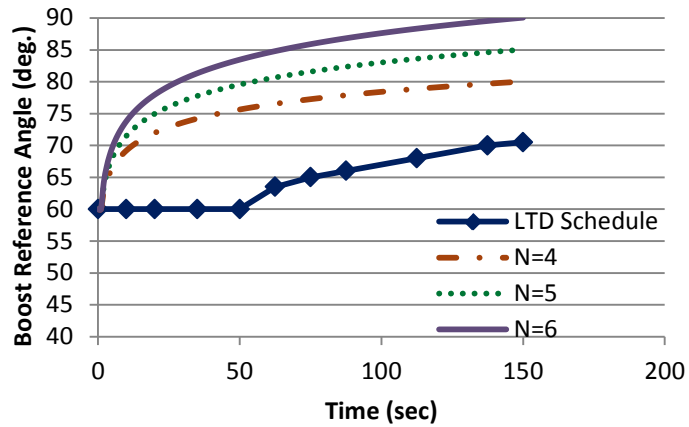


Figure 4.18. Laser beam boost reference angle schedules with respect to launch pad.

A third study examined the performance improving effects of Mach 0.6 “pop-up” maneuvers to altitudes of 12, 20, and 30 km, before accelerating through Mach 1. As before, this study invoked 511 kg of ablative PTFE propellant consumed in the rocket mode for a MR of 2.02 (with 50 kg of unexpended RCS propellant), and ideal delta-V of 4443 m/s. By maintaining a subsonic ascent Mach number of ~0.6 throughout the

thickest parts of Earth's atmosphere, much propellant and beamed energy can be preserved. The highlighted section in Fig. 4.43 identifies the Mach 0.6 portion of the 12 km pop-up launch trajectory.

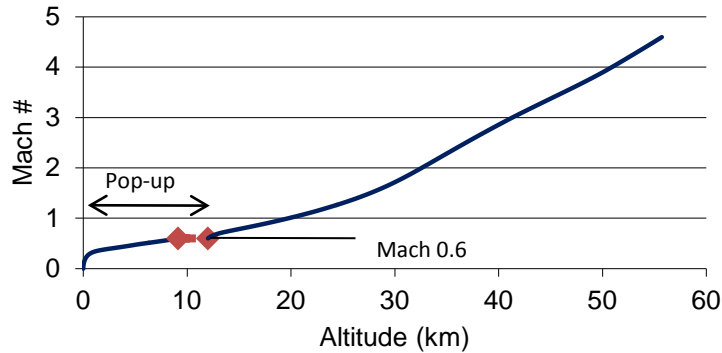


Figure 4.19. Mach number vs. altitude for pop-up to 12 km; 100 MW beam power; 511 kg initial PTFE propellant; 240 cm lightcraft; variable zenith angle with an initial value of 60 degrees, for $N=5$.

Figures 4.44a and 4.44b reveal that substantial increases in suborbital “burnout” velocity and peak altitude are achievable from subsonic pop-up maneuvers, wherein much propellant is saved for later consumption at the top of the atmosphere where aerodynamic drag is greatly reduced. Note that the 20 km and 30 km pop-ups give significantly increased performance over the 12 km pop-up, which provided nearly identical results to the “no pop-up” case. In all, the 30 km pop-up achieved a 140% increase in maximum altitude and 60% increase in “burnout” velocity compared to runs without pop-ups. Figure 4.45 reveals the substantial PTFE propellant conservation secured through the Mach 0.6 pop-up to 30 km, before accelerating through Mach 1. Figure 4.46 gives the RCS propellant consumption vs. time; due to the longer boost duration for the 30 km pop-up, note that only 16.1 kg of RCS propellant remains at burnout.

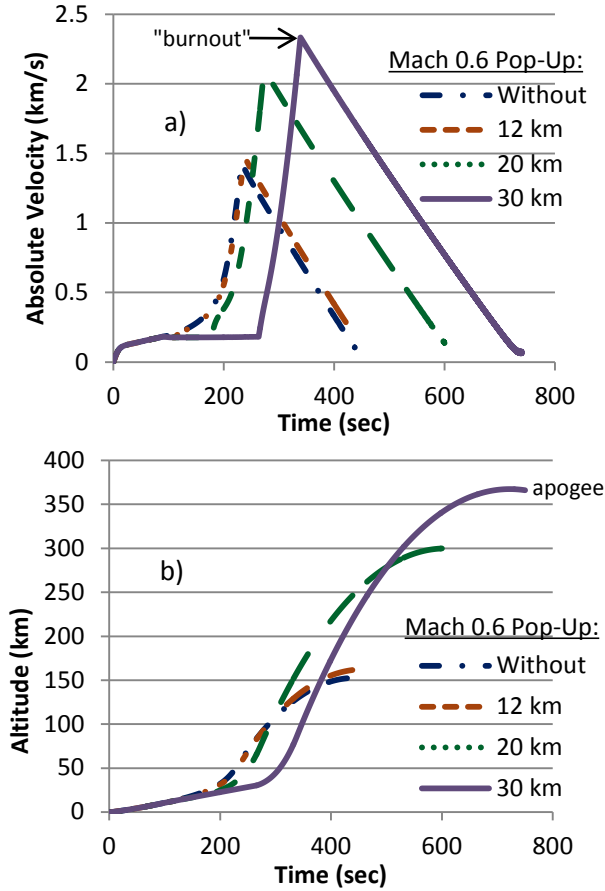


Figure 4.20. a) Absolute vehicle velocity vs. time for several Mach 0.6 pop-up schedules; b) Altitude vs. time for several pop-up schedules; 100 MW beam power; 511 kg initial PTFE propellant; 240 cm lightcraft; variable zenith with initial value of 60° , for $N=5$.

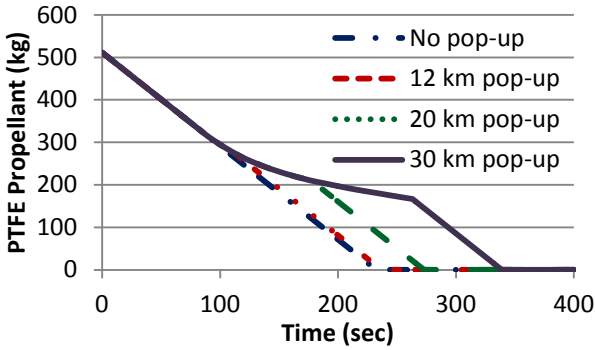


Figure 4.21. Remaining PTFE propellant mass vs. time for several Mach 0.6 pop-up schedules; 100 MW beam power; 511 kg initial propellant; 240 cm lightcraft; variable zenith with initial value of 60° , for $N=5$.

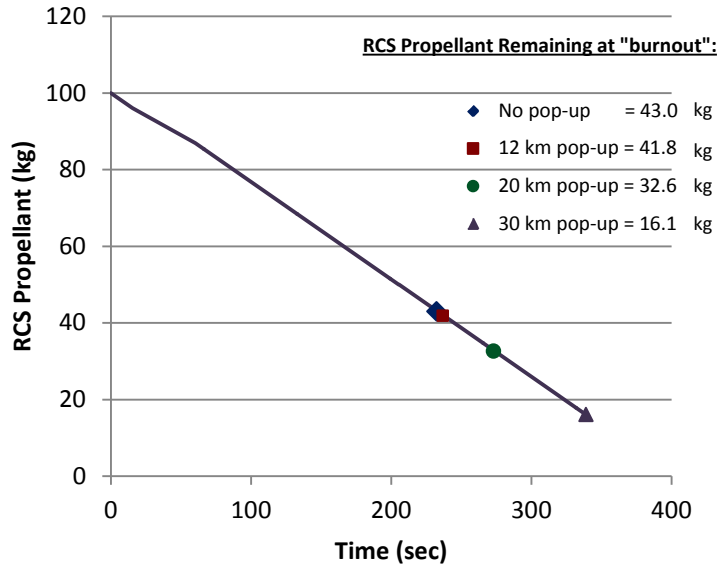


Figure 4.22.RCS propellant mass vs. time for several Mach 0.6 pop-up schedules; 100 MW beam power; 511 kg initial propellant; 240 cm lightcraft; variable zenith with initial value of 60, for N=5).

The fourth study reported here (see results in Table 4.6 below) was actually carried out just prior to the previous one, and invoked a Mach 0.6, 12 km pop-up with 767 kg of PTFE propellant for all runs. This 40% increased propellant load gave a MR of 2.49 and suborbital ideal delta-V of 5.75 km/s; in contrast, note that MR=3.55 is needed for 8 km/s LEO velocity with I_{sp} =644 seconds. As shown in Table 4.6, several different boost reference angle schedules were applied in this study, with initial zeniths ranging from 50 to 63 degrees. All seven examples successfully rode the beam to “burnout” using just the autonomous beam-riding #200 engine with the RCS system active, of course. The results from Flight 5 are highlighted in Figs. 4.47 and 4.48 below; its *launch-point-to-apogee* range was 1300 km and “burnout” azimuthal velocity was 2.8 km/sec— both exceed all other runs. Flight 1 had the highest absolute “burnout” velocity of 5.34 km/s, closely followed by Flights 4 and 6 at 5.27 km/s and 5.21 km/s, respectively. Note that “azimuthal” velocity in Table 4.6 refers to the “burnout” velocity vector component which is directed parallel to the Earth surface.

Table 4.5. Initial launch conditions and results for selected suborbital flights of 240 cm lightcraft.

Flight Run Ref #	Beam slew constant "N"	Initial zenith (deg)	Initial mass of PTFE propellant (kg)	Apogee altitude (km)	Range to apogee (km)	Time to peak altitude (s)	Velocity at "burnout" (km/s)	absolute azimuthal
1	4	50	767	2750	440	1200	5.34	0.894
2	4	60	767	1100	1050	800	3.87	2.60
3	4	63	767	1410	1100	800	4.46	2.50
4	5	50	767	2620	960	1200	5.27	1.42
5	5	60	767	990	1300	1100	3.73	2.80
6	6	50	767	2460	1270	1200	5.21	1.92
7	6	60	767	652	1100	800	3.30	2.68

Note: Time of PTFE propellant "burnout" = 362 seconds for all flights; Pop-up altitude = 12 km for all.

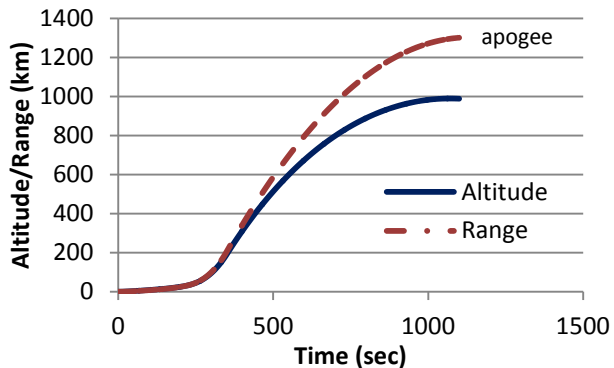


Figure 4.23. Flight 5 altitude and range vs time; 100 MW beam power; 767 kg initial PTFE propellant; 240 cm lightcraft; variable zenith, initial value of 60° —see schedule in Eqn. 30, for N=5.

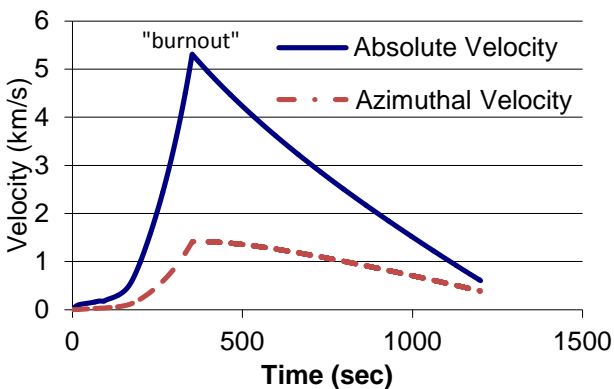


Figure 4.24. Flight 5 absolute and azimuthal velocity vs. time (100 MW beam power; 767 kg PTFE propellant; 240 cm lightcraft; variable zenith, initial value of 60° —see schedule in Eqn. 30, for N=5).

Using what was learned in the above simulations and the previously discussed "Aim Point" strategy, trajectories to LEO were simulated using two phases. For the first phase, the beam does not actively target a specific spot on the engine during the Mach

0.6 “pop-up maneuver” phase. As mentioned earlier, this preserves much propellant and beamed energy from being lost to aerodynamic drag. During this “pop-up” phase, the autonomous beam-riding feature maintains the vehicle’s lateral position within the beam, while the RCS propellant maintains the tipping angle (pitch/roll) of the craft. Once the lightcraft clears the dense portion of the atmosphere, it continues accelerating, now using the “Aim Point” strategy. As a result, stable trajectories were flown reaching speeds greater than 8 km/s at 510 km in ~480 s (see Figs. 4.49 and 4.50, respectively), launching a 100 kg payload (upper limit of microsatellite class) using a 100 MW ground-based laser (GBL), “optimized” for 100 kJ pulses at 1 kHz pulse repetition frequency; these runs assumed an idealized liquid propellant performance with a specific impulse of 900 seconds, C_M of 190 N per MW, and optimistic ablative laser propulsion efficiency of 88%. The pop-up maneuver was performed to an altitude of 10 km in ~150 seconds, at which time the “Aim Point” strategy (21 cm linear offset) was implemented. This study proved the feasibility of the “Aim Point” strategy to achieve near orbital velocities and altitudes. Final orbit circularization would be performed by a brief “kick” by an on-board chemical rocket burn.

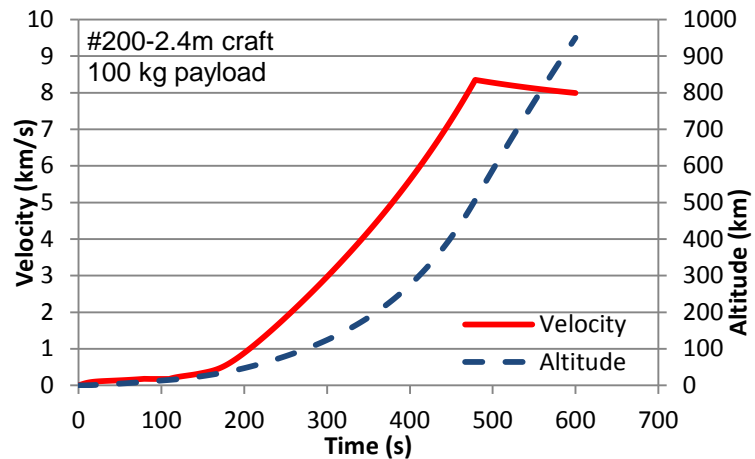


Figure 4.25. Launch vehicle velocity and altitude vs. time (100 MW beam power).

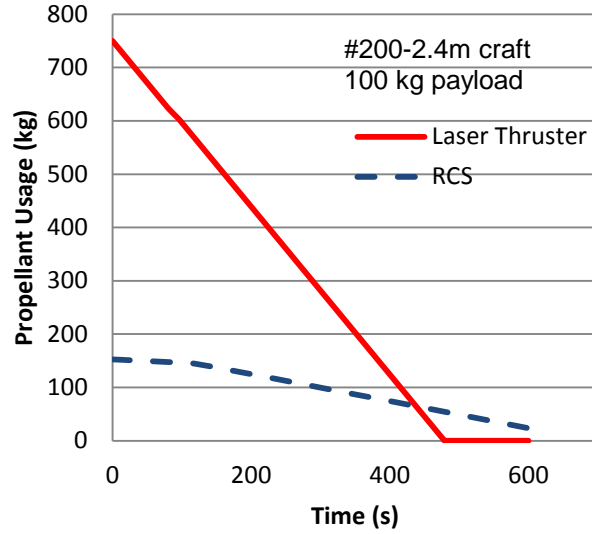


Figure 4.26. Laser thruster and RCS propellant usage vs. time (100 MW beam power).

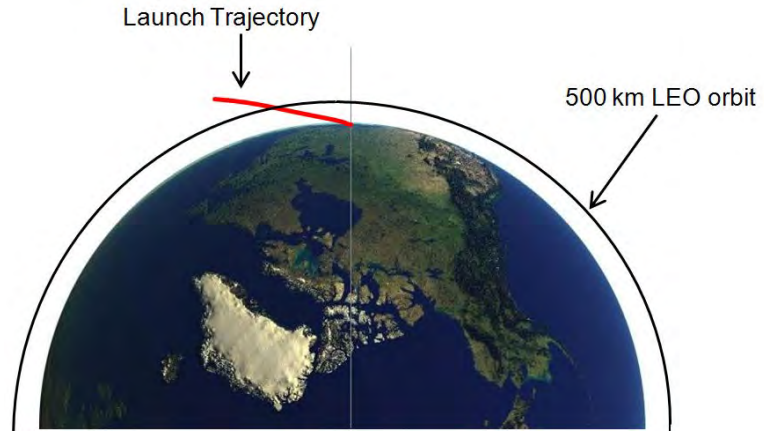


Figure 4.27. Visualization of launch trajectory to scale over Earth.

4.4.4 Simulations Using Experimental Results

Finally, using the axial and lateral engine performance data experimentally obtained on the K-922M laser system, free flight trajectories of 2/3 scale (97.7 mm diameter) were simulated. Using an advanced, 30x35 mm, 10kW K-922M laser beam, a divergence of 0.15 mrad (measured experimentally for the unstable resonator optics used at RPI), altitudes of 57 and 80 m were reached by the #200-2/3 AB and RM geometries, respectively, as seen in Fig. 4.52. The #250-2/3 and #150-2/3 geometries were only able

to achieve altitudes of 54 and 10 m, respectively, due to inferior beam-riding capabilities. As expected, the #200 and 250 geometries far exceed the experimental launch trajectories performed on PLVTS at WSMR [2], with the #200-2/3 geometry and 10 kW laser beam power. This study confirms the improved performance obtained with short (100 ns) pulse duration (FWHM) will result in superior launch trajectories.

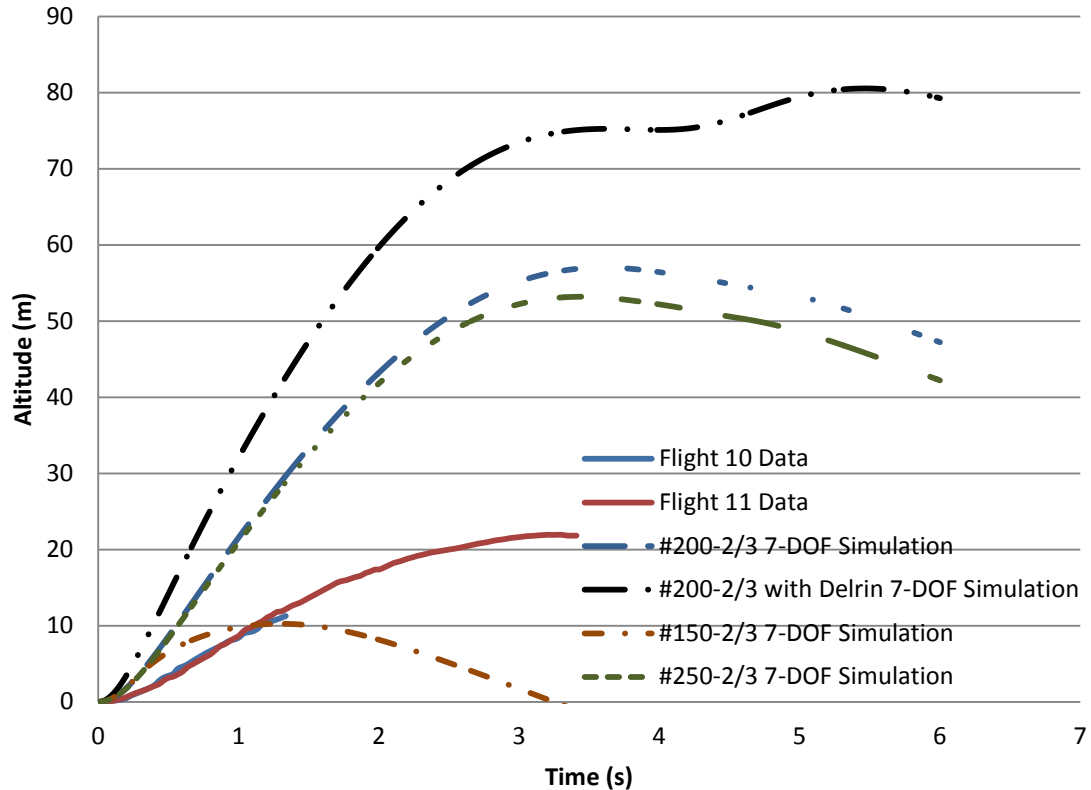


Figure 4.28. . WSMR Flights 10 and 11 vs. updated model simulations on advanced K-922 laser system, (100 ns pulse duration, 0.15 mrad divergence, 10kW, 250 Hz).

DISCUSSION AND CONCLUSIONS

The laser propulsive characteristics of a series of lightcraft engine geometries has been investigated experimentally and used to numerically investigate and define their “flight envelope” along boost trajectories to extreme altitudes. This combined experimental and numerical effort has: 1) determined why the #200 lightcraft geometry flies so well, and others don’t; 2) obtained an understanding of the beam-riding phenomenon in varying engine geometries both experimentally and numerically; and, 3) determined the performance of the #200 lightcraft geometry for trajectories that can transport 1-100 kg payloads to Low Earth Orbit (LEO).

5.1 AIMD and LWBP Experimental Results

A sensitive ballistic pendulum was used to measure the axial impulse generated by a family of lightcraft engines and a bell geometry, using the twin Lumonics K922M laser system. Using the AIMD, side impulses and pitching angular impulses vs. lateral offset were measured for this same series of engines. Momentum coupling coefficients (C_M) were then calculated using the initial angular velocity of the ballistic pendulum and AIMD rotors. Additionally, wind tunnel experiments were able to determine aerodynamic coefficients of lift, drag and moment and validate previous CFD studies. The aerodynamic center of the #200 geometry was found for a range of angles of attack. The principal conclusions from the experimental portion of the present research effort are:

- The *laser gas study* found High Gain laser mix, with its short pulse duration (100 ns FWHM) and truncated tail (i.e., much shorter than the LM5 mix), derives optimum engine performance from the K922M TEA laser system for the 2/3 to 5/6 scale engines (i.e., 97.7 mm to 122.2 mm);

- The *axial performance of #200 engines* study found K922M pulse energies are modest (10-40 J) and more suited for these small lightcraft engine sizes than prior PLVTS experiments at 420 J/pulse;
- The *LWBP axial performance of #200 engines* study shows at 225 N/MW, peak axial C_M results for the airbreathing #200-2/3 engine are 1.9x higher than the ~120 N/MW previously reported for long pulse (e.g., 10-18 μ s) CO₂ electric discharge lasers [9];
- The *AIMD investigations of #200 engines* study found that by reaching 75 N/MW (again with the airbreathing #200-2/3 engine), peak lateral C_M performance is 5x higher than prior results from the PLVTS laser [32] with its 18 μ s pulse duration;
- For the first time, pitching angular impulses of the 2/3 scale lightcraft engine family have been measured, falling in the range of only +/- 0.6 x10⁻⁵ to 1.2 x10⁻⁴ N-m-s for airbreathing and “rocket” modes, respectively;
- Regardless of the laser gas mix, lateral (i.e., beam-riding) C_M performance of smaller lightcraft engines is more reliable (less erratic) at larger included focus angles (α), on the unexpanded K922M beam;
- During the *LWBP propellant experiments*, axial C_M values of 467 N/MW were found using Delrin® propellant in the #200-2/3 “rocket mode,” exactly twice the airbreathing value;
- The *AIMD propellant experiments* measured Lateral C_M values for the first time in “rocket mode,” and were also 2x their airbreathing counterparts;
- In the series of *German Bell experiments* the parabolic bell engine geometry demonstrated axial C_M values similar to the #250 lightcraft geometry, but gave lateral C_M values roughly an order of magnitude smaller;
- *Engine refresh time* studies found the refresh time for a static airbreathing #200-2/3 engine at 1 atmosphere with 16 J pulses indicates that PRFs of ~350Hz and below should be feasible;
- *Sanded vs. unsanded focus* studies (as seen in Fig. 7.36 in Appendix E), indicate a sanded or roughed up annular focal ring acts as a “spark plug,” enhancing laser induced breakdown. (Note that all WSMR flights had sanded optical focal rings.)

5.2 7-DOF Flight Dynamics Code Results

A 7-DOF flight dynamics code was generated and calibrated against a 16 flight database from WSMR. Lightcraft vehicles were scaled for larger diameters, and flown on simulated launch trajectories to extreme altitudes and velocities. Engine propulsive models were updated using the experimental data obtained in the present effort, and the trajectories further proved the superior flight performance of the #200 lightcraft geometry. Principal conclusions from the numerical flight dynamics research effort are as follows:

- The “flight envelope” of our 7-DOF flight dynamics and control code has now been successfully expanded into the suborbital regime, simulating launches of beam-riding 240 cm lightcraft carrying 100 kg payloads to extreme altitudes, relying on ablative rocket propellant with PTFE-like performance.
- Volumetric constraints of the Type 200 annular shroud limit PTFE propellant loads to 511 kg (MR=2.02; ideal delta-V of 4.44 km/s), although 767 kg was also run (MR=2.49; ideal delta-V of 5.75 km/s). PTFE-type propellant is assumed to give a vacuum specific impulse of 644 seconds, momentum coupling coefficient of 190 N/MW, and ablative laser propulsion efficiency of 60%.
- The *vertical-flight-in-crosswinds tolerance* study indicates that passive beam-riding engines may be THE essential ingredient for a stable launch to orbit—with minimal RCS propellant requirements. When the RCS system allows the autonomous beam-riding feature to dominate, and only maintains the lightcraft’s axis parallel to the laser beam, RCS propellant usage is dramatically reduced compared with a non-beam-riding engine or vehicle.
- For vertical flights in crosswinds below 75 m/s, the 240 cm lightcraft maintains small orbiting radii about the laser beam axis, and continues to climb until the PTFE propellant load is exhausted. In crosswinds of 70-150 m/s, the craft orbits the beam at larger radii, wherein power is “spilled” and lost, causing a loss of

thrust and resulting in lesser altitudes. In crosswinds of 150 m/s or greater, the craft is blown entirely off the beam shortly after launch.

- The *constant zenith boost angle* study indicates that smaller initial zenith angles (i.e., launch close to vertical) are desirable, but large zenith angles (i.e., $\sim 90^\circ$) at “burnout” will of course be mandatory for orbital insertion. Larger zenith angles result in lower apogees and/or velocities, and require the craft to spend too much time accelerating through the dense atmosphere, thus wasting propellant (lost to drag) and beam power (lost to high atmospheric attenuation, which is not yet modeled here).
- The *Mach 0.6 Pop-Up* study reveals that the 30 km pop-up altitude is superior to the 20 km pop-up, and both give significantly increased performance over the 12 km pop-up which has nearly identical results to the “no pop-up” case. The 30 km pop-up achieved a 140% increase in maximum altitude and >60% increase in “burnout” velocity compared to runs without pop-ups. The PTFE propellant conservation secured through the Mach 0.6 pop-up to 30 km, before accelerating through Mach 1, is sizeable.
- The *scheduled zenith angle* study specified a Mach 0.6 12 km pop-up with 767 kg of PTFE propellant, investigated several boost-reference-angle schedules with initial zeniths of 50 to 63 degrees, and beam slew constants (“N”) ranging from 4 to 6. As with all trajectories reported in this paper, these seven examples successfully rode the beam to “burnout” on the autonomous beam-riding #200 engine with the RCS system active, of course. The best results from this 12 km pop-up study were obtained from Flight #5 for initial zenith= 60° and $N=5$, which secured an apogee of 990 km, absolute “burnout” velocity of 3.73 km/s, and launch-point-to apogee range of 1300 km.
- The *orbital launch trajectory* study simulated trajectories with an idealized liquid propellant ($C_M = 190$ N/MW, $I_{sp} = 900$ s, $\eta_{ALP} = 0.88$) and vehicle mass ratio of 2.5, to speeds greater than 8 km/s at an altitude of 500 km. The simulations proved the feasibility of the “Aim Point” strategy to achieve near orbital velocities and altitudes.

- Engine propulsive models have been updated in the flight dynamics code and trajectories were simulated that further proved the superior performance of the Type #200 engine geometry.

6 FUTURE WORK

The next step in the ongoing basic research program is the experimental investigation of airbreathing LP engine physics under subsonic, transonic, and low supersonic conditions. The requirements for such facilities come from the flight regimes a vehicle encounters along its boost trajectory into orbit [32]. As a multi-cycle LP engine climbs up through the atmosphere, it may transition through as many as five different laser-thermal propulsion modes: e.g., airbreathing Pulsed Detonation Engine (PDE), ramjet, scramjet, ducted rocket, and upon leaving the atmosphere, purely rocket (i.e., onboard propellant only). It is necessary to analyze each propulsion mode separately within its respective optimum flight envelope.

6.1.1 Flight Simulation and Flow Facilities

Small-scale supersonic, blow-down type flow facilities [33] can be designed and manufactured at modest cost, and tailored to support a wide variety of LP experiments, thus yielding an excellent cost/return ratio. Two of these facilities have been thoroughly designed, with all the required equipment dimensioned and component suppliers selected. The construction and assembly of the down-selected facility is now dictated largely by manufacturing time and available research funds.

The first of these flow facilities is a supersonic blow down wind tunnel [34], capable of simulating transonic through Mach 3.0 conditions, expected from launch up to the high altitude flight regime. This tunnel consists of a high pressure, dry air reservoir composed of stacked DOT-E 9421 – 4500 psi storage tanks, fed by a high pressure compressor/dryer (Star Air 6000 compressor unit), followed by a Fisher 1" HPS Body ball-type valve connected to a 4160K 2-Mode electrically actuated pressure controller for the control of the air feed pressure as the reservoir is emptied.

Following the pressure control valve is a settling chamber to guarantee flow uniformity in the test section. Due to the flow facility's modular design concept several different test sections can be inserted, as dictated by the goal of the experimental research: e.g., a "direct-connect" 2D inlet test section modeling any given vehicle geometry; or a "straight

through,” constant area test section measuring 50mm×50mm. To simulate the desired flight altitude, the test section exit station is evacuated to a vacuum tank, with its discharge pressure controlled by throttling another fast-action valve that assures the desired static pressure within the test section. The whole system can be easily integrated and run on a LabView equipped computer. A simplified representation of the entire flow and laser system is given in Fig. 6.1, showing the distribution of the main components within the laboratory.

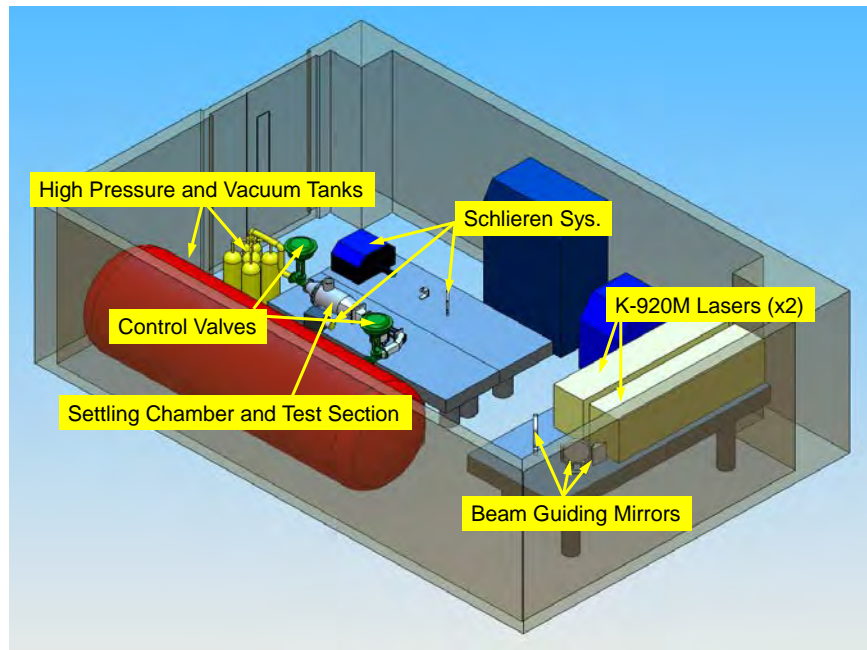


Figure 6.1: Integrated setup in the present 7.9 m x 5.2 m available laboratory space with altitude supersonic flow facility.

The second candidate flow facility is a Ludwieg tube-driven system, capable of simulating both transonic and low supersonic flight conditions, depending on the test section and model inserts. This facility has a simpler design and reduced costs (as compared with the previous option), but is not capable of simulating high altitude flight conditions: i.e., the test section always discharges directly into a 1 bar laboratory environment. This facility is basically composed of a high pressure reservoir equipped with a pressure actuated sting for diaphragm rupture, a truncated convergent nozzle, and a modular test section. The test conditions are dictated by the reservoir pressure and the geometry of the model installed inside the test section, which acts to throttles the flow.

This facility would have reduced precision and increased limitations, but considerably lower costs and reduced complexity.

The objective in designing/ assembling these flow facilities is to create research tools capable of simulating all essential phenomena involved in supersonic airbreathing laser propulsion, from the inlet flow field, to laser energy absorption and impulse generation. The facilities' small size, simple operational procedures, and low acquisition cost present an optimum match with the available Lumonics K-922M laser system. Several of the research objectives stated previously in this paper will require such tools. Furthermore, these flow systems are also an important asset to the *calibration* of CFD codes that can rapidly evolve the design of future Lightcraft. Without such experimental data it will be impossible to assess the accuracy of any numerical predictions, nor the validity of their assumptions.

6.1.2 Static Experiments

The principal goal of stationary laser propulsion experiments is to study the *temporal force history* delivered by laser-induced blast waves as they expand rapidly over thruster/vehicle surfaces. Direct thrust measurements of this force/time history for several 2-D and 3-D lightcraft engine geometries will be taken with piezoelectric force sensors, using the high speed Schlieren visualization system (with the Cordin digital camera) for insight into the hydrodynamic phenomena. The integrated impulse obtained from force sensors traces would then be compared and contrasted with ballistic pendulum data, using Schlieren movie frames to track expanding shock positions, for validation.

Another static test campaign will investigate the physics of liquid propellant injection schemes for pulsed laser rocket propulsion. Essentially, a fine mist or cloud of water vapor (or other liquid propellant of interest) will be injected into the laser focal point of an absorption chamber, to examine the hydrodynamics and efficiency of the laser heating process. A family of parabolic mirrors, sized for the unexpanded K922M laser beam, has already been manufactured, and their injection systems are now being

installed. Subsequent static and dynamic LP experiments will involve liquid propellant injection into various 2-D Lightcraft geometries.

6.1.3 Vacuum Chamber LP Experiments

Further investigations into laser ablative propellants will be performed to complement the “rocket-mode” and PRF studies performed above. A proposed vacuum chamber [35], as seen in Fig. 6.2, would provide ample opportunity to investigate the laser ablative performance of propellants without augmentation from a 1-bar background atmosphere. These “rocket-mode” experiments will be performed in a static environment with decreased atmospheric pressure ranging from 0-1 bar. Eventually, the effects of PRF on the impulses generated by laser ablative propellants inside a lightcraft will also be investigated.

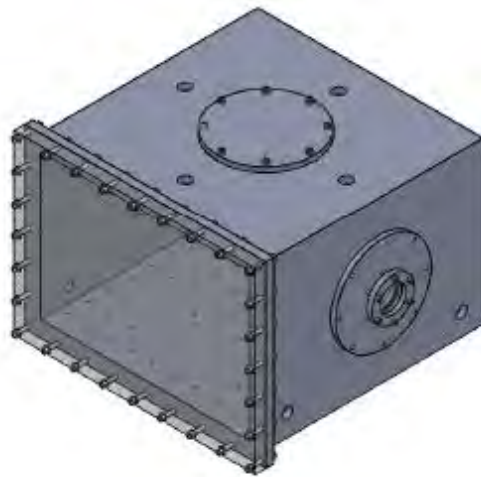


Figure 6.2: Proposed vacuum chamber for LP experiments. [35]

6.1.4 LP Engine Geometry Optimization Studies

The search for the optimum engine geometry for each stage of a launch trajectory, and the associated axial and lateral impulses, can be performed using CFD. It will be necessary to model pulsed laser energy deposition in various engine geometries and flow speeds. This CFD study will also provide further insight into the nature of the autonomous beam riding force as a function of laser beam offset, PRF, and energy, as well as engine-to-beam diameter ratio.

6.1.5 Windtunnel Experiments

Significant progress has been made towards understanding the subsonic aerodynamics of the acorn-shaped, Type 200 lightcraft configuration. Further progress will be made with a study of Magnus effects on rotating lightcraft, which will shed light on the observed phenomena of tipping into a cross-wind. Note that the Magnus force has its own “center” which has yet to be determined, but for the present it is assumed to act through the aerodynamic center (AC) which was found in the 2006 wind tunnel test. Note also that the other aerodynamic forces must act through the lightcraft’s aerodynamic center, which until this present study had been assumed co-incident with its center of mass. Further research will define the movement of the AC as a function of AOA and flight Mach number. Figure 6.3 presents the design of the spinning lightcraft model that will be used to study Magnus effects. The electric motor to which it is mounted is an AXi 2208/20 brushless “out-runner” that can be programmed for any rotation rate up to the maximum desired 13,000 RPM, using software recently developed at RPI.

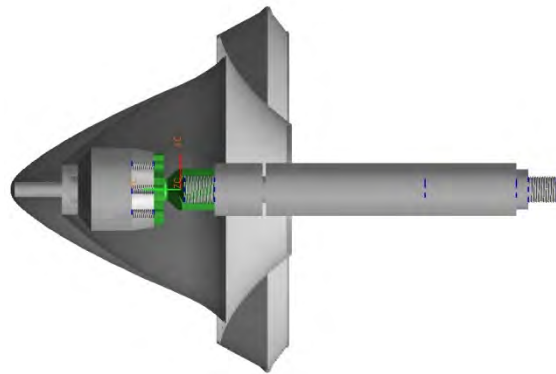


Figure 6.3: Lightcraft model with AXi brushless outrunner motor, mounted to sting balance.

The current 200-5/6 wind tunnel model and its sting mount can only enable angles of attack from zero to 30 degrees. New sting adapters will be fabricated to capture a 30-to-90 angle of attack range for the non-spinning model, so that the test envelope can be expanded. Eventually, a rigorous program of subsonic wind tunnel testing for the spinning model will produce the data required to calibrate future CFD simulations of spinning lightcraft models in flight.

7 REFERENCES

1. D.A. Kenoyer, "Validation and Calibration of a 6-DOF Laser Propelled Lightcraft Flight Dynamics Model vs. Experimental Data," M.S. Thesis, Rensselaer Polytechnic Institute, Troy, N.Y., Dec. 2007.
2. L.N. Myrabo, "World Record Flights of Beam-Riding Rocket Lightcraft: Demonstration of 'Disruptive' Propulsion Technology," AIAA Paper 2001-3798, 37th AIAA/ASME/SAE/ASEE Joint Propulsion Conference, Salt Lake City, Utah, July 2001.
3. Kantrowitz, A., "Propulsion to Orbit by Ground-Based Lasers," *Astronautics and Aeronautics*, Vol. 10, No. 5, pp.74-76, 1972.
4. L.N. Myrabo, et. al., "Transatmospheric Laser Propulsion," Final Technical Report, Rnsselaer Polytechnic Institute, Prepared under Contract No. 2073803 for Lawrence Livermore National Laboratory and the SDIO Laser Propulsion Program, 30 June 1989.
5. L.N. Myrabo, M.A. Libeau, E.D. Meloney, R.L. Bracken, Pulsed laser propulsion performance of 11-cm parabolic 'bell' engines within the atmosphere, in: 33rd Plasmadynamics and Lasers Conference, Maui, Hawaii, May 2002, Paper AIAA 2002-2206.
6. W.L. Bohn and W.O. Schall, Laser propulsion activities in Germany. In: A.V. Pakhomov, Editor, *Proceedings of the First International Symposium on Beamed Energy Propulsion, Huntsville, Alabama, November 2002, AIP Conference Proceedings* vol. 664, American Institute of Physics, Melville, New York (2003), pp. 79–91.
7. M.A. Libeau, L.N. Myrabo, M. Filippelli, and J. McInerney, "Combined Theoretical and Experimental Flight Dynamics Investigation of a Laser-Propelled Vehicle," AIAA 2002-3781.
8. C.G. Ballard, K.S. Anderson, and L.N. Myrabo, "Flight Dynamics and Simulation of Laser Propelled Lightcraft," Paper 35660, Proc. of IDETC/CIE 2007.
9. D.A. Kenoyer, K.S. Anderson, and L.N. Myrabo, "Calibration and Validation of a 6-DOF Laser Propelled Lightcraft Flight Dynamics Model vs. Experimental Data,"

Fifth International Symposium on Beamed Energy Propulsion. AIP Conference Proceedings, Volume 997, pp. 325-337 (2008).

10. D.A. Kenoyer, K.S. Anderson, L.N. Myrabo, "Trajectory Simulations For Laser-Launched Microsatellites Using a 7-DOF Flight Dynamics Model," Paper 86664, Proc. of IDETC/MSNDC7, 2009.
11. A.V. Pakhomov and K.E. Mahaffy, "Binary Solid Propellants for Constant Momentum Missions," *5th International Symposium on Beamed Energy Propulsion*, edited by A.V. Pakhomov, AIP Proceedings 997, New York: American Institute of Physics, pp. 266-279 (2008).
12. Stefan Scharring, Daniela Hoffmann, Hans-Albert Eckel, and Hans-Peter Röser. "Stabilization and steering of a parabolic laser thermal thruster with an ignition device." *Acta Astronautica*, Volume 65, Issues 11-12, December 2009, Pages 1599-1615
13. M.A. Libeau, L.N. Myrabo, M. Filippelli, J. McInerney, "Combined Theoretical and Experimental Flight Dynamics Investigation of a Laser-Propelled Vehicle," First International Symposium on Beamed Energy Propulsion. AIP Conference Proceedings, Volume 664, pp. 125-137 (2003); Further CFD Calculations performed by McInerney.
14. I.M. Droz, L.N. Myrabo, J.P. McInerney, "Combined Experimental and Numerical Investigation of Lightcraft #200 Aerodynamics at Mach 3," Fifth International Symposium on Beamed Energy Propulsion. AIP Conference Proceedings, Volume 997, pp. 338-350 (2008).
15. Tobias Langener, Leik Myrabo, Zvi Rusak, "Inlet Aerodynamics and Ram Drag of Laser-Propelled Lightcraft Vehicles," Sixth International Symposium on Beamed Energy Propulsion. AIP Conference Proceedings Volume 1230, pp. 44-60 (2009).
16. D.A. Kenoyer, L.N. Myrabo, "Subsonic Aerodynamics of Spinning and Non-Spinning Type 200 Lightcraft: Progress Report," Sixth International Symposium on Beamed Energy Propulsion. AIP Conference Proceedings Volume 1230, pp. 30-40 (2009).

17. A.D. Panetta, "Low Speed Wind Tunnel Testing of a Laser Propelled Vehicle," M.S. Thesis, Rensselaer Polytechnic Institute, Troy, NY, 1999; further wind tunnel testing performed by M. Filippelli (Campaign I) and C. Misiewicz (Campaign II).
18. S.F. Hoerner, and H.V. Borst, "Fluid-Dynamic Lift: Practical Information on Aerodynamic and Hydrodynamic Lift," Hoerner Fluid Dynamics, Great Britain, 1975
19. M.A. Libeau, "Off Axis and Angular Impulse Measurements on a Lightcraft Engine," Third International Symposium on Beamed Energy Propulsion. AIP Conference Proceedings, Volume 766, pp. 166-177 (2005).
20. Jones, J.E., Wang T., "Time Dependent Measurements of Electron Temperature and Density in a Laser Lightcraft," AIAA Paper 2001-3796.
21. Libeau M. A., "Experimental Measurements of the Laser-Induced Reaction on a Lightcraft Engine," AIAA 2003-300.
22. Myrabo, L.N., Messitt, D.G., and Mead, F.B., "Ground and Flight Tests of a Laser Propelled Vehicle," AIAA Paper 98-1001, 1998.
23. Mead, F.B., Myrabo, L.N., and Messitt, D. G., "Flight and Ground Tests of a Laser-Boosted Vehicle," AIAA Paper 98-3735.
24. Bohn, W.L., "Laser Lightcraft Performance," DLR Institute of Technical Physics, D-70569 Stuttgart, Germany.
25. M.A. Libeau, "Exerimental Measurements of the Laser-Induced Reaction on a Lightcraft Engine," M.S. Thesis, Rensselaer Polytechnic Institute, Troy, NY. May 2002.
26. W.T. Thomson, Introduction to Space Dynamics, Dover Publications, NY, 1986 (original printing 1961).
27. URL <http://www.autolev.com>, last visited August 2008.
28. T.R. Kane and D.A. Levinson, Dynamics: Theory and Application, McGraw-Hill, NY, 1985.
29. W.E. Wiesel, Spaceflight Dynamics, McGraw Hill, 1989.
30. D.A. Kenoyer, L.N. Myrabo, S.J. Notaro, P.W. Bragulla, "Experimental Investigation into Beam-Riding Physics of Lightcraft Engines: Progress Report,"

Sixth International Symposium on Beamed Energy Propulsion. AIP Conference Proceedings Volume 1230, pp. 17-29 (2009).

31. Stefan Scharring, Hans-Albert Eckel, Hans-Peter Röser, "High Speed Analysis Of Free Flights With A Parabolic Thruster," Sixth International Symposium on Beamed Energy Propulsion. AIP Conference Proceedings Volume 1230, pp. 77-88. (2009).
32. Frazier, S.R., "Trajectory Analysis of a Laser Energized Transatmospheric Vehicle", MSc. Thesis, Rensselaer Polytechnic Institute, 1987.
33. Pope, A. and Goin, K., *High-Speed Wind Tunnel Testing*, Wiley, New York, 1965.
34. I.I. Salvador, D.A. Kenoyer, L.N. Myrabo, S.N. Notaro, "Dedicated Laboratory Setup for CO₂ TEA Laser Propulsion Experiments at Rensselaer Polytechnic Institute," 2010 International High-Power Laser Ablation Conference, AIP Conference Proceedings (2010).
35. I.I. Salvador, Rensselaer Polytechnic Institute, 2010, private communications.

8 APPENDICES

8.1 Appendix A: AIMD Spring Calibration

Table 8.1. AIMD Spring Calibration

Spring	Mass (kg)	Force (N)	Initial Length (mm)	Final Length (mm)	Deflection (mm)	Spring Constant (N/M)
Old 1	0.2254	2.211174	29.96	32.51	2.55	867.1270588
Old 2	0.2254	2.211174	29.7	32.19	2.49	888.0216867
80252-1	0.4467	4.382127	34.77	56.56	21.79	201.107251
80252-2	0.4467	4.382127	35.17	56.73	21.56	203.2526438
80252-3	0.4467	4.382127	35.65	57.26	21.61	202.7823693
80252-4	0.4467	4.382127	35.13	56.86	21.73	201.6625403
5305-1	0.2258	2.215098	26.56	113.73	87.17	25.4112424
5305-2	0.2258	2.215098	26.75	112.84	86.09	25.73002672
5305-3	0.2258	2.215098	26.84	114.18	87.34	25.36178154
5305-4	0.2258	2.215098	26.52	114.17	87.65	25.27208214
5436-1	0.2254	2.211174	74.05	99.74	25.69	86.07138965
5436-2	0.2254	2.211174	74.3	100.25	25.95	85.20901734
5436-3	0.2254	2.211174	70.87	94.11	23.24	95.14518072
5436-4	0.2254	2.211174	74.33	100.21	25.88	85.43948995
5509-1	0.2254	2.211174	51.97	66.95	14.98	147.6084112
5509-2	0.2254	2.211174	51.81	66.05	14.24	155.279073

8.2 Appendix B: Sample RVDT Outputs

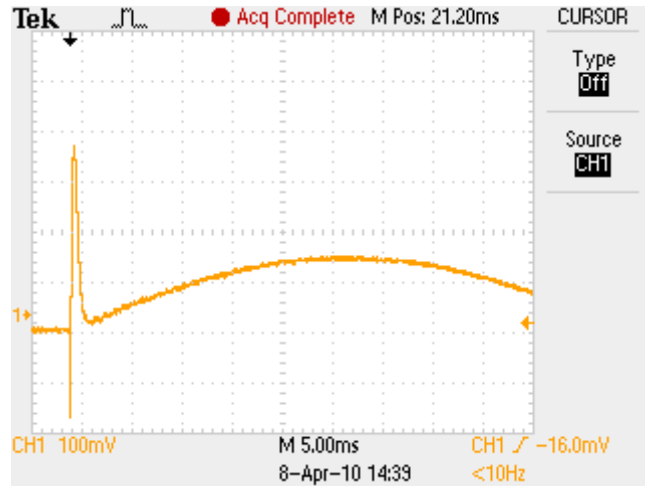


Figure 8.1. Sample output from AIMD (#200-2/3 with Delrin® propellant, 30 mm offset, ~20 J pulse, HG Mix, retracted position).

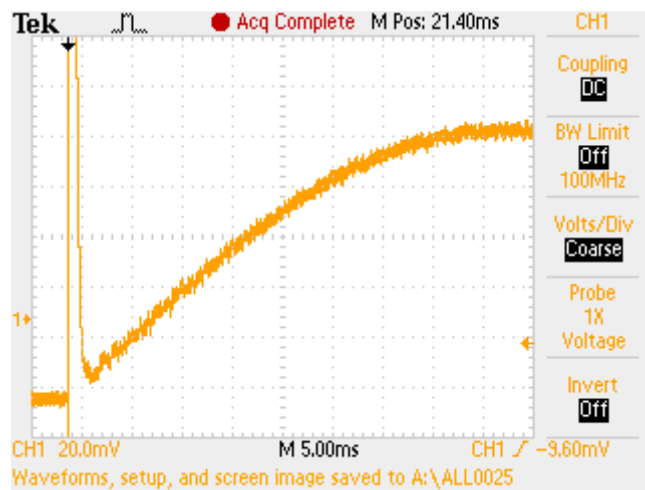


Figure 8.2. Sample output from AIMD (#200-2/3 with Delrin® propellant, 30 mm offset, ~20 J pulse, HG Mix, extended position).

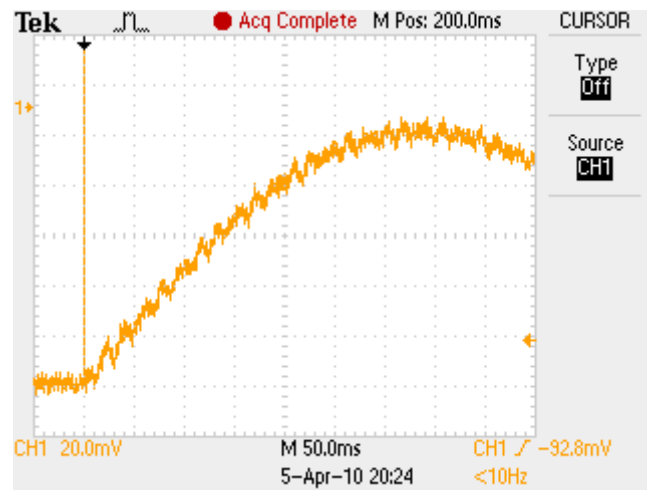


Figure 8.3. Sample output from LWBP (#250-2/3, ~39 J pulse, HG Mix).

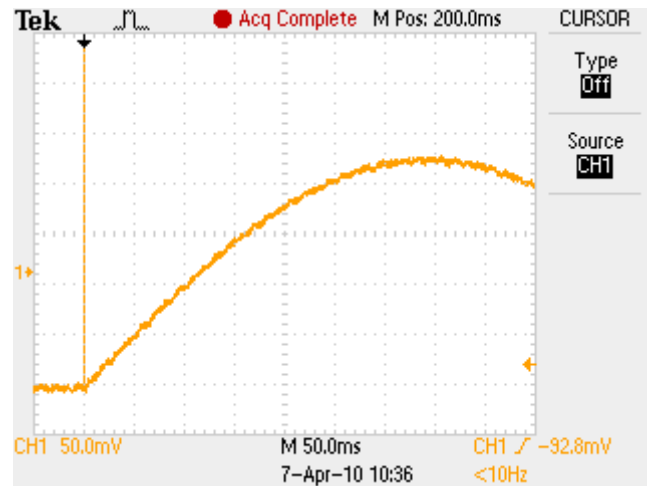


Figure 8.4. Sample LWBP output (#200-2/3, Delrin® propellant, ~38J pulse, HG Mix).

8.3 Appendix C: Simulations

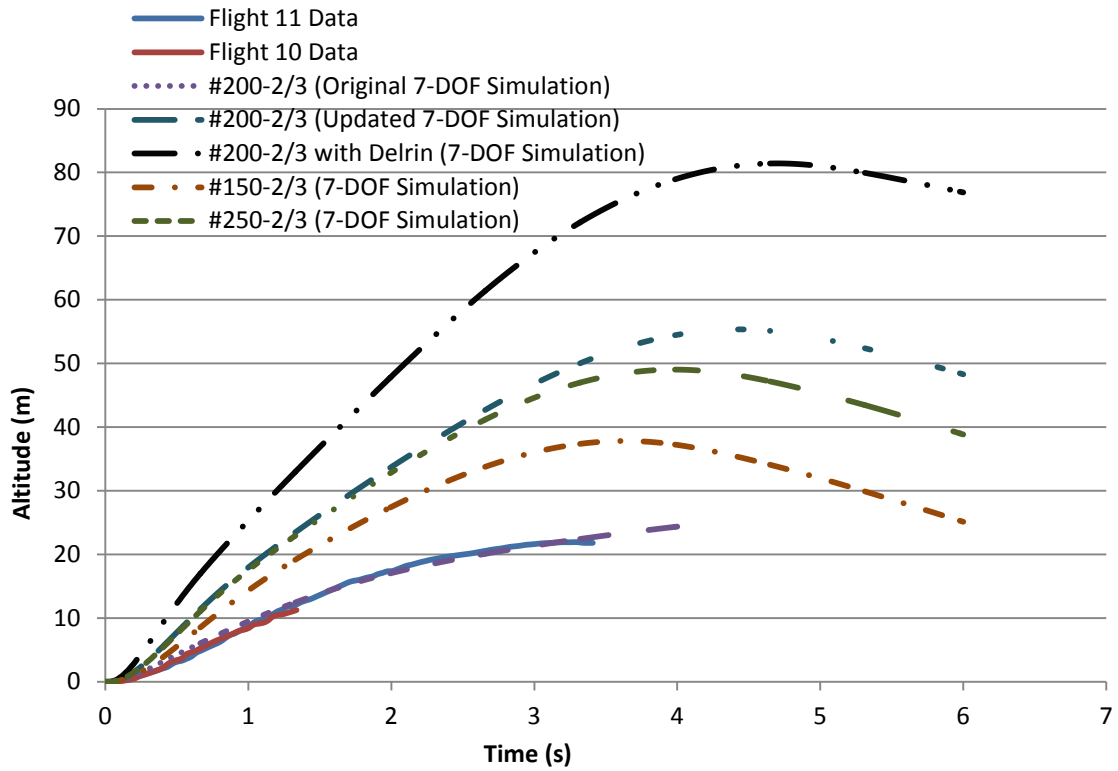


Figure 8.5. WSMR Flights 10 and 11 vs. updated model simulations on PLVTS-like laser (100 ns pulse duration for new simulations, 3.22 m telescope, 10kW, 25 Hz).

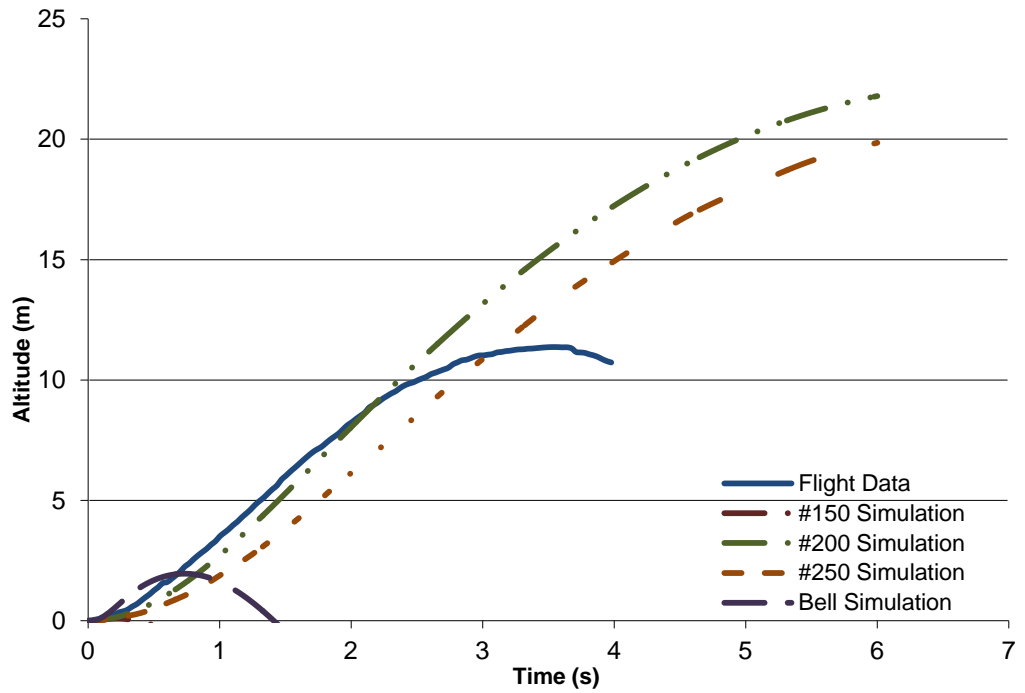


Figure 8.6. Simulation vs. climb trajectory data for Flight #2 (25 Hz at 400 J, 10 kW power; 200-11/10 airbreathing mode; 2.974m telescope spacing).

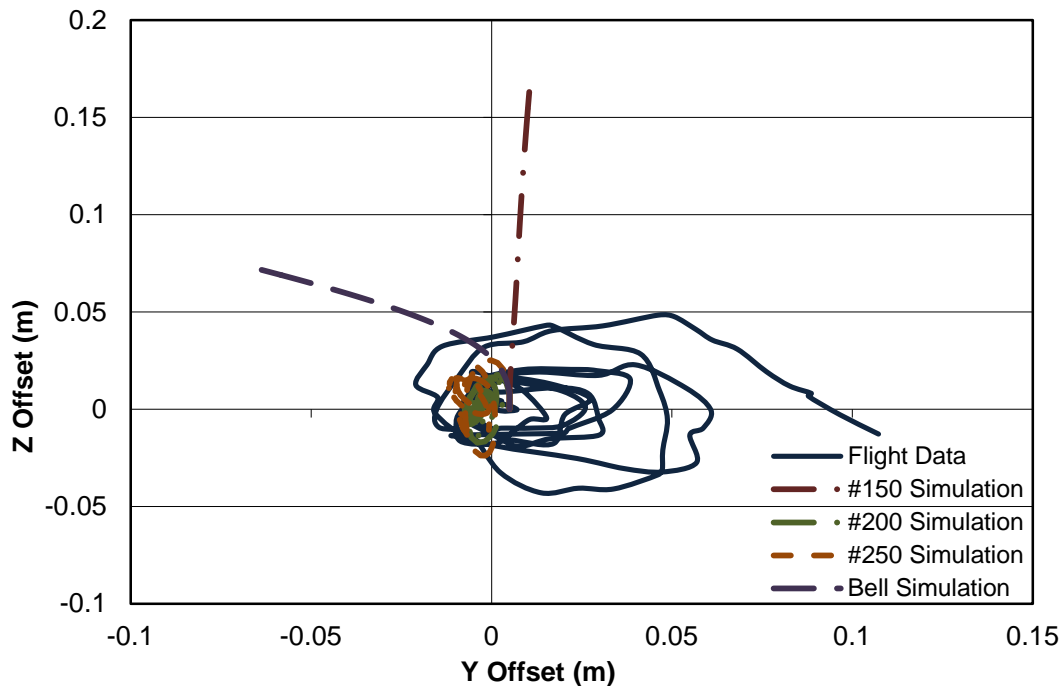


Figure 8.7. Simulation vs. trajectory data in the Y-Z plane for Flight #2 (25 Hz at 400 J, 10 kW power; 200-11/10 airbreathing mode; 2.974m telescope spacing).

8.3.1 Flight 1

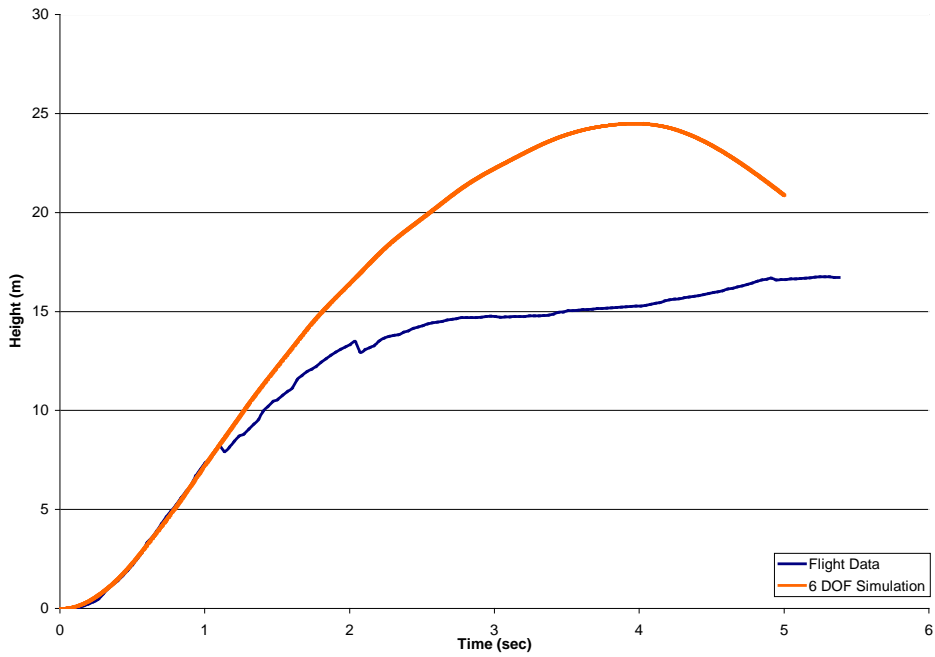


Figure 8.8. Simulation vs. trajectory data of Flight #1 (25 Hz at 400 J, 10 kW power; 200-5/6 size Airbreathing mode; 2.7m Telescope Spacing).

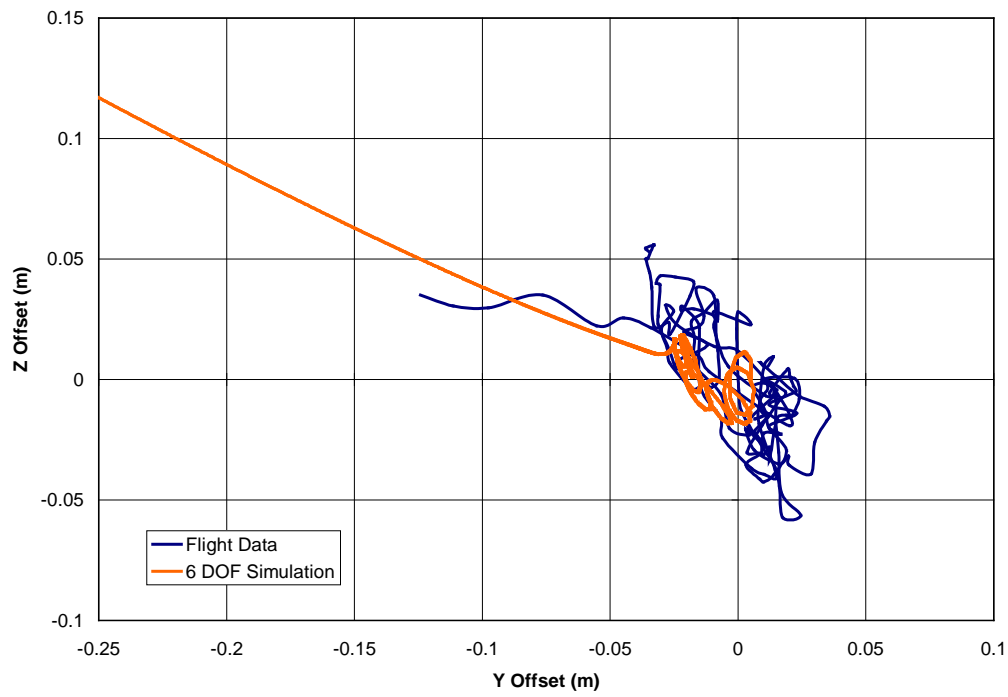


Figure 8.9. Simulation vs. trajectory data in the Y-Z plane for Flight 1.

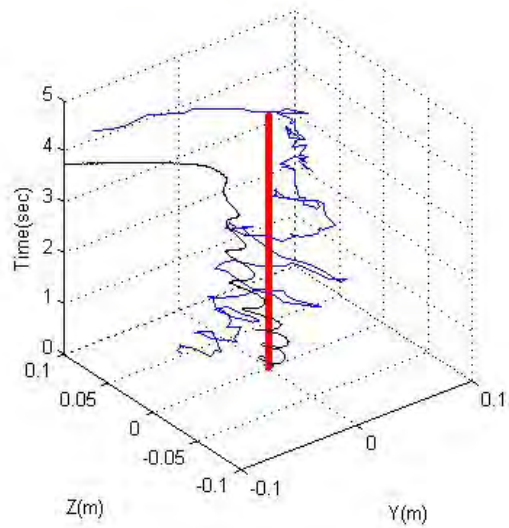


Figure 8.10. 3-D Simulation vs. trajectory for Flight 1.

8.3.2 Flight 3

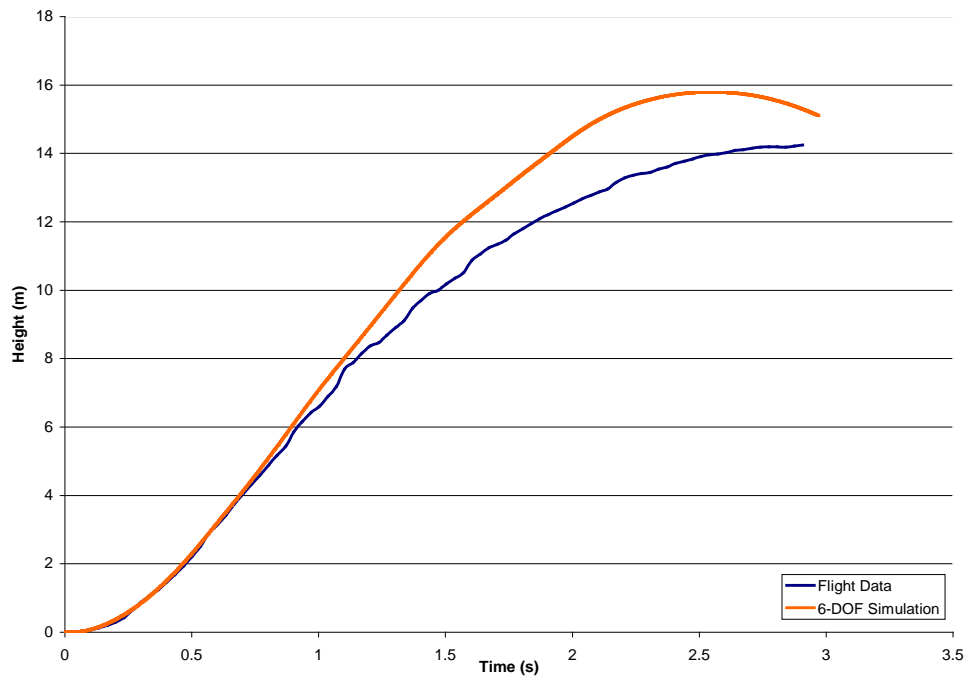


Figure 8.11. Simulation vs. trajectory data of Flight #3 (25 Hz at 400 J; 200-5/6 size Airbreathing mode; 3.22m Telescope Spacing).

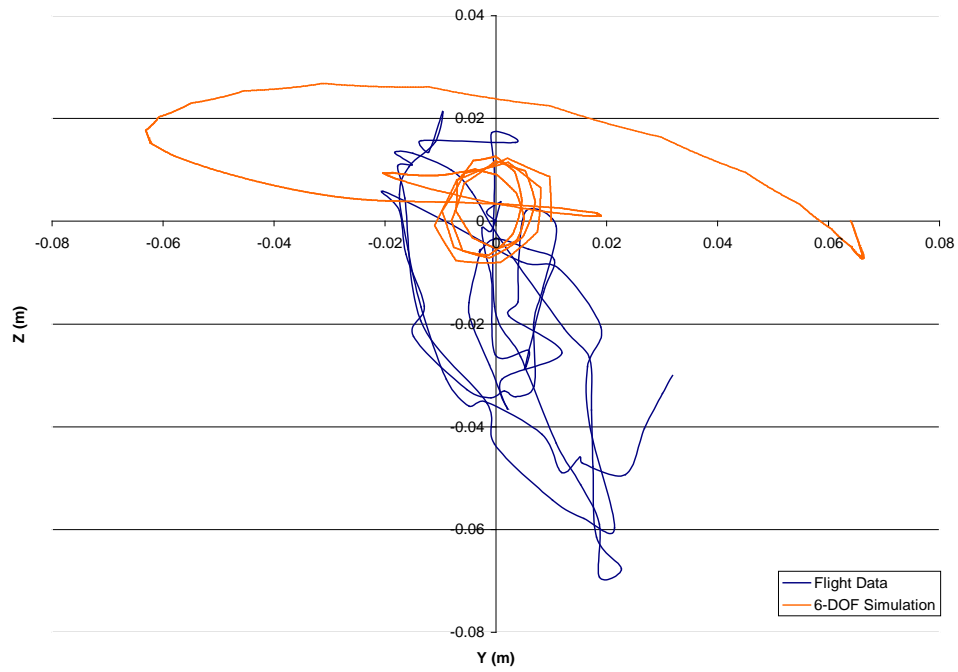


Figure 8.12. Simulation vs. trajectory data in the Y-Z plane for Flight #3 (25 Hz at 400 J, 200-5/6 airbreathing mode; 3.22m Telescope Spacing).

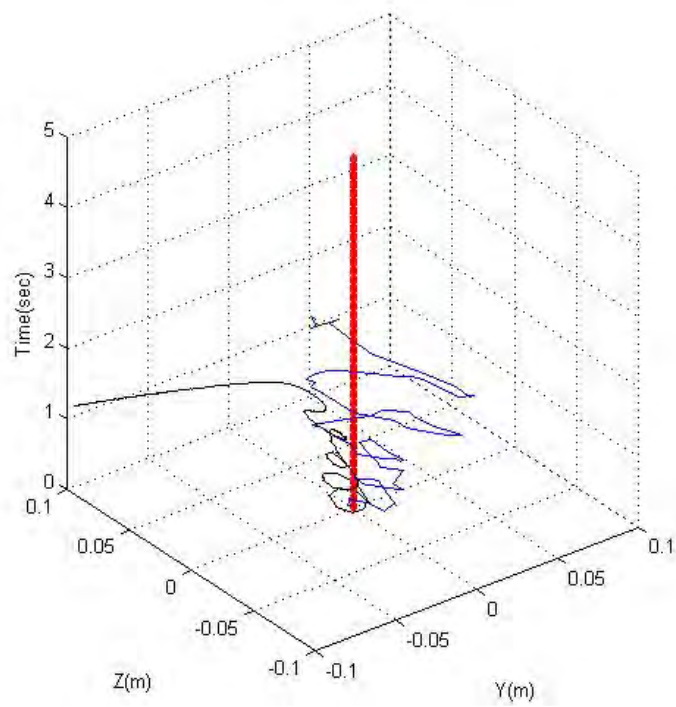


Figure 8.13. 3-D Simulation vs. trajectory for Flight 3.

8.3.3 Flight 4

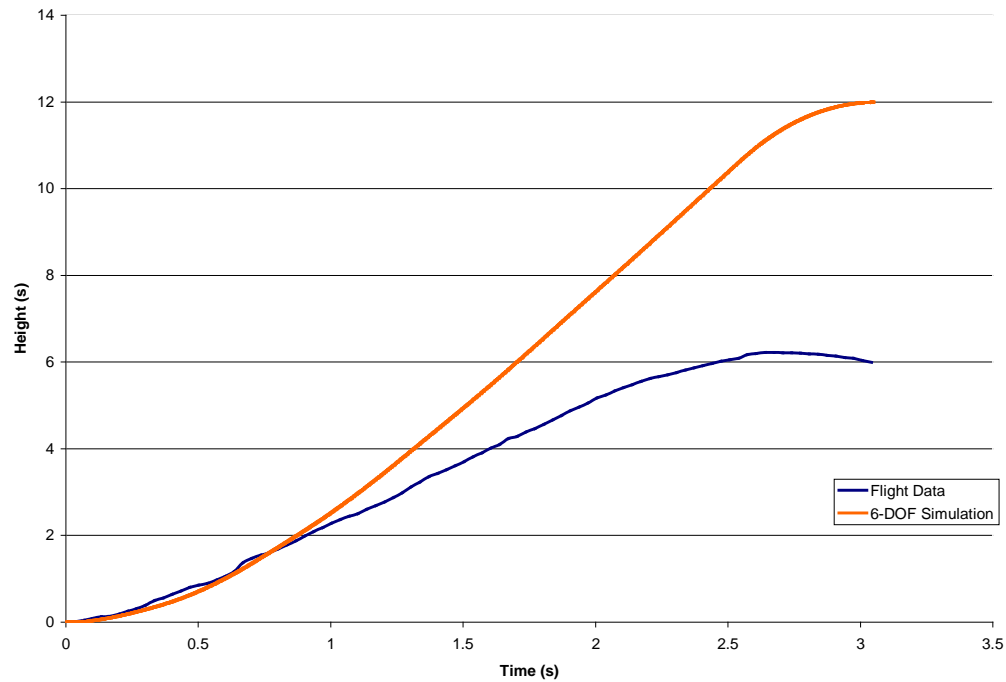


Figure 8.14. Simulation vs. trajectory data of Flight #4 (25 Hz at 400 J; 200-11/10 size Airbreathing mode; No Telescope).

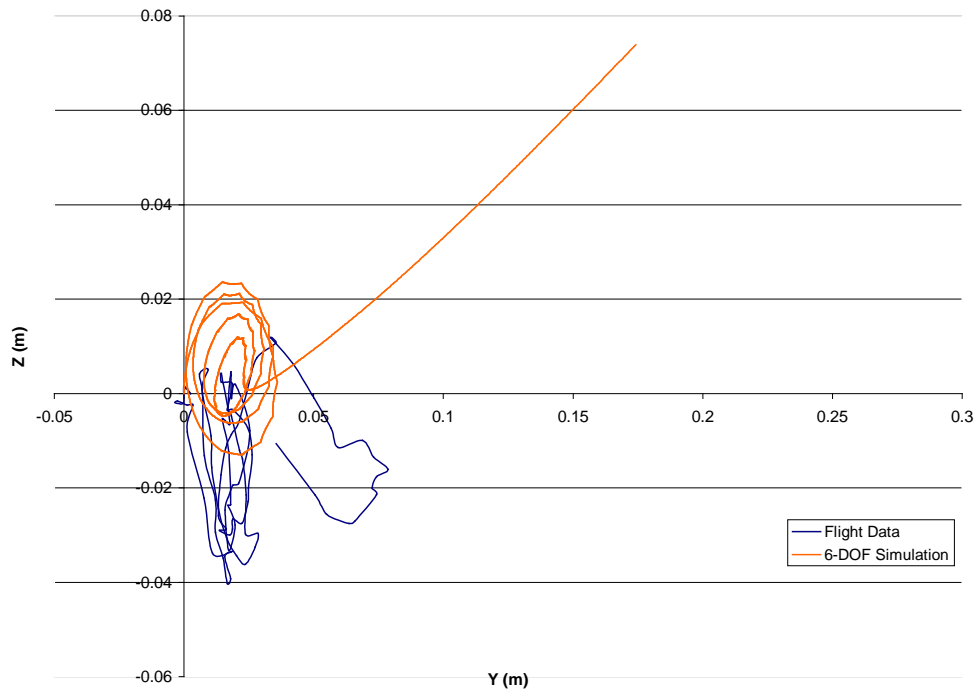


Figure 8.15. Simulation vs. trajectory data in the Y-Z plane for Flight #4 (25 Hz at 400 J, 200-11/10 airbreathing mode; No Telescope).

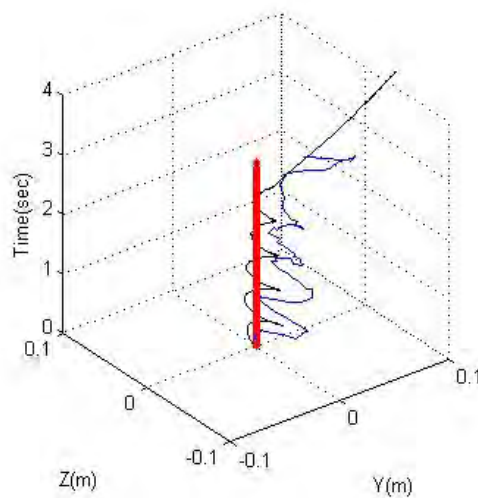


Figure 8.16. 3-D Simulation vs. trajectory for Flight 4.

8.3.4 Flight 6

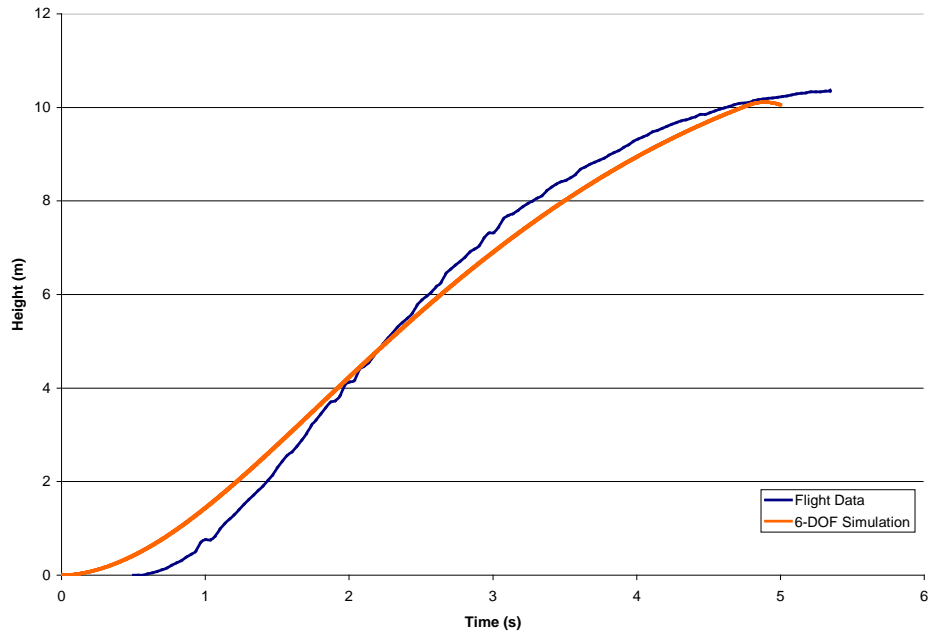


Figure 8.17. Simulation vs. trajectory data of Flight #6 (25 Hz at 400J; 200-11/10 size Airbreathing mode; No Telescope).

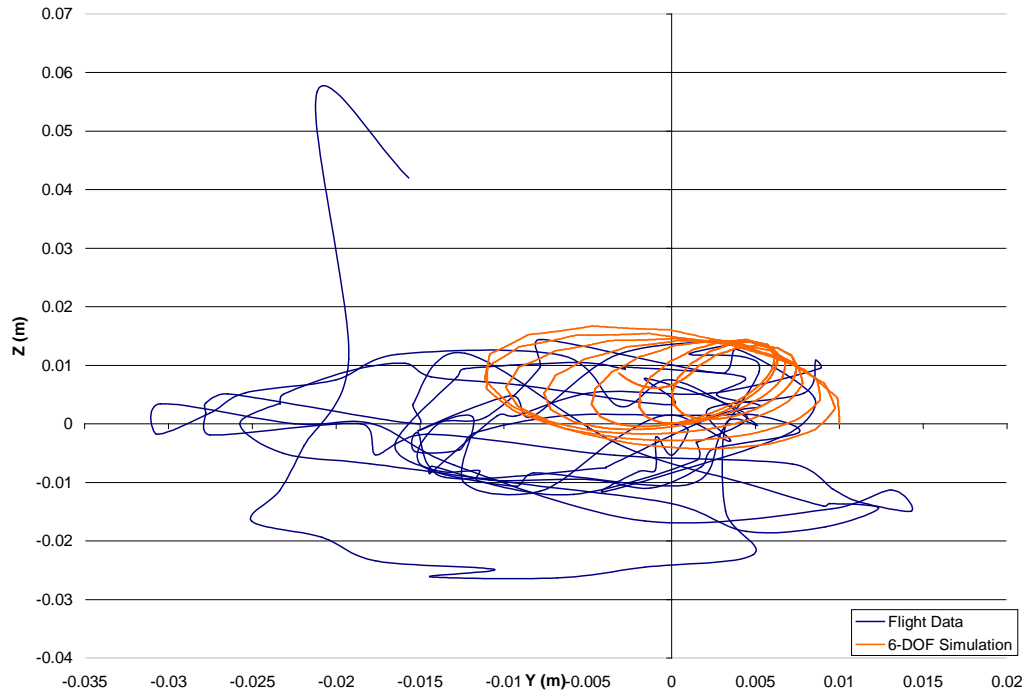


Figure 8.18. Simulation vs. trajectory data in the Y-Z plane for Flight #6 (25 Hz at 400 J, 200-11/10 Airbreathing mode; No Telescope).

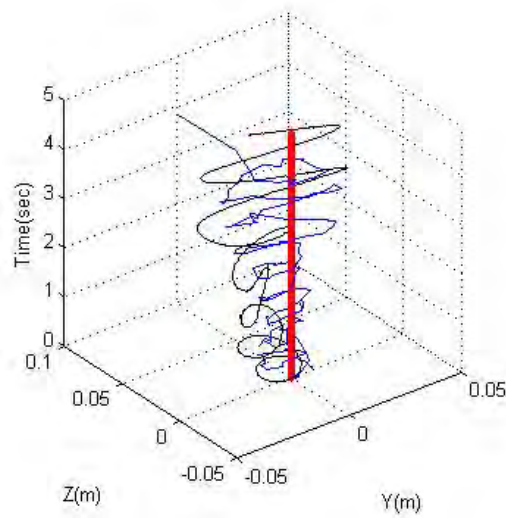


Figure 8.19. 3-D Simulation vs. trajectory for Flight 6.

8.3.5 Flight 7

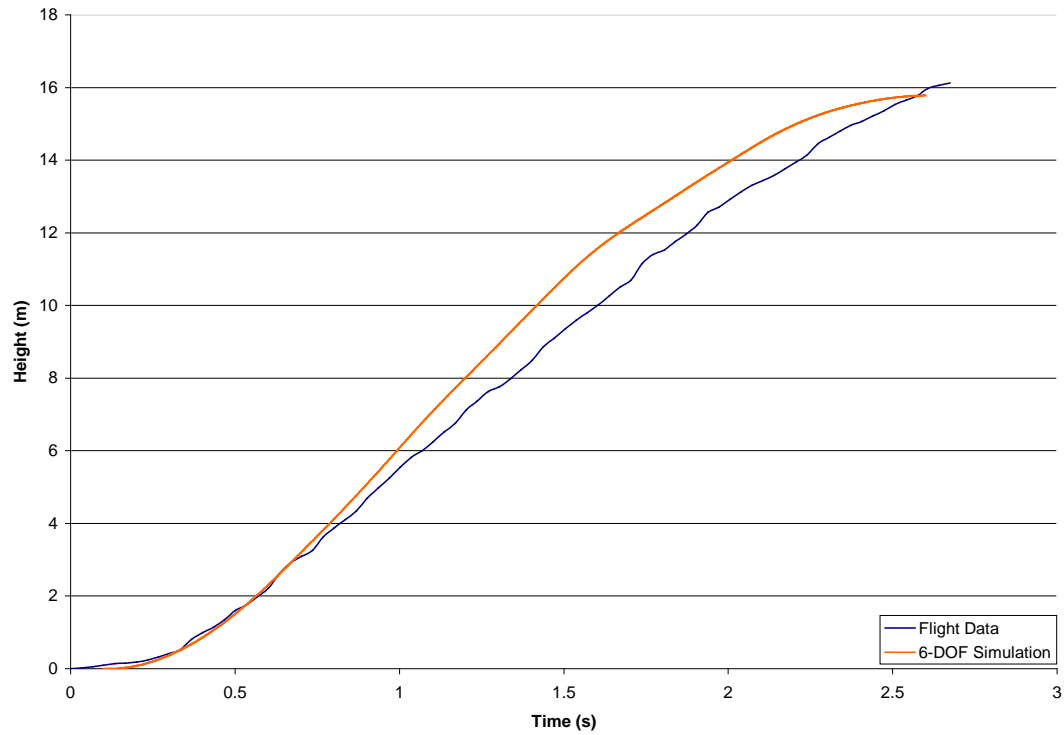


Figure 8.20. Simulation vs. trajectory data of Flight #7 (25 Hz; 200-5/6 size Airbreathing mode; 3.22m Telescope Spacing).

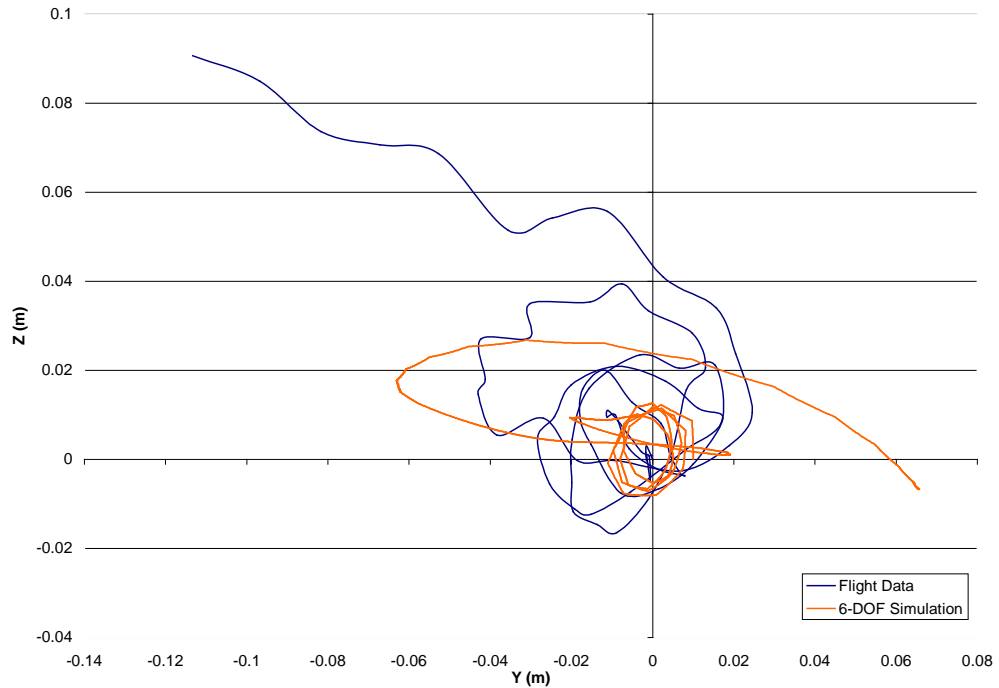


Figure 8.21. Simulation vs. trajectory data in the Y-Z plane of Flight #7 (25 Hz; 200-5/6 size Airbreathing mode; 3.22m Telescope Spacing).

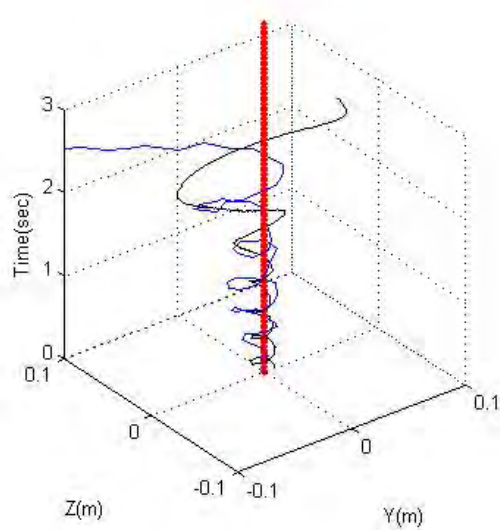


Figure 8.22. 3-D Simulation vs. trajectory data of Flight #7 (25 Hz; 200-5/6 size Airbreathing mode; 3.22m Telescope Spacing).

8.3.6 Flight 8

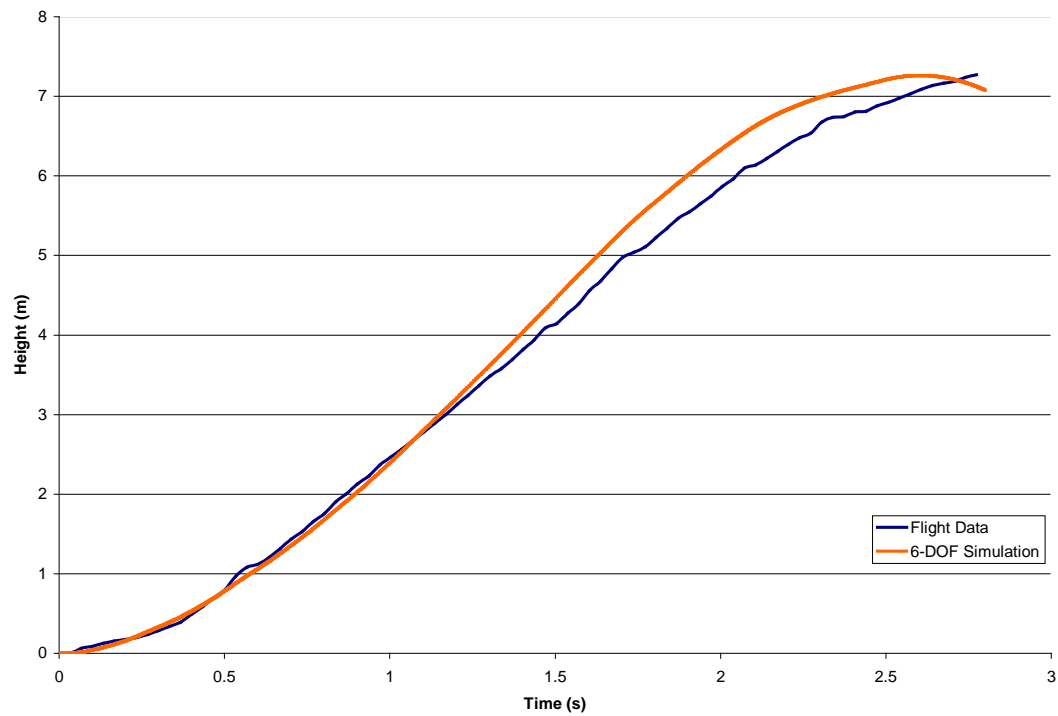


Figure 8.23. Simulation vs. trajectory data of Flight #8 (25 Hz; 200-10/10 size Airbreathing mode; 3.22 Telescope Spacing).

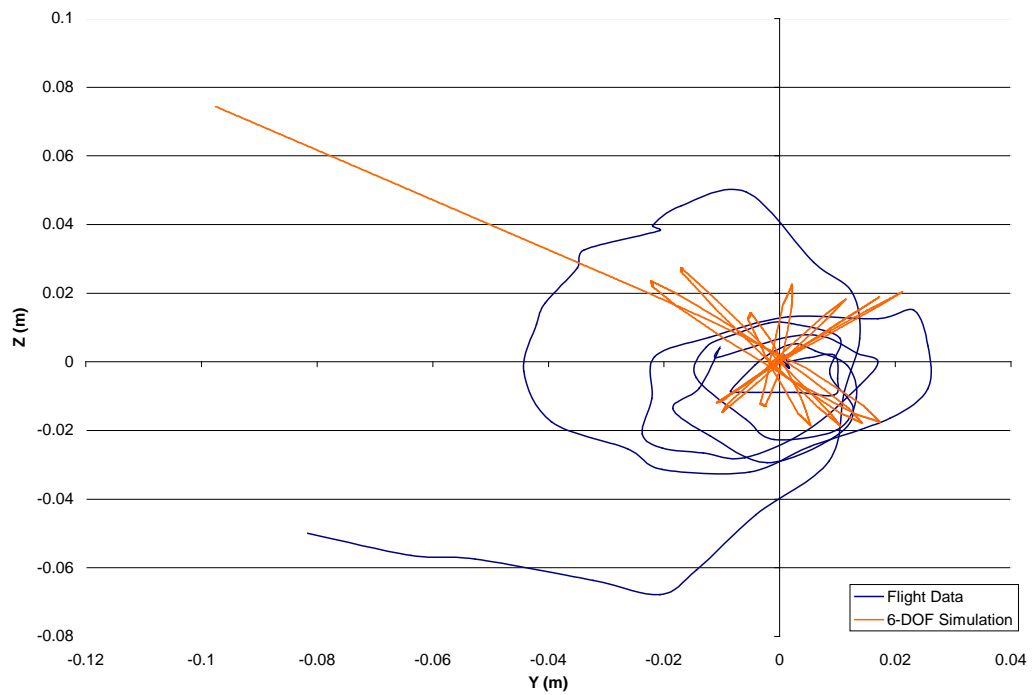


Figure 8.24. Simulation vs. trajectory data for the Y-Z plane of Flight #8 (25 Hz; 200-10/10 size Airbreathing mode; 3.22 Telescope Spacing).

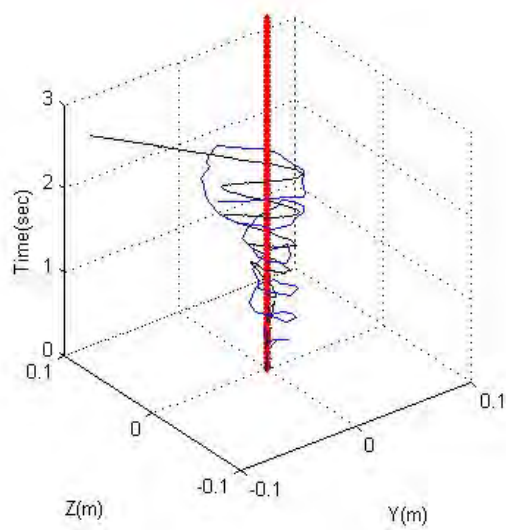


Figure 8.25. 3-D Simulation vs. trajectory for Flight 8.

8.3.7 Flights 10 and 11

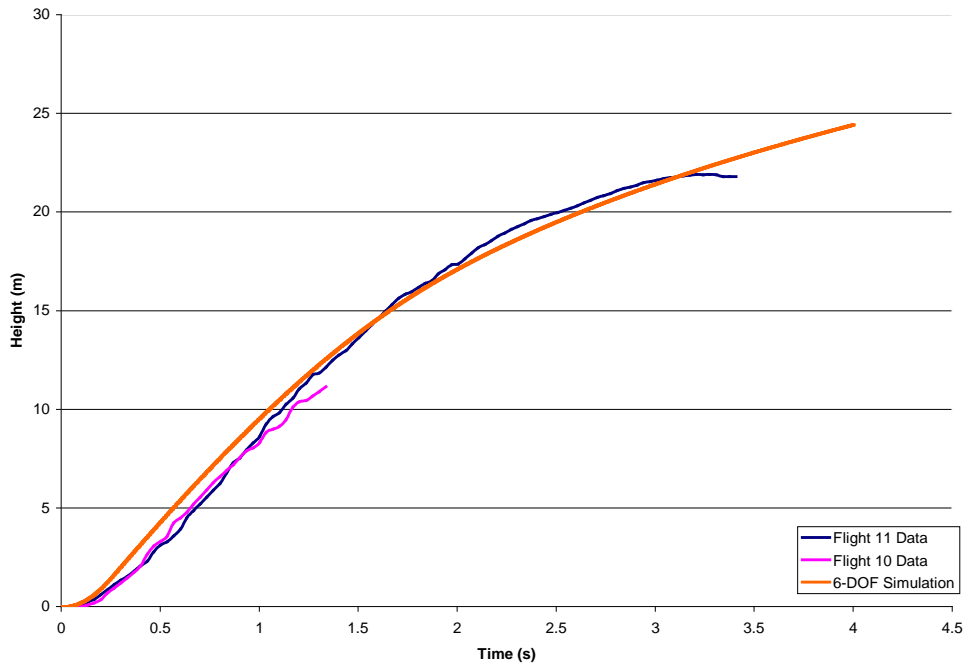


Figure 8.26. Simulation vs. trajectory data of Flights #10 and #11 (25 Hz; 200-2/3 size Airbreathing mode; 3.22m Telescope).

8.3.8 Flight 12

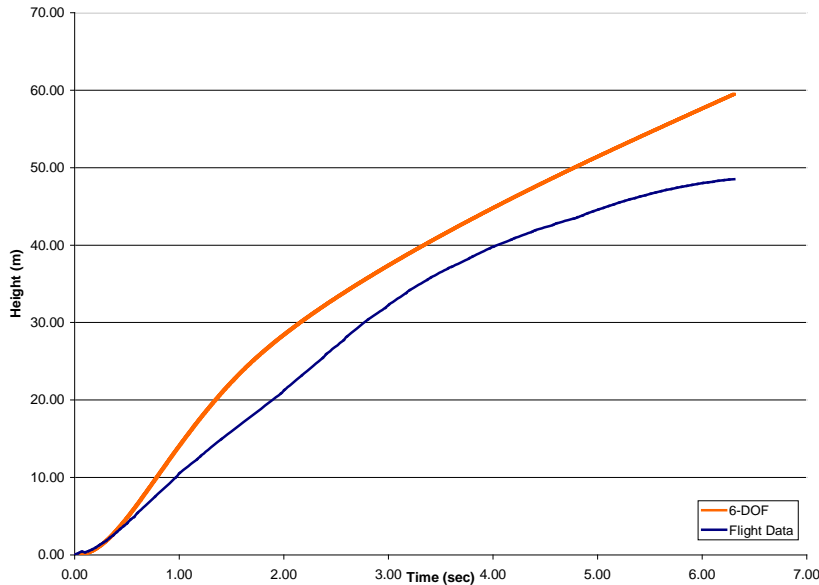


Figure 8.27. Simulation of Flight #12 vs. trajectory data (400 J @ 25 Hz; 200-5/6 SAR; 2.965m telescope spacing).

8.3.9 Flight 13

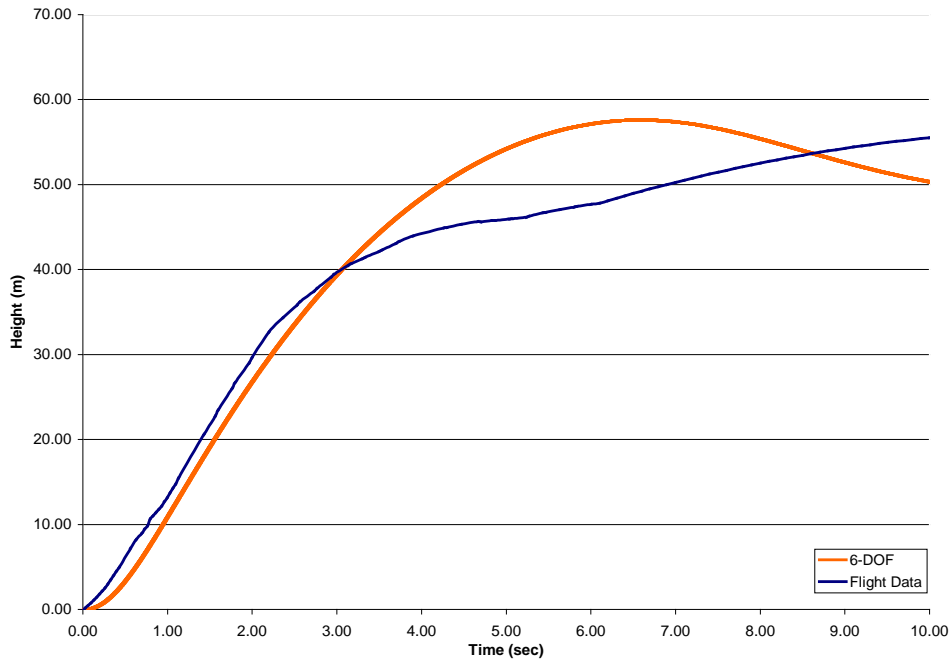


Figure 8.28. Simulation of Flight #13 vs. trajectory data (400 J @ 25 Hz; 200-3/4SAR; no telescope).

8.3.10 Flight 14

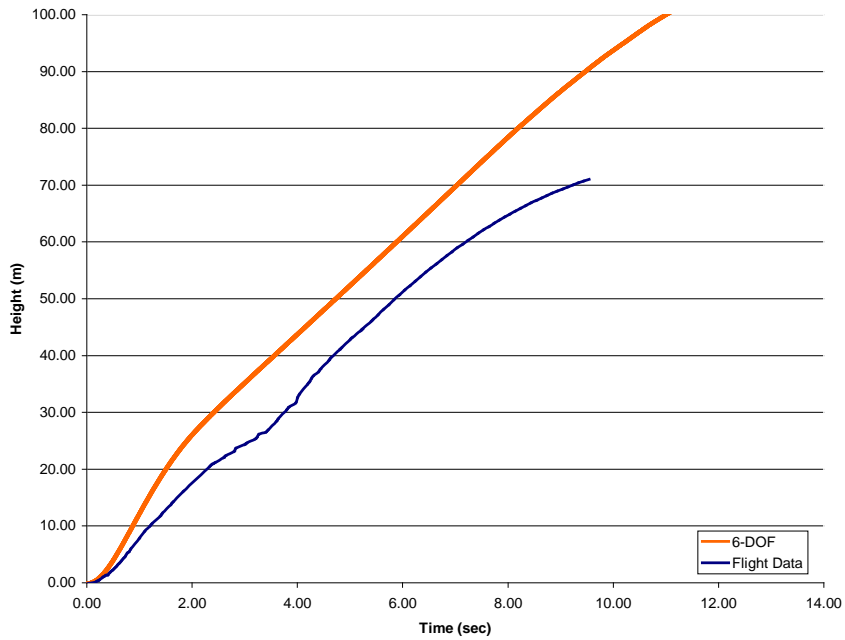


Figure 8.29. Simulation of Flight #14 vs. trajectory data (400 J @ 25 Hz; 200-5/6 SAR; 2.965m telescope spacing).

8.3.11 Flight 15

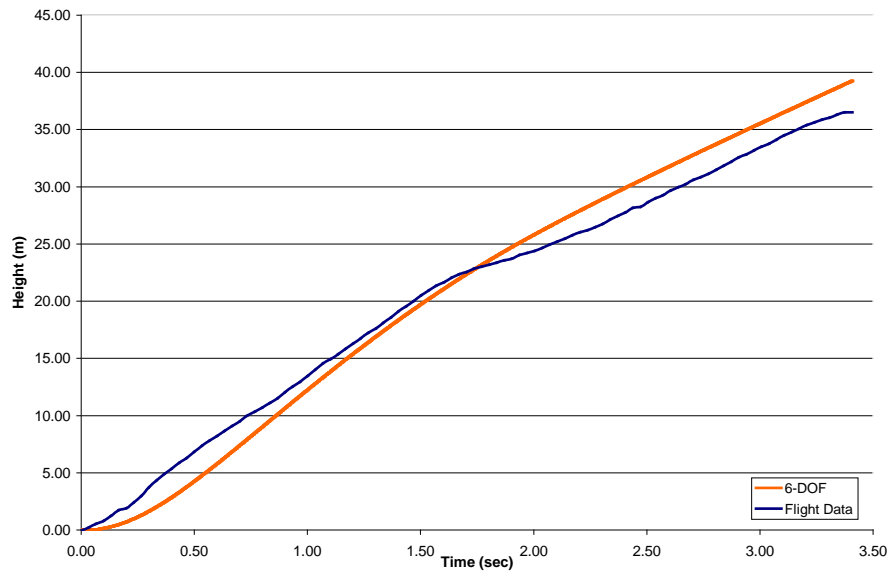


Figure 8.30. Simulation of Flight #15 vs. trajectory data (400 J @ 25 Hz; 200-3/4SAR; 2.965m telescope spacing).

8.3.12 Flight 16

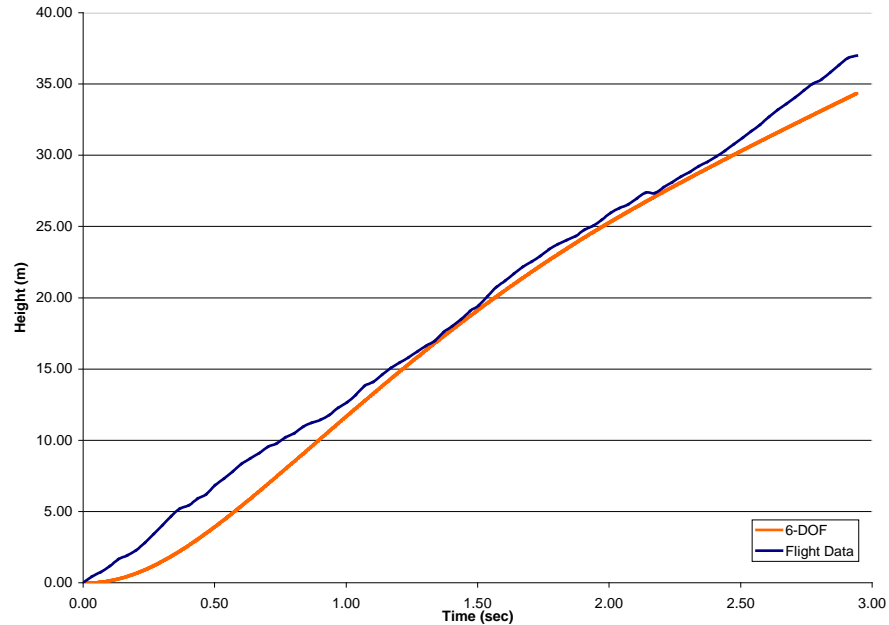


Figure 8.31. Simulation of Flight #16 vs. trajectory data (400 J @ 25 Hz; 200- 3/4SAR; 2.965 m telescope spacing).

8.4 Appendix D: Impact Hammer Calibrations

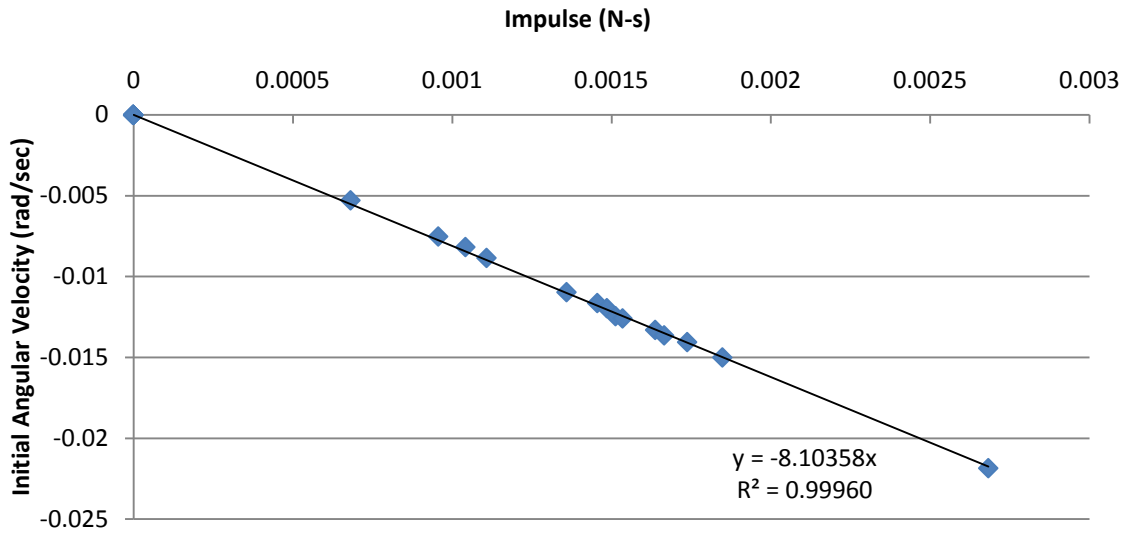


Figure 8.32. LWBP Impulse vs. initial angular velocity calibration for #200-2/3 with Delrin® propellant ring.

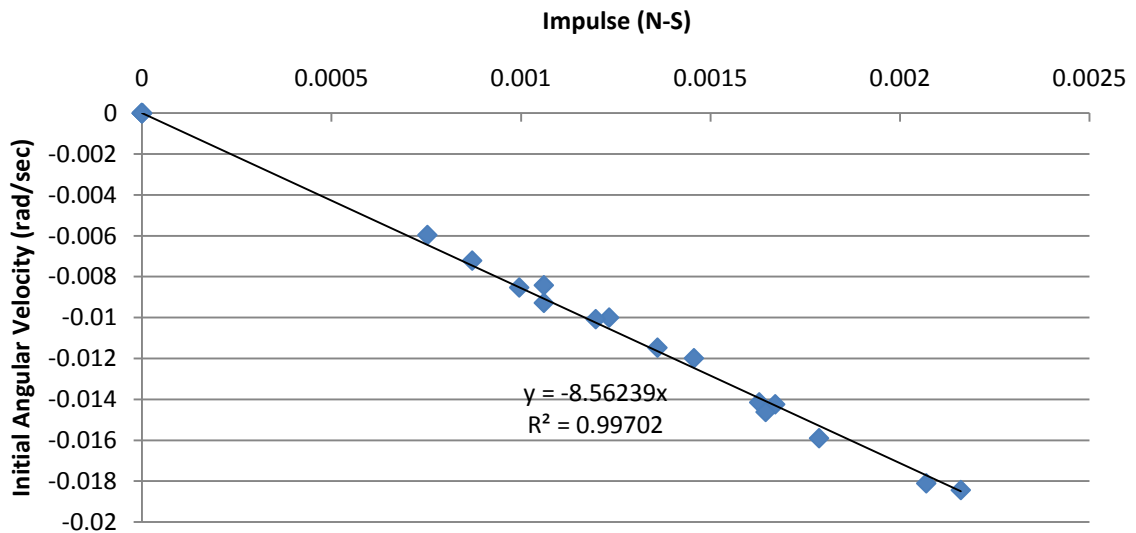


Figure 8.33. LWBP Impulse vs. initial angular velocity calibration for #150-2/3.

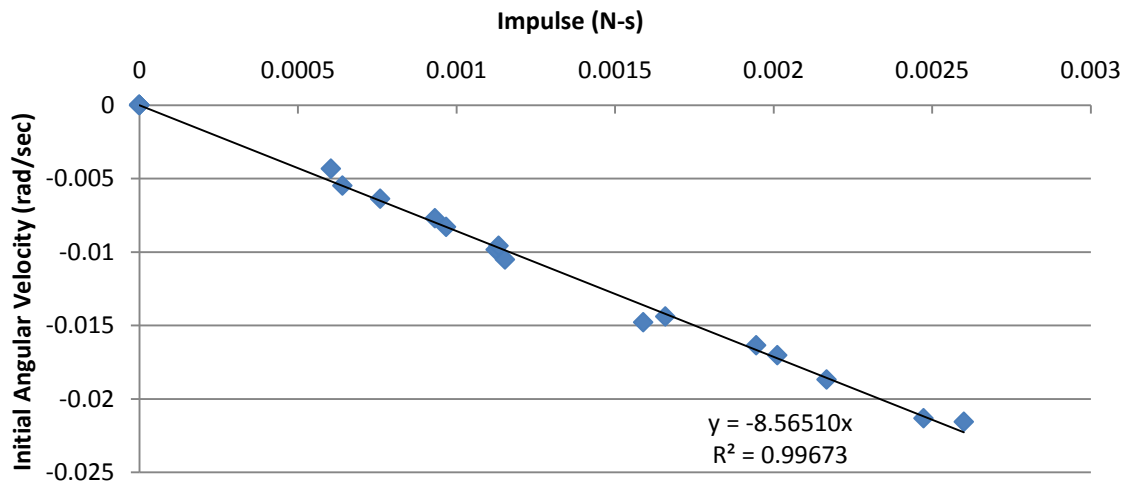


Figure 8.34. LWBP Impulse vs. initial angular velocity calibration for #250-2/3.

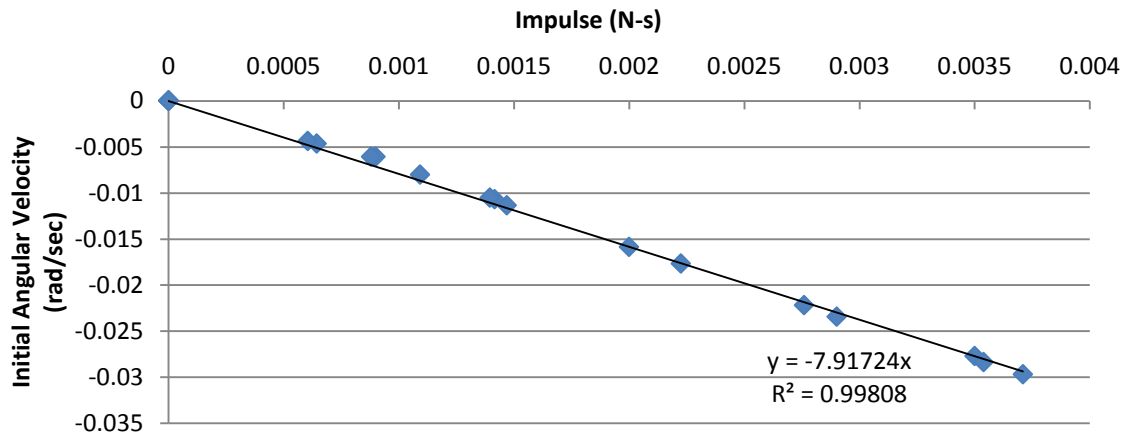


Figure 8.35. LWBP Impulse vs. initial angular velocity calibration for German Bell.

Table 8.2. Calibration data for models on LWBP.

Engine Geometry	Magnitude Initial Angular Velocity per Impulse
#200-2/3 Airbreathing (AB)	8.56340
#200-2/3 Delrin Propellant	8.10358
#200-3/4 AB	9.62072
#200-5/6 AB	6.96548
#150-2/3 AB	8.56239
#250-2/3 AB	8.56510
10 cm German "Bohn" Bell	7.91724

8.5 Appendix E: Sanded vs. Unsanded Optics

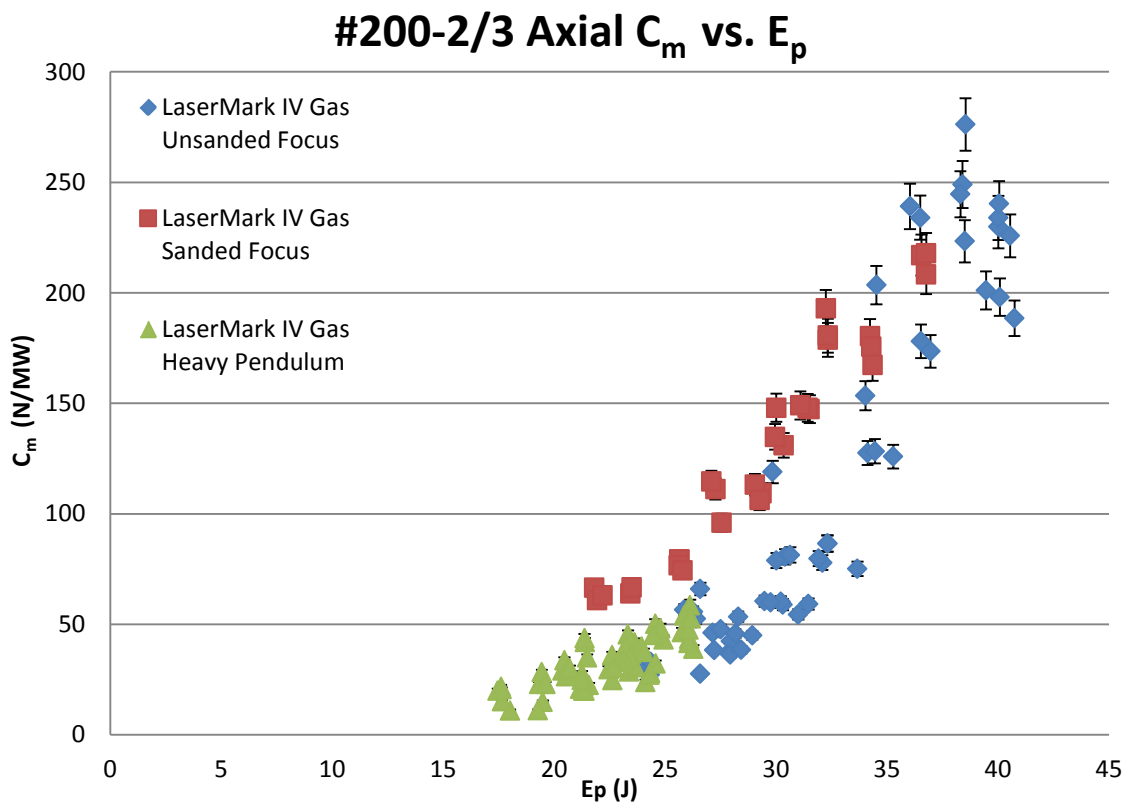


Figure 8.36. Axial C_m for sanded vs. non-sanded foci of #200-2/3 on heavy and lightweight ballistic pendulums.

9 Acronyms

LP	Laser Propulsion
LEO	Low Earth Orbit
GBL	Ground Based Laser
7-DOF	7 Degree of Freedom
WSMR	White Sands Missile Range
PLVTS	Pulsed Laser Vulnerability Test System
BEP	Beam Energy Propulsion
CFD	Computational Fluid Dynamics
GEO	Strategic Defense Initiatives Office
PDE	Pulsed Detonation Engine
HELSTF	High Energy Laser System Test Facility
PTFE	Polytetrafluoroethylene, or Teflon®
AP	Delrin®
AC	aerodynamic center
CM	Center of Mass
AoA	Angle of Attack
RVDT	Rotary Variable Differential Transformer
AIMD	Angular Impulse Measuring Device
LWBP	Lightweight Ballistic Pendulum
LM5	LaserMark 5
HG	High Gain
PRF	Pulse Repetition Frequency
FWHM	Full Width Half Maximum
RCS	Reaction Control System
MR	Mass Ratio
RPM	Rotations Per Minute